PROCEEDINGS

of the

15th MINI CONFERENCE ON VEHICLE SYSTEM DYNAMICS, IDENTIFICATION AND ANOMALIES

Held at the

Faculty of Transportation Engineering and Vehicle Engineering
Budapest University of Technology and Economics, Hungary
BUDAPEST, 7-9 November, 2016

Edited by Prof. I. Zobory

VSDIA 2016

BUDAPEST UNIVERSITY OF TECHNOLOGY AND ECONOMICS

PROCEEDINGS

of the

15th MINI CONFERENCE ON VEHICLE SYSTEM DYNAMICS, IDENTIFICATION AND ANOMALIES

Held at the

Faculty of Transportation Engineering and Vehicle Engineering
Budapest University of Technology and Economics, H u n g a r y
BUDAPEST, 7-9 November, 2016

Edited by Prof. I. Zobory

VSDIA 2016

BUDAPEST UNIVERSITY OF TECHNOLOGY AND ECONOMICS

THE CONFERENCE ORGANISING COMMITTEE GRATEFULLY ACKNOWLEDGES THE GENEROSITY OF THE FOLLOWING *MAJOR SPONSORS* AND SPONSORS:

BME Faculty of Transportation and Vehicle Engineering (H)
BME Intelligent Transportation and Vehicle Systems Co. (ITS ZRt.) (H)
Knorr Bremse Brake Systems Ltd. (H)
Knorr Bremse Brake R&D Institute Budapest (H).
Knorr-Bremse Railway Vehicle Systems Hungaria Ltd. (H).,
Stadlertrains Hungary Ltd. (H)
Ganz Motor Ltd. (H)
Grampet Debrecen Vagon Factory (H)

CONFERENCE PRESIDENT

INTERNATIONAL SCIENTIFIC COMMITTEE

The Organising Committee thanks the authors for their efforts providing the electronic version of the full paper manuscripts. Issued by the ***BME ITS ZRt***. Budapest, 2017. **ISBN** 978-963-313-266-1

Participants of the VSDIA 2016 International Scientific Conference in front of the Vehicle Engineering Building of the Faculty of Transportation Engineering and Vehicle Engineering at the Budapest University of Technology and Economics

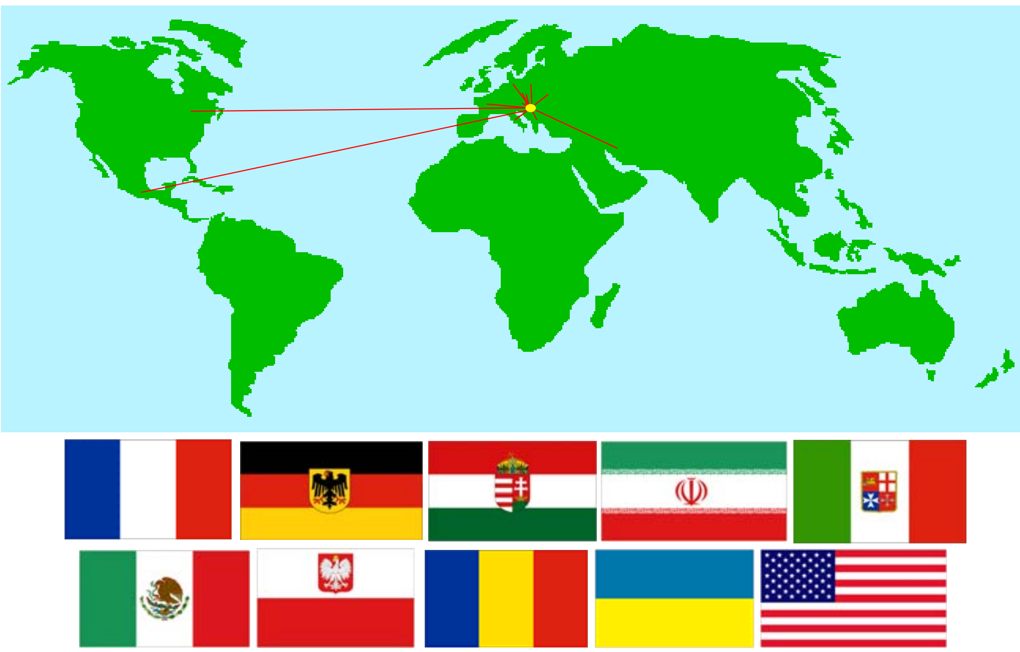

The 10 Countries interested in VSDIA 2016

Editor in Chief:
Prof. István Zobory

This volume was prepared using files submitted by the authors.
No scientific or linguistic revisions were provided by the Organisers.

CONTENTS

PREFACE

The Budapest VSDIA MINI Conference series on *Vehicle System Dynamics, Identification and Anomalies* began in 1988 on the basis of the initiative of the academic staff members of the *Faculty of Transportation Engineering* dealing with railway vehicle, road vehicle, aerospace vehicle, as well as ship dynamics and control at the *Technical University of Budapest*. The rapid development in this special field and the great interest of industrial/transport enterprises in the intensive research and development made it reasonable to think of widening the possibilities in Central Europe for the international exchange of views and experience on *dynamics, identification and parameter anomaly problems* of vehicle systems.

Since 1988 the Faculty of Transportation Engineering methodically organises the VSDIA Conferences *in a biannual order* under increasing international interest. By 2016, the Conference series achieved its 28th birthday. The VSDIA conferences became world-wide known among the representatives of the special field, first of all in Europe but the published conference proceedings volumes are known in a rather wide circle all through the world due to the intensive dissemination realised by the organisers.

Considering the twentyeight-year-long history of the VSDIA Conferences and the fact that also the 15th Conference of Jubilee character on Vehicle System Dynamics, Identification and Anomalies has been successfully realised, it can be stated that the original strategic goals of the initiators, namely to give a scene of high scientific level for the treatment of all dynamical/control system and operation process models commonly valid for both ground vehicles and flying/floating vehicles have been fulfilled. Parallely, the intended integration of the recent results of modern control theory, as well as those of applied mechanics and mathematics have been successfully realised in the contributions received in the vehicle control/interdisciplinary sessions of the Conferences.

The VSDIA 2015 Conference was held at the Budapest University of Technology and Economics between 7 and 9 November, 2016. The International Scientific Committee accepted 38 paper offers from 10 countries, while the final number of participants was 55. High quality papers were presented in all the five Sessions. The atmosphere of the Conference was as usual excellent, and provided an outstanding opportunity for direct communication and exchange of ideas on an international level between researchers and specialists working in industry or practising as executive engineers. Theory and praxis could meet and fertilise each other.

In this volume the electronic versions of the camera-ready manuscripts received from the authors at the end and after the Conference are published. The members of the Organising Committee are convinced that the material represented will provide a wide-scale view of the latest developments in the special field over the past two years.

Budapest, 31 December, 2016

Prof. István Zobory
Conference President

MONTE-CARLO SIMULATION OF MAINTENANCE PROCESSES

László POKORÁDI

Institute of Mechatronics and Vehicle Engineering
Óbuda University
H-1081 Népszínház u. 8. Budapest, Hungary

Received: November 7, 2016

ABSTRACT

The maintenance is one of the most important territories of practical vehicle engineering. From the mathematical point of view, this process is a discrete state space stochastic one without after-effects, so it can be depicted mathematically as a Markov-chain. After setting up the transition probability matrix, matrix-algebraic tools can be used for investigating the process with system approach analysis. Monte-Carlo Simulation is a classical simulation method. The essence of the Monte-Carlo Simulation is the invention of games of chance whose behaviour and outcome can be used for studying some interesting phenomena. The paper is aimed to show the possibilities of the use of Markov matrix-based Monte-Carlo Simulation of maintenance processes. The proposed simulation method can be used for the assessment of requested number for spare part, availability, maintenance cost of a technical system operation depending on required estimating uncertainty.

Keywords: maintenance processes, Markov chains, modelling, Monte-Carlo Simulation

1. INTRODUCTION

A maintenance system can be characterized by the availability of equipment. Availability may be generically be defined as the percentage of time that a repairable system is in the operating condition.

The availability can be characterized as the capability of a system to be ready to perform its functions when required. Failure is the total or partial loss of the capability of a system. Repair is restoration of an object. In many analyses, the "repair" means restoration to an operable condition."

From mathematical point of view, the operation of technical systems and equipment is a discrete state space stochastic process without after-effects, so it can be approximated with a Markov-chain [9].

Monte-Carlo (MC) is one of the classical simulation techniques. MC is only one particular application of another general method, which is applicable in both deterministic and probabilistic settings. At the heart of MC there is a computational procedure in which a performance measure is estimated using samples drawn randomly from a population with appropriate statistical properties. The selection of samples, in turn, requires an appropriate random number generator. Ideally, the generated "random" sequence is a completely faithful software counterpart of the non-determinism underlying the actual process.

The idea of the MC calculation is much older than the computer. The name "Monte-Carlo" is relatively recent – it was coined by Nicolas Metropolis in 1949 – but under the older name of "statistical sampling" the method has a history which goes back well into the last century, when numerical calculations were performed by using pencil and paper and perhaps a slide rule. An early example was a MC calculation of the motion and collision of the molecules in gas was described by William Thomson (Lord Kelvin) in 1901 [5]. Kelvins' calculations were aimed at demonstrating the truth of the equipartition theorem for the internal energy of a classical system. The exponential growth in computer power since those early days is a familiar story to us all by now, and with this increase – in computational resources MC techniques have looked deeper and deeper into the subject of statistical physics. The Monte-Carlo Simulations (MCS) have also become more accurate as a result of the invention of a new algorithm.

The essence of the MCS is the invention of games of chance whose behavior and outcome can be used for studying some interesting phenomena. While there is no essential link to computers, the effectiveness of numerical or simulated gambling as a serious scientific pursuit is enormously enhanced by the availability of modern digital computers [6].

The term MC method is generally used to refer to any simulation techniques related to the use of random numbers [4]. Numerical experiments of MCS lead us to run the simulation on many sampled inputs before we can infer the values of the system performance measures of interest.

There are several books and papers that state theory of the MCS and its applications. Rubinstein depicted detailed treatment of the theoretical backgrounds and the statistical aspects of these methods in his book [10].

Paper of Chinedu et.al. described the procedure for using Markov modelling and Monte Carlo simulation to determine the reliabilities of internally corroded pipelines. The research used Markov modelling and Monte Carlo simulation for predicting the survival probability of corroded pipelines at a given time for different corrosion wastage rates whilst using Weibull probability function to calculate the time lapse for pipeline leakage. Markov modelling and Monte Carlo simulation was used for the model developed in this paper because it has been used for estimating the failure probability of corrosion defect growth of corroded pipelines and other structures by numerous researchers [2].

Garavaglia and Sgambi proposed the study of strategies of selective maintenance for a steel bridge immersed in an aggressive environment, starting from the simulation of each individual member [3]. Simulation of deterioration is obtained through the application of an appropriate damage law implemented with a Monte Carlo methodology, while the time prediction of occurrence of the deterioration is obtained through the application of a Markovian probabilistic approach. The results of the Markovian approach were the starting point for choosing strategies of selective maintenance, as the Markov process allowed the identification, in probabilistic terms, of the structure members with the highest risk of collapse and the timing for achieving levels of damage related to the possible collapse of compromised members. This timing was used to identify possible intervals of maintenance. Proposed scenarios are compared with each other both in terms of associated risk, and in terms of life-cycle cost effectiveness.

Paper of Nannapaneni and Mahadevan proposed a systematic probabilistic framework to include both aleatory uncertainty and epistemic uncertainty in reliability analysis. The proposed Monte Carlo methodology results in a single loop sampling approach due to the use of auxiliary variables.

Pokorádi showed the possibilities of the use of Markov matrix in the case of stationary maintenance processes [9]. A well-algorithmizable method for mathematical modeling of stationary stochastic industrial process was presented by Pokorádi [7]. This model-

ing method can be used to estimate maintenance cost and the time of availability of equipment.
The aims of this investigation are the followings:

- apply the method proposed by Pokorádi [7] [8] to depict Markovian model of the investigated maintenance process;
- use MCS of the investigated maintenance process based on its stochastic model;
- propose a method determining availability and Required Number for Spare Part (*RNSP*) depending on required estimating uncertainty;
- propose a method estimating the Numbers of Failures (*NoF*) depending on required estimating uncertainty.

The outline of the paper is as follows: Section 2 shows the MCS. Section 3 presents the stochastic model of investigated maintenance process. Section 4 depitcs the proposed simulation method and its possibilities use to determinate *RNSP* and *NoF* depending on required estimating uncertainty. Section 5 summarizes the paper, outlines the prospective scientific work of the Author.

2. THE MONTE-CARLO SIMULATION

Monte Carlo is a classical simulation technique. The name Monte Carlo was applied to this class of mathematical methods first used by scientists working on the development of nuclear weapons during the Manhattan project in Los Alamos [5]. The most common features of MCSs are the followings:

1) A known probability density function *f(x)* over the set of system inputs.
2) Random sampling of inputs based on the distribution specified in feature 1), and simulation of the system under the selected inputs.
3) Numerical aggregation of experimental data collected from multiple simulations conducted according to feature 2) [4].

Numerical experiments of MCS lead the modelers to run the simulation on many sampled inputs before they can infer the values of the system performance measures of interest.
At its subsitance is a computational procedure in which a performance measure is estimated using samples drawn randomly from a population with appropriate statistical properties. The selection of samples, in turn, requires an appropriate random number generator.
Basically three generation methods are used [10]:

- Inverse Transform Method (ITM);
- Composition Method (CM);
- Acceptance–Rejection Method (ARM).

During our investigation the Acceptance–Rejection Method was used. This method is due to John von Neumann and consists of sampling a random variant from an appropriate distribution and subjecting it to a test to determine whether or not it will be acceptable for use [5].
The probability density function *f(x)* and interval of the generated parameter should be determined (see Fig. 1.). Then two independent random values x from $[x_{min}; x_{max}]$ and y_x from (0; 1) intervals should be generated, and test to see whether or not the inequal-

ity

$$y_x < f(x) \tag{1}$$

holds:

- if the inequality is violated, reject the pair x, y_x (see **A** point in Figure 1.) and try again;
- if the inequality holds, then accept x as a variable generated from *f(x)* (see **B** point in Figure 1.).

The HMM is simple to implement and can generate random numbers according to any distribution [8].

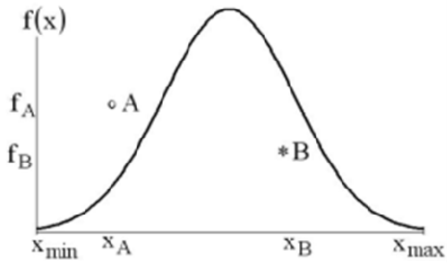

Fig. 1 Illustration of Acceptance-Rejection Method

3. MARKOV-MODEL OF THE INVESTIGATED MAINTENANCE PROCESS

For MCS modelers should have the mathematical model of simulated system or process. In this chapter the Markov model maintenance process of an equipment used in a large number will be shown.

During the operation of this equipment four different (***A***, ***B***, ***C***, ***D***) types component-related failures have been distinguished. The feature of the repairs of equipment (except ***C*** type failure) is a long – approximately 45 day (1080 hours) – period because of logistical matters. This investigation is done from point of view of end-user; therefore the repairs are characterized by Mean Repair Turnaround Times (MRTT). Additionally it can be established that the time of replacement of faulty equipment is negligible. So these times are not taken into account during simulation modeling.

The Figure 2 shows weighted directed graph of the process. In the graph, the weights of the edges show probability densities (failure and turnaround rates) of changes of operational states.

The failure rate λ_i is equal to the probability of the ith failure in a unit time interval given that no failure has occurred before it [9]. The turnaround rate μ_j can be interpreted analogically:

$$\lambda_i = \frac{1}{MTBF_i} \quad \text{and} \quad \mu_i = \frac{1}{MRTT_i} \quad . \tag{2}$$

The system of differential equations of this process that describes the changes in time of the probability of staying in different states can be determined as

$$\begin{aligned}
\frac{dP_W}{d\tau} &= -(\lambda_A + \lambda_B + \lambda_C + \lambda_D)P_W + \mu_A P_A + \mu_B P_B + \mu_C P_C + \mu_D P_D \\
\frac{dP_A}{d\tau} &= \lambda_A P_W - \mu_A P_A \\
\frac{dP_B}{d\tau} &= \lambda_B P_W - \mu_B P_B \\
\frac{dP_C}{d\tau} &= \lambda_C P_1 - \mu_C P_C \\
\frac{dP_D}{d\tau} &= \lambda_C P_1 - \mu_D P_D
\end{aligned} \quad . \tag{3}$$

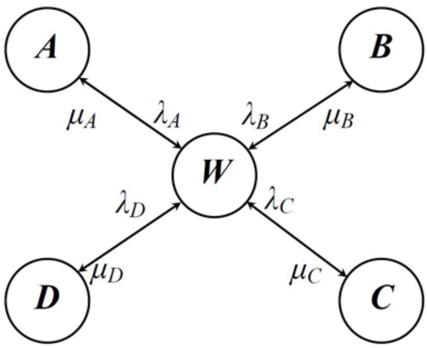

Fig. 2 The Graph Model of Investigated Maintenance Process

If the investigated process is stationary, the differential coefficients of equipment (3) are:

$$\frac{dP_W}{d\tau} = \frac{dP_A}{d\tau} = \frac{dP_B}{d\tau} = \frac{dP_C}{d\tau} = \frac{dP_D}{d\tau} = 0 \quad . \tag{4}$$

A further condition of the solution is the

$$\sum_{i=W}^{D} P_i(\tau) = 1 \tag{5}$$

probability of event space. This equation expresses that the equipment has to stay only in one of five states. Then on the basis of equations (3) – (5) stochastic model of the investigated stationary operation process can be depicted as the following matrix formula by [7]:

$$\begin{bmatrix} -(\lambda_A + \lambda_B + \lambda_C + \lambda_D) & \mu_A & \mu_B & \mu_C & \mu_D & 1 \\ \lambda_A & -\mu_A & 0 & 0 & 0 & 1 \\ \lambda_B & 0 & -\mu_B & 0 & 0 & 1 \\ \lambda_C & 0 & 0 & -\mu_C & 0 & 1 \\ \lambda_D & 0 & 0 & 0 & -\mu_A & 1 \\ 1 & 1 & 1 & 1 & 1 & 0 \end{bmatrix} \begin{bmatrix} P_W \\ P_A \\ P_B \\ P_C \\ P_D \\ 1 \end{bmatrix} = \begin{bmatrix} 1 \\ 1 \\ 1 \\ 1 \\ 1 \\ 1 \end{bmatrix} \tag{6}$$

4. SIMULATION OF PROCESS

In this Chapter the MCS of operational process modeled above will be done to investigate effects of parametric uncertainties of probability densities (failure and turnaround rates) of changes of operational states. Based on the simulation results the possibility of use in maintenance management decision of MCS will be shown.
The block diagram of the simulation can be seen in Fig. 3.

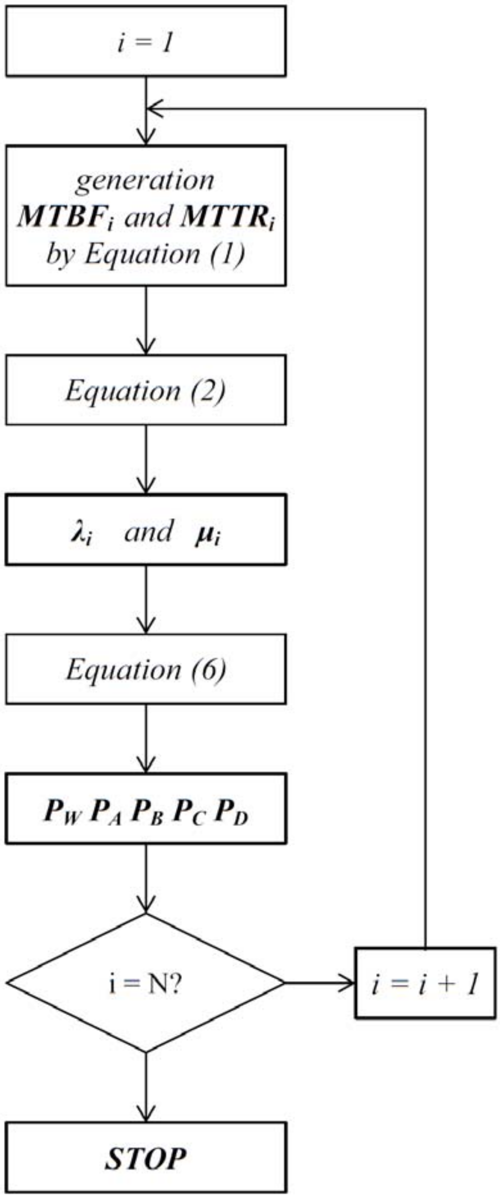

Fig. 3. Block Diagram of the Monte-Carlo Simulation

4.1 Creating of Initial Data

Firstly, the available failure and turnaround data were analyzed statistically. The standard deviation and expected values of times between failures, and repair turnaround times were determined. These expected values are the MTBF (Mean Time Between Failures) and MRTT (Mean Repair Turnaround Time) parameters that commonly used to characterize the operational processes (see Table 1).
Due to the relatively small number of available data, the goodness-of-fit tests have been left out. According to general engineering practice it is assumed that the measured parameters have normal (Gauss) probability distribution.

Failure	***A***	***B***	***C***	***D***
Number of samples	23	24	25	21
Mean Time Between Failures *MTBF* [hour]	183627	162059	152800	179789
Standard deviation of Times between Failures [hour]	2033	1881	1659	2198
Mean Repair Turnaround Time *MRTT* [hour]	1080.8	1081.1	167.13	1079.8
Standard deviation of Repair Turnaround Times [hour]	23.9	23.7	23.16	24.3

Table 1. Results of the Main Statistical Analysis of Input Data of Simulation

4.2 Determination of Number of Excitations

One of the most essential questions of MCS is the applicable number of excitations. During our investigation the number of excitations was increased from 50 to the applicable number. The the applicable number was defined when relative differents of Mean Values and Standrd Deviations of probability of aviability P_w in actual and precedent cases are less then 10^{-3}.

N_{Ex}	Mean	Rel.Dif.	St.Dev.	Rel.Dif.
50	0,98074	–	0,000275	–
100	0,98076	$2,03928 \cdot 10^{-5}$	0,000302	$9,81818 \cdot 10^{-2}$
250	0,98074	$2,03923 \cdot 10^{-5}$	0,000285	$5,62914 \cdot 10^{-2}$
500	0,98071	$3,05891 \cdot 10^{-5}$	0,000284	$3,50877 \cdot 10^{-3}$
750	0,98072	$1,01967 \cdot 10^{-5}$	0,000285	$3,52113 \cdot 10^{-3}$
1000	0,98071	$1,01966 \cdot 10^{-5}$	0,000287	$7,01754 \cdot 10^{-4}$

Table 2. Results and Relative Deviations of Simulations with Different Number of Excitations

The Table 2 and Figure 4 show the results of simulations with different number of excitations. Seeing the relative differences, the applicable number of excitations can be determined as 1000.

	Mean	St.Dev.
P_w	0,980710	0,000287
P_a	0,005769	0,000144
P_b	0,006546	0,000157
P_c	0,001081	0,000150
P_d	0,005888	0,000152

Table 3. Results of Simulation (N_{ex} = *1000*)

The Table 3 shows the Mean Values and Standard Deviatons of probabilities of staying in different states by *“N_{ex} = 1000*” simulation.

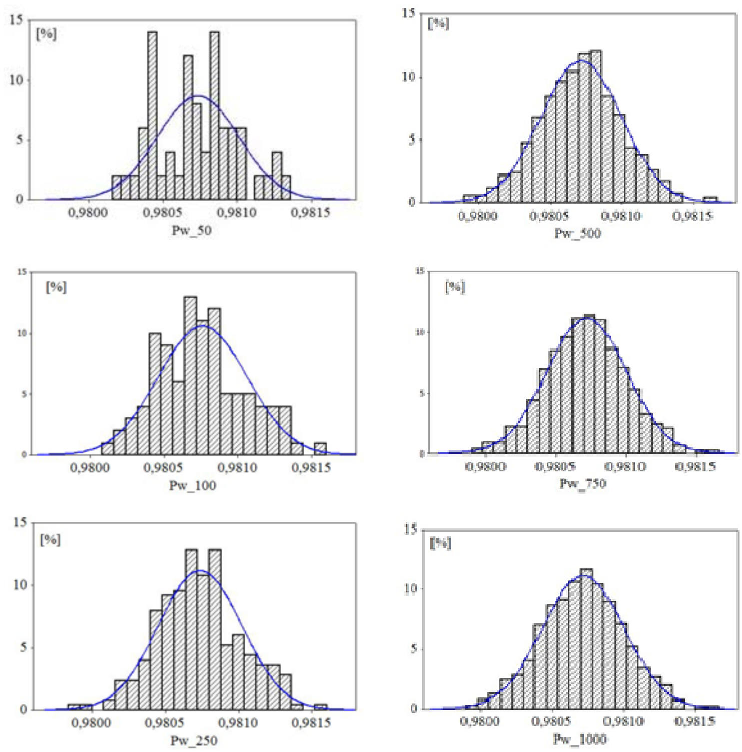

Fig. 4. Histograms of Simulations with Different Number of Excitations

4.3 Determination of Requested Number for Spare Part

This model simulation is done from point of view of end-user fundamentally. Thus, the most important question is the Required Number of Spare Part (*RNSP*). Knowing probability of the availability P_w, the *RNSP* can be determined by the following equation:

$$N_{RNSP} = \left\lceil \left(\frac{1}{P_W} - 1 \right) N \right\rceil \quad , \tag{7}$$

where N is the number of equipment in the system.
Using the probability distribution of simulation results (see Table 3), it should be determined, in case of which, value *PRNS* the probability of availability P_w will be less than the acceptable assessing uncertainty R.
The *RNSP*s were determined in cases of different assessing uncertainty values. These results are shown in Table 4.

Assessing Uncertainty R	Availability P_w	Requested Number for Spare Part N_{RNS}
10 %	0,98030	101
1 %	0,98008	102
0,5 %	0,98001	103

Table 4. Required Number for Spare Part Depending on Estimating Uncertainty ($N = 5000$)

4.4 Determination of Numbers of Failures

The Number of i^{th} type Failure (NoF_i) can be determined by the following equation:

$$NoF_i = \left\lceil \frac{T \cdot P_i}{MRTT_i} N \right\rceil \quad , \tag{7}$$

where T is the length of investigational time.
The model simulation data presented by Table 7 can be used to estimate the NoFs, maintenance cost and work expenditures of operated systems in investigated time (in the present case: $T = 1\ year = 365 \cdot 24 = 8760\ hours$) interval depending on required estimating uncertainties.
Comparing data of Tables 4 and 5, it is easily remarked that sum of *NoF*s are more than *RNSP*. At first it may seem to be contradictory. However, it should also be taken into account that the NoFs were estimated by a time interval, but the *RNSP* is time-independent. Be it remembered that the repaired equipment will be returned to the end-user, where firstly they might be spare ones, and later they will replace the other failed ones.

i	$R = 10\%$		$R = 1\%$		$R = 0{,}50\%$	
	P_{iE}	NoF_i	P_{iE}	NoF_i	P_{iE}	NoF_i
A	$5.959\ 10^{-3}$	241	$6.110\ 10^{-3}$	247	$6.145\ 10^{-3}$	249
B	$6.748\ 10^{-3}$	273	$6.915\ 10^{-3}$	280	$6.953\ 10^{-3}$	281
C	$1.265\ 10^{-3}$	329	$1.422\ 10^{-3}$	370	$1.457\ 10^{-3}$	379
D	$6.086\ 10^{-3}$	246	$6.244\ 10^{-3}$	253	$6.281\ 10^{-3}$	254

Table 5. Number of Failures Depending on Estimating Uncertainty ($T = 8760\ hours$; $N = 5000$)

5. CONCLUSIONS, FUTURE WORK

This paper discussed a Monte-Carlo Simulation-based method of maintenance processes analysis. Its possibility of use was demonstrated by a case study. The proposed method can be used:

- for analyzing of maintenance processes;
- for supporting decision making in maintenance management;
- for estimating the availability and Required Number for Spare Part depending on required estimating uncertainty;
- for assessing the Numbers of Failures depending on required estimating uncertainty.

The Author's planned prospective scientific research related to this field of applied mathematics and maintenance management decision making includes the study of methodologies of mathematical tools for analysis of maintenance systems and processes for example stochastic model and simulation-based weighted sensitivity analysis of maintenance systems and processes.

6. REFERENCES

[1] **Bera, J. – Pokorádi, L.**: Monte-Carlo Simulation of Helicopter Noise. Acta Polytechnica Hungarica 12:(2), p.21-32.

[2] **Ossai C.I. - Boswell, B. – Davies, I.J.**: Application of Markov modelling and Monte Carlo simulation technique in failure probability estimation – A consideration of corrosion defects of internally corroded pipelines. Engineering Failure Analysis Vol. 68, p.159–171.

[3] **Garavaglia, E. - Sgambi, L.**: Selective maintenance planning of a steel truss bridge based on the Markovian approach, Engineering Structures Vol. 125, p.532–545.

[4] **Guizani, M. - Rayes, A. - Khan, B. - Al-Fuqaha, A.**: Network Modeling and Simulation, A Practical Respective, John Wiley & Sons, Chichester, 2010., p.281.

[5] **Kalos, M.H. - Whitlock, P.A.**: Monte Carlo Methods. Second Edition, WILEY-VCH Verlag GmbH & Co. KGaA, Weinheim, 2008, p.204.

[6] **Nannapaneni, S. - Mahadevan, S.**: Reliability analysis under epistemic uncertainty, Engineering & System Safety Vol. 155, p.9-20.

[7] **Pokorádi, L.**: Systems and Processes Modeling, Campus Kiadó, Debrecen, 2008, p. 242. (in Hungarian)

[8] **Pokorádi, L. – Molnár, B.**: Monte-Carlo simulation of the pipeline system to investigate water temperature's effects, Polytechnical University of Bucharest. Series D: Mechanical Engineering Vol. 73:(4), p.223-236.

[9] **Pokorádi, L.**: Availability Assessment Based on Stochastic Maintenance Process Modeling, Debreceni Műszaki Közlemények vol. 2013, no. 1, p.37-46.

[10] **Rubinstein, R.Y.**: Simulation and the Monte-Carlo Method, New York: John Wiley & Sons; 1981.

OPTIMAL SELECTION OF WEIGHTING FUNCTIONS BY GENETIC ALGORITHMS TO DESIGN H_∞ ANTI-ROLL BAR CONTROLLERS FOR HEAVY VEHICLES

Van Tan VU[1], Olivier SENAME[1], Luc DUGARD[1] and Peter GÁSPÁR[2]

[1]Univ. Grenoble Alpes and CNRS, GIPSA-lab, F-38402 Grenoble Cedex, France
E-mail: {Van-Tan.Vu, olivier.sename, luc.dugard}@gipsa-lab.grenoble-inp.fr
[2]Systems and Control Laboratory, Institute for Computer Science and Control,
Hungarian Academy of Sciences, Kende u. 13-17,
H-1111 Budapest, Hungary, E-mail: gaspar@sztaki.mta.hu

Received: November 7, 2016

ABSTRACT

Multi-criterion optimization is so far popular for many complex engineering problems. The objective of active anti-roll bar of heavy vehicles is to maximize roll stability to prevent rollover in dangerous cases. However, such a performance objective must be balanced with the energy consumption of the anti-roll bar system, which is not a trivial task. In a previous work, the authors proposed an H_∞ active anti-roll bar controller for which the weighting functions were chosen by trials and errors during the design step. In this paper, Genetic Algorithms (GAs) are proposed to find optimal weighting functions for the H_∞ control synthesis. Such a general procedure is applied to the case of active anti-roll bar control in heavy vehicles. Thanks to GAs, the conflicting objectives between roll stability and torques generated are handled using one high level parameter only. The multi-criterion optimization solution is illustrated via the Pareto frontier. Simulations, performed in the frequency and time domains, emphasize the efficiency of the proposed method.

Keywords: H_∞ control, Genetic Algorithms, Heavy vehicle, Active anti-roll bar control, Rollover, Roll stability.

1. INTRODUCTION

1.1 Context

Rollover of heavy vehicle is an important road safety problem world-wide. Although rollovers are relatively rare events, they are usually deadly accidents when they occur. Moreover, the roll stability loss is the main cause of traffic accidents in which heavy vehicles are involved. In order to improve the roll stability, several schemes with possible active intervention into the vehicle dynamics have been proposed. One of them employs active anti-roll bars, that is, a pair of hydraulic actuators, which generates a stabilizing moment to counter balance the overturning moment [17].

On the other hand, the H_∞ control design approach is an efficient tool for improving the performance of a closed-loop system in pre-defined frequency ranges. The key step of the H_∞ control design is the selection of weighting functions, which depends on the engineer skill and experience. In many real applications, the difficulty in choosing the weighting functions still increases highly because the performance specification is not accurately defined i.e it is simply to achieve the best possible performance (optimal design) or to achieve an optimally joint improvement of more than one objective (multi-objectives design). So the optimization of weighting functions to satisfy the desired performances is still an interesting problem. Recently, the idea to use an optimization tool was proposed in [1] and [10]. The choice of GAs seems natural because their formulation is well suited for this type of problematic [4].

1.2 Related works

Some of the control methods applied to active anti-roll bar control on heavy vehicle are briefly presented below:

a- Optimal control: Sampson et al [12], [13], [14] have proposed a state feedback controller which was designed by finding an optimal controller based on a linear quadratic regulator (LQR) for single unit and articulated heavy vehicles.

The LQR was also applied to an integrated model including an electronic servo-valve hydraulic damper model and a yaw-roll model of a single unit heavy vehicle. The input current of the electronic servo-valve is the input control signal [17].

b- Neural network control: A reinforcement learning algorithm using neural networks proposed to improve the roll stability for a single unit heavy vehicle [2].

c- Robust control (LPV): Gaspar et al. [5], [6], [7] have applied Linear Parameter Varying (LPV) technique to control active anti-roll bars combined with active brakes on the single unit heavy vehicle. The forward velocity is considered as the varying parameter.

1.3 Paper contribution

Based on the H_∞ active anti-roll bar control presented by the authors in [18], this paper proposes the use of Genetic algorithms to define automatically the weighting functions. Hence the following contributions are brought:

- The Genetic algorithms method is applied to define the weighting functions of the H_∞ robust controller for active anti-roll bar system on the single unit heavy vehicle. Thanks to GAs, the conflicting objectives between the normalized load transfers and the generated torques are handled using a single high level parameter only, denoted α.

- The simulation results in frequency and time domains show the normalized load transfers at two axles when the tuning parameter value α moves from 0 to 1, compared with the case of passive anti-roll bar and to the results of the previous paper [18]. In time domain, a cornering manoeuvre is used for the heavy vehicle. The forward velocity of the heavy vehicle is considered up to 160 km/h in order to evaluate the roll stability, as well as to determine the maximal forward velocity at which the normalized load transfers and the generated torques reach their limits.

The paper is organised as follows: Section 2 gives a brief introduction about multi-objective optimization using GAs. Section 3 presents the model of a single unit heavy vehicle. Section 4 develops the H_∞ control synthesis to prevent rollover of heavy vehicles. Section 5 illustrates how to use the GAs to define the weighting functions of the H_∞ active anti-roll bar. Section 6 presents some simulation results in frequency and time domains. Finally, some conclusions are drawn in section 7.

2. GENETIC ALGORITHMS AND MULTI-CRITERION OPTIMIZATION

2.1 Genetic algorithms

Genetic algorithms are now widely used since the first study in [9], confirmed by a popular theory-oriented book [8] and an application-oriented book [3]. The algorithms are based on the natural selection mechanism and have been proven to be very effective in optimization in many real applications such as finance and investment strategies, robotics, engineering design, telecommunications, etc. They are likely global optimization techniques (despite the high computational expense) using probabilistic, multi-points search, random combination (crossover, mutation) and information of previous iteration to evaluate and improve the population. A great advantage of GAs compared with other searching methods (for example gradient methods) is that they search regardless of the nature of the objective functions and constraints.

GAs initializes with a random population. Through the genetic operation: *selection*, *crossover* and *mutation*, a new population is obtained. By using a selection process, the fittest individuals based on their fitness values are chosen; crossover and mutation are then applied to create the new population. The genetic operation on individuals of population continues until the optimization criterion is satisfied or a certain number of generations is reached.

Fitness function: The fitness of an individual is useful for choosing between “good” and “bad” individuals. An individual with a high fitness value will have a great chance to be selected.

Selection: This step is to sort and copy individuals by order of satisfaction of the fitness function. The higher the value of the fitness associated to an individual, the greater the individual's chances to be selected to participate in the next generation. “Proportionate selection” [9] and “tournament selection” [11] are two most popular selection methods.

Crossover: This is the main operation acting on the population of parents. It consists of an exchange of parts of chains between two selected individuals (parents) to form two new individuals (children). This exchange may be due either to a single point or to multiple points.

Mutation: Mutation operates on a single individual by changing randomly a part of it. In the case of binary coding, this is done by reversing one or more bits in a chromosome.

2.2 Multi-criterion optimization

One well-known application of the GAs is to find the optimal solution for the multi-objective optimization problem involving multiple and conflicting objectives. This is a very popular problem in practice and can be described as follows

$$\min_{x \in C} F(x) = \begin{bmatrix} f_1(x) \\ f_2(x) \\ \vdots \\ f_{n_{obj}}(x) \end{bmatrix}, \; n_{obj} .. 2, \tag{1}$$

where x is called the decision vector, C the set of possible decision vectors (or the searching space), and $F(x)$ the objective vector.

The existence of an ideal solution x^* that can minimize simultaneously all objective functions $f_1, f_2, \ldots f_{nobj}$ is in fact rarely feasible.

There are many formulations to solve the problem (1) like *weighted min-max method*, *weighted global criterion method*, *goal programming methods* [4] and references therein. One of the most popular and simple approaches is the weighted sum method which converts the multi-objective problem into a single objective one. In this paper, one uses a particular case of the weighted sum method, where the multi-objective functions vectors F are replaced by the convex combination of objectives:

$$\min J = \sum_{i=1}^{n_{obj}} \alpha_i f_i(x), \; s.t\, x \in C, \sum_{i=1}^{n_{obj}} \alpha_i = 1 \tag{2}$$

Vector $\alpha = (\alpha_1, \alpha_2, ..., \alpha_{n_{obj}})$ represents the gradient of function *J*. By using various sets of *α*, one can generate several points in the Pareto set [4].

3. SINGLE UNIT HEAVY VEHICLE MODEL

Fig. 1 illustrates the combined yaw-roll dynamics of the vehicle modelled by a three-body system, where m_s is the sprung mass, m_{uf} the un-sprung mass at the front including the front wheels and axle, and m_{ur} the un-sprung mass at the rear with the rear wheels and axle. The variables of the yaw-roll model are shown in Table (1) and the parameters are shown in [5].

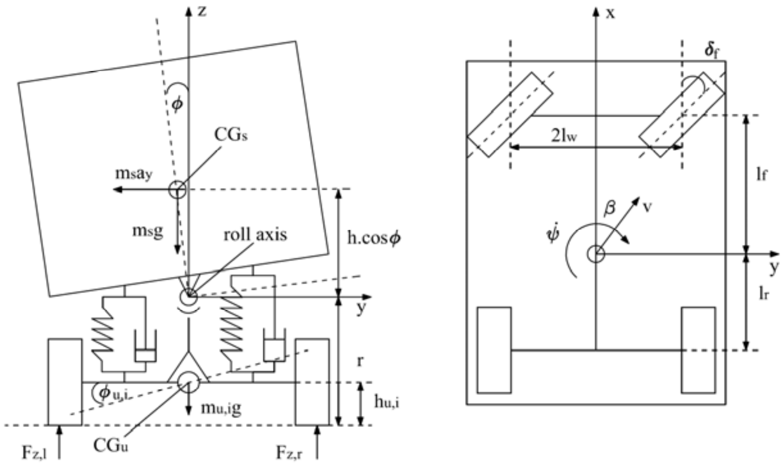

Fig. 1 Yaw-Roll model of single unit heavy vehicle [5].

Table 1. Variables of yaw-roll model.

Symbols	Description	Symbols	Description
m_s	Sprung mass	δ_f	Steering angle
$m_{u;f}$	Un-sprung mass on the front axle	C_f	Tire cornering stiffness on the front axle
$m_{u;r}$	Un-sprung mass on the rear axle	C_r	Tire cornering stiffness on the rear axle
m	The total vehicle mass	k_f	Suspension roll stiffness on the front axle
v	Forward velocity	k_r	Suspension roll stiffness on the rear axle
v_{wi}	Components of the forward velocity	b_f	Suspension roll damping on the front axle
h	Height of CG of sprung mass from roll axis	b_r	Suspension roll damping on the rear axle
$h_{u;i}$	Height of CG of un-sprung mass from ground	k_{tf}	Tire roll stiffness on the front axle
r	Height of roll axis from ground	k_{tr}	Tire roll stiffness on the rear axle
a_y	Lateral acceleration	I_{xx}	Roll moment of inertia of sprung mass
β	Side-slip angle at centre of mass	I_{xz}	Yaw-roll product of inertial of sprung mass
ψ	Heading angle	I_{zz}	Yaw moment of inertia of sprung mass
$\dot{\psi}$	Yaw rate	l_f	Length of the front axle from the CG
α	Side slip angle	l_r	Length of the rear axle from the CG
ϕ	Sprung mass roll angle	l_w	Half of the vehicle width
$\phi_{u,i}$	Un-sprung mass roll angle	μ	Road adhesion coeffcient

In the vehicle modelling, the differential equations of motion of the yaw-roll dynamics of the single unit vehicle, i.e. the lateral dynamics (3.1), the yaw moment (3.2), the roll moment of the sprung mass (3.3), the roll moment of the front (3.4) and the rear (3.5) unsprung masses, are formalized in the equations (3):

$$\begin{cases} mv(\dot{\beta}+\dot{\psi})-m_s h\ddot{\phi}=F_{yf}+F_{yr} & (3.1)\\ -I_{xz}\ddot{\phi}+I_{zz}\ddot{\psi}=F_{yf}l_f-F_{yr}l_r & (3.2)\\ (I_{xx}+m_s h^2)\ddot{\phi}-I_{xz}\ddot{\psi}=m_s gh\phi+m_s vh(\dot{\beta}+\dot{\psi})-k_f(\phi-\phi_{uf})-b_f(\dot{\phi}-\dot{\phi}_{uf})+M_{ARf}+U_f & \\ \qquad -k_r(\phi-\phi_{ur})-b_r(\dot{\phi}-\dot{\phi}_{ur})+M_{ARr}+U_r & (3.3)\\ -rF_{yf}=m_{uf}v(r-h_{uf})(\dot{\beta}+\dot{\psi})+m_{uf}gh_{uf}\phi_{uf}-k_{tf}\phi_{uf}+k_f(\phi-\phi_{uf})+b_f(\dot{\phi}-\dot{\phi}_{uf})+M_{ARf}+U_f & (3.4)\\ -rF_{yr}=m_{ur}v(r-h_{ur})(\dot{\beta}+\dot{\psi})-m_{ur}gh_{ur}\phi_{ur}-k_{tr}\phi_{ur}+k_r(\phi-\phi_{ur})+b_r(\dot{\phi}-\dot{\phi}_{ur})+M_{ARr}+U_r & (3.5) \end{cases}$$

The lateral tire forces F_{yf} and F_{yr} in the direction of velocity at the wheel ground contact points are modelled by a linear stiffness as:

$$\begin{cases} F_{yf}=\mu C_f\alpha_f \\ F_{yr}=\mu C_r\alpha_r \end{cases}. \tag{4}$$

where the tyre side slip angles are given as:

$$\begin{cases} \alpha_f=-\beta+\delta_f-\dfrac{l_f\dot{\psi}}{v} \\ \alpha_r=-\beta+\dfrac{l_r\dot{\psi}}{v} \end{cases}. \tag{5}$$

The moment of passive anti-roll bar impacts the un-sprung and sprung masses at the front and rear axles as follows [17], [18]:

$$\begin{cases} M_{ARf}=4k_{AOf}\dfrac{t_At_B}{c^2}\phi-4k_{AOf}\dfrac{t_A^2}{c^2}\phi_{uf} \\ M_{ARr}=4k_{AOr}\dfrac{t_At_B}{c^2}\phi-4k_{AOr}\dfrac{t_A^2}{c^2}\phi_{ur} \end{cases}, \tag{6}$$

where k_{AOf}, k_{AOr} are respectively the torsional stiffness of the anti-roll bar at the front and rear axles, t_A half the distance of the two suspensions, t_B half the distance of the chassis and c the length of the anti-roll bars's arm.

Using the previous equation, the single unit heavy vehicle can be represented by the linear system in the state space form (7):

$$\begin{cases} \dot{x}=Ax+B_1w+B_2u \\ y=Cx \end{cases}, \tag{7}$$

with the state vector: $x=\begin{bmatrix}\beta & \dot{\psi} & \varphi & \dot{\varphi} & \varphi_{uf} & \varphi_{ur}\end{bmatrix}$, the exogenous disturbance input: $w=\begin{bmatrix}\delta_f\end{bmatrix}$,

the control inputs: $u=\begin{bmatrix}U_f & U_r\end{bmatrix}$ and the output vector: $y=\begin{bmatrix}\beta & \dot{\psi} & \varphi & \dot{\varphi} & \varphi_{uf} & \varphi_{ur}\end{bmatrix}$.

4. H$_\infty$ CONTROL SYNTHESIS OF ACTIVE ANTI-ROLL BAR ON HEAVY VEHICLES

4.1 Control objective, problem statement

The objective of the active anti-roll bar control system is to maximize the roll stability of the vehicle. Usually, an imminent rollover detected when the calculated normalized load transfer reaches 1 (or -1), as explained hereafter. First, the lateral load transfer can be given by:

$$\Delta F_z = \frac{k_u \varphi_u}{l_w}, \tag{8}$$

where k_u is the stiffness of tire, φ_u the roll angle of the un-sprung mass and l_w the half of vehicle's width. Then, the lateral load transfer can be normalized w.r.t. the total axle load F_z as follows:

$$R = \frac{\Delta F_z}{F_z} . \tag{9}$$

The normalized load transfer $R=\pm 1$ corresponds to the largest possible load transfer. In that case, the inner wheel in the bend lifts off.

While attempting to minimize the load transfer, it is also necessary to constrain the roll angles between the sprung and un-sprung masses $(\varphi-\varphi_u)$ so that they stay within the limits of the suspension travel (7-8 deg), see [5].

The performance characteristic which is of most interest when designing the active anti-roll bar, is then the normalized load transfer. The chosen control objective is to minimize, the effect of the steering angle on the normalized load transfer R, in the H$_\infty$ framework. As explained later, the limitation of the torques $U_{f;r}$ generated by the actuators is also crucial for practical implementation.

4.2 Background on H$_\infty$ control

The H$_\infty$ control problem is formulated according to the generalized control structure shown in Fig. 2 [15], [16].

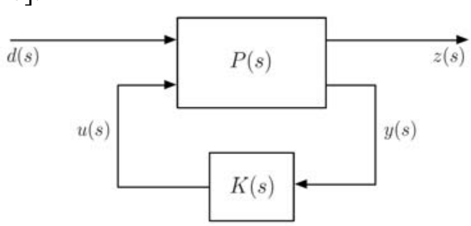

Fig. 2 Generalized control structure.

with P partitioned as:

$$\begin{bmatrix} z \\ y \end{bmatrix} = \begin{bmatrix} P_{11}(s) & P_{12}(s) \\ P_{21}(s) & P_{22}(s) \end{bmatrix} \begin{bmatrix} d \\ u \end{bmatrix} \tag{10}$$

and $u = K(s).y$, which yields

$$\frac{z}{d} = F_l(P,K) := \left[P_{11} + P_{12}K\left[I - P_{22}K\right]^{-1} P_{21} \right] \tag{11}$$

The aim is to design a controller K that stabilizes the closed loop system and also reduces the signal transmission path from disturbances d to performance outputs z. This problem is then to find a controller K which minimizes γ such that

$$\left\| F_l(P,K) \right\|_\infty < \gamma \tag{12}$$

By minimizing a suitably weighted version of $F_l(P,K)$ the control aim is achieved.

4.3 H∞ control synthesis for the active anti-roll bar of the single unit heavy vehicle model

In this section, the H_∞ control design is presented for the active anti-roll bar system on a single unit heavy vehicle. Consider the closed-loop system given in Fig 3, which includes the feedback structure of the nominal model G, the controller K and the weighting functions W_{ij}. In this diagram, U_f and U_r are the control inputs, y_1 and y_2 are the measured outputs, n_1 and n_2 are the measurement noises. δ_f is the steering angle considered as a disturbance signal, which is set by the driver. The variables z_1, z_2, z_3, z_4 and z_5 represent the performance outputs.

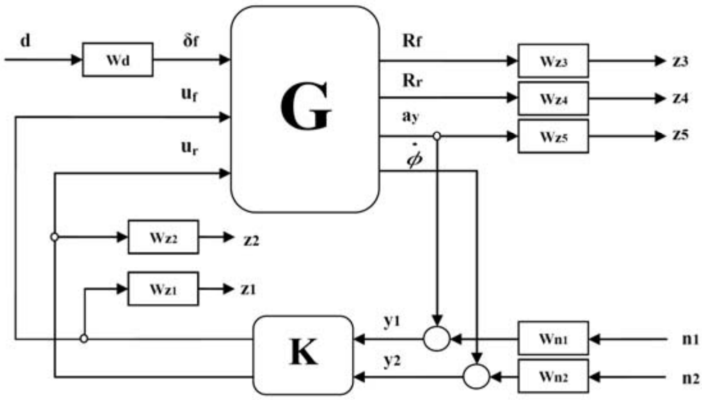

Fig. 3 G-K control structure of H_∞ active anti-roll bar control.

According to Fig. 3, the concatenation of the linear model (7) with performance weighting functions lead to the state space representation of P(s):

$$\begin{bmatrix} \dot{X} \\ Z \\ Y \end{bmatrix} = \begin{bmatrix} A & B_1 & B_2 \\ C_1 & D_{11} & D_{12} \\ C_2 & D_{21} & D_{22} \end{bmatrix} \begin{bmatrix} X \\ W \\ U \end{bmatrix}, \tag{13}$$

with the exogenous input (disturbance): $W = [d \;\; n_1 \;\; n_2]$, the control input: $U = [U_f \;\; U_r]^T$, where U_f is the torque at the front axle and U_r at the rear axle, the performance output vector: $Z = [z_1 \;\; z_2 \;\; z_3 \;\; z_4 \;\; z_5]^T$, the measured output vector: $Y = [a_y \;\; \dot{\varphi}]^T$, and A, B_1, B_2, C_1, D_{11}, D_{12}, C_2, D_{21}, D_{22} are matrices of appropriate dimensions.

The next section proposes an automatic and systematic way to obtain the optimal weighting functions used to solve the H_∞ control design problem.

5. SELECTION OF WEIGHTING FUNCTIONS OF H∞ ANTI-ROLL BAR CONTROLLERS BY GENETIC ALGORITHMS

In industrial applications, multiple goals have to be taken into account, which often are conflicting. Multi-criterion optimization (MCO) is then a powerful tool to find the best compromise solution balancing the conflicts, and therefore is of great importance in practice. In this section, MCO problem for the weighting function selection of the H_∞ active anti-roll bar control on heavy vehicles is introduced and solved using the Genetic algorithms method. But first, the criterion for MCO problem must be defined.

5.1 Optimization objectives

The objective of the active anti-roll bar control system is to maximize the roll stability of heavy vehicles to prevent rollover in dangerous cases. However, such a performance objective must be balanced with the energy consumption of the anti-roll bar system due to the torques generation by the actuators. Therefore the objective function is selected as follows:

$$f = \alpha f_{\text{Normalized\_load\_transfer}} + (1-\alpha) f_{\text{Torque}}, \tag{14}$$

where $f_{\text{Normalized\_load\_transfer}}$ and f_{Torque} are performance indices corresponding to the normalized load transfers and torques generated at two axles. They are defined as follows:

$$\begin{cases} f_{\text{Normalized\_load\_transfer}} = \dfrac{1}{2}\left(\sqrt{\dfrac{1}{T}\displaystyle\int_0^T R_f^2(t)dt} + \sqrt{\dfrac{1}{T}\displaystyle\int_0^T R_r^2(t)dt} \right) \\ f_{\text{Torque}} = \dfrac{1}{2}\left(\dfrac{\sqrt{\dfrac{1}{T}\displaystyle\int_0^T U_f^2(t)dt}}{\sqrt{\dfrac{1}{T}\displaystyle\int_0^T U_f^2(t)_{\max}dt}} + \dfrac{\sqrt{\dfrac{1}{T}\displaystyle\int_0^T U_r^2(t)dt}}{\sqrt{\dfrac{1}{T}\displaystyle\int_0^T U_r^2(t)_{\max}dt}} \right) \end{cases}, \tag{15}$$

where $R_{f;r}$ are the normalized load transfers and $U_{f;r}$ the torques generated at front and rear axles. $U_{f;rmax}$ are defined when the optimal problem focusses only on the normalized load transfers (i.e. the torques are then not considered in the optimisation problem). In that case, $\alpha = 1$ and $f = f_{\text{Normalized\_load\_transfer}}$.

5.2 Multi-criterion optimization problem formulation

The weighting functions used in Fig 3 are detailed in this part.
The input scaling weight W_d normalizes the steering angle to the maximum expected command and is selected as $W_d = \frac{\pi}{180}$. This value corresponds to a 1^0 steering angle command.
The weighting functions W_{n1} and W_{n2} are selected as: $W_{n1} = W_{n2} = 0.01$, which accounts for small sensor noise models in the control design. The noise weights are chosen as $0.01(m/s^2)$ for the lateral acceleration and $0.01(^0/sec)$ for the derivative of the roll angle $\dot{\varphi}$ [5]. Note that other low pass filters could be selected if needed.

The weighting functions W_{zi} represent the performance outputs *(W_{z1}, W_{z2}, W_{z3}, W_{z4} and W_{z5})*. The purpose of the weighting functions is to keep small the control inputs, normalized load transfers and the lateral acceleration over a desired frequency range. The weighting functions chosen for performance outputs can be considered as penalty functions, that is, weights should be large in the frequency range where small signals are desired and small where larger performance outputs can be tolerated.
The weighting functions W_{z1} and W_{z2} corresponding to the front and rear control torques generated by active anti-roll bars are chosen as:

$$W_{Z1} = \frac{1}{Z_1};\ W_{Z2} = \frac{1}{Z_2}\ . \tag{16}$$

The weighting functions W_{z3} and W_{z4} corresponding to the normalized load transfers at front and rear axles are selected as:

$$W_{Z3} = \frac{1}{Z_3};\ W_{Z4} = \frac{1}{Z_4}\ . \tag{17}$$

The weighting function W_{z5} is selected as:

$$W_{Z5} = Z_{51}\frac{Z_{52}s + Z_{53}}{Z_{54}s + Z_{55}}\ . \tag{18}$$

Here, the weighting function W_{z5} corresponds to a design that avoids the rollover situation with the bandwidth of the driver in the frequency range up to more than *4rad/s*. This weighting function will directly minimize the lateral acceleration when it reaches the critical value, to avoid the rollover, where Z_{ij} are constant parameters.
From equations (16) - (18), the following variables will then be defined: Z_1, Z_2, Z_3, Z_4, Z_{51}, Z_{52}, Z_{53}, Z_{54}, Z_{55}.
The MCO problem for the H_∞ active anti-roll bar control can be defined as:

$$\begin{aligned} &\min_{p\in P} f(p), f(p) := \left[f_{Normalized\_load\_transfer} \quad f_{Torque} \right]^T \\ &P := \left\{ p = [Z_1, Z_2, Z_3, Z_4, Z_{51}, Z_{52}, Z_{53}, Z_{54}, Z_{55}]^T \in R \mid p^l \le p \le p^u \right\} \end{aligned}, \tag{19}$$

where *f(p)* is the vector of objectives, *p* denotes the vector of weighting function parameters, and p^l, p^u represent the lower and upper bounds of the weighting function selection.
The lower and upper bounds of the weighting function parameters are given in Table (2). Besides the minimization of the objective function from equations (14) and (19), we also have to account for the limitations of the normalized load transfers, roll angle of suspensions as well as torques generated at each axle. These limitations are considered as the optimality conditions (binding conditions) shown in the Table (3).

Table 2: Lower and upper bounds of the weighting functions.

	W_{z1}	W_{z2}	W_{z3}	W_{z4}	W_{z5}				
	Z_1	Z_2	Z_3	Z_4	Z_{51}	Z_{52}	Z_{53}	Z_{54}	Z_{55}
Lower bound	50	50	0.1	0.1	0.5	$\frac{1}{3000}$	1	1	0.001
Upper bound	300000	300000	10	10	100	1	500	$\frac{1}{0.001}$	2

Table 3: Binding conditions.

No	Note	Maximum value	Unit
1		< 7	deg
2	$\lvert\phi-\phi_{ur}\rvert$	< 7	deg
3	$\lvert R_f\rvert$	< 1	-
4	$\lvert R_r\rvert$	< 1	-
5	$\lvert U_f\rvert$	< 120000	Nm
6	$\lvert U_r\rvert$	< 120000	Nm

5.3 Genetic operation

The selection method used in this paper is the proportionate selection developed by Holland [9]. This method assigns a probability of selection to each individual, proportional to its relative fitness. Proportionate selection can be illustrated by a roulette wheel. The crossover happens with a probability of 0.9 and the mutation happens with a very small probability 0.095.

The proposed weighting function optimization procedure for H_∞ active anti-roll bar control synthesis is as follows:

Step 1: Initialize with the weighting functions as in the previous paper [18], the vector of weighting function selected as $p=p_0$.

Step 2: Select lower bound, upper bound, scaling factor, offset and start point.

Step 3: Format optimal algorithm, select the vector of objectives with the variation of switch value from 0 to 1 and then solve the minimization problem.

Step 4: Select the individuals, apply crossover and mutation to generate a new generation: $p=p_{new}$.

Step 5: Evaluate the new generation by comparing with the binding conditions. If the criteria of interest are not satisfied, go to step 3 with $p=p_{new}$; else, stop and save the best individual: $p_{opt}=p_{new}$.

6. SIMULATION RESULTS

6.1 Optimization results

Thanks to the Genetic algorithms method, Table (4) synthesis the values of the variables Z_i, Z_{5j} in five cases for $\alpha=[1;0.85;0.65;0.5;0]$. When $\alpha=1$, it means that $f=f_{\text{Normalized\_load\_transfer}}$, the optimal problem focuses only on the normalized load transfers and when $\alpha=0$, it means that $f=f_{\text{Torque}}$, the optimal problem focuses only on the torques generated.

Table 4: Optimization results for the weighting functions of H_∞ active anti-roll bar.

Controllers	W_{z1}	W_{z2}	W_{z3}	W_{z4}	W_{z5}				
	Z_1	Z_2	Z_3	Z_4	Z_{51}	Z_{52}	Z_{53}	Z_{54}	Z_{55}
SSSC2016 [18]	150000	200000	1	1	1	0.0005	50	100	0.01
$\alpha=1$	258762.34	259996.91	0.91	0.64	0.97	0.46	392.54	801.38	0.22
$\alpha=0.85$	273598.36	295104.17	0.45	0.26	1.17	0.80	334.15	968.50	0.16
$\alpha=0.65$	112322.78	110837.28	0.72	0.75	0.63	0.54	139.23	97.46	0.02
$\alpha=0.5$	166902.22	196036.53	1.09	0.92	0.97	0.0005	54.19	116.64	0.01
$\alpha=0$	50	50	1.59	0.83	0.50	0.43	1	683.05	0.024

Fig. 4 shows the conflicting relation between the normalized load transfers and torques generated with some Pareto-optimal points, computed for the active anti-roll bar on heavy vehicle. They are generated for different values of α in the range of [0;1]. For $\alpha=0$, f_{Torque} is minimized and conversely for $\alpha=1$, $f_{\text{Normalized\_load\_transfer}}$ is minimized.

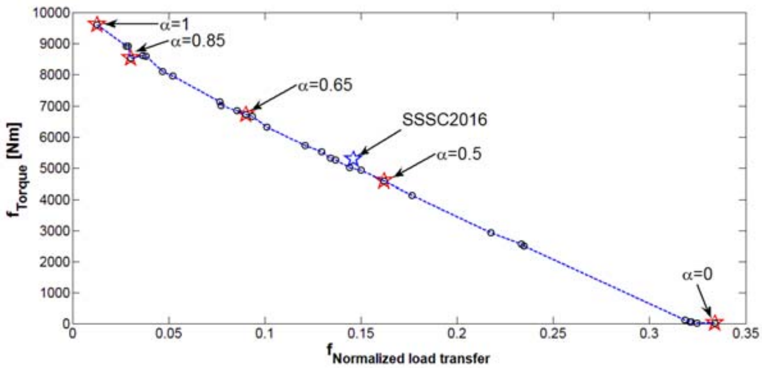

Fig. 4 The optimization results of some points in the Pareto frontier for the active anti-roll bar on heavy vehicle.

6.2 Evaluation of optimization results in frequency domain

The limited bandwidth of the driver must be considered up to *4rad/s* to identify any resonances in the response that may be excited by the driver [5]. Therefore, it is necessary to consider the behaviour of the heavy vehicle in a wider frequency range. In this section, the frequency response of heavy vehicle is shown in the nominal parameters case of the single unit heavy vehicle considered, characterized by the sprung mass $m_s = 12487kg$, the forward velocity V at *70 km/h* and the road adhesion coefficient $\mu = 1$.

Figs. 5 and 6 show the normalized load transfers at the two axles $R_{f,r}$. They show that in the cases $\alpha = [1;0.85;0.65]$, H_∞ active anti-roll bar controllers reduce well the normalized load transfers compared to that of the case passive anti-roll bar and of the case of the previous paper [18] which are chosen by trials and errors.

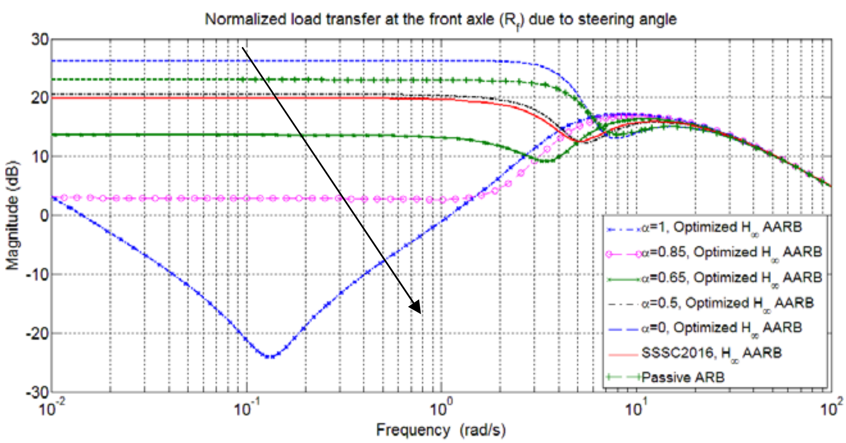

Fig. 5 Frequency responses of the normalized load transfer at the front axle (R_f) due to steering angle.

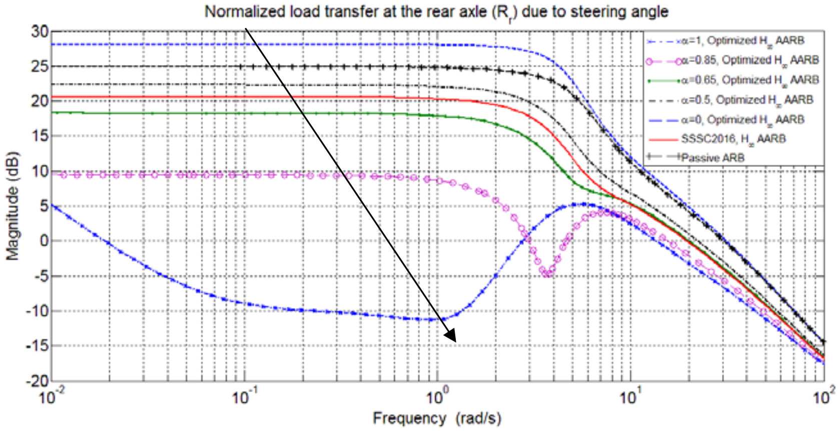

Fig. 6 Frequency responses of the normalized load transfer at the rear axle (R_r) due to steering angle.

6.3 Evaluation of optimization results in time domain

In this section, the considered vehicle manoeuvre is cornering [5].

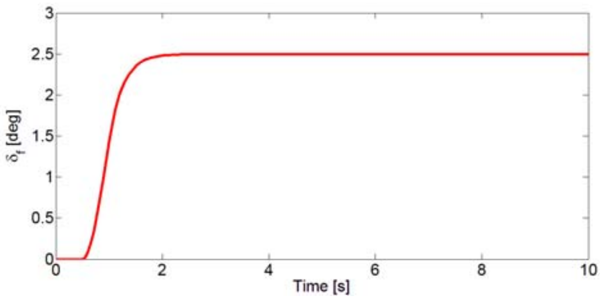

Fig. 7 Steering angle δ_f during cornering maneuver.

Fig. 8 a,b show the normalized load transfers and *Fig 8c,*d show the torques generated at two axles when the forward velocity is considered at *70 km/h*. When the value of α increases, the controllers reduce the normalized load transfers, but the torques generated by the actuators are higher. This fulfils consistently the objective of optimal design.

The forward velocity of the heavy vehicle continuously varies during operation of the heavy vehicle, especially in the case of an emergency. The rollover of heavy vehicle often occurs for forward velocity within *60* to *110 km/h*. In Figs. 9 and 10 we consider the forward velocity of the heavy vehicle up to *160 km/h* in order to evaluate the roll stability, as well as to determine the maximum forward velocity at which the normalized load transfers and the torques generated reach the limitations. In what follows, the disturbance is the steering angle *(δ_f)* corresponding to a cornering maneuver. From Fig. 9*,* we can see that the maximum absolute value of normalized load transfers at the front axle reaches the limit *"1"* in the case of $\alpha = [1; 0.85; 0.65; 0.5]$ where the forward velocities are respectively *134, 131, 123, 104 km/h.* Note that in the previous paper [18] we got *107 km/h* for the forward velocity.

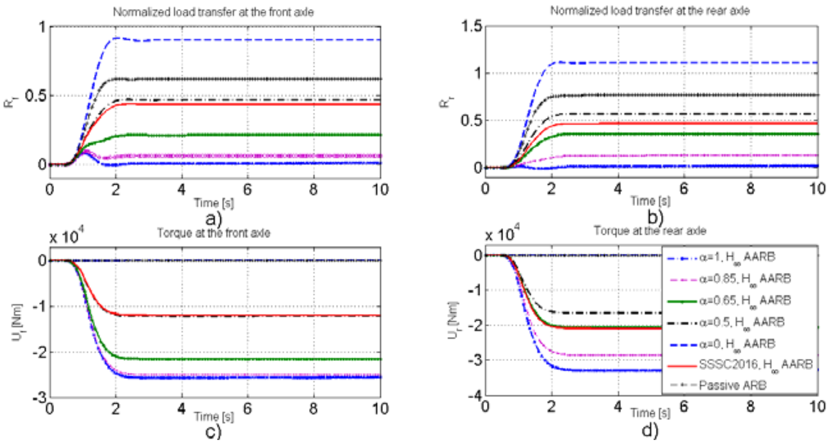

Fig. 8 Time responses of the normalized load transfers ($R_{f,r}$) and torques generated at the two axles.

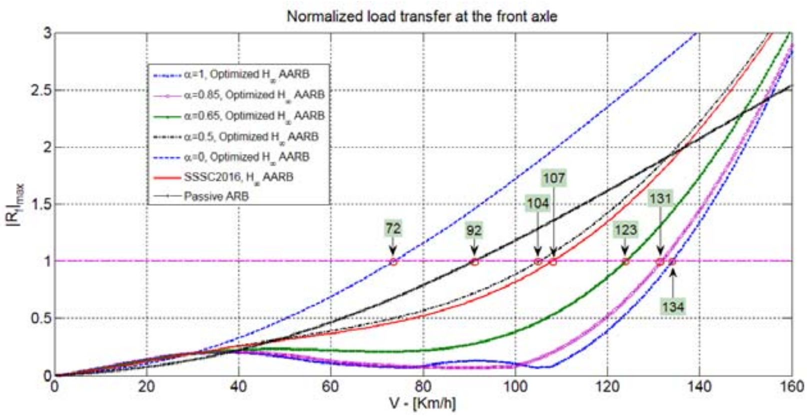

Fig. 9 Effect of the forward velocity on the normalized load transfer: front axle R_f.

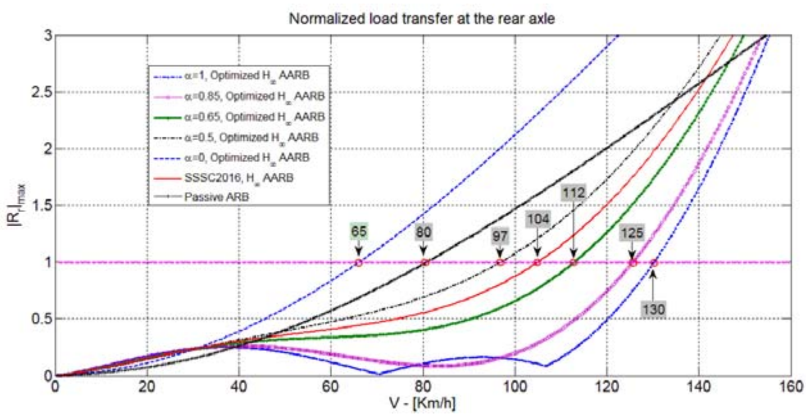

Figure. 10 Effect of the forward velocity on the normalized load transfer: rear axle R_r.

Considering Fig. 10, the maximum absolute value of the normalized load transfers at the rear axle reachs the limit *"1"* in the case of $\alpha = [1; 0.85; 0.65; 0.5]$ where the forward velocities are respectively *130, 125, 112, 97 km/h.* Note that in the previous paper [18] we got *104 km/h* for the forward velocity. In fact, the forward velocities of heavy vehicles are often considered up around *100 km/h*, so that choosing α between 1 and 0.65 is convenient.

7. CONCLUSIONS

In this paper, a weighting function optimization procedure using GAs for H_∞ active anti-roll bar control on single unit heavy vehicle has been proposed. The conflicting objectives between the normalized load transfers and generated torques are handled using only one high level parameter, which is a great advantage to solve the multi-objective control problem. The simulation results in frequency and time domains have shown the efficiency of GAs in finding a suitable controller to satisfy some performance objectives.

Even if other structures for the weighting functions could be used, the ones used in this paper are shown to be simple enough while being efficient to solve the problem. For future works, the comparison with an LPV controller (scheduled by the vehicle velocity) will be of interest.

8. REFERENCES

[1] Alfaro-Cid, E. - McGookin, E.W. - Murray-Smith, D.J.: Optimisation of the weighting functions of an H_∞ controller using genetic algorithms and structured genetic algorithms. International Journal of Systems Science, 2008, p.335–347.

[2] **Boada, M. - Boada, B. - Quesada, A. - Gaucha, A. - Daz, V.:** Active roll control using reinforcement learning for a single unit heavy vehicle. In 12th IFToMM World Congress. Besancon, France, 2007.

[3] **Davis, L.D.:** Handbook of genetic algorithms. Van Nostrand Reinhold, 1991.

[4] **Do, A.L. – Soualmi, B. - Lozoya-Santos, J. - Sename, O. - Dugard, L. - Ramirez-Mendoza, R.:** Optimization of weighting function selection for H_∞ control of semi-active suspensions, Proceedings of the 12th MINI Conference on Vehicle System Dynamics, Identification and Anomalies (VSDIA 2010). (Ed. by Prof. I. Zobory), BME, Department of Railway Vehicles and Vehicle System Analysis, Budapest, Hungary, 2011, p.471- 484.

[5] **Gáspár, P. - Bokor, J. - Szászi, I.** The design of a combined control structure to prevent the rollver of heavy vehicles. European Journal of Control, 2004. (p.148–162).

[6] **Gáspár, P. - Bokor, J. - Szászi, I.:** Reconfigurable control structure to prevent the rollover of heavy vehicles. Control Engineering Practice, 2005a. (p.699–711).

[7] **Gáspár, P. - Szabó, Z. - Bokor, J.:** Prediction based combined control to prevent the rollover of heavy vehicles. In Proceedings of the 13th Mediterranean Conference on Control and Automation. Limassol, Cyprus, 2005b.

[8] **Goldberg, D.:** Genetic Algorithms in Searching Optimisation and Machine Learning. Addison-Wesley Longman, 1989.

[9] **Holland, H.J.**: (1975). Adaptation in natural and artificial systems, an introductory analysis with application to biology, control and artificial intelligence. Ann Arbor, The university of Michigan Press.

[10] **Kitsios, I. - Pimenides, T.:** H_∞ controller design for a distillation column using genetic algorithms. Mathematics and Computers in Simulation, 2002.

[11] **Miller, B.L. - Miller, B.L. -, Goldberg, D.E., and Goldberg, D.E.** Genetic algorithms, tournament selection, and the effects of noise. Complex Systems, 1995, p.193–212.

[12] **Sampson, D. - Cebon, D.:** An investigation of roll control system design for articulated heavy vehicles. In 4th International symposium on Advanced Vehicle Control, AVEC1998. Nagoya, Japan, 1998.

[13] **Sampson, D. - Cebon, D.:** Achievable roll stability of heavy road vehicles. In Proceedings of the Institution of Mechanical Engineers, Part D: Journal of Automobile Engineering, volume 217, United Kingdom, 2002.

[14] **Sampson, D. - Cebon, D.:** Active roll control of single unit heavy road vehicles. Vehicle System Dynamics: International Journal of Vehicle Mechanics and Mobility, 40(4), 2003, p.229–270.

[15] **Scherer, C. Weiland, S.:** Linear matrix inequalities in control, University Lecture, 2005.

[16] **Skogestad, S. - Postlethwaite, I.:** Multivariable Feedback Control. John Wiley & Sons, 2 edition, 2001.

[17] **Vu, V.T. - Sename, O. - Dugard, L. - Gáspár, P.:** Active anti-roll bar control using electronic servo-valve hydraulic damper on single unit heavy vehicle. In IFAC Symposium on Advances in Automotive Control - 8th AAC 2016, Sweden, 2016.

[18] **Vu, V.T. - Sename, O. - Dugard, L. - Gáspár, P.:** H_∞ active anti-roll bar control to prevent rollover of heavy vehicles: a robustness analysis. In IFAC Symposium on System Structure and Control - 6th SSSC 2016, Turkey, 2016.

OPTIMIZATION OF RAILWAY TRANSITION CURVES FOR DIFFERENT CURVE RADII

Krzysztof ZBOINSKI and Piotr WOZNICA

Department of Transport Infrastructure, Faculty of Transport
Warsaw University of Technology
Koszykowa 75, 00-662 Warsaw, Poland

Received: November 7, 2016

ABSTRACT

In this article the assessment of the dynamical properties and shape optimization of railway transition curves (TCs) for the range of curve radii was made. The search for the proper shape means the evaluation of the curve properties based on chosen dynamical quantities and generation of a such shape with use of mathematically understood optimization methods. As a transition curve in the studies performed the authors adopted a polynomial of *n*-th degree, where *n*=9, 11. In the study one model of vehicle was used. The model represents 2-axle freight car of the average values of parameters. The authors took the so-called standard transition curves of 9^{th} and 11^{th} degrees as an initial TCs in the optimization processes. As objective functions (evaluation criteria) authors used the 5 functions concerning the vertical dynamics, namely the displacements and accelerations of vehicle body. In optimization process the authors used two sets of stiffness values of the suspension elements in the vehicle model and observed their influence on optimization results and on the vehicle body dynamics. In this work results of the optimisation – the curvatures of the optimum transtion curves and both lateral and vertical displacements and accelerations of vehicle body – were presented and compared.

Keywords: railway transition curve, optimisation, computer simulation

1. INTRODUCTION

The subject of the research done by the authors of this article is the assessment of the dynamical properties and shape optimization of railway polynomial transition curves (TCs). Here, the search for the proper shape means the evaluation of the TC properties based on chosen dynamical quantities and generation of a such shape with use of mathematically understood optimisation methods. As a TC in the studies performed the authors adopted a polynomial of *n*-th degree, where *n*=9 and 11. For these two degrees formulas for curve lateral co-ordinate, curvature, superelevation, and inclination of superelevation ramp were determined ([3], [4]). The authors took into account only basic condition, which the transition curve must satisfy, i.e. proper values of curvature and superelevation ramp in start and end point of the curve. Number of the terms of the polynomial for the basic condition was *n*-2.

The degree of polynomial (*n*=9 and 11) was not chosen accidentally. TCs of higher degrees, due to higher number of polynomial terms, are more flexible and thereby the set of number of potential solution is bigger. Also in the earlier works of authors of current article TCs of such degrees had the best dynamical properties (e.g. [5]).

The aim of this work is the optimization of railway polynomial TCs of 9^{th} and 11^{th} degrees with use of non-traditional assessment criteria (quality functions *QFs* concerning the vertical dynamics) and full rail vehicle model. The optimization of the shape meant always the minimization of the value of *QF* adopted. In this work the authors also wanted to check, whether new assessment criteria taken to the analysis will give in result so-called smooth TCs (the class of the function of curvature is C^1 and there exists G^1 continuity in the terminal points of the curve). Radii *R* of circular arc were equal to 600 m, 1200 m and 2000 m, while superelevations H were assumed to be equal to 0.15 m, 0.075 m and 0.045 m, respectively. For the given values of R and H, the authors always calculated two velocities of vehicle. The lower velocity always corresponded to lateral acceleration in the plane of track a_{lim} equal to 0 m/s^2, whereas higher velocity corresponded to unbalanced lateral acceleration equal to 0.3 m/s^2 or 0.6 m/s^2. The lengths of TCs were calculated according to the algorithm given in detail in [1]. The authors also took two TCs (of 9th and 11th degree) from [2] as an initial TCs in these processes.

2. VEHICLE MODEL

In the study one model of wagon was used. The same model was used in previous works of the authors, e.g. in [4]. The model represents 2-axle freight car of the average values of parameters. One can find all parameters of the vehicle-track system analysed in [6]. In current work the authors used two values of longitudinal and lateral stiffness in the suspension elements of the vehicle model - k_{zx}=800 kN/m and k_{zy} =800 kN/m (soft suspension) and k_{zx}=4000 kN/m and k_{zy} =4000 kN/m (stiff suspension).

3. QUALITY FUNCTIONS

In the study the authors used the following 5 quality functions:

$$QF_1 = max\left|z_b\right|, \tag{2.1}$$

$$QF_2 = L_C^{-1}\int_0^{L_C}\left(z_{lp} + z_{rp} + z_{lk} + z_{rk}\right)dl\,, \tag{2.2}$$

$$QF_3 = max\left|\varphi_b\right|, \tag{2.3}$$

$$QF_4 = L_C^{-1}\int_0^{L_C}\varphi_b\,dl\,, \tag{2.4}$$

$$QF_5 = L_C^{-1}\int_0^{L_C}\ddot{\varphi}_b\,dl\,, \tag{2.5}$$

where: L_C – length of whole TC and the adjacent 100 m of circular arc, z – vertical displacement of vehicle mass element, φ – angular displacement (roll rotation) around x axis, $\ddot{\varphi}$ – angular acceleration (roll acceleration) around x axis. Indices l, r, p, k and b refer to left hand-side, right hand-side, front (leading) wheelset, rear (trailing) wheelset, and vehicle body, respectively.

The *QFs* were not also chosen accidentally. The courses of the selected parameters – z, φ and $\ddot{\varphi}$ – differed significantly in the TC and circular arc sections. For the other parameters the differences were relatively small – also for the other routes – and it was difficult to state, which TC had the best dynamical properties. The authors did also the second selection of *QFs* among the 5 *QFs* initially chosen. They were aware, that the improvement of value of *QF* doesn't mean the improvement of vehicle dynamics. Here such case has place for QF_2 and QF_4. Fig. 3.1 shows the angular displacements of vehicle body before and after the optimization for QF_4. The integral from this criterion has in fact miminum value, but the vehicle dynamics is worse. Despite this fact the authors used these 2 *QFs* in TC' shape optimization.

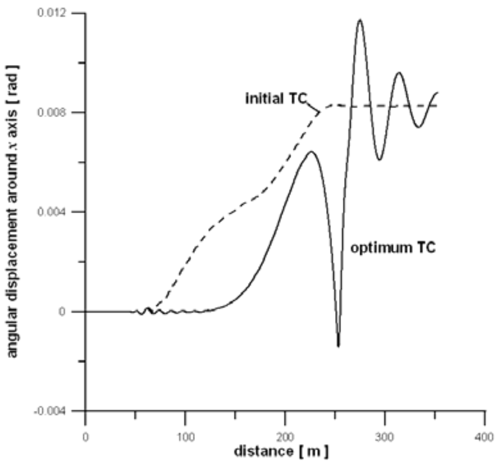

Fig. 3.1. Angular displacement of vehicle body around *x* axis

4. THE RESULTS OF TCs' SHAPE OPTIMIZATION

In order to achieve the aim of this work the authors obviously performed optimization of the TCs' shape. As the quality function they adopted 5 *QFs* decribed in section 3 of current work. The values of parametres applied in optimization for given values of *R* and *H* (l_0, v and a_{lim}) are presented in Tabs. 4.1-4.3.

Generally each polynomial TC obtained in the work had the curvature (superelevation ramp), which may be qualified to one of 4 groupes. These 4 groupes (types) and extra group for 3rd degree parabola are:

1) type 1 – curvature (superelevation ramp) is in practise very similar to the curvature of standard TC of 9th and 11th degree ([5]),
2) type 2 – curvature (superelevation ramp) is something between standard TC of 9th and 11th degree and 3rd degree parabola ([5]),
3) type 3 – linear curvature (superelevation ramp) of 3rd degree parabola,
4) type 4 – curvature (superelevation ramp) has convex character. It has slope subtype (4a) or G_1 continuity subtype (4b) at the beginning of TC and it has slope at the end,
5) type 5 – curvature (superelevation ramp) has concave character. It has slope at the beginning of TC and it has slope subtype (5a) or G_1 continuity subtype (5b) at the end.

Going to the analysis of the types of TCs presented in Tabs. 4.1-4.3, we see, that, despite the same starting point, program found different optimum shapes of TCs. The majority of the curvatures obtained had only G_0 continuity in terminal points of the curve. The biggest number of TCs obtained – 74 among 120 cases analysed – had the type no. 4 of the curvature. Here, the system tended to keep the large curve radius *R* as long as possible. It is the most visible for QF_2. For the rest *QFs*, it is not so obvious. It is also the most visible for the larger curve radii *R*=1200 and 2000 m (Tabs. 4.2 and 4.3) and the smaller lenghts of TCs (<120 m). For the curve radius *R*=600 m and big lengths (Tabs. 4.1), optimum TCs had all the types of curvature.

Note, that the authors assumed 60 different conditions of optimization (3 *R* x 2 *n* x 2 *v* x 5 *QFs*). For each of conditions two optimization were always made, namely for vehicle model with the soft and stiff suspension. In 46 cases among all 60 conditions the program found optimum TCs having the curvature of the same type. It is equally visible for the all curve radii. It may indicate, that two considered suspension types of the vehicle had relatively small impact on the shape of the optimum TCs.

Tab. 4.1. Types of curvatures - *R*=600 m, *H*=150 mm

n	*v* [m/s]	a_{lim} [m/s^2]	Suspension	QF_1	QF_2	QF_3	QF_4	QF_5	Length [m]
9	24.26	0	soft	1	4b	3	4a	2	142.15
			stiff	1	4b	4a	4a	2	
	30.79	0.6	soft	1	4b	2	4b	2	180.46
			stiff	1	4b	1	4b	1	
11	24.26	0	soft	1	4b	3	4a	2	159.86
			stiff	1	4b	3	4a	2	
	30.79	0.6	soft	1	4b	2	4b	1	202.94
			stiff	1	4b	1	4b	1	

Tab. 4.2. Types of curvatures - *R*=1200 m, *H*=75 mm

n	*v* [m/s]	a_{lim} [m/s^2]	Suspension	QF_1	QF_2	QF_3	QF_4	QF_5	Length [m]
9	24.26	0	soft	4a	4a	4a	3	4a	71.07
			stiff	4a	4a	4a	3	4a	
	36.17	0.6	soft	1	4a	4a	5b	4a	105.98
			stiff	1	4a	4a	5b	4a	
11	24.26	0	soft	4a	4a	4a	4	3	79.93
			stiff	2	4a	4a	4	4a	
	36.17	0.6	soft	2	4a	3	2	4a	119.18
			stiff	2	4a	4a	5b	4a	

Tab. 4.3. Types of curvatures - *R*=2000 m, *H*=45 mm

n	*v* [m/s]	a_{lim} [m/s^2]	Suspension	QF_1	QF_2	QF_3	QF_4	QF_5	Length [m]
9	24.26	0	soft	4a	3	3	4a	4a	42.64
			stiff	4a	4a	3	3	4a	
	34.47	0.3	soft	4a	3	4a	5a	4a	60.60
			stiff	4a	4a	4a	3	4a	
11	24.26	0	soft	4a	4a	3	3	4a	47.95
			stiff	4a	4a	4a	4a	4a	
	34.47	0.3	soft	4a	4a	4a	4a	4a	68.15
			stiff	4a	4a	4a	4a	4a	

In Fig. 4.2 the authors have shown example curvatures of the obtained optimum polynomial TCs for 9th degree - *R*=1200 m, *H*=75 mm, *v*=24.26 m/s - for vehicle with two kinds of suspension and the superelevation ramp slopes coresponding to them compared with courses for standard initial TC. Courses for the initial TC are marked

INI TC, whereas the courses for the soft and stiff suspension – optimum TC 1 and optimum TC 2, respectively. Figure 4.2a shows, that the program has found the optimum curvatures (of type no. 4) only slightly different from each other. All of them do not have a tangence (G_1 continuity) in the terminal points, although theoretically it was possible to find TCs possessing which have such a tangence. Figure 4.3 shows both the lateral displacements and accelerations of the mass centre of the vehicle body. Figures 4.4-4.5 show both the vertical and angular displacements and accelerations of the vehicle body.

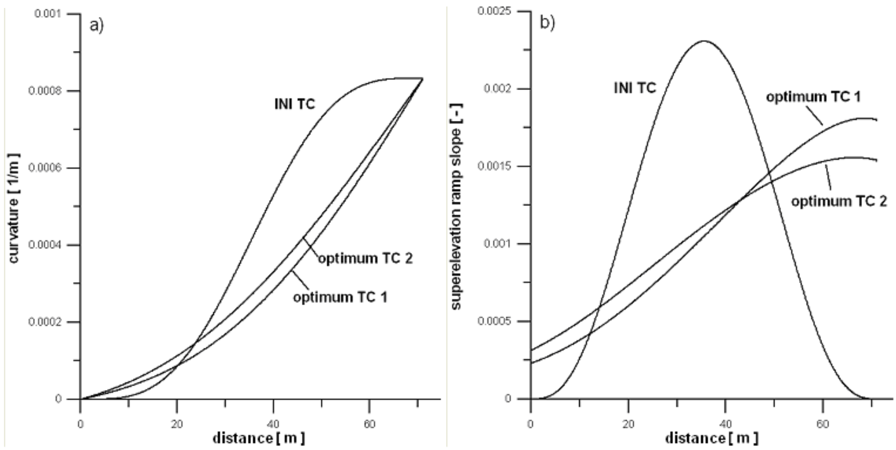

Fig. 4.2. a) curvatures, b) superelevation ramp slopes of the optimum TCs

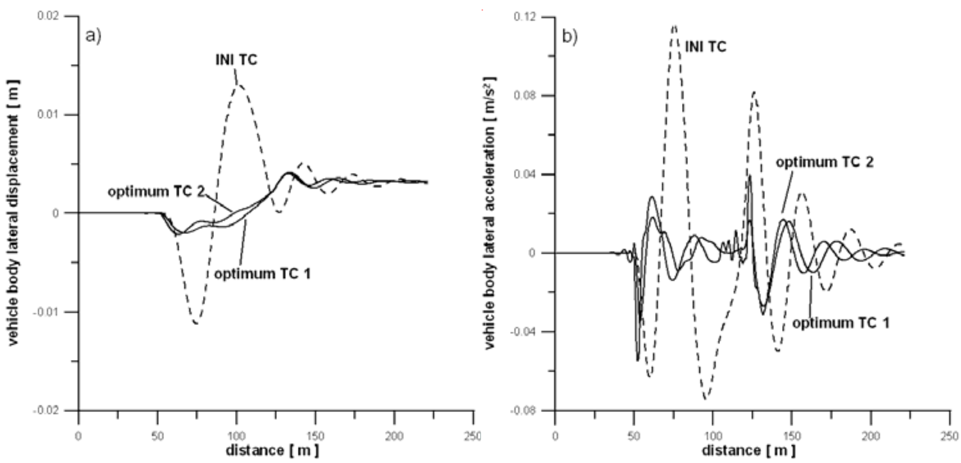

Fig. 4.3. Dynamical characteristics: a) lateral displacements, b) lateral accelerations of vehicle body mass centre

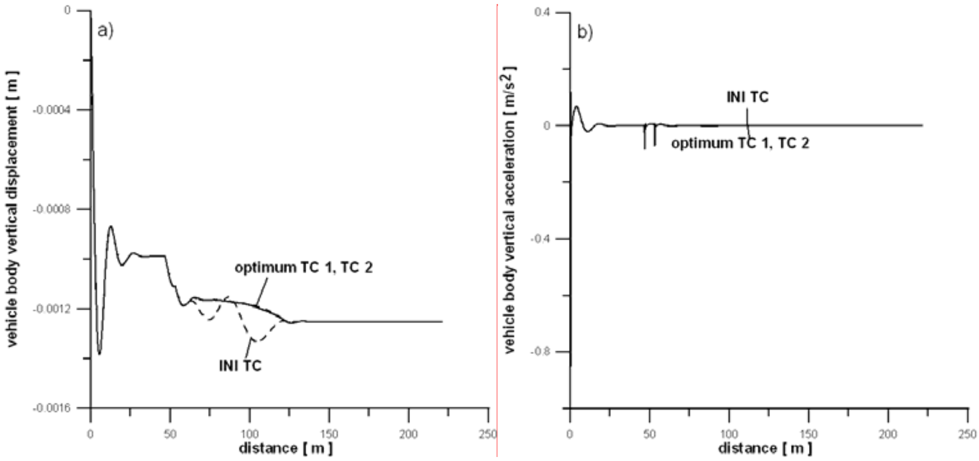

Fig. 4.4. Dynamical characteristics: a) vertical displacements, b) vertical accelerations of vehicle body mass centre

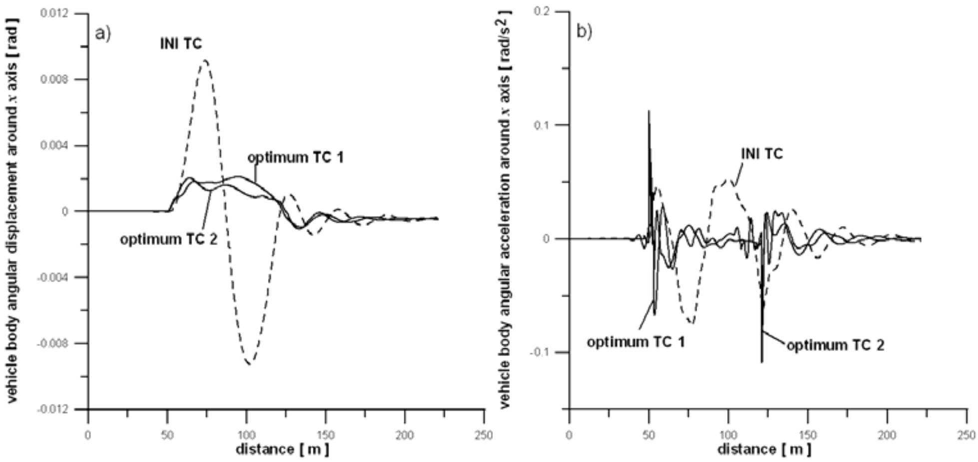

Fig. 4.5. Dynamical characteristics: a) angular displacements, b) angular accelerations of vehicle body around x axis

Analysis of Figs. 4.2-4.5 leads to conviction, that apart from the obvious improvement of vehicle dynamics after the optimization, the use of 2 types of vehicle suspension gives the chance to obtain very similar TCs. This off course results in similar vehicle dynamics and the values of *QFs*. The lateral coordinate of optimum TC for case with soft suspension is:

$$y=\frac{1}{600}\left(-0.0021\cdot\left(\frac{l^9}{142.15^7}\right)+0.0065\cdot\left(\frac{l^8}{142.15^6}\right)+0.0137\cdot\left(\frac{l^7}{142.15^5}\right)+0.0068\cdot\left(\frac{l^6}{142.15^4}\right)\right.$$
$$\left.+0.0279\cdot\left(\frac{l^5}{142.15^3}\right)+0.0320\cdot\left(\frac{l^4}{142.15^2}\right)+0.0364\cdot\left(\frac{l^3}{142.15^1}\right)\right). \tag{5.1}$$

5. THE LOCAL MINIMA PROBLEM

The problem of finding the local optimum instead of the global one by optimization algorithms is as old as the optimization algorithms. Most of the algorithms find only a local minimum, in a neighborhood of the starting point. Therefore finding the global minimum depends on the choice of the starting point. The library procedure used by the authors belongs to a such group of algorithms. If the system studied has physical characteristics resulting in the occurrence of local minimum, instead of only a single global minimum, we have to face the problem of proper selection of the starting point (initial TC). It is highly recommended, that a few starting points are tested, e.g. 3.

In the previous section the authors presented examples, where despite the same starting point (a significant influence on the solution had the choice of *QF*) the program found different TCs. In this section the authors present the examples, where different starting point was the main cause of finding different solutions.

The reason of undertaking the research of this issue is fourth column in Tab. 4.1. In all cases for QF_1 the program found the optimum TC having the curvature of type no. 1. It means, that initial TC is probably at least local optimum. The authors therefore made additionall 8 optimizations for 9th degree and QF_1, where the new starting points were: 3rd degree parabola and the TC marked by the formula (5.1). In Tab. 5.1 the authors presented types of the curvatures and the values of *QFs* obtained in these optimizations and compared with the types and the values from the previous section.

Going into the analysis of the types of TCs obtained and presented in Tab. 5.1, we may conclude, that for 4 cases analyzed (2 vehicle velocities and 2 types of suspension) the smallest values of *QFs* exist for the optimum TC having the curvature of types no. 1, 2 and 5. All values of *QFs* are given in brackets while the smallest ones are in bold. The optimizations performed showed, that TC having the curvature of type no. 1 is probably the global optimum in 2 cases analyzed. The differences in *QFs* values are very small for them. It is probably caused by the fact, that for big lengths of the TC, i.e. 142.15 m and 180.46 m, the differences in values of the curvatures for particular length are relatively small.

This case shows the sensibleness of the use of bigger number of starting points. It is also worth of noting, that two types of suspension of the vehicle, as before, had relatively small impact on the optimum shape of the TCs. It can be seen, when one compares the values of *QFs* for each of 12 optimizations performed.

Tab. 5.1. Types of curvatures - *R*=600 m, *H*=150 mm

n	***v* [m/s]**	**Suspension**	**Initial TC= standard TC**	**Initial TC= 3rd degree parabola**	**Initial TC= TC (5.1)**	**Length [m]**
9	24.26	soft	1 (0.0015278 m)	**5b (0.0015269 m)**	4a (0.0015351 m)	142.15
		stiff	**1 (0.0015283 m)**	1 (0.0015319 m)	4a (0.0015350 m)	
	30.79	soft	**1 (0.0020044 m)**	5b (0.0020094 m)	2 (0.0020132 m)	180.46
		stiff	1 (0.0020038 m)	5b (0.0020042 m)	**2 (0.002005 m)**	

6. CONCLUDING REMARKS

As a result of the discussed studies quite a few original and important conclusions can be presented.

First of all, the inclusion into the analysis of the vertical displacements and accelerations of vehicle body centre of mass and the angular displacement and acceleration of the body has changed both the assessment of the curves and the results of optimization. Generally, for QF_1, QF_3 and QF_5 the biggest number equal to 39 of the optimum shapes of transition curves of 9th and 11th degree had the curvatures of type no. 4. The curves of these degrees obtained previously [5] and having the curvatures of type no. 2 were optimum TCs in 10 cases, mainly for big lenghts of the curves.

Secondly, the new *QFs* used in the work did not let to obtain in all cases the optimum *TCs* with curvatures (superelevation ramps slopes) having G^1 continuity in terminal points of a curve. Such continuity, both in the first and the last point of the curve, had only the some TCs.

Lastly, the study showed the examples illustrating the difficulties, that may be encountered due to the existence of local minima. According to the authors, the problem is feasible. However, if we want to recommend new shapes for practical use, it is necessary to ascertain, whether we did not omit solutions better than we have found. In this context, an important for practice remark is that in the case of high degrees of TCs and the maximum number of terms the probality of a such omission drops significantly.

7. REFERENCES

[1] **Koc, W. – Radomski, R.**: Analiza krzywych przejściowych z nieliniowymi rampami przechyłowymi (Analysis of transition curves with nonlinear superelevation ramps - in polish). Drogi Kolejowe, 11, 1985.

[2] **Long, X.Y. – Wei, Q.C. – Zheng, F.Y.**: Dynamical analysis of railway transition curves. Proc. IMechE part F Journal of Rail and Rapid Transit, 224(1), 2010.

[3] **Zboinski, K. – Woznica, P.**: Formation of railway transition curves based on advanced dynamic vehicle models. Proc. of the Tenth International Conference on Computational Structures Technology, Civil-Comp Press, 2010.

[4] **Zboinski, K. – Woznica, P.**: Optimisation of the railway transition curves' shape with use of vehicle-track dynamical model. Archives of Transport, 22(3), 2010.

[5] **Zboinski, K. – Woznica, P.**: Optimisation of railway polynomial transition curves: a method and results. Proc. of the First International Conference on Railway Technology: Research, Development and Maintenance, Civil-Comp Press, 2012.

[6] **Zboinski, K.**: Dynamical investigation of railway vehicles on a curved track. European Journal of Mechanics A-Solids, Vol. 17, no. 6, 1998.

MODEL OF HIGH-SPEED TRAIN ENERGY CONSUMPTION

P-O. VANDANJON[1], R. BOSQUET[2], A. COIRET[1] and M. GAUTIER[3]

[1]Université Bretagne-Loire, Ifsttar, AME, EASE, Ifsttar, Route de Bouaye, F-44341 Bouguenais, France

[2]SNCF-Direction du matériel/Ingéniérie du matériel-Centre d'ingéniérie du matériel – F-72100 Le Mans France

[3]Université de Nantes, IRCCyN 1, rue de la Noë BP 92 101, F-44321 Nantes France

Received: November 7, 2016

ABSTRACT

The current transport system is not sustainable because of its high consumption of finite resources (mainly oil) and its impact on the environment (air quality, global warming, etc.). In this context, rail has several advantages: lower consumption and emissions than road and air modes, larger passenger flow, etc. That is why, many rail infrastructures are planned in the world. Today, the impact of energy is not taken into account during the project design. At the project phase of new rail infrastructures, it is nowadays important to characterize accurately the energy that will be induced by its operation phase, in addition to other more classical criteria as construction costs and travel time. Current literature consumption models used to estimate railways operation phase are obsolete or not enough accurate for taking into account the newest train or railways technologies. In this paper, an updated model of consumption for high-speed is proposed, based on experimental data obtained from full-scale tests performed on a new high-speed line. The assessment of the model is achieved by identifying train parameters and measured power consumptions for more than one hundred train routes. Perspectives are then discussed to use this updated model for accurately assess the energy impact of future railway infrastructures.

Keywords: identification, consumption model, high-speed line, high-speed train

1. INTRODUCTION

According to the International Transport Forum at the OECD [1]: Greenhouse gases emissions (GHG) due to the transport sector will increase by 34 % to 106 % between 2010 and 2050 depending on different economic scenarios. In the same time, the experts of the intergovernmental panel on climate change recommend to stabilize these GHG emissions from the transport sector in order to follow the representative concentration pathway 2.6 (RCP 2.6) to keep the global warming below 2° [2]. These two studies imply that our actual transport system is not sustainable.

One solution, among others, is to switch from the petrol to the electricity as energy source for the transport system. It will be very advantageous for countries where the electricity mix has a low carbon content as in France (due to the nuclear power) or in Norway (due to the hydraulic power).

In this context, high speed trains offer many advantages, as consuming significantly less energy than road or air transports. According to Akerman [3], high-speed transport consuming roughly 4 times less energy use than road transport and 9 times less than air transport (expressed as kilowatt-hour by passenger-kilometer - kWh/pkm). Even if Chester and Horvath [4] moderates this result with the life cycle assessment point of view, rail modes have the smallest energy consumption. So, about 10,000 km of tracks are under construction in the world and more than 15,000 km are planned as determined by UIC [5].

At a railway project, several alternative routes are usually studied. The final choice of the rail line is the output of a complex process including numerous actors as described by

Leheis [6]. The different stakeholders (national government, local authorities, local residents, economic sector, ecological associations, etc.) request objective methods in order to enlighten public debates. Our contribution is to propose a consumption model for high speed train in order to simulate different scenarios. Our first result was described in [7]. In this actual paper, an updated model is proposed which is a major improvement in comparison with this first paper by modelling the power for the mechanical and electrical part of the system. Moreover, the identification process is based on a robotic technique called IDIM-LS, more robust than the technique used in the first paper. This new approach yields to a more consistent and more accurate comprehensive model.
The next section builds the consumption model. This model depends linearly on parameters which are identified in the section 3 through experimental data. The last section concludes this paper.

2. COMPREHENSIVE MODEL

In this topic, the first approach is to reduce the train to a point and to apply the Newton's second law to this point. Lukaszewicz [8] or Rochard and Schmid [9] give an interesting general formulation of running resistance as a function of train characteristics like mass, number of bogies, inter-vehicle gap, number of pantographs, etc. Unfortunately in those models, the maximum speed is generally lower than 300 km/h although the projects speed of a new high-speed line are at least 350 km/h. Formulation presented in the current paper is an adaptation of these literature models to higher speeds by taking into account test data. Particularly, for high speeds, aerodynamic have to be analysed more accurately. Raghunathan et al. [10] study it for Shinkansen and their approach is adapted to the TGV Dasye in this paper.
Then, the second step of the model review is to gather knowledge on the method to convert the force developed by the train (based on a physical model) in energy consumption. Lindgreen and Sorenson [11] and Boullanger [12] propose a consumption model with information about engine efficiency, loss of auxiliary equipment and transformer. These models will not directly be used in this paper since they are not suitable for the electric French case (25 kV 50 Hz AC) and high-speed train.
Our comprehensive model is the union of a mechanical model and an electrical model. They are described in the following paragraphs.

2.1 The Mechanical Model

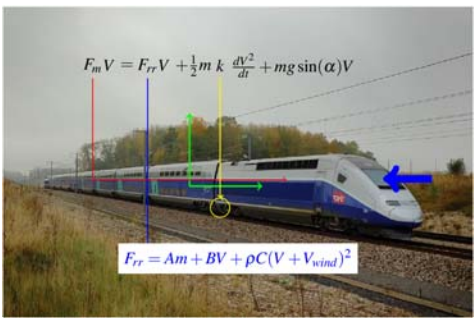

Fig. 1 The Mechanical model

The mechanical model, described by figure 1, associated with the theorem the derivative of the mechanical energy is equal to the power of the non-conservative forces yield to the following equation :

$$F_m V = F_{rr} V + \frac{1}{2} mk \frac{dV^2}{dt} + mg \sin(\alpha) V \tag{1}$$

F_m is the tractive force produced by the driving chain including the motor at the drive wheels; V is the speed of the train; m is the mass; k is the conventional coefficient, it represents inertia of rotating masses; α is the slope of the rail line;

F_{rr} is the running resistance and is composed of the following physical effects.

- Rolling resistance: it is related to the contact wheel rail. As a first approximation, it is considered as constant. Because of sticking effect, this value is not the same when the train is stop or sets in motion.
- Mechanical resistance: it consists of friction which are viscous friction F_c, depending mainly of the velocity, and the dry friction F_s , which can be considered as constant (unless when the train starts for the same reason as for the rolling resistance).
- Aerodynamic resistance, related to drag coefficient C_x , and the weather conditions (wind, rain, etc...). This resistance depends mainly on the squared velocity.

By taking into account the previous physical interpretation, this resistance force (F_{rr}) is approximated by a second order polynomial [9]:

$$F_{rr} = Am + BV + \rho C (V + V_{wind})^2 \tag{2}$$

ρ is the air density; V_{wind} is the speed of the wind along the direction of the speed of the train; A, B, C are coefficients depending on the rolling stock.

One speciality of our model is to multiply only A by the mass m. In [9], all the right side of the equation (2) is multiplied by the mass m. Our model is an adaptation of the classical models to High-Speed train for which the C term plays a major role and is not substantially influenced by the mass.

In our model, the resistance force in curve is not modelled. Knowing that the radius of high speed line is superior to 3,000m, and considering the model of this force given in [9], this resistance force can be neglected in a first approach.

2.2 Electrical model

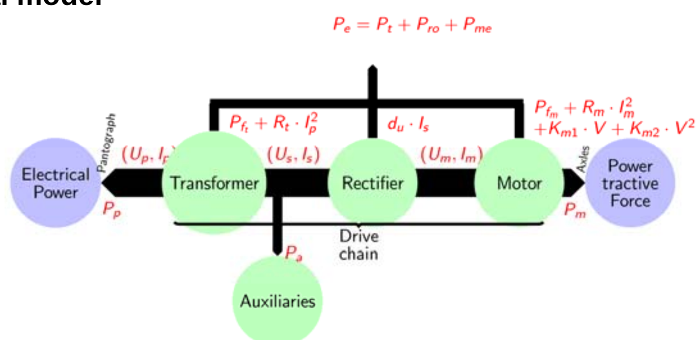

Fig. 2 Electrical model

Fig. 2 displays the electrical model and the different losses at each step of the transformation of the electrical power to the mechanical power. It is based on classical results in Electrical Engineering.

The input of this scheme is P_p the active power exchanged at the catenary with the pantograph. $P_p = U_p I_p \cos(\Phi)$. $U_p I_p$ is the *rms* voltage and current delivered by the pantograph. Φ is the current-voltage phase shift. P_p is positive while the engine is providing traction and is negative while energy-recovery braking system is used.

The output of this scheme is the power computed with the tractive force $P_m = F_m V$. The first step is done by the transformer which decreases the initial voltage: 25 kV to 1kV, the copper losses are $P_{ct} = R_t I_p^2$. As the voltage is assumed constant, the iron losses P_{ft} are constant.

One part of the power after the transformer P_a, is consumed by the auxiliary equipment, they are the cooling of the motor, the air-conditioning system, the lighting. As the tests were carried out in summer during the day, this loss is assumed to be constant.

The rectifier transforms alternative current (AC) to direct current (DC). The losses of the rectifier are proportional to I_s, the secondary current output of the transformer.

$$P_{ro} = d_u I_s.$$

The motor of the train is asynchronous. The power loss is approximated by the following equation.

$$P_{me} = P_{fm} + K_{m1} \cdot V + K_{m2} \cdot V^2 + R_m \cdot I_m^2$$

P_{fm}, K_{m1}, K_{m2} are constant in relation with the iron losses in the stator; I_m is the current in the stator, R_m is an equivalent resistor.

The following equation is calculated by rearranging the previous equations and replacing the currents by the current delivered by the pantograph,

$$P_e = P_F + D_u \cdot I_p + R \cdot I_p^2 + K_{m1} \cdot V + K_{m2} \cdot V^2 \qquad (3)$$

P_F, K_{m1} and K_{m2} are constant in relation with the iron losses; D_u is a constant in relation with the losses in the rectifier; R models the copper losses.

2.3 Comprehensive model

Finally, by combining equations 3 and 1 and regrouping parameters, the final equation of the power is

$$P_p = P_{co} + D_u \cdot I_p + R \cdot I_p^2 + \left[A \cdot m + B \cdot V + \rho \cdot C \cdot (V + V_{vent})^2\right] \cdot V \qquad (4)$$
$$+ m \cdot k \cdot \frac{1}{2} \cdot \frac{dV^2}{dt} + m \cdot g \cdot V \cdot sin\,(\alpha)$$

P_{co}, D_u, R, A, B, C, m, k are parameters of the train (P_{co} regroups the constant terms). V, I_p is the state of the system; ρ, V_{wind} are the meteorological conditions, α is the local slop of the train line.

3. IDENTIFICATION

In the previous equation, some parameters are known thanks to public technical data: the mass of the train, m = 380 tons + estimated weight of the passengers, the model of the rotating inertia, k = 1.04, but most of them are unknown: P_{co} , D_u , R, A, B, C. In order to identify them, data of the acceptance tests of the High-Speed Line Rhin-Rhône were processed. It is the purpose of this section.

4. EXPERIMENT

The acceptance tests of the French Rhin-Rhône high- speed line have been used to obtain experimental data. The line has been opened to the traffic since the end of 2011 and links Mulhouse to Dijon, via Belfort-Montbéliard and Besançon

Numerous tests have been performed on this high-speed line. Among these tests, 130 trial runs (half in the east/west direction, half in the west/east direction) (79 hours of travels) have been carried out for the purpose of this study within a period of three months between June and August 2011. For field testing, 20 sensors were added to the test train. During these tests, geometry, energy, dynamic measurements, direction and velocity of the wind were recorded. A special attention was dedicated to the aerodynamic drag [13]. The test train is the standard French TGV Duplex DASYE (duplex asynchronous ERTMS). Speed, position and active power measured at the pantograph have been recorded at a 5 Hz.

5. RESULTS

A first analysis of the comprehensive model (equation 4) is that the equation is linear in relation to parameters. Then, this equation is rearranging to:

$$y = W \cdot \chi_{bs}$$

W is the observation matrix : $W = \begin{bmatrix} m \cdot V & V^2 & \rho \cdot V \cdot (V + V_{wind})^2 & 1 & I_p & I_p^2 \end{bmatrix}$

χ_{bs} is the vector of the basic parameters: $\chi_{bs} = \begin{bmatrix} A & B & C & P_{co} & D_u & R \end{bmatrix}^t$

$$y = P_p - m \cdot k \cdot \frac{1}{2} \cdot \frac{dV^2}{dt} - m \cdot g \cdot V \cdot \sin(\alpha)$$

A well-known identification technique is to use linear least-squares which solve the optimization program $\hat{\chi}_{bs} = \arg \min_{\chi_{bs}} \|y_m - y\|^2$ where y_m is computed from the measurements. However, the observation matrix is also built with measurements. In this case, the least-squares estimate does not converge to the true value. It is the reason why, a method coming form Robotic: IDIM-LS (Identification Dynamic Inverse Model – Least-Squares) was used (see [14]). It consists, mainly, to apply a filter on each signal and a parallel filter on each column of the observation matrix.

The identification process warns us that two parameters are not identifiable with the given experimental data: A and R. Finally, the following table presents the value of the essential parameters, their standard deviations, their units and the ratio between standard deviation and the value of the parameter.

Essential parameters	$\hat{\chi}_{bs}$	sd($\hat{\chi}_{bs}$)	**SI**	sd($\hat{\chi}_{bs}$)/$\hat{\chi}_{bs}$
B	154	4	kg/s	2 %
C	5.04	0.04	Kg/m	0.8 %
P_{co}	287×10^3	5.3×10^3	W	2 %
D_u	425×10^1	1.4×10^1	V	0.3 %

The parameters are well identified, the ratio sd($\hat{X}_{bs}$)/$\hat{X}_{bs}$ is small. Moreover, we checked the physical meaning of the values by comparing them with fragmented technical data.

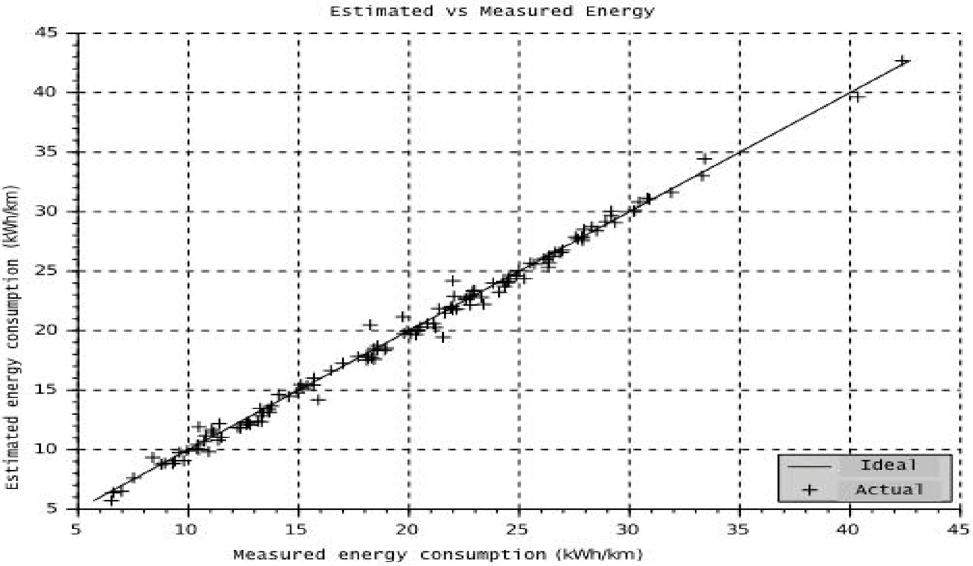

Fig. 3 Validation of the model

Fig. 3 displays a comparison between the measured and estimated energy consumption of the 130 trial runs. 95 % of the energy spent during the tests is explained by our model.

6. CONCLUSION

Numerous high-speed line projects arise due to the energy efficiency of this system of transport. However, it is important to assess in advance the impact of future energy lines. Unfortunately, there was no bibliography for consumption model which can be used to assess different routes from an energy point of view. In this paper, an energy consumption model is proposed to assess operation phase. Along a route, the model provides instantaneous power supply as well for acceleration, deceleration and constant speed phases in function of route profile. Thanks to this model, key infrastructure parameters affecting the energy consumption can be identified (see [15]). The energy consumption of the new 15,000 km of high-speed line, which are planned in the world, represents the issue of such energy models. This study is part of a global methodology called PEAM (Project Energy Assessment Method) which takes into account too the consumption of construction phase. This methodology was applied on the project of the High Speed Line Montpellier-Perpignan [16]. An unintended outcome of this study is a contribution to the eco-driving of train [17].

7. ACKNOWLEDGMENT

This investigation is part of a partnership with SNCF Réseau, the French railway owner. Tests were performed by SYSTRA (http://www.systra.com), EURAILTEST (http://www.eurailtest.com) and SNCF/AEF.

8. REFERENCES

[1] *ITF Transport Outlook 2015*. OECD Publishing, 2015.

[2] **Pachauri, R.K. - Meyers,L.A.:** *Climate Change 2014: Synthesis Report. Contribution of Working Groups I, II and III to the Fifth Assessment Report of the Intergovernmental Panel on Climate Change*, IPCC. Geneva, Switzerland, 2014.

[3] **Akerman, J.:** The role of high-speed rail in mitigating climate change – The Swedish case Europabanan from a life cycle perspective, *Transp. Res. Part Transp. Environ.*, vol. 16, n^{o} 3, 2011, p.208-217.

[4] **Chester, M. V. - Horvath, A.:** Environmental assessment of passenger transportation should include infrastructure and supply chains, *Environ. Res. Lett.*, vol. 4, n^{o} 2, avr. 2009, p.024008.

[5] High Speed - International Union of Railways (UIC). [En ligne]. Disponible sur: http://www.uic.org/highspeed. [Consulté le: 03-nov-2016].

[6] **Leheis, S.:** High-speed train planning in France: Lessons from the Mediterranean TGV-line, *Transp. Policy*, vol. 21, n^{o} 0, 2012, p.37-44

[7] **Bosquet, R. - Vandanjon, P.-O. - Coiret, A. - Lorino, T.:** Model of High-Speed Train Energy Consumption, in *World Academy of Science, Engineering and Technology*, 2013, vol. 78.

[8] **Lukaszewicz, P.:** Running resistance - results and analysis of full-scale tests with passenger and freight trains in Sweden, *Proc. Inst. Mech. Eng. Part F J. Rail Rapid Transit*, vol. 221, January, 2007, p.183-192.

[9] **Rochard, B. - Schmid, F.:** A review of methods to measure and calculate train resistances, *Proc. Inst. Mech. Eng. Part F J. Rail Rapid Transit*, vol. 214, n^{o} 4, 2000, p.185–199.

[10] **Raghunathan, R. S. - Kim, H.-D. - Setoguchi, T.:** Aerodynamics of high-speed railway train », *Prog. Aerosp. Sci.*, vol. 38, n^{o} 6–7, 2002, p.469-514.

[11] **Lindgreen, E. - Sorenson, S. C.:** Simulation of energy sinsumption and emissions from rail traffic, Technical University of Denmark, Department of Mechanical Engineering, February, 2005.

[12] **Boullanger, B.:** Modelling and simulation of future railways, BANVERKET, 2008.

[13] **Coiret, A. - Vandanjon, P.-O. - Bosquet, R. - Soubrié, T. - Baty, G.:** Experimental assessment of wind influence on high-speed train energy consumptions, in *Proc. Transport Research Arena 5th conference*, Paris, France, 2014, p. 6.

[14] **Janot, A. - Vandanjon, P.-O. - Gautier, M.:** A Generic Instrumental Variable Approach for Industrial Robot Identification, *IEEE Trans. Control Syst. Technol.*, vol. 22, n^{o} 1, January. 2014, p.132-145.

[15] **Bosquet, R. - Vandanjon, P.-O. - Gautier, M. - Coiret, A. - Cazier, O.:** Influence of railway gradient on energy efficiency of high speed train », in *Proc. Transport Research Arena 5th conference*, Paris, France, 2014, p. 8 p.

[16] **Bosquet, R. - Jullien, A. - Vandanjon, P.- Dauvergne, O. M. - Sanchez, F.**: Eco-design model of a railway: A method for comparing the energy consumption of two project variants, *Transp. Res. Part Transp. Environ.*, vol. 33, December, 2014. p.111-124.

[17] **Lejeune, A. - Chevrier, R. - Vandanjon, P.-O. Rodriguez, J.:** Towards eco-aware timetabling: evolutionary approach and cascading initialisation strategy for the bi-objective optimisation of train running times. *IET Intell. Transp. Syst.*, vol. 10, n^{o} 7, September, 2016. p. 483-494.

IRREGULAR BRAKE DISC WEAR CAUSED BY DYNAMICALLY UNSTABLE RUNNING

István ZOBORY

Budapest University of Technology and Economics
Faculty of Transportation Engineering and Vehicle Engineering
Group of Railway Vehicles and Vehicle System Analysis
H-1111 Budapest, Műegyetem rkp.3, Hungary

Received: November 9, 2016

ABSTRACT

The phenomena of loss of dynamical running stability should be avoided in the normal operation of railway vehicles. Loss of dynamical stability emerges with increasing travelling speed v due to certain lateral force components acting on the wheel-set at the wheel/rail contact spots. There are always some force components which feed back positively in the motion equation of the wheel-set, which represent the *destabilising effect* causing *auto-excitation*. The other dissipative, lateral force components providing negative feed-back in the motion equations represent *stabilising effects,* but they have a multiplier coefficient ($1/v$), thus with increasing travelling speed v the stabilizing effect decreases, and on exceeding a certain speed limit v_0 – the so-called critical speed – auto-excitation emerges causing dynamic instability. However, due to certain non-linear lateral displacement or lateral speed dependent force components in the wheel-set motion equations, the lateral and yawing motion do not increase without bound, but periodic motion forms emerge, the so called *limit-cycles*. When travelling at above the critical speed v_0, auto-excitation causes periodic lateral and yawing motion affecting all components of the vehicle. In the course of unstable running in *brake application-free operation state*, the limit-cycle-form lateral motions of the wheel-sets and the bogie frames lead to unwanted impacts like intermittent grinding contact between the brake discs mounted on the wheel-sets and the brake pads mounted by hinge-joints on the movable calliper mechanism of the brake unit which is connected laterally to the bogie frame by rubber-sprung joints (silent blocks). The process described above takes place if the travelling speed of the vehicle exceeds the critical speed value v_0, and causes *irregular two-bay-form wear pattern* on the sliding interfaces of the brake-discs. Parallel to the intermittent grinding, the impact like lateral forces acting on the brake-pads are transmitted to the hinge-joints of the pad-holders and the callipers, causing severe damage to the pin and the bearing surfaces, to the point of complete failure. The secondary negative result brought about by the seizure damage to the pins in the hinge-joints is skew-wear of the brake pads. This lecture introduces the elaborated dynamical model representing the irregular brake disc wear under dynamically unstable vehicle motion. Wear is treated on the basis of the frictional work dissipated in the intermittent grinding process in the course of *running in brake application-free state* at a speed over the critical speed v_0.

Keywords: dynamically unstable motion state, critical speed, auto-excited motion, intermittent grinding of brake discs, seizure damage to pins, skew wear

1. INTRODUCTION

In railway operation several problems arise with *irregular wear* in friction brake systems. A special problem has emerged in form of the *"two-bay" wear pattern* on brake discs, on trains of 140 km/h permitted speed. Another very severe problem is the *seizure of the hinges* of the brake-pad-holders. In addition to irregular disc wear patterns *irregular skew wear pattern* of the brake pads can also emerge, which can be traced back to the seizure of the hinges. This lecture deals mainly with the *two-bay brake disc wear pattern*, and traces it cause to the occurrence and continuous presence of *dynamically unstable running* of the vehicle.

2. IRREGULAR WEAR OF THE BRAKE DISC

The *regular wear pattern* of the discs should follow the radial distribution of the *specific energy dissipation* $q = \mu p v$. Here μ stands for the coefficient of sliding friction, p stands for the pressure between the disc and the pad and v stands for the sliding velocity. The unit of measure of q is W/m^2. This quantity shows a convex distribution, which should lead to a regular ***„single-bay”*** radial wear pattern; see the upper side of Fig. 1. The *irregular radial wear pattern*, as opposed to the regular case, shows a „*two- bay*” radial wear pattern shown in the lower side of Fig. 1.

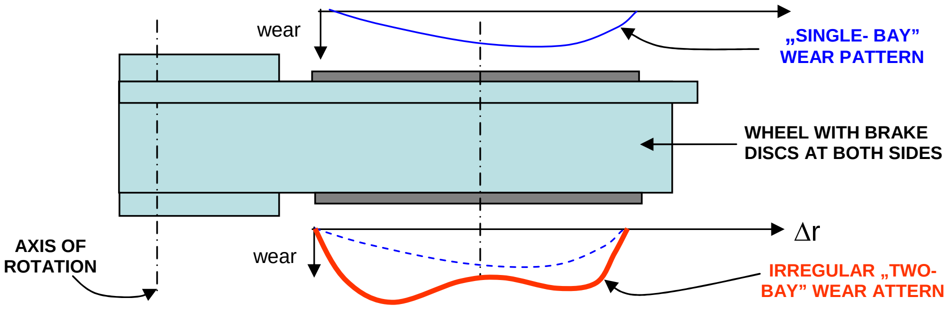

Fig 1. The regular single-bay and irregular two-bay radial wear patterns on the friction interfaces of the brake discs mounted on both sides of the wheel discs.

3. DYNAMICALLY UNSTABLE RUNNING

The running of a railway vehicle remains dynamically stable under a speed level v_0 called *critical speed*. The existence of such a critical speed can be shown by using the linearized dynamical model constructed for treating the horizontal in-plane motions of a two-bogie four axle railway vehicle. Such a model consists of minimum of 14 degrees of freedom for the unknown motions. The unknown time functions of the motions are included in the vector-valued time-function $\boldsymbol{x}(t)$, and the following linear second order set of motion equations can be deduced:

$$\boldsymbol{M}\ddot{\boldsymbol{x}}(t)+\boldsymbol{D}\dot{\boldsymbol{x}}(t)+\boldsymbol{S}\boldsymbol{x}(t)=\boldsymbol{0}\,.$$

Concerning the problem of loss of dynamical stability, the damping matrix $\boldsymbol{D}$ and the stiffness matrix $\boldsymbol{S}$ are relevant. The root of the problem is hidden into the force transfer realising between the wheel profile and the rail surfaces in the course of the track directional rolling motion.

Based on *Kalker*’s linearized description of the rolling contact, de-stabilizing entries appear both in matrix $\boldsymbol{D}$ and in matrix $\boldsymbol{S}$ (causing positively fed back forces). In case of $v < v_0$, the damping matrix can dominate over the destabilizing effects represented by some terms in the stiffness matrix $\boldsymbol{S}$ and damping matrix $\boldsymbol{D}$. Damping matrix $\boldsymbol{D}$ can be decomposed into the speed dependent $(1/v)\boldsymbol{B}$ and the constant $\boldsymbol{G}$ member matrices:

$$\boldsymbol{D}=\left(\frac{1}{v}\boldsymbol{B}+\boldsymbol{G}\right).$$

With increasing speed, the damping effect of $(1/v)\boldsymbol{B}$ and associated with dissipation caused by rolling decreases hyperbolically with v, and the remaining de-stabilizing effects in $\boldsymbol{G}$ and $\boldsymbol{S}$ become significant. With the introduction of the motion-state vector

$$\boldsymbol{y}(t) = \left[\dot{\boldsymbol{x}}(t), \boldsymbol{x}(t)\right]^T,$$

the motion equations can be transformed, using the state-space formulation as follows:

$$\dot{\boldsymbol{y}}(t) = \begin{bmatrix} -\boldsymbol{M}^{-1}\boldsymbol{D} & -\boldsymbol{M}^{-1}\boldsymbol{S} \\ \boldsymbol{E} & \boldsymbol{0} \end{bmatrix} \begin{bmatrix} \dot{\boldsymbol{x}}(t) \\ \boldsymbol{x}(t) \end{bmatrix} = \boldsymbol{A}(\boldsymbol{M}, \boldsymbol{D}, \boldsymbol{S})\boldsymbol{y}(t), \ \forall t$$

The loss of stability occurs if speed v reaches or exceeds the *critical speed* v_0, which indicates that one of the complex eigenvalues $\lambda = \beta + i\gamma$ of the system matrix $\boldsymbol{A}(\boldsymbol{M}, \boldsymbol{D}, \boldsymbol{S})$ has a positive real part, i.e. $\beta > 0$.

The motion-state solution $\boldsymbol{y}(t)$ of the linear set of motion equations with known eigenvector $\boldsymbol{h}$ for eigenvalue λ of coefficient matrix $\boldsymbol{A}$ has the form, such that in the case of $\beta > 0$ the motion co-ordinates will exponentially increase without limitation if t increases, in accordance with the formula below:

$$\boldsymbol{y}(t) = \boldsymbol{h}e^{\beta t}e^{i\gamma t}.$$

Fortunately, under real vehicle/track conditions exponentially increasing, unbounded motion cannot evolve as in the linearized system, due to *non-linearities* always present in the dynamical system in the case of larger lateral displacements and velocities occurring in the *trace-canal*, and the loss of dynamical stability leads only to a *bounded* periodic motion form of angular frequency γ. This motion form is called a *limit cycle*. The form of the non-linear differential equation system is as follows:

$$\boldsymbol{M}\ddot{\boldsymbol{x}}(t) + \boldsymbol{D}\dot{\boldsymbol{x}}(t) + \boldsymbol{S}\boldsymbol{x}(t) + \boldsymbol{f}(\boldsymbol{x}(t), \dot{\boldsymbol{x}}(t)) = \boldsymbol{0}$$

The characteristic process taking place in the case of loss of stability due to increasing speed can be introduced by using *cubic non-linearity* in the *lateral restoring force* acting on the wheel-set.

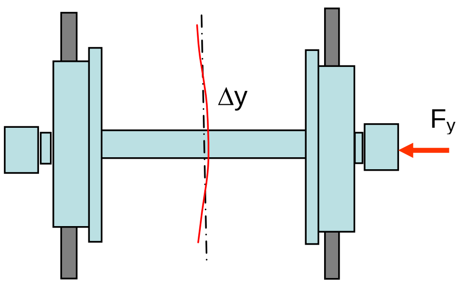

Fig. 2 Lateral restoring force F_y acting F_y on the wheel-set when Δy occurs

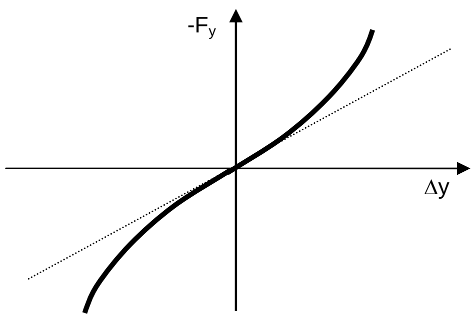

Fig. 3 Non-linear lateral restoring force vs. Δy ensuring the limit cycle formation

The unstable, lateral- and yawing motions of the wheel-set lead to limit cycles, shown in the following two diagrams. The loss of dynamical stability occurs at $t = 0$ (i.e. when the real part of one eigenvalue becomes non-negative, $\beta > 0$).

The transient evolution and the stabilised (steady state) limit cycle of the lateral displacement y(t) of the wheel-set is shown in Fig.4

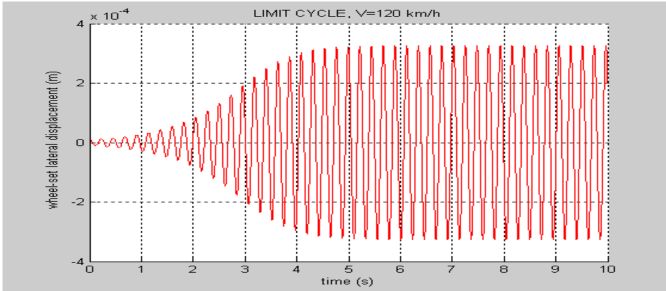

Fig. 4 Time evolution of the limit cycle of the lateral motion of the wheel-set

The transient evolution and the stabilised (steady state) limit cycle of the angular displacement $\psi(t)$ (yawing) of the wheel-set is shown in Fig.5

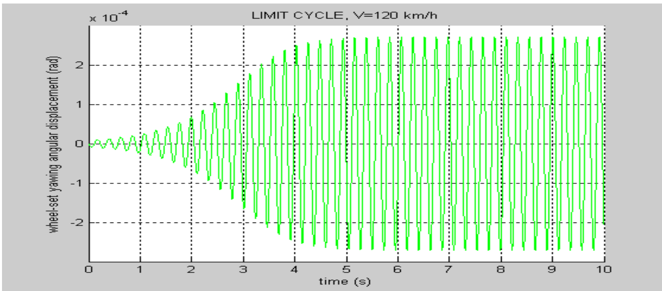

Fig. 5 Time evolution of the limit cycle of the yawing motion of the wheel-set

In the *motion-state-space* the steady-state limit cycles appear with *closed loops* traced by spiral trajectories in the course of the transient motion plotted in Fig. 6 and Fig. 7.

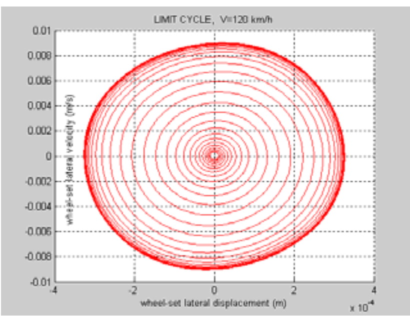

Fig. 6 Evolution of the limit cycle of the lateral motion of the wheel-set

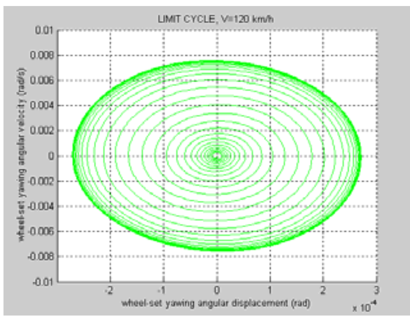

Fig. 7 Evolution of the limit cycle of the yawing motion of the wheel-set

4. DYNAMICAL MODEL FOR DETERMINING THE WEAR LOAD OF THE BRAKE DISC SURFACES

The top view of the bogie is shown in Fig. 7. It can be seen that each of the four disc brake units is mounted by two lateral pins in rubber bushes which span between the bogie side frame and a small cantilever extending from the inner side of the transom. The brake units themselves are shown in Fig. 8. In the isometric view the rubber silent blocks with their connecting pins can be seen. The latter have rectangular ends with vertical bolt holes to allow fixing to the bogie frame.

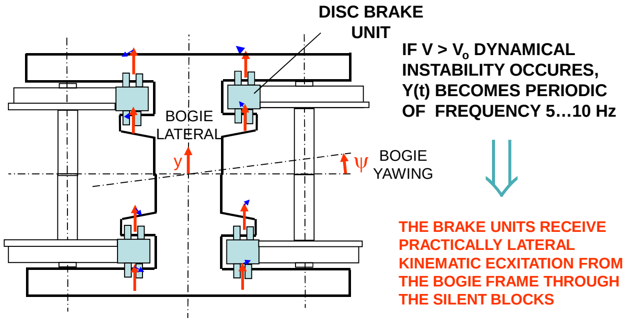

Fig. 7 Top view of the bogie with the brake units

The lateral and yawing displacements of the bogie frame are transmitted to the brake units through the silent blocks. Thus the brake units undergo lateral excitation by lateral motion of the bogie-frame through the rubber springs of the silent blocks.

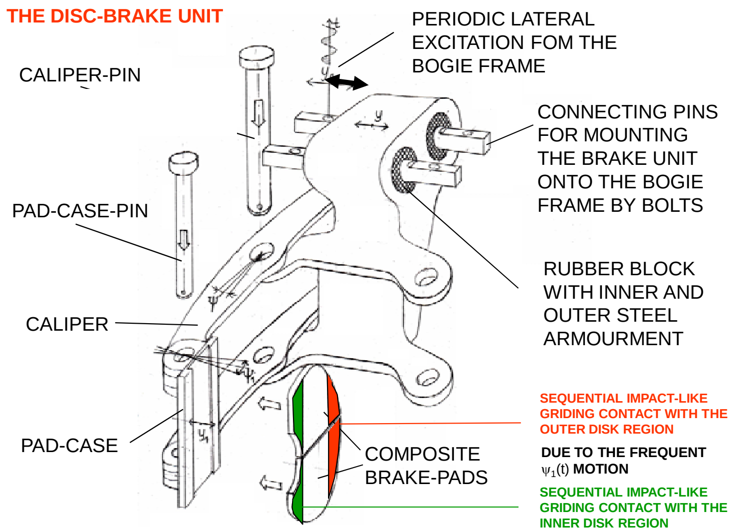

Fig. 8 The disc brake unit

The layout of the hinged joints between the callipers and the central brake unit casting and between the callipers and the pad-holders requires no further explanation. The two half-pads are retained in the pad-holder by a dove-tail joint, thus the half-pads can be inserted into the pad-holder from below one after the other and pushed upwards against a stop. A fixable, hinged member at the lower end of the pad-holder is closed to prevent the pads from dropping out. In Figs. 8 and 9 the shaded vertical strips on the both sides of the half-pads show which parts of the half-pad surfaces come into impact/rubbing contact with the brake-disc-surface while the brakes are released and lateral- and yawing motion of the pad-holder arises due excitation of the brake unit (and sometimes also on the wheel-set) caused by the *dynamically unstable* running state of the bogie.

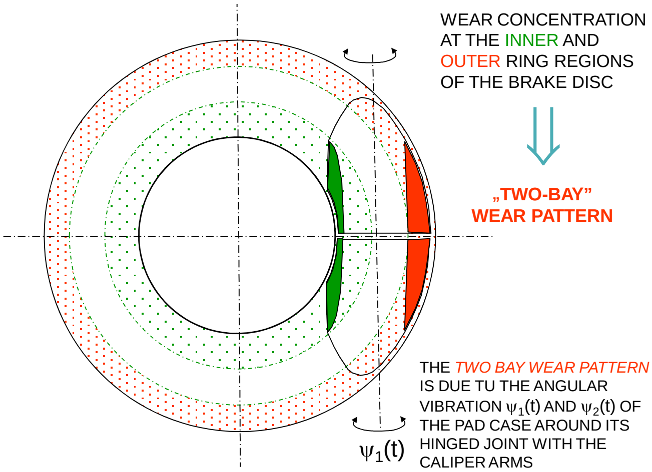

Fig. 9 Rubbed circular strips on the brake disc interacting with the brake pads when quasi periodic angular motion ψ_1(t) evolves in the course of running in dynamically unstable state of motion

In Fig. 9 the inner and outer circle-rings represent the areas touched by the inner and outer edges of the half-pads when lateral and yawing motion of the brake-pad occurs as a consequence of the lateral excitation of the brake unit and/or the wheel-sets due to the emergence of the dynamically unstable motion state of the vehicle. In Fig. 10 the simplified top view of the brake unit and the lumped parameter dynamical model of the latter are shown.

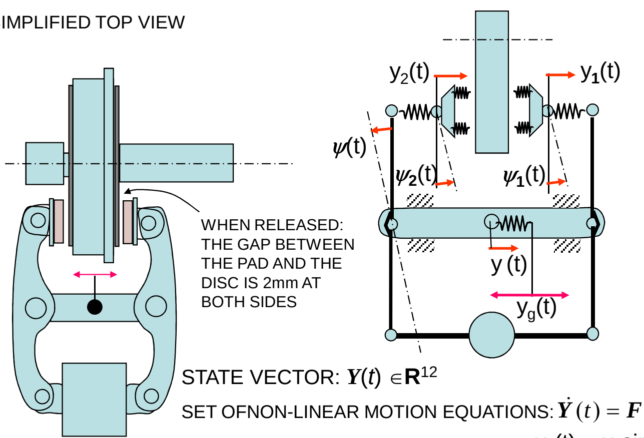

STATE VECTOR: $\boldsymbol{Y}(t) \in \mathbf{R}^{12}$

SET OFNON-LINEAR MOTION EQUATIONS: $\dot{\boldsymbol{Y}}(t) = \boldsymbol{F}(\boldsymbol{Y}(t), t)$

EXCITATION DUE TO NON_STABLE RUNNING: $y_g(t) = y_0 \sin(\Omega t)$

SOLUTION OF THE INITIAL VALUE PROBLEM BY **NUMERICAL METHOD**

$$\boldsymbol{Y}(t) = [\dot{y}(t), \dot{y}_1(t), \dot{y}_2(t), \dot{\psi}(t), \dot{\psi}_1(t), \dot{\psi}_2(t), y(t), y_1(t), y_2(t), \psi(t), \psi_1(t), \psi_2(t)]^T$$

Fig. 10 Dynamical model of the brake unit in released, but periodically excited state

The brake unit receives lateral *displacement excitation* $y_g(t)$ through a spring from the bogie frame being in dynamically unstable motion state, i.e. the vehicle runs over the critical speed v_0. The lateral and yawing motions of the brake unit are represented by the time functions $y(t)$, $y_1(t)$, $y_2(t)$, $\psi(t)$, $\psi_1(t)$, $\psi_2(t)$ of the free displacements and angular displacements. Obviously, their time-derivatives also enter the state-space treatment of the dynamical system.

In Fig. 10 the state vector $\boldsymbol{Y}(t)\in R^{12}$ and the first order non-linear set of the motion equations are also shown, together with the form of the applied lateral excitation: $y_g(t)= y_o \sin(\Omega t)$. The solution of the formulated initial value problem $\dot{\boldsymbol{Y}}(t)=\boldsymbol{F}(\boldsymbol{Y}(t),t);\ \ \boldsymbol{Y}(t_0)=\boldsymbol{Y}_0$ was carried out by means of numerical integration (*Euler*'s method, [1]).

5. SIMULATION RESULTS

In Fig. 11 the characteristic variation with time of the excited lateral and yawing vibrations of the brake-unit is shown. The amplitude of the *kinematic excitation* coming from the bogie frame in form of periodic lateral displacement was $y_o = 5mm$, the frequency: $f = (\Omega/2\pi) = 7Hz$.

It is apparent that the lateral displacement $y_1(t)=y(t)-a\psi(t)$ of the pad-holder-hinge moves in the interval [*-2mm, 2mm*], i.e. the interval of the nominal back-lash between the pad and disc surfaces in *released state* of the brake-gear. End values *2 mm* and *-2 mm* represent the limiting *impact events* and the emerging *sliding contact* between the brake-disc and the pads at both sides.

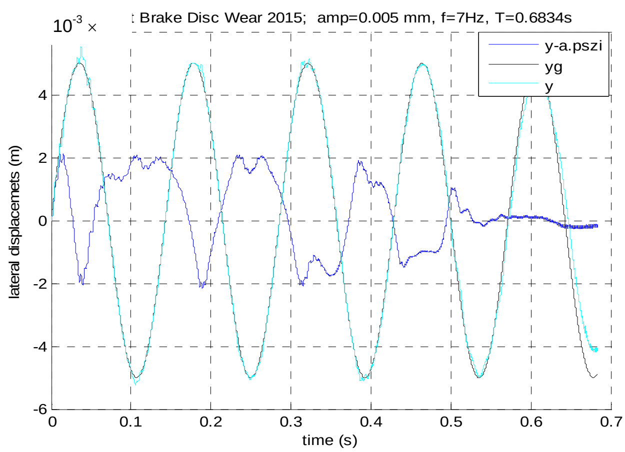

Fig. 11 Lateral motion of the brake unit and the pad-holder hinge

The results of the simulation show the sequential *impact-caused normal forces* arising in the course of the pad/disc sliding frictional contact process. In Fig. 12 the simulated normal contact forces are shown. It is very characteristic, that a fibrillation of frequency higher than **7** *Hz* is superimposed on the basic motion response, due to the very small moment of inertia of the brake-pad-holders with respect to the vertical axis of the hinged connection between the pad-holders and the callipers. The positive and negative signs identify if the contact takes place at the right or at left side of the disc.

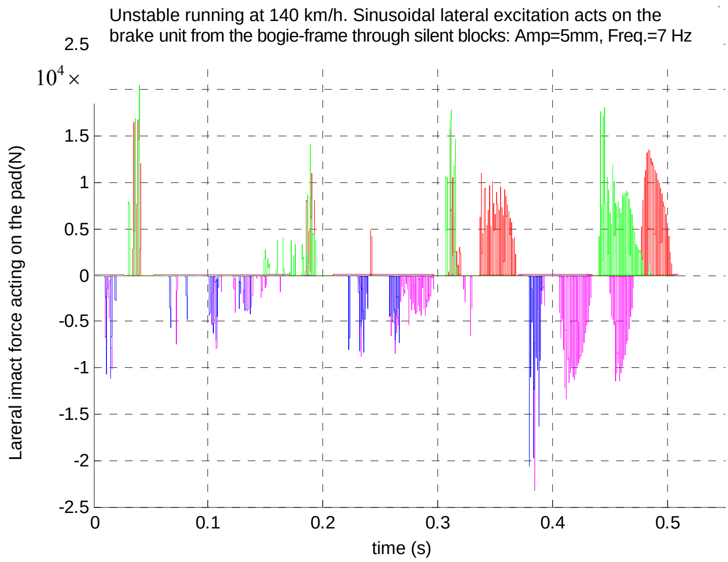

Fig. 12 Impact-like contact forces acting perpendicularly on the brake disc in the course of brake-released running in dynamically unstable state of motion

The *intermittent grinding process* is due to the normal forces caused by the sequential impacts and the evolving sliding frictional interaction between the brake-pads and the brake disc. In the background of the phenomenon is the excitation effect caused by the brake-effect-free dynamically unstable running of the vehicle. The *frictional energy dissipated* by the evolving frictional connection was also simulated. Knowing the normal forces $F_n(t)$ caused by the elastic impacts and the medium frictional coefficient μ for the pad/disc frictional pair, the frictional force acting in tangential direction could be determined in form: $F_f(t) = \mu F_n(t)$. To compute the frictional work done by the friction forces so determined, one should also take into consideration the arc-lengths of the contact traces at the outer and inner radii r_1 and r_2.of the disc. Thus, the frictional work done by the friction forces arising in the course of the intermittent contact process can be computed for both sides of the disc by using the formulae below:

$$W_{f1}(t) = \int_0^t F_{f_{r_1}}(\tau) ds_{r_1}(\tau), \quad W_{f2}(t) = \int_0^t F_{f_{r_2}}(\tau) ds_{r_2}(\tau).$$

In Fig. 13 the diagrams of the friction work done by the impact induced tangential friction forces are shown. The frictional work done over a time interval is approximately proportional to the *material mass worn out from the pads and the disc over this time interval.*

To define the *medium frictional energy flow* (the medium frictional power) in the course of the so determined friction process, the slopes of the *linear trends* of the friction work processes can be used, as it is shown with the straight lines in Fig. 13. It is surprising, that at 140 km/h running speed the medium friction power loss on one of the friction surfaces was P = 2 x 3.57 kW

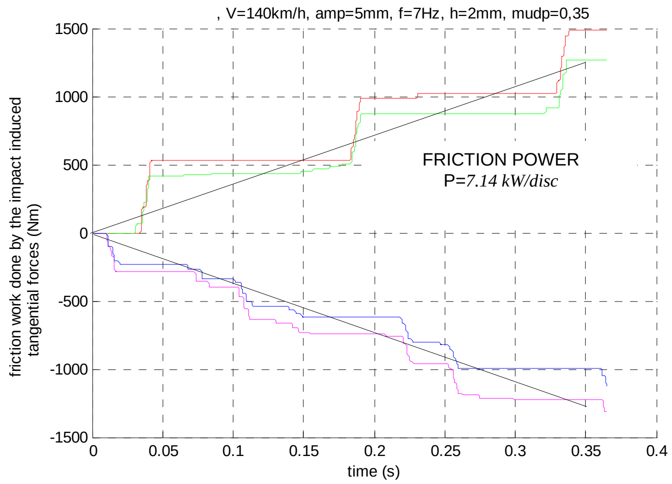

Fig. 13 Friction work done by the intermittent grinding at a speed 140 km/h

The medium *frictional energy flow* over a time interval is approximately proportional to the *medium debris mass flow valid over this time interval.*

The result of the *intermittent grinding* described is the evolution of the *two-bay* wear pattern on the sliding surfaces of the brake-discs, see Fig. 14.

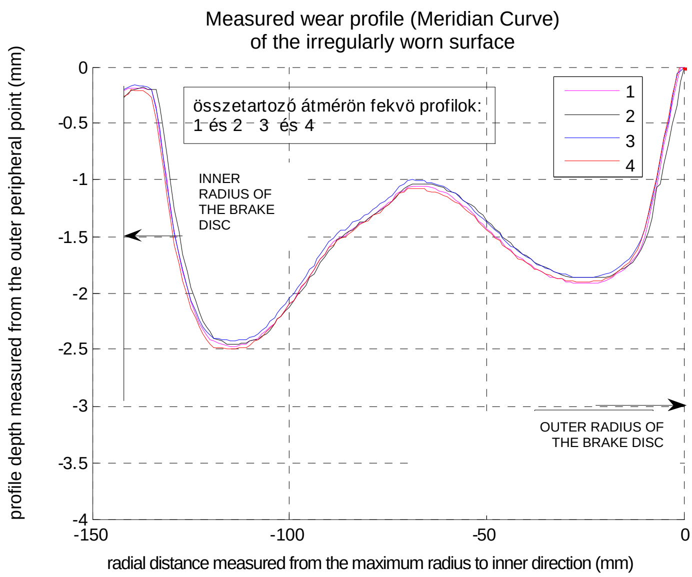

Fig. 14 Evolution of the *two-bay* wear pattern

6. CONCLUSIONS

From the results of the investigations into the irregular wear patters of brake discs in the presence of dynamically unstable motion form of the vehicle, due to exceeding the critical speed, the following conclusions can be drawn:

- The elaborated *simulation model and the numerical solution process worked in a reliable way,*
- The simulation results *explained the evolution of the „two-bay" irregular wear patterns* experienced on the brake discs, namely *the phenomenon was traced back to the occurrence of the intermittent grinding process* arising when travelling above the critical speed,
- A *medium power loss of cca. 7.14 kW/disc* has been identified in the course on unstable running at a speed 140 km/h,
- The cause of the *seizure damage to the journal pins* of the brake-pad-holders experienced *has also been recognised in the impact-like forces* arisen perpendicular to the disc,
- The cause of the *skew-wear of the brake pads* has also been recognised in the *severe seizure damage to the journal pins.*

7. REFERENCE

[1] **Zobory , I.**: Vehicle Dynamics. Lecture notes. BME, Department of Railway Vehicles, Budapest, 1999.

THE IMPACT OF SUSPENSION PARAMETERS ON SELECTED FEATURES OF BOGIES DYNAMICS IN THE TRANSITION CURVES

Krzysztof ZBOINSKI and Milena GOLOFIT-STAWINSKA

Faculty of Transport
Warsaw University of Technology
Koszykowa 75, 00-662 Warsaw, Poland

Received: November 7, 2016

ABSTRACT

The article presents results of the authors' studies aimed at the impact of the suspension parameters on selected features of bogies dynamics in the sections of transition curves for velocities below and above non-linear critical velocity. Parameters which were tested are the coefficients of lateral k_{zy} and longitudinal k_{zx} stiffness in primary suspension. The following three 2-axle bogies were examined: 25TN bogie of the freight car, bogie of MK111 passenger car and bogie of the average parameters. In the study two values of circular curve radii in the range from R=300 m to R=2000 m will be selected.

Keywords: non-linear dynamics, transition curve, critical velocity, numerical simulation, vehicle dynamics, self-exciting vibrations

1. INTRODUCTION

The article presents results of research on the impact of the suspension parameters on selected features of bogies dynamics in the sections of transition curves (TC). From the geometric point of view, TC sections are lying between the straight track (ST) and the circular curve (CC). TC is of transient character, i.e. they possess variable superelevation (h) and variable radius of curvature (R). Therefore, the study of motion along the section of transition curve are difficult but very interesting and often surprising. The subject is to some extent related to studies of railway vehicle non-liniear lateral stability, e.g. [1, 2, 3, 4, 8, 9, 10, 11, 12, 17 and 18] The authors are focused on variation of velocities (v) above and below the critical velocity (v_n). All the bogies among the three ones refer to the real objects. As mentioned in the abstract these objects are: 25TN bogie of the freight car, bogie of MK111 passenger car and bogie of the average parameters.

Each of the bogies moved at a fixed route consisting of three aforementioned consecutive sections, namely straight track, transition curve and circular curve. The influence of value of the circular curve radius on the dynamics of objects was additionally studied. In the study two values of circular curve radii (the smaller and larger ones) in the range from R=300 m to R=2000 m were further selected. For: bogie of the average parameters and bogie of MK111 passenger car the circular curve radii are R=600 m and R=2000 m and for 25TN bogie the circular curve radii are R=300 m and R=900 m. The selected value of circular curve radius results from the earlier studies and graphs representing the motivation reference to this study (the exact parameters are given in the captions under the pictures - Figs. 1-6). The authors are interested in behaviour of bogies in the section of transition curve around the critical velocity v_n, i.e. the study was conducted for velocities below and above v_n. Velocity of the objects was varied, than. In addition, the non-zero initial conditions (i.c.) $y_i(0)$=0.0045 m were imposed on the objects lateral displacements y_i. The denotations used in the figures are as follows: lat-

eral displacements y, vertical displacement z, roll angle ϕ and yaw angle ψ. Indices b, l and t denote bogie frame, leading wheelset and trailing wheelset, respectively.
Besides (at the above described motion conditions), influence of the suspention selected parameters on bogies' dynamics will also be tested. Parameters which influence was tested are the coefficients of lateral k_{zy} and longitudinal k_{zx} stiffness in primary suspension.

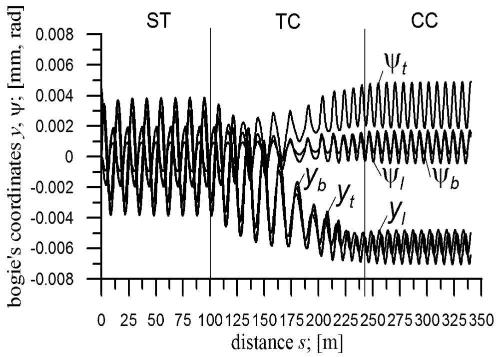

Fig. 1 Selected co-ordinates of 2-axle <u>bogie of average parameters</u>: non zero i.c. $y_i(0)$=0.0045 m, <u>***R*=600 m**</u>, h=0.15 m, v=54 m/s, k_{zy}= 3890000 N/m, k_{zx}=2615000 N/m – basic value of stiffness k_{zy} and k_{zx}

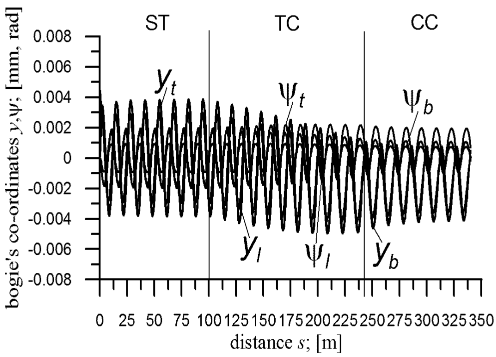

Fig. 2 Selected co-ordinates of 2-axle <u>bogie of average parameters</u>: non zero i.c. $y_i(0)$=0.0045 m, <u>***R*=2000 m**</u>, h=0.045 m, v=54 m/s, k_{zy}= 3890000 N/m, k_{zx}=2615000 N/m – basic value of stiffness k_{zy} and k_{zx}

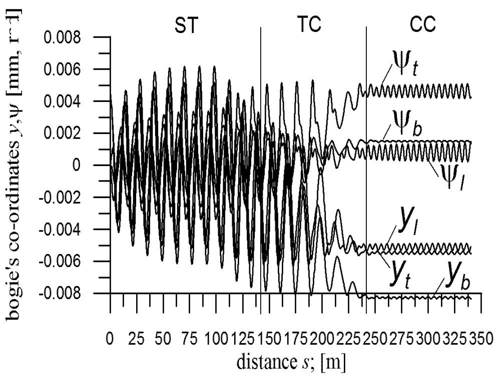

Fig. 3 Selected co-ordinates of 2-axle <u>bogie of MK111 passenger car</u>: non zero i.c., $y_i(0)$=0.0045 m, <u>***R*=600 m**</u>, h=0.15 m, v=54 m/s, k_{zy}= 1308000 N/m, k_{zx}=2667000 N/m – basic value of stiffness k_{zy} and k_{zx}

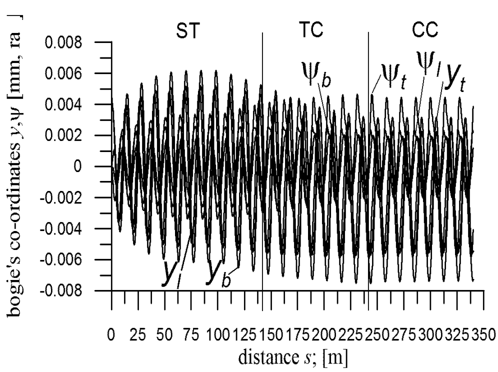

Fig. 4 Selected co-ordinates of 2-axle <u>bogie of MK111 passenger car</u>: non zero i.c., $y_i(0)$=0.0045 m, <u>***R*=2000 m**</u>, h=0.045 m, v=54 m/s, k_{zy}= 1308000 N/m, k_{zx}=2667000 N/m – basic value of stiffness k_{zy} and k_{zx}

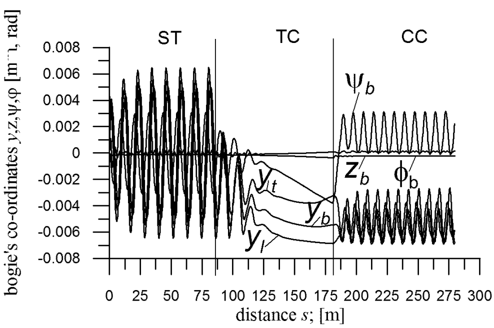

Fig. 5 Selected co-ordinates of 2-axle <u>25TN bogie of the freight car</u>: non zero i.c., $y_i(0)$=0.0045 m, ***R*=300 m**, h=0.15 m, v=29.5 m/s, k_{zy}= 3890000 N/m – basic value of stiffness k_{zy}

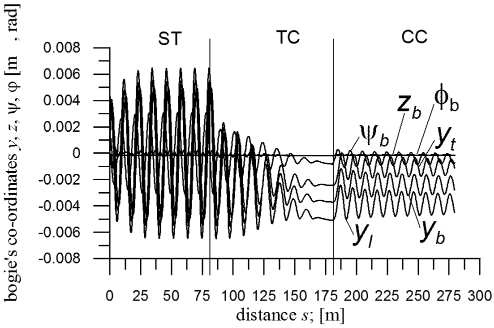

Fig. 6 Selected co-ordinates of 2-axle <u>25TN bogie of the freight car</u>: non zero i.c., $y_i(0)$=0.0045 m, ***R*=900 m**, h=0.142 m, v=29.5 m/s, k_{zy}= 3890000 N/m – basic value of stiffness k_{zy}

2. THE OBJECTS AND SIMULATION MODELS IN STUDIES

The subject of research in this article are the bogies of 2-axle type referring to the objects as follows: 25TN bogie of freight car, bogie of MK111 passenger car and bogie of the average parameters.

The structure of nominal models of all three objects is similar. The structure of nominal models of the bogies alone are shown in Figure 7c. The bogie's models are supplemented with flexible track models for both the lateral and vertical directions. Structures of the track nominal models are shown in Figures 7a and 7b, respectively.

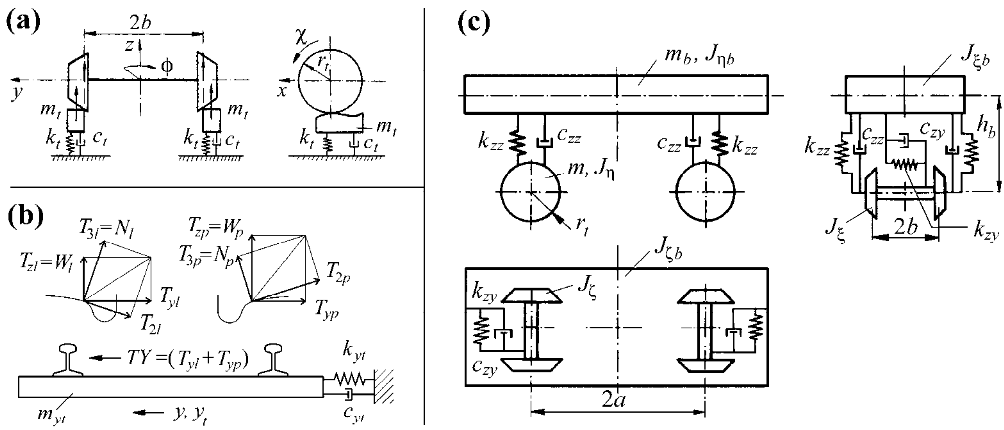

Fig. 7 System's nominal model: (a) track vertically, (b) track laterally, (c) bogie [14]

The 25TN bogie of freight car – track model has got 16 degrees of freedom (DOFs). The bogie of MK111 passenger car - track model and the bogie of the average parameters – track model have 18 degrees of freedom. Their parameters are given in [17 and 18].

To simulate the models' motion the authors used computer program that utilizes Lagrange second type equations adapted to describe relative motion [7]. In the models of all three objects and track linear characteristics of stiffness and dumping were introduced. The wheel-rail contact model includes non-linear geometry of the wheel and rail profiles and non-linear calculation of the tangential contact forces. The contact geometry is calculated with use of the RSGEO software [6], while the forces with use of the FASTSIM procedure [5]. Nominal (not worn) wheel and rail profiles are applied. The S1002 wheel profile is used in vehicle model. The UIC60 rail profile is used in the track model. Inclination of rails equals 1:40, while track gauge equals 1435 mm. Coefficient of friction in the contact forces calculation equals 0.3 [13, 15 and 16].

3. THE RESULTS OF STUDIES

3.1 Introduction to the resuls

Motivation and reference to present study were the former results indicated in section 1 of this article (Figs. 1-6). As these graphs were a motivation to the study, they were named "original graphs" and indicated by index *o*. For bogie of the average parameters *o* (original graphs) always corresponds to v=54 m/s, k_{zy}= 3890000 N/m (basic value), k_{zx}= 2615000 N/m (basic value), R=600 m and R=2000 m. For bogie of MK111 passenger car *o* (original graphs) always corresponds to v=54 m/s, k_{zy}= 1308000 N/m (basic value), k_{zx}= 2667000 N/m (basic value), R=600 m and R=2000 m. For 25TN bogie of the freight car *o* (original graphs) always corresponds to v=29.5 m/s, k_{zy}= 3890000 N/m (basic value), k_{zx} - no longitudinal stiffness due to the smaller number of degrees of freedom, R=300 m and R=900 m. The above given values used in tests as reference are presented below in Table 1.

Figures presented in current section represent the effect of various parameters such as values of lateral k_{zy} and longitudinal k_{zx} stiffness, velocity, circular curve radius on the dynamics of railway vehicle in transition curves at velocities below and above critical one. The three already mentioned objects shall be subject to testing.

The authors carried out studies for a wide range of stiffness values:

*lateral k_{zy} - 0,001; 0,01; 0,1; 0,2; 0,4; 0,6; 0,8; 0,9; 2; 3; 4; 5; 6; 7; 8; 10; 20; 40; 60; 80; 100 and 1000 times enlarged as compared to the basic value,

*longitudinal k_{zx} - 0,001; 0,01; 0,1; 0,2; 0,4; 0,6; 0,7; 0,8; 0,9; 10; 20; 40; 60; 80; 90; 100 i 1000 times enlarged as compared to the basic value. The range of velocities was also wide, i.e. velocity value changes from v=5 m/s to moment of the numerical derailment. In the authors study two different circular curve radius values (small and large), were used for each object. As mentioned before, for bogie of the average parameters and bogie of MK111 passenger car the circular curve radii are R=600 m and R=2000 m and for 25TN bogie the circular curve radii are R=300 m and R=900 m. The numerical simulations done for bogies move always for routes that include ST, TC and CC. For: bogie of the average parameters and bogie of MK111 passenger car the lengths individual sections are: ST=100 m, TC=140 m and CC=100 m. But for 25TN bogie of the freight car the lengths individual sections are: ST=86.5 m, TC=95 m and CC=98 m. The transition curves were always of 3rd degree parabola type. Precise superelevation values *h* are given in the figures captions. The indices in the figures not defined so far are: /10, /11, /12, /14, /15, /20, /26, /29.5, /30, /32, /33, /34, /35, /36, /37,

/38, /39, /40, /42, /44, /45, /50, /54, /60, /62, /63, /65, /70, /80, /90, /110, /130. They represent velocities v in m/s.

Denotation	Meaning	Unit	Bogie of the average parameters	Bogie of MK111	25 TN bogie
k_{zy}	lateral stiffness in 1st level of suspension system	kN/m	3890	1308	3890
k_{zx}	longitudinal stiffness in 1st level of suspension system	kN/m	2615	2667	-
v	velocity	m/s	54	54	29.5
R	circular curve radius	m	600 2000	600 2000	300 900

Table 1: Parameters of the nominal models

3.2 The results of current studies

The authors devided results of the studies into three groups depending on the type of bogie. They are as follows: bogie of the average parameters – Figs. 8-15, bogie of MK111 passenger car – Figs. 16-23 and 25TN bogie of freight car – Figs. 24-27. In each group:

*the first couple of Figures was made for smaller lateral stiffness k_{zy} than the basic value and velocities lower than the nominal velocity (Figs. 8, 9, 16, 17, 24 and 25) - $k_{zy}\downarrow$ $v\downarrow$,

*the second couple of Figures was made for bigger lateral stiffness k_{zy} than the basic value and velocities higher than the nominal velocity (Figs. 10, 11, 18, 19, 26 and 27) - $k_{zy}\uparrow$ $v\uparrow$,

*the third couple of Figures was made for smaller longitudinal stiffness k_{zx} than the basic value and velocities lower than the nominal velocity (Figs. 12, 13, 18 and 19) - k_{zx} v $\downarrow$, $\downarrow$

*the forth couple of Figures was made for bigger longitudinal stiffness k_{zx} than the basic value and velocities higher than the nominal velocity (Figs. 14, 15, 22 and 23) - $k_{zx}\uparrow$ $v\uparrow$.

In order to get better illegibility of figures (large number of the lines) just some coordinates were selected to be presented.

For **bogie of the average parameters** while reducing the lateral stiffness k_{zy} (k_{zy}=1556000 N/m – 0.4 of the basic value) and the velocity the authors have found that the higher velocities cause vehicle derailment independly of the circular curve radius value (R=600 m and R=2000 m) (Figs. 8 and 9). While gradually reducing velocity the limit cycle is established. In the case of R=600 m the limit cycle establishes only in first section, i.e. in ST. In CC there is no limit cycle (Fig. 8). In the case of R=2000 m the limit cycle establishes in CC at first. At the same time in ST vibrations grow or the limit cycle in the ST and CC appears immediately. Vibrations always go smoothly from the ST to the TC and CC (Fig. 9). In both cases (Fig. 8 and 9) with the further velocity reducing the vibrations decrease (disappear) in ST and TC and no vibrations in CC exist. The vibrations amplitude is quite large. In Fig. 8 it is approx. 0.5 cm in the beginning section and then it gradually decreases but in Fig. 9 it is approx. 0.5 cm within the whole route.

While increasing the lateral stiffness k_{zy} (k_{zy}=311200000 N/m – 80 times more than the basic value) and the velocity, the authors concluded that the vehicle does not derail (with few exceptions). In Figs. 10 and 11 the vibrations in ST tend to disappear quickly. In the case of R=600 m the vibrations in TC momentarily appear and then quickly disappear, and never appear again. In CC the vibrations do not occur (Fig. 10). In Fig. 11 the vibrations in ST and TC tend to disappear and in the case of lower velocity disappear completely. For v=80 m/s the vibrations rapidly disappear in TC and then reappear at the end of TC but of a different nature and tend to increase in CC. For v=90 m/s the limit cycle in CC establishes but with small amplitude. Further velocity increase leads to the limit cycle also in ST. Then, with a further velocity increase the vibrations in CC disappear completely again.

While reducing the longitudinal stiffness k_{zx} (k_{zx}=1046000 N/m – 0.4 of the basic value) and the velocity the authors have found that in both cases (R=600 m and R=2000 m) the higher velocities cause vehicle derailment (Figs. 12 and 13). While gradually reducing velocity the limit cycle is established in ST and CC but in Fig. 12 with smaller amplitude than in Fig. 13. With reducing velocity futher the vibrations tend to disappearing initially only in CC and later in TC, too. For small velocities the vibrations do not occur in TC and CC (Figs. 12 and 13).

In case of reducing the lateral stiffness k_{zy} and the velocity (Fig. 8) the limit cycle in CC never appeared (no vibrations in CC). On the other hand in Fig. 12 while reducing the longitudinal stiffness k_{zx} and the velocity the limit cycle in CC appears. But in case of larger circular curve radius R=2000 m the limit cycle in CC appears on both graphs (Figs. 9 and 13).

While increasing the longitudinal stiffness k_{zx} (k_{zx}=156900000 N/m – 60 times more than the basic value and k_{zx}=209200000 N/m – 80 times more than the basic value) and the velocity in Figs. 14 and 15, the authors concluded that the bogie behaves similarly as in Figs. 10 and 11. In Fig. 14 and 15 the vibrations in ST tend to disappear quickly. In the case of R=600 m the vibrations in TC rapidly appear and then quickly disappear. In CC the vibrations do not occur (Fig. 14). In Fig. 15 the vibrations in ST and TC tend to disappear and in the case of lower velocity disappear completely. For v=70 m/s the vibrations rapidly disappear in TC and then reappear in CC but of a different nature and the limit cycle in CC establishes. For bigger velocities the vibrations reappear at the end of TC and establish the limit cycle in CC. For smaller velocities v=60 m/s the vibrations do not occur in CC. For v=70 m/s they establish the limit cycle but with small amplitude while for v=80 m/s and v=90 m/s the limit cycle amplitude is bigger. Finally for v=110 m/s the limit cycle amplitude decreases again.

For **bogie of MK111 passenger car** while reducing the lateral stiffness k_{zy} (k_{zy}=1177200 N/m – 0.9 of the basic value) and the velocity the authors have found in Fig. 16 that for v=54 m/s and v= 50 m/s the corresponding courses are similar to the original one. The vibrations are increasing in ST and establish the limit cycle in CC but with very small amplitude. For v=40 m/s which is close to critical velocity the limit cycle in CC is established for the last time. For velocities smaller than v=40 m/s the vibrations are decreasing in ST and TC and in CC the vibrations do not occur. In Fig. 17 for bigger circular curve radius R=2000 m and for higher velocities the limit cycle in ST and CC exist with big amplitude equal aprox. 4-5 mm. With reducing the velocity the amplitude decreases in the limit cycle while for further reduction in the velocity the vibrations tend to decay in ST and CC and disappear completely in CC.

While increasing the lateral stiffness k_{zy} (k_{zy}=5232000 N/m – 4 times more than the basic value) and the velocity, the authors concluded in Fig. 18 that for R=600 m and v=54 m/s the vibrations in CC increase and establish the limit cycle with big amplitude. For v=60 m/s the graph is similar to previous graph but the limit cycle amplitude in CC is smaller. For v=65 m/s the result is interesting because the vibrations disappear in the middle of the TC and then become rapidly reborn. At the end of TC they disappear and establish the limit cycle in CC of very small amplitude. Above v=65 m/s the vibrations in CC disappear completaly. In all cases the limit cycle in ST establishes. In Fig. 19 for v=54 m/s the limit cycle in CC is established but in contrast to Fig. 18 with smaller amplitude than on the original graph. The limit cycle in ST is also established. With increasing velocities the vibrations tend to decrease in TC and CC. For v=90 m/s the vibrations tend to increase in CC and finally the bogie derails.

While reducing the longitudinal stiffness k_{zx} (k_{zx}=1066800 N/m – 0.4 of the basic value) and the velocity the authors have found that in both cases (R=600 m and R=2000 m) the higher velocities cause the bogie's derailment (Figs. 20 and 21). In the case of R=600 m for v=33 m/s the vibrations fluent passage from ST to the TC and CC happens. In CC the limit cycle is established. For v=32 m/s the vibrations tend to decrease. The vibrations disappear completaly in CC. The critical velocity is between v=32 and 33 m/s (these two cases are not given in Fig. 20). While gradually reducing velocity the vibrations disapper in ST, TC and CC. In Fig. 20 for v=30 m/s the vibrations disappear completaly at the beginning of the CC. For smaller velocities the vibrations disappear completaly in ST. In Fig. 21 for v=33 m/s the vibrations tend to decrease in ST and tend to increase in CC. For smaller velocities they establish the limit cycle in ST and CC. While gradually reducing velocity the vibrations tend to decrease in ST, TC and CC.

Reducing both the stiffness values - lateral stiffness k_{zy} and the longitudinal stiffness k_{zx} bring similar influence on bogie of MK111 passenger car for a given circular curve radius value.

While increasing the longitudinal stiffness k_{zx} (k_{zx}=53340000 N/m – 20 times more than the basic value and the velocity in Fig. 22 for R=600 m the bogie behaviour is similar regardless of the velocity. The limit cycle in ST is established. The vibrations decrease completaly in TC and do not occur in CC. For v=63 m/s the bogie derailment occurs. In case of Fig. 23 for higher velocities the limit cycle in ST and CC is established but with the smaller amplitude than on original graph.

In case of reducing both the stiffness values bring similar influence on bogie but in case of growing both the stiffness types bring different behaviour. In case of Fig. 22, when R=600 m for each case the limit cycle in CC does not exist but in Fig. 18 the limit cycle establishes in CC even with a relatively big amplitude. In case of Fig. 23 where R=2000 m, for higher velocities the limit cycle amplitude in CC are smaller than on original graph. But in Fig. 19 the limit cycle amplitude were first smaller and then bigger in relation to the original.

For **25TN bogie of the freight car** while reducing the lateral stiffness k_{zy} (k_{zy}=389000 N/m – 10 times less than the basic value) and the velocity the authors have found that in Fig. 24 for v=15 m/s the object numerically derailed. For velocity above v=12 m/s the limit cycle in ST was obtained. In all cases the vibrations in ST pass to the TC and then to CC fluently. In Fig. 25, in contrast to Fig. 24, at velocity v=16 m/s the object derailed numerically. For v=15 m/s the limit cycle in ST and CC establishes with amplitude of aprox. 4 mm. For v=12 and 11 m/s the limit cycle in CC is established, too but with the smaller amplitude. For velocities v=10 and 11 m/s the limit cycle in ST was not obtained. For v=10 m/s the limit cycle in CC does not occur. The vibrations fluently pass from ST, by TC to CC for all velocities. Distinguishing phenomenon occurs at the passage from the TC to the CC for v=15 m/s. It consists in a quick increase of the amplitude after entering the CC.

While increasing the lateral stiffness k_{zy} (k_{zy}=7780000 N/m – 2 times more than the basic value) and the velocity in Fig. 26 an original result and results for velocities v=29.5 and 38 m/s are shown. For velocities lower than v=38 m/s the limit cycle in ST was not obtained while for a higher one the bogie derailment occured. In case of Fig. 27 for all tested velocities no limit cycle in the ST exists (the limit cycle exist only for the original case). At a velocity v=40 m/s the object numerically derailed (no line in the figure). The vibrations in the ST disappear, do not exist in TC and reborn in CC. With increase of velocity the increased amplitudes of vibration in the CC exist. While the bogie enters TC and CC a sudden change solutions follows.

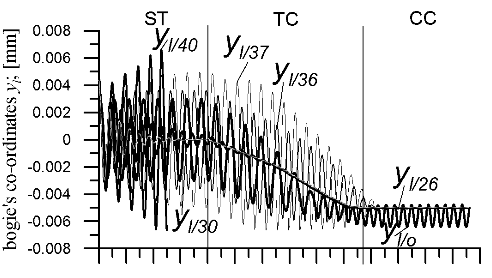

Fig. 8 Selected co-ordinates of 2-axle <u>bogie of average parameters</u>: non zero i.c. $y_i(0)$=0.0045 m, ***R*=600 m**, h=0.15 m, ***k*$_{zy}$= 1556000 N/m (0.4x)**, ***v* - different**, k_{zx}=2615000 N/m

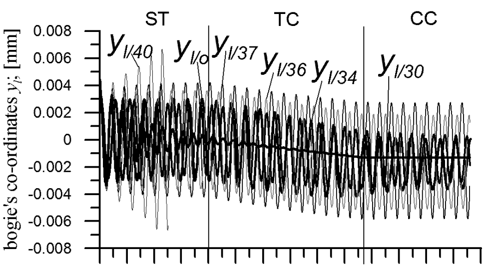

Fig. 9 Selected co-ordinates of 2-axle <u>bogie of average parameters</u>: non zero i.c. $y_i(0)$=0.0045 m, ***R*=2000 m**, h=0.045 m, ***k*$_{zy}$= 1556000 N/m (0.4x), *v* - different,** k_{zx}=2615000 N/m

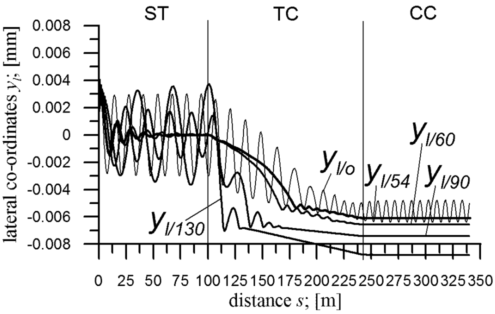

Fig. 10 Selected co-ordinates of 2-axle <u>bogie of average parameters</u>: non zero i.c. $y_i(0)$=0.0045 m, ***R*=600 m**, h=0.15 m, **k_{zy}= 311200000 N/m (80x)**, ***v* - different**, k_{zx}=2615000 N/m

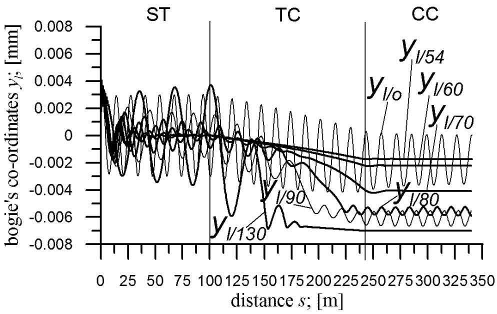

Fig. 11 Selected co-ordinates of 2-axle <u>bogie of average parameters</u>: non zero i.c. $y_i(0)$=0.0045 m, ***R*=2000 m**, h=0.045 m, **k_{zy}= 311200000 N/m (80x), *v* - different,** k_{zx}=2615000 N/m

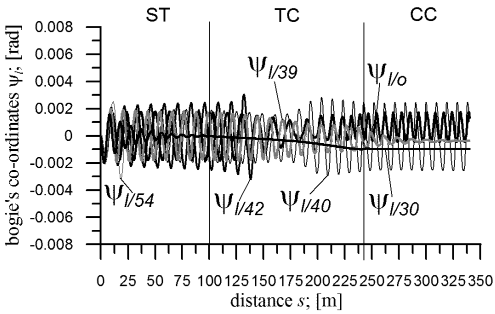

Fig. 12 Selected co-ordinates of 2-axle <u>bogie of average parameters</u>: non zero i.c. $y_i(0)$=0.0045 m, ***R*=600 m**, h=0.15 m, k_{zy}=3890000 N/m, ***v* - different**, **k_{zx}=1046000 N/m (0.4x)**

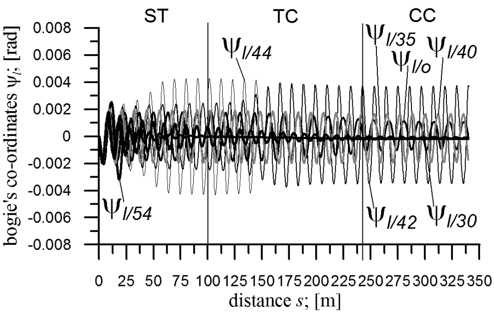

Fig. 13 Selected co-ordinates of 2-axle <u>bogie of average parameters</u>: non zero i.c. $y_i(0)$=0.0045 m, ***R*=2000 m**, h=0.045 m, k_{zy}= 3890000 N/m, ***v* - different,** **k_{zx}=1046000 N/m (0.4x)**

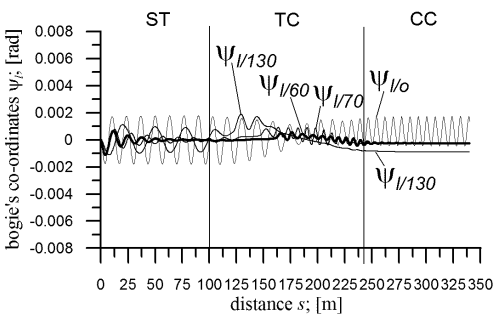

Fig. 14 Selected co-ordinates of 2-axle <u>bogie of average parameters</u>: non zero i.c. $y_i(0)$=0.0045 m, ***R*=600 m**, h=0.15 m, k_{zy}=3890000 N/m, ***v* - different**, **k_{zx}=156900000 N/m (60x)**

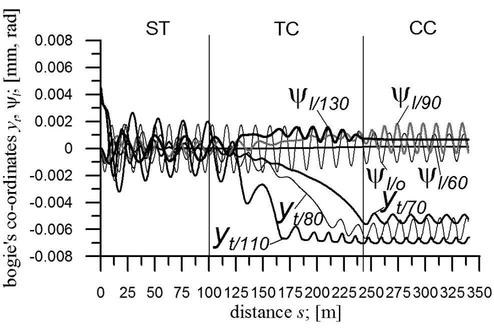

Fig. 15 Selected co-ordinates of 2-axle <u>bogie of average parameters</u>: non zero i.c. $y_i(0)$=0.0045 m, ***R*=2000 m**, h=0.045 m, k_{zy}= 3890000 N/m, ***v* - different,** **k_{zx}=209200000 N/m (80x)**

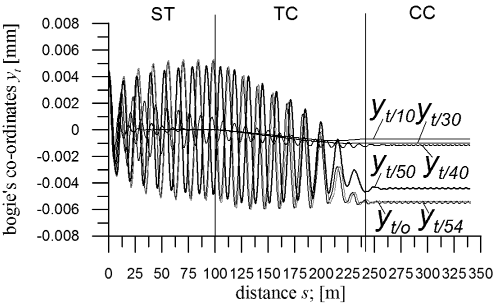

Fig. 16 Selected co-ordinates of 2-axle <u>bogie of MK111 passenger car</u>: non i.c., $y_i(0)$=0.0045 m, ***R*=600 m**, h=0.15 m, **k_{zy}= 1177200 N/m (0.9x)**, ***v* - different**, k_{zx}=2667000 N/m

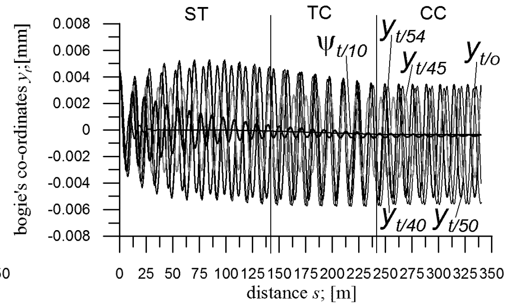

Fig. 17 Selected co-ordinates of 2-axle <u>bogie of MK111 passenger car</u>: non zero i.c., $y_i(0)$=0.0045 m, ***R*=2000 m**, h=0.045 m, **k_{zy}= 1177200 N/m (0.9x),** ***v* - different,** k_{zx}=2667000 N/m

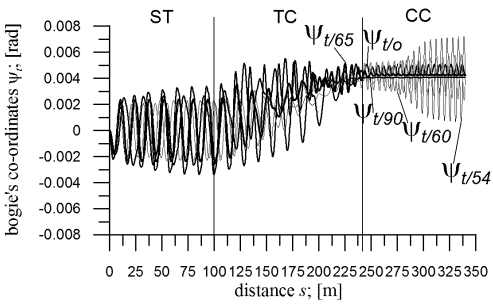

Fig. 18 Selected co-ordinates of 2-axle <u>bogie of MK111 passenger car</u>: non zero i.c., $y_i(0)$=0.0045 m, ***R*=600 m**, h=0.15 m, **k_{zy}= 5232000 N/m (4x)**, ***v* - different**, k_{zx}=2667000 N/m

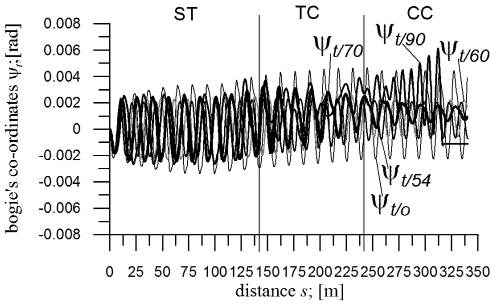

Fig. 19 Selected co-ordinates of 2-axle <u>bogie of MK111 passenger car</u> : non zero i.c., $y_i(0)$=0.0045 m, ***R*=2000 m**, h=0.045 m, **k_{zy}= 5232000 N/m (4x),** ***v* - different,** k_{zx}=2667000 N/m

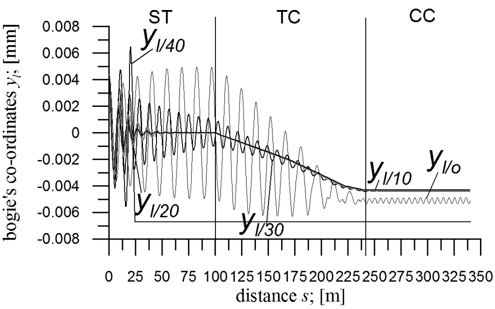

Fig. 20 Selected co-ordinates of 2-axle <u>bogie of MK111 passenger car</u>: non zero i.c., $y_i(0)$=0.0045 m, ***R*=600 m**, h=0.15 m, k_{zy}= 1308000 N/m, ***v* - different**, **k_{zx}=1066800 N/m (0.4x)**

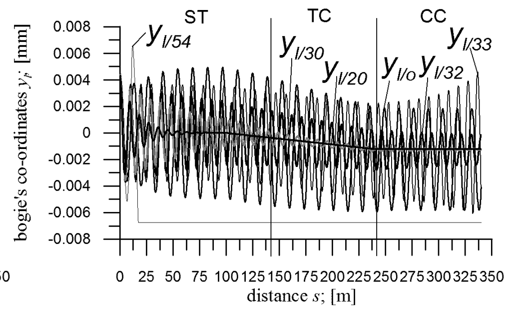

Fig. 21 Selected co-ordinates of 2-axle <u>bogie of MK111 passenger car</u> : non zero i.c., $y_i(0)$=0.0045 m, ***R*=2000 m**, h=0.045 m, k_{zy}= 1308000 N/m, ***v* - different,** **k_{zx}=1066800 N/m (0.4x)**

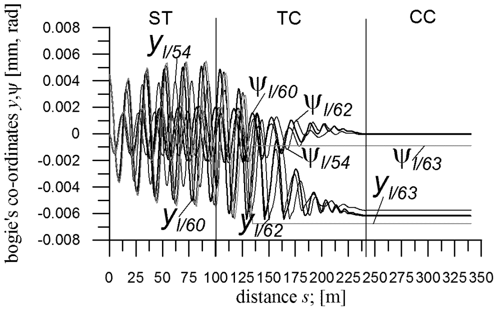

Fig. 22 Selected co-ordinates of 2-axle bogie of MK111 passenger car: non zero i.c., $y_i(0)$=0.0045 m, ***R*****=600 m**, h=0.15 m, k_{zy}= 1308000 N/m, ***v* - different**, $\boldsymbol{k_{zx}}$**=53340000 N/m (20x)**

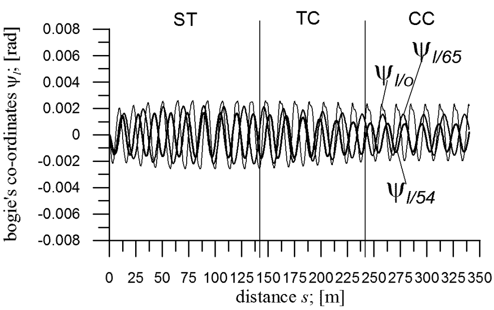

Fig. 23 Selected co-ordinates of 2-axle bogie of MK111 passenger car : non zero i.c., $y_i(0)$=0.0045 m, ***R*****=2000 m**, h=0.045 m, k_{zy}= 1308000 N/m, ***v* - different,** $\boldsymbol{k_{zx}}$**=53340000 N/m (20x)**

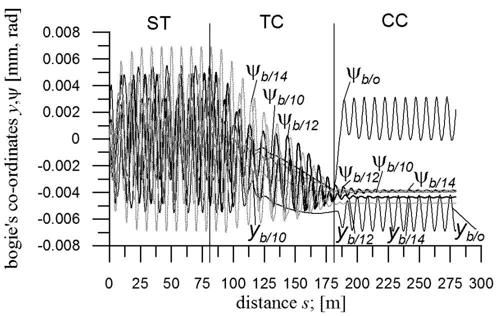

Fig. 24 Selected co-ordinates of 2-axle 25TN bogie of the freight car: non zero i.c.
$y_i(0)$=0.0045 m, ***R*****=300 m**, h=0.15 m, $\boldsymbol{k_{zy}}$**= 389000 N/m (0.1x)**, ***v* - different**

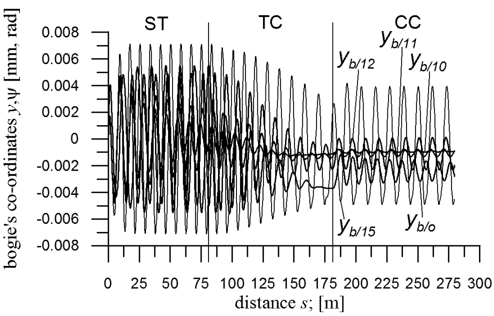

Fig. 25 Selected co-ordinates of 2-axle 25TN bogie of the freight car: non zero i.c.
$y_i(0)$=0.0045 m, ***R*****=900 m**, h=0.142 m, $\boldsymbol{k_{zy}}$**= 389000 N/m (0.1x), *v* - different**

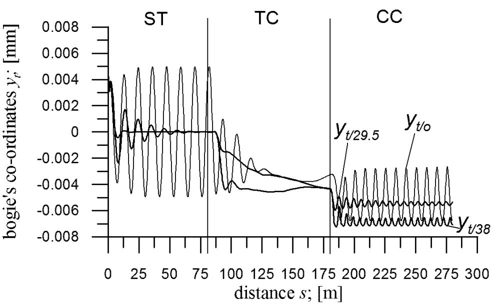

Fig. 26 Selected co-ordinates of 2-axle 25TN bogie of the freight car: non zero i.c.
$y_i(0)$=0.0045 m, ***R*****=300 m**, h=0.15 m, $\boldsymbol{k_{zy}}$**= 7780000 N/m (2x)**, ***v* - different**

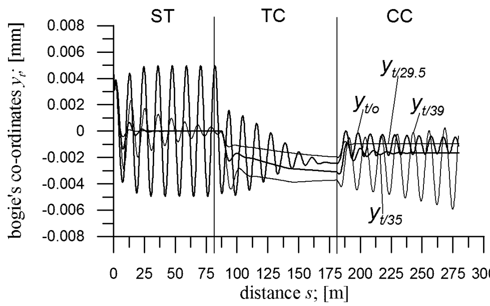

Fig. 27 Selected co-ordinates of 2-axle 25TN bogie of the freight car: non zero i.c.
$y_i(0)$=0.0045 m, ***R*****=900 m**, h=0.142 m, $\boldsymbol{k_{zy}}$**= 7780000 N/m (2x), *v* - different**

4. CONCLUDING REMARKS

By testing the impact of the lateral k_{zy} and longitudinal k_{zx} stiffness, velocities and the circular curve radius values on bogies' dynamics in the transition curves the authors have received a lot of different results for velocities below and above non-linear critical velocity. Some of them require further study. These behaviours may represent, e.g. fluent passage from the behaviour in ST to that one in CC. The disappearance of vibrations in TC is surprising while the vibrations in ST and CC have the form of limit cycles. The vibrations rapidly disappear in the middle of TC, suddenly reborn for the moment and disappear again. There is also a change in the nature of solutions for individual sections of the route. The vibrations in TC may often represent decreasing tendencies in relation to the values in ST and CC. It has been shown that a lot of factors may influence different behaviours of the vehicle in TC.
Taking into account the individual bogies authors can draw the following conclusions:

*for bogie of the average parameters in case of reducing the lateral stiffness k_{zy} and the velocity (Fig. 8) the limit cycle in CC never appeared (no vibrations in CC) but in Fig. 12 while reducing the longitudinal stiffness k_{zx} and the velocity the limit cycle in CC appeared. But in case of larger circular curve radius *R*=2000 m the limit cycle in CC appears in both graphs (Figs. 9 and 13);

*for bogie of MK111 passenger car in case of reducing both the stiffness types bring similar behaviour of bogie but in case of growing both the stiffness bring different behaviour. In case of Fig. 22, when *R*=600 m the limit cycle does not exist in CC for each case but in Fig. 18 the limit cycle in CC establishes even with a rather big amplitude. In case of Fig. 23, when *R*=2000 m for higher velocities the limit cycle amplitude in CC are smaller than for original graph but in Fig. 19 the limit cycle amplitude were first smaller and then bigger in relation to the original;

*for 25TN bogie of the freight car in case of both stiffness types the authors have found that in Figs. 24 and 26 (*R*=300 m) the vibrations in CC have always a smaller amplitude than on original graphs but in Figs. 25 and 27 (for bigger *R*) some amplitudes are smaller and some are bigger than on the original graphs.

In the future, the authors are going to examine different circular curve radii from *R*=300 m to *R*=10000 m range and whole railway cars (vehicles of more complex construction).

ACKNOWLEDGEMENTS

Scientific work financed as research project no. 2014/15/N/ST8/02668 from funds of National Science Centre, Poland.

5. REFERENCES

[1] **Cheng, Y.C. – Lee, S.Y. – Chen, H.H.:** Modelling and nonlinear hunting stability analysis of high-speed railway vehicle on curved tracks. Journal of Sound and Vibration, 324(1-2), 2009, p.139-160.

[2] **Hoffmann M.:** Dynamics of European two-axle freight wagons. PhD thesis, Technical University of Denmark, Informatics and Mathematical Modelling, Lyngby, Denmark 2006.

[3] **Hoffmann, M. – True, H.:** The dynamics of European two-axle railway freight wagons with UIC standard suspension, Proc. 20th IAVSD Symposium on The Dynamics of Vehicles on Roads and on Tracks. Vehicle System Dynamics, 46(suppl.), 2008, p.225-236.

[4] **Kaiyun, W. – Peng, L.:** Lateral stability analysis of heavy-haul vehicle on curved track based on wheel/rail coupled dynamics. Journal of Transportation Technologies, 2, 2012, p.150-157.

[5] **Kalker, J.J.:** A fast algorithm for the simplified theory of rolling contact. Vehicle System Dynamics, 11, 1982, p.1-13.

[6] **Kik, W.:** Comparison of the behaviour of different wheelset-track models. Proc. 12th IAVSD Symposium. Vehicle System Dynamics, 20 (suppl.), 1992, p.325-339.

[7] **Kisilowski, J. – Knothe, K.:** Advanced railway vehicle system dynamics. WNT, Warszawa, 1991.

[8] **Polach, O.:** Characteristic parameters of nonlinear wheel/rail contact geometry. Proceedings of 21st IAVSD Symposium, August 2009, KTH, Stockholm, Sweden. Paper 95, 2009, p. 1-12, 17-21.

[9] **True, H.:** Multiple attractors and critical parameters and how to find them numerically: the right, the wrong and the gambling way. Vehicle System Dynamics 51(3):, doi: 10.1080/ 00423114.2012. 738919, 2013. p.443-459.

[10] **True, H. – Hansen, T. G. – Lundell, H.:** On the Quasi-Stationary Curving Dynamics of a Railroad Truck. Proc. ASME/IEEE/AREA Joint Railroad Conference, ASME-RTD 29, 2005, p.131-138,

[11] **Wang, K. – Liu, P.:** Lateral stability Analysis of Heavy-Haul Vehicle on Curved Track Based on Wheel/Rail Coupled Dynamics. Journal of Transportation Technologies 2: 2012, p.150-157.

[12] **Zboinski, K. – Dusza, M.:** Extended study of rail vehicle lateral stability in a curved track, Vehicle System Dynamics, 49(5), 2011, p.789-810.

[13] **Zboinski, K. - Golofit-Stawinska, M.:** Simulation study into non-linear properties of railway vehicles in transition curve at velocities around the critical one, 23rd International Symposium on Dynamics of Vehicles on Roads and Tracs, Qingdao, conference materials, IAVSD2013-20.3-ID452.

[14] **Zboinski, K. - Golofit-Stawinska, M.:** Dynamics of 2- and 4-Axle Railway Vehicles in Transition Curves above Critical Velocity, in J. Pombo, (Editor), Proceedings of the Second International Conference on Railway Technology: Research, Development and Maintance, Civil-Comp Press, Stirlingshire, UK, Paper 265, 2014. doi:10.4203/ccp.104.265.

[15] **Zboinski, K. - Golofit-Stawinska, M.:** Vehicle-track system parameters influencing dynamics in transition curves. In J. Pombo (ed.), Proceedings of the Third International Conference on Railway Technology: Research, Development and Maintenance. Stirlingshire, UK: Civil-Comp Press, Paper 89, 2016, doi:10.4203/ ccp.110.089.

[16] **Zboinski, K. - Golofit-Stawinska, M:** Dynamics properties of railway bogie of average parameters in transition curve at velocities around critical one. Proceedings of 20th International Scientific Sonference, Transport Means, 2016.
[17] **Zboinski, K.:** Dynamical investigation of railway vehicles on a curved track. European Journal of Mechanics, Part A Solids, 17(6), p. 1001-1020, 1998.
[18] **Zboiński, K.:** Non-linear dynamics of rail vehicles in curves. ITE PIB Scientific Publishers. Warsaw – Radom 2012, ISBN 978-83-7789-129-2 (in Polish).

AXIAL RUBBING IN HUB-AXLE PRESS FIT JOINT DUE TO BENDING

Ferenc KOLONITS

Department of Railway Vehicles, Aircraft and Ships
Faculty of Transportation Engineering and vehicle Engineering
Budapest University of Technology and Economics
H-1521 Budapest, Hungary

Received: November 7, 2016

ABSTRACT

Fretting is a kind of surface degradation originated by an (even micro) slip between surfaces pressed together while the worn-off particles cannot leave the contact zone. It is an imminent danger for press-fit joints of railway axles and wheel hubs. The vicinity of hub end is very prone to this fault, because there is a peak pressure which has to descend to zero at the end of the hub-axle contact. There, the decreasing pressure cannot produce enough friction force against axial load to prevent rubbing. Such axial load is surely produced by the moment acting on the axle due to weight of the vehicle. More than that, the mutual effect of friction, fitting tolerance and weight may result repeated relative motion of contacting surfaces farther in the hub, extending the zone endangered by fretting. The conditions of relative motion will be studied by finite element calculations on a model including the peak at hub end and the internal part of the contact characterized by Lamé's pressure. The model is detailed enough to be able taking a Navier style load on the axle cross section into account equivalent to a moment load. The appearing of an internal slipping zone cannot be excluded.

Keywords: shrink fit, bending, slip, rubbing, fretting

1. INTRODUCTION

The railway axle and wheel are joined customarily by interference fit. That can be realized pushing directly the axle into the hub of the wheel (press fit) or mounting them with different temperatures and the thermal dilatation will do the job (shrink fit). The joint undergoes to various loads while the vehicle is rolling. For the analysis of events due that, the bulid-up of the fit gives the initial condition. The further studies here will concern the shrink fit technology.

1.1 Introductory remarks: the model

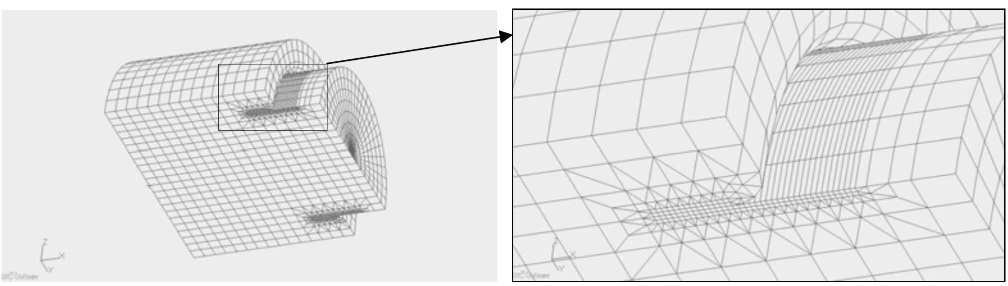

Fig. 1 FEM model and detail at roundoff

The object to be studied is a half of a joint, **Ø160**, length **190** axle, **Ø160/Ø220**, length **150**, **R10** rounded-off hub. Fig. 1 shows the FEM mesh. The size of the finite elements in the axial section is **10x10**, reduced to **1.25x1.25** at the rounded-off end of the hub. This plane mesh will be rotated around the symmetry axle with **2π/50** steps, defining

50 spatial slices consisting of hexahedral finite elements. The nodes in the left cross section of the model will be constrained to move in plane (of symmetry) only.

1.2 Loads and process studied

The hub and axle are fitted with a **H8/v6** tolerance. The resulting overclosure is at least **0.165**, the radial difference is **0.0825**. If it were realized by temperature difference at mounting, that has to be **85.938°C**. The radial contact pressure at full overclosure will be **51.15** MPa according to the formula of Lamé. The mating bodies during mounting and while running under various loads undergo relative displacement. Whether that happens as slip on the surfaces or they remain sticked, that depends on the friction force between. A moderate friction (coeffiecient **μ=0.1**) is supposed to take effect in bi-linear Coulomb form [2]. There, a growing relative displacement of bodies below a certain limit **δ** generates a linearly growing friction force while the surfaces do not slip (The following calculations were made with the MARC program default **0.01969**) . If a greater relative displacement were constrained, the surfaces begin to slip. The displacement/friction force diagram is similar to that of elastic-ideally plastic bodies.

The model will be analysed first under the shrinking process, then a periodic bending moment will be applied on the right end of the axle. In order to guess the magnitude of bending, be a 25-ton wagon of 4 wheels and 0.25 m wheel-chassis support distance taken. With those, a **38 MPa** maximal bending stress can be calculated for the axle [1].

2. SHRINK FIT PROCEDURE

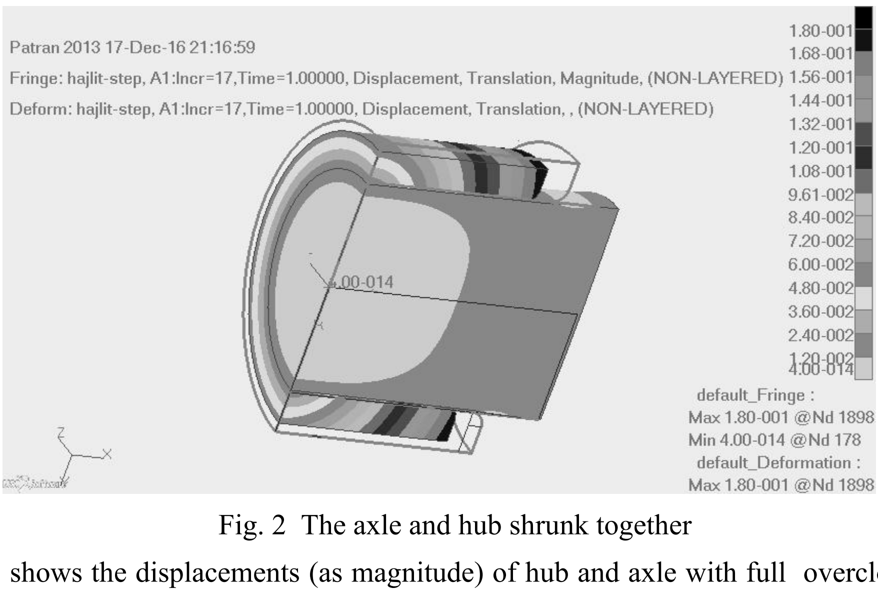

Fig. 2 The axle and hub shrunk together

Fig. 2 shows the displacements (as magnitude) of hub and axle with full overclosure. This can be made by heating the hub to **85.938°C** over the actual temperature of the axle. If they had been manufactured with proper tolerances, the thermal dilatation ceases the radial difference, the parts can be united. Then, letting them to cool down,

the shrink produces the overclosure needed. The procedure has to consider some additional conditions e.g. maintaining the proper relative position of parts.
The contour lines show the original, mounting position of the parts. The fringes show that while the hub recedes on the axle, the latter puts up a small elongation due the radial pressure.
This initial step will be followed with repeated bending cycles. The software lines up and calculates the steps according to “time”. This is now purely symbolic, because no inertial forces are included – no more than an index. Therefore, the “time” of shrink fit mounting will be referred as 0…1. A full sinusoidal cycle will be 2 units long, containing a positive and a negative (0…π…2π) part. The process will be followed through three cycles to discover running-in effects. Start-end ndexes/times of load cases will be 1…3…5…7, respectively.

3. REPEATED CYCLIC BENDING

The Figs 3-5 contain the displacements around the end of second bending cycle. The maximal bending stress Sb had been taken to 75 MPa. Later it will be shown, this load is high enough to produce repeated slipping in the shrink fit.

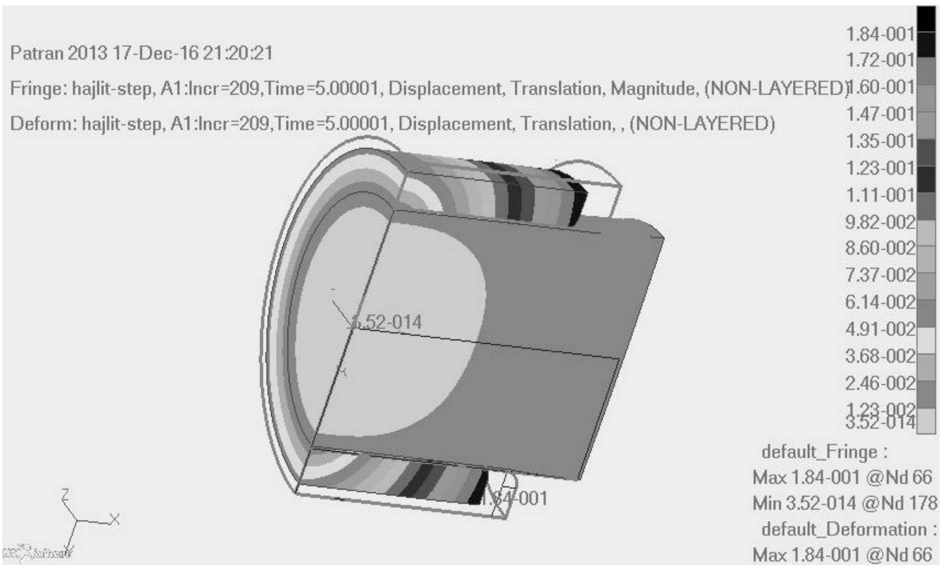

Fig. 3 Displacements at the end of 2. bending cycle (t=5)

The Fig.3 shows the neutral, unloaded position, which is very similar to that in Fig.2. Small differences in values and –most salient – the vanishing the little patch before the hub front may be attributed to shakedown effects.
Fig.4 and 5 shows the displacements under maximal moment load deforming the axle upwards and downwards, respectively. The values and fringes are symmetric enough to suppose that the running-in process were finished and the further cycles are stabilized.

The following calculations/figures show the values of the variation of normal forces and friction forces during the shrinkage and three moment load cycles, i.e. t=0…7, at the Nodes 130 (hub) and 482(axle), respectively. They lay at X=131.25 location, near to the hub end in the zone of small elements.

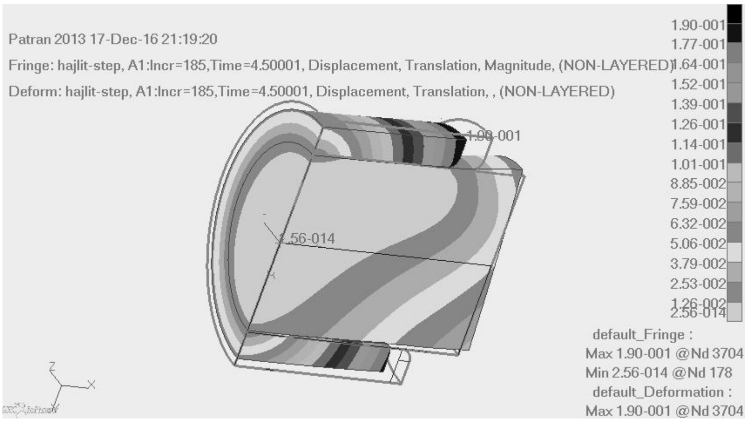

Fig. 4 Displacements at t=4.5, maximal bending upwards

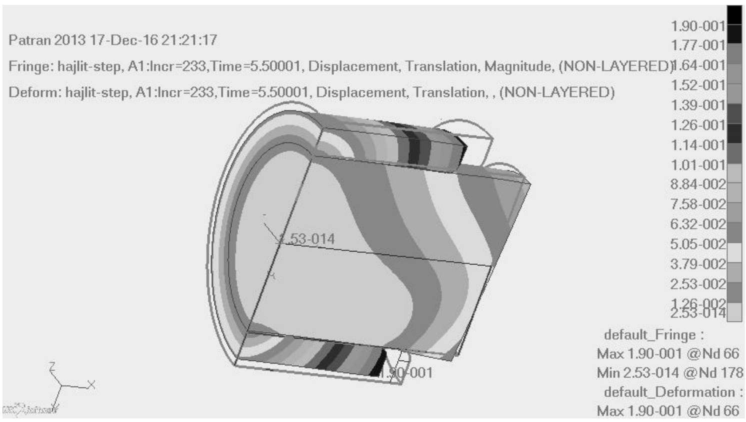

Fig. 5 Displacements at t=4.5, maximal bending downwards

Thus, they may reflect the relative displacements and forces most decisive with respect to stick or slip but outside of possible numerical difficulties at hub end. The maximal bending stress will be started with 38 MPa. In an earlier study [1], the Navier stress distribution of bending could not be applied onto axi-symmetric ring-like elements, the upper triangle of the distribution had been rotated around in the axle cross section. The resulted eventually axial load had been periodically applied onto axle. That is a gross estimate to a real bending load, at end's end shows only, what can happen under periodic axial load somewhat milded in distribution. The axi-symmetric model had been a choice to avoid excessive node/element number but to keep a fine net of element in the axial section. This should help to detect local singular effects, but they did not put up as decisive.

The forces and friction forces in the diagrams are nodal ones. They consist of forces acting on proportional parts on finite elements around the actual node. In order to make easy to confer the forces, the contact normal ones are multiplied with μ=0.1 showing thus the limit what friction forces may reach without slip.

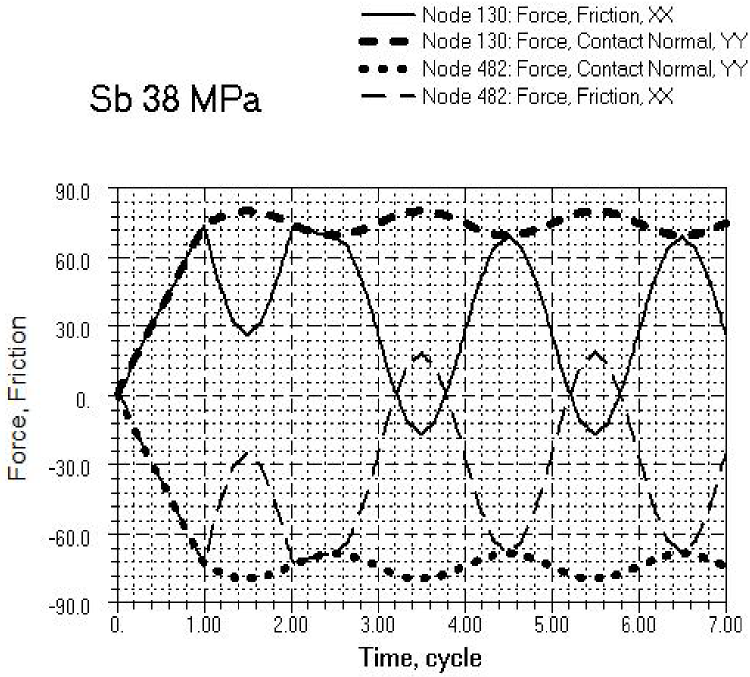

Fig.6 Contact and friction force vs time, under Sb=38 MPa maximal bending stress at location X=131.25

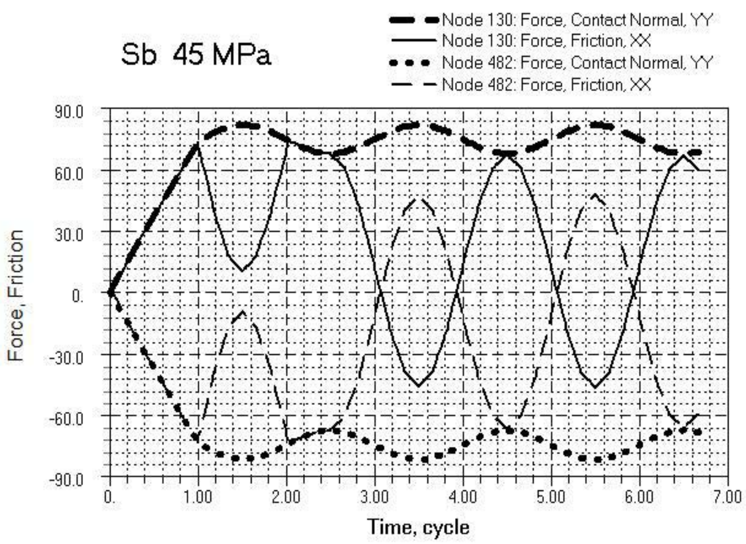

Fig.7 Contact and friction force vs time, under Sb=45 MPa maximal bending stress at location X=131.25

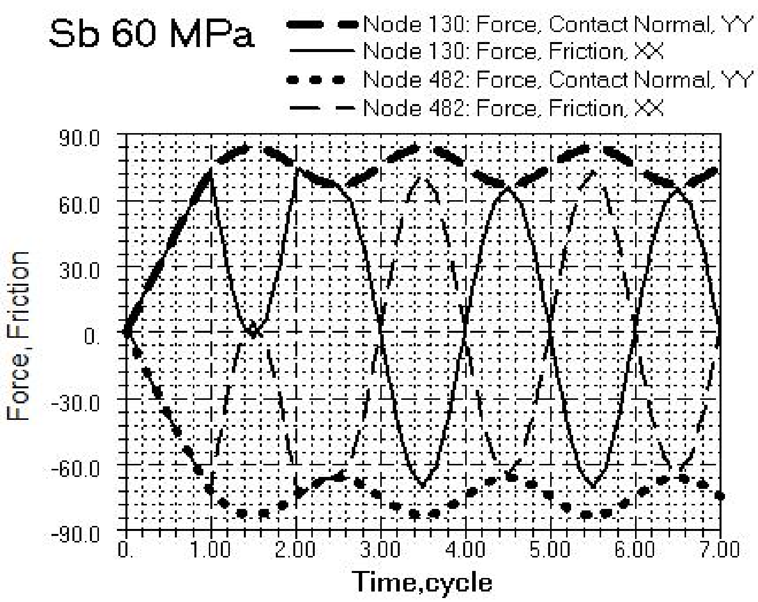

Fig.8 Contact and friction force vs time, under Sb=60 MPa maximal bending stress at location X=131.25

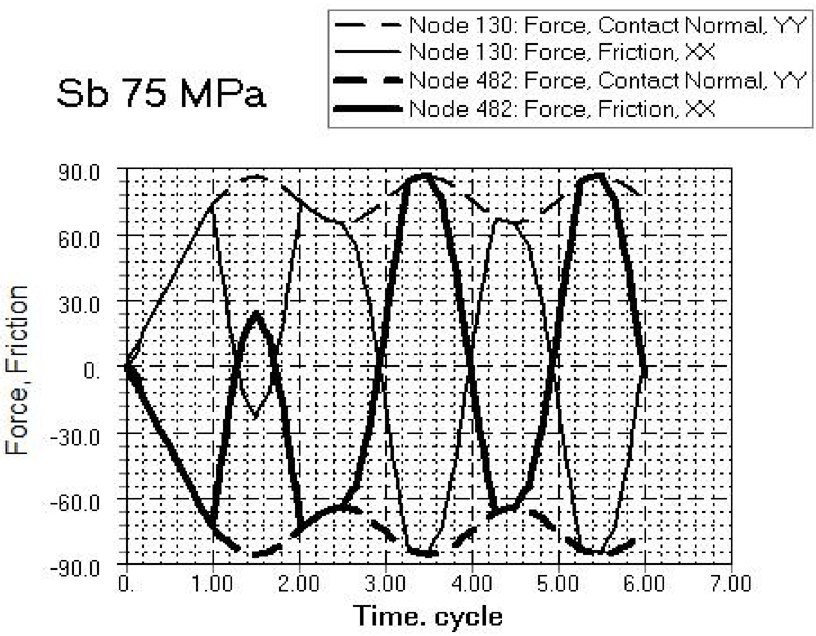

Fig.9 Contact and friction force vs time, under Sb=75 MPa maximal bending stress at location X=131.25

The Sb=38 depicts a process where the pattern produced by the mounting the shrink fit will be modified in the first bending load cycle. There must be a slip due that the hub and axle change their relative position and these will be not modified by any further slip, although the friction force changes periodically but remain mostly under the slip limit. Although it reaches pointwise them at the top of vawes of variation, this is only a local event if any. This curves remain for Sb=45… 60 of same character although the variation of friction forces goes nearer to the limiting (contact normal force)xμ. Somewhere between Sb=60 and 75, respectively, the slip limits are reached and as the Fig.9 shows, a consecutive to and fro slipping occurs.

The displacements under maximal up- and downward bending are shown in Figs 4 and 5, respectively, in specific times. Let us see the variation of axial displacement at specific nodes.

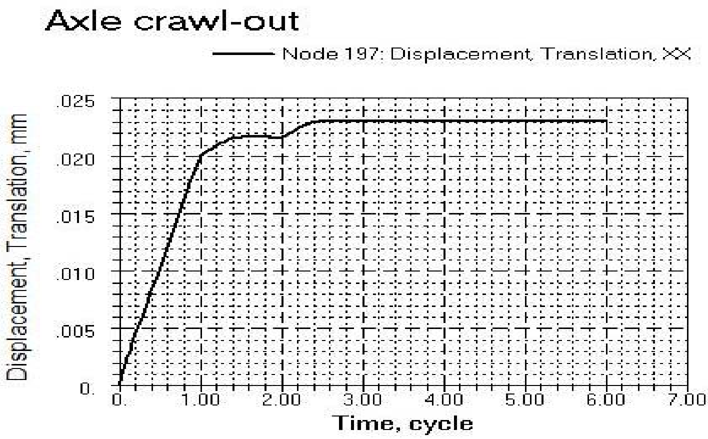

Fig.10 Displacement of axle end center during mounting and load cycles

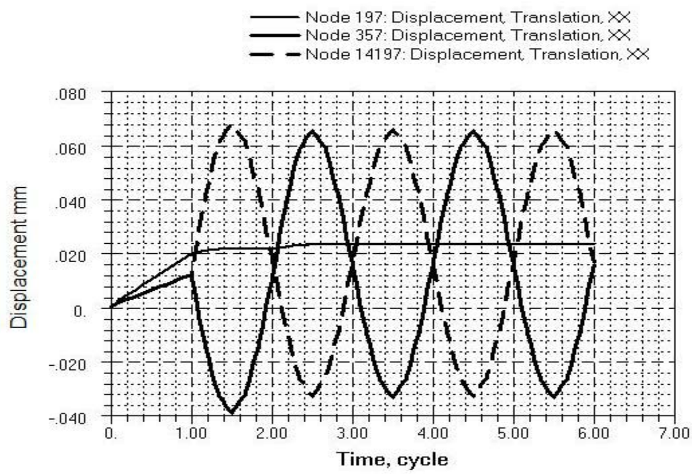

Fig.11 Displacement of axle end contour nodes

The Node 197 is at the central point of the axle end (X=190) In Fig.10, up to t=1, the dilatation due to shrink fit can be seen, after that until t=2 and t=3, respectively, two shakedown crawling-outs appear. However, with these a position of parts are stabilized and no more motion follows under further load cycles. The same curve is drawn also on Fig. 11, along with varying motion of nodes on the end of axle (X=190, Y=±80). They are far greater than the displacement of the center and after the first shakedown cycle show unchanged sine waves.

4. CONCLUDING REMARKS

- Thermal shrink produces remanent stresses, subject to shakedown under repeated loads
- An earlier study had shown that a repeated axial load has the contact surfaces rubbing near the end of the hub or to creep the axle outwards. The load had been simulated by rotating the Navier stress distribution – this grossly over-estimates the load with tespect to a real bending.
- Repeated bending of the same peak intensity produces a shakedown but a stable periodic deformation after that
- A bending of double intensity goes to a shakedown and a stable periodic stick-slip later on

5. REFERENCES

[1] **Kolonits, F.**: Initial conditions for load history of a wheel-hub/wheel-seat contact realized by thermal shrink fit joint. Proceedings of the 10th International Conference on Railway Bogies and Running Gears (Bogie'16) (Ed. by Prof. I. Zobory),SSME (GTE), Budapest, 2016, p.233-242.

[2] **MacNeal-Schwendler Software Co.:** MSC MARC 2013.1 User Manual

INTEROPERABILITY – CONFORMITY ASSESSMENT OF THE ROLLING STOCK SUBSYSTEM - NEW CHALLENGE AND EXPERIENCES

Sándor MALATINSZKY

Head of Rolling Stock Certification Office
KTI Institute for Transport Sciences Non-Profit Ltd.
Railway Certification
H-1119 Budapest, Than Károly u.3-5, Hungary

Received: November 9, September 2016.

ABSTRACT

Rolling stock manufacturers, railway undertakings and wagon keepers shall meet the legal and contractual requirements related to the design, construction, production, modernisation, functions and operation of the railway vehicles. The orientation in the jungle of mandatory and voluntary requirements of the "Technical Specifications for Interoperability of the Rail System in the European Union" is a challenge that needs a lot of time for the manufacturers and also for the applicants of the authorisation, while the risks for incompliance of the products to the new demands are very high.

Keywords: interoperability, rolling stock, certification, conformity assessment

1. INTRODUCTION

Railway Interoperability Directives, the 96/48/EC on the interoperability of the Trans-European High-speed network and the 2001/16/EC on the interoperability of the Trans-European Conventional network have been changed the way that railway infrastructure, rolling stock and the so-called interoperability constituents are designed, assessed and accepted before placing them into service or putting them on the market. The liberalization, the free access of the railway infrastructure opened the door for new actors to participate in the railway transportation. Notified Bodies and Designated Bodies took over the role of the classic national railway companies in case of design review, quality management system approval, testing and verification of the new products. The new term "interoperability" was invented to destroy the technical barriers of the national railway systems to ensure the free movement of the trains across the European Union.

2. RAIL SYSTEM OF THE EUROPEAN UNION

The Council Directive 96/48/EC of 23 July 1996 on the interoperability of the trans-European high-speed rail system and the Directive 2001/16/EC of the European Parliament and of the Council of 19 March 2001 on the interoperability of the trans-European conventional rail system, brought fundamental changes in the life of the companies of the railway industry. New actors appeared on the market exchanging the national railway companies, and sweeping away the 150 years old railway system. New terms should be learnt, for example interoperability and new processes had to be invented in order to keep in operation the system. The interoperability means by the definition of the Directives: the ability of a rail system to allow the safe and uninterrupted movement of trains which accomplish the required levels of performance.

The aim of the interoperability directives is to set up the common European railway market by creating unified subsystems, that ensure the safe movement of trains without obstacles on the whole rail system within the European Union. Further expected result is to place harmonised railway equipment and installations on the market, that make competitive the railway transportation against the road traffic.
The idea of interoperability comes from the necessity to eliminate the obstacles from the international traffic of the European high speed trains. Although, these train systems were developed on national industrial bases and on the requirement of the national railway companies separately, the interoperability of the conventional European rail network has a long history in the international railway traffic.

2.1 The History of Railway Interoperabilty

The origin and the history of interoperability goes back to the Gauge Act of the British parliament in 1846, when it was declared first time that the same rail gauge had to be used in railway passenger traffic to avoid the uncomfortable change of trains and reload of goods at the transfer stations. Or even to the age of the Stockton—Darlington Railway (S&DR), when George Stephenson decided to make profitable the company's operation by running so many coal loaded Chaldron waggons from Darlington to the harbour of Stockton as much as possible.[1] The S&DR was an infrastructure railway company running on the model of the water channels without time table, and everyone could use its service, who had sufficient rolling stock, let it be a hand operated vehicle, a horse or steam locomotive drown train. The experiences gained by the operation of S&DR could lead George Stephenson to the recognition, that the railway infrastructure and the rolling stock constitute a common, closed system. Its optimal operation is the adequate function of the subsystems, the and the rolling stock. The Liverpool & Manchester Railway, opened in 1830, was operated by this principle. This principle was used for 150 years, and is used even today for the operation of the railway systems.
At the same time, when the British Parliament passed the Gauge Act, the ten biggest Prussian railway directorates established the first railway association on the continent, on 10 November 1846. The aim of the association was to support the endeavours of the member-railway companies in unanimity, and thus to serve their own interests as well as those of the public. All German railway companies joined to the association in the next six months. It changed the name to Verein der Deutschen Eisenbahnverwaltungen – Union of German Railways, in December 1847. The Union had 40 members in 1850, four Austro-Hungarian railway companies among them, including the Magyar Középponti Vasúttársaság, which opened the first public steam railway in Hungary between Pest and Vác, in 1846. The Union had defined the most important operational, commercial and technical requirement, developed and offer standardised

[1] The first steam operated Stockton & Darlington Railway was opened for public service on 27th of September 1825. It was built for coal transportation from the collieries of Shildon in County Durham, to the port of Stockton-on-Tees. George Stephenson was asked to construct the railway line and the steam locomotives for hauling the trains. Since few hundred „*chaldron waggons*" with 1,164 m^3 loading capacity had been operated on the Shildon colliery railways carrying coal to the river Tyne, he chose the very similar 4 feet 8 Inches (1422 mm) track gauge for the S&DR company, so the "c*haldron waggons*", could run after minor modifications without restrictions on the new Stockton and Darlington line. George Stephenson increased this gauge by ½ inch at constructing the Liverpool & Manchester Railway, five years later. - Csíkvári Jákó: *A közlekedési eszközök története 1 kötet (The History of Means of Transportation part 1 - in Hungarian),* 1883, reprint kiadás, p. 77

processes for the free movement of goods and rolling stock between the individual networks of the member companies.

The Berne Agreement was the first convention of European states adopted by the German Empire, France, Italy, Austria, Hungary and Switzerland, in 1887. It specified the technical requirement for the international railway traffic across the borders. The Agreement fixed the standard gauge as 1435 mm, defined the dimensions of wheels and wheel-sets and standardised the carriage key. The so called “Technische Einheit” (TE) contained the specified technical requirement related to infrastructure and rolling stock. Famous trains run across the continent by fulfilling the requirement of the TE. like the Orient Express from Paris to Istambul.

The International Union of Railways was set up with Paris headquarters to regulate the railway traffic crossing the new borders traced out by the conqueror nations after the First World War as the result of Treaty of Versailles.[2] In 1922, the UIC had 51 member railway companies from 29 countries, including Japan and China. UIC played an important role in standardization of railway parts, data and terminology. Therefore, UIC Leaflets were developed since the beginning of its establishment, and the these were the technical base of the RIC and RIV agreements, since 1922, which regulated the exchange of passenger coaches and freight wagons running in international traffic.

The PPV regulation was put into force after the second world war, in 1956, to control the railway traffic between the friendly Eastern European countries and the Soviet Union. The PPV, similar to the RIC and RIV regulations, were based on the UIC and UIC- OSJD Leaflets.

Fig. 1 The RIC Frame indicating the maximum speed complying with the provisions of RIC point 31.1 and the additional signs for fulfilling the conditions in RIC appendix IV.

2.2 The Rail System within the European Union

The interoperability Directives 96/48/EC and 2001/16/EC were substantially amended by Directive 2004/50/EC of the European Parliament and of the Council. Since the necessary introduction of further, new amendments the Directives were recast into the new Directive 2008/57/EC on the interoperability of the rail system within the Community, which was published on 17 June 2008. Because of the further amendments the Directive 2016/797/EU on the interoperability of the rail system within the European Union was introduced at the end, on 11 May 2016. The Directive divides into three major parts of the rail bounded network of the Union establishing three levels of the regulations. The first, the highest level is the rail system of the European Union. The second is the field of the open questions and special cases defined in the Technical Specifications for Interoperability (TSIs) and the derogations regulated by the national requirement. Finally, he third is the level of local public transport systems. Since metros, trams and other light railway systems do not need to be interoperable and are functionally separate from the Union rail system, are not in the scope of the Directive.

[2] The new Trianon borders cut the Hungarian railway network at 46 points creating border crossings, in 1920.

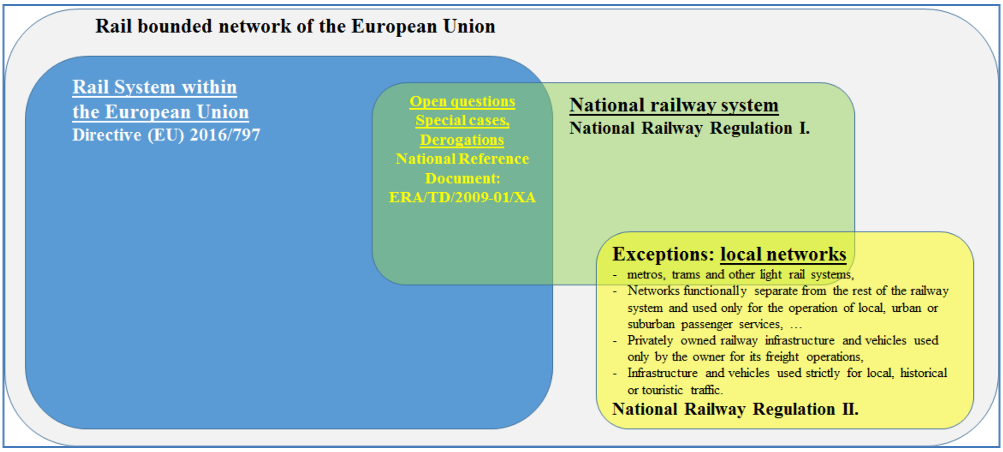

Fig. 2 Rail bounded network of the Euoropean Union

3. INTEROPERABILITY – REQUIREMENT

The Directive defines the essential requirements, that means all the conditions set out in Annex III of the it, which must be met by the Union rail system, the subsystems, and the interoperability constituents, including interfaces. These are:

- safety,
- reliability and availability,
- health,
- environmental protection,
- technical compatibility,
- accessibility

The Technical Specification for Interoperability (TSI) is a specification adopted in accordance with the Directive by which each subsystem or part of a subsystem is covered in order to meet the essential requirements and ensure the interoperability of the Union rail system. The subsystem is the structural or functional part of the Union rail system, as set out in Annex II of the Directive:

(a) structural areas:

- infrastructure,
- energy,
- trackside control-command and signalling,
- on-board control-command and signalling,
- rolling stock,

(b)functional areas:

- operation and traffic management,
- maintenance,
- telematics applications for passenger and freight services.

The structural areas are divided to three parts containing three different groups of TSIs:

- the vehicles,
- the fix installations, and
- the common TSIs.

The group of the vehicles contains three TSIs. For the conformity assessment of the rolling stock further three common TSIs and the NRMM Directive 97/68/EC also contain requirements. The TSIs specify only the basic parameters for the relevant areas. Basic parameters are the regulatory, technical or operational conditions which are critical to the interoperability.

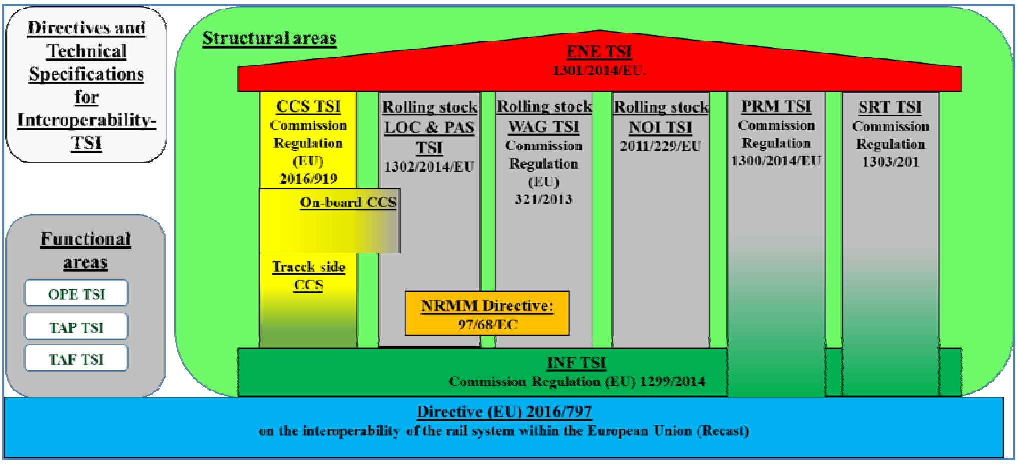

Fig. 3 The Directives and Technical Specifications for Interoperabilility

4. INTEROPERABILITY – CONFORMITY ASSESSMENT

4.1. Conformity Assessment Procedures

Conformity assessment is a set of processes that show that a product, a service or a system meets the requirement of a standard. The first notified conformity assessment bodies appeared in the European Community, already in 1985, to check and certificate the products, whether they meet the demands of the essential requirements of the new directives, when placing into market of them had high risk.

There are three different types of conformity assessment procedures. The first when the manufacturer makes all the checks and tests and declares that its product meets the requirement of the relevant technical documentation. The second, when independent accredited laboratories make the tests, and the last, when independent accredited third parties, conformity assessment bodies certify the conformity of he product. The relevant TSIs define the possible procedures and the Commission Decision 713/2010/EC contains the modules for the procedures for assessment of conformity, suitability for use and EC verification to be used in the technical specifications for interoperability adopted under Directive 2008/57/EC. The conformity assessments shall be carried out by the modules or module combinations defined by the relevant TSIs.

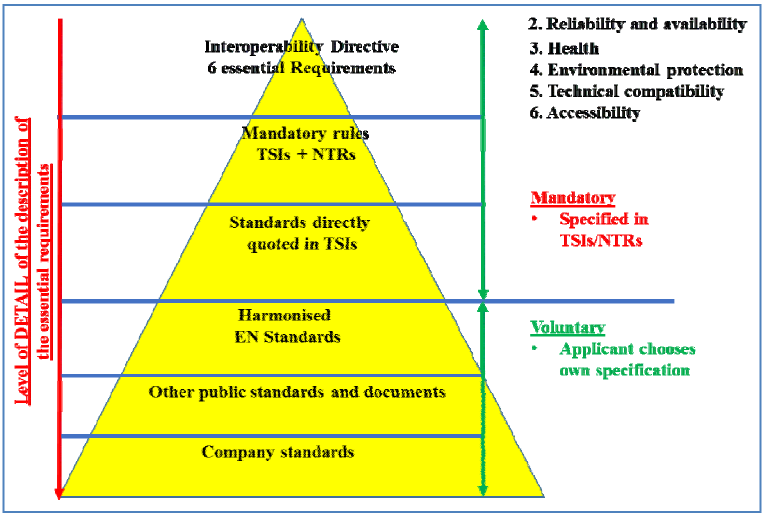

Fig. 4 The hierarchy and levels of detail of the specifications containing the requirements of the products (2014/897/EU)

4.2 The Conformity Assessment Bodies

The conformity assessment body has been notified or designated to be responsible for conformity assessment activities, including calibration, testing, certification and inspection. These bodies are classified as a Notified Body (NoBo) and either as a Designated Body (DeBo).

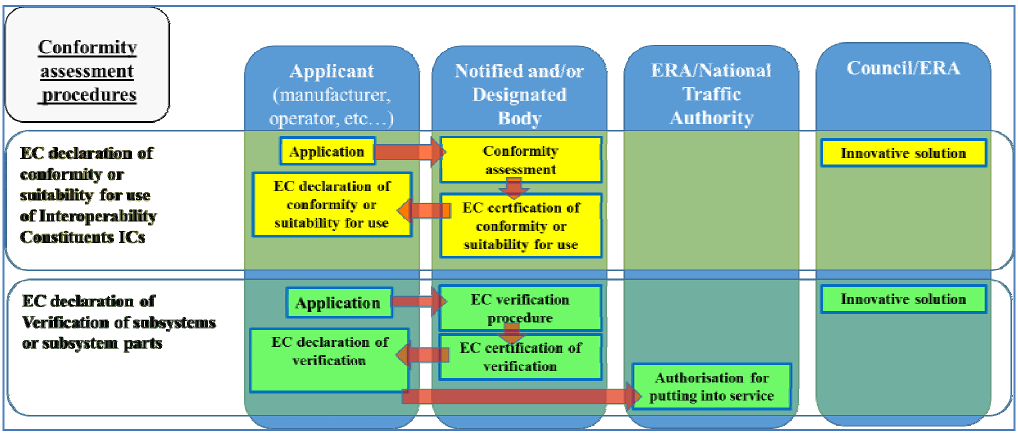

Fig. **5** The process of conformity assessment procedures

The notification of a NoBo is an act whereby a Member State informs the Commission and the other Member States that a body, which fulfils the relevant requirements, has been designated to carry out conformity assessment according to a directive, on the territory of the European Union[3]. The DeBo is a conformity assessment body, which fulfils the relevant national requirements, and has been designated to carry out conformity assessment according to national regulations.

[3] http://ec.europa.eu/growth/tools-databases/nando/

The conformity assessment body shall be a legal entity, independent from the manufacturer, the operator and the dealer of the product, shall have: liability insurance, professional competence, professional experiences and the equipment necessary for the testing procedures.

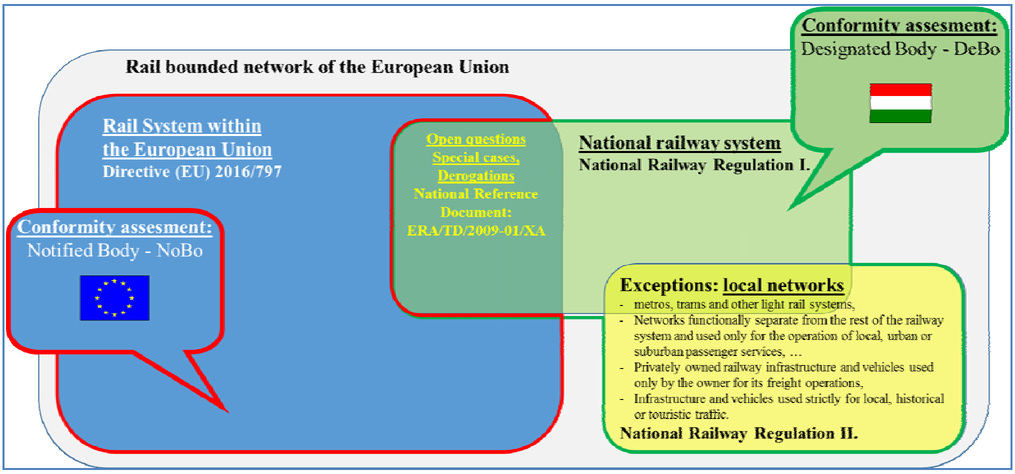

Fig. 6 The ares of NoBo and DeBo certifications

4.3. The Authorisation for Placing into Service of the Subsystems

The authorisation for placing in service of a railway subsystem is the recognition by a Member State that the applicant for this subsystem has demonstrated that it meets, in its design operating state, all the essential requirements of Directive 2008/57/EC when integrated into the rail system. According to Article 17(1) of the Directive, this is provided in the form of an EC-declaration of verification[4].

The Commission adopted its Recommendation 2011/217/EU to clarify the procedure for authorising the placing in service and use of structural subsystems including the vehicles as set out in Directive 2008/57/EC. The following diagram summarises the activities before and after an authorisation for placing in service of a structural subsystem and putting into service of the rolling stock.

4.4. Conformity Assessment and the Reliability Theory

Since reliability and availability are essential requirements, the detection of the lack of the safety relevant functions of the rolling stock shall be subject to a reliability study considering the failure mode of components, redundancies, software, periodic checks and other provisions, and the estimated failure rate of the function.

The reliability of safety related components shall be demonstrated by failure mode analyses, safety analyses and either risk analyses. These components and equipment are the brake system, the control system, the passenger access doors, the system for the detection of driver's activity, some kind of Fire Containment and Control Systems. The knowledge and application of the reliability theory, as additional requirement, is very important in the conformity assessment processes.

---

[4] Comission Recommendation of 5 December 2014 on matters related to the placing in service and use of structural subsystems and vehicles under Directives 2008/57/EC and 2004/49/EC of the European Parliament and of the Council (Text with EEA relevance) *(2014/897/EU*

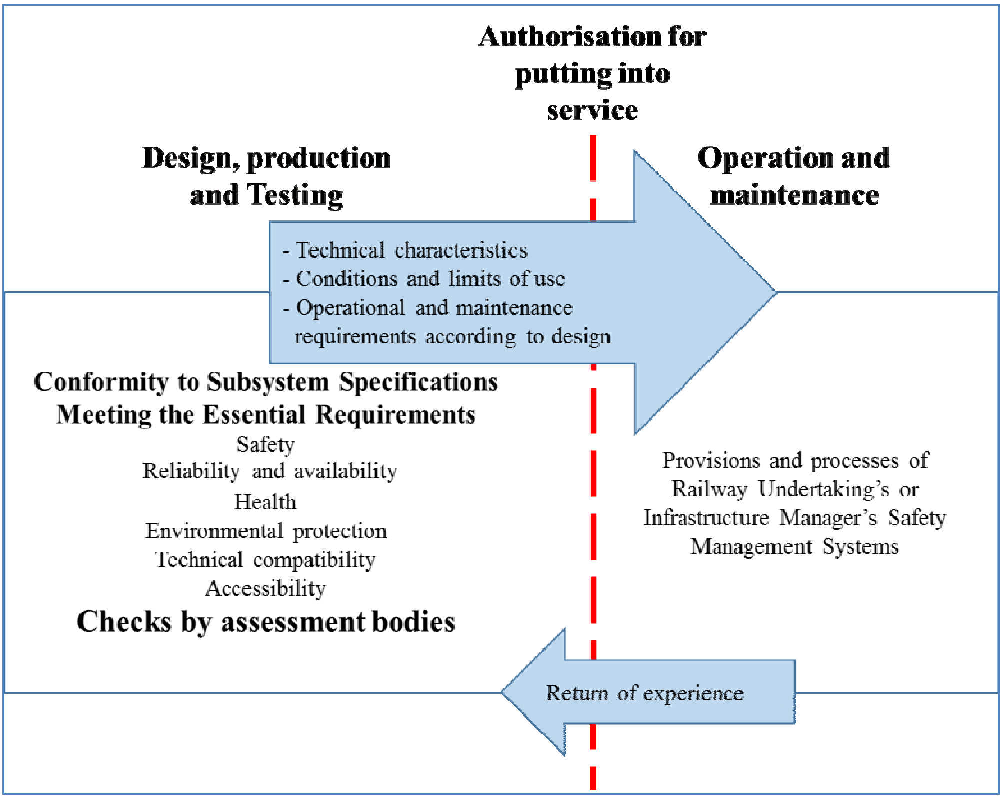

Fig. 7 The procedure for authorisation as set out in Directive 2008/57/EC and the activities before and after an authorisation for placing in service of a structural subsystem

To maintain and improve the operational safety of these parts and equipment is also a demand for the operators, which needs rather theoretical, than practical knowledge.

5. THE EXPERIENCES

5.1. From the Point of view of the Manufacturers

The last two cartoons represent very well the situation caused by the invention of the conformity assessment procedures in the rolling stock manufacturing industry. Unnecessary checks and expansive tests hinder the authorisation of the vehicles and hold up the manufacturing processes. Needless and useless documentation, plus expenses that are the opinions of the applicants are pointed out.

5.2. From the Point of view of a Conformity Assessment Body

It is a fact that involving an additional party into a process, where the customer, the manufacturer and authorising national authorities played only the main roles before, makes the procedures more difficult. The experiences show that the applicants should be better prepared for the participation in these processes. They should know better the requirements, the related documents, and the possibilities offered by the necessary use of the module system.

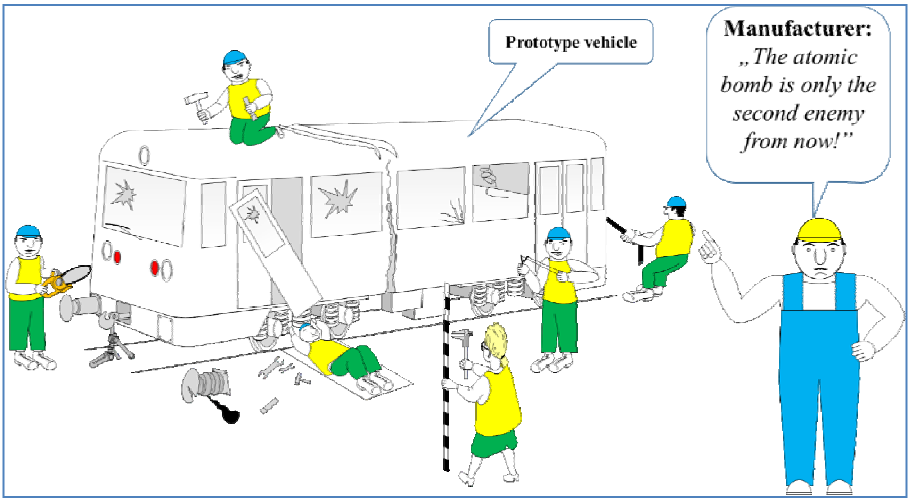

Fig. 8 Conformity assessment tests 1

When a contract is made a time demand for the conformity assessment is not taken into consideration. Generally, the time is too late, when the applicants turn to a NoBo or DeBo for the certification and the product does not meet all the requirements. The correction of the deviations takes time and more expenses.

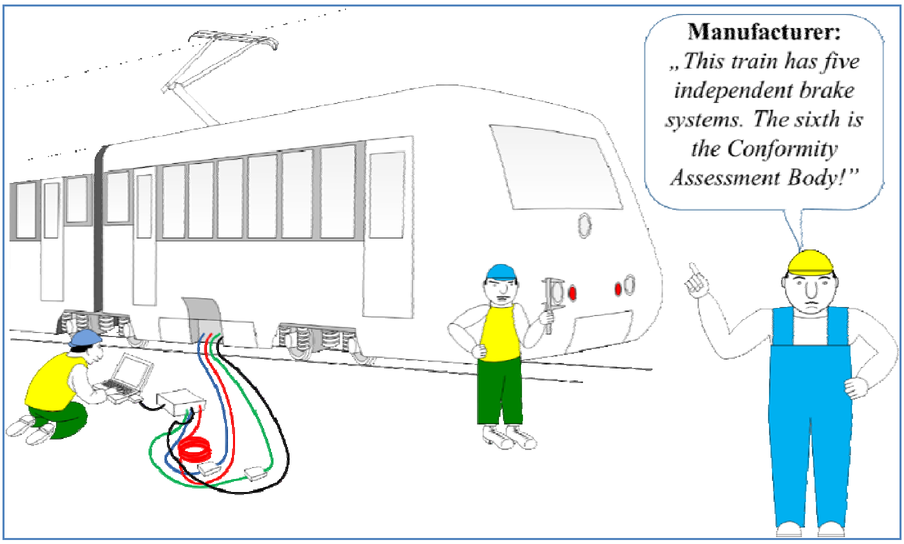

Fig. 9 Conformity assessment tests 2.

6. CONCLUDING REMARKS

The manufacturers' responsibility is to check, weather their products need EC declaration of conformity or suitability for use before putting them on the market, or EC declaration of verification to get the authorisation to operate them on the European or the national rail networks. The manufacturer of the product must declare the conformity or suitability for use or the verification that it meets the requirements of the European

Union's legal obligations, or fulfil the national requirements on the bases of a certification issued by a NoBo or a DeBo. The conformity assessment should be started at the very beginning of the design of the new products, as early as possible.

The TSIs are opened for the new innovative solutions which do not have accepted certification processes yet. So, the laboratories of the universities and the research institutes also can join to this activity to elaborate new technologies and define new conformity assessment methods.

„The biggest obstacle of the certification is the proficiency."

Dr. János SZÉKELY
Expert for railway certification KTI

7. REFERENCES

[1] **Csíkvári, J.:** A közlekedési eszközök története 1 kötet (The History of Means of Transportation part 1), 1883, reprint issue, p. 77. (in Hungarian)

[2] **Malatinszky, S.**: A Bejelentett szervezetek - Notified Body-k feladata az európai vasútközlekedési iparban, Vasútgépészet, Budapest, 2014/1, p.24-28. (in Hungarian)

[3] Council Directive 2008/57/EC on the interoperability of the rail system within the Community, 17 June 2008,

COMPARATIVE INVESTIGATION OF THE COMPONENTS DETERMINING THE RELIABILITY OF RAILWAY CARRIAGE BOGIES BY USING LONG TIME-SPAN OPERATION DATA

József CSIBA

Head of Railway Certification (NoBo & DeBo)
Budapest University of Technology and Economics,
Intelligent Transport and Vehicle Systems Non-Profit Co.
H-1521 Budapest, Hungary

Received: November 9, 2016

ABSTRACT

The carriage stock of the Hungarian State Railways Co and their bogie types are rather heterogeneous and they have got different upgraded versions. The aim of this investigation is to get an answer to the question: how do the operation conditions of the structural elements determining the running technical characteristics of different types of bogies change during operation. In what form can the reliability distribution function $F_\tau(t)$, the failure rate $\lambda(t)$ and other safety characteristics related be given in the time span of the investigation based on the available data. It could be the objective of further investigations whether there is a uniquely determined relationship among the failures of the components selected for investigation, or only a certain measure of stochastic connection can be recognised. The time span of the investigation is from 01.01.2010 to 31.08.2016. The vehicles selected for investigation are carriages built for international and domestic traffic. The vehicles are built on the basis of traditional principles. 4- and 2-axle EMU and DMU stocks can also be found among them. 2-axle rail-buses with 2-axle trailers for side line traffic have also been chosen as targets of this investigation. The general overhauls and inspections were given for the vehicles with variant age and building construction in different workshops. A natural workshop system was operated during the first period of operation of the vehicles. This old system had a lot of advantages in connection with the lead-times and costs of the maintenance. The natural workshop system was eliminated in the last decade by changing of philosophy of the carriage maintenance. Cycle time periods were extended and workshop tasks were passed over the depots. The depots based maintenance and repair events concerning those structural elements that make worse the running technical characteristics will be analyzed in this investigation. All of anomalies and failure data constituting the basis of the investigation are brought concerning a determined time span. But the time span sequences determined in this way can be considered as realisations of random time span sequences. These time spans can be identified as random variables ordered to the bogie numbers and the difficulties in operation processes of the chosen bogie types can be recognised by the help of the random variables mentioned. Data of maintenance and repair events and wheel-set failures requiring wheel-set changing can be brought in connection with time and with the mileage of the carriages, too. The extent of the wheel-wear can be better expressed by the latter characteristics. The events in connection with the whole bogie, wheel-set and its structural elements, bolster, suspension gear, dampers and wheel-slide protection will be analyzed from the anomaly and failure events recorded in connection with bogies. This investigation gives an opportunity to compare the running gears of vehicles built by different Hungarian and foreign companies and workshops of the Hungarian State Railways with regard to the reliability, availability, maintainability and safety (RAMS), too. There is a comparison opportunity in connection with the different vehicle bogie types by the help of operation and maintenance data.

Keywords: running gear, reliability, anomaly, maintenance and repairing event, mileage performance

1. INTRODUCTION

Numerous technical and organisational conditions are needed for the economical vehicle operation. Reliability, availability, maintainability and the result of the maintenance activity are determining factors in connection with the economical operation. Exact maintenance and vehicle data are necessary for the analysis of operation. Anyway a very valuable and useful information package is given to the operators, maintenairs, manufacturers, designers, vehicle owners and a lot of different experts by the continuous collection, comparative investigation and variation with time of maintenance data of different type of railway vehicles.

A comparative investigation method and evaluation procedure of maintenance data of different bogie types of railway carriages for same traffic tasks will be shown in this paper.

2. PRELIMINARES

The presentation under title "The Investigation into the Reliability of Bogies of the 2nd Generation InterCity Carriages at the MÁV" was delivered in the 9th International Conference on Railway Bogies and Running Gears in 2013, [6].

The identification of the weak points of the vehicle and the bogie constructions was submitted by the presentation. There was an opportunity to study an exact analysis of failure causes in a combined cost and time analysis considering the failure events.

Some proposals and suggestions were pointed out from the aspect of the continuous and future works in connection with the determination of weak points of different bogie types and the calculation of numerous maintenance key performance indicators (KPI). Among others Systematic evaluation of available data, survey of grouping of data, permanent control of data fixing and collecting can be found in the paper [2].

3. TASKS DERETMINED BY FORMER EXAMINATIONS

An adequate task series is given by the above mentioned observations and the results of the previous examinations lectured in the course of the last Budapest VSDIA 2014 and BOGIE' 16 conferences. This series are generated by the following elements:

- Systematic application of results given by this investigation and the development of informatics background of vehicle maintenance to increase the human and technical reliability in operation and maintenance of vehicles in passenger traffic and to reduce the cost indexes in connection with the above mentioned activities.
- Development of the software package to reduce the failure data acquisition.
- Increasing of the software effectiveness through increased human reliability.
- Extension of the introduced investigation method to possibly all types of bogies and vehicles operated by the railway company.
- The completion of the software package by suitable considered time data is unavoidable needed in the interest of computation and control of the vehicle availability.
- Investigation into the reasons of wheel-set failures.
- Examination the possibility of technology changing in wheel-set repair.
- Overview of the difficulties with dampers of different types.

4. VEHICLES AND THEIR TASKS, BOGIES

Vehicle types of this examination partly are rebuilt types for InterCity traffic and partly for suburban traffic. The vehicles for the first purpose are loco hauled ones, the other ones are EMU vehicles and loco hauled. One group of the InterCity carriages are composed by the types 10-67 (open first) and 20-67 (open standard). These 2nd generation IC carriages originally manufactured in Győr between 1974-1976, built Y type carriages for domestic traffic are rebuilt in Dunakeszi Vehicle Repair Workshop. Their bogies are also modernised types: RÁBA – Dk (IC). The other type family of InterCity purpose is designated by 19-57 (open first) and 29-57 (open standard). These originally in 1979-1980 in Poznan built Y type 3rd generation IC carriages for domestic traffic are rebuilt in the Dunakeszi Vehicle Repair Workshop. The bogie type of this vehicle generation is designated by Dk.

The vehicle group for suburban traffic consists of the vehicles: 11-05 open first, 21-05 open standard, 22-05 open standard, built in Ganz – MÁVAG Co. and Ganz-Hunslet Co. between 1987-1994 these vehicles are able to run in EMUs (type BDv), the bogie type of these latter ones is of type GH-250-2, with a permitted speed of120 km/h.

The designations of the loco hauled vehicles for suburban traffic are as follows: 20-05 550-… open standard, 80-05 400-… driving trailer brake open standard, carriages rebuilt in Dunakeszi Vehicle Repair Workshop, 1998-2008. As for the bogie types in question: 90, 90 modernized, GH – 120 S and type 130.

5. MAINTENANCE DATA

The examined maintenance data come from time interval: 01.01.2010…30.09.2016.

The data collections contain:

- Vehicles by running numbers
- Naming of (carriage, motive power) depot
- Kind of work
- Time of entering depot
- Leaving time of depot
- Work (failure) denomination
- Time consumption
- Number of exchanged (repaired) parts

6. COMPARATIVE INVESTIGATION

By the help of the following three tables and four Figures a detailed comparative investigation can be executed. Maintenance events, maintenance hours, yearly and daily mileage performances can be investigated for the different type of vehicles and the different usage and application fields of the carriage types. A very useful information package can be found in connection with the applied maintenance practice by the analysis of brake shoe/pad changing events for the different vehicle types. There is an adequate opportunity to plan the component supply by the analysis of failure events of the main components of bogies and other structural units of the vehicles.

Vehicle type	Vehicle number	Maintenance events			Maintenance hours /vehicle	Yearly mileage	Daily mileage
		assortment	number				
			total	/vehicle			
1	2	3	4	5	6	7	8
10-67	26	21	3711	142,73	346,43	221000	605
20-67	97	180	11628	119,88	242,29	193287	530
19-57	3	18	311	103,67	348,4	180488	494
29-57	7	24	571	81,57	283,89	123267	338
20-05 550 -	293	105	61978	211,53	371,96	117474	322
80-05 400	55	67	10626	193,20	349,56	98973	271
11-05 0	4	8	63	15,75	72,15	58451	160
21-05 0/100	53	12	251	4,74	448,92	74568	204
22-05 0	32	17	211	6,59	55,56	54222	149

Table 1 Maintenance and vehicle information

ANALYSIS OF BRAKE PAD CHANGINGS (10-67)

NUMBER OF BRAKE PADS	0	1	2	3	4	5	6	7	8	9	10	12	14	16	18	20	22	24	26	28	32
FREQUENCY	8	645	357	40	431	14	54	2	188	2	14	85	10	100	8	25	1	14	1	3	40

Table 2 Data brake pad change of the carriage type 10-67

7. EVALUATION

An absolute exact wide-spread evaluation can be executed by a comparative investigation into the available comprehensive maintenance data basis. The aim is only to show the opportunities through some short examples in connection with a few traffic safety relevant parts of the chosen bogies. The mileage performances of vehicles are not too high and they spread strongly. The reliability of the wheel-sets can be acceptable, since the number of wheel set changes is low, it means: the maintenance plan is reasonable or the mileage performance is too low between two maintenances in workshop. The changing time of the brake pads and brake shoes are too high and they spread on a wide scale. Mostly not the total brake pad/shoe set is changed. It can be a reason of surplus vehicle residence in depots. Lack of vehicles can make an anomaly in the availability of the passenger trains.

After the introduction above let be constructed a Table wise comparison about the vehicles and their bogies of identical types or members of a vehicle families considering the different constructional components or units. This evaluation can generate questions concerning the vehicle economy, as well. Let this carriage family the most spread domestic InterCity carriage family having obviously identical bogies.

	EVENTS OF MAIN PARTS OF BOGIES								
VEHICLE TYPES	10-67	20-67	19-57	29-57	20-05 550-	80-05 400-	11-05 0	21-05 0/100-	22-05 0
NUMBER OF VEHICLE TYPE	26	97	3	7	293	55	4	53	32
BRAKE PAD CHANGE	3628	4017	232	430			30	191	93
BRAKE PAD CHANGE/VEHICLE	140	41	77	61			8	4	3
NUMBER OF CHANGED BRAKE PADS	14965	30996	2725	5133			299	1282	1143
NUMBER OF CHANGED BRAKE PADS/VEHICLE	576	320	908	733			75	24	36
BRAKE SHOE LINING CHANGE					53457	8959			
BRAKE SHOE LINING CHANGE/VEHICLE					182	163			
NUMBER OF CHANGED BRAKE SHOE LININGS					625695	114998			
NUMBER OF CHANGED BRAKE SHOE LININGS/VEHICLE					2135	2091			
WHEELSET CHANGE	2	116	3	8	189	47	0	0	7
WHEELSET CHANGE/VEHICLE	0	1	1	1	1	1	0	0	0
NUMBER OF CHANGED WHEELSETS	8	418	12	26	668	180	0	0	28
NUMBER OF CHANGED WHEELSETS/VEHICLE	0	4	4	4	2	3	0	0	1
WHEELSET TURNING	6	319	8	14	846	185	9	30	72
WHEELSET TURNING/VEHICLE	0	3	3	2	3	3	2	1	2
NUMBER OF TURNED WHEELSETS	28	1116	25	32	3148	716	12	30	75
NUMBER OF TURNED WHEELSETS/VEHICLE	1	12	8	5	11	13	3	1	2
DAMPER CHANGE	6	1911	13	42	1738	445	0	9	2
DAMPER CHANGE/VEHICLE	0	20	4	6	6	8	0	0	0
NUMBER OF CHANGED DAMPERS	22	3146	22	55	3961	992	0	21	2
NUMBER OF CHANGED DAMPERS/VEHICLE	1	32	7	8	14	18	0	0	0

Table 3

Maintenance data of main components of bogies

Table 1 contains the main data about the maintenance and vehicle identifying information. Consider the two first vehicle types in the table. The types 10-67, 20-67 are the determining ones of the domestic IC traffic of the Hungarian Railways. (In the earlier years also buffet cars belonged to the type family considered which performed also restaurant service. The vehicles belonging to the carriage types mentioned today are stopped, i.e. they are out of service. The two open carriage types perform a mileage performance of 605 and 530 km pro year. These figures both from the point of view of the absolute values and of the relation of the two numbers are satisfactory. The numbers of the carriage types are: 26 and 97, thus one open first covers four open standard. Due to the decreased traffic in the train build up the IC trains in the majority of cases and of destinations – especially on weekdays and out of peak hours – eventually only one or two, earlier three but maximum four open standard and only one open first vehicle can be found in the IC trains. It amplifies the daily performance that the vehicles run the highest performance on the lines of highest train density, at given trains mileage value 1080 km/day. All these mean that the longest trains operate on the lines mentioned above.

Considering the two types the number of maintenance activities is proportional, in the time span in question the number of the maintenance evens were 3711 and 11628. (Obviously the due activities, the regularity, the quality of the maintenance work and the waiting times of the vehicles in workshops and storing tracks do not belong to the scope of this analysis.) The number of maintenance activity per vehicle is approximately proportional the values are 142.73 and 119.88, rounded: 143 and 120. The differing number of maintenance operation kinds is questionable. The number of operational kinds is 21 for open first, while 180 for open standard. This significant deviation in numbers is found for two carriage types of almost identical layout. The only difference is in the number of seats, while seat arrangement is approximately identical. The bogies are nearly of congruent layout. Both of the two mentioned vehicle classes had been manufacturing throughout years in almost identical layout and of almost identical bogies. The question arises, how could be generated this significant deviation, namely the number of maintenance operation kinds is 21 for open first while 180 for open standard? From what can be originated this deviation? Is it be possible at all? The answer is a determinate yes. The source of the deviation in question can be identified in the fact that the maintenance information system has been introduced without appropriate preparation and professional background. It is also probable that the data preparing personals did not go under appropriate training. The personals mentioned have not been provided with auxiliary materials for studying the data preparing activities.

It can be true that the data preparing personals had a not bounded freedom when doing data preparation. The former means the un-appropriate preparation of the activity introduction. It is likely that the same maintenance operations or vehicle components are identified by using different names. It can also cause a trouble that the new personals applied for operating the new system have not had a proper training or the personals in questions have not had the awaited pre-training. The mentioned phenomenon appoints the fact that no comprehensive analysis and examination of the maintenance information system was made in the almost seven year duration, so the correction of the system has not been performed. Remaining at Table 1 one should mention yet a further data pair for the two carriage types, namely the number of maintenance hours per vehicle. The data pair in question: 346 hours/vehicle for open first and 242.29 hours/vehicle for open standard. The question remains, how it can be possible taking into consideration the practically identical layouts, identical maintenance cycle order and cycle activity elements. Though in the first part of the cycle order the mileage performances are not taken into consideration because the cycle elements are jointed to the calendar days, but the necessity of the workshop maintenance influencing the technical state of the vehicle in a crucial way is determined on the basis of mileage performance for these vehicle types, which mileage performance can be overwritten by the calendar years as final bounds. (The drawback of the regulation is the fact that it refers for calendar duration, not for the real time of operation and service days.)

Table 2 gives an overview about the number of changed brake pads realised in the course of maintenance of carriage type 10-67. (Obviously with the knowledge of the data available similar Table can be constructed for other vehicle types.) In the context of brake pad changing the ideal number pair would be 0 or 32, reflecting the fact that no or all pads should be changed when maintenance is done. Other figures reflect unsatisfactory maintenance activity. More unsatisfactory maintenance procedure emerges when the number of changed pads is odd, or if the changing is not performed in a pair-wise way.

Table 3 shows the maintenance data of the main bogie components of the vehicle types included into the analysis. The Table contains for the types considered also the specific data concerning the vehicles. (Regarding the Table the main role carriers are the data of the two IC-carriage types for domestic traffic.) Considering the maintenance of the wheel-sets two facts are by all means to be mentioned: at both of the types relatively few maintenance events emerge due to the structure of the bogies, furthermore the maintenance practice is not identical concerning the two carriage types. The wheel-event of carriages 10-67 are almost decaying: in the considered time span there was no wheel-set change, further more in the considered time span carriage-wise only a single wheel-set turning occurred. Here the question arises, what the cause can be of the two order of magnitude higher number of failure events at the open standards, though the mileage performance of this carriage type is 14% less than that at the open first carriages. (This phenomenon requires further analysis, since the failures of wheels and the wheel-repair mean considerable cost component, furthermore the extraction of the vehicles from service has considerable consequences concerning the increase in operation and service costs. It should be analysed if in the background of the mentioned phenomenon there is not only the inappropriate practice of one-two service places). The final item in the table is the damper: the damper change as maintenance event, the number of the changed dampers vehicle-wise, and the specific characteristics of the former numbers for each carriage. In connection with the dampers, quite similar relations can be recognised as those at the wheel-sets: the dominance of the events and number of changes emerge at the carriage type 20-67.

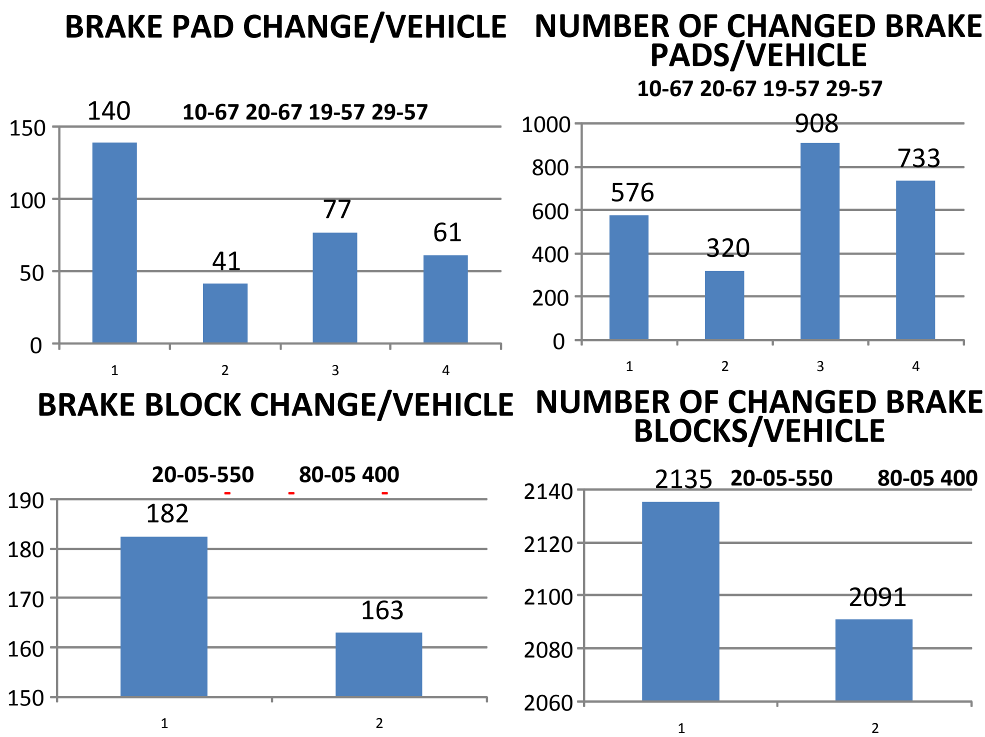

Fig. 1 Specific values of the number of the changing of different brake components in bogies during the maintenance process

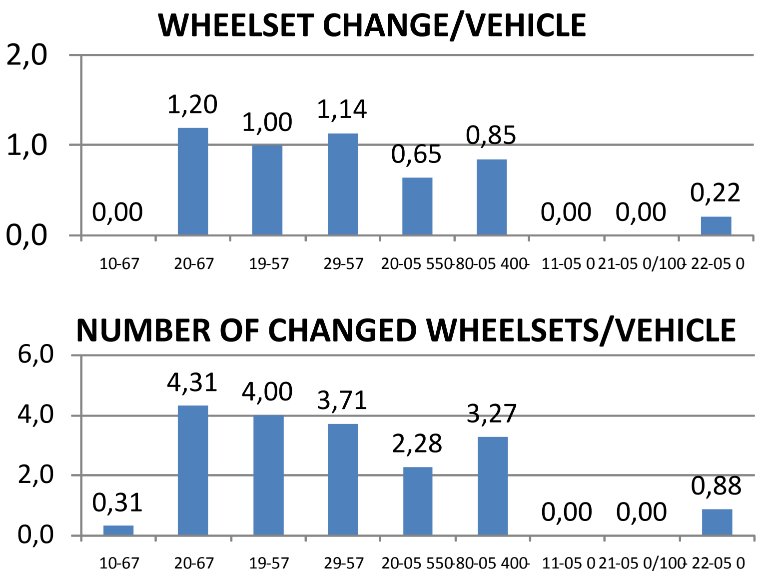

Fig. 2 Specific values of the wheel-set changes

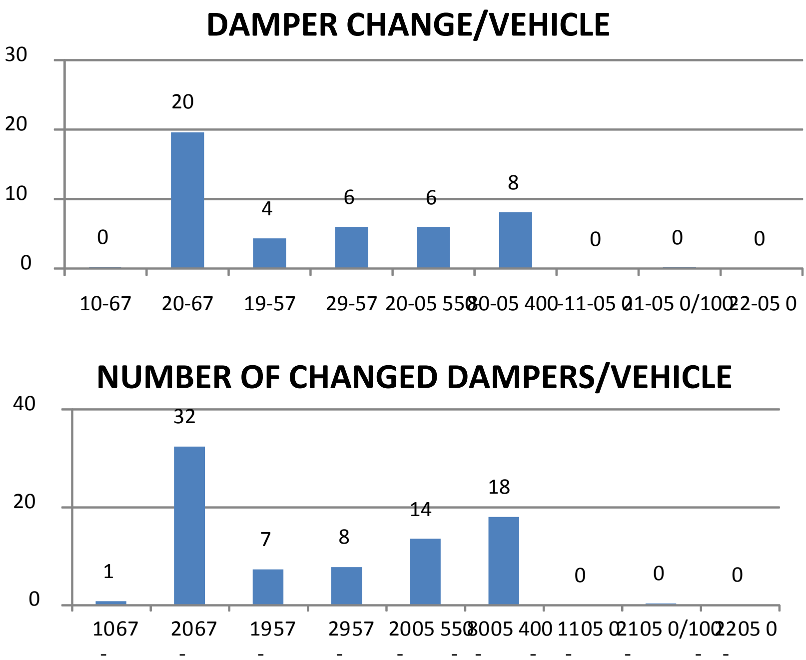

Fig. 3 Specific values of the damper changes

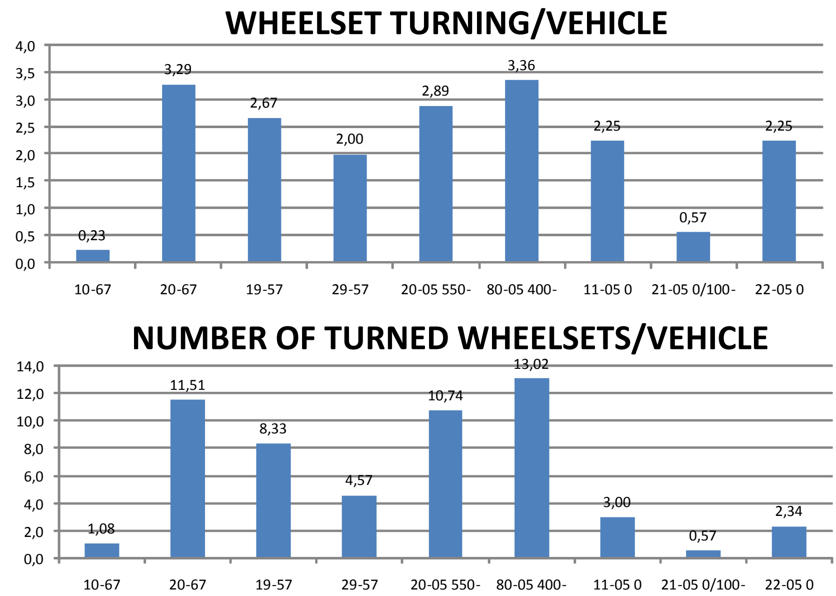

Fig. 4 Specific values of the wheel-set turning

8. SUMMARY

The necessity of collection and evaluation of maintenance data of railway vehicles and several results of the data evaluation were shown in the paper. The following main topics are treated in the paper :

- Preliminaries
- Vehicles and their tasks, bogies
- Maintenance data
- Comparative investigation
- Evaluation
- Further tasks and proposals
- Summary

9. FURTHER TASKS AND PROPOSALS

It can be stated that different tasks and proposals can professionally be elaborated by the analysis of the maintenance, failure and operation data. These tasks and proposals are the next ones:

- Revision of data-system
- Systematic evaluation of available data
- Survey of grouping of data
- Permanent control of data fixing and collecting, even using of software technology
- Increasing of the reliability of fixed data
- Data control based on data fixed in other systems
- Trainings on the basis of the results of control activity
- Collecting of experiences, consultations

By the solution and analysis of the listed tasks a higher reliability of operation and lower maintenance cost data will be realised.

10. REFERENCES

[1] **Zobory, I. – Győri, J. – Kolonits, F. – Békefi, E.:** On Reliability Analysis of Bogies and Running Gears. Proceedings of the 7th International Conference on Railway Bogies and Running Gears (Edited by Prof. I. Zobory), BME Department of Railway Vehicles, Budapest, 2007, p.367-383.

[2] **Zobory, I.:** Data Needed for Determination of Reliability of InterCity Carriages Type Eurofima by Managing Based Software VAJAR, Maintenance Development by Information Technological Tools. Research closing report. 28th December 2005. p.90 +110+5. (In Hungarian)

[3] **Zobory, I.:** Railway Operation, Reliability and diagnostics. Lecture Notes for MSc Courses. BME Department of Railway Vehicles, Budapest, 2010, p.86. (In Hungarian)

[4] **Zobory, I.:** Reliability Theory and Mathematical Statistics. Lecture Notes for Training Engineer Specialists. BME, Department of Railway Vehicles, and Vehicle System Analysis. Budapest, 2013, p.86. (In Hungarian)

[5] **Csiba, J.:** Comparative Investigation of the Elements Determination the Running Technical Characteristics of Railway Carriage Bogies. Proceedings of the 14th MINI Conference on Vehicle System Dynamics, Identification and Anomalies. (Edited by Prof. I. Zobory). BME, Knowledge Centre for Electric and Electronic Vehicle Control (EJJT), Budapest, 2015, p. 263-274.

[6] **Csiba, J.:** Investigation into the Reliability of Bogies of the 2nd Generation InterCity Carriages at the MÁV Co. Proceedings of the 9th International Conference on Railway Bogies and Running Gears (Ed. by Prof. I. Zobory). BME, Department of Railway Vehicles, Aircraft and Ships, Budapest, 2014. p. 339-350.

LIFETIME EXTENSION POSSIBILITIES OF STADLER BOGIE FORCE TRANSMISSION ELEMENTS ON THE BASIS OF TEST RESULTS

Péter FERENCZ

STADLER Rail Service Hungary
BRCC – Bogie Revision Centre of Competence
H-5000 Szolnok, Hungary

Received: November 8, 2016

ABSTRACT

The STADLER Rail Service Bogie Revision Centre of Competence provides full range os services on bogies in concern of revision, overhaul and repair tasks. Each operated fleet has different operational circumstances, environmental conditions demands, running performance. Thus tailor made technical content of bogie revision procedure is provided. The tailor made tasks are determined on basis of test revision results, which is meant that special, mainly force transmission elements are tested at the stage of mileage performance tthat the bogie needs to be overhauled. This paper describes how the test process and how the basics are created to evaluate test results in order to provide the most efficient service, special focus on the fleet size provided aspects and differences as well.

Keywords: STADLER, bogie revision, tailor made products, part lifetime determination, deterioration curve, leet size, risk minimalization;

1. INTRODUCTION

In the state-of-the-art railway vehicle maintenance and repair strategies the diagnostic database creation methods provide us growing importance. The STADLER Rail Service Bogie Revision Centre of Competence (BRCC) in Szolnok, Hungary represents service for its Customers on high quality, on high quality products. Customers of STADLER Rail operate tailor made standardized product applications of bogies. BRCC provides wide range of services in bogie overhaul, repair and condition diagnosis. Getting more frequently Customers are interested in high quality and sustainable safe operation of bogies on less cost. The Original Equipment Manufacturer STADLER specified certain level of revision cycles for bogies, but as quite new products, the revision scope of supply may vary depending on operational circumstances and final condition of concerned date of revision. This paper describes throughout focus on samples the process of gathering data, determining further usage possibilities of force transmission elements in STADLER, particularly FLIRT and KISS type bogies.

Fig. 1 Overhauled “Flirt 1” type driven bogie

For instance as for rubber-to-metal components placed in primary suspension system, longitudinal force transmitting behaviour may be reserved as long as one revision cycle more after a million kilometre of mileage performance. The parameters of such components lead to develop test methods, evaluation of results, and on basis of results checking technique of elements can be developed to easily decide extension of lifetime, as well as to exchange to new. The parameters are giving us criteria as limits of usage, determining the diagnostic database. Beyond the rubber-to-metal elements this paper describes shortly the issue in concern of wheel mounted brake disc condition check methods, and lifetime on a statistic data-field from several operators of FLIRT type bogies.

1. PURPOSE OF TESTS

Condition based maintenance philosophy has the aim to keep parts in operation to the technically safe limit described with exact border conditions. The original equipment manufacturer of bogie and its parts described the expected lifetime and stated the limit of exchange.

By testing processes for all suppliers it is required to use 3 simple categories to form adequate groups for results. This concerns the condition of part whether it is further usable for a second cycle of bogie revision mileage, or conditionally further usable which means the part does not have the possibility to reach a second revision cycle but further usable at time being. Last the not further usable condition.

Qualifikationen und Farben:	In Ordnung
	Unbedenklich
	Nicht in Ordnung

Fig. 2 The simple categories of condition level

Before the normal conditional record evaluation there are not “normal” damages that are not casued by the normal operation, these are exceptional items which shall be considered as outliars for any kinds of statistical evaluation. Of course these items are ranked in the not further usable category, but considered separated.

Fig. 3 Sample of a damper that has outliar damage

As end-result of testing the components gives the opportunity to decide on further usage. A component that have the certainty to reach a second revision cycle considered

as real cost reduction item of revision. These have the “real” influence of costs, and maintenance procedures shall be modified.
On basis of the traditional maintenance strategy the guidelines are the following that shall be considered. Control and revision **cycles** of element groups provides the regular cycles of maintenance tasks. Comparing to condition based **strategy,** basis criterias shall be formed to step out from traditional task lists. The task lists shall be flexible depending on the control and test results;

Stadler vehicle fleets are quite new - experience and feedback needed, which are originated from operational aspects, as well as the data gathered during the revision process. The parts lifetime determination methods on classical basis at production development level has the influence on the **LCC** evaluation and determination. The original data might be misdrived with re-consideration of data of certain part sor structures, thus lifetime extension on group of parts level is possible. Generally this process shall be customized to application of standard products to all fleets.
On basis of classic description of statistical evaluation of component and system deterioration process the following method was developed. For instance wear, as a geometry size decreasing, change, function of time shows the figure No.4. The curve has 3 main sections, divided by 2 inflection points, so the derivative of first section is negative, the middle is considered constant, the third as positive. The change velocity of function is given by the plausible description as of

$$v_z = (z_2-z_1)/(t_2-t_1) = dz/dt$$

A certain part lifetime can be determined on basis of this function as the near surround of the second inflection of the curve, the „end” of the quasy linear section.

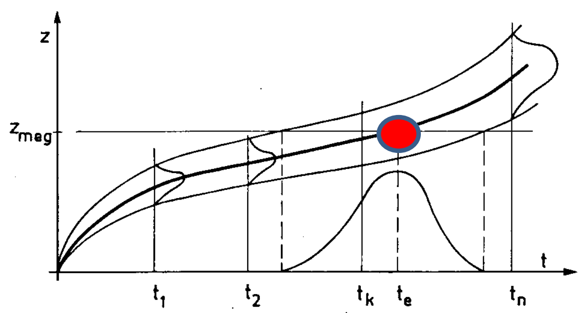

Fig. 4 Deterioration function of part

If one consideres the same parts but a batch of samples to be investigated into, the individual results give the collection of curves from which the expected value remains as basis of the investigation goal and serves as statistical database to determine the reference point, so the „red dot” on the figure curve.
Named and related as follows:

$$t_e = z_{meg}/v_z\ ;$$

Out of the description the „z_{meg}” determines the target limit value maximum allowed size, measure of wear for instance.

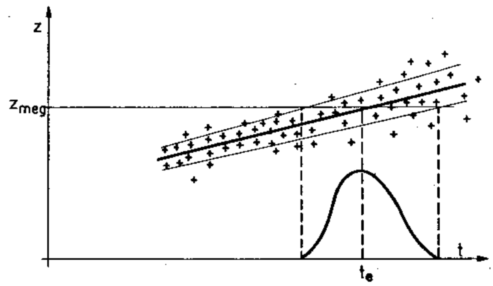

Fig. 5 Statistical results of limit

To determine the the limit out of a batch of samples is based as process of statistic evaluation. The criteria of maximum „wear” or deterioraion allowed is located as the geometry cross of expected value of quasy linear results and the maximum value of the distribution maximum of inflection location values.
The basis leads to the optimization process with results to be evaluated on the action parameter of „part lifetime”, target function to minimize the RISK!, minimize the COSTS! and maximize the Quality!. The basic question is that at the certain point of the investigation is carried out, can it be determined that the certain part would last one revision cycle more in operatio as of 1 – 1.2 million kiometers of mileage performance? How would the reliability and certainty of the parts, so the structure will change?
The optimization boundary conditions shall be taken into account as safety, warranty responsibility allocation, original equipment manufacturer specifications, operational circumstances, original life cylce cost determination method, and the lead time of the bogie revision process itself.

2. COMPONENT GROUPS THAT SHALL BE CONSIDERED

Component goups are formed in accordance with the force transmission stages of a certain bogie. From wheels to bearings, all kinds of force transmission rods, rubber-to-metal bushes, bearings, longitudinal and vertical components are considered to be tested. Especially the rubber-to-metal parts are simply tested with static loads. The spring characteristics of elements are compared with new items features. The comparison provides the ranking in possible further usage opportunities. There are rubber-to-metal components which considered generally further usable, but a new technology step defined in revision tasks, it is a visual check method to make decision whether to exchange the item.

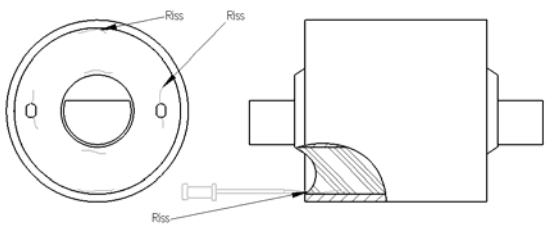

Fig.6 Features to be checked on axle guide bearing bush

Suspension system elements shall be checked on characteristical features. Primary suspension elements considered on workload point surrounding evaluated stfinness parameters to compare. Dampers are fully tested against charateristical features. The rubber-to-metal parts and dampers are all considered as **"more uncertain" parts** due to the more difficult investigation methods that shall be considered to determine the deterioration conditaion.

Wheels, axle bearings as well as brake discs also give us more fields for deep controls and results evaluation, but considered as **"less uncertain" items** as defined features of limits of usage. It can be generally stated as highlighted feature of importancy from practice, that a more than 50% of FLIRT type trailer wheel mounted brake disc wear rings are further usable at the revision cycle point of 1 - 1.2 million km of mileage performance.

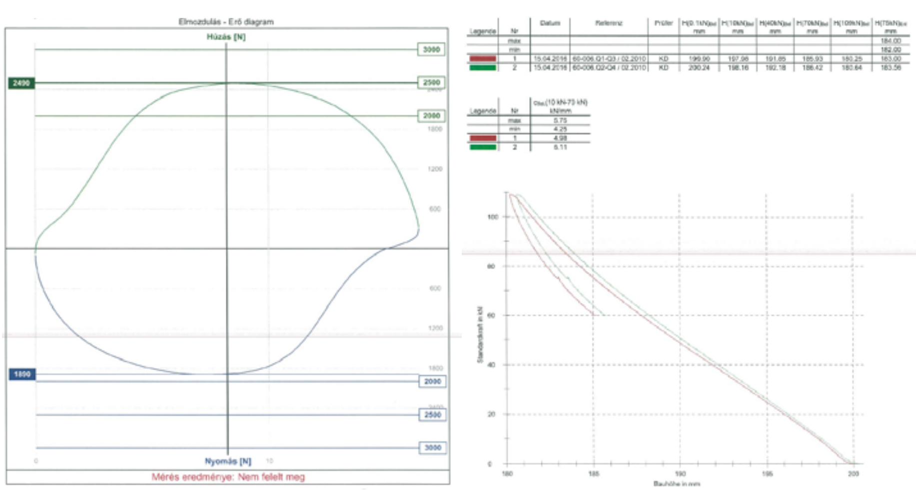

Fig.7 Sample of damper and spring test characteristics

Fig.8 Wheel mounted brake disc under machining

3. TEST RESULTS AND APPLICATION

On basis of this simple evaluation comes the bogie part tests' results related method. Usually the sample size is so low that the certainty of result is low that the „real t_e" is calculated according to the above described deterioration function. Thus the evalautaion result can be considered on the following way. *To Perform „**test revision**" of each type of bogie unit from a certian vehicle fleet:*

- Considering mainly exchange of certain items, besides the disassmbled ones are controlled;
- To be controlled: the „deterioration situation" on basis of the „deterioration curve model";
- Help of OEM part manufacturers, or performed on own developed technical specifications or indepedent experts – SUPPLIER CHAIN feedback importancy;

The decision point at first is that the revealed defect on a certain part is caused by normal deterioration or an unexpected damage detect? In case the "normal" deterioration condition is identified the next decision point comes as to determine criteria of further usage certainty. What is the reliable test method for a certain part? What does a result show? It shall be decided even though the sample size is low, that "where" the result point point is located on the quasy linear section of the basis function?

To be more certain with the result usually operational input data are considered besides the investigation results. These are usually maintenance control visual check results gathered as in-advance data before the revision starts. Nevertheless after the investigations carried out feedback are given to the operator of trains as well as the original equipment manufacturer, on the basis of feedback technical content modification of the bogie revision process, maintenance procedure modification, even part lifetime modification can be implemented.

There are two different ways defined at BRCC how to consider the resulted values of the tested items. As it was stated above, the uncertainty is originated from the fact that the position of the result is unknown "where" the on the quasy linear section located on, "more closer" to the progressive section, or more certain to be no change in deterioration velocity.

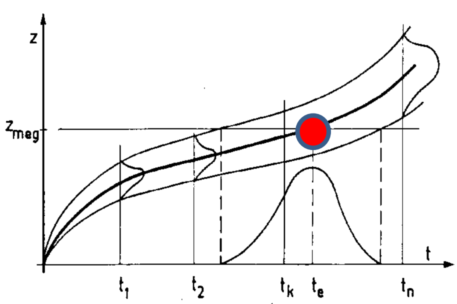

Fig. 9 Worst and the best passed case

Depending on the feature of the part group, the so called "more uncertain" and the "less uncertain" structures and items are leading to have the theory as the "**worst" and the "best" passed case to be applied on the certain group of parts or part.**

Fig. No. 9 on the left shows the “worst passed case” method, so the result is considered as the inspected part is having still good condition, but at the end of its usability, so shall be exchanged.
Fig. No. 10 shows the “best passed case”, so the result of the inspected part is considered as good result, and still has the lifetime to reach even another revision cycle in operation.

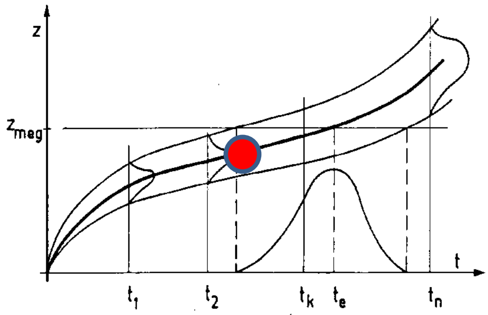

Fig. 10 Worst and the best passed case

4. CONTRADICTION OF RESULTS TO APPLY IN MIRROR OF FLEET SIZE

Fleet size matters. STADLER as railway vehicle manufacturer has young fleets all over Europe in operation.

Let consider a sample of trainset fleet consisting of 100 vehicles. Each vehicle has 2 driven bogies, and 4 trailer bogies. Besides the “big” fleet we shall consider another type of operator, the “small” fleet type. It means i.e. 5 trains from the same platform type of trainsets, but with contracted availability performance indicator of 100%.
What parameters and how shall be considered? Testing the elements of 1 bogie out of the whole fleet means questionable certainty and reliability of results depending on the fleet size.

As the considered sample if a fleet consisting of 5 trains, having a sum of 10 driven bogies, the testing of elements providing us much larger certainty of safety of results to be applied on the whole fleet comparing to the results that a fleet would provide out of 100 trains. The reliability of the tests results be applied leads us to the question how shall these be applied and what influences shall have on the technical content of a revision work package.

The operator of 5 trainsets fleet might have no opportunity to finance spare bogies, so unexpected damage of a part or a bogie can have much larger effect on unexpected lifecycle costs, such as missing out a train from operation. A “small-size” fleet has more risk to keep the bogies running with old parts.
Simple evaluation of parameters used behind the 2 fleet sizes considered:

<u>Sample brake down analysis of a „SMALL” OPERATOR FLEET</u>

Quantity of the operated trainsets is: 5
Bogie type distribution in trainset:

Driven bogie 2 units,
Jacobs trailer 3 units
Sum:
Driven bogie 10 units
Jacobs trailer 15 units

The most important RISK of the certain type of fleet is:
brake down of 1 trainset has strong influence on fleet availability.

Yearly mileage performance of the fleet is : 450 000 – 600 000 km

Auxiliary fleet float conditions are:

No or low amount of spare sub-systems or components, or bogies;
Strong sensitivity on process LEAD time shall be considered.
Sensitivity on COST reduction is high, keeping trains at 100% availability.
Resultant fleet availability sensitivity:

AS = 1 / 5 = 20%

The „Less uncertain" items are considered to be exchanged in case no possibility to reach the next revision cycle period.

For the „More uncertain" items the application of „**WORST or BEST PASSED CASE** abstraction" applied depending mainly on experiences with certain part usage in other applications.

Despite the simple reliability factor of i.e. tested axle guide bearing units case for driven bogies is:

R = 4 / 10*4 = 0,1 -> 10%

Besides on increment sensitivity of the parameter is:

S = 1 / 10*4 = 2,5%

<u>Sample break down analysis of a „BIG" OPERATOR FLEET</u>

Quantity Operated trainsets is: 105

Bogie type distribution in trainset:

Driven bogie 2 units
Jacobs trailer 3 units
Sum:
Driven bogie 210 units
Jacobs trailer 315 units

The most important RISK of the certain type of fleet is:
The unexpected brake down or malfunction of a component in higher amount.

Yearly mileage performance is: 180 000 – 250 000 km

Auxiliary fleet float conditions are:

Significant amount of spare sub-systems or components, or bogies.
Sensitivity on process LEAD time lower then small fleet operator
Sensitivity on COST reduction with keeping items on further usage.
Resultant fleet availability sensitivity:

AS = 1 / 105 = 0,95%

The „Less uncertain" items are considered to be further used even in case no possibility to reach the next revision cycle period but a certain futher mileage.

For the „More uncertain" items of Application of „**BEST PASSED CASE** abstraction" applied relying on maintenance check and higher certainty, less sensitivity.

Despite the simple reliability factor of i.e. tested axle guide bearing units case for driven bogies is:

R = 4 / 210*4 = 0,0047 -> 0,47%

Besides on increment sensitivity of the parameter is:

S = 1 / 210*4 = 0,12%

On the basis of the above described data flow, the „small fleet operator" decision point are influenced by other risks comparing to the „big fleet operator". The dependency of on „AS" sensitity value is high at a small fleet. Thus even the „less uncertain" parts and goups, even in case of exisiting possibility of further usage are considered to be exchanged, i.e. the wheels or brake discs, in order to not to stop any of the train out of the fleet.

The „big fleet operator" decides strongly relying on the size and features of the available exchange float of parts, even a higher quantity of complete spare bogie units. Therefore the risk is considered more depending on a certain part failure in a high quantity. The „less uncertain" type of items are always considered to be further used. The tchnical conent of revision process can be adjusted in accordance with the test results.

5. CONCLUDING REMARKS

Fig. 11 Overhauled "Flirt" type Jacobs trailer bogie at BRCC

- Bogie force transmission elements as defined gorups have possibility for further usage comparing to OEM determined revision cycle, lifetime extension;
- The optimization has the main goal of risk minimalization besides cost minimalization;
- The remained „effective" lifetime is depending on the optimization boundary conditions;
- The fleet size has contradiction feature in decision making of components further usability;

- Special supplier chaine co-operation and own technologies are developed at SRS HU BRCC for control methods;
- Customized bogie revison technical content provided;

6. REFERENCES

[1] STADLER Rail Service BRCC company documents

DETERMINATION OF THE DYNAMICAL EFFECT OF THE WHEEL FLATTENING BY MEANS OF SIMULATION METHOD

András SZABÓ and János PARÁZSÓ

Department of Aeronautics, Naval Architecture and Railway Vehicles
Faculty of Transportation Engineering and vehicle Engineering
Budapest University of Technology and Economics
H-1521 Budapest, Hungary

Received: September 12, 2016

ABSTRACT

During the operation of rail vehicles often occurs that a flattening appears on the running surface of the wheel blocked due to sliding without rolling. Further operation of the flattened wheels causes significant dynamic load both for the vehicle and track. This is the reason why many procedures have been developed to detect the flattened wheels under the normal railway operation and take them out of the traffic. In this paper the relationships between the results given by a wheel-flattening measuring system and the wheel flattening itself are investigated.

Keywords: flattening of the railway wheel, dynamical modelling, modelling of the measuring system.

1. INTRODUCTION

There is a typical failure of the running gears of railway vehicles when due to the intensive break application a flattening appears on the running surface of the blocked wheel which was sliding on the rail without rotation. When the flattened wheel remains in operation then each rotation causes one impact on the rail-head. The magnitude of the impact depends on the dimension of the flattening, and causes dynamical load for the track, excites undesirable vibrations both in the track and in the running gear of the railway vehicle. That's why to detect, select and as soon as possible to stop the further operation of vehicle having flattened wheel is one of the most important task for the railway vehicle operators.

The problem to determine the dynamical loads caused by the flattened railway wheels is well known in the international literature. Some experiments were performed in this field by the authors of [2], other cases of this problem was analysed by the simulation methods in time or frequency domain [3],[4], or finite elements methods were applied [5].

To select the vehicles having flattened wheels measuring systems should be elaborated for detecting these failures during the normal operation of vehicles. In these systems the appropriate conclusions are drawn on the basis of the signals given by the sensors installed along the track.

We introduce system shown in Fig. 1 based on [2], where the flattening is detected by the measuring of the track deformation between two sleepers, because this system is similar to the system investigated in this paper.

At the Department of Aeronautics, Naval Architecture and Railway Vehicles of the BME it is usual to solve dynamical problems in the framework of the computer based simulations, both the track-vehicle system [6] and the track dynamical behaviour with respect to sources [7] and [8]. On the basis of the latter in the present paper a procedure and its results are introduced based on a nonlinear dynamical model of concentrated parameters.

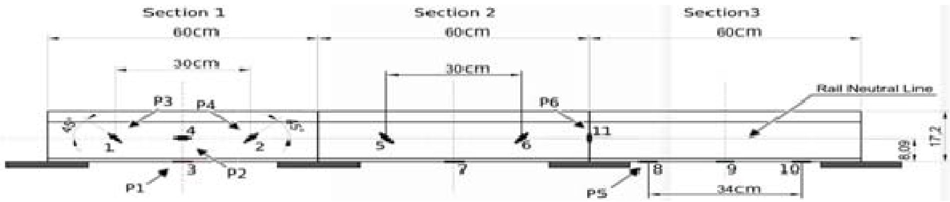

Fig. 1 Optical method based measuring system laying along the track. [2]

2. FEATURES OF THE MODELLED SYSTEM

In our investigations a real measuring system is modelled. Our target was to determine the relations between the magnitude of the wheel flattening and the received measured signals taking into consideration the properties of the measuring system.

In case of the considered measuring system the measured signals are the shear-deformations of the rail. The strain gauges positioned in the middle section between two sleepers on the rail stem. There are two measuring cross sections (later measuring points), the distance between the two cross sections is 320 mm. From the measured shear deformations the shear forces could be determined. In static case the difference of the two computed shear forces is equal to resultant vertical external force acting in the sector between the two cross sections, so this force is the effect originated from the wheel tread to the rail.

In the course of modelling on the following factors was paid emphasized attention:

a.) The vertical stiffness of the rail is variable between the two sleepers.

b.) When the flattened part of the wheel is in rolling, the contact point emerging between the wheel and the rail jump-like evolves in the longitudinal direction.

c.) In the course of measuring when using the filtering method the real force process differs from the observed (measured) one.

In the course of modelling one wheel and the track section connected to he former are treated (Fig. 5). The mass $m_p(x)$ represents the mass of the track (rail) under the wheel, so this is an equivalent replacing mass. This mass always represents the rail being actually under the wheel, so due to the motion of the wheel, this mass is variable depending on the longitudinal co-ordinate x. Because of this, the stiffness $s_s(x)$ and the damping coefficient $d_s(x)$ of the support of the equivalent "track-mass" $m_p(x)$ are also variable depending on the longitudinal co-ordinate x. The zero value of co-ordinate x is at the middle point of the measuring section. (Fig. 2).

The stiffness function $s_s(x)$ in accordance with the above point a.) is varying periodically between the two sleepers. To determine the function of the fluctuation a pre-computation was elaborated. In the course of this pre-computation the rail and the support of the rail was modelled based on the model shown in Fig.2. In this model the rail is a flexible beam apt for flexural deformation, and the supports under the sleepers have also elastic property.

The stiffness s_a stands for the stiffness of the elastic support of the sleeper. The stiffness s_b is similar, but it must be determined in such a way, that it must represent also the further farer sections of the track. If stiffness s_a is correct, then the stiffness-function $s_s(x)$ has extreme values (maximums and minimums) at the middle point over the sleepers and at the middle point between two sleepers.

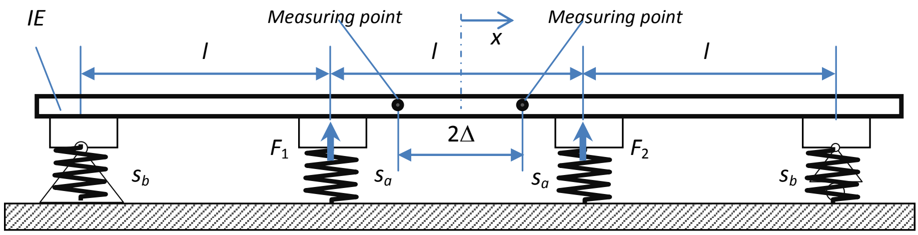

Fig. 2 Model of the rail/track to determine stiffness function $s_s(x)$.

In case of rail type UIC 54 and sleepers distance 600 mm the stiffness function $s_s(x)$ is shown in Fig.3. In the Figure $\beta = s_b/s_a$ stands for the ratio of the two stiffnesses.

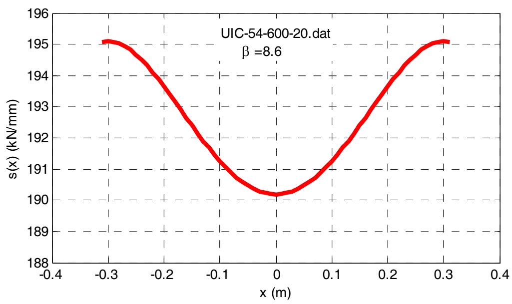

Fig. 3 The stiffness function of the support (UIC 54, 600 mm).

When treating the fluctuation of track-mass $m_p(x)$ a piece-wise linear transition "roof" was taken into consideration (see Fig. 4). In the Figure m_Δ is the equivalent track-mass of the rail sections without sleepers, and m_{ka} means the additional mass of the sleeper attached to one rail.

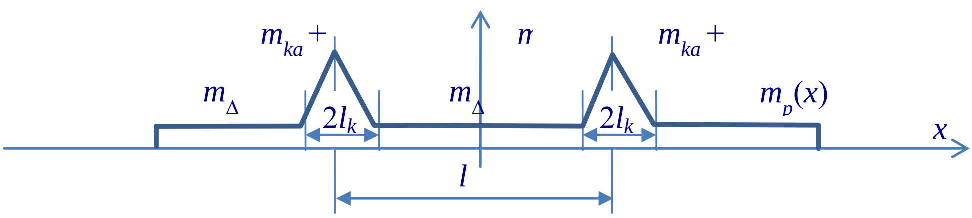

Fig. 4 The equivalent track-mass $m_p(x)$ as a function of co-ordinate x.

When the equivalent track-mass function $m_p(x)$ and the stiffness function $s_s(x)$ are known, the function of damping coefficient $d_s(x)$ is determined form the actual critical damping value by using suitable multiplying factor λ according to formula:

$$d_s(x) = \lambda\, 2 \sqrt{s(x)\, m_p(x)}\ . \tag{1}$$

2. THE DYNAMICAL MODEL

The construction of the concentrated parameter dynamical model is shown in Fig. 5. In the model the concentrated mass m_f represents the masses of the bogie and the car body belonging to one wheel, while mass m_k means the mass of the wheel. Function $m_p(x)$ is the equivalent „track-mass" and - as written above - this mass represents always the track section being actual under the wheel, so it is variable depending on the longitudinal co-ordinate x.

In the course of the simulation the wheel moves at a constant velocity parallel to axis x. The actual value of the x co-ordinate is computed by e numerical integration of the above mentioned constant velocity, the integration starts at the given initial value and steps forwards by the same time step, what is used at the actual solution of the differential equation system constructed for the vertical motions of the dynamical model.

In the model between the pairs of concentrated masses and between the track-mass $m_p(x)$ and the environment there are connection forces with linear elastic and dissipative properties. These properties are given by the actual stiffness s and actual damping coefficient d.

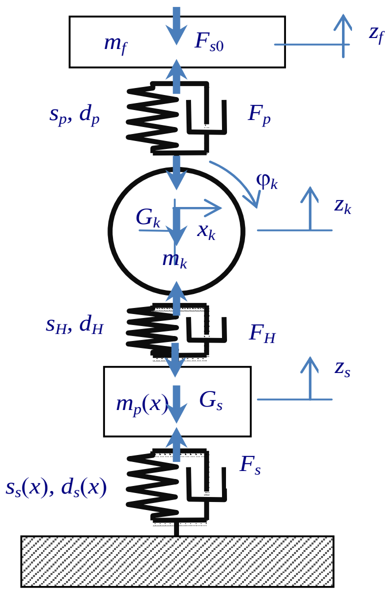

Fig. 5 Wheel-track dynamical model.

In Fig. 5 the forces are shown which were taken into consideration. There are designated the elastic and dissipative inner forces mentioned above, which ones depend on the vertical motion state of the system. There are also the gravity forces acting on the masses and force F_{s0}, which is the constant wheel load without the own-weight of the wheel.

The forces evolved between the concentrated mass-pairs of the model are computed by the relationships to be written as follows. The force F_p evolved in the primary suspension system is computed from the vertical displacement z_f of upper mass m_f and from the vertical displacement z_k of the wheel by formula:

$$F_p = s_p\,(\,z_k - z_f\,) + d_p\,(\,\dot{z}_k - \dot{z}_f\,)\,. \tag{2}$$

The force F_H between the wheel and equivalent track-mass is computed by formula:

$$F_H = s_H\,(\,z_s - z_e\,) + d_H\,(\,\dot{z}_s - \dot{z}_e\,)\,, \tag{3}$$

Where z_s means the vertical displacement of track-mass. Finally, the force arising under the track-mass is:

$$F_s = -\,s_s(x_e)\,z_s - d_s(x_e)\,\dot{z}_s\,. \tag{4}$$

At this point must be taken into consideration that the horizontal co-ordinate x_e of the wheel-rail contact point can be different from the horizontal position co-ordinate x of of the wheel mass centre, when the contact is just in the section of wheel flattening (see later).
On the basis of the forces emerging in the system the equations of the system motion are constructed by using Newton's second law. Thus, for the mass m_f moving vertically it reads:

$$m_f\,\ddot{z}_f = F_p - F_{s0}\,, \tag{5}$$

for the vertical motion of the wheel:

$$m_k\,\ddot{z}_k = F_H - F_p - G_k\,, \tag{6}$$

and for the vertical motion of the equivalent track-mass, it reads:

$$m_s(x_e)\,\ddot{z}_s = F_s - F_H - G_s\,. \tag{7}$$

The differential equations above are solved by using numerical method. To use the well-known standard numerical method it is necessary to reduce the second order differential equation system to a first order one, in accordance with the state space formulation. To this end a *state vector* **X** is introduced, which contains the vertical velocities and displacements of the masses in the system:

$$\mathbf{X} = [\,\dot{z}_f\,,\dot{z}_k\,,\dot{z}_s\,,\,z_f,,\,z_k\,,\,z_s\,]^{\mathrm{T}} \tag{8}$$

Using this *state vector* there emerges a differential equation system of 6 first order differential equations:

$$\begin{bmatrix} \ddot{z}_f \\ \ddot{z}_k \\ \ddot{z}_s \\ \dot{z}_f \\ \dot{z}_k \\ \dot{z}_s \end{bmatrix} = \dot{\mathbf{X}}\,(t) = \begin{bmatrix} (F_p - F_{s0})/m_f \\ (F_H - F_p - G_k)/m_k \\ (F_s - F_H - G_s)/m_s \\ \dot{z}_f \\ \dot{z}_k \\ \dot{z}_s \end{bmatrix} = \Phi(\mathbf{X}(t))\,. \tag{9}$$

For the solution of the initial value problem belonging to this differential equation system *Euler's* method is used with non-constant time steps. The solution is started at the initial time t_0 from the initial state vector:

$$\mathbf{X}(t_0) = \mathbf{X}_0\,, \tag{10}$$

and is going on by successive usage of formula

$$\mathbf{X}(t_i+\Delta t) = \mathbf{X}(t_{i+1}) = \mathbf{X}(t_i) + \dot{\mathbf{X}}\,(\mathbf{X}(t_i),t_i)\,\Delta t = \mathbf{X}(t_i) + \mathbf{\Phi}(\mathbf{X}(t_i),t_i)\,\Delta t\,. \tag{11}$$

The time step Δt is the time increment used in the course of simulation. During the simulation there are some criteria for the selection of time step Δt as follows:

1. Δt should be greater than the specified Δt_{min} and less than the specified Δt_{max}.
2. During one time step the maximum change of any force in the model must be less than the specified value ΔF_{max}.
3. The Δt time step can be increased at any next step, but the ratio of the previous time step and the new time step must be less than a specified ratio.
4. The critical points of the computation – for example the points where the flattened section of the wheel steps into or out of the contact – must always be limit points.

Remark: Criterion No 4 overwrites criterion No 1.

3. MODELLING OF THE MEASURING SYSTEM

The vertical motions and the inner forces in the system become known by the solution of the differential equation system. On the basis of these, the force arising in the measured section should be computed. The middle of the measured section is situated at the position $x = 0$ and its half-length is Δ to the left and to the right. There emerges force in measured section, when at least a part of the contact area of wheel and the rail intersects the measured section.

In present investigation the wheel-rail contact area is taken into consideration as an ellipse of constant longitudinal dimension, designated by $2a$. Over the contact surface there is assumed an ellipsoid-form distribution of the normal pressure, and the integral of this pressure distribution is corresponding to the actual vertical force arising between the wheel and rail.

When the rail cross sections at the start point or at the end point of the measured section (measure limit points) only partially intersecting the wheel-rail contact area, than only a fraction of the vertical force emerging between the wheel and rail is sensed by the measuring system. To determine the sensed force fraction a volumetric ratio is taken into consideration. This is the ratio of the partial-volume of the pressure distribution of half ellipsoid-form, defined over the intersection area of the contact area and the measured rail section and of the volume of the whole ellipsoid pressure distribution (see Fig. 6).

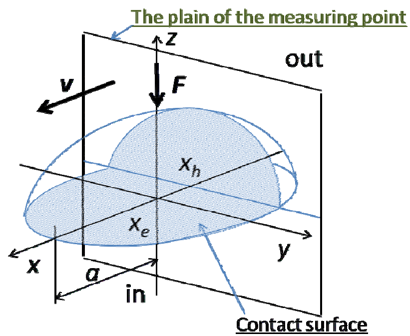

Fig. 6 Passage over the measuring section "limit-point".

The co-ordinate of the measuring section limit point (start or end point of the section) is x_h, and a means the half-length of the contact ellipse in longitudinal direction. It is necessary to compute the "force-ratio", when relation abs(ξ) < 1 is valid for the variable $\xi = (x_e - x_h)/a$. In this case at the entry point (start point of the measuring section) the effective part F_{Nx} of the normal force F_N reads:

$$F_{Nx} = F_N\, V(\xi) \,/\, \mathrm{V}(1)\,, \tag{12}$$

where $V(\xi)$ is the volume of the half-ellipsoid over the interval [-1, ξ], and the $V(1)$ means the volume of the whole half-ellipsoid. At the "exit point" (end point of the measuring section) the sign of ξ takes the inverse one.

As written above, the computation of the measured force means, that the variation of the force during entering and rolling trough the measured section, as well as rolling out of this section always has smooth form, and in case of a constant normal force F_N its variation is similar as it is shown in Fig .7.

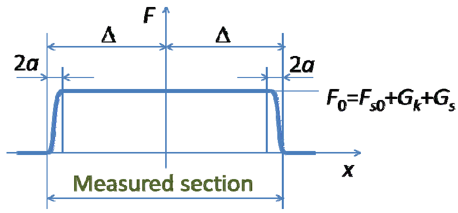

Fig. 7 Variation with length of the measured force in case of constant normal force F_N.

The other important property of the measuring systems is the method of using filtering of the measured signals. In the simulation the filtering-method is modelled by continuous computation of the moving-averaging of the actual results.

4. TREATING OF THE WHEEL FLATTENING

To introduce the computation method for the passage on the section of the wheel flattening let us look at Fig. 8. In the figure a wheel is shown in that situation, when the flattening has already entered the measured section.

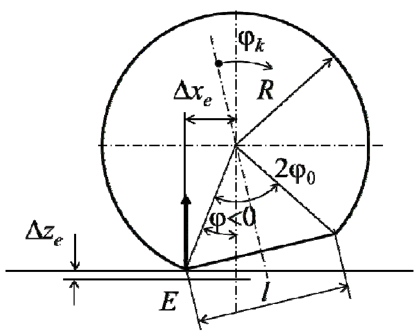

Fig. 8 Passage on the section of the wheel flattening.

Contact point E between the wheel and rail does not fit on the vertical line going through the centre of the wheel, so a distance Δx_e appears and at the same time also a vertical distance Δz_e emerges measured from the point of the original rail surface position valid in flattening-free case. The angle φ means the angular distance between the vertical central line going through the wheel centre and the wheel radius intersecting the starting point or the end point of the flattening. (At the position shown in Fig.8. the angle φ takes negative value.) Position φ_0 belongs to the starting and end points of the flattening section, and the zero value of the wheel rotation angle φ_k belongs to the axis of symmetry of the flattening section. Thus,

$$\varphi = -\varphi_k - \varphi_0 \ \text{ if } \ \varphi_k < 0 \ \text{ and } \varphi = \varphi_0 - \varphi_k \ \text{ if } \ \varphi_k \geq 0 \ . \tag{13}$$

If abs(φ) < φ_0 = arc sin($l/2R$) is true, then the wheel is rolling in the flattened peripheral section, and the vertical and horizontal distances introduced above are:

$$\Delta x_e = R \sin(\varphi) \ \text{ and } \ \Delta z_e = R\,(1-\cos(\varphi)) \ . \tag{14}$$

The variables in formulas (3) and (4) are:

$$x_e = x_k + \Delta x_e \ , \ z_e = z_k + \Delta z_e \ \text{ and } \ \dot{z}_e = \dot{z}_k + \Delta\dot{z}_e = \dot{z}_k + R\,\dot{\varphi}\sin(\varphi) \ , \tag{15}$$

where $\dot{\varphi} = \omega_k = v/R$ is the angular velocity of the wheel.

5. THE RESULTS OF SIMULATIONS

So in the course of the solution of the differential equation system (9) the force acting on the considered rail section is also determined when the wheel passages over the section. The length of the specified section is 320 mm, and the wheel flattening is activated after entering the specified section. The wheel-rail contact point at the starting point of the flattening is 100 mm prior to the centre of specified (assigned for measurement) track section. In this case the force fluctuations generated by the influence of flattening for the mean is observed by the simulated measuring system.

In the present investigation 4 different axle load cases (50,100, 150 and 200 kN) are simulated, at any axle load there are 3 different wheel velocities (of levels 40, 80, and 120 km/h) and at any case there are 3 different flattening sizes (of lenghts l = 10, 20 and 40 mm).

Because in the measuring system always used some filter-method as written above, so the filtered values of the force is also determined, and the further conclusions are based on these filtered value fluctuations. The filter system is modelled by the computation of the continuous moving-averaging value over the time duration of 0.0025 s. In Figs. 9 – 11 there are shown the “raw” functions on the left hand side and on the right hand side the filtered functions of the observed forces are shown depending on the length coordinate x. For instance the results belonging to axle load 150 kN are displayed in the Figures.

The „filtered” values of the forces are nearer to force values measured, but they strongly depend on the measure of the filtering and significantly decrease the peaks of the force fluctuations as shown in Figs 9 – 11. The higher duration of the filtration means the more decreasing in the peaks.

The simulated force fluctuations of cases of different axle loads are in one diagram in Fig 12. In this figure one can see, that the magnitude of the axle-loads has no measurable effect on the profile of the force fluctuation, until the wheel and rail are in continuous contact.

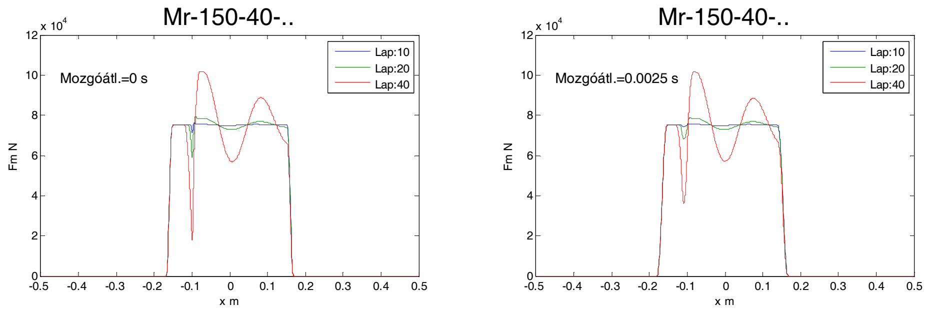

Fig. 9 The “raw” and “filtered” force fluctuations: F_N =150 kN, v =40 km/h.

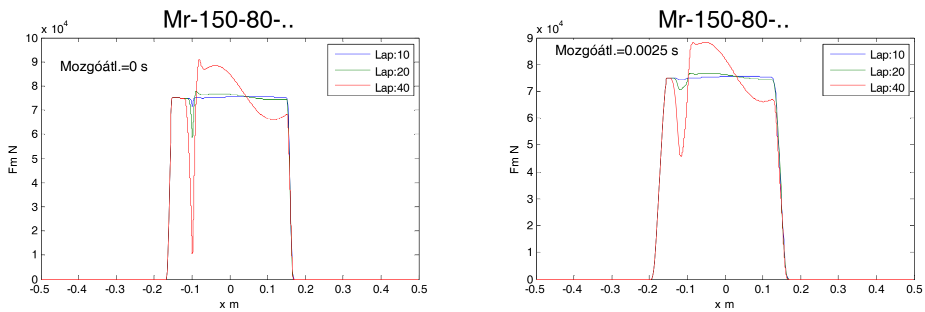

Fig. 10 The “raw” and “filtered” force fluctuations: F_N =150 kN, v =80 km/h.

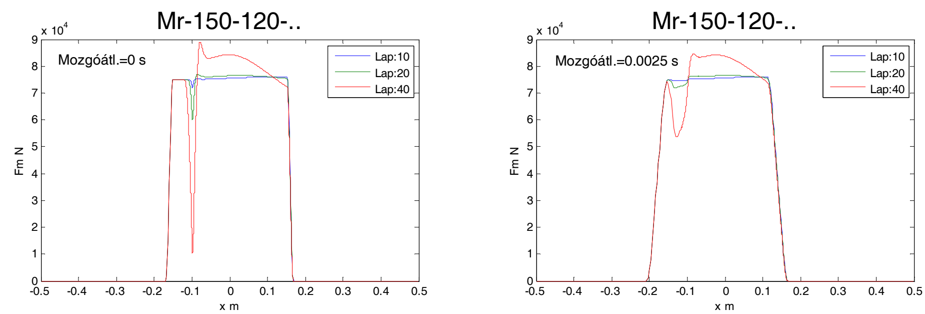

Fig. 11 The “raw” and “filtered” force fluctuations: F_N =150 kN, v =120 km/h.

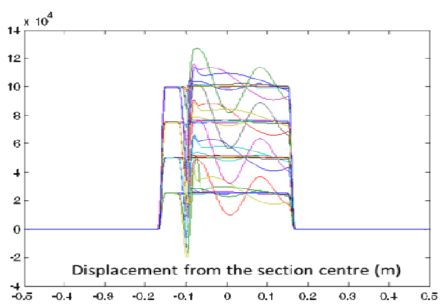

Fig. 12 The “raw” force fluctuations in one diagram in UIC 54 track:
l = 10, 20, 40 mm; F_N = 50, 100, 150, 200 kN, v = 40, 80, 120 km/h.

As further evaluation, in Fig.13 the force-jump $\Delta F = F_{max} - F_{min}$ is also indicated in the filtered fluctuation diagram

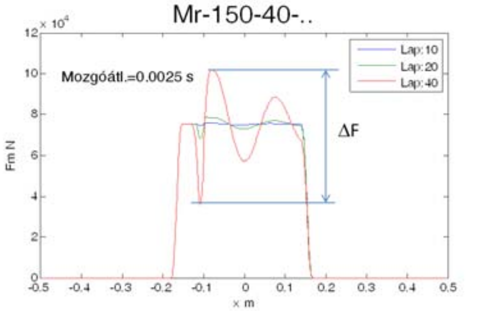

Fig. 13 „Force-jump" in the filtered fluctuation.

In Figs. 9 – 11 at the left hand side the diagrams of the force fluctuation without filtration the force-jumps are increasing but on the right hand side in the diagrams of the filtered force fluctuations the force-jumps are decreasing when the velocity is increasing. The reason is that if the velocity increases, then the force fluctuation becomes faster, so the effect of the filtering-procedure occurs in a stronger way.

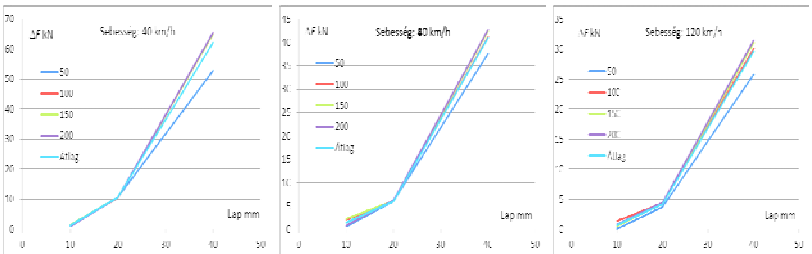

Fig. 14 Force-jump of different flattening sizes and different velocities.

In Fig. 14 the force-jumps of different specified velocities are shown depending on the size (length) of the flattening. In the Figure one can see that the force-jump does not depend on the axle load. In Fig. 15 the force-jumps depending on the velocity are shown. Fitting exponential functions on the velocity dependent force-jump values, at each flattening size approximately the same exponent values of value 0.01 h/km has been resulted.

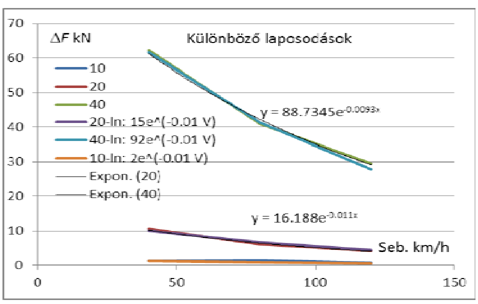

Fig. 15 Force-jump depending on velocity at different flattening sizes.

So based on Fig. 15 as a general rule for the dependence of force-jumps on the velocity the formula

$$\Delta F_f = F_a(l)\, e^{-0,01\,V} \tag{16}$$

is yielded, where the $F_a(l)$ is a coefficient depending on the size of flattening defined by the l length (dimension) of the latter. As for the values of the coefficient mentioned the power function

$$F_a(l) = 0,005912\, l^{2.6167} \tag{17}$$

represents a good approximation, as it can be seen in Fig. 16.

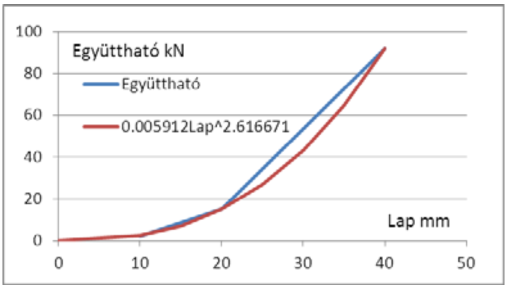

Fig. 16 The coefficient of the force-jump function depending on the size of flattening.

6. CONCLUDING REMARKS

In the present investigation the objective of the elaborated simulation method is to determine the measurable effect of the force effect acting on the due to the motion of flattened wheels. On the basis of the results received the following tendencies can be identified:

- The magnitude of the axle-loads has no measurable effect for the profile of the force fluctuation.
- Because of the filtration applied in the measuring system the force-jump defined by the difference of the first maximum and minimum in the force fluctuation decreases in an exponential way with increasing velocities.
- The increase in the magnitude of the force-jump vs. increasing lengths of the flattening can be approximated by a power function.
- The small change in the track construction (e.g. UIC54 or UIC60) has no measurable effect on the shape and magnitude of the force fluctuation due to flattening.

7. REFERENCES

[1] **Szabó, A. - Zobory, I. - Parázsó, J:** Determination of the dynamic wheel loads caused by the wheel flattening. Research Report. BME VRHT, Budapest, 2015. (in Hungarian)

[2] **Filograno, M. L. - Corredera, P. - Rodríguez-Plaza, M. - Andrés-Alguacil, A. - González-Herráez, M.**: Wheel flat detection in high-speed railway systems using fiber bragg gratings. IEEE Sensors Journal, 13 (2013), p.4808-4816.

[3] **Uzzal, R. U. A. - Ahmed, A. K. W. - Bhat, R. B.:** Modelling, validation and analysis of a three-dimensional railway vehicle-track system model with linear and

nonlinear track properties in the presence of wheel flats. Vehicle System Dynamics, 51 (2013), p.1695-1721.

[4] **Liang, B. - Iwnicki, S. D. - Zhao, Y.:** Crosbee, D., Railway wheel-flat and rail surface defect modelling and analysis by time-frequency techniques. Vehicle System Dynamics, 51 (2013), p.1403-1421.

[5] **Bian, J. - Gu, Y. - Murray, M. H.:** A dynamic wheel-rail impact analysis of railway track under wheel flat by finite element analysis. Vehicle System Dynamics, 51 (2013), p.784-797.

[6] **Szabó, A. - Zobory, I.**: On Deterministic and Stochastic Simulation of Wheel and Rail Profile Wear Process. Periodica Polytechnica-Transportation Engineering Vol.26:(1-2), Budapest, 1998, p.3-17.

[7] **Zoller, V. – Zobory, I.**: On dynamics of the track/vehicle system in presence of inhomogeneous rail supporting parameters. Periodica Polytechnica-Transportation Engineering Vol.39:(2), Budapest, 2011, p.83-85.

[8] **Zoller, V. – Zobory, I.**: Railway track dynamics with periodically varying stiffness and damping in the Winkler foundation. Periodica Polytechnica-Transportation Engineering Vol.39:(2), Budapest, 2011, p.87-90.

DERAILMENT DYNAMICS OF RAILWAY FREIGHT CARS

Lajos T. VÉGH

Department of Railway Vehicles, Aircraft and Ships
Faculty of Transportation Engineering and Vehicle Engineering
Budapest University of Technology and Economics
H-1521 Budapest, Hungary

Received: November 7, 2016

ABSTRACT

The target of the analysis concerning the derailment accident of an asymmetrically loaded railway freight car (with different wheel loads) that ran through a singular irregularity is to determine the rate of the role of the asymmetrical loads and of the track irregularity in the occurrence of the accident. The substance of the research is to construct a model, which based on the rail and vehicle parameters, such as: layout of the track, superelevation, speed limit, measure and the shape of the rail failure, measure of the asymmetricity of the load, actual speed of the train, etc. The adjustments of the model parameters could be checked, or the parameter identification could be done by the process of the derailment recognized based on the traces found after the accident. Further targets: to develop a vehicle and track model, which is suitable to analyze similar derailment accidents. After developing the software, which is apt to make simulations, there will be opened the possibility of analyzing the running safety of asymmetrically loaded vehicles, to reduce the risk of similar accidents. Further analysis is needed to investigate the joint effects of the asymmetrical loads. The analysis is to be extended to take into consideration also the effects caused by the wheel/rail running surfaces, the bearings, the eventual overloads, the local thermal and wear processes.

Keywords: derailment, accident, asymmetrical load, railway freight car, track irregularity

1. INTRODUCTION

The research started with an investigation of a derailment accident of an asymmetrically loaded freight car that ran through a singular track irregularity. Fig. 1. shows the derailmented car and its derailmented axles. The load asymmetricity – the didtance between the payload mass centre and the geometrical centre of the vehicle – was more than 500 mm to the right side. The track irregularity depth was 15-35 mm on 2 m length at right rail of the track, and the left rail was superelevated.

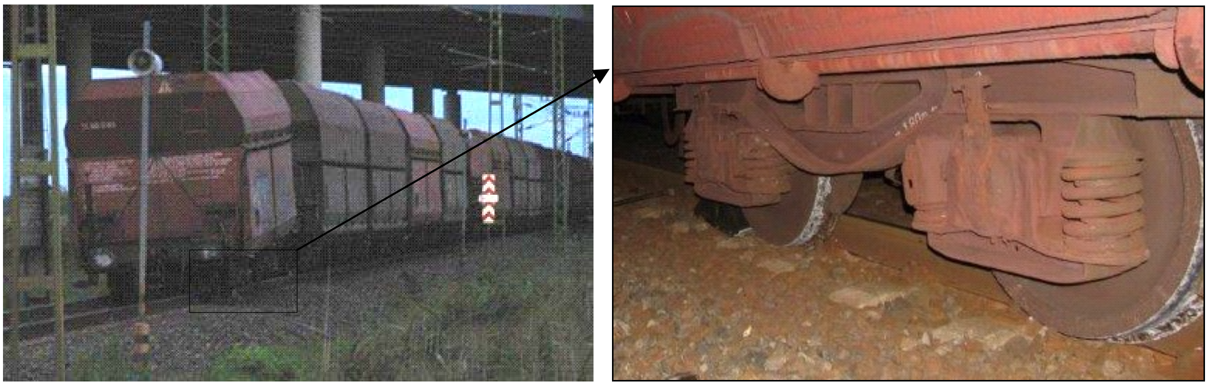

Fig. 1 Freight car after derailment

The train traversed more than 200 km before the occurance of the accident without any kind of noted problem. There were no other accident occurred through many years at that track irregularity. The question put by the court to bee answered was to appraisal the rate of the role of asymmetrical loads and role of the track irregularity in the occurrence of accident. Therfore the investigation was a collective work of a railway track expert and a wehicle-mechanical expert.

2. THE ACCIDENT

Fig. 2 The track irreguarity and the wearing on the left side rail

The accident occurred at 3:42 am in September under night visibility conditions. The railhead was dry, the ballast and the subgrade was very wet after two rainy days. The second freight car behind the locomotion derailmented running through the singular irregularity wich was in a right curve at right rail after a road crossing. Fig. 2. and Fig. 3. show the singular irregularity (sinking). The train moved forward an estimated 500 meters with derailmemted car until it stopped, while the sleepers demaged.

Fig. 3 The track irreguarity (sinking) at right side rail, the sleepers and the ballast

2.1. The track and the singular irregularity

The track parameters were the follows in the train movement direction:

- straight track
- 95 m transition curve to 600 m radius right, the superelevation growes up from 0 to 130 mm
- 128 m curve, 600 m radius right
- 90 m transition curve from 600 m radius right to straight, superelevation decrease down from 130 mm to 0 mm
- strait track
- original speed limit was 100 km/h
- actual speed limit was 60 km/h, because of the irregularity

- optimum speed at 600 m radius and 130 mm superelevation is 81,31 km/h calculated by the following equations and Fig. 4:

$$v = \sqrt{\frac{mRg}{n}} \text{ , where } tg\alpha = \frac{M\frac{v^2}{R}}{Mg} \cong \frac{m}{n} \text{ and } a' = \frac{v^2}{R} - \frac{m}{n}g$$

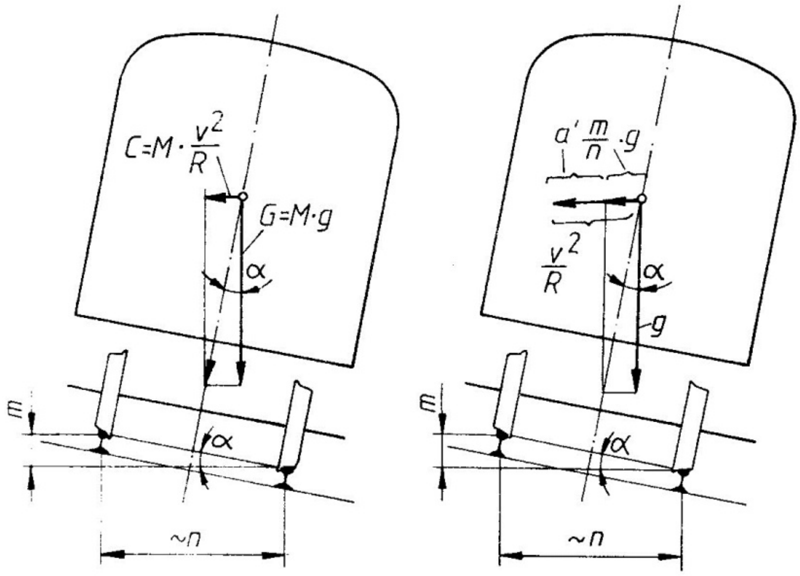

Fig. 4 The forces and the accelerations in a curve with superelevation

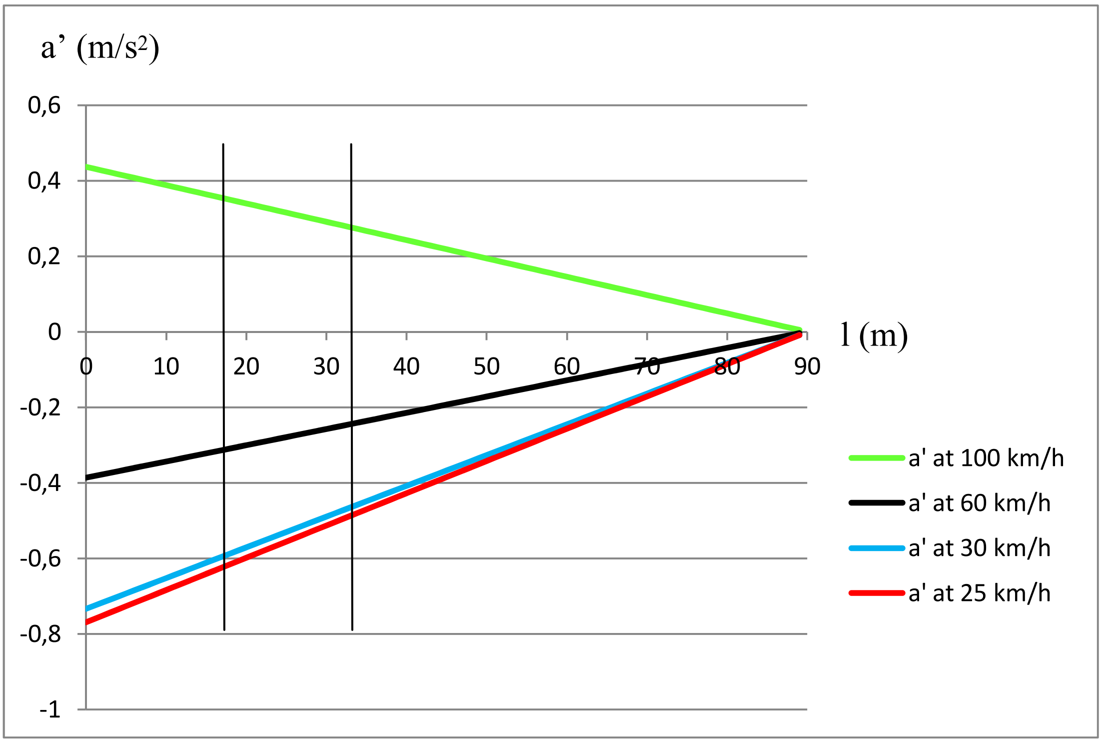

Fig. 5 Noncompensated horizontal accelerations (a') in transition curve

- Fig. 5. shows the noncompensated horizontal acceleration (a') due the transition curve negotiated at different speeds

- Fig. 2. shows the inner wall wear of the left rail, the angle was 70 degrees
- the accident occurred in the get-out transition curve after the road crossing (Fig. 2, Fig. 3), the right rear wheel of the car was running through the irregularity (sinking) in the 17th meter of the transition curve, the flange of the left leading wheel climbed on the top of the left rail, and the left leading wheel dropped down on the sleepers at the 33rd meter of the transition curve (Fig. 6)
- the depth of the irregularity (sinking) was 15-35 mm, and the length was 2 m – measured by 11 t axle-load car.

Fig. 6 The traceof derailment on the sleepers and on the inner side of the right rail

2.2. The train and the derailed car

The main datas of the train and the car was the followings:

Train length (m):	345
Train mass (t):	1931
Locomotive:	MÁV Class V63
Freight car:	Fals
Freight car axles:	4
Bogie:	Y25
Wheelbase (bogie) (mm):	1800
Bogie distance (mm):	7200
Length (mm):	13500
Net weight (t):	28,9
Payload (t):	45,4
Gross weight (t):	74,3

Fig. 7 The locomotive and the freight car

2.3. The asymmetric load

The asimmetricity of the payload could be guessed by the pictures about the bukk and the drawing of the car (Fig. 8), and could be calculated by the deformations of the springs measured after the accident.

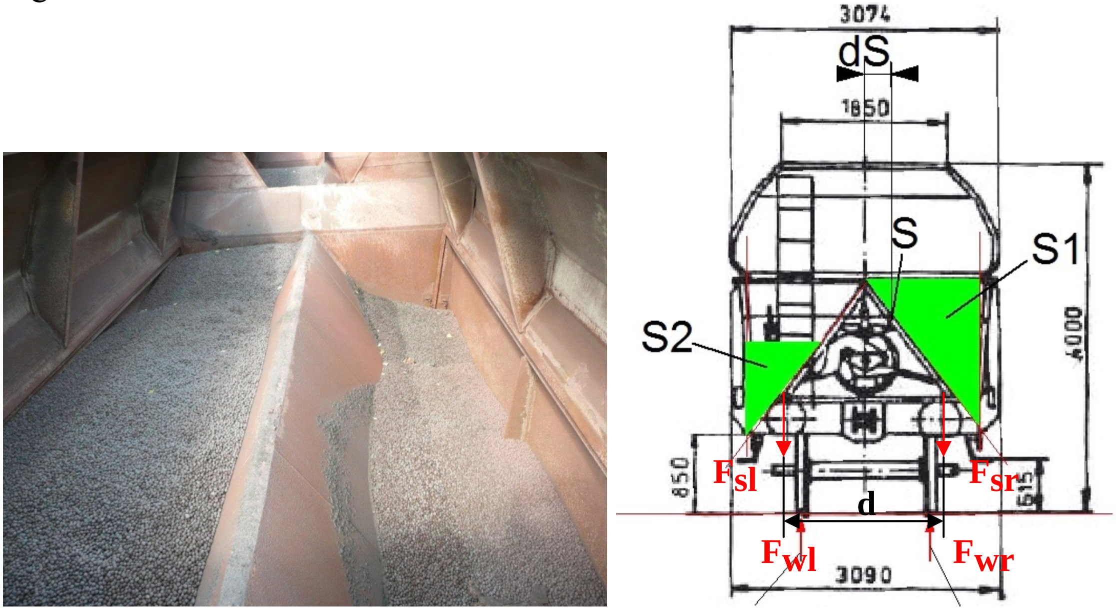

Fig. 8 The load and its asymmetricity

Spring deformations and forces:

				height (mm)			c (mm/kN)		Forces (kN)		
		spacer	height	spring height	outer free	inner free	outer	inner	outer spring	inner spring	sum
1.	journal	8	225	217	264	234	2,4	1,3	39,17	26,15	65,32
2.	journal	8	235	227	264	234	2,4	1,3	30,83	10,77	41,60
3.	journal	8	225	217	264	234	2,4	1,3	39,17	26,15	65,32
4.	journal	8	225	217	264	234	2,4	1,3	39,17	26,15	65,32
5.	journal	8	205	197	264	234	2,4	1,3	55,83	56,92	112,76
6.	journal	8	197	189	264	234	2,4	1,3	62,50	69,23	131,73
7.	journal	8	200	192	264	234	2,4	1,3	60,00	64,62	124,62
8.	journal	8	200	192	264	234	2,4	1,3	60,00	64,62	124,62
							sum (kN)		386,67	344,62	731,28
							sum (t)		39,42	35,13	74,54

The overall loads on the left and right side wheels could be calculated by the following equations and Fig. 8:

$$Fsl + Fs = Fwl + Fwr = Faxle$$

$$dFs = Fsr - Fsl$$

$$dFw = \frac{dFs * d}{n}$$

$$Fwl = \frac{Faxle}{2} - dFw \text{ and } Fwr = \frac{Faxle}{2} + dFw$$

	sum forces (kN)						
ratio (w/w)	left springs	left wheels	right wheels	right springs	axle	d springs	d wheels
2,7526	237,56	194,87	536,41	493,72	731,28	128,08	170,77
av. forces (kN)	59,39	**48,72**	**134,10**	123,43	182,82	32,02	42,69
av. load (t)	6,05	**4,97**	**13,67**	12,58	18,64	3,26	4,35

The loads calculated by the pictures about the bukk and the load centres (S1, S2) of the green triangles on Fig. 8:

	left whhels	right wheels
Net weight (t):	28,900	
Wheel load from net weight (t):	3,613	3,613
Payload (t):	45,400	
Gross weight (t):	74,300	
Payload offset (dS) (m):	0,573	
Wheel load from payload (t):	1,338	10,012
Gross wheel load (t):	4,950	13,625
Wheel load ratio:	1,000	2,752
Gross weight offset (m):	0,350	

2.4. The movement of the train

The movement of the train could be reconstructed by the graficons of the locomotive's tachograph. The actual speed of the train was 25-30 km/h at the moment of the derailment.

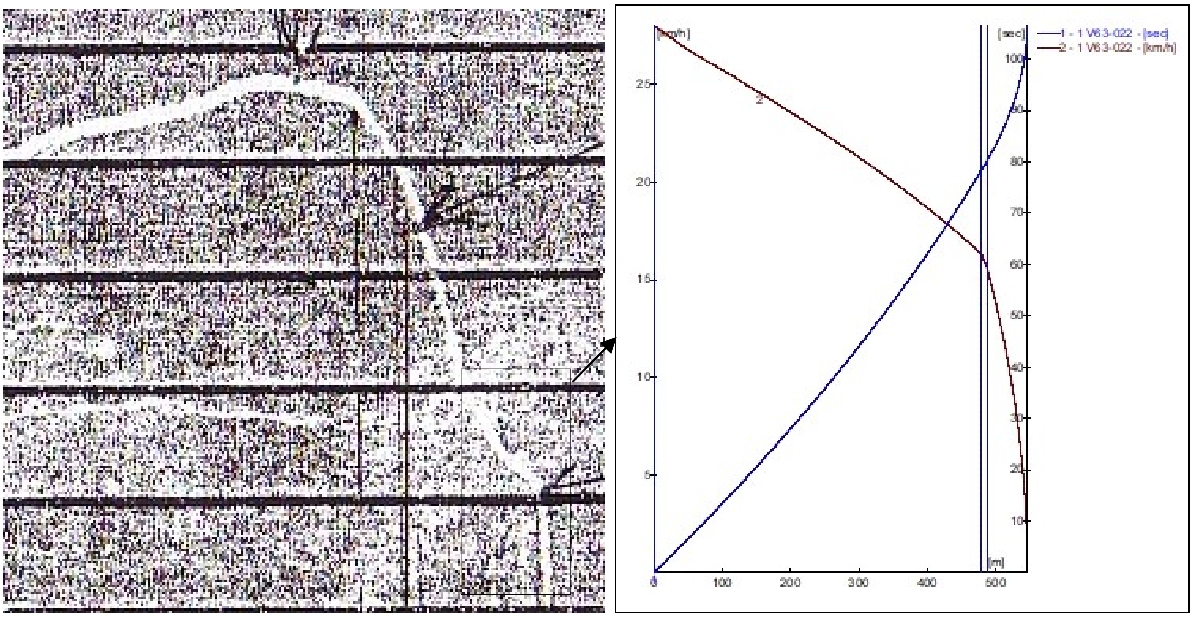

Fig. 9 The v(s) and t(s) functions of the train (tachograph and reconstructed)

2.5. The investigation

The investigation demonstrated that the differences of the wheel load came from four main circumstances:

- payload asimmetricity
- uncompensated horizontal acceleration
- changing of the superelevation in the transition curve
- the depth of the irregularity (sinking).

The wheel loads and the differences are included into the Table below:

	left leading wheel	right rear wheel	av. %	sum %
av. wheelload (t):	9,288	9,288	100	
dif. from payload asimmetricity (t):	-4,337	4,337	-47	**64**
dif. from uncompensated acc. (t):	-1,092	1,092	-12	16
dif. from changing of superelevation (t):	-0,314	-0,314	-3	5
dif. from singular irregularity (t):	-1,058	-1,058	-11	**16**
sum of dif. (t):	-6,801	4,057	-73	100
wheelload (t):	2,486	13,344		
wheelload %:	27	144		

The loads at different conditions of the critical left leading wheel:

payload asimmetricity	irregularity	left leadingwheel load %	critical
exists	exists	**27**	**critical**
not	exists	73	not critical
exists	not	38	probably critical
not	not	85	not critical

The appraisal the rate of the role of asymmetrical loads and role of the track irregularity in the occurrence of accident after the first investigation was 75-25 %.

3. THE DYNAMICAL MODEL

For the precisely modification of the rate of the role of asymmetrical loads and role of the track irregularity in the occurrence of the accident – to construct a track and vehicle model and make a several simulation is needed.

3.1. The vehicle model

We have 7 object at vehicle model: body, 2 bogies, 4 axles. Each of them has 4 parameters (m, θ_x, θ_y, θ_z) and 6 free coordinates (x, y, z, φ_x, φ_y, φ_z).

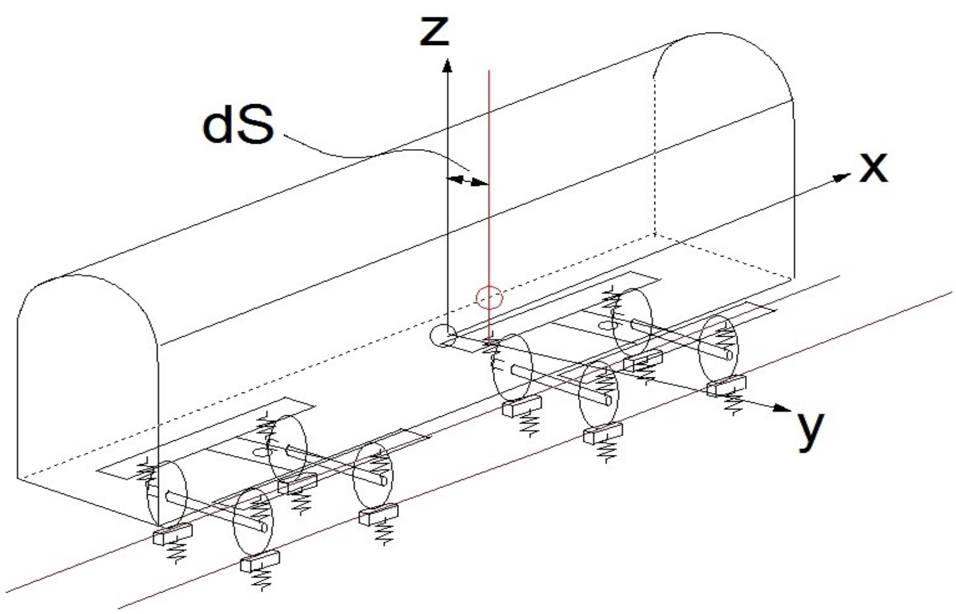

Fig. 10 Dynamical model of the car

3.2. The track model

We have 8 rail elements under each of wheels representing the mass of the rail. Each have parameter m (mass) and free z coordinates. The superelevation e(x), the irregulation h(x), the radius r(x) and the stiffness of the ballast si(x) depend on the place coordinate of the track, x.

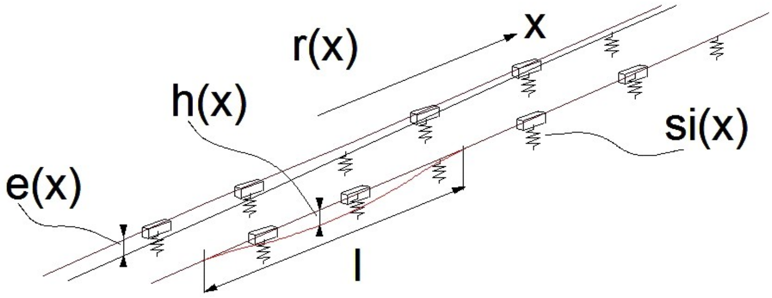

Fig. 11 Dynamical model of the track

3.3. The equations of motions

So there are 50 free coordinates of $\underline{x}(t)$ and the statement vector, $\underline{Y}(t)$ has 100 free coordinates. The equations of motion in matrix formulation:

$$\mathbf{M}\ddot{\underline{x}}(t) + \mathbf{D}\dot{\underline{x}}(t) + \mathbf{S}\underline{x}(t) = \underline{g}(t);\ \forall\ t \in T$$

There are nonlinear contact forces:

- frictional damper forces in Y25 bogies
- contact forces between the frame and bogies
- contact forces between the wheels and rail

We have to calculate the nonlinear contact forces in each step of of the integration in the solution of the equations.


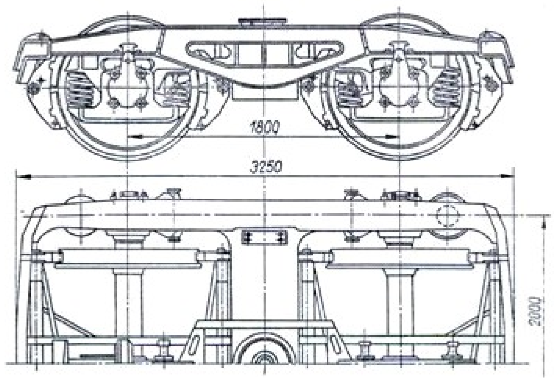

Fig. 12 The Y25 type bogie

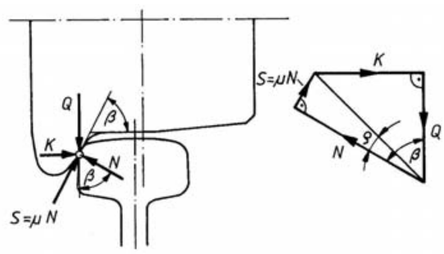

Fig. 12 Wheel-rail contact forces

The wheel-rail contact forces can be computed by the Nadal's formula (Fig. 12):

$$\frac{Y}{Q} = tg(\beta - \rho) = \frac{tg\beta - \mu}{1 + \mu tg\beta} = f(\beta, \mu) \quad .$$

4. MODEL PARAMETERS

The parameters of the model are included into the vector below:

$$\mathbf{p} = [m_i, \theta_{ix}, \theta_{iy}, \theta_{iz}, d_i, s_i] \in \boldsymbol{R}^{92}$$

The components of the parameter vector could be set on the basis of measured parameters of the track and through the reconstruction of the accident occured.

After the identification of the parameters of the wehicle and the rail, and reconstruct the occoured accident – we will able to run several simulation with steping the load asimmetricity (dS) from zero up to the certain derailment and steping the depth of the irregularity (sinking) (h) from sero up to the certain derailment. In this way the probability of the derailment (P) chiefly depend on the load asimmetricity and on the sinking depth could be constructed.

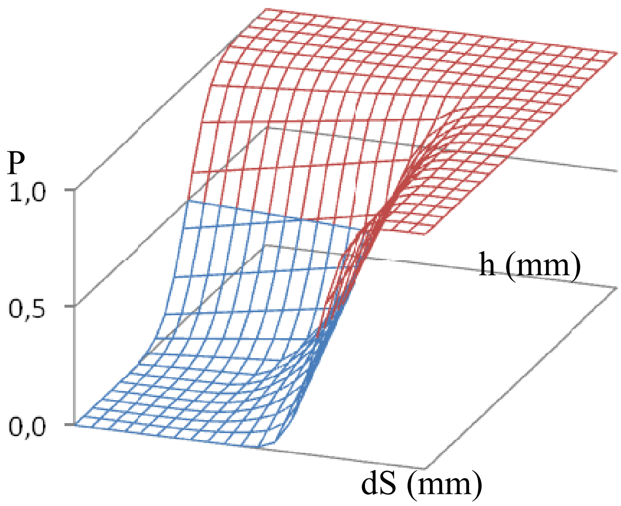

Fig. 13 The anticipated function of derailment probability

5. CONCLUDING REMARKS

- The modell is apt to analyse derailment accidents through the identification of parameters using the existing data and the arosed traces,
- With several simulations using different parameters the probability of the derailment event can be studied,
- The model can be developed to be apt to investigate the joint effects, the effects caused by the wheel/rail running surfaces, the bearings, the eventual overloads, the local thermal and wear processes.

6. REFERENCES

[1] **Sostarics, Gy. – Balogh, V.**: Railway vehicles. (Vasúti járművek). Tankönyvkiadó, Budapest, 1991. (In Hungarian)

[2] **Szabó, A.:** Possibilities for computer based investigations into the accidents caused by the common failures of the track and the vehicle (A pálya és a jármű együttes hibájából történt balesetek számítógépes vizsgálatának lehetőségei.) http://www.vrht.bme.hu/vasut/targyak/jegyzet/Kisikdin.pdf (In Hungarian)

HOMOLOGATION TESTS OF ETR1000-V300ZEFIRO TRAIN UP TO 350 KM/H

Stefano BIONDA, Francesco BRAGHIN, Gabriele CAZZULANI, Egidio DI GIALLEONARDO and Ferruccio RESTA

Dipartimento di Meccanica
Politecnico di Milano
Via La Masa 1, I-20131, Milan, Italy

Received: November 9, 2016

ABSTRACT

The homologation of railway vehicles in Europe is ruled by EN-14363. It defines testing scenarios, experimental setups, data post-processing procedures and limit values for a number of different parameters mainly associated with vehicle safety and ride quality. In particular, in the case of high speed and/or high axle load vehicles, a testing methodology based on the measurement of wheel-rail contact forces at several wheel-sets of the vehicle and accelerations at a number of other places is required. However, for the homologation of very high speed trains (i.e. trains having an operating speed above 300km/h) it should be taken into account that limit values for track geometry quality of the test track provided by the standards go up to a maxi-mum speed of 300km/h. Thus, the homologation process of a very high speed train has to face a number of uncertainties and open questions that require accurate evaluations and will provide very important data for the extension of existing standard requirements to higher speeds than the ones considered today. The present paper presents the work carried out for the dynamic homologation of ETR1000-V300Zefiro train up to an operating speed of 350km/h. The homologation sensor layout as well as the distributed acquisition system for monitoring the whole vehicle will be presented. It should be noted that, for the first time, dynamometric wheel-sets were provided with accuracy information that was constantly monitored during line tests. The influence of vehicle speed on vehicle safety and ride quality up to 350km/h will be presented through the most relevant parameters accounted for by the standards and considerations on how to extend existing standards will be provided.

Keywords: high speed train, homologation, measuring wheelset.

1. INTRODUCTION

In Europe acceptance of running characteristics of railway vehicles is ruled by EN 14363 [1] which is based on present state of the art knowledge of railway vehicle dynamic behaviour. It defines testing scenarios, experimental measurements, post-processing algorithms and limiting values for a number of different parameters associated with vehicle and track safety as well as ride quality. For high speed to very high speed trains, the "normal" method should be applied that requires the measurement of wheel-rail contact forces at several wheel-sets of the vehicle. These forces are both due to the railway vehicle and track characteristics.

In particular, the knowledge of magnitude and characteristics of track irregularities is essential for homologation and acceptance tests. It should be noted that their influence on the dynamic interaction between wheel and rail grows more than linearly with vehicle speed. However, for cost reasons, existing homologation standards prescribe limit track irregularity parameters for the track on which acceptance tests will be carried out that decrease less than linearly with the maximum vehicle speed. Even more critical is the fact that existing standards do not prescribe any track irregularity parameters above 300 km/h. Thus, constant extrapolation is typically adopted, e.g. for any speed above 200 km/h the absolute maximum lateral misalignment should be less or equal to 4 mm for track quality level QN1.

In parallel, for safety and comfort reasons, acceptable wheel-rail contact force and bogie/car-body acceleration limits are independent of vehicle running speed (except the maximum wheel force limit). Thus, the dynamic performances of railway vehicles have to increase more than linearly with their maximum speed. This cannot typically be achieved by passive solutions and active solutions are there-fore sought for. However, this shift of requirements from the track to the vehicle poses at least one fundamental question: which is the optimal balance between track and vehicle requirements?

The present paper presents the work carried out for the dynamic homologation of ETR1000-V300Zefiro train up to an operating speed of 350km/h and tries to propose a reasonable answer to the above fundamental question.

2. LAYOUT OF THE MEASURING SYSTEM

The ETR1000-V300 Zefiro train is an 8-car train-set characterised by a symmetrical formation (Bo′Bo′+2′2′+Bo′Bo′+2′2′+2′2′+Bo′Bo′+2′2′+Bo′Bo′). The power is distributed along the train-set in order to guarantee better traction performances. The train-set used for the homologation with respect to running dynamics was instrumented in different ways: three bogies belonging to DM8, TT7 and T5 cars were equipped with instrumented wheel-set so to apply the normal method as prescribed by EN 14363, while all the other bogies were equipped with accelerometers in order to guarantee the monitoring of safety parameters according to the simplified method.

The train-set was equipped with a measurement chain capable of acquiring and recording a great number of signals. The different signals acquired on board can be grouped depending on physical quantity that they represent and are listed below:

- odometric parameters of the train (eg. running speed and position along the line);
- forces;
- accelerations;
- displacements.

Odometric parameters are acquired by a dedicated system that uses as input the signal from the tachometer mounted directly on the train. This system generates as output the train speed and the position of the train along the railway track which are continuously transmits speed to the main acquisition system.

Forces at wheel-rail interface are measured by means of instrumented wheel-sets using a system which is developed by the research group of Politecnico di Milano that will be described more into details in the following section. This system transfers the data to the main acquisition system in order to have a real-time estimation of lateral and vertical forces. Additionally, forces are also measured on the rods of the active lateral suspension on the same bogies equipped with instrumented wheel-sets. Strain gauges are mounted on each rod and the force applied by the lateral suspension is derived by means of a preliminary calibration performed in laboratory.

Acceleration are measured using mems accelerometers mounted in various locations, for different both for homologation or investigation purposes, including:

- bogie frame;
- axle boxes;

- car-body floor.

Bogie frame accelerations are used mainly for monitoring of the train during test runs plus some investigative measures with “non-standard” placement of the sensors (e.g. centre of the bogie, vertical direction, etc..) to check the vibration level on the bogie. Car-body accelerations are used for homologation purposes (ride quality) or for the evaluation of the passenger comfort.

Displacements, by means of linear potentiometers, are measured between the car-body and the bogie in the lateral direction in order to evaluate the effectiveness of the active lateral suspension and between the bogie frame and the traction motor. Additionally, the deflections of the primary suspension are also measured, using laser transducers, in order to increase the reliability of the wheel-rail contact force estimation system guaranteeing the functionality of the system even in case of faults.

The total number of signals acquired is above 200, depending on the configuration. Sensors are placed along the whole train in a length of about 200 meters. In order to avoid a large number of cables running all over the train the acquisition system was also distributed over three cars, in each of these cars there is an IMC Cronos instrument connected with a set of sensors. The data acquisition systems communicate between them via LAN protocol and an appropriate signal is used in order to achieve correct synchronization between channels.

An additional acquisition system based on National Instruments hardware also distributed along the train is present in order to continuously monitor the data acquired by the telemetry systems of the instrumented wheel-sets and check in real-time the good functioning of the system for the estimation of wheel-rail contact forces.

3. INSTRUMENTED WHEELSET

The ETR1000-V300 Zefiro experimental train was equipped with 6 instrumented wheel-sets, 4 belonging to a trailer bogie and 2 to a motor one. The trailer wheel-sets were instrumented using 22 full Wheatstone bridges: 16 for the measure of the bending of the axle, 4 for the measure of the bending of the wheels and 2 for the measure of the torsion of the axle. A similar arrangement was also used for the motor wheel-sets apart from the fact that two additional bridges were used for the measure of the torsion of the axle on account of the discontinuity given by the presence of the gearbox, directly mounted on the wheel-set. The wheel-set is divided into sections where two bridges for the measure of axle bending are mounted 90° apart, as shown in Figure 1 (right). A number (32 or 16) of strain gauges are mounted on the wheel-web and are connected in series/parallel in order to obtain a full Wheatstone bridge, whose output signal is almost directly proportional to the lateral force minimising the crosstalk effects due to the other forces and to the position of the contact point.

The method used for the estimation of wheel-rail contact forces was developed in the last decades by the research group established in the Department of Mechanical Engingeering of Politecnico di Milano [2,3,4]. As described into details in [5] the optimal set of measurements needed for a good estimation of the three components of wheel-rail contact forces is composed by: two sections on the spindles (e.g. A-H), two sections along the axle between the wheels (e.g. C-F) and two wheel-web signals (e.g. R1A-R1B), one torsional bridge is additionally for the estimation of the longitudinal forces in case of trailer axles, while this number increases to two in case of motor axles.

The basic idea of this instrumented is to guarantee a reliable system even in case of faults of some strain gauges, which may occur during the test runs for different reasons (e.g. flying ballast phenomena). In case one of the strain gauges belonging to a section is faulty the section can be replaced with an analogous one (for example section A can be replaced by section B, section C can be replaced by sections D and E, and section R1A can be replaced by section R2A), guaranteeing full performances of the systems without any loss in accuracy. Additional independent signals can be used as backup, like for example the deflection of the primary suspension which, in this specific case, were measured using laser transducers.

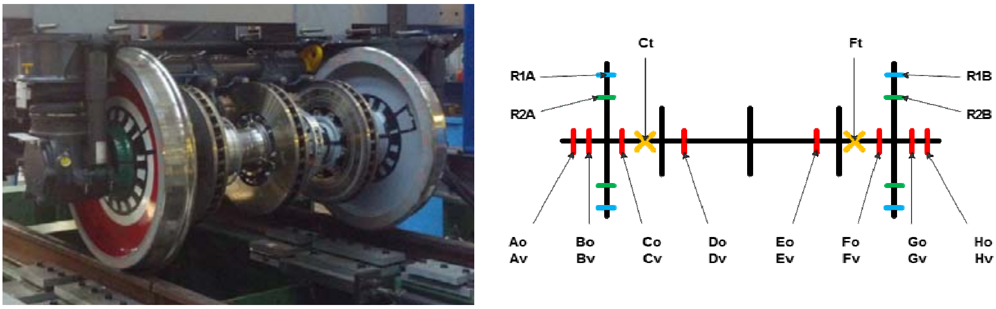

Fig. 1 instrumented wheel-set under calibration and scheme of the disposition of the measurement sections.

3.1 Calibration Test Rig

In order to impose and directly measure the loads at wheel-rail interface a dedicated test-rig have been developed by the Department of Mechanical Engineering of Politecnico di Milano. More details on the design and construction of the test-rig can be found in [7]. This test rig has been designed with the aim to create a totally reconfigurable system, capable to house the entire bogie which the dynamometric wheel-set belongs to. Due to this fact the boundary conditions on the wheel-set are exactly the same which will be experienced during inline service. It is important to remember that the deformation field, especially on the axle, is influenced by the boundary conditions imposed through the suspensions. Moreover, the forces are applied to the wheels by means of two pieces of rail having a UIC 60 rail profile posed with an angle of 1/20. These solutions allow to correctly reproduce the geometrical conditions of the contact.

Fig. 2 shows the layout of the test-rig: the vertical load is imposed by a couple of hydraulic actuators, while a third actuator is mounted on one side of the structure and is used to generate the lateral reaction force necessary to keep in place the bogie. The lateral and longitudinal forces are imposed directly at the contact points by means of the two dynamometric balances depicted in Figure 3.The first element, called Balance1, is composed by four instrumented rods in the vertical direction in order to measure the vertical force. In the lateral direction an actuator having a maximum load of 50kN imposes and, together with a load cell in series, measures the lateral force, while in the longitudinal direction, the measurement and imposition of the loads is obtained by means of a couple of actuators each one having a maximum load of 15kN. The element Balance2 is specular to the first one, with the exception that instead of the longitudinal actuators two instrumented rods are used.

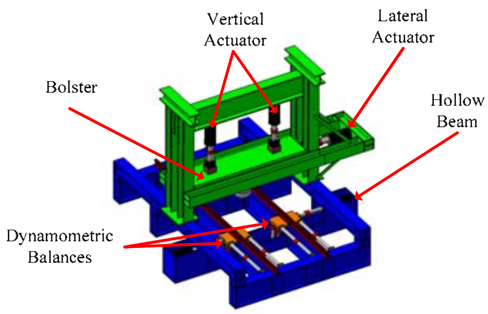

Fig. 2 Test-rig lay-out

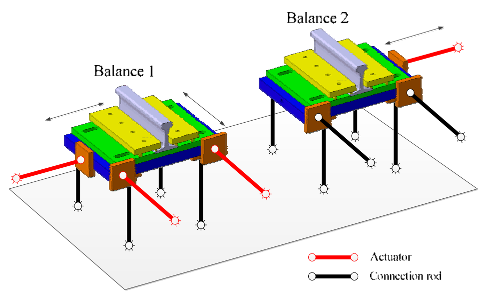

Fig. 3 Dynamometric balances

3.2 Calibration Results

The test plan used for the calibration has been designed in order to consider all the possible conditions that the wheel-set may encounter in regular service. Three lateral position have been considered: central, left flanging and right flanging. The load cases have been then designed by means of a factorial combination of the loads acting on the wheel-set. Table 1 shows the load levels used for the calibration.

Table 1. Summary of the load condition applied in the calibration process.

Factor	Symbol	Levels
Vertical Force (Left) [kN]	Q1	55, 70, 85, 100
Vertical Force (Right) [kN]	Q2	55, 70, 85, 100
Lateral Force (Left) [kN]	Y1	-40, -20, -10, 0, 10
Lateral Force (Right) [kN]	Y2	-40, -20, -10, 0, 10

The entire test plan was repeated for two angular position in order to verify the independency of the dynamometric wheel-set from its angular position. Finally, some specific tests were added to introduce the effects of longitudinal forces. In total, the calibration test plan was composed by 514 tests, 210 repeated tests for two angular position (i.e. 0° and 90°) and 94 tests for the longitudinal forces.

Fig. 4 and Fig. 5 show the calibration results for a trailer wheel-set obtained considering an optimal measurement set i.e. bridges A-H-C-F-R1A-R1B for the measurement of the vertical and lateral forces. For the sake of briefness, only the results concerning the vertical and lateral forces acting on wheel A are presented. The index used to evaluate the performances of the various calibration models is σ, which is the standard deviation of the estimation error for each force, as defined in Equation (1).

$$\underline{\sigma} = std\left([F] - [\hat{F}]\right) = std([F] - [K][\varepsilon]) \tag{1}$$

being [F] the matrix containing the measured forces for each calibration test and [F^] the estimated ones by means of the calibration matrix [K] and the matrix [ε] containing the measured signals by means of strain gauges.

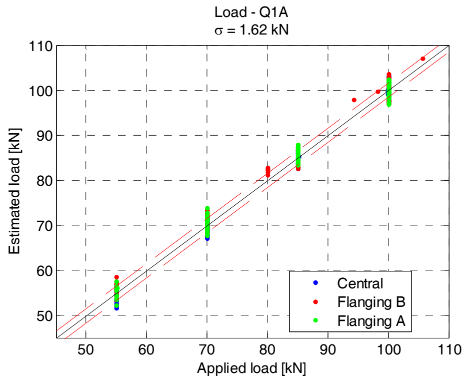

Fig. 4 vertical force estimation on the left wheel with optimal measurement set.

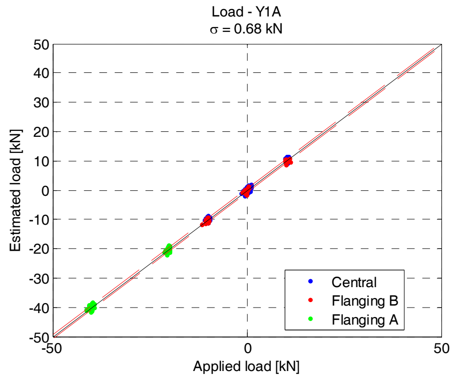

Fig. 5 lateral force estimation on the left wheel with optimal measurement set.

It can be shown that increasing the number of measurement sections does not reduce significantly the σ values, rather, the increase of the linear dependant inputs in the model causes over-fitting problems with a consequent greater sensitiveness of the model to signal noises. The final output of the calibration process is the uncertainty of the instrumented wheel-set which is obtained combining σ with the other sources of uncertainty in the test-rig (for example the uncertainty of the balances.)

4. EXPERIMENTAL TESTS

An example of the results of the homologation tests performed at the maximum speed of 385 km/h are shown in this section. The test runs were performed on the High-Speed Line from Turin to Milan. Two different tests are briefly analysed in the following considering the train in two different conditions: with the active lateral suspension operated in active mode (in the following shown using a red line) or simply operated in passive mode (in the following shown using a blue line).

The results of two different track sections are shown:

A) two opposite curves, with a radius of 11000 m and 10500 m and a cant equal to 55 mm negotiated at the maximum speed;
B) two opposite curves, with a radius of 6000 m and 10000 m and a cant equal respectively to 95 mm and 60 mm, negotiated at speed larger than 360 km/h so to reach a non-compensated lateral acceleration around 1.1 m/s2 in the first curve.

The speed profile and the non compensated lateral acceleration in the two track sections are reported in Figure 6 considering both conditions of the vehicle. In track section A, the speed is almost constant and equal to 385 km/h, while the non compensated lateral acceleration is equal to 0.7 m/s^2 in the first curve (which has a radius of 11000 m and a cant of 55 mm) and to 0.75 m/s^2 in the second one (which has a radius of 10500 m and a cant of 55 mm). On the contrary, in track section B the speed is larger than 360 km/h so to obtain in the first curve a non-compensated lateral acceleration larger than 1.05 m/s^2. This condition should be met in order to guarantee the fulfilment of the requirements of the test sections according to EN 14363, being 1 m/s^2 the permissible non-compensated lateral acceleration.

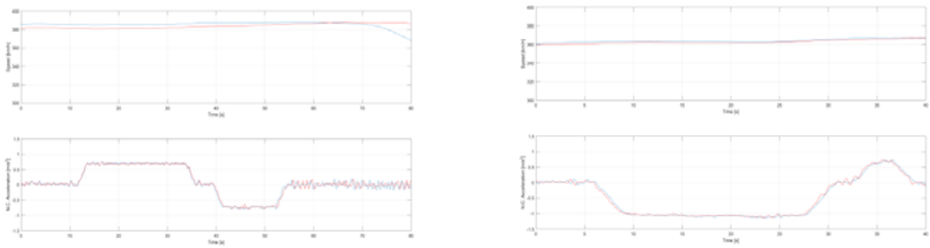

Fig. 6 speed (on the top) and non compensated lateral acceleration (on the bottom) on the considered track sections (track section A on the left, track section B on the right).

The sum of the lateral forces on both axles of the three instrumented bogie are reported in Figure 7 together with the corresponding limit defined according to EN 14363. It is observed that also in this case where the maximum speed of 385 km/h was reached there was a large safety margin especially forTT7 and DM8 cars which are the heavier cars. T5 car is characterised by a lower axle-load and thus a lower limit value for the sum of the lateral forces.

Also considering the quantities to be assessed by means of the simplified method the safety margin is relevant. In fact, the lateral accelerations on the same bogie are also shown in Figure 8. Even in this case the distance with respect to the limit is large. It is worth noticing that being the limit value depending only on the bogie mass T5 and TT7 cars have the same limit whereas a lower limit is defined for DM8 being the motor bogie heavier with respect to the trailer one.

6. CONCLUSIONS

In the present paper the work carried out for the dynamic homologation of ETR1000-V300Zefiro train up to an operating speed of 350km/h was presented. The homologation sensor layout as well as the distributed acquisition system for monitoring the whole vehicle was described.

Additionally, the layout of the instrumented wheel-set and the calibration process which permitted to define its accuracy was presented.

Finally, the results of two homologation tests performed at the maximum speed of 385 km/h were shown proving that the vehicle has a sufficient safety margin even in these extreme speed conditions.

6. REFERENCES

[1] **EN 14363**: "Railway applications - Testing for the acceptance of running characteristics of railway vehicles - Testing of running behaviour and stationary tests", 2005.

[2] **Benigni, E. - Braghin, F. - Cervello, S. - Cigada, A. - Resta, F.:** Determinazione delle forze di contatto tra ruota e rotaia a partire da misure di deformazione dell'assile, Ingegneria Ferroviaria, 57(12), 2002, p.1059-1075.

[3] **Diana, G. - Resta, F. - Braghin, F. - Bocciolone, M. Di Gialleonardo, E. – Crosio, P.**: Methodology for the calibration of dynamometric wheel-sets for the measurement of the wheel-rail contact forces [Metodologia di calibrazione di sale dinamometriche per la misura delle forze di contatto tra ruota e rotaia], Ingegneria Ferroviaria, 67 (1), 2012, p.9-21.

[4] **Cazzulani, G. - Di Gialleonardo, E. - Bionda, S. - Bassetti, M. - Crosio, P. - Braghin, F.**: A new approach for the evaluation and the improvement of the metrological characteristics of an instrumented wheel-set for the measure of wheel–rail contact forces, Proceedings of the Institution of Mechanical Engineers, Part F: Journal of Rail and Rapid Transit, 231 (4), 2016, p.381-393.

DYNAMICAL ANALYSIS OF A SPECIAL ANTI-SKID-SYSTEM FOR RAILWAY CARS AND TRACTION UNITS

István ZOBORY[1] and Dezső NAGY[2]

Budapest University of Technology and Economics
[1] Faculty of Transportation Engineering and Vehicle Engineering
[2] Faculty of Electrical Engineering and Informatics
H-1111 Budapest, Műegyetem rkp 3, Hungary

Received: November 9, 2016

ABSTRACT

It is of paramount importance to maintain the rolling motion of the wheels under braking, in other words to avoid total wheel sliding, i.e. when the rotation of the wheel ceases (blocking), as a consequence of over-braking. In the case of excessive braking torque exerted by the braking system, the adhesion region contracts and finally vanishes in the wheel/rail contact spot, and with further longitudinal motion, pure sliding takes place in the wheel/rail contact, which can lead in the end to stopping of the wheel rotation, bringing about the wheel-tread damage called wheel flattening. In this paper a "creep-control" procedure is formulated so that the time dependent braking torque exerted on the wheel-set can ensure that the prescribed longitudinal creepage ν^* *remains stable*. The known principle of "Inverse Dynamics" [1], [2] is applied for a traction unit with two bogies, in which creep-controlled time dependent brake torque is exerted on all four wheel-sets. The traction unit dynamical model has 11 degree of freedom (four rotatory, and seven translatory coordinates). The train pulled or braked by the traction unit is modelled by a single mass, connected by a linear elastic spring and damper. The longitudinal braking forces transmitted by the wheel/rail contacts of the wheel-sets are described by creep-dependent, non-linear force connection coefficients. Thus, a lumped parameter system model of 12 degrees of freedom in total is considered. In the paper the principle of control for constant (prescribed) longitudinal creepage is first explained on an elementary system model. Based on the control principle, braking of the dynamical model train is then simulated in the time domain by using a numerical integration method. The simulation results for stop braking will be presented, and the effect of the selection of the gain-constants of the equivalent linear control equation will be shown.

Keywords: creepage, nonlinear dynamics, inverse dynamics, creep-control, stability, railway vehicle anti-skid device

1. INTRODUCTION

Improving the effectiveness of the anti-skid devices is one of the most important tasks in the development of railway brake systems, [2], [4]. There are various control procedures for increasing the probability of avoiding the macroscopic wheel sliding under low adhesion conditions. In general the basic requirement for realising the control strategies is to have information on the creep-dependent *force connection coefficient* (*FCC*) defined by the ratio: $\mu = F_t/F_n$ either in a deterministic or a stochastic scheme [3]. From among the available control strategies we selected the approach which uses the measured acceleration and velocity of the longitudinal motion and the angular acceleration and angular velocity of the wheel-set to select the appropriate time variation of the braking torque exerted on the wheel-set, to eliminate macroscopic wheel-sliding using the principle of "inverse dynamics". This method does not need explicit knowledge of the *FCC* function, but is still able to ensure the prescribed creepage in the wheel/rail connection. The authors extended the "*creep control*" strategy for the case when an elastic/dissipative sub-system is connected to the braked (or driven) wheel-sets. Obviously, the method elaborated can be applied for the brake systems of all ground vehicles.

2. CREEP CONTROL

When rolling along the rail, the *FCC* reflecting the force transmitting property of the wheel/rail contact is a creepage (ν) and distance covered (s) parameter *stochastic process: $\mu = \mu(\nu,s,w)$,* where w stands for the *elementary event*, for the occurrence indicator [3].

During a brake application, the occurrence of macroscopic sliding leading to wheel flats can be avoided if the brake control system (by adjusting the braking torque acting on the wheel-sets based on the actual motion characteristics of the jointed sub-systems) can maintain a prescribed small and *constant* creepage value ν*, in the framework of an *always dynamically stable* system property.

The control procedure presented, based on the principle of "Inverse Dynamics", gives an *always stable* final linear system with controlled longitudinal creepage as ouput, and *the method does not require the explicit knowledge of the actual FCC value.*

First, an elementary system of DF=3 will be treated by creep-control based on "Inverse Dynamics", then the method elaborated will be applied to all four braked wheel-sets of a "locomotive" represented as an extended brake-dynamical system model.

3. THE ELEMENTARY DYNAMICAL MODEL

3.1 Model structure and designations

The elementary dynamical model consists of the mass and rotational inertia of the braked wheel-set, and the bogie mass which is connected to the wheel-set by a longitudinal, linear elastic/damping axle-guidance member, see Fig. 1. The linear elastic/damping member consists of a linear spring of stiffness *s* connected in parallel with a linear damper of damping coefficient *d*.

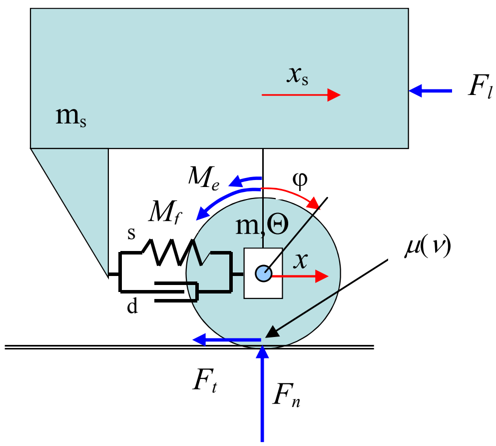

Fig. 1 The elementary dynamical model for the braked wheel-set

There are three degrees of freedom, namely the angular displacement φ of the wheel-set, and the longitudinal displacements x and x_s of the wheel-set and the bogie, respectively.

For non-zero travelling speeds the *longitudinal creepage* ν is defined by the following ratio:

$$\nu = \left.\frac{R\dot{\varphi} - \dot{x}}{\dot{x}}\right|_{\dot{x}\neq 0} .$$

During free running or braking on horizontal track, the longitudinal creepage takes negative values: $\nu < 0$.

The *force connection coefficient* (*FCC*) μ is defined as the ratio of the creep-force $F_f < 0$ (i.e. the tangential braking force) acting on the wheel tread in the wheel/rail contact and the vertical wheel load $F_n > 0$:

$$\mu = \frac{F_f}{F_n} \quad .$$

When braking, force connection coefficient (*FCC*) values are negative ($\mu < 0$). Thus, in accordance with theory and experience, the force connection coefficient μ is essentially *creep-dependent*: creep and *FCC* values are negative during braking or free running, while under driving (tractive effort exerted) creep and *FCC* values are positive, see Fig. 2. It is clear, that with constant F_n the maximum braking force can be exerted at creepage $-\nu_0$. The prescribed creepage ν^* for the controlled braking process, must obviously fall somewhere between $-\nu_0$ and zero. The air resistance force acting on the bogie-mass is a quadratic function of speed: $F_l = -sign(\dot{x})C\dot{x}^2$.

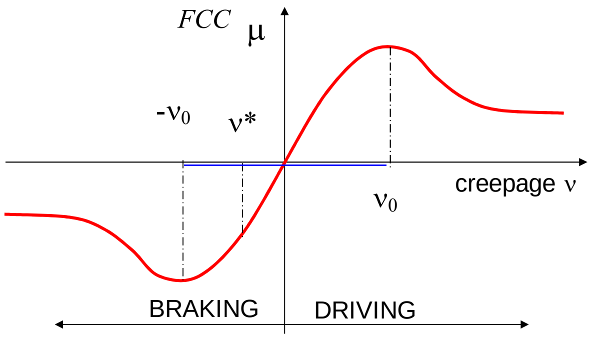

Fig. 2 Force connection coefficient (FCC) μ vs. longitudinal creepage ν

3.2 The motion equation system

The system equations (the motion equations) are generated by using Newton's 2^{nd} law both for the single rotatory motion and for the two translatory motions.

1. Wheel-set rotation: $$\Theta\ddot{\varphi} = -F_n\mu(\nu)R - M_e(\dot{\varphi}) - M_f(t) \qquad (1)$$

2. Wheel-set translation: $$m\ddot{x} = F_n\mu(\nu) + s(x_s - x) + d(\dot{x}_s - \dot{x}) \qquad (2)$$

3. Bogie translation: $$m\ddot{x}_s = -s(x_s - x) - d(\dot{x}_s - \dot{x}) - C\dot{x}_s^2 \qquad (3)$$

In explicit form: $$\ddot{\varphi} = \frac{1}{\Theta}\left[-F_n\mu(\nu)R - M_e(\dot{\varphi}) - M_f(t)\right]$$

$$\ddot{x} = \frac{1}{m}\left[F_n\mu(\nu) + s(x_s - x) + d(\dot{x}_s - \dot{x})\right]$$

$$\ddot{x}_s = \frac{1}{m_s}\left[-s(x_s - x) - d(\dot{x}_s - \dot{x}) - C\dot{x}_s^2\right]$$

3.3 The control requirement

The objective of the creep-control is to maintain the prescribed *constant creepage value* ν^* in the course of braking, also in the presence of perturbations, thus the task is to determine the appropriate variation with time of the applied braking torque $M_f(t)$ to achieve this objective.

In order to determine the appropriate function M_f(t), consider first the deviation of the actual creepage $\nu(t)$ from the prescribed (commanded) creepage value ν^*:

$$\Delta\nu(t) \overset{def}{=} \nu(t) - \nu^* \quad .$$

Let us determine the *time derivative* of the *deviation function* $\Delta\nu$(t) defined above:

$$\frac{d}{dt}\Delta\nu(t) = \dot{\nu}(t) = \frac{d}{dt}\left(\frac{R\dot{\varphi} - \dot{x}}{\dot{x}}\right) = \frac{(R\ddot{\varphi} - \ddot{x})\dot{x} - (R\dot{\varphi} - \dot{x})\ddot{x}}{\dot{x}^2} =$$

$$= \frac{R\ddot{\varphi}}{\dot{x}} - \frac{R\dot{\varphi}\,\ddot{x}}{\dot{x}^2} \quad .$$

The derivative $\ddot{\varphi}$ is known from the motion equation (1), and creep force F_f in the wheel/ rail contact can be expressed from motion equation (2):

$$F_f = F_n\mu(\nu) = m\ddot{x} - s(x_s - x) - d(\dot{x}_s - \dot{x}) \, .$$

Thus:

$$\frac{d}{dt}\Delta\nu(t) = \frac{R\ddot{\varphi}}{\dot{x}} - \frac{R\dot{\varphi}\,\ddot{x}}{\dot{x}^2} = \frac{R}{\dot{x}}\left(-\frac{m\ddot{x} - s(x_s - x) - d(\dot{x}_s - \dot{x})}{\Theta} - \frac{M_e(\dot{\varphi})}{\Theta} - \frac{\mathrm{M_f(t)}}{\Theta}\right) - \frac{R\dot{\varphi}}{\dot{x}^2}\ddot{x} \, .$$

The whole right hand side of the expression can be transformed into $-K\,\nu\Delta$(t), if the braking torque M_f(t) to be applied is determined based on the actual (measured) motion characteristics of the vehicle using the principle of "Inverse Dynamics" ([1], [2]) as follows :

$$\mathrm{M_f(t)} = \frac{\dot{x}\Theta K}{R}\Delta\nu - M_e(\dot{\varphi}) - m\left(R + \frac{\Theta\dot{\varphi}}{m\dot{x}}\right)\ddot{x} + sR(x_s - x) + dR(\dot{x}_s - \dot{x}) \quad .$$

The above torque variation with time can be realised if quantities

$$x_s(t) - x(t),\ \dot{x}(t),\ \dot{x}_s(t) - \dot{x}(t),\ \ddot{x}(t)\ and\ \dot{\varphi}(t)$$

have been *measured continuously or with frequent sampling* in the course of the actual operation process. The application of such a special *motion-state-dependent braking torque $M_f(t)$* results in a *homogeneous linear resultant system* , i.e. the creepage-process obeys the simple *linear homogeneous first order differential equation*:

$$\frac{d}{dt}\Delta\nu(t) = -K\Delta\nu(t)$$

the equilibrium state $\Delta\nu = 0$ of which is *asymptotically stable.* Thus, in the case of the occurrence of perturbations, i.e. when the actual creepage value is forced to deviate with time from the prescribed stationary (target) value ν^**,* then after having the disturbance decayed, the creepage value ν of the controlled system returns to the prescribed value ν^* in an exponential way. Obviously the selection of gain coefficient K will play a decisive role in the dynamical processes emerging in the creep-controlled system.

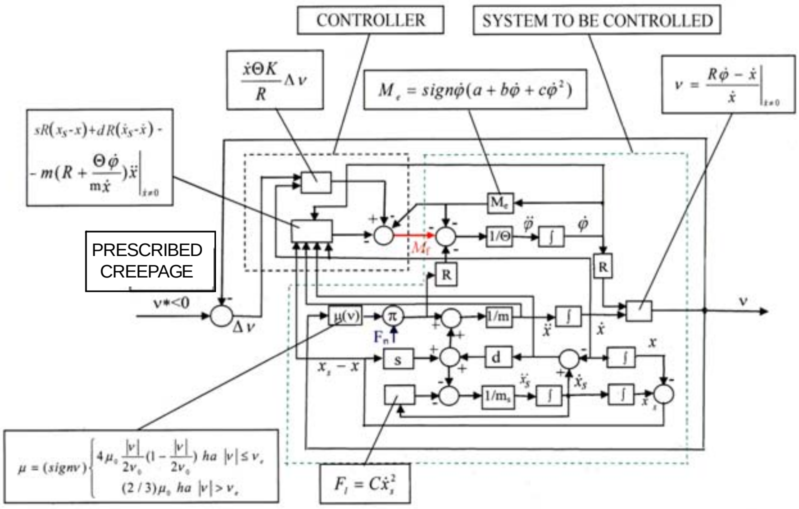

Fig. 3 Flow chart of the creep-control of one wheel-set

The logical flow-chart of the creep-controlled system is shown in Fig. 3. In the Figure the sub-system *to be controlled* (the plant) and the *controller* are clearly distinguished. The control effect itself is exerted by the indirectly time dependent braking torque $M_f(t)$.

4. JOINT DYNAMICAL MODEL OF THE TRACTION UNIT AND THE TRAIN

The system model of the complete brake-controlled locomotive + train system is shown in Fig. 4.

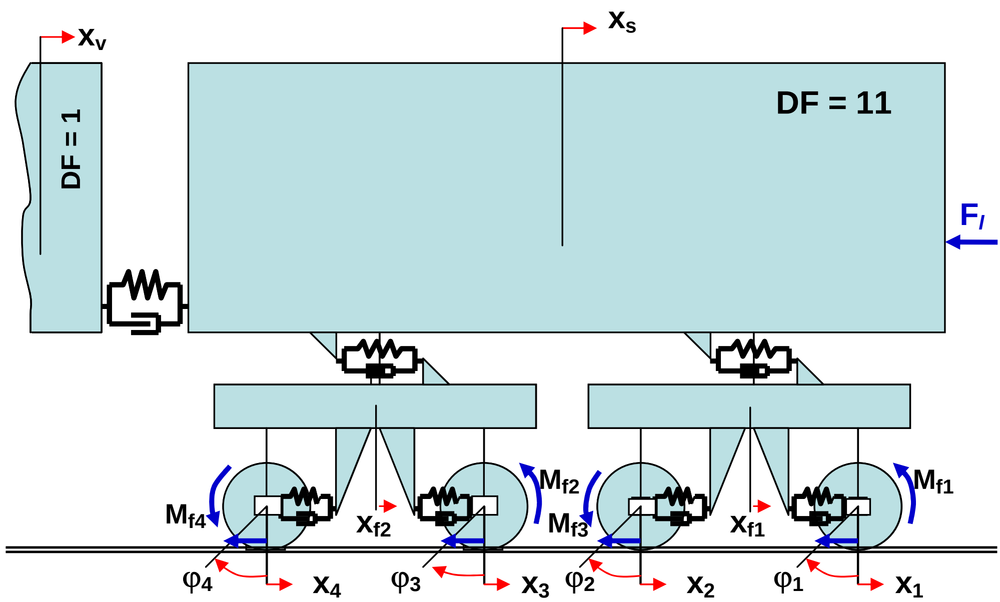

Fig. 4 The dynamical model for the braked loco + train system

The motion equations can be characterised as follows:

- Strongly **non-linear *implicit*** set of motion equations (wheel/rail contact, journal friction torque, air drag, braking torque),

  $$\mathbf{F}(\mathbf{x}, \dot{\mathbf{x}}, u(t)) = \mathbf{0},\ \mathbf{x}(t_0) = \mathbf{x}_0\,,$$

  Where $\mathbf{x}_0$ is the initial value vector of the simulation process at initial time t_0. The *state vector* is built up as follows:

  $$\mathbf{x} = \begin{bmatrix} \dot{\varphi}_1 & \dot{\varphi}_2 & \dot{\varphi}_3 & \dot{\varphi}_4 & \dot{x}_1 & \dot{x}_2 & \dot{x}_3 & \dot{x}_4 & \dot{x}_{f1} & \dot{x}_{f2} & \dot{x}_s & \dot{x}_v & \varphi_1 & \varphi_2 & \varphi_3 & \varphi_4 & x_1 & x_2 & x_3 & x_4 & x_{f1} & x_{f2} & x_s & x_v \end{bmatrix}^T \in R^{24}$$

  The *control process* u(t) appears in the form of an *indirectly* (through the motion states) *time dependent braking torque* u(t) = M_f(t) = $M_f(\mathbf{x}(t), \dot{\mathbf{x}}(t))$.
- In the dynamical equations the four wheel-sets were treated separately when computing their motion characteristics determining the creepage conditions on the contact spots. The traction resistance torques acting continuously on wheel-sets were computed using quadratic functions of the angular velocity with constant coefficients.
- The air drag F_l was modelled by a pure quadratic function of the locomotive velocity. Its action point was located at the centre of the for-head surface of the locomotive.
- To approximate the dynamical environment of the locomotive the train was somewhat crudely modelled by a single mass joined to the locomotive body by a linear spring and damper.
- The difficulties due to the implicit character of the initial value-problem for the deducted implicit differential equation system can be reduced by reasonable numerical approximation methods.

As the *approximating method* to be used in the following, the motion state dependent braking torque in the equation at time instant t_i was computed by using the motion state-dependent values from the previous instant t_{i-1} of the simulation. Thus, the solution procedure works in a "two tact" operation mode:

1. Computation of M_f at t_{i-1}, is designated by $M_f(t_{i-1})$
2. Computation of the accelerations at t_i **using** $\mathbf{M_f}(t_{i-1})$

5. SIMULATION RESULTS

- The train model of *11 + 1* degrees of freedom presented in Fig. 4 was numerically simulated.
- First the motion characteristics necessary to feed back for computing the appropriate (Inverse Dynamics induced) braking torques were the "pure" simulated acceleration, velocity and displacement characteristics, i.e. no measuring errors were taken into consideration. Later, there attempts were made to add noise to the "pure" computed dynamical system responses, thus slightly perturbed motion characteristics were fed into the controller to generate the appropriate braking torques acting on the wheel-sets.

- The creep-controlled *stop braking process* was analysed in the case of an initial velocity 30 km/h. The mass of the loco was 80 t and that of the train was of 100 t. Brake effect was exerted only by the locomotive brake system.
- The anticipated deceleration of the braked train was $a_b = -1$ m/s^2
- The prescribed longitudinal creepage was computed based on the anticipated deceleration. Its value was determined as $\nu^* = -0.0055$.
- The simulation program was written in MATLAB.

5.1 Longitudinal forces acting on one wheel-set

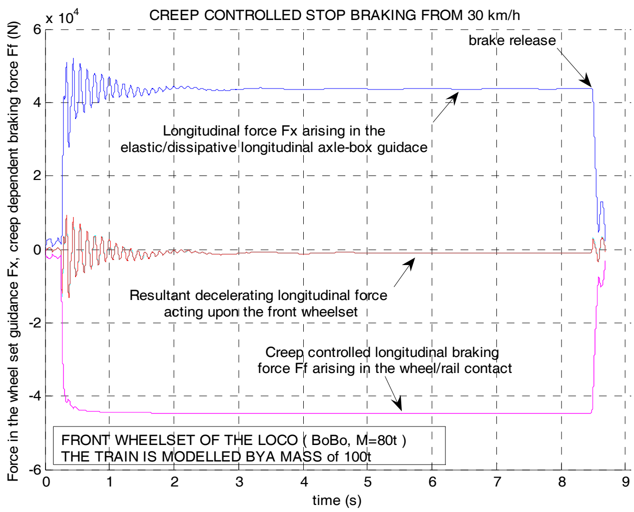

Fig. 5 Longitudinal forces acting on one wheel-set vs. time

In Fig. 5 the clear *force-play* of the longitudinally moving wheel-set is shown. It can be seen that the resultant longitudinal force influencing the longitudinal motion of the wheel-set is the sum of the (negative) creep/force emerging on the contact surface F_f induced by the controlled braking moment M_f, and the (positive) connection force F_x arising in the longitudinal axle-box guidance. Initial time: $t_0 = 0.25$ s.

5.2 Stop braking due to the creep-controlled deceleration process

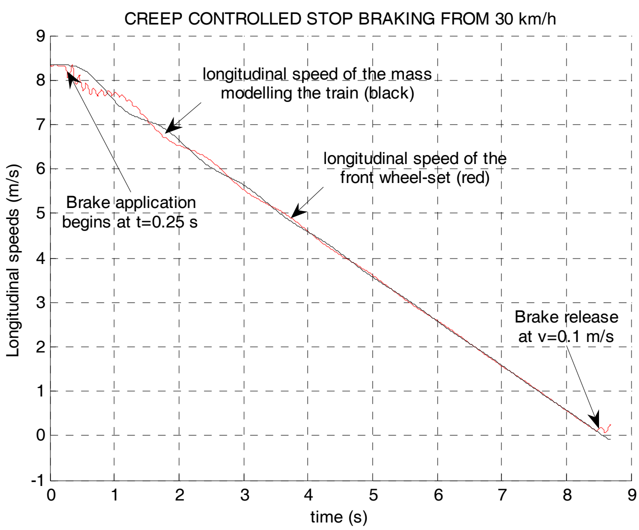

Fig. 6 The speed "profile" due to the action of appropriate braking torque $M_f(t)$

In Fig. 6 the longitudinal velocity conditions are shown. From among the four braked wheel-sets of the locomotive only the time dependent longitudinal velocity of the front wheel-set is shown, since the other three velocity functions were practically congruent to the front one. The initial time of the brake application (= intended stop braking) was at $t_0 = 0.25$ s. The longitudinal velocity process of the wheel-set shows certain wavy variation after the brake application certainly due to the similar property of the controlled braking moment acting on the wheel-sets, see Fig. 5. The velocity of the train shows slow damped and decaying variation with time being in counter phase with the variation with time of the wheel-set longitudinal velocity process. The quasi constant acceleration is ensured in the whole system from the fourth second after the brake application. The control process seems to complete its mission.

5.3 The controlled longitudinal creepage vs. time

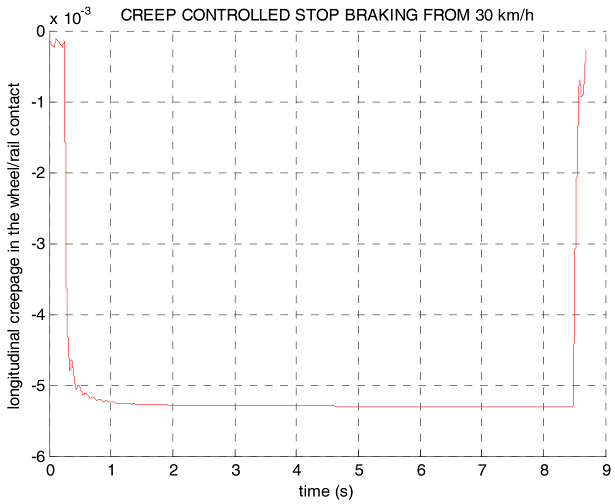

Fig. 7 The variation with time of the controlled longitudinal creepage

In Fig. 7 the longitudinal creepage of the front wheel-set is shown. The creepage has been enforced by the appropriately controlled braking torque exertion on the wheel-set. It can be seen that after a 0.75 s long transient period the control target creepage $\nu^* = -0.0055$ has practically been maintained up to the time instant of the brake release at instant 8.5 s. After having released the brake, the creepage returns to the value enforced only by the traction resistance torque (bearing resistance) acting on the wheel-set.

5.4 The braking torque ensuring the quasi constant creepage

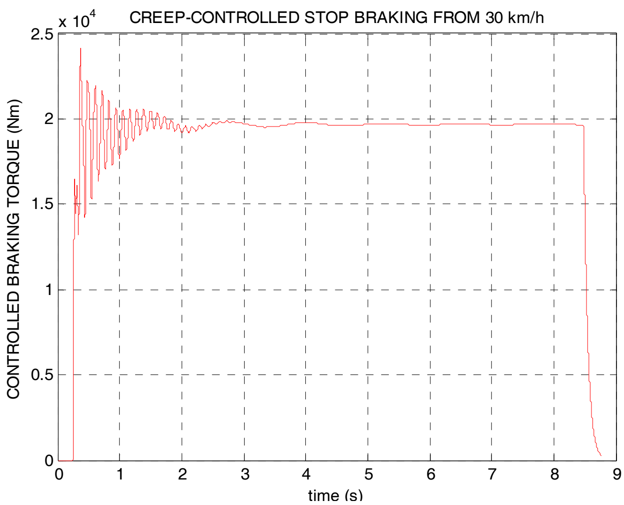

Fig. 8 The “appropriately” creep-controlled braking torque exertion vs. time

In Fig. 8 the creep-controlled braking torque applied on the front wheel-set is shown. The effects on the creep-controlled braking torque due to vibrations induced by the brake application in the whole dynamical system model can be identified. The transient torques decay in the first 3 *s* and after this period the creep-controlled braking torque was stabilized and took a practically stationary value up to the instant of brake release. After having released the brake, the creep controlled braking torque rapidly vanishes.

5.5 FCC vs. longitudinal creepage

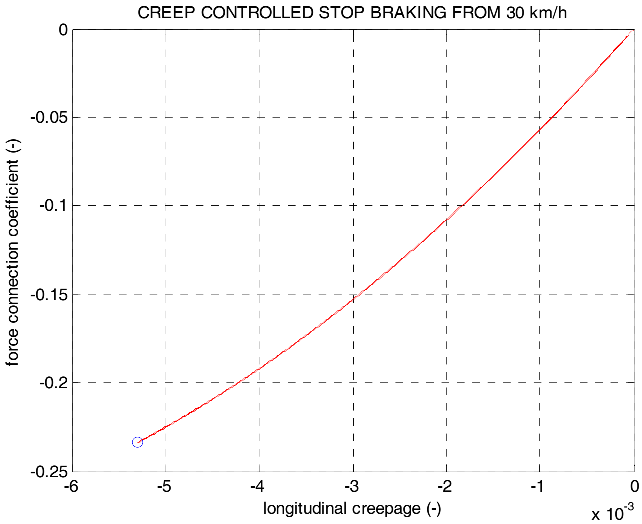

Fig. 9 Variation of the *FCC* vs. longitudinal creepage. Initial speed: 30 km/h, at a quasi-constant deceleration of -1 m/s^2. Commanded creepage: ν^* = -0.0055

In Fig. 8 the variation of the FCC with longitudinal creepage is shown for the whole creep-controlled braking process simulated. At the beginning of the process the creepage starts from zero. In the course of the first 0.25 s only the traction resistance (journal friction) torque enforces a very small negative creepage on the wheel-set considered (the front wheel-set is the leader or representative one). After having applied the creep-controlled braking torque, the creepage increases up to the constant intended (commanded) creepage: ν^* = -0.0055, following the time process shown in Fig. 7. The *FCC* achieves the constant value -0.23 necessary for the intended constant brake deceleration. The reverse process started when the brake was released. The *FCC* decreases in accordance with the creepage dependence indicated in Fig. 2. After brake release the decreasing in creepage tends to zero (when stopping).

5.6 Creepage time-derivative vs. creepage

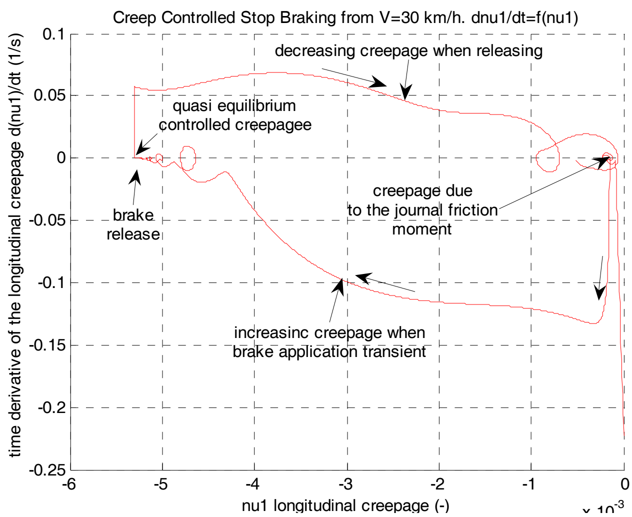

Fig. 10 Variation of the time derivative dν/dt vs. the creepage ν itself for the creep-controlled stop braking process from initial speed 30 km/h.

In Fig. 10 the variation with longitudinal creepage of the time derivative of the longitudinal creepage (the creep-velocity) is shown. The braking process begins at the coordinate-pair containing a zero initial creep-velocity and a very small negative creepage related to the journal friction moment (traction resistance moment) acting on the wheel-set. The creep-controlled brake application process enforces negative creep-velocities, while the creepage itself takes greater negative values. Achieving the control-target creepage value ν* certain damped variations of periodic components can be recognised. The creep-control is effective, i.e. the target state value is practically achieved at point (0, ν*), and after having initiated the brake release, the process takes an initially very slowly varying positive span of creep-velocity and prior to stopping it performs certain small, decaying loops around zero.

5.7 Creep control ensuring braking torque vs. longitudinal creepage

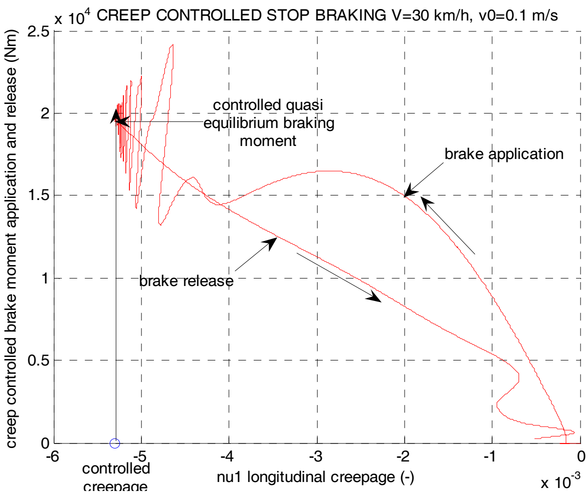

Fig. 11 Variation of the creep-controlled braking moment vs. the creepage itself for the creep-controlled stop braking from initial speed 30 km/h. Controlled (commanded) creepage: ν* = 0.0055.

In Fig. 11 the variation of the creep-controlled braking moment (torque) with longitudinal creepage is shown. In the diagram it is easy to recognise the transient torque oscillations of bottleneck-form prior to arriving at the practically constant quasi equilibrium state near to the controlled creepage (commanded creepage) value ν*. When brake release occurs, the controlled braking torque decreases almost linearly with the (in absolute value) decreasing longitudinal creepage values. The final near-zero state is reached by certain oscillation-like variation

6. PARAMETER VARIATIONS FOR TESTING CONTROL SENSITIVITY

6.1 Varying control gain *K*, effect on the variation of braking torque $M_{f1}(t)$

To test the effect of variation in control gain K on the braking torque $M_{f1}(t)$ acting on the front wheel-set of the front bogie, a simulation sequence was carried out. The control gain values K applied were as follows:

$$K = 75000, 65000, 40000, 10000.$$

The results of the simulation sequence are shown in Fig. 12.

It can be clearly seen that there are two characteristic effects of the variation in K on the time variation of the braking torques. High values of K lead to a fast reaction in the creep control process, but inconvenient fluctuations of large amplitude appear just after the brake application. The fluctuations show damped character and after 2 seconds the unwanted fluctuations disappear, and the “control representing” braking torque $M_{f1}(t)$ tends to be stabilized.

The low gain value $K = 10000$ is “too low”. The inconvenient fluctuations have practically disappeared, but the control process becomes very slow, i.e. after 2 seconds stabilization is still not achieved.

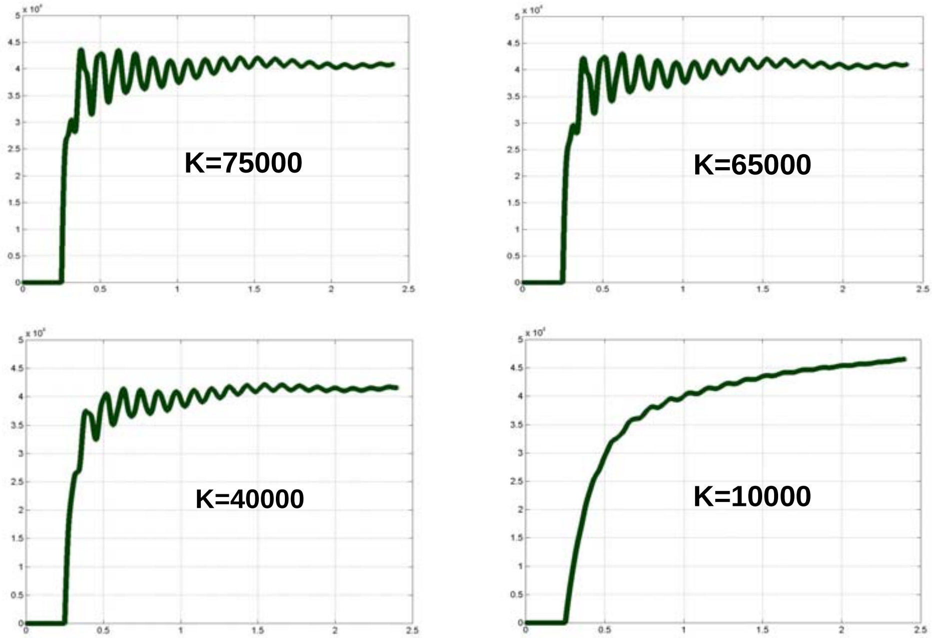

Fig. 12 The effect of the applied gains K on M_{f1}

6.2 Varying control gain K, effect on the FCC $\mu_1(t)$

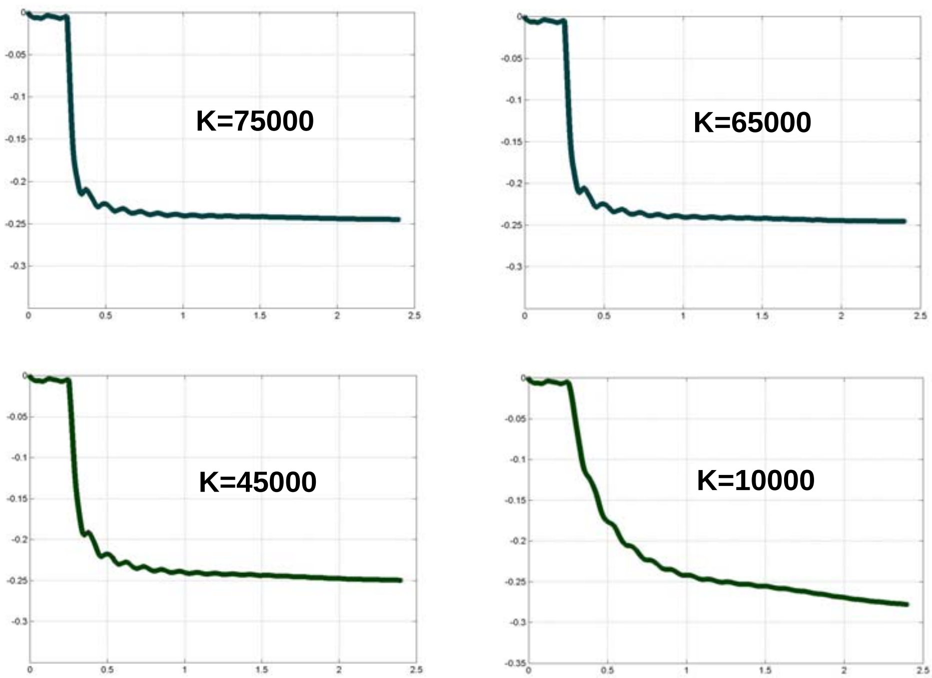

Fig. 13 The effect of the applied gains K on $FCC\mu_1$

Fig. 13 shows results of the previously mentioned simulation for the variation with time of the controlled *FCC* $\mu_1(t)$ for the different gain values. It can be seen that the variation with time of the controlled *FCC* functions do not take on the intensive fluctuations from the controlling torques M_{f1}(t). The functions are practically smooth even for the highest gain, and the target value *FCC* = - 0.25 is firmly achieved and maintained. The effect of decreasing gain can be seen in the slower reaction and for gain *K = 10000* there is a considerable deviation from the target value at the end.

6.3 Varying axle loads along the track

To test the effect of varying axle load on the "appropriately" fed back braking torques M_{f1}(t) and on the resultant *FCC* $\mu_1(t)$, a *sinusoidal variation* was considered in the function of axle-load vs. distance covered, with constant (nominal) mean axle-load F_{n1}, i.e. this procedure gives a preliminary model of the effects caused by vertical vibrations in the forces normal to the wheel/rail contact area. The amplitude of the sinusoidal axle load variations was $0.05F_{n1}$, while the spatial angular frequency of the variation in the axle load was Ω = 6 rad/m. The effect on the braking torques for different gain values *K* applied in the basic equation are shown for the front axle (subscript 1) of the loco in Fig. 14 . In Fig. 15 the effect on *FCC* $\mu_1(t)$ is shown.

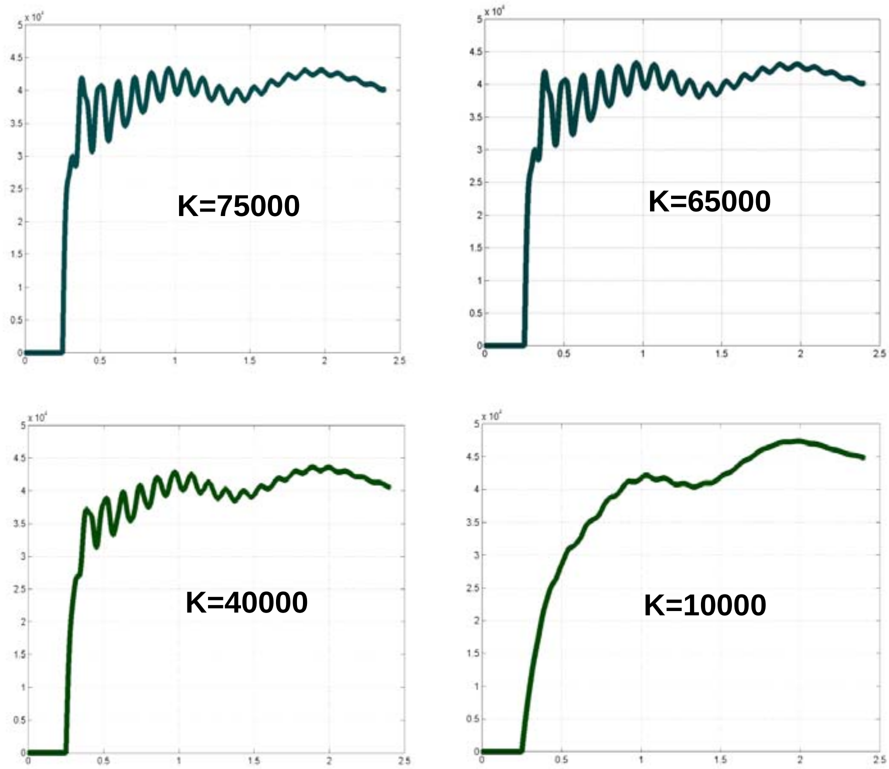

Fig. 14 The effect of axle load variation of amplitude 5% and the gains K on M_{f1}

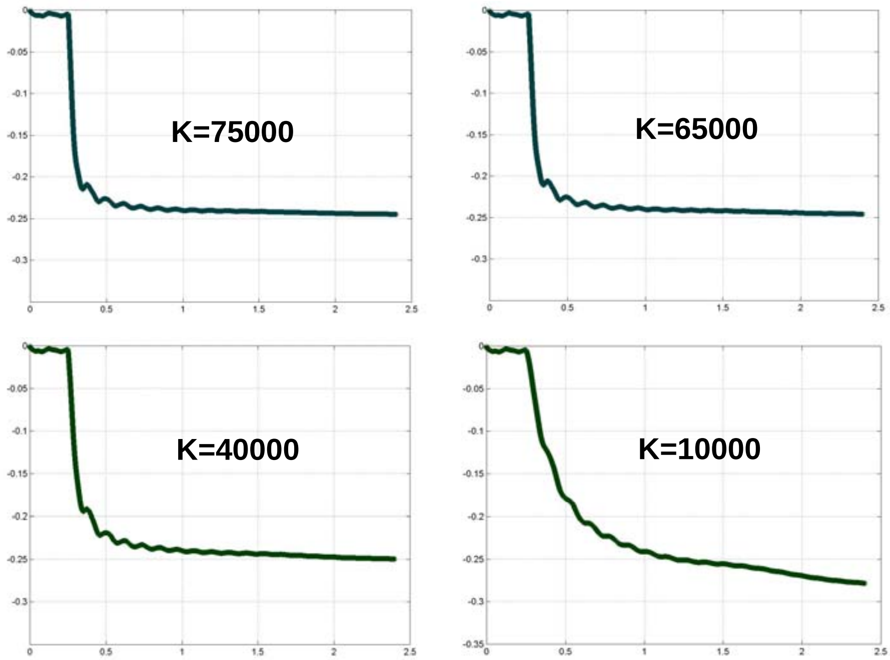

Fig. 15 The effect of sinusoidal axle load variation of amplitude 5% of $F_{n1}$and the gains K on $FCC\mu_1$

7. CONCLUSIONS

Based on the investigations described above the following conclusions can be drawn:

- The elaborated elementary creep-control model based on the principle of „Inverse Dynamics" gives the possibility of recognising a proper strategy for developing *novel antiskid-devices*.
- The creep-control principle elaborated is proper for the parallel application for realising the independent creep-controlled braking of more wheel-sets
- Further investigations are needed to test perturbed (by measurement noise) processes used as feed-backs for generating the appropriate braking torque that can ensure the constant creepage prescribed.
- With the knowledge of the appropriate torque application functions further research and development is needed to determine and assign the real torque generating machines (friction brake, electro-dynamical brake, etc.) to be applied.
- The sensor system to be used for a real system also needs detailed research and development activities

8. REFERENCES

[1] **Ariyur, K.B. – Krstič, M.:** Real-Time Optimization by Extremum Seeking Control. Wiley&Sons, Inc. New-York, 2003.

[2] **Gáspár, P. – Szabó, Z. – Bokor, J.:** An Estimation Method For The Wheel-Rail Friction Coefficient. Proceedings of the 10th MINI Conference on Vehicle System Dynamics, Identification and Anomalies (VSDIA 2006). (Ed. by Prof. I. Zobory). BME, Department of Railway Vehicles, Budapest, 2007, p.237-244. ISBN: 9789634209683

[3] **Zobory, I.**: On Stochastic Field Model of the Wheel/Rail Rolling/Sliding Contact Force Transfer. Proceedings of the 10th MINI Conference on Vehicle System Dynamics, Identification and Anomalies. (VSDIA 2006). (Ed. by Prof. I. Zobory) BME, Department of Railway Vehicles, Budapest, 2007, p. 95-114. ISBN: 9789634209683

[4] **Zobory, I. – Békefi, E.:** Control Strategies of Brake Dynamics for Railway Vehicles Equipped with Anti-Slip-Device. Proceedings of the 9th MINI Conference on Vehicle System Dynamics, Identification and Anomalies (VSDIA 2004). (Ed. by Prof. I. Zobory), BME Budapest, p. 227-236. ISBN: 9634208754

AN APPLICATION OF KALMAN FILTERING ESTIMATION TO THE CONDITION MONITORING OF THE GEOMETRIC QUALITY OF THE RAILWAY TRACK

Francesco LEONARDI, Stefano ALFI and Stefano BRUNI

Department of Mechanical Engineering, Politecnico di Milano
Via La Masa 1, 20156 Milano, Italy
e-mail francesco.leonardi@.polimi.it
ph. +39 02 2399 8357

Received: November 9, 2016

ABSTRACT

In this paper, an application of the treatment of dynamic datasets of a railway vehicle, as previously described by the same authors in Reference [1], is presented. In the preceding work, the proposed track condition monitoring system was designed to be implemented on board of train being operated in standard revenue service. Through the use of Kalman filter state estimator it was possible to replace some direct measures with their estimation. This paper provides a more comprehensive framework for the study, by investigating the observability of the system. Moreover, the proposed methodology, previously validated exploiting a multi-body simulator, is herein applied to real data collected during measurements campaign on Italian railway network.

Keywords: Rail vehicle dynamics, monitoring of the track, Kalman filter.

1. INTRODUCTION

In the last decade diagnostic condition activities in the railway field have been moving from periodic maintenance to that so called "*on condition*" maintenance in order to improve the railway quality and decrease the operating cost. This new approach involves the collection of data regarding the geometric quality condition of railway framework. For several years, specialized inspection vehicles have been used to carry this work out. Of course the use of dedicated trains produces high costs and collides with the necessity to cover the railway network. In order to improve this situation, measurements collected by in-service train can be used in addition to those gathered by inspection vehicles, see e.g. [2-4]. As outlined in [1], this requires to reduce the number of systems used in order to meet the stringent constraint in term of space available for transducer and wiring, power supply, gauge, etc. Previous work from the same authors of the paper was aimed at meeting the requirements through the use of Kalman filter to replace the direct measure of vehicle dynamics at some meaningful locations by stochastically optimal state estimation [1]. Kalman filter state estimator was developed for different reduced sets of transducers, with the aim of the defining a best deal between the complexity of the measuring set-up and the overall accuracy of the monitoring system. A performance index was defined to summarize the performances of the diagnostic unit. All Kalman filter state estimators were validated on the base of virtual measurements obtained through numerical simulation of a fully non-linear multi-body model of the vehicle having an excess of 100 states.

Continuing along the same research stream, this paper provides a more comprehensive framework for the study, by investigating the observability of the system.

Furthermore, in this paper the proposed method is applied to line measurements performed on an ETR500 class High Speed Train and the actual applicability of the approach is discussed.

2. IDENTIFICATION MODEL

A model with 6 *d.o.f.* (vertical displacements z and pitch rotation ϑ of car body C, leading bogie LB and trailing bogie TB) aimed to describe the vehicle dynamics in the vertical plane has been obtained. During this work some simplifying assumptions are introduced such as rigid bodies and constant speed of the train.

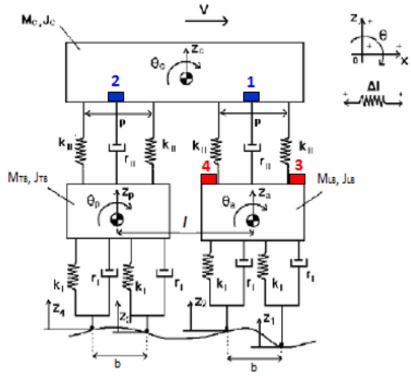

Fig. 1 Identification model

The model shown in Fig. 1 is composed by three rigid bodies: a car body and two bogies. Each of them is linked to the car body through elastic and viscous damping elements. Moreover, it has been considered that wheels always keep in contact with the rail and that the wheels and the rail have much higher stiffness with respect to primary suspensions. Under these conditions it is possible to consider vertical irregularity of the track equal to vertical motion of axle-boxes represented by the displacements z_1, z_2, z_3, z_4 of the four axles.

Furthermore, in Fig.1 is represented the measurement set which involves four accelerometers, two on car body (blue squares) and two on leading bogies (red squares). The numbering of these sensors will be useful in the evaluation of a figure of merit for state identification proposed in section 5.

The equations of vertical motion are obtained using Lagrange equation and secondly they are re-written in the standard state equation form shown in Eq. (1). The output vector has been chosen composed by the vertical accelerations evaluated at two distinct points on the car body and on the leading bogie.

$$\begin{cases} \dot{\underline{x}}(t) = A \cdot \underline{x}(t) + B \cdot \underline{u}(t) \\ \underline{y}(t) = C \cdot \underline{x}(t) + D \cdot \underline{u}(t) \end{cases} \tag{1}$$

Where:

$$\begin{gathered} \underline{x} = \left| \dot{z}_C \quad \dot{\theta}_C \quad \dot{z}_{LB} \quad \dot{\theta}_{LB} \quad \dot{z}_{TB} \quad \dot{\theta}_{TB} \quad z_C \quad \theta_C \quad z_{LB} \quad \theta_{LB} \quad z_{TB} \quad \theta_{TB} \right|^T \\ \underline{u} = \left| \dot{z}_1 \quad \dot{z}_2 \quad \dot{z}_3 \quad \dot{z}_4 \quad z_1 \quad z_2 \quad z_3 \quad z_4 \right|^T \\ \underline{y} = \left| \ddot{z}_{C,front} \quad \ddot{z}_{C,rear} \quad \ddot{z}_{LB,front} \quad \ddot{z}_{LB,rear} \right|^T \end{gathered} \tag{2}$$

The described model allows the description of vertical dynamic behavior of the whole system. Under assumed hypotheses it is possible to obtain the imposed movement, unknown at the beginning, through the double integration of the vertical measured accelerations on one axle. In this paper, the fourth axle is considered. Before proceeding with the mathematics integration, it is indispensable to remove both the high frequency content of the axle box acceleration signal, to avoid aliasing problem and to consider the rigid three bodies, and the low frequency content to avoid an offset component in the result of integration. So, a band-pass filter and integration have been developed in the frequency domain. In this way filtered signals of position and speed have been obtained. In order to obtain all input signals, in terms of speed and position for each axle, it is necessary to shift forward the signal related to the fourth axle by a time amount that depends on geometry and speed of train (track irregularity estimation). For more details, see [1].

3. ANALYSIS OF THE SYSTEM OBSERVABILITY

To investigate the feasibility of using Kalman filter in this study, an investigation of the observability of the system was performed. Unfortunately, the complexity of the system does not allow to compute accurately the rank of observability matrix M_O, which will be numerically singular as reported in [5]. Exploiting the knowledge of linear algebra and Singular Value Decomposition (SVD), it is possible to deal with this problem.

Specifically, developing the SVD of M_O according to the theory it is possible to obtain the following expression:

$$M_O = U\Sigma V^T \tag{3}$$

In figure 2 [6], are specified the size of matrixes and is given a graphics intuition on how to exploit the SVD for the desired purpose.

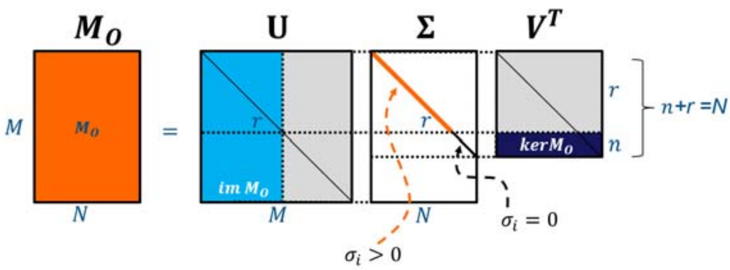

Fig. 2 Singular Value Decomposition for a generic matrix

In fact, the numbers of singular values different from zero provides a useful information about the observability property of the system. The results obtained applying the SVD approach to the observability matrix of the system described in Section 2, are shown in figure 3b in which each blue dot represents an element different from zero. In this way it is easy to check that all the elements located on diagonal of the Σ matrix are strictly positive (cfr. figure 2b). In other words, it has been verified that the dimension of the vector $(\sigma_1, \ \sigma_2, \ \dots, \ \sigma_r)$ is equal to $p = \min\{M, N\}$ (cfr. Fig. 2a). That means the observability matrix has full rank and so the vehicle model in fig. 1 is completely observable.

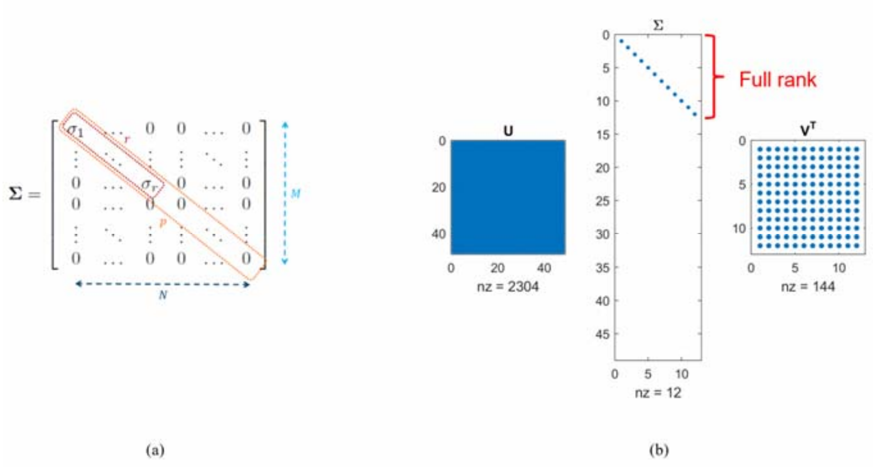

Fig. 3 Singular Value Decomposition applied to the observability matrix

Moreover, through the same analysis it is possible to obtain another important property of the system regarding the sensitivity to the input variation. In fact, the ratio between the maximum and the minimum singular value represents the condition number k_2. A large value of this parameter would mean the system is ill-conditioned and so a small variation on the inputs produces a large variation on the outputs. Unfortunately, the condition number of this system is $k_2 = 9.33 \cdot 10^{15}$ which is a large value and therefore shows that the identification problem might be ill-conditioned.

4. STATE ESTIMATE THROUGH KALMAN FILTER

Kalman filter [7] is a state observer with feature of optimality that is applied when systems are affected by stochastic disturbances. Exploiting the proof given in section 3 it is allowable to use the Algebraic Riccati Equation (ARE) instead of Differential Riccati Equation (DRE) with enormous benefits in term of computational load. As reported in [1], it is possible to obtain the final formulation of Kalman filter:

$$\dot{\hat{\underline{x}}}(t) = [A - \bar{L}C] \cdot \hat{\underline{x}}(t) + [B - \bar{L}D \quad \bar{L}] \cdot \begin{vmatrix} \underline{u}(t) \\ \underline{y}(t) \end{vmatrix} \tag{4}$$
$$\hat{\underline{y}}(t) = C_{new} \cdot \hat{\underline{x}}(t) + D_{new} \cdot \begin{vmatrix} \underline{u}(t) \\ \underline{y}(t) \end{vmatrix}$$

Where $\bar{L} = \bar{P}CR^{-1}$ is the Kalman filer matrix gain that minimizes the quadratic form of prediction error's covariance and $\bar{P}$ is the solution of ARE. For more details regarding the setting of the covariance matrices on the state Q and on the measurements R, refer to [1]. The new formulation of Kalman filter allows the choice of new matrices in the second Eq. (4) in order to obtain the same output signals of the model.

5. NUMERICAL EXPERIMENTS

Numerical experiments shown in figure 4 have been performed in order to validate the treatment of datasets, the proposed model and developed Kalman filters. A multibody (MB) simulator called *ADTreS* [8], developed at the Department of Mechanical Engineering of Politecnico di Milano, has been used for this purpose.

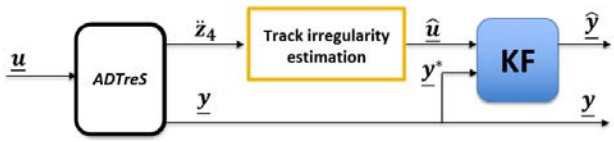

Fig. 4 Numerical experiment implemented

With the aim of finding a trade-off between the number of saved sensors and a good performance level of diagnostic system, several Kalman filters have been developed, that differ in the number of measures they need to receive as input. The $\underline{y}^*$ represents a partitioning of the whole output vector $\underline{y}$. It would be ideal to save as many sensors as possible without decreasing significantly the performance. Every designed observer has been tested using numerical experiments. In order to allow an easy comparison between different solutions, a figure of merit in the frequency domain has been introduced that is able to summarize the performance level in each Kalman filter applied.

$$J_{tot} = \sum_{n=1}^{4} J_n, \qquad J_n = \sqrt{\frac{\sum_i \frac{\left[A_z(i) - A_{z,ref}(i)\right]^2}{2}}{\sum_i \frac{\left[A_{z,ref}(i)\right]^2}{2}}} \cdot 100, \qquad n = 1,2,3,4 \qquad i = i-th\ frequency \tag{5}$$

Where *n* means the measuring point (Cf. Figure 1). The figure of merit in Eq. (5) considers differences between each reference variable and its estimation. The reference variables considered are "virtual measurements" obtained as the output of a numerical simulation performed with *ADTreS*. For more detail about the validation of the treatment of datasets and the model refers to [1]. Only results of numerical experiment when estimators have been applied on the *ADTreS* data are reported in Table 1 for purpose of clarity. In the table the contribution of every variable estimated is recognisable. The table shows a desirable trend of level performance according to the number of measures used. Each of these tests represents the best case in comparison with other characterised by the same number of used measures but with different sensor locations. Specifically, the best cases for increasing number of sensors have been obtained respectively using $\ddot{z}_{C,front}$ (case with 1 measure), $\ddot{z}_{C,front}$ and $\ddot{z}_{C,rear}$ (case with two measures), $\ddot{z}_{C,front}$, $\ddot{z}_{C,rear}$ and $\ddot{z}_{LB,rear}$ (case with three measures). The worst performance is obtained obviously in the case when the measures are obtained by inputting in the identification model the axle-box acceleration without leaving any feedback correction based on Kalman filter estimator.

Number of measures	J_1	J_2	J_3	J_4	J_{TOT}
0	9,73	13,82	6,02	5,48	35,04
1	0,05	11,50	6,53	6,09	24,17
2	0,05	0,04	6,37	5,88	12,34
3	0,06	0,04	5,16	0,01	5,26
4	0,06	0,04	0,68	0,01	0,79

Table 1 - Kalman filters validation applied on ADTreS data

On the contrary, using all four measures the best performance has been achieved. Based on the results in Table 1 solutions characterized by two and three measures seem feasible. The performance level obtained with four measures proves that Kalman filter works very well. In view of the final aim of this work, it is important to reduce the number of sensors necessary to obtain a satisfactory value as figure of merit. So the solution with three measures seems to be the best solution reaching a good trade-off between performance level and saved sensors

6. APPLICATION TO LINE MEASUREMENTS

In this section, the method is applied on experimental data collected during measurements campaign on the Italian railway network. The experiment set-up used here is the same with the difference that now all the variables are not produced numerically but they are experimental data previously acquired on the Italian railway network.

6.1 The Measuring set-up

Two different trains, belonging to the family of ETR500, are used to carry diagnostic activities out on the high speed railway network: ETR-Y1 and ETR-Y2. In the following only the ETR-Y1 (figure 5, [9]) will be presented in detail because the data have been collected by this vehicle.

Fig. 5 ETR500-Y1

The ETR500-Y1 has been equipped by MEMS accelerometers, due to the fact the frequency range is approximately 0-150 Hz, their properties of robustness and cheapness. Furthermore, they allow measuring the static component of acceleration.
More in detail, the transducer set-up installed on the ETR-Y1 train consist of (cfr Fig. 6):

- Four tri-axial accelerometers, measuring the vertical, lateral and longitudinal axle-boxes in one bogie (dark green square);
- Four mono-axial accelerometers measuring lateral accelerations of the bogie frame above the leading and trailing wheel-sets on both bogies (light green square with prefix *y"*+ in the labels);
- Three mono-axial accelerometers measuring the vertical accelerations of three vertexes of the frame in one bogie (light green square with prefix *z"*+ in the labels). Transducers are placed above the two axle-boxes of the external axle and over one axle-box of the internal axle (see figure 7);
- Four accelerometers, measuring the vertical and lateral accelerations of head and tail of the car-body.

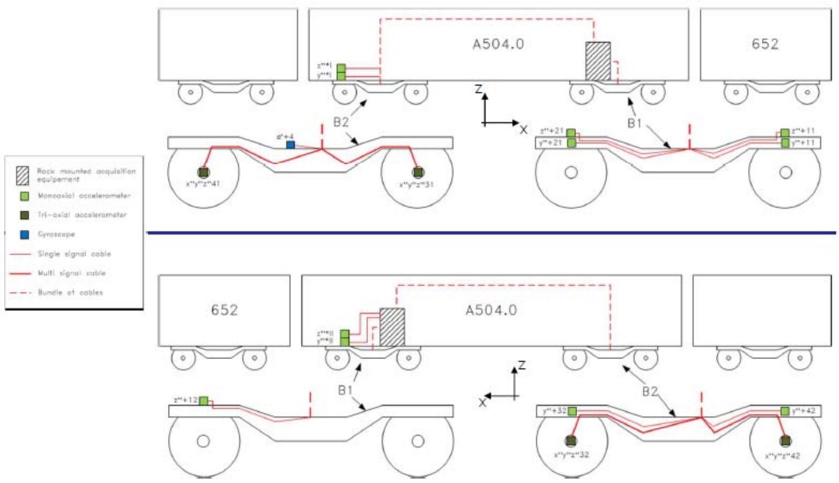

Figure 6: Measuring set-up

With the purpose of completeness in figure 7 has been shown the actual position of the tri-axial accelerometer located on the axle-box and the lateral accelerometer on situated on bogie.

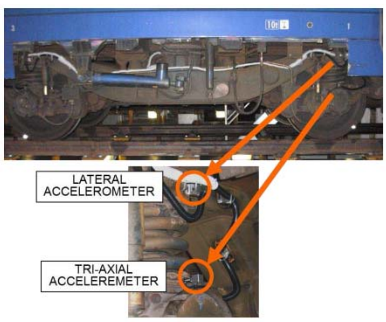

Figure 7: Axle-box and bogie accelerometers

Naturally, during this work the measurements obtained by actual 3D layout sensors have been managed in order to get the equivalent information into the vertical plane only.

6.2 Results

More in detail these data regard the route from Naples to Bologna. During the travel history five records from the data acquired characterized by constant speed have been recognized and extracted. Then, the proposed methodology has been applied to each record independently. In figure 8 are reported the performances of different Kalman filters applied to five time history selected.

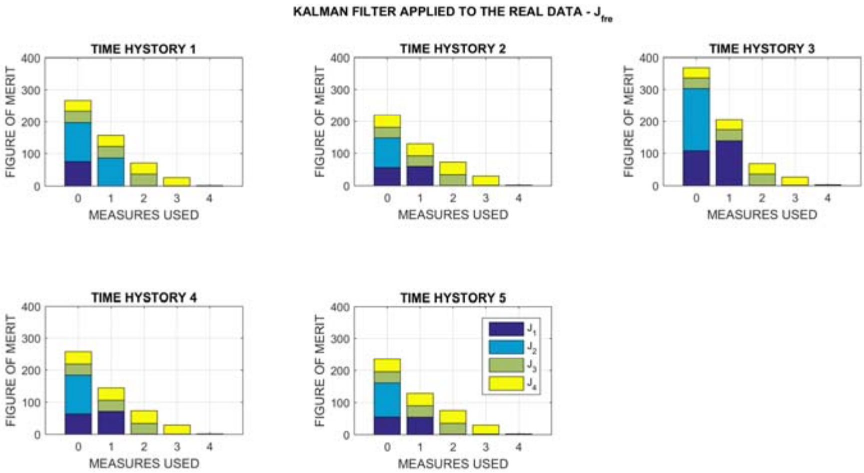

Fig. 8 Performance of Kaman filters applied on real data

Fig. 8 shows that the five plots have the same desired trend. For sure, it would have been desirable to obtain a lower index performance value. In fact, using 3 measures it is reachable an index value belongs to the range 23%-29%. In order to show the effectiveness of the Kalman filters applied to the real data a deeper investigation is reported in the following regarding only one of the five segments with the purpose of clarity and conciseness.

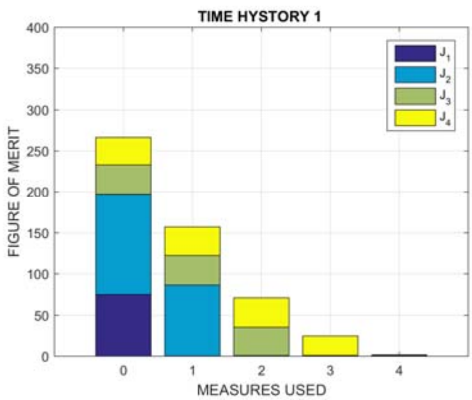

	J_1	J_2	J_3	J_4
0	74,5	122,7	35,9	37,7
1	0,35	85,8	36,0	34,6
2	0,49	0,33	34,6	35,4
3	0,51	0,33	0,17	23,7
4	0,65	0,44	0,17	0,35

Fig. 9 Result of Kalman filters applied to the first segment, graphically in the bar plot (left) and numerically into the table (right)

Just for example, the first time history has been considered. Starting from the worst case characterized by only the model knowledge and increasing gradually the number of measures used it is possible to see that the effectiveness of Kalman filters improves not only in terms of the performance value strictly related to the same channel, but also in terms of performance connected to a different channel.In fact, adding the measured output 1 ($\ddot{z}_{C,front}$) obviously the performance level related J_1improves (it means the figure of merit decrease). But also, the performance related to the J_2 improves. In the same way, moving from 1 to 2 measures used, adding the measured output 2 ($\ddot{z}_{C,rear}$), the performance indexes J_2 and J_3 improve. Only in this case the improvement on the performance unrelated with information just given is slightly. Then, moving from 2 to 3 measure adding the measured output 3 ($\ddot{z}_{LB,front}$), both the performance J_3 and J_4 improve.

7. CONCLUSIONS

This paper discusses the application to a real data of a method presented in [1], which is based on a treatment of measurements composed by filtering and integration carried out in frequency domain combined with the Kalman filter estimation. The effectiveness of the condition monitoring system has been tested both numerically and experimentally: in the first case the method shows good results whereas when the same is applied to experimental data lower performances are obtained.
The difference in the performance of the method when applied to numerical or real data can be attributed at the following reasons:

- Experimental data are inevitably corrupted by measurement noise;
- The problem is strongly ill-conditioned.

So starting from these considerations, the future further improvement could be:

- Investigate on the setting the covariance matrixes on the state Q and on the measurements R;
- Investigate on the possible layout sensors such that the conditioning number decreases.

8. REFERENCES

[1] **Leonardi, F. – Alfi, S. – Bruni, S.**: Treatment of driving dynamic datasets of a railway vehicle aimed at condition monitoring of the track. Proceeding of the Mini Conference on Vehicle System Dynamics, Identification and Anomalies (VSDIA 2014) (Ed. by Prof. I. Zobory), BME EJJT Vehicle Technologies Knowledge Center, Budapest, 2015, p. 219-225.

[2] **Ward, C. et al.**: Condition monitoring opportunities using vehicle-based sensors. Proc. of IMechE Part F. Journal of Rail and Rapid Transit 2011; 225:F2, p.202-218.

[3] **Tsunashima, H. – Naganuma, Y. – Kobayashi, T.:** Track geometry estimation from car-body vibration, Vehicle System Dynamics 52 suppl., 2014; p.207-219.

[4] **Alfi, S. - Bruni, S.:** Estimation of long wavelength track irregularities from on board measurements. 4th IET International Conference on Railway Condition Monitoring (RCM 2008). Derby, UK, 18-20 June, 2008

[5] **Paige, Chris C.:** Properties of Numerical Algorithms Related to Computing Controllability, IEEE Transaction on automatic control, vol. AC-26, n.° 1, 1981

[6] **Ghezzi, L.**: Inverse problem and data assimilation for process diagnosis, Lecture Notes of PhD course 2015/2016

[7] **Simon, D.**: Optimal State Estimation: Kalman, H infinity and nonlinear approaches. Wiley, 2006

[8] **Alfi, S. - Bruni, S.:** Mathematical modelling of train turn-out interaction, Vehicle System Dynamics, 47 (5) 2009, p.551-574.

[9] Gasparetto, L.: Fault Diagnosis of the running gear in high speed railway vehicle, PhD Thesis, 2014.

DYNAMICS OF THE TRAIN/TRACK SYSTEM IN THE PRESENCE OF CONTINUOUSLY VARYING, FOURIER TRANSFORMABLE VISCOELASTIC PARAMETERS OF THE SUBGRADE

Vilmos ZOLLER

S. Rejtő Faculty
Óbuda University
Mailing address: Doberdó út 6, H-1034 Budapest, Hungary
E-mail: `zoller.vilmos@rkk.uni-obuda.hu`

Faculty of Transportation Engineering and Vehicle Engineering
Group of Railway Vehicles and Vehicle System Analysis
Budapest University of Technology and Economics
Mailing address: H-1521 Budapest, Hungary
E-mail: `railveh@rave.vjt.bme.hu`

Received: *November 7, 2016*

ABSTRACT

In the paper we investigate the dynamics of the train/track system in case of an inhomogeneous longitudinal subgrade stiffness/damping distribution varying in a discrete, compactly supported way or in a Fourier transformable fashion along the track. In our study the track is modelled by a Bernoulli–Euler beam laying on a Winkler foundation of continuous stiffness/damping parameters varying either discretely or continuously. The damped oscillatory load is moving along the track at a constant velocity. In order to have a closed-form solution to the boundary problem associated to the system above, we build up first a discretization method for approximating the solution with the help of the closed-form answer given to the case, where elastic parameters of the subgrade are varying by step functions. In the second step we obtain an integral formula for the solution in the case, when the viscoelastic parameters of the subgrade vary continuously. At the end we obtain a fastly computable solution with the help of Fourier tranforms.

Keywords: Train/track system, dynamics, Fourier-transform, viscoelasticity, inhomogeneous subgrade

1. INTRODUCTION

A rapidly developing direction in the investigation of beam problems on viscoelastic supports systems under the action of moving loads is the inclusion of support systems having inhomogeneous viscoelastic coefficients, cf. [3],[7] in the periodically varying case.

In this paper we investigate the moving, damped oscillatory load problem of the form

$$EI\ \partial_x^4 u + \rho A\ \partial_t^2 u + (k_0 + k(x))\ \partial_t u + (s_0 + s(x))\ u = F_0 \exp(wt)\delta(x - vt), \quad w \in \mathbf{C},$$

$$\lim_{x \to \pm\infty} u(t,x) = 0, \quad t \in \mathbf{R}$$

on an infinite Bernoulli-Euler beam laying on a Winkler foundation of varying damping and stiffness parameters in cases, where the viscoelastic parameter functions

$$k, s : \mathbf{R} \to \mathbf{R}$$

of the subgrade vary pointwise along the track.

The varying parameter functions in this paper can be either

(1) discretely varying step functions of compact supports (i.e. they are piecewisely constant, and vanishing outside a given finite interval),

or

(2) continuously varying, Fourier transformable functions.

Let us introduce auxiliary functions

$$e_k(x) := \frac{1}{4EI\lambda_k^3}(\sigma_k \exp(\sigma_k \lambda_k x) + \sigma_{k+1}\mathrm{i}\,\exp(\sigma_{k+1}\mathrm{i}\lambda_k x)),$$

$$f_k(x) := s(x) + (w - \lambda_k v)k(x),$$

$$g_k(t,x) := \frac{F_0 \sigma_k}{\partial_\lambda P_w(\lambda)} \exp(\lambda_k x)\mathrm{H}(\sigma_k(x - vt))$$

for $k = 1,\ldots,4$, symbolizing the motion forms generated by the excitation coming from the moving load

$$F_0 \exp(wt)\delta(x - vt),$$

where characteristic roots λ_k, $k = 1,\ldots,4$ stand for the roots of the characteristic polynomial

$$P_w(\lambda) = EI\lambda^4 + \rho A v^2 \lambda^2 - v(k + 2\rho A w)\lambda + (s + kw + \rho A w^2)$$

of the system, cf. [1], [5], and $P_w(\lambda)$ stands for its derivative with respect to variable λ.

The characteristic roots are positioned in the complex plane as it is shown in Fig. 1 with additional correspondence $\lambda_5 := \lambda_1$. This way the first characteristic root has a negative real part and a positive imaginary part, while the other roots follow by rectangular rotations in the positive direction. Such a positioning is possible if conditions in [1],[4],[5] are met.

$$\begin{array}{c|c} \lambda_1 & \lambda_4 \\ \hline \lambda_2 & \lambda_3 \end{array}$$

Fig. 1 The positioning of the characteristic roots in **C**

Signs σ_k are defined by correspondences $\sigma_k = -\operatorname{sgn} \operatorname{Re} \lambda_k$, for $k = 1,..,4$, i.e. σ_k is positive, if characteristic root λ_k lies in the left halfplane, while it is negative in the opposite case.

1. THE DISCRETELY VARYING PROBLEM

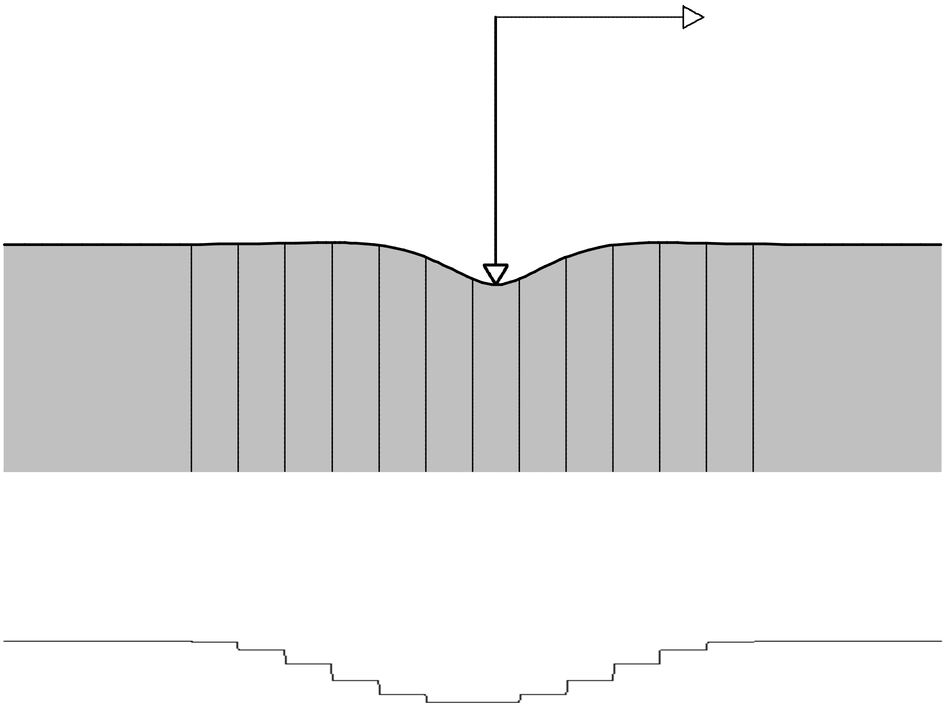

2. Fig. 2 The discrete model of the track

In the case of discretely varying viscoeslastic parameters of the subgrade our problem can be transformed into the form

$$EI\,\partial_x^4 u + \rho A\,\partial_t^2 u + k_0\,\partial_t u + s_0\,u =$$

$$F_0 e^{wt}\delta(x - vt) - \sum_{j=0}^{2n} h\,(k(x_j)\partial_t u(t, x_j) + s(x_j)u(t, x_j))\,\delta(x - x_j),$$

$$\lim_{x\to\pm\infty} u(t, x) = 0,\ t \in \mathbf{R},\ x_j = -L + jh,\ h = L/(n+1),\ j = 1,2,\dots,2n+1,$$

where

$$s(x) = s_j,\ k(x) = k_j$$

is satisfied in intervals $[x_{j-1}, x_j),\ j = 1,2,\ldots,2n+1$, while

$$s(x) = 0,\ k(x) = 0$$

hold outside the interval $[-L, L)$, i.e. we have discrete, viscoelastic supports of discrete valued stiffness and damping parameters varying at the points $x_1, x_2, \ldots, x_{2n+1}$.

The effect of the vibration of the supports is switched back by the last sum on the right-hand side of the boundary value problem representing the continuosly varying case.

It is acting on the fixed elements of the discrete support system, and generates solution functions of the form

$$\exp((w - \lambda_k v)t + \varepsilon_j \lambda_k x),\ \varepsilon_j = \mathrm{i}^{j-1},\ j = 1,\ldots,4,$$

as given in [6].

The components $u_k(x)$ of the solution function

$$u(t,x) = \sum_{k=1}^{4} \mathrm{e}^{(w-\lambda_k v)t} u_k(x)$$

can be computed by solving the system of linear equations

$$\sum_{j=1}^{2n+1} (\mathbf{I} + \mathbf{A}_k)_{ij} u_k(x_j) = g_k(t, x_i),\ i = 1,2,\ldots,2n+1$$

with matrix $\mathbf{A}_k$ composed of elements

$$a_{k,ij} = e(\mathrm{sgn}(x_i - x_j)x_i) f(x_j) h,\ i,j = 1,2,\ldots,2n+1$$

for $k = 1,\ldots,4$.

Altough matrix $\mathbf{A}_k$ itself is not a dyadic matrix, one can easily prove, that its square

$$(\mathbf{A}_k^2)_{ij} = (c_{k1} e_k(x_i) + c_{k2} e(-x_i)) f_k(x_j) h$$

is, and it has the property

$$\mathbf{A}_k^3 = c_k \mathbf{A}_k^2,$$

where

$$c_{k1} = \sum_{j=1}^{n} e(x_j) f_k(x_j) h, \; c_{k2} = \sum_{j=n+2}^{2n+1} e(-x_j) f_k(x_j) h$$

and

$$c_k = c_{k1} + c_{k2}$$

hold.

We are able to invert matrix $\mathbf{I} + \mathbf{A}_k$ in case $|c_k| < 1$ in the way

$$(\mathbf{I} + \mathbf{A}_k)^{-1} = \mathbf{I} - \mathbf{A}_k + \frac{1}{1+c_k} \mathbf{A}_k^2$$

for any $k = 1, \ldots, 4$, and the solution to our problem in the discretely varying case takes the form

$$u(t,x) = \sum_{k=1}^{4} \mathrm{e}^{(w-\lambda_k v)t} \Big(g_k(t,x) -$$

$$\sum_{j=0}^{2n} \Big(e_k(\mathrm{sgn}(x-x_j)x) - (1+c_k)^{-1} \big(c_{k1} e_k(x) + c_{k2} e_k(-x) \big) \Big) f_k(x_j) g_k(t,x_j) h \Big).$$

3. THE CONTINUOUSLY VARYING PROBLEM

Our problem in this case has the form

$$EI\, \partial_x^4 u + \rho A\, \partial_t^2 u + (k_0 + k(x))\, \partial_t u + (s_0 + s(x))\, u = F_0 \mathrm{e}^{wt} \delta(x - vt),$$

$$k, s : \mathbf{R} \to \mathbf{R} \text{ Fourier transformable, } \lim_{x \to \pm\infty} u(t,x) = 0, \; t \in \mathbf{R}.$$

First we approximate this, continuously supported case by discretely supported cases occuring in the previous section.

Then, in order to build up an integral formula for the continuously supported case, we calculate the limit

$$\lim_{h \to 0} u(t,x)$$

of the discrete solution function $u(t,x)$ in the case, when step h tends to 0.

Finally, we apply limit transition $L \to +\infty$ for the length of the finite supports in order to get rid of the finite character of the system.

The calculation of the limits of constants c_{k1}, c_{k2} and c_k of the previous section can be carried out as

$$c_{k1} = \sum_{m \le n} e_k(-x_m) f(x_m) h \to I_{k1} = \int_{-\infty}^{0} e_k(-y) f_k(y)\,\mathrm{d}y\,,$$

$$c_{k2} = \sum_{m > n} e_k(x_m) f(x_m) h \to I_{k2} = \int_{0}^{+\infty} e_k(y) f_k(y)\,\mathrm{d}y = \int_{-\infty}^{0} e_k(-y) f_k(-y)\,\mathrm{d}y$$

and

$$c_k = \sum_{m=1}^{2n+1} e_k(|\,x_m\,|) f(x_m) h \to I_{k0} = \int_{-\infty}^{+\infty} e_k(|\,y\,|) f_k(y)\,\mathrm{d}y = \int_{-\infty}^{0} e_k(-y)(f_k(y) + f_k(-y))\,\mathrm{d}y$$

where $h \to 0$ and $L \to +\infty$ hold.

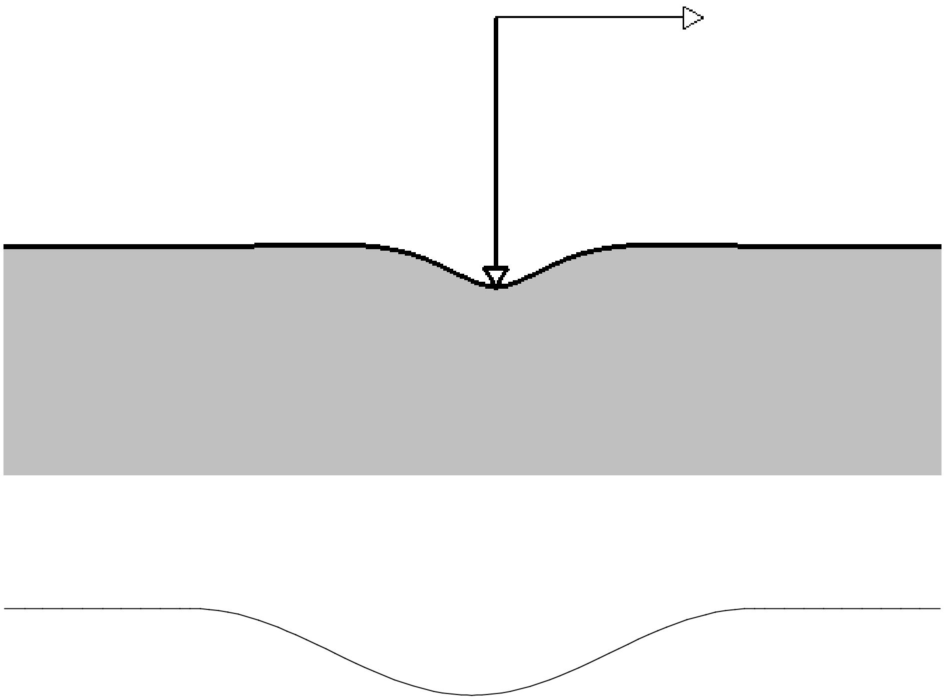

Fig. 3 The continuous model of the track

For the computation of the solution function we need the limits of the components

$$\sum_{j=1}^{2n+1} A_{k,ij}\, g_k(t, x_j) \quad \text{and} \quad \sum_{j=1}^{2n+1} A_{k,ij}^2\, g_k(t, x_j)$$

of the solution to the above system of linear equations.

These limits can be calculated by formulae

$$\sum_{j=1}^{2n+1} a_{k,ij} g_k(x_j) = \frac{F_0\sigma_k}{\partial_\lambda P_w(\lambda_k)}\Big(\sum_{j\le n} e_k(-x_i) f(x_j)\exp(\lambda_k x_j)\mathrm{H}(\sigma_k(x_j - vt)) +$$

$$\sum_{j>n} e_k(x_i) f(x_j)\exp(\lambda_k x_j)\mathrm{H}(\sigma_k(x_j - vt))\Big)h \to$$

$$\frac{F_0\sigma_k h}{\partial_\lambda P_w(\lambda_k)}\left(e_k(\sigma_k x)H(\sigma_k vt)\int_{vt}^{\sigma_k\cdot\infty} \exp(\lambda_k y) f_k(y)\,\mathrm{d}y - e_k(-\sigma_k x)H(\sigma_k vt)\int_0^{vt}\exp(\lambda_k y) f_k(y)\,\mathrm{d}y \right)$$

and

$$\sum_{j=1}^{2n+1} (\mathbf{A}_k^2)_{ij}\, g_k(x_j) = (c_{k1}e(x_i) + c_{k2}e(-x_i))\sum_{j=1}^{2n+1} f_k(x_j) g_k(x_j)h,$$

where

$$\sum_{j=1}^{2n+1} f_k(x_j) g_k(x_j)h \to \frac{F_0\sigma_k}{\partial_\lambda P_w(\lambda_k)}\int_{-\infty}^{+\infty} f_k(y)\exp(\lambda_k y)\mathrm{H}(\sigma_k(y - vt))\,\mathrm{d}y =$$

$$\frac{F_0\sigma_k}{\partial_\lambda P_w(\lambda_k)}\int_{vt}^{\sigma_k\cdot\infty}\exp(\lambda_k y) f_k(y)\,\mathrm{d}y,\ k = 1,\ldots,4$$

holds in the case $h \to 0,\ L \to +\infty$.

Substituting the results of the calculations above into the solution formula for the discretely supported case, the limits provide the following integral formula for the final solution in the continuously supported case.

$$u(t,x) = F_0\sum_{k=1}^{4}\frac{\sigma_k}{\partial_\lambda P_w(\lambda_k)}\Big(\exp(\lambda_k x)\mathrm{H}(x - vt) -$$

$$e_k(\sigma_k x)H(\sigma_k vt)\int_{vt}^{\sigma_k\cdot\infty} \exp(\lambda_k y) f_k(y)\,\mathrm{d}y + e_k(-\sigma_k x)H(-\sigma_k vt)\int_0^{vt}\exp(\lambda_k y) f_k(y)\,\mathrm{d}y +$$

$$\left.\frac{(I_{k1}e(x) + I_{k2}e(-x))}{1 + I_{k0}}\int_{vt}^{\sigma_k\cdot\infty}\exp(\lambda_k y) f_k(y)\,\mathrm{d}y\right).$$

4. FAST COMPUTATION OF THE SOLUTION

In the consequence of the fulfilment of properties

$$\int_{vt}^{-\infty} \exp(\sigma_k \lambda_k \,|\, y \,|) f_k(y)\,\mathrm{d}y = -\int_{-\infty}^{vt} \exp(\sigma_k \lambda_k \,|\, y \,|) f_k(y)\,\mathrm{d}y =$$

$$\int_{vt}^{+\infty} \exp(\sigma_k \lambda_k \,|\, y \,|) f_k(y)\,\mathrm{d}y - S_{k1} - S_{k2},$$

and

$$\int_{0}^{+\infty} \exp(\sigma_k \lambda_k y) f_k(y)\,\mathrm{d}y = S_{k2},$$

where the auxiliary integrals S_{k1} and S_{k2} with $\mathrm{k} = 1,\ldots,4$ are defined by correspondences

$$S_{k1} = \int_{-\infty}^{0} \exp(\sigma_k \lambda_k \,|\, y \,|) f_k(y)\,\mathrm{d}y, \;\; S_{k2} = \int_{0}^{+\infty} \exp(\sigma_k \lambda_k \,|\, y \,|) f_k(y)\,\mathrm{d}y,$$

we have only the four integrals

$$\int_{vt}^{+\infty} \exp(\sigma_k \lambda_k y) f_k(y)\,\mathrm{d}y, \;\; k = 1,\ldots,4.$$

to be computed at each step.

Let

$$\hat{f}_k(p) =: \mathrm{F}(f_k)(p) := \int_{-\infty}^{+\infty} f_k(y) \exp(-\mathrm{i}py)\,\mathrm{d}y$$

denote the FOURIER transform of function

$$f_k(y) = s(y) + (w - \lambda_k v) k(y).$$

The integral in question may be written into the following form:

$$\int_{vt}^{+\infty} \exp(\sigma_k \lambda_k y) f_k(y)\,\mathrm{d}y = \int_{vt}^{+\infty} \exp(\sigma_k \lambda_k y) \cdot \frac{1}{2\pi} \int_{-\infty}^{+\infty} \hat{f}_k(p) \exp(\mathrm{i}py)\,\mathrm{d}p\,\mathrm{d}y =$$

$$\frac{1}{2\pi} \int_{-\infty}^{+\infty} \int_{vt}^{+\infty} \exp((\sigma_k \lambda_k + \mathrm{i}p) y)\,\mathrm{d}y\, \hat{f}(p)\,\mathrm{d}p = \frac{1}{2\pi} \int_{-\infty}^{+\infty} \frac{\exp((\sigma_k \lambda_k + \mathrm{i}p) vt)}{\sigma_k \lambda_k + \mathrm{i}p} \hat{f}(p)\,\mathrm{d}p =$$

$$\frac{1}{2\pi}\exp(\sigma_k\lambda_k vt)\int_{-\infty}^{+\infty}\frac{\hat{f}(p)}{\sigma_k\lambda_k+\mathrm{i}p}\exp(\mathrm{i}pvt)\,\mathrm{d}p=$$

$$\exp(\sigma_k\lambda_k vt)\,\mathrm{F}^{-1}\left(\frac{\hat{f}(p)}{\sigma_k\lambda_k+\mathrm{i}p}\right)(vt).$$

The computation of the solution to the continuously supported case can be deduced from the computation of the integrals above.

4. CONCLUSION

In case of the discretely and inhomogeneously supported beam problem subjected to moving, viscoelastic loads we obtained a closed-form solution with the help of using methods from (multi)linear algebra.

If the support has continuously varying viscoelastic parameters, then the integrals corresponding to the solutions can be approximated by sums of solutions to discretely varying sytems, and finally a closed-form integral formula can be found in order to describe the full motion of the continuously supported system.

If the parameter functions are Fourier-transformable, then the integrals in the above formula, and hence the solution itself are fast computable.

5. ACKNOWLEDGEMENT

The author thanks Professor István Zobory for introducing him into the subject and for stimulating discussions.

6. REFERENCES

1. **Belotserkovskiy, P.M.:** Periodic string response to an impact and a suddenly applied concentrated stationary force. *J. Sound Vib.* 228, No. 1, 51-68 (1999)
2. **De Pater, A.D.:** Inleidend onderzoek naar het dynamisch gedrag van spoor-staven, Thesis: Waltman, Delft, 1948.
3. **Verichev, S.N. - Metrikine, A.V.:** Instability of vibrations of a mass that moves uniformly along a beam on a periodically inhomogeneous foundation, *J. Sound Vib.* 260, No.1, 901-925 (2003)
4. **Zobory, I. - Zoller, V.:** Dynamic response of a railway track in case of a moving complex phasor excitation. In: M. Brøns, M.P. Bendsøe and M.P. Sørensen (Eds) Progress in Industrial Mathematics at ECMI 96, Teubner/Stuttgart, 85-92 (1997)
5. **Zobory, I. - Zoller, V. - Zibolen, E.:** Theoretical investigations into the dynamical properties of railway tracks using a continuous beam model on elastic foundation. *Periodica Polytechnica*, *Ser. Transp. Eng.* 22, No.1, 35-54 (1994)
6. **Zoller, V. – Zobory, I.**: Relations between the motion-responses caused by fixed and moving loads acting on discretely supported strings and beams. In: M. Anile, V.

Capasso and A. Greco (Eds) Progress in Industrial Mathematics at ECMI 2000, *Mathematics in Industry* **1**, Springer/Berlin, 657-661 (2002)

7. **Zoller, V. - Zobory, I.:** On the dynamics of the railway track/vehicle system in the presence of inhomogeneous rail supporting parameters. *Periodica Polytechnica*, *Ser. Transp. Eng*. 39 (2) 83-85 (2011)

IMPROVEMENTS OF THE ESTIMATION OF WHEEL-RAIL CONTACT FORCES USING INSTRUMENTED WHEEL-SETS

Stefano BIONDA, Francesco BRAGHIN, Gabriele CAZZULANI and Egidio DI GIALLEONARDO

Dipartimento di Meccanica
Politecnico di Milano
Via La Masa 1, I-20154, Milan, Italy

Received: November 9, 2016

ABSTRACT

In the present work, the accuracy of the measurement of wheel-rail contact forces through instrumented wheel-sets is analyzed. In previous works the minimal number of independent measurements needed for a consistent measurement was defined, highlighting the need of six independent measurement sections for estimating vertical and lateral forces. Anyway, cross-talk effects related to contact point position and longitudinal forces lead to a reduction in accuracy of the method, especially while negotiating narrow curves. By introducing an absolute angular reference system, it is possible to separate the different force components thus overcoming cross-talk effects. The effectiveness of the proposed method is tested both by means of quasi-static tests performed on a full-scale dedicated test-rig and by means of dynamic tests performed inline. Results obtained with an optimally and non-optimally instrumented wheel-set are presented and compared.

Keywords: instrumented wheelset, calibration.

1. INTRODUCTION

The understanding of the contact mechanics between wheels and rails is a relevant issue in rail-way engineering. Thus, the possibility of measuring contact forces exchanged at wheel-rail interface may have important implications in several railway engineering related fields such as ride comfort, fatigue and wear of the components, noise, etc. More important, it is of fundamental importance to investigate vehicle's safety against derailment and its performances in straight and curved track.

According to the European standard [1], the homologation of new vehicles must be performed measuring not only accelerations but also contact forces exchanged at wheel-rail interface. So far, several measurement systems have been developed in order to achieve this goal. The one that provides the best results in terms of accuracy is the instrumented wheel-set [2]. This method is based on the instrumentation of a wheel-set by means of strain gauges: from the deformation state of the wheel-set it is possible to infer the forces causing it, given a calibration matrix. In previous work [3], the minimal measurement set required for a consistent estimation of contact forces was defined, high-lighting the need of at least six independent measurement sections.

The main drawback of minimum measurement sets is that it is not easy to identify independent measurement sections (or they don't even exist) thus leading to sub-optimal installations and cross-talk effects that reduce measurement accuracy. Moreover, strain gauges may die due to harsh environment and, for high speed trains, due to impacts with flying ballast. Thus, redundant measurement sections should be considered. Unfortunately, this leads to a significant in-crease in setup time and costs.

Previous works from the authors [4,5] showed that, with the use of specific algorithms, it is possible to minimize the influence of cross-talk effects related to contact point position. However, the cross-talk of force components is still an issue. In the present work the cross-talk effects related with the interaction between contact forces will be analyzed and a method for their reduction will be proposed.

2. CROSS-TALK EFFECTS

The accuracy of the estimated contact force components is a function of the applied boundary conditions, i.e. the contact point position and the co-existence of different contact force components, especially during the negotiation of small radius curves or turnouts.

In fact, contact point variation generates a bending moment similar to the one caused by vertical and lateral contact forces. To discriminate between contact point variation and vertical/lateral force components, one should increase the number of independent measurement sections (e.g. adding wheel-web deformation signals). Other strategies have been analyzed in previous work [4,5].

Of course, the wheel-set is rotating. Thus, to obtain a signal independent of the absolute angular position of the wheel-set two strain bridges are placed 90° apart on each axle section. The two signals are squared and summed in order to obtain the deformation magnitude. This operation provides a more robust signal with respect of the single bridge signal since it is independent of the absolute angular position of the wheel-set. However, it can be easily verified that the resulting signal is proportional to the total bending moment generated by both the vertical/lateral contact force components and the longitudinal contact force components as shown in Figure 1.

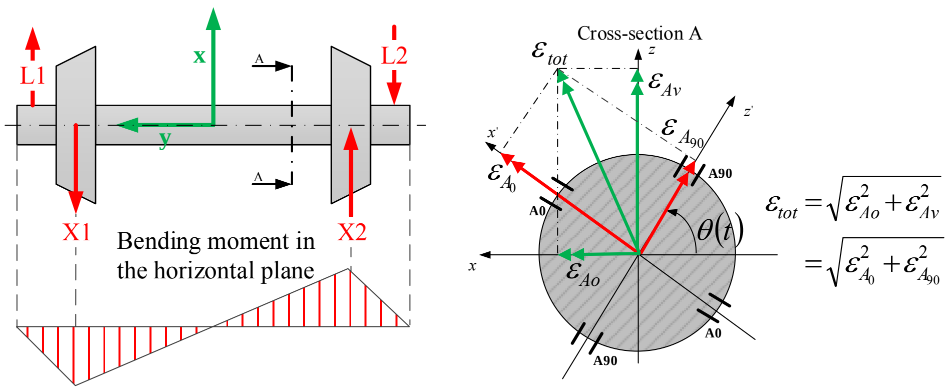

Fig. 1 Measurement of the deformation in the vertical plane.

To separate the vertical/lateral force contribution from the longitudinal one it is useless to in-crease the number of measurement sections. The solution proposed in this paper relies on the projection of the resultant bending moment on the absolute reference system of the axle, thus allowing to decouple the bending moments in the absolute vertical and horizontal planes.

2.1 Correction of the angular misalignment of a single section

Each measurement section along the axle is instrumented with two flexional full bridge placed 90° apart. The installation process may lead to two errors: one associated to electrical offsets between the bridges and the other associated to an angular misalignment between the bridges. It is easy to show that the introduction of electrical offsets in the bridge signals causes a ripple that is isofrequent with the angular speed of the wheel-set whilst the angular misalignment produces a ripple that has a frequency twice the one of the wheel-set's angular speed. Electrical offsets can be adjusted by differently gaining the bridges (offsets c_0, c_{90}) and the angular misalignment can be recovered by identifying the relative phase angel angle φ:

$$\begin{Bmatrix} \tilde{\varepsilon}_{A_0} \\ \tilde{\varepsilon}_{A_{90}} \end{Bmatrix} = \begin{bmatrix} 1 & -\cos\varphi \\ 0 & \sin\varphi \end{bmatrix} \cdot \left(\begin{Bmatrix} \varepsilon_{A_0} \\ \varepsilon_{A_{90}} \end{Bmatrix} - \begin{Bmatrix} c_0 \\ c_{90} \end{Bmatrix} \right) \tag{1}$$

In order to identify these correction coefficients it is necessary to measure the signals during the wheel-set's rotation under constant applied loads. The simplest way is to perform rotation tests with the wheel-set lifted from the ground. Thus, the strain gauge bridges measure the bending deformation due to the wheel-set's weight. Through Carnot's formula the angle φ and the (offsets c_0, c_{90}) can easily be determined. The formulae is reported in (2), whilst in Figure 2 the effects of the angular correction are shown.

$$\begin{aligned} &(\varphi, c_0, c_{90}) = \min_{\varphi, c_0, c_{90} \in \mathbb{R}} J \\ &J(\varphi, c_0, c_{90}) = \mathrm{std}(f(\varphi, c_0, c_{90})) \\ &f(\varphi, c_0, c_{90}) = \sqrt{(\varepsilon_{A_0} + c_0)^2 + (\varepsilon_{A_{90}} + c_{90})^2 - 2(\varepsilon_{A_0} + c_0)(\varepsilon_{A_{90}} + c_{90})\cos\varphi} \end{aligned} \tag{2}$$

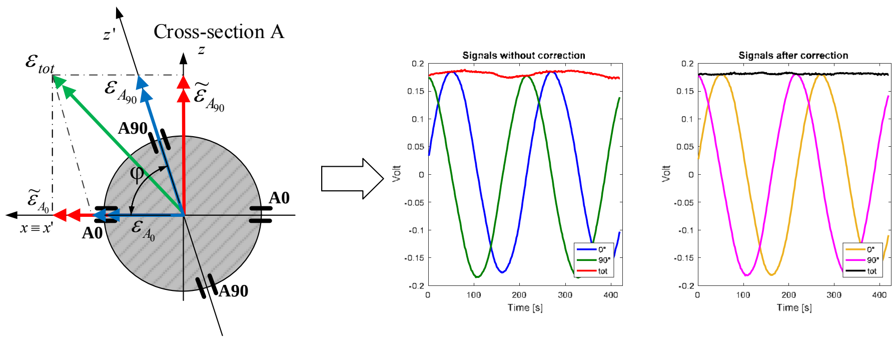

Fig. 2 Effects of the angular misalignments.

2.2 Correction of the angular misalignment between different sections

The absolute angular orientation of different sections may be different due to installation errors as shown in Figure 3. The misalignment between sections results in the impossibility to correctly reconstruct the bending moment. By means of a rotation test with the wheel-set lifted from the ground it is possible to derive the angular displacement between the sections with respect a reference one. For instance, as shown in Figure 3, choosing section A as the reference section, it is possible to derive α and β_i (one for each measurement section) by means of this rotation test and thus calculate the angular displacement as defined in Equation (3).

$$\alpha = \mathrm{atan}\left(\frac{\tilde{\varepsilon}_{A90}}{\tilde{\varepsilon}_{A0}}\right); \beta_i = \mathrm{atan}\left(\frac{\tilde{\varepsilon}_{i90}}{\tilde{\varepsilon}_{i0}}\right) \Rightarrow \Delta\theta_i = \beta_i - \alpha \tag{3}$$

Once the $\Delta\theta_i$ values are calculated for each section it is possible to numerically re-align all the sections by means of a rotation matrix as depicted in (4).

$$\begin{Bmatrix} \hat{\varepsilon}_{io} \\ \hat{\varepsilon}_{iv} \end{Bmatrix} = \begin{bmatrix} \cos\Delta\theta_i & -\sin\Delta\theta_i \\ \sin\Delta\theta_i & \cos\Delta\theta_i \end{bmatrix} \cdot \begin{Bmatrix} \tilde{\varepsilon}_{i_0} \\ \tilde{\varepsilon}_{i_{90}} \end{Bmatrix} \tag{4}$$

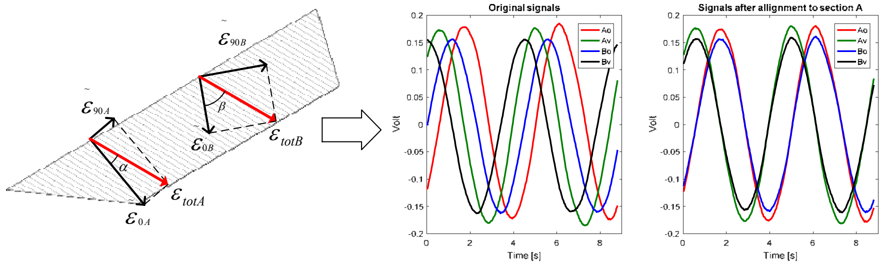

Fig. 3 Misalignment between two flexional bridges and correction.

2.3 Projection of the deformation amplitude on the absolute reference system

To project the original signals on the absolute non-rotating reference system retrieving, for each section, the deformation acting both in the absolute vertical and horizontal planes. This goal is achieved by introducing an angular sensor. The simplest possibility is to use an eddy current sensor that measures the passage of a marker fixed on the wheel-set (Fig. 4). If more than 1x wheel turn positions are required (e.g. for achieving higher angular accuracy) the encoder mounted in the axle-box can be used. In the tests carried out a 95 teeth/turns encoder was used.

Fig. 4 Eddy current sensor for absolute angular positioning.

Thus, given the rotation matrix derived in the previous paragraph and knowing the absolute angular position of the wheel-set it is possible to derive the two deformation components acting on the absolute vertical and horizontal planes as in (5).

$$\begin{Bmatrix} \varepsilon_{i_O} \\ \varepsilon_{i_V} \end{Bmatrix} = \begin{bmatrix} \cos\theta(t) & -\sin\theta(t) \\ \sin\theta(t) & \cos\theta(t) \end{bmatrix} \cdot [R(\Delta\theta_i)] \cdot [R(\varphi_i)] \cdot \left(\begin{Bmatrix} \varepsilon_{i_0} \\ \varepsilon_{i_{90}} \end{Bmatrix} - \begin{Bmatrix} c_{i_0} \\ c_{i_{90}} \end{Bmatrix} \right) \tag{5}$$

3. CALIBRATION AND RESULTS

The method presented in paragraph 2 was applied on an instrumented wheelset equipped with an optimal measurement set (four measurement sections on the axle, two measurement sections on the wheel-web) as well as a redundant (non-optimal) measurement set. Table 1 shows the measurement accuracy (equal to the standard deviation of the estimation error $\sigma_F = std(F - [k]\underline{\varepsilon})$) for both optimal and non-optimal measurement sets using the squared sum method and the projection method. The calibration was performed via least square minimisation applying known loads through a dedicated test-rig [6].

Table 1. Comparison between various calibration methods.

Contact Force	*Non-optimal set Squared sum*	*Non-optimal set Projection*	*Optimal set Squared sum*	*Optimal set Projection*
	σ_F [kN]	σ_F [kN]	σ_F [kN]	σ_F [kN]
Q_A	1.60	0.59	0.59	0.33
Q_B	1.30	0.78	0.79	0.54
Y_A	0.67	0.68	0.65	0.62
Y_A	0.78	0.77	0.72	0.73

It can be seen that the projection method generally achieves a more accurate estimation of the forces. Moreover, the estimation accuracy considering a reduced measurement set (only four sections on the axle) is comparable with that of the optimal measurement set especially for what concern the vertical forces (see central columns in Table 1). The effectiveness of the method has been assessed by means of quasi-static tests performed on the test-rig [7] (see Fig. 5).

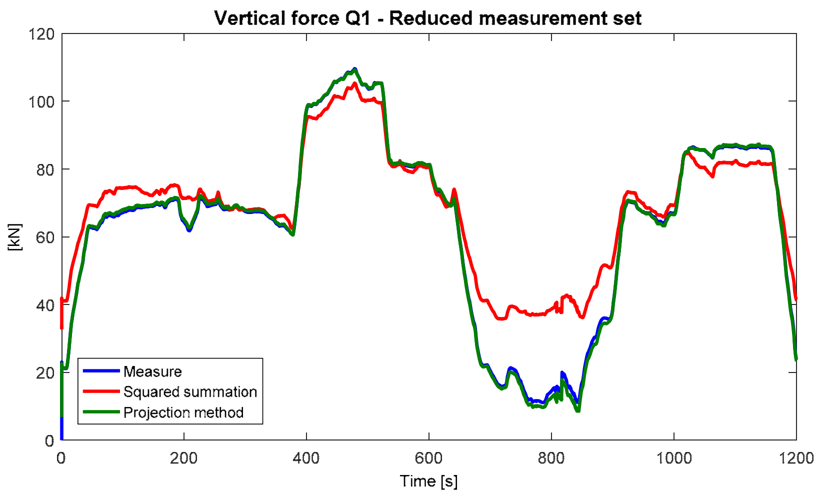

Fig. 5 Results of a quasi-static test with a reduced measurement-set.

Fig. 5 shows that the projection method allows not only to estimate contact forces with higher accuracy but also a better extrapolation capability in ranges outside the calibration range (from 55 to 100 kN). In fact, as shown in Fig. 6, the projection method pre-serves the sign of the measured deformation. Thus, a reduced measurement set can perform as an optimal measurement set.

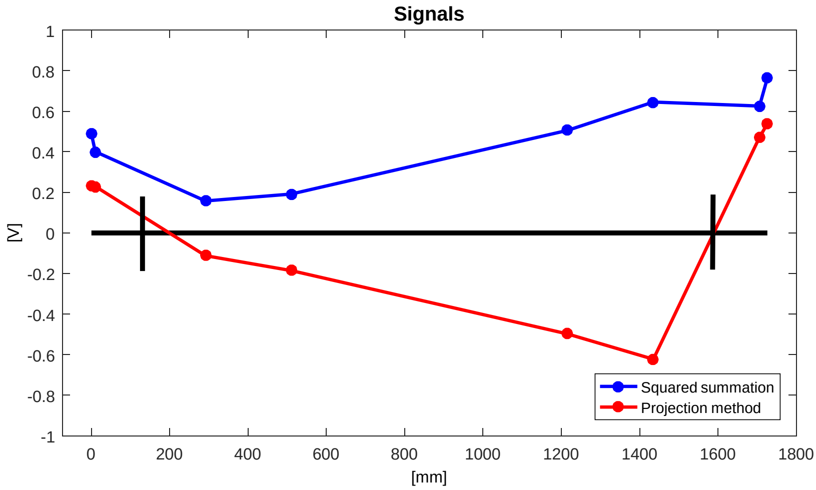

Fig. 6 Signals measured during the application of a load condition.

4. RESULTS FROM INLINE TESTS

Results from inline tests with a passenger train running at 85 km/h are shown in Fig. 7. The considered track section is characterized by two sharp curves of 292 m and 606 m negotiated at the maximum allowed speed.

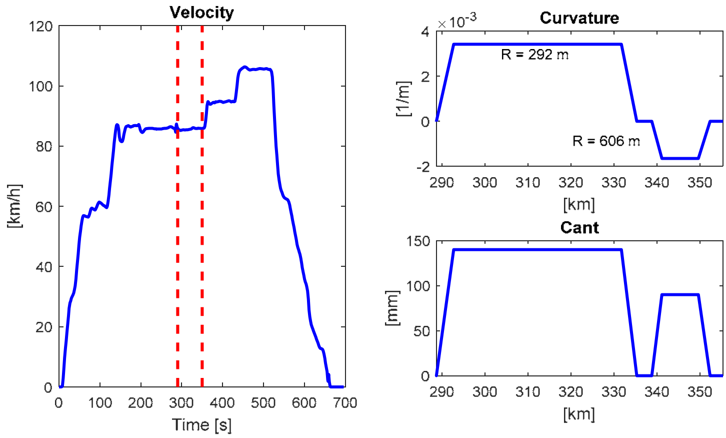

Fig. 7 Speed profile and characteristics of the track.

Both the speed profile, the track curvature and the cant are reported. Fig. 8, instead, shows the comparison between the forces estimated by means of an optimal measurement set (four measurement sections on the axle, two measurement sections on the wheel-web and a torsional bridge for the longitudinal forces) considering the two calibration methods presented before. No improvement for the lateral force components is achieved by the projection method since the major contribution to the estimation of these force components comes from the wheel-web signals that are not affected by longitudinal force components. Instead, major differences in the estimation of vertical force components, especially during the negotiation of the first curve characterized by high longitudinal force components, are obtained. In fact, longitudinal force components affect the estimation of vertical force components, leading to an overestimation of the forces with the squared sum method. The better accuracy of the projection method is clearly visible in the estimation of the total axle load that remains constant throughout the considered track section.

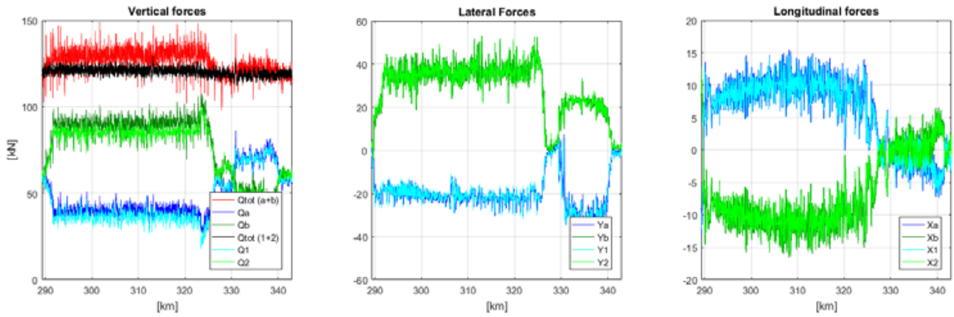

Fig. 8 Comparison between estimation via squared summation (a,b) and via projection method (1,2).

5. CONCLUSIONS

A method to increase the accuracy of the wheel-rail force estimation via dynamometric wheel-set has been presented. The research aimed at defining a numerical procedure to account for mounting misalignments of the stain gauge bridges and to project the measured deformations in an absolute non-rotating reference system. The outcome of the procedure allows to achieve more accurate estimations of the contact force components with reduced cross-talk effects due to the interactions between the forces acting on the wheel-set at the cost of an additional wheel-set's angular position sensor. A second outcome of the research is the preservation of the sign of the measured bending deformations thus further increasing the accuracy of the developed methodology in presence of cross-talk effects related to the contact point position. The methodology has been tested both in laboratory on a full-scale test-rig and during inline tests. The results confirmed the effectiveness of the methodology and its feasibility in real applications.

6. REFERENCES

[1] **EN14363.** Railway applications - Testing for the acceptance of running characteristics of railway vehicles - Testing of running behaviour and stationary tests. 2005.
[2] **Roeleveld, T.:** Measurement of wheel-rail contact forces. Proceedings of Symposium of Advances in Contact Mechanics a tribute to Prof. J. J. Kalker, 2008.
[3] **Bionda, S. - Di Gialleonardo, E. - Cazzulani, G. – Braghin, F.:** Evaluation of the metrological characteristics of an instrumented wheelset for the measurement of wheel-rail contact forces. Proceedings of the 13th MINI Conference on Vehicle System Dynamics, Identification and Anomalies (Ed. by Prof. I. Zobory), BME,

Department of Railway Vehicles and Vehicle System Analysis, Budapest, 2013, p.131-140.

[4] **Bionda, S. - Di Gialleonardo, E. - Cazzulani, G. – Braghin, F.:** Development of a new algorithm for wheel-rail contact force estimation using reduced measurement sets. Proceedings of the 14th MINI Conference on Vehicle System Dynamics, Identification and Anomalies (Ed. by Prof. I. Zobory), BME, EJJT, Budapest, 2015, p.111-122.

[5] **Bionda, S. - Di Gialleonardo, E. - Cazzulani, G. – Braghin, F.:** An application of the Interactive Multiple Model to the measurement of wheel-rail contact forces. The Dynamics of Vehicles on Roads and Tracks - Proceedings of the 24th Symposium of the International Association for Vehicle System Dynamics, IAVSD 2015, 2016, p.1145-1154.

[6] **Diana, G. - Resta, F. - Braghin, F. - Bocciolone, M. - Di Gialleonardo, E. – Crosio, P.:** Metodologia di calibrazione di sale dinamometriche per la misura delle forze di contatto tra ruota e rotaia. Ingegneria Ferroviaria 12, no. 1 (2012), p.9-21.

[7] **Cazzulani, G. - Di Gialleonardo, E. - Bionda, S. - Bassetti, M. - Crosio, P. – Braghin, F.** A new approach for the evaluation and the improvement of the metrological characteristics of an instrumented wheelset for the measure of wheel-rail contact forces. Proceedings of the Institution of Mechanical Engineers, Part F: Journal of Rail and Rapid Transit 231, no. 4 (2017), p.381-393.

SOUND- AND VIBRATION ANALYSIS IN THE OPERATION OF METRO VEHICLES

Gergely TULIPÁNT and András SZABÓ

Budapest University of Technology and Economics
Department of Aeronautics, Naval Architecture and Railway Vehicles
Group of Railway Vehicles and Vehicle System Analysis
H-1111 Budapest, Műegyetem rkp. 3. Hungary

Received: November 9, 2016

ABSTRACT

The moving railway vehicles generate noise-load in the neighbourhood of the track section covered in operation. The generated noise is measurable and can be recorded by means of appropriate measuring equipment. The measured signal carries both the effect of the local track characteristics and the responses coming from the singular properties of the vehicle passing through the track. Certain singular property emerging at a given point of the track for instance, a track irregularity exerts a characteristic effect on all vehicles passing through it which effect appears in the vibration signal, as well a sin the noise effect caused by the moving vehicles. That part of the vibration and noise effect emerging in the course of motion of a singular vehicle along a given track, which can be ordered to the singular properties of the vehicles, can obviously traced back to the singular anomalies and eventual failures of the vehicles. In this paper conclusions are drown concerning both the track and the singular vehicles, based on the evaluation of the vibration signals measured in the environment in the course of passage of a well specified vehicle set of small number through a given track section. The vibration measurement was realised in a metro tunnel, where further outer factors did not mean unwanted vibration-load, disturbing the investigations, so the measured signals represent the properties of the track-vehicle system.

Keywords: metro operation, vibration-load and noise-load, vibration measurement

1. INTRODUCTION

In the course of traversing a given tracks section, the railway vehicles generate characteristic noise and vibration load in the neighbourhood of the track section in question.
The signal determined by using an appropriate measuring device carries both the effect of the local track characteristic and that of the information contained in the individual qualities of the vehicles moving on the track.
In the present lecture well defined, only small number of vehicle set caused vibration signals, measured in the environment in the course of the motion of the vehicles mentioned, have been evaluated and have been drawn conclusions concerning both the track and the individual vehicles.
The vibration measurement was taking place in the metro tunnel where other outer factors did not mean vibration load that would have disturbed the examination, thus the measured signals could carry the properties of the track/vehicle system.

2. DYNAMICAL ANALYSIS

The track/vehicle dynamical system:

- It is excited by the environmental effect
- It is an excitation source with respect to the environment
- The track and the vehicle as two subsystems cause inner excitation interaction

Vibration caused by vehicles:

- Excitations originated in the motion of vehicles-parasitic motions
- Excitations effect caused by the operation of the inner equipment of the vehicle

Vibrations caused by track:

- The geometric unevennesses of the track
- Inhomogenity of the mass-, stiffness- and damping charasteristics of the track along the longitudinal coordinate

3. THE WHEEL/RAIL CONNECTION AS EXCITATION SOURCE

Excitation recurrence caused by the wheels rolling through after another over a given measurement point of the track. Rolling through durations and associated frequencies at a vehicle speed 60 km/h are as follows:

	Axle base in bogie	**Distance of king-pins**	**Distance of king-pins of to adjacent cars**
a_i [m]	2	12.6	7.552
T [s]	0.12	0.756	0.453
f [Hz]	8.3	1.32	2.21

4. MEASURING-TECHNIQUE

Processing of the measure signals were as follows: computing *rms* values with continuous windowing, and graphical plotting of their variation with time were carried out.
The *rms* time functions concerning the running through of a selected metro train are plotted in common diagrams (more oscillograms in a common co-ordinate system).

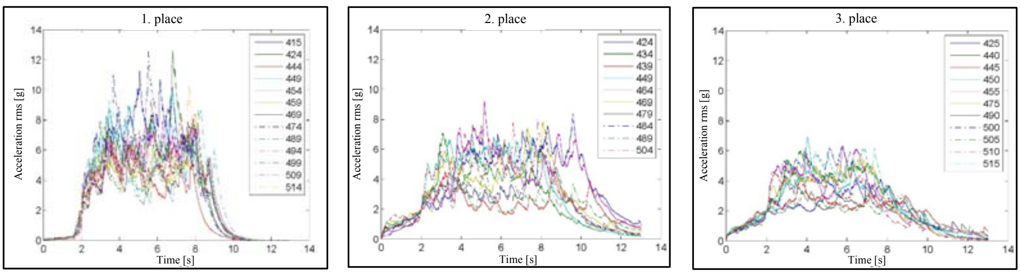

Fig. 1 Lower plane of the rail-head or on the rail tread in vertical measuring direction

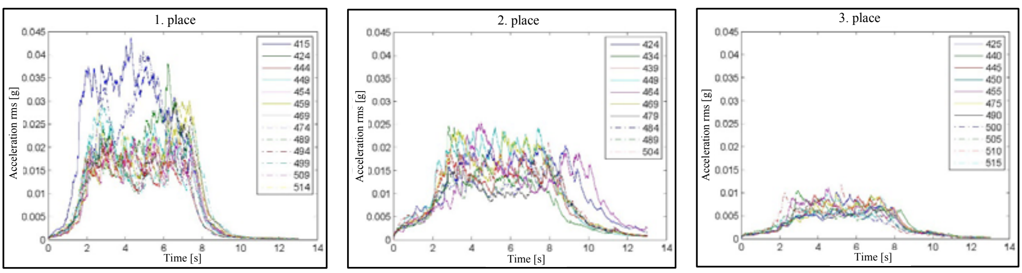

Fig. 2 Sidewall of the tunnel the measurement direction is perpendicular to the wall

5. THE METRO-TRAIN UNDER EXAMINATION

Alstom Metropolis AM5-M2:

- At the both ends of the train there is a powered car with driver's cab named MC
- The 2nd and 4th vehicles there are powered cars named M
- In the middle of the train there is a car named T
- Central sprung draw-bar
- Axle-base of the bogie: 2 m
- Distance of king-pins: 12.6 m
- The non-front car length: 20.2 m

6. PLACES OF MEASUREMENTS

Examination point No. 1 (place 1)

- Right track
- The track is of straight line-formation
- 1,93 ‰ track inclination (prior 6,94 ‰ and after 11,84 ‰ is the inclination)
- Structure of the line tunnel: monolitic concrete wall with iron plate and reinforced concrete jacket insolation (prior monolitic concrete wall with inner reinforced concrete jacket, after cast iron tubing)

Examination point No. 2 (place 2)

- Right track
- The track is of straight line-formation
- 5,06 ‰ track inclination (prior 5,29 ‰ and after 6,24 ‰, resp. 5,13 ‰ is the inclination)
- Structure of the line tunnel: block wall structure constructed of waterproof concrete

Examination points No. 3 (place 3)

- Left track
- The track is of curved line-formation (R = 400 m)
- 2,44 ‰ track inclination (prior 2,67 ‰, resp. 2,42 ‰, after 30,57 ‰ is the inclination)
- Structure of the line tunnel: block wall structure constructed of waterproof concrete (prior cast iron tubing, block wall structure constructed of waterproof concrete, monolitic concrete wall with iron plate jacket, alternating)

7. ANALYSIS OF RESULTS RECEIVED FOR THE METRO-TRAINSETS

In this Chapter the characteristic examination results received for the metro train-sets under consideration are shown.

420-424 metro-trainset

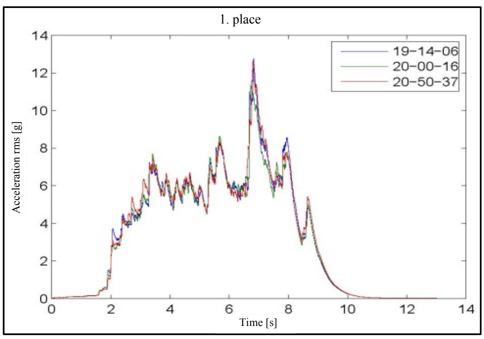

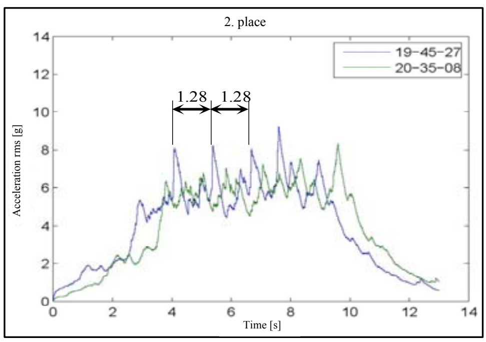

Fig. 3 Examination result of 420-424 metro-trainset

- The *rms* values measured at the given place of the track show intensive increased sections in the neighbourhood of the passage of the last but on vehicle in the case of passage of car No 423 the maximum vibration gain caused by track unevenness is about the twice value measured in *rms* of the values (experienced) characteristic in average cases. A slight increase was experienced also in the case of the passage of neighbour vehicle No 422.
- At the measuring place No 2 all these are much less intensive, the variation *rms* function is much more uniformed.
- At the metro-train (19-45-27) passage the distance in time 1.285 s between the peak values of the rail vibration evaluation can be connected to the length 20.156 m of the vehicles at a speed 56.46 km/h.

425-429 metro-trainset

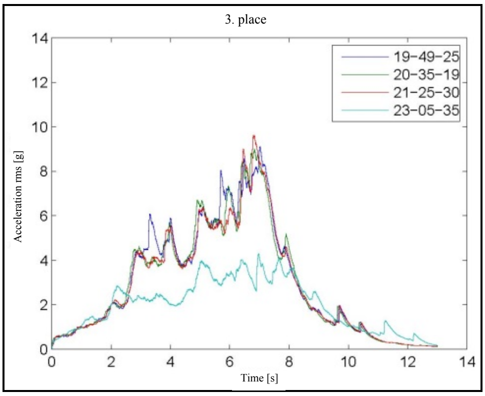

Fig. 4 Examination result of 425-429 metro-trainset

- In the (23-05-35) procession the traversing speed was cca. by 20 km/h lower, then the average speed. This relation can be stated that the speed reduction rate indicated significantly reduced the *rms* values of the excited vibrations of the assembly, in the case of rail vibrations the reduction was about 50%.
- The measured vibrations show that there is a substantial difference between the first train-part and the rear train-part from the point of view of vibration excitation. Considering the motion of the metro train in a given track therms values of vibrations generated by the two front running vehicles – namely cars 425 and 426 – are about the half values, than the vibrations generated by the rear running, cars of number 427-429. → extra-ordinary wheel-turning has been made at the first front running cars (No. 425-426), so the running distance less than the other car's running distance by cc. 7400 km. This is the reason, that the first part of the train has shown not so severe vibration generation.

440-444 metro-trainset

- At examination point 1. the track error is recognizable in vibration image but along the train the change of vibration-excitation effect is also observable. The front and rear part of the train generate higher *rms* levels than the middle section.

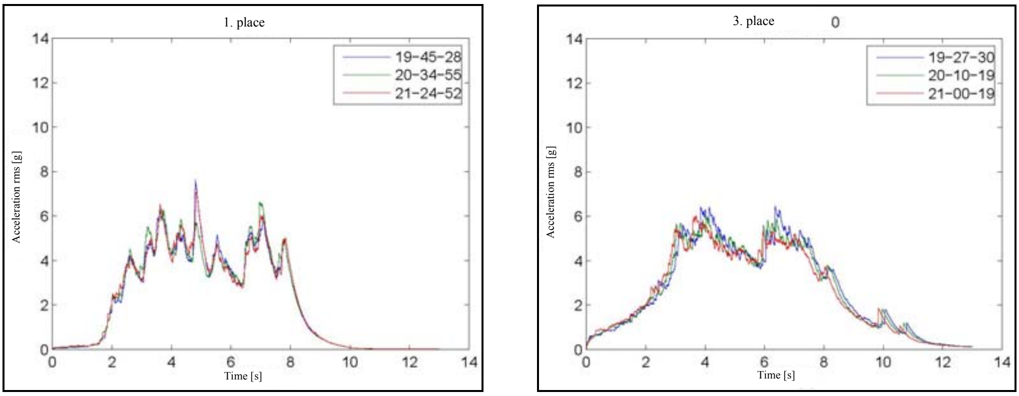

Figure 5. Examination results of 440-444 metro-trainset

- At examination point 3. it can be observed that in the case of curved track sections the excitation-effect generated by the train is characteristically different from those at the straight sections of track. At the same time at the two examination points the rail-vibrations have approximately the same *rms* levels.

445-449 metro-trainset

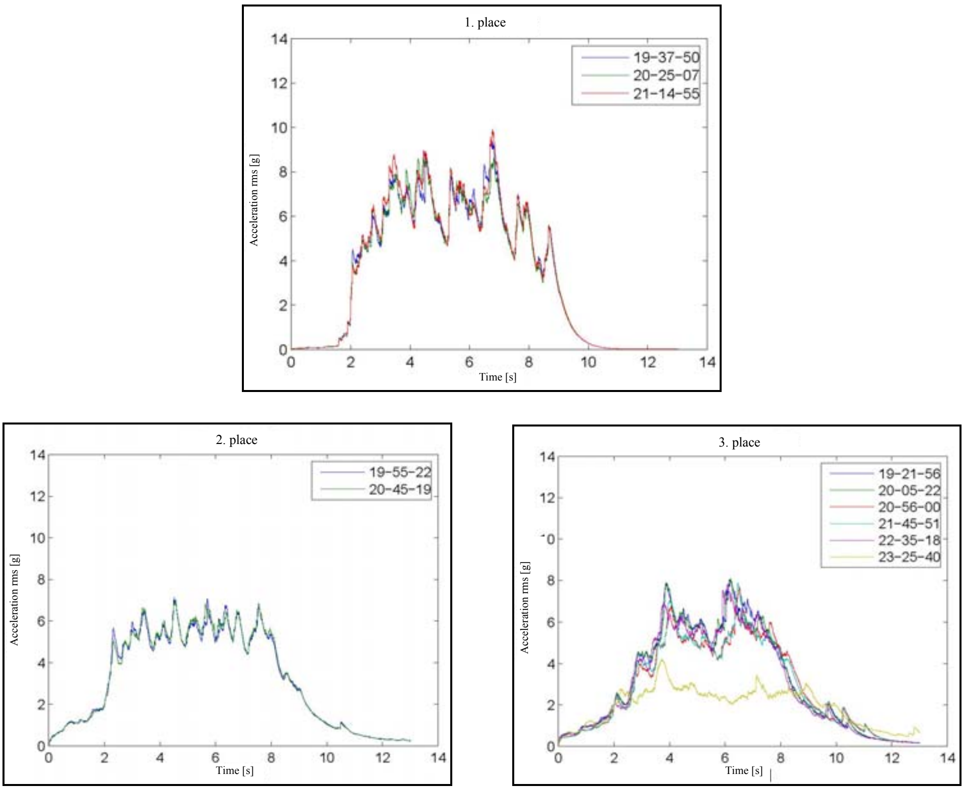

Fig. 6 Examination results of 445-449 metro-trainset

- At examination point 1., it is clearly visible that the successive peak appearances are in accordance with the bogie king-spin distances (caused by the track unevennesses).
- At examination point 2. to the local track unevenness caused excitation does not suppress other excitations, and approximately same track vibrations processes are experienced.
- At examination point 3. characteristic variation *rms* functions are obtained along the train, whereas the central part of the train seems to cause in lower values, and this variation of the acceleration signal can also be observed in the case of the last passage of lower speed.
- As a summarized statement for the three examination points, it can be stated that the train from the last turning on the lathe has run about 20.000 km, thus its wheel profiles are probably less worn, and considering the vibration diagrams, the profiles went under more or less the same wear load.

450-454 metro-trainset

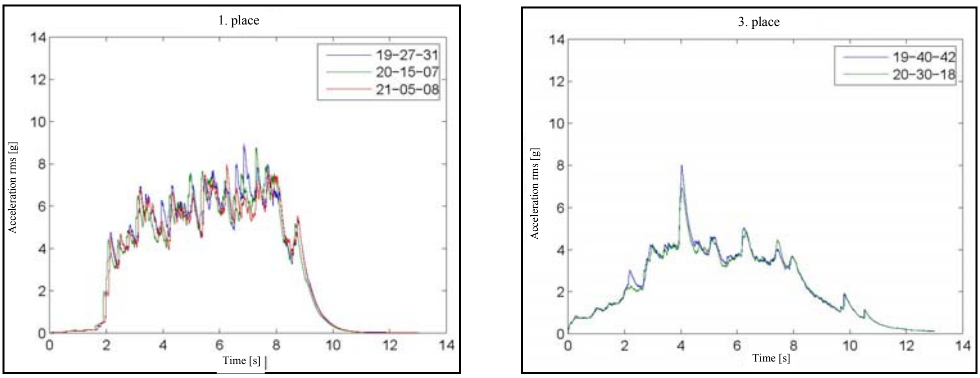

Fig. 7 Examination results of 450-454 metro-trainset

- acceleration *rms* functions do not show significant peaks, they are rather of low level.
- At examination point 1., it is clearly visible that the vibrations caused by the local track unevenness are dominant.
- A smaller increase in the *rms* function can be detected when the second part of the train passes over the point No 1. Accordingly, at examination point 3. in the case of the backward moving train one can observe a minor decrease in the variation of the *rms* functions.
- The examination point 3. from the beginning of the intensive increasing acceleration *rms* values (the time point at 4 s) almost identical peak formation can be observed in the accelerations measured on the rail in the case of both passages of the same metro-train. At the given case it is probably the result of a certain individual effect – some individual irregularity caused effect – belonging to the second car (No 451). Since the mentioned peaks do not observable on straight track, it is more probably, that certain problem is hidden in the background associated with the curving of the wheel.

475-479 metro-trainset

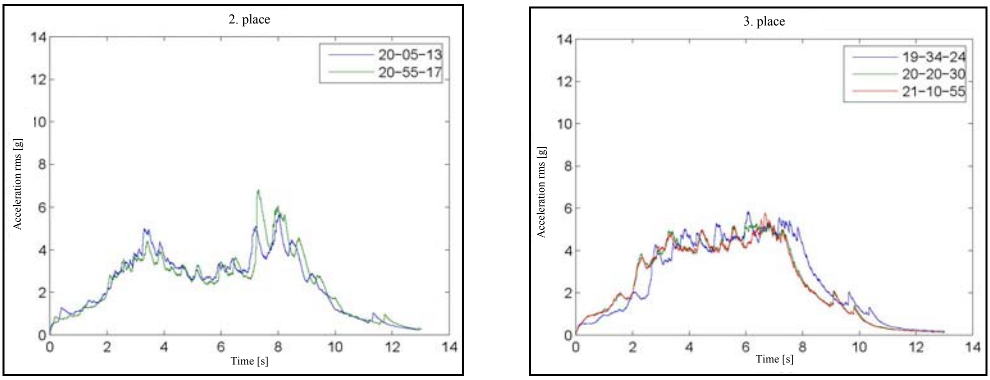

Fig. 8 Examination results of 475-479 metro-trainset

- In the course of passing through straight track section, it is the case also at this train, that a two maxima vibration process can be observed, thus both the front and the rear end of the train caused significantly higher *rms* levels compared to the effect of the middle section of train. In curves all the former are not typical, so in curving the contact between the rail and the wheels are less different among individual cars of the train.
- According to data of the maintenance of the vehicles the turning on the lathe of the wheels of car No 475 has been made out of plane. The effect of turning on the lathe, rather just at examination point 3., in the course of curving can be recognised, where the vehicle is repaired vehicle as the front vehicle causes recognisable smaller rail vibration *rms* values.

490-494 metro-trainset

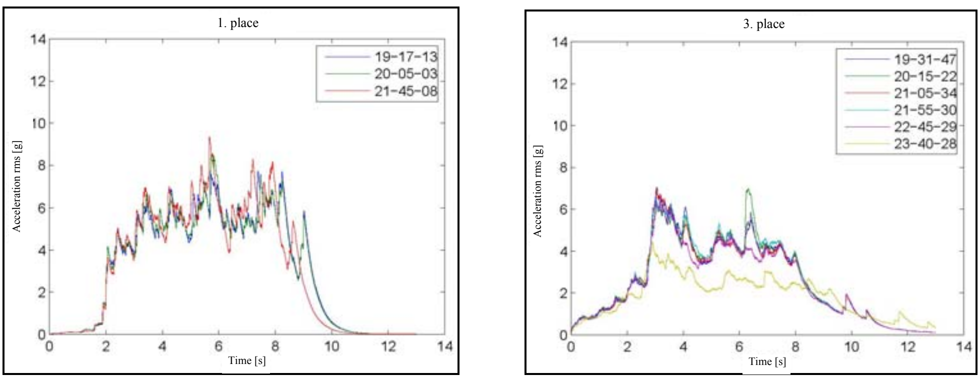

Fig. 9 Examination results of 490-494 metro-trainset

- At the examination point 1., the vibration mirror shows many peaks and frequencies, what is the sign of the presence of further excitation sources, especially this phenomenon proofs the more expressed effect of the rear half of the metro-train. At the examination point 3. the aforesaid is in accordance with the higher signal level belonging to the front part of the train..

- According to the maintenance of data before the measurements the entire train has received wheel turning on lathe after 6.000 km mileage performance. Thus, during the measurements the wheel profiles were only mild worn, but due to the measurement results the tire wear has achieved noticeable difference during this short period of time.

495-499 metro-trainset

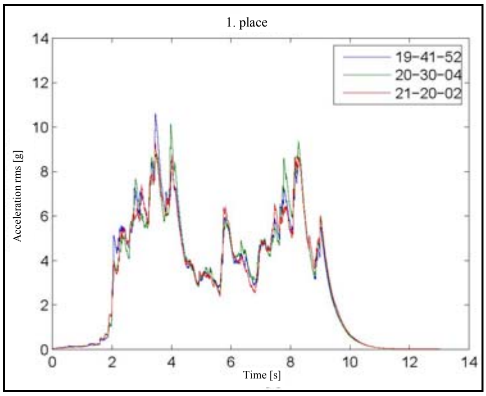

Fig. 10 Examination result of 495-499 metro-trainset

- The *rms* functions, which can approximately be considered of „Two hump" form, the peak belonging to the front part of the train achieves about the double value, to that of the characteristic level belonging to the event when the middle part of the train passes over the examination point. The shape of the signal shows intensive variations, and achieves very high levels in comparison with the similar functions of the other trains.
- The high vibration generating effect is explained by the maintenance data, due to the latter in the case of the operating trains since about 80.000 km running there was no turning on the lathe, except car No 495, which was turned on the lathe about 25.000 km distance covered before the measurement. This effect of the latter turning has disappeared, and it is likely, that the as a whole analysed vibration conditions are caused by the presence of wheel-sets having rather worn tread profiles.

505-509 metro-trainset

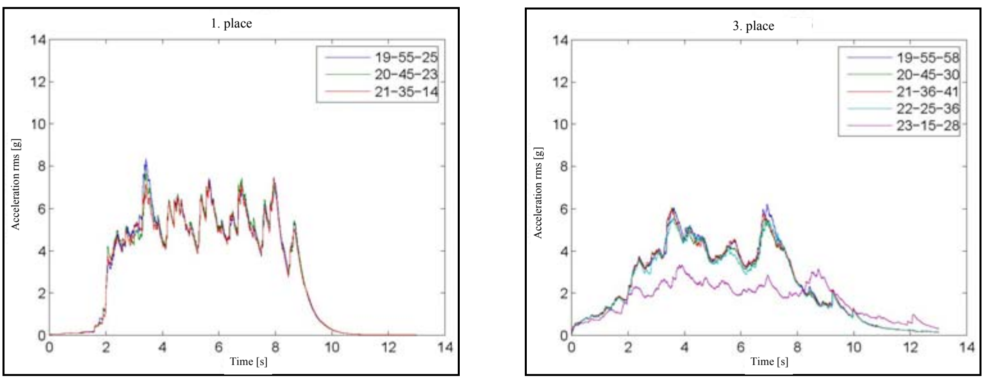

Fig. 11 Examination results of 505-509 metro-trainset

- The measured vibration images reflect "good" vehicles. Accordingly, at examination point 1., there appears the conventional variation of the vibrations caused by the track unevennesses.
- At examination point 3. some irregularities emerge in the *rms* function patterns, but as a whole, the signal level is low. At this train in the course of the last running it was also possible to perform measurements at a lower train speeds, and it has also resulted in significantly lower *rms* values.
- According to maintenance data when the measurements occurred with this train the wheel profiles performed about 18.000 km mileage performance, thus, they were not severely worn.

8. CONCLUSIONS

- At a given measuring place the vibration process caused by a specified metro-train shows similarity of great measure in the case of identical vehicle speeds and sequential traversing.
- At the given measuring place the vibration processes caused by different metro-trains shows characteristically deviating, metro-train specific realisation functions.
- In case of specified metro-train the vibration processes at the measuring places on the track show also common characteristics but there are certain characteristic deviations, as well.

Possibilities of further analyses: Diagnostic application of the results of vibration measurements:

- Detecting of the technical state of the metro-trains/vehicles by means of continuous/regular vibrations measurements at a selected point of the track.
- Detecting the technical state of the track by means of continuous/regular vibrations measurements realised by measuring system installed on selected vehicles.

9. REFERENCES

[1] **Zobory, I.- Szabó, A.:** Kerék- és sínkopás szimuláció metró üzemben. Közlekedéstudományi Szemle; LIV. évf., 2004/8. Budapest, 2004. p.307-314. (In Hungarian)

[2] **Zobory, I.- Szabó, A.:** Valószínűségelméleti hátterű kerék és sínkopás előrejelzés egy adott vasúti hálózatra. GÉP, LV. évfolyam, 2004/12. Budapest, 2004. p.81-84. (In Hungarian)

[3] **Heckl, M.:** Körperschallerstehung bei Schienenfahrzeugen. Vorträge des Kollokviums Schallemission und –Immission von Schienenfahrzeugen und Referate im Rahmen der DAGA ’90 Konferenz, Wien (1990)

[4] **Thompson, D.:** Railway Noise and Vibration. Elsevier, Amsterdam, Boston, Heidelberg, London, New York, Oxford, Paris, San Diego, San Francisco,Sydney, Tokyo,2009.

[5] **Tulipánt, G.:** A zajterhelés változása a 2-es metróvonal felújított szakaszán. Városi Közlekedés, 2005. október, XLV. évfolyam 5. szám. Budapest, 2005. p.275-280. (In Hungarian)

[6] **Tulipánt, G.:** A budapesti metró zajcsökkentési lehetőségei. Konferencia előadás, OPAKFI Zajvédelmi Szeminárium. Gyula, 2005. október 19-21. (In Hungarian)

THE IMPACT OF EN13749 REQUIREMENTS ON THE FATIGUE STRENGTH DESIGN OF FREIGHT BOGIES

Cornel RAICOV and Ioan VETRO

ICPV SA, DESIGN TESTING RAILCARS
(Company of ASTRA RAIL INDUSTRIES)

Calea Aurel Vlaicu, nr. 29-31,
310141 – Arad, Romania

Received: November 9, 2016

ABSTRACT

The paper refers to the impact of additional requirements from EN 13749 for design the freight wagon bogies, in comparison with the UIC 510, under the application of mandatory European Directives to TSI (Technical Specification for Interoperability). The requirements of calculation and testing proof for a bogie frame to fulfil UIC 510-3 are Exceptional Static Forces, and Static Forces for Simulation of Dynamic Service Loads, inclusively rail track induced twist. As well, fatigue loads in the testing facility of 10 millions cycles were requested. Nowadays, during the TSI era, the application of EN 13749 became mandatory, and the designer of the bogie has faced with several new challenges. The purpose of the paper is to show the differences between the two standards (UIC vs. EN) and to show the simulation results using detailed FEA (Finite Element Analysis). The accurateness of the simulation is nowadays a god argument to predict bogie frame behaviour in the testing stage, as well in service stage – but there are a lot of calculations and optimizations during the design stage, in order to achieve the goal to have a bogie with higher performances. The main impact is that the design of new developed bogie is influenced by the new requirements; as well the ways of testing and the interpretation of testing results have been changing in the recent years (i.e. the crack occurrence in any location is not accepted any longer in the second stage, etc.).

Keywords: Bogie frame strength, fatigue stress

1. INTRODUCTION

1.1 UIC 510-3 requirements for design and testing

The requirements of calculation and testing for a new bogie frame according to UIC 510-3 leaflet are the following:

- test with Static Exceptional Forces,
- test with Static Forces for Simulation of Dynamic Service Loads,
- fatigue test in a test rig.

The tests presented above contain vertical and transversal forces applied in the pivot area, forces due to the roll of the vehicle applied on the side bearings, forces arising from twisting of the track, forces arising from braking of the vehicle.
The criteria of allowance for these tests are various, from not exceeding elastic limit of the material for Static Exceptional Loads, to not exceeding fatigue limits (i.e. Goodman diagram) for Forces for Simulation of Dynamic Service Loads, generally speaking the stress based approach. As well, there are requirements regarding non-occurrence of cracks after a number of cycles during test in the fatigue test rig.

1.2 EN 13749 Requirements

The requirements of calculation and testing for a new bogie frame according to EN 13749 are mostly similar with those prescribed in UIC 510-3. However there are a few new requirements regarding forces to be applied on the bogie structure.

These requirements consist of additional application of loads in the x – longitudinal direction, called “lozenging forces” and also in studying of an additional load case due to twisting of the bogie. Longitudinal lozenging forces have to be applied to each wheel and in the opposite sense on the opposite sides of the bogie frame. These forces are given by the relations (1) as Exceptional Load and (2) as Dynamic Service Load.

$$F_{x1max} = 0.1(F_z + m^+g) \quad (1)$$

$$F_{x1} = 0.05(F_z + m^+g) \quad (2)$$

Twisting load consists of studying of a load case under vertical load, considering a complete unloading of one wheel, with the vertical displacement being limited to rail height. This case simulates the effects of a slow speed derailment on depot track.

Additional to these loads, EN 13749 requires application of forces due to components attached to the bogie frame. These are inertia loads generated by the bogie motion and any loads generated by the operation of the equipment.

The acceleration levels required by EN 13749 for bogie frame mounted equipment are given in the Table 1.

Direction	Exceptional acceleration	Fatigue acceleration
Vertical	20g	6g
Lateral	10g	5g
Longitudinal	3g	2.5g

Table 1

These requirements regarding accelerations are sometimes practically impossible to fulfil and they are not usually applicable for freight bogies.
In consequence, in order to avoid design of the freight bogies in an ultra conservative way, the results of the track tests with similar reference bogies are used. By doing this, the accelerations values for attached components could be decreased approximately 2...3 times.

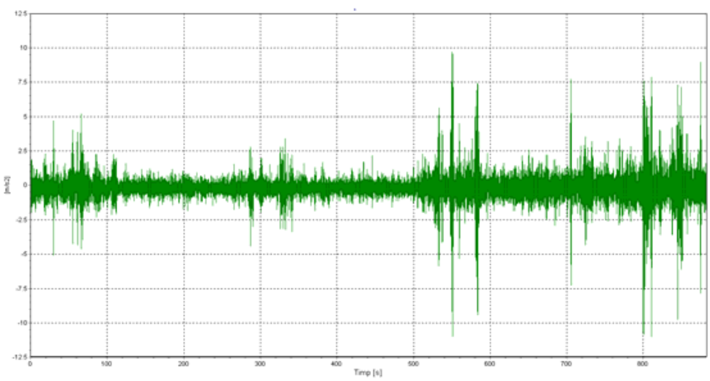

Fig. 1 Measured accelerations in a dynamic test on rail track

However, due to the high values of accelerations, it is necessary to change the design solution of different bogie components supports (attachments) and also new assembling techniques by welding or fastening of the supports with the bogie frame.
The methods for improvement of welding quality are well known, they allowing higher fatigue limits and in consequence higher fatigue strength of the bogie frame.

2. THE INFLUENCE OF THE EN 13749 ON THE DESIGN OF THE Y25 BOGIE FRAME

In Fig. 2 is presented a rendering of the CAD complete model of an Y25 bogie and in Fig. 3 is presented the model of the same bogie frame.

Fig. 2 CAD model of the complete Y25 disk brake bogie

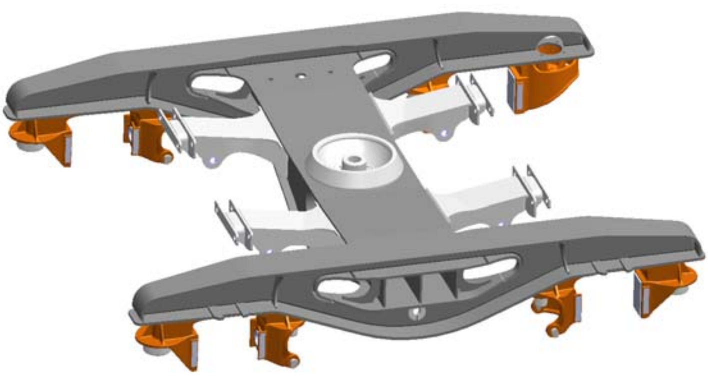

Fig. 3 CAD model of the bogie frame

The main affected area of the bogie frame as result of the additional requirements of EN 13749 is the joint area between the transversal beam (pivot beam) and the lateral sill, this area being well known as the most stressed in the frame structure (Fig.4).

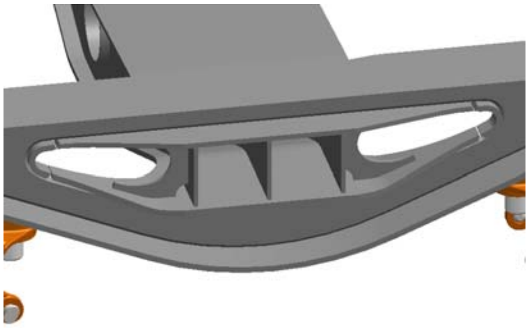

Fig. 4 Detail of CAD model, area affected by additional loads

The next step was structure optimization in the affected area, taking into account the most important dimensional parameters (Fig.5).

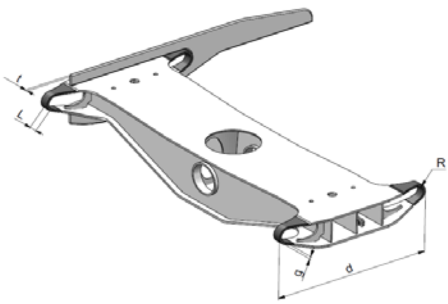

- d maximum opening window
- g   thickness of the closing area
- R   radius of the closing area
- L width of the closing area
- t   thickness of lateral sill web

Fig. 5 Parameters to be optimised in the transverse beam

The optimization has been made by FEM simulation using NX Nastran software. All of exceptional and normal load cases from EN 13749 have been simulated. A detail of the simulation model regarding the interest area are presented in Figs. 6 and 7.

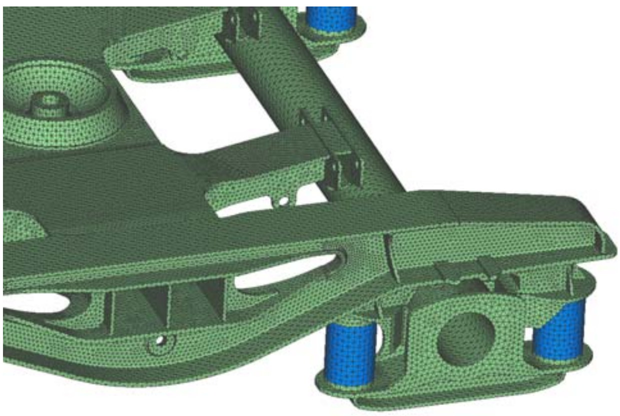

Fig. 6 Meshing detail of the model

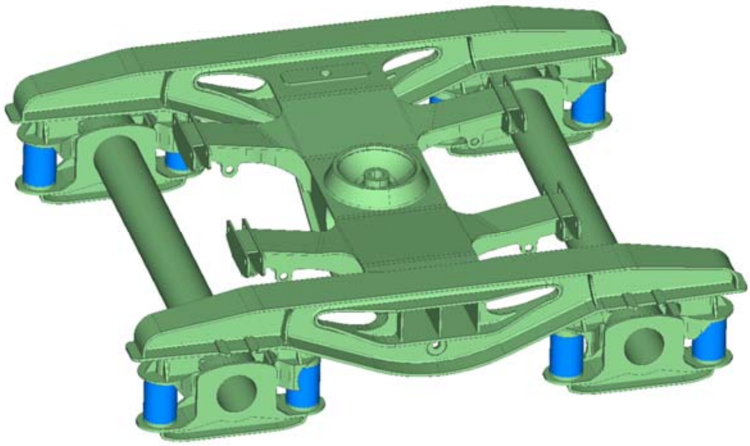

Fig.7 Simulation model

3. FEM SIMULATION RESULTS

The following results are presented as equivalent von Mises stress diagrams.

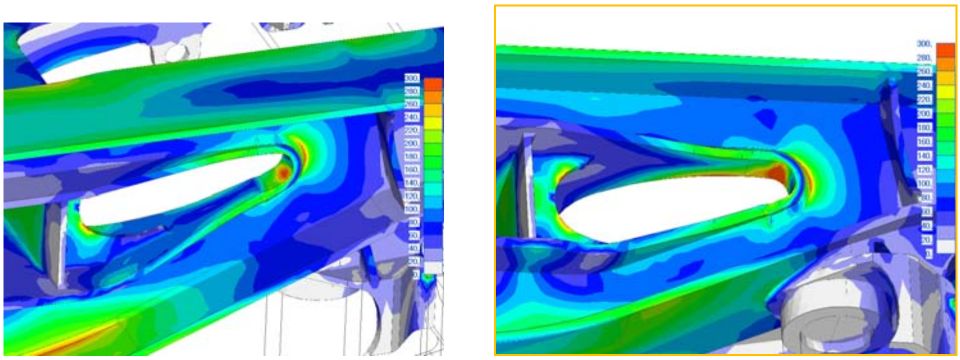

Fig. 8 Stress distribution before optimization process

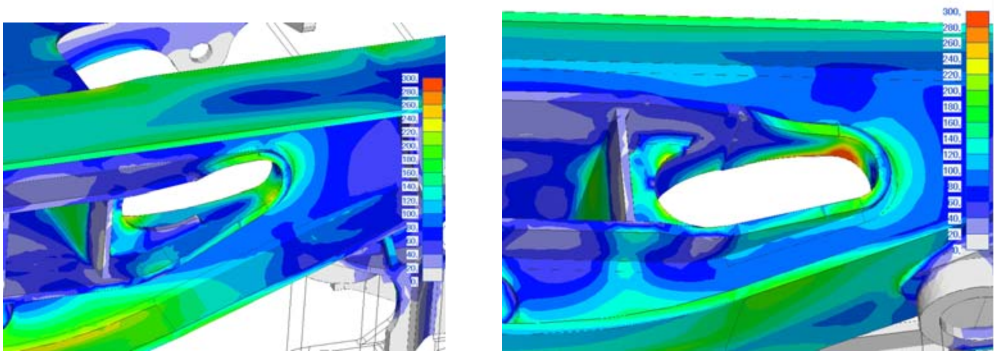

Fig. 9 Stress distribution after optimization process

4. CONCLUSIONS

On the basis of theoretical investigations and numerical simulations, the following conclusions can be drawn:

- additional requirements of EN 13749 regarding loads applied on bogie frame lead to necessity of improvement in some important areas of the bogie frame
- the dimensional optimization of the area of intersection between transversal beam and lateral sill leads to a lower stress by about 15%, as well as to easier manufacturing of the modified parts
- it is also necessary to optimize the bogie frame welded supports in order to ensure their capability to bear the real accelerations from the rail track. In case of lack of railtrack measurements, the attachments and the bogie frame must be over dimensioned (due to excessive value of required acceleration - see table 1)
- the full TSI certification of a new bogie implies performing further full static and fatigue tests (10 millions cycles for fatigue) on a bogie frame, as well as dynamic tests on rail track in conformity with EN 14363 requirements

5. FUTURE WORK

The study presented in this paper represents a bogie under development in ICPV/ARI. Following the design, a bogie frame prototype has been built. The bogie frame will be subjected to complete static and fatigue tests according EN 13749, in an accredited testing laboratory.

Fig.12 Prototype of Y25 disk brake bogie at InnoTrans Berlin exhibition

After all tests, final certification of the bogie will be made, following by its mass production. This process will be ended by middle of 2017.

6. REFERENCES

[1] EN 13749, March 2011– Method of specifying the structural requirements of bogie frames

[2] UIC 510-3 – Essais de resistance au banc des bogies a 2 et 3 essieux

[3] UIC B12/RP 17, 9th edition, July 2012 – Programme of tests to be carried out on wagons with steel structure

[4] ERRI B12/RP 60, 2nd edition, June 2001 – Tests to demonstrate the strength of railways vehicles. Regulations for proof tests and maximum permissible stresses

[5] TSI CE 321 / 2013

CONTROL ORIENTED MODELLING AND VALIDATION OF AN EXHAUST BRAKE SUPPORTED LOW PRESSURE EXHAUST GAS RECIRCULATION ON A MEDIUM DUTY DIESEL ENGINE

Ádám NYERGES and Huba NÉMETH

Department of Automobile Technology
Faculty of Transportation Engineering and Vehicle Engineering
Budapest University of Technology and Economics
Stoczek str. 6, -1111 Budapest, Hungary

Received: November 11, 2016

ABSTRACT

Due to modern modelling and simulation possibilities it has become easier to understand the working processes and to design the control strategies of complex systems. The more and more stringent emission norms for internal combustion engines make it necessary to use modern modelling procedures to develop advanced combustion processes and air path systems. Apart from greenhouse gas emissions the main problem with diesel engines is the reduction of NO_x and particulate matter emission at the same time. The difficulty is that the formation of the two pollutants is counterproductive. The pollutants' quantity in the exhaust gas is reducible by cleaner combustion processes or by exhaust gas after-treatment. To achieve cleaner combustion processes precise control strategies are necessary in the air path system. With external exhaust gas recirculation (EGR) the composition of the intake charge and the temperature of the combustion are controllable. By the mass flow rate of the recirculated exhaust gas the fresh air (or the burnt gas) fraction can be controlled in the combustion chamber. Due to the larger heat capacity of the inert burnt gases the temperature of the combustion process becomes lower which achieves lower NOx emission. Exhaust gas recirculation leads to better results in lower load operation points because it decreases the air-fuel ratio. The standard measurement cycles usually do not demand high load operation points. This means that EGR is effective in the most common operation points. The quantity of the recirculated exhaust gas can be controlled by several valves. If the exhaust side pressure is higher than the intake side pressure, then through the EGR valve the exhaust gas can be fed back to the intake side. The mass flow rate of the EGR can be increased with an intake throttle or with an exhaust flap. In this paper a control oriented model of a medium duty diesel engine will be presented. The engine is equipped with a low pressure EGR system. The EGR is supported with an exhaust flap. In the simplified engine model the equations, the state variables, the measured and the estimated parameters and the validation will be presented.

Keywords: diesel engine, dual loop exhaust gas recirculation, exhaust brake, engine model validation

1. INTRODUCTION

Today one of the most significant problems in transportation are CO_2 and pollutant emissions of internal combustion engines. The environmental impact of transport is controlled by international regulations, for instance the EURO emission norms in ECE R49 [1]. The EURO restrictions are becoming increasingly strict. To comply with them, more and more complex internal combustion engine systems are needed. The EURO VI norms have been recently applied to commercial vehicles, future regulations will also include stricter restrictions. The CO_2 and pollutant emissions of internal combustion engines are analysed by stationary and transient cycles. The most important stationary cycle of trucks is the WHSC (World Harmonised Stationary Cycle) (Fig. 1). The applied transient cycle is the WHTC (World Harmonised Transient Cycle).

The exhaust gas of modern diesel engines contains mainly two pollutants: particulate matter and NO_x. Decreasing both is a difficult task because their formation is counterproductive. By improving the combustion process the quantity of the pollutants can be decreased.

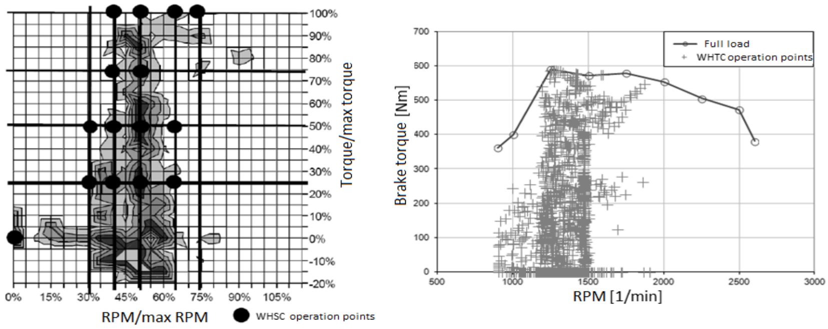

Fig. 1 The WHSC and the WHTC cycles

With EGR a significant NO_x emission reduction is achievable, and in some engine operation points the brake specific fuel consumption (BSFC) can be reduced as well.

2. DUAL LOOP EXHAUST GAS RECIRCULATION

In turbocharged internal combustion engines there are two ways to feed back the exhaust gas to the intake side of the engine. These are the low pressure and the high pressure EGR systems. Both of them have advantages and disadvantages, these are shown in Tab. 1. The most important advantage of the HP EGR system is the fast response because of the shorter recirculation loop. Due to this, the HP EGR behaves better in transients. On the other hand, the maximum recirculated gas quantity with HP EGR is usually lower than that of the LP EGR, due to the given pressure difference by the turbo charger.

HP EGR	LP EGR
fast response, favourable in transient cycles	slower response, higher boost pressure because all exhaust gas go through the turbine, favourable in stationary cycles
the time for mixing the intake air and the exhaust gas is shorter	longer time for mixing, but the condense water can demage the compressor
it increases the fuel consumption, but in high power demand operation points it can provide lower BSFC	it increases the BSFC less than the HP EGR, because of the higher boost pressure
using both systems on the same engine has advantages, this is an optimisation task	

Tab. 1 Advantages and disadvantages of HP and LP EGR

The LP EGR has a longer response, but the brake efficiency is in many operation points higher because the entire exhaust gas amount is utilised by the turbine. This means that the boost pressure is also higher, and the BSFC can reduce. The advantages of the two systems are able to complement each other. For example in a transient cycle in the first period the HP EGR is able to provide fast response to keep the NO_x emission lower. Later in the stationary phase of the cycle the LP EGR is able to provide lower BSFC.

Under low engine loads it is possible to use very high EGR rates because the air-fuel ratio is much higher than the smoke limit. In these operation points the pressure differ-

ence between the exhaust and the intake side is not enough to achieve the required EGR rate (by using an EGR valve only). To achieve higher levels it is necessary to use some support e.g. by the intake throttle or the exhaust flap/brake.
The dual loop EGR systems with LP and HP loops on heavy duty diesel (HDD) engines are not yet widespread and the effects of the very high EGR rate have not yet been fully analysed (see [2, 3, 4, 5]). In any serial production engines the application of the dual loop EGR is also not so widely used. Up to now these systems have appeared only in few passenger car diesel engines, e.g. [6, 7]. The control methods of the EGR systems are usually very simple and not very accurate.

3. ENGINE TEST BENCH

To have a high freedom in the flow controls several controllable flaps are used to apply into the engine. The quantity of the EGR is increasable by an intake throttle or by an exhaust flap. The main parameters of the engine test bench setup are in Tab. 2. The layout of the tested engine is shown in Fig. 2. The pressure and the temperature are measured in each important position of the air path. The fuel consumption is measurable in a gravimetric way.

Type:	turbocharged diesel, in-line, 4 cylinder
Maximum power:	125kW (2500 1/min)
Maximum torque:	600Nm (1200-1600 1/min)
Displacement:	3.9l
Stroke/bore ratio:	1.176
Compression ratio:	17.3
Injection system:	direct injection, common rail
Maximum boost pressure:	2.5bar

Tab. 2 Technical data of the tested engine

The quantity of the LP EGR can be increased by a low pressure intake throttle or a low pressure exhaust brake as well. These flaps are placed to the atmospheric side of the turbo charger. The quantity of the HP EGR is increasable by a high pressure intake throttle or a high pressure exhaust flap. These flaps are placed to the engine side of the turbo charger. The low pressure exhaust flap is applicable upstream and downstream to the diesel particulate filter (DPF) too.

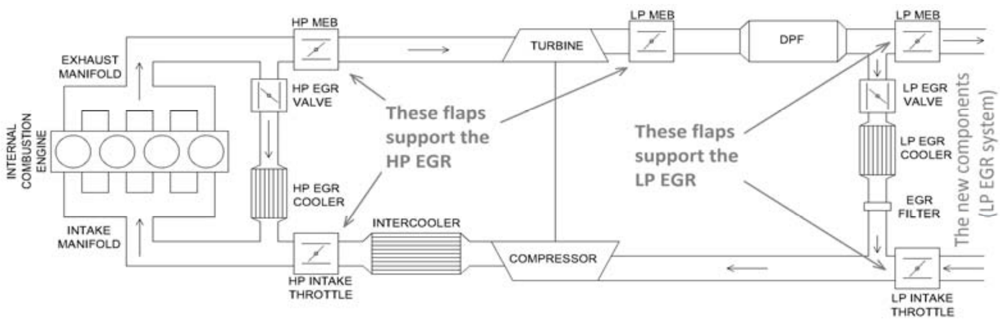

Fig. 2 Schematic drawing of the air path in the simulation model

The aim of this research is to create a validated, control oriented air path model of a medium duty diesel engine. The engine model contains the LP EGR system and a low pressure mechatronic exhaust brake (MEB).

4. ENGINE MODEL

4.1 Basic equations

The basic building block in the air path system is a fixed volume (a receiver) for which the thermodynamic states (pressures, temperatures, composition, as shown in Fig. 3) are assumed to be the same over the entire volume.

Fig. 3 A basic building block of the engine model [9]

The general laws which can be used for the basic blocks are derived from the ideal gas law, from the mass conservation law and from the energy conservation law [9].

$$p(t)V = m(t)RT(t) \tag{1}$$

$$\frac{dm(t)}{dt} = \sigma_{in}(t) - \sigma_{out}(t) \tag{2}$$

$$\frac{dU(t)}{dt} = \dot{H}_{in}(t) + \dot{H}_{out}(t) + \dot{Q}(t) \tag{3}$$

In a control oriented model the small number of the states is important, the model has to be as simple as possible. For instance in a turbocharged internal combustion engine model the transient changes of the pressures is more important than the change of the temperatures.

The differential equation of the pressure can be used as follows [9]:

$$\frac{dp(t)}{dt} = \frac{RT}{V}\left[\sigma_{in}(t) - \sigma_{out}(t)\right] \tag{4}$$

If there is a heat transfer through the wall, then the pressure changes can be estimated as [10]:

$$\frac{dp(t)}{dt} = \frac{\kappa R}{V}\left[\sigma_{in}(t)T_{in}(t) - \sigma_{out}(t)T_{out}(t) + \frac{\dot{Q}(t)(\kappa-1)}{\kappa R}\right] \tag{5}$$

The air fraction changes can be estimated in a similar way [9]:

$$\frac{dx(t)}{dt} = \frac{RT}{p(t)V}\left[\sigma_{in}(t)x_{in}(t) - \sigma_{out}(t)x(t)\right] \tag{6}$$

4.2 The state variables of the engine model

The subdivision of the engine air path system can be seen in Fig. 4. There are six fixed volumes. Every volume has three states, but the changes of most of them are less important i.e. it is negligible.

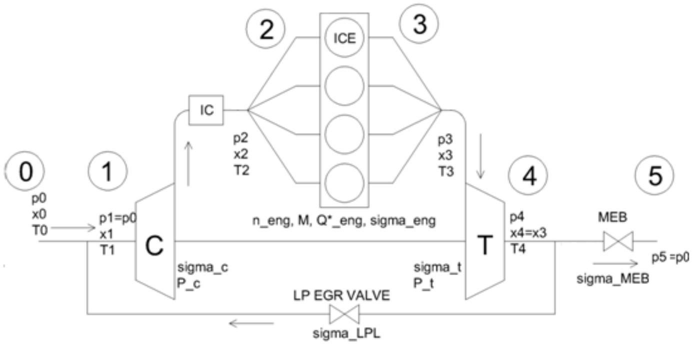

Fig. 4 The subdivision of the air path system

The state variables of the engine model are: compressor outlet pressure, turbine inlet pressure, turbine outlet pressure, turbocharger power. For air fraction estimation and model validation the air fraction defined as a state variable in blocks (2), (3) and (4).
The differential equation of the turbocharger is a mechanic equation. It can be estimated as follows [10]:

$$\frac{\mathrm{dP_c}(t)}{\mathrm{dt}} = \frac{1}{\tau_{\mathrm{tc}}}\left[-P_c(t) + \eta_{m\_tc} P(t)_t\right] \tag{7}$$

4.3 Additional equations

The mass flow rates through the flap valves (LP EGR, MEB) can be estimated by the orifice equation [9]:

$$\pi = \frac{p_{high}}{p_{low}} \qquad \pi_{crit} = \left(\frac{\kappa+1}{2}\right)^{\frac{\kappa}{\kappa-1}} \tag{8), (9}$$

$$\pi \le \pi_{crit} \Rightarrow \sigma_{orifice} = A_{eff}\,\frac{p_{high}}{\sqrt{RT_{high}}}\sqrt{\frac{2p_{low}}{p_{high}}\left(1-\frac{p_{low}}{p_{high}}\right)} \tag{810}$$

$$\pi \succ \pi_{crit} \Rightarrow \sigma_{orifice} = A_{eff}\,\frac{p_{high}}{\sqrt{RT_{high}}}\frac{1}{\sqrt{2}} \tag{11}$$

Regarding the air path system, the engine itself can be modelled as a volumetric pump, i.e. a device that enforces a mass flow rate as a function of its speed. A formulation for the model is [10]:

$$\sigma_{eng} = \eta_{vol}(n_{eng})\rho_2\frac{V_d n_{eng}}{2\cdot 60} \tag{16}$$

The mass flow rate of the compressor and the turbine depends on many parameters. In the model the isentrophic efficiencies are modelled as constants. In this case the formula of the compressor mass flow rate estimation is [11]:

$$\sigma_c = \frac{\eta_c}{\frac{R\kappa}{\kappa-1}T_1}\frac{P_c}{\left(\frac{p_2}{p_1}\right)^{\frac{\kappa-1}{\kappa}}-1} \tag{12}$$

The formula for the turbine mass flow rate contains two constants [10]:

$$\sigma_{t,red} = c_t \sqrt{1-\left(\frac{p_3}{p_4}\right)^{k_t}} \tag{13}$$

Finally the formulas for the turbine power and outlet temperature can be seen below [11]:

$$P_t = \eta_t T_3 \frac{\kappa R}{\kappa - 1}\left[1-\left(\frac{p_3}{p_4}\right)^{\frac{\kappa-1}{\kappa}}\right]\sigma_t \qquad T_4 = T_3\left\{1-\eta_t\left[1-\left(\frac{p_3}{p_4}\right)^{\frac{1-\kappa}{\kappa}}\right]\right\} \qquad (14), (15)$$

5. MODEL VALIDATION

5.1 Input signals

The control oriented model has to be accurate in typical operation points. In order to achieve that, representative operation points were selected from the WHSC cycle and a representative interval was selected from the WHTC cycle.

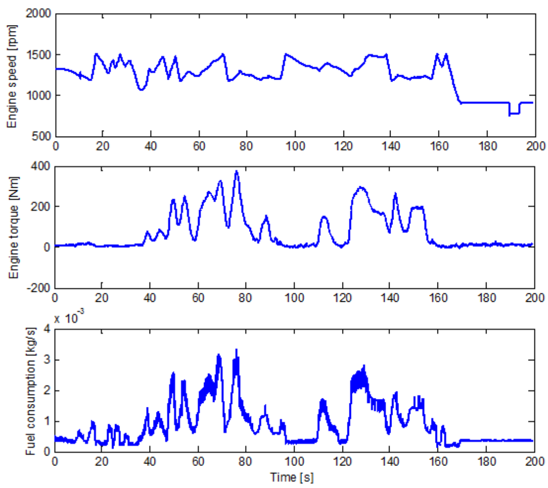

Fig. 5 Input signals from the WHTC cycle for the model validation [1]

The engine model requires three input signals: the engine speed, the engine brake torque and the fuel consumption. The input signals from the WHTC cycle can be seen in Fig. 5. The WHTC cycle mainly uses the small torque and low speed operation points.

5.2 Validation signals

The engine model is validated to measurement results. The validation signals were:

- compressor outlet pressure,
- turbine inlet pressure,
- air fuel ratio on the exhaust side,
- oxygen concentration on the intake side (to estimate LP EGR rates).

6. SIMULATION RESULTS

The purpose of this chapter is to prove that the engine model with its four state variables is suitable for control design aims in further researches. Fig. 6 shows the differences between measured and simulated compressor outlet and turbine inlet pressures without LP EGR. The curve of the simulated compressor inlet pressure fits well to the measured curve, smaller errors can be detected at lower pressures. The properties of the turbine inlet pressure are similar, but the errors at lower pressures are bigger.

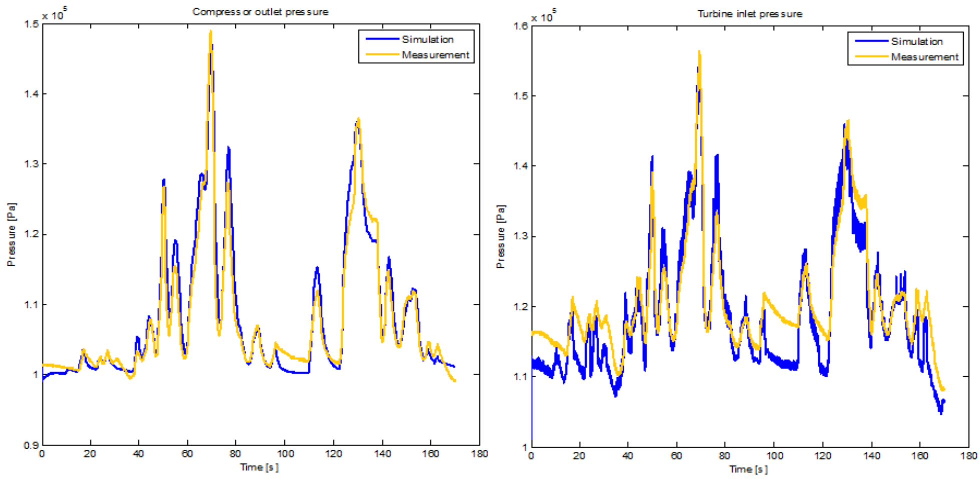

Fig. 6 The comparison between the measured and the simulated compressor outlet and turbine inlet pressures without LP EGR

With closed LP EGR valve the intake side O_2 concentration is constant. However, the exhaust side O_2 concentration changes significantly, and the comparison of the measured and the simulated results demonstrates the accuracy of the achieved mass flow rates in stationary and in transient opration cycles too. In Fig. 7 the measured and the simulated exhaust side O_2 concentration is shown. In some cycles the dynamics of the change in the simulation is faster and in some other cycles it is slower. In these three comparison results (without EGR) the RMS tolerances were below 3%.

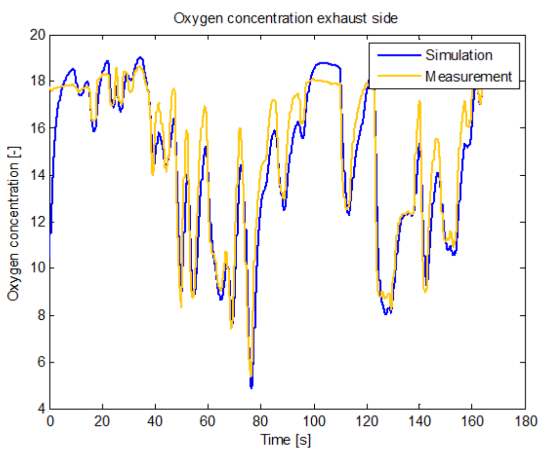

Fig. 7 The comparision between the measured and the simulated oxygen concentration without LP EGR

Experience showed that the properties of the compressor outlet and the turbine inlet pressure do not change with smaller EGR rates, typically with open LP EGR valve. With open LP EGR valve both the exhaust and the intake side O_2 concentration decrease. These results are shown in Fig. 8. The RMS error is below 5%. In low power operation points the relative error is bigger and the dynamic response of the simulation model is slower than the measurement results. In future researches the parameters of the model with strong effect on the dynamic response to the simulation results have to be checked to improve the accuracy of the model.

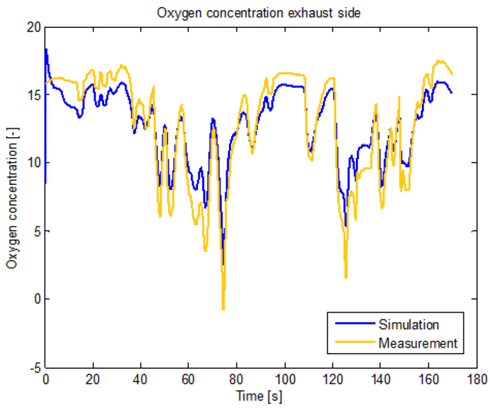

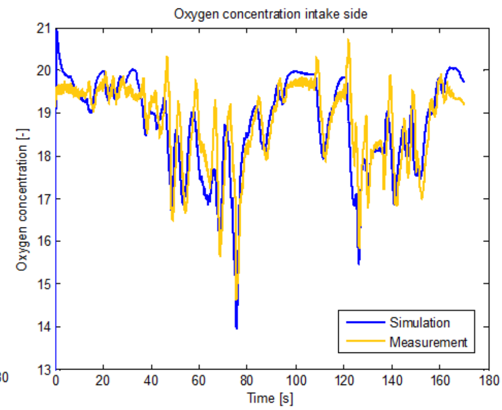

Fig. 8 The comparison between the measured and the simulated compressor outlet and turbine inlet pressures with LP EGR

7. LP EGR BENCH EXPERIENCES

Some measurement results have important effects on the engine behaviour with LP EGR. As mentioned in the introduction, the main aim of the application of the EGR is the reduction of NO_x emission. The achievements can be seen in the first diagram in Fig. 9.

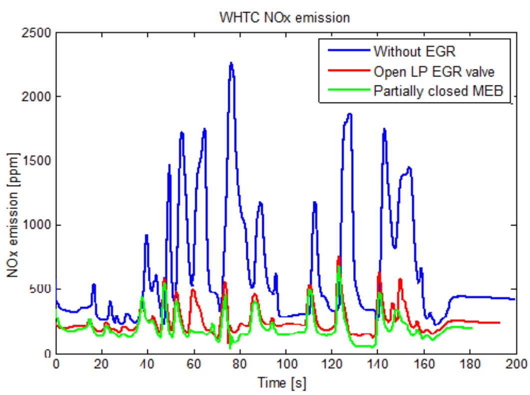

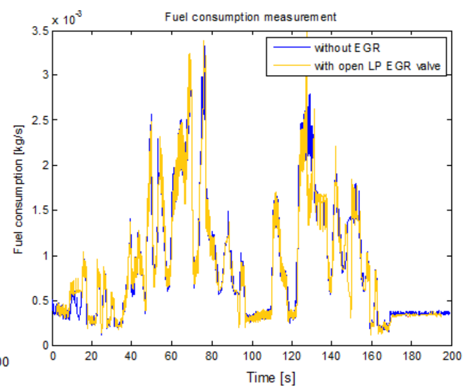

Fig. 9 The NO_x concentrations with different EGR valve and MEB valve positions and the comparison of the measured fuel consumptions with different EGR valve positions

With closed LP EGR valve the average NO_x emission is nearly 1000ppm, the maximum is near 2300ppm. The opening of the LP EGR valve signifiantly decreases the NO_x emission: its average is less than 300ppm, and the maximum is 500ppm. Further reduction can be achieved with partially closed MEB. In future researches on the control of the MEB the NO_x emission can be kept on a continuously low level.
The second diagram in Fig. 9 compares the fuel consumptions with and without LP EGR. The LP EGR does not make significant changes in the operation of the turbocharger. Therefore, differences between the two cases cannot be shown in this 200s interval.

8. CONCLUDING REMARKS

In this paper the effects of the MEB supported LP EGR system were analysed and a control oriented model and validation on a medium duty diesel engine was presented.
The main aim of the application of EGR systems is NO_x emission reduction. With LP EGR the NO_x was decreased to approximately a third level. Apart from the NO_x emission, the operation point of the turbocharger remains nearly the same with LP EGR, therefore the fuel consumption does not change significantly int he investigated cycles.
In the control oriented engine model four state variables were defined to estimate the pressures and the mass flow rates. To estimate the air fractions more state variables are necessary. For future research opportunities where the HP EGR system is going to be implemented where more state variables are considered.
According to the validation results the engine model showed an accuracy of 2-3%. WHTC requires high accuracy in low torque operation points where the boost pressure is low. In these operation points the model accurracy is not satisfactory. Further research is necessary in order to tune the parameters, typically the properties of the turbocharger.

9. REFERENCES

[1] United Nations Global technical regulation No. 4; 25 January 2007
[2] **Banks, A. – Niven, M. – Andersson, P.**: Boosting technology for Euro VI and Tier 4 final heavy duty diesel engines without NO_x aftertreatment, Ricardo Consulting Engineers Ltd, Shoreham-by-Sea, UK
[3] **Zamboni, G. – Capobianco, M.**: Experimental study on the effects of HP and LP EGR in an automotive turbocharged engine, Internal Combustion Engines Group (ICEG), Department of Thermal Machines, Energy Systems and Transportation (DIMSET), University of Genoa, via Montallegro 1, 16145 Genoa Italy, Elseiver (September 2011)
[4] **Reifarth, S.**: Efficiency and Mixing Analysis of EGR-Systems for Diesel engines (Doctorate Thesis), Department of Machine Design Royal Institute of Technology (Stockholm), TRITA-MMK 2014:01

[5] **Nyerges, Á. – Németh, H.**: Low pressure intake throttle and exhaust brake support assessment on the low pressure loop exhaust gas recirculation on medium duty diesel engines, Proceedings of VSDIA 2014 (Ed. by Prof. I. Zobory), BME ITS nonprofit ZRT. Budapest, 2015, p.315-324.

[6] **Neußer, H.J. - Kahrstedt, J. - Jelden, H. - Engler, H.J. - Dorenkamp, R. - Jauns-Seyfried, S. – Krause, A.:** Volkswagen's new modular TDI® generation, 33. Internationales Wiener Motorensymposium 2012

[7] **Yamano, J. - Ikoma, K. - Matsui, R. - Ikegami, N. - Mori, S. – Yano, T.**: The New "Earth Dreams Technology i-DTEC" 1.6 L Diesel Engine from Honda, 34. Internationales Wiener Motorensymposium 2013

[8] **Bárdos, Á. – Vass, S. – Németh, H.**: Validation of a detailed commercial vehicle turbocharged diesel engine model, A Jövő Járműve 1-2, 2014, p.25-31.

[9] **Guzella, L. – Onder, Ch.H.:** Introduction to Modeling and Control of Internal Combustion Engine Sytems, DOI 10.1007/978-3-642-10775-7, Springer 2010

[10] **Bárdos, Á. – Németh, H.:** Control oriented air path model for compressed air boosted Diesel engines, Periodica Polytechnica doi: 10.3311/PPtr.7093, 2013

[11] **Jung, M. - Ford, R.G. - Glover, K. - Collings, N. – Christen, U. - Watts M.J.:** Parameterization and Transient Validation of a Variable Geometry Turbocharger for Mean-Value Modeling at Low and Medium Speed-Load Points, Powertrain & Fluid Systems, Conference & Exhibition San Diego, California USA October 21-24 2002, SAE International, 2002

COMPARISON OF DIFFERENT APPROACHES FOR ANALYSING CROSS-WIND EFFECTS ON HIGH SIDED VEHICLES PASSING BY A BRIDGE TOWER

G. QUATTROMANI, D. ROCCHI, E. SABBIONI, L.SALATI and P. SCHITO

Dipartimento di Meccanica
Politecnico di Milano
Via La Masa 1, I-20131, Milan, Italy

Received: November 9, 2016

ABSTRACT

One of the risks connected to running safety of heavy vehicles is associated to rollover due to the high cross winds which may occur in exposed sites such as embankments, bridges, etc. Specifically, the present paper compares two methodologies for investigating the interaction between a tractor semi-trailer combination and the wake of a tower bridge in cross wind conditions. The first methodology employs moving vehicle CFD simulations to evaluate the aerodynamic loads acting on the vehicle. In particular, motion of the vehicle is introduced into the CFD model using a moving mesh approach. The second methodology is instead base on a multi-body vehicle model coupled with a force distribution approach to calculate the aerodynamic forces acting on the vehicle during the tower wake crossing, which relies on static vehicle CFD simulations/wind tunnel tests. In the paper, the results of the two methodologies are presented and compared, illustrating relative advantages and drawbacks.

Keywords: Heavy-vehicles, cross-wind, moving vehicle CFD simulations, moving-mesh technique, force-distribution approach, rollover.

1. INTRODUCTION

High-sided vehicles experience sudden changes in the aerodynamic forces when passing through the wake of towers of largely exposed bridges under cross-wind. This may lead, in the worst case, to vehicle rollover or undesired lane changes and so, it represents a serious concern for running safety. To address these issues, specific fences are placed both at the edges of the bridge and close to the tower, shielding the vehicle from cross-wind.

The design of these devices however requires taking into account the driver-vehicle-wind interaction to choose the best performing solution in terms of safety. Since the complexity of the system makes an experimental reproduction of the problem on a reduced scale an extremely challenging task, the use of numerical models appears a preferable solution.

Specifically, in this paper two different approaches are proposed and compared to simulate and investigate the dynamic vehicle-bridge tower wake interaction.

The first approach applies Computational Fluid Dynamics (CFD). Open-source CFD codes *OpenFOAM*© and *ParaView*© are used on the purpose. Motion of the truck is introduced in the CFD model using a moving mesh technique coupled with Arbitrary Coupled Mesh Interface (ACMI).

The second methodology instead employs a Multi-Body (MB) model of the truck and a quasi-static force distribution approach to calculate the aerodynamic loads acting on the vehicle when passing by the bridge tower. Aerodynamic coefficients and wind horizontal profile in the tower wake needed for aerodynamic loads calculation can be

obtained using static vehicle tests (either wind tunnel experiments or CFD simulations).
In the paper the results of the two methodologies are presented and compared, illustrating relative advantages and drawbacks.

2. METHODOLOGY

The developed numerical model is made of the following subsystems:

- a multi-body model representing the dynamic behaviour of the considered heavy vehicle, which is coupled with a driver model;
- a model reproducing the aerodynamic forces and moments acting on the vehicle during the tower wake crossing, which is based on a force distribution approach and static vehicle tests (either wind tunnel experiments or CFD simulations).

2.1 Aerodynamic forces

The aerodynamic forces and moments acting on the vehicle are computed using a Force Distribution Approach (FDA, [1]-[3]), to account for wind non-uniformity as the truck crosses the tower wake. On purpose, the vehicle is divided into 5 cross-plane slices along its lengths as shown in **Fig. 1**.

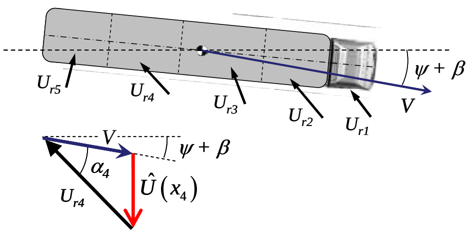

Fig. 1 Relative wind speed on vehicle slices.

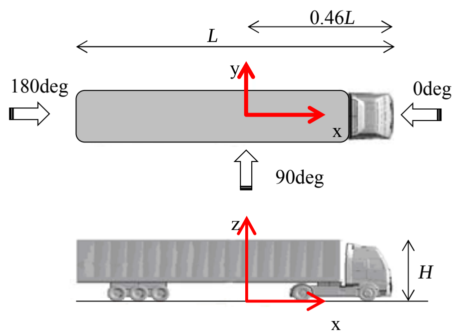

Fig. 2 Reference system for aerodynamic forces calculation and truck dimensions (H=3.84m, L=16.56m full scale).

Making reference to **Fig. 1** and **Fig. 2**, aerodynamic forces ($F_{k,i}$) and moments ($M_{k.i}$) are computed independently for each slice, according to:

$$F_{k,i}=\frac{1}{2}\rho LHC_{Fk,i}(\alpha_i)U_{ri}^2; \qquad (k=x,y,z)$$
$$M_{k,i}=\frac{1}{2}\rho L^2HC_{Mk,i}(\alpha_i)U_{ri}^2; \qquad (k=x,y); \qquad M_{z,i}=\frac{1}{2}\rho LHb_iC_{Fy,i}(\alpha_i)U_{ri}^2 \tag{1}$$

where b_i is the distance between the *i-th* slice center from the origin of the truck reference system, while L and H are respectively the vehicle length and height (**Fig. 2**).
Aerodynamic forces and moments therefore depend on the relative wind speed (U_{ri}) and the agle of attack (α_i) at the considered slice, which are calculated combining the vehicle speed (V) and the cross wind velocity horizontal profile ($\hat{U}(x_i)$) in corres-

ondence of the position of the *i-th* slice (x_i). It is worth nothing that the relative wind speed U_{ri} and the relative wind angle of attack α_i also account for vehicle yaw (ψ) and sideslip (β) angles according to the sketch of Fig. 1.
The speed of each slice is assumed to be the same and equal to the truck speed *V*, while the cross wind speed $\hat{U}(x_i)$ is calculated accounting for the *i-th* slice position in the tower wake (x_i). As it will be described in Section 4, the wind horizontal profile in the tower wake is estimated based on static vehicle CFD simulations with the truck placed at different locations with respect to the bridge tower.
The aerodynamic coefficients ($C_{Fk,i}$, $C_{Mk,i}$, see eq. (1)) of the *i-th* slice are instead evaluated based on static vehicle CFD simulations in flat ground scenario (Section 3).
In the following sections, a description of the CFD model developed to evaluate the aerodynamic coefficients of the different vehicle slices and the wind horizontal profile in the tower wake will be provided.

3. CFD SIMULATIONS

As mentioned earlier, aerodynamic coefficients of each slice and horizontal wind profile in the tower wake, which are needed by the MB vehicle model, were obtained by means of static vehicle CFD simulations. Moreover, to assess reliability of obtained results, moving vehicle CFD simulations were performed to calculate aerodynamic force/moments in the tower wake.
On purpose, a CFD model of the truck was developed using the open-source code *OpenFOAM*©: the *snappyHexMesh* pre-processor was used, the solver *simpleFoam* and the *paraView* post-process were adopted.

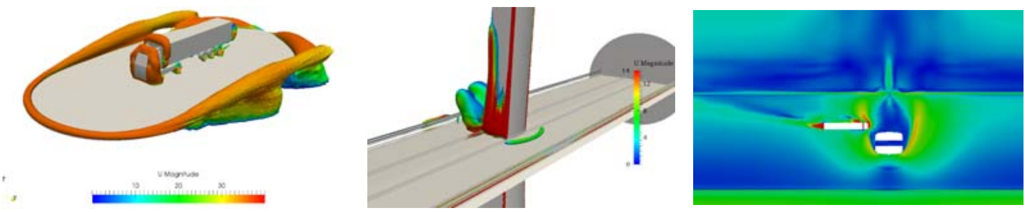

(a) (b) (c)

Fig. 3 FD simulations: (a) static vehicle in flat ground scenario, (b) deck-tower scenario, (c) moving vehicle in deck-tower scenario

Static vehicle CFD simulations were carried out both in flat ground scenario (**Fig. 3**-a) to assess aerodynamic properties of the truck for different exposure angles and in bridge deck-tower scenario (**Fig. 3**-b) to evaluate the aerodynamic forces and the wind horizontal profile in the tower wake. In this latter scenario, the vehicle was placed at different locations in the wake of the bridge tower and cross wind conditions (wind perpendicular to the vehicle) were considered. Then motion of the vehicle was introduced into the CFD simulation using moving mesh technique coupled with Arbitrary Coupled Mesh Interface (ACMI) to evaluate the moving vehicle-bridge tower wake interaction (**Fig. 3**-c).

3.1 Static vehicle CFD simulations: flat ground scenario

The developed CFD model was used to evaluate the aerodynamic coefficients of the truck in a flat ground scenario at different exposure angles. The CFD approach proposed in [4] was adopted, accounting for best practices available [8]. Specifically, since the aim was the calculation of vehicle static aerodynamic coefficients, steady-state RANS equations supplemented by SST (Shear Stress Transport) k-ω SST turbulence model [6] were solved.

3.2 Moving vehicle CFD simulations: deck-tower scenario

To estimate the horizontal wind profile in the tower wake, static vehicle CFD simulations were carried out with the developed model in bridge deck-tower scenario. In this configuration, a central tower whose cross section is 10m long and 8.5m wide (full scale) is placed in the middle of the deck (Fig. 4). It is worth noting that the tower never completely shields the truck, which is 16.65m long in full scale. Wind shields are present along all the edges of the deck. Wind fences are characterized by a porosity of 40%.

CFD simulations were performed varying the relative position between the vehicle and the bridge tower (truck-tower relative positions are reported in **Table 1**). During all the simulations the vehicle was placed in the nearest lane downwind the tower (L3, **Fig. 4**) and cross wind conditions were considered (wind direction equal to 90°, see **Fig. 2**). Even in this case, since static vehicle simulations are performed, steady-state RANS equations supplemented by SST k-ω SST turbulence model were solved.

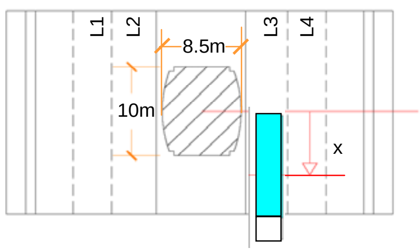

Fig. 4 Tower section and reference system for truck-tower relative position. Dimensions in full scale.

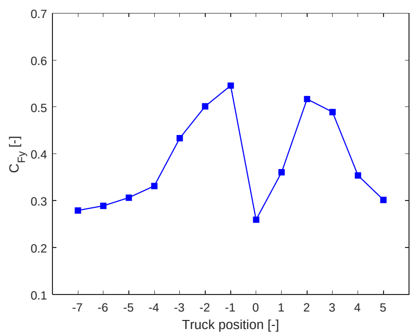

Fig. 5 Side force coefficient vs. truck position.

As an example of the obtained results, **Fig. 5** shows the overall lateral force coefficient for different truck–tower relative positions. At each position, the lateral force coefficient is calculated according to (make reference to **Fig. 2**):

$$C_{Fy} = \frac{F_y}{0.5\rho L H \overline{U}^2}, \tag{2}$$

where $\overline{U}$ is the imposed mean wind speed (undisturbed flow), H and L are the reference dimensions of the truck (**Fig. 2**), ρ is the air density, F_y is the lateral aerodynamic force acting on the truck.

As it can be seen, the lateral force increases as the truck approaches or leaves the tower, while it reaches its minimum value when the vehicle is shielded by the tower (position 0, see **Table 1**).

Position #	-7	-6	-5	-4	-3	-2	-1	0	1	2	3	4	5
x [m]	-60	-50	-40	-30	-20	-15	-10	0	10	15	20	30	40

Table 1: Tested truck-tower relative positions (measures in full scale, make reference to Fig. 4)

3.3 Moving vehicle CFD simulations: deck-tower scenario

To evaluate the aerodynamic loads acting on the vehicle as it crosses the tower wake, moving vehicle CFD simulations were performed. Motion of the vehicle was introduced into the CFD model using moving mesh technique [7]. According to this technique, cells are rigidly moved with the vehicle, without changing their topology, in order to reproduce the relative velocity between the vehicle and the infrastructure. In this way, quality of the mesh does not change during motion. A special treatment of the patches around the moving part of the domain is required by this approach, which can be solved using Arbitrary Coupled Mesh Interface (ACMI).
In this case the analysis is transient, therefore the unsteady RANS (URANS) formulation is adopted, using the k-ω SST turbulence model [6] and the solver *pimpleDyMFoam*, which couples URANS solution with dynamic mesh analysis. Second order upwind discretization scheme is adopted for all variables and the SIMPLEC algorithm is used for the pressure and velocity coupling. Time step is fixed to 10^{-3}s to guarantee a maximum Courant number lower than 1.2.

4. ESTIMATION OF WIND PROFILE IN THE TOWER WAKE

Since the wind speed is not uniform along the vehicle height (**Fig. 6**), the wind profile allowing to reproduce the aerodynamic loads acting on the vehicle as it crosses the tower wake has to be identified. To estimate the horizontal wind profile in the tower wake, an optimization procedure based on a least squares approach was implemented. Aim of the optimization procedure is the minimization of the error (e_i) between the aerodynamic lateral force and yaw moment acting on each of the 5 slices predicted by the model ($\hat{F}_{yi}$, $\hat{M}_{zi}$) described by eq. (1) and the results of CFD simulations (F_{yi}, M_{zi}):

$$e_i = \left|F_{yi}(x_j) - \hat{F}_{yi}(x_j)\right| + \left|M_{zi}(x_j) - \hat{M}_{zi}(x_j)\right| \tag{3}$$

As the estimates of the aerodynamic lateral force and yaw moment on the *i–th* slice at the *j-th* position are a function of the horizontal wind speed profile

$$\hat{F}_{yi}(x_j) = \frac{1}{2}\rho LHC_{Fy,i}(\alpha_i(x_j))\hat{U}_{ri}^2(x_j); \qquad \hat{M}_{z,i}(x_j) = \hat{F}_{yi}(x_j)b_i \tag{4}$$

the minimization of the error leads to the identification of the horizontal wind profile at the *j-th* position ($\hat{U}_{ri}(x_j)$). It must be pointed out that since the same (or a similar) position is reached by different vehicle slices, the estimate of the wind profile at the *j-th* position is the value minimizing the error associated with the different slices. Specifically, the 13 positions reported in **Table 1** were used and only vehicle slices overlapping more than 80% at a given position were averaged to estimate the wind profile. Fig. 7 compares the estimated wind horizontal profile (red dashed line) vs. the distance from the tower with the horizontal wind profile at different heights (3m, 4m, 5m).

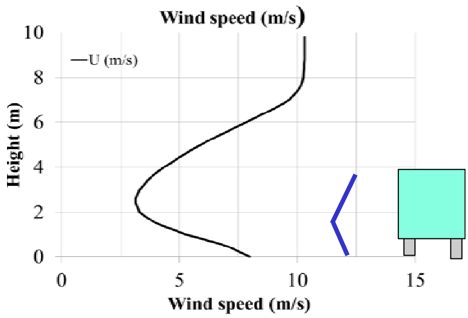

Fig. 6 Vertical wind profile away from the bride tower.

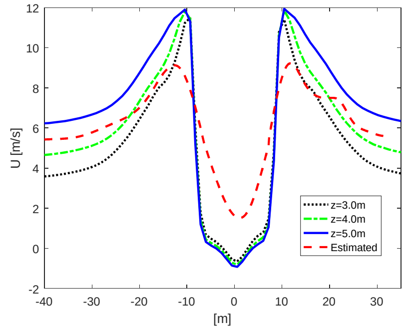

Fig. 7 Estimated wind horizontal profile vs. distance from the tower centre: comparison with wind profile at different heights.

5. VEHICLE MB MODEL

Vehicle dynamic response is simulated using a multi-body (MB) model implemented in MatLab/SimuLink/SimMechanics environment. The considered vehicle is composed of a two axles tractor and a three axles semi-trailer. The model is made of 7 rigid bodies (i.e. the tractor and the semi-trailer carbodies and the 5 axles) and has 22 degrees of freedom (dofs). Tractor and semi-trailer are connected by a non ideal spherical joint. Tires are introduced by means of MF-Tyre model, accounting for combined slip effects and vertical load dependency.

The overall aerodynamic forces and moments are computed as the sum of the five slices contribution (see eq. (1) of Section 2.1).

The vehicle model is coupled with a path-follower driver model to perform closed loop manoeuvres ([3],[5]). To keep the vehicle on the desired trajectory, the driver model calculates the steer angle, δ, according to a proportional-integrating-derivative (PID) regulator aimed at minimizing the error between the reference and the actual path followed by the vehicle.

6. RESULTS

Results of the MB vehicle model supplied by the developed quasi-static force distribution approach for aerodynamic load calculation were compared with moving vehicle CFD simulations.

The passage of the truck (moving on a straight line in the lane nearest to the tower) in the tower wake at the constant speed of 20m/s was simulated. A cross-wind of 10m/s (about 6m/s in correspondence of the truck away from the tower) before the wind shields placed at the bridge edges (characterized by a porosity of about 40%) was considered.

The comparison between the aerodynamic loads predicted by the moving vehicle CFD model (solid blue line) and the ones calculated using the MB model + force distribution approach (red-dashed line) is shown in Fig. 8.

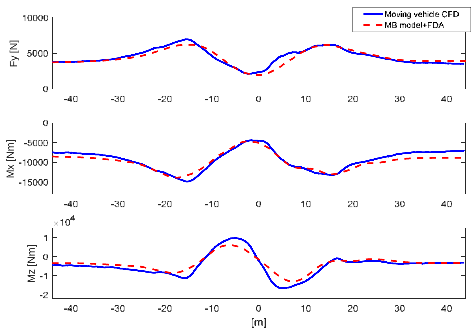

Fig. 8 Comparison between CFD and MB results: overall aerodynamic loads on vehicle.

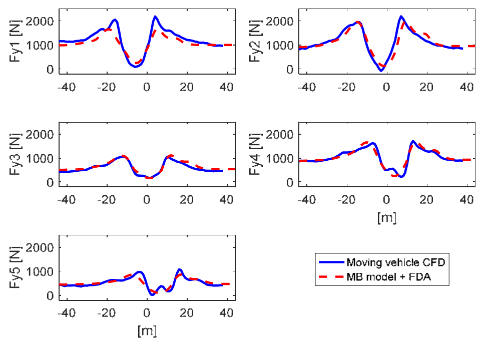

Fig. 9 Comparison between CFD and MB results: side aerodynamic force on vehicle slices.

Overall aerodynamic side force (F_y, top of the figure), overturning moment (M_x, centre of the figure) and yaw moment (M_z, bottom of the figure) are shown. The centre of gravity of the truck is aligned with the centre of the bridge tower at 0m. As it can be seen, a good agreement can be noticed between CFD and MB data. A slight underestimation of the aerodynamic loads at tower enter/exit can be observed. This issue may be recovered improving wind profile estimation in the tower wake. To deepen the analysis the aerodynamic lateral force acting on the 5 vehicle slices is reported in **Fig. 9**. The highest error occurs at the first vehicle slice (i.e. the tractor). This may suggest a refinement of vehicle slices for the tractor for improving estimation of the aerodynamic loads.

7. CONCLUDING REMARKS

A MB model supplied by a force distribution approach for aerodynamic load calculation during the crossing of a bridge tower wake was compared with a moving vehicle CFD model employing the moving mesh technique. Simulation results stated the capability of the MB model + FDA to reproduce moving vehicle CFD data, whist significantly reducing computational effort.

The key point for aerodynamic loads calculation with FDA is the estimation the wind horizontal profile in the tower wake. The more accurate is the estimate, the higher is the accuracy of obtained results with respect to CFD data.

It is to point out that the force distribution approach for aerodynamic load calculation is based on static vehicle CFD simulations (or alternatively static vehicle wind tunnel tests) and this allows to limit computational effort (or complexity of the experimental setup in the case of wind tunnel tests) with respect of moving vehicle CFD simulations.

Moreover, MB model + FDA allows the coupling with a driver model, so to investigate vehicle + driver response under cross-wind conditions for different wind shielding solutions. Thus the proposed model could represent a valuable tool for assisting bridge engineers in designing/comparing different solutions for ensuring running safety under cross-wind.

8. REFERENCES

[1] **Charuvisit, S. – Kimurab, K. – Fujinoc, Y**.: Experimental and semi-analytical studies on the aerodynamic forces acting on a vehicle passing through the wake of a bridge tower in cross wind. Journal of Wind Engineering and Industrial Aerodynamics, 92(9), 2004. p.749-780.

[2] **Belloli, M. -, Rocchi, D. – Rosa, L. – Sabbioni, E. – Sbrosi, M.:** A numerical–experimental methodology for simulating the aerodynamic forces acting on a moving vehicle passing through the wake of a bridge tower under crosswind. Journal of Wind Engineering and Industrial Aerodynamics, 104-106, 2012. p.256-265.

[3] **Galeotti, R. - Rocchi, D. - Sabbioni, E. - Sbrosi, M.:** Dynamic Response of Vehicle-Driver Couple to the Aerodynamic Loads due to the Crossing of a Bridge Tower Wake. SAE International Journal of Commercial Vehicles, 5(1), 2012. p.83-93.

[4] **Salati, L. – Schito, P. – Cheli, F.:** Heavy Truck Drag Reduction Obtained from Devices Installed on the Trailer", SAE International Journal of Commercial Vehicles, 8(2), 2015. p.747-760.

[5] **Cheli, F. – Belforte, P. – Melzi, S. – Sabbioni, E. – Tomasini, G.:** Numerical-experimental approach for evaluating cross-wind aerodynamic effects on heavy vehicles. Vehicle System Dynamics, 44 Supplement, 2005. p.791-704.

[6] **Menter, F.R.:** Review of the shear-stress transport turbulence model experience from an industrial perspective. International Journal of Computational Fluid Dynamics, 23(4), 2009. p.305-316.

[7] **Jasak, H.:** Dynamic mesh handling in OpenFOAM. Proc. 47th AIAA Aerospace Sciences Meeting Including The New Horizons Forum and Aerospace Exposition, 5-8 January, Orlando, Florida, 2009.

[8] **SAE International Surface Vehicle Recommended Practice,** Guidelines for Aerodynamic Assessment of Medium and Heavy Commercial Ground Vehicles Using Computational Fluid Dynamics. SAE Standard J2966, Rev, 2013.

STRUCTURE AND ARCHITECTURE PROBLEMS OF AUTONOMOUS ROAD VEHICLE TESTING AND VALIDATION

Zsolt SZALAY

Department of Automobiles and Vehicle Manufacturing
Faculty of Transportation Engineering and Vehicle Engineering
Budapest University of Technology and Economics
Stoczek street 2, H-1111 Budapest, Hungary,
zsolt.szalay@gjt.bme.hu, phone: +36 1 463 1615 fax: +36 1 463 3978

Received: September 12, 2016

ABSTRACT

In the not-too-far vision of autonomous driving (e.g. level 4 according to SAE J3016) the human driver is no longer responsible for the fallback performance of certain automated driving tasks. In case of level 5 automation the human driver will be substituted in all driving modes without any human fallback responsibility of the dynamic driving tasks. This article draws the attention to this change (human driver exchange for electronic control system) from the electronic control perspective and its effect to the future system testing and validation methodologies. Today vehicle testing and type approval are based on completely standardized processes that rather focus on the vehicle endurance characteristics and vehicle dynamics, extended with limited, but well reproducible use cases for the advanced drives assistance systems (ADAS). While in the future systematic testing and repeatability will still be a big part of the testing and validation methodology, automated driving will also require new approaches and this is where the Hungarian autonomous vehicle proving ground can make a difference. The proving ground is designed specifically for autonomous vehicles and planned to be built by end of 2017 in Zalaegerszeg. As the BME and the RECAR (REsearch Center for Autonomous Road vehicles) took major role in the technical specification process, this article will also explain the methodology of the composition of the technical requirement together with the industry lead automotive suppliers, governmental bodies and authorities.

Keywords: testing, validation, autonomous driving, connected and automated vehicles, proving ground, test track

1. INTRODUCTION

Connected and automated driving created new challenges to the automotive industry. Beyond providing safe technical solutions there are new areas that have to be considered, when talking about the deployment of automated driving. First of all, the missing legal environment delays the deployment. Until there are no internationally harmonized rules for regulating insurance and liability questions there will always be a question after a road accident: how to identify liability and how to program liability into automated road vehicles? Since automated vehicles will be connected as well and each of them will generate a huge amount of vehicle related data, data collection and ownership rules has to defined: how to make the data access and data handling transparent and still guarantee the protection of the personal data? Recent attacks have shown that todays' vehicles are already vulnerable to cyber-attacks. In an automated vehicle where steering and braking will happen based on electronic commands by design, cyber security of vehicles is an essential portion to maintain public acceptance of automated driving. But experts still do not know how to prevent the malice or bad intended use of the vehicles intelligent functions. Last but not least driverless vehicle technology requires new methodology for testing and validation to make sure that AD vehicles are safe and reliable.

2. DISRUPTIVE CHANGES DUE TO AD VEHICLES

The technology transformation due to the challenges of connected and automated driving are no longer just based on incremental improvements, but rather on disruptive in-

novation. On one hand, automated vehicles are no longer separate entities they are embedded into the traffic and surrounding environment. On the other hand, in automated driving the human driver is getting out of the control loop. These two major alterations result in several new phenomena in the automotive development, especially in the testing and validation processes.
To explain how disruptive the change that we have to face let just take vehicle dynamics control (VDC) applications as an example. They were designed to interfere when the human driver based control result in a deviation from the ideal or safe state of the vehicle. When there is no human driver in the loop there will be no need for corrective actions for erroneous driver intention.
From control point of view the differences between a human driver and an electronic control system can be categorized into three layers, namely the capability to access information (1), to make the right decision (2) and finally the capability of the intervention (3). Although ADAS testing and validation reveals already the limitations of the state-of-the-art testing and validation processes (e.g. malicious behaviour of the camera based systems in case of special lighting conditions) this is just the top of the iceberg. Today's testing is concentrated on dedicated scenarios and the rest of the real cases are the drivers' liability. In autonomous driving, the number of the potential cases is so high that they cannot be physically tested. New approaches are required and the testing and validation focus will shift towards special circumstances that may have an influence on the AD system performance.

3. NEW APPROACH FOR TESTING & VALIDATION

Within the framework of the RECAR program (REsearch Center for Autonomous Road vehicles) a new systematic approach has been worked out for meeting this future challenge in vehicle testing and validation. This new approach is visualized below as a so-called testing and validation pyramid, which layers will be explained in details in the following chapters.

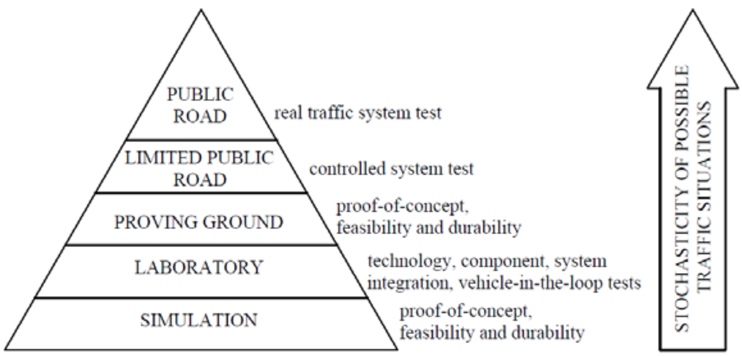

Fig. 1 Autonomous Vehicle Testing & Validation Pyramid

There are different testing levels required by the connected and automated vehicles starting from virtualization to reality testing: computer simulation (1), laboratory testing (2), test track/proving ground testing (3), limited/controlled public road testing (4), open public road testing (5).

Thy pyramid is composed to be able to cover conventional vehicle tests and automated driving related vehicle tests as well. It became obvious that vehicle dynamics testing in itself will not be enough for the future. The test cases should also address testing the vehicles' environment perception capabilities, the interaction to other vehicles, other road users and the infrastructure. Additionally, connected vehicles require the testing of different communication technologies, either DSRC based or cellular based solutions. On top new algorithms validation will not work like before for example in the case of deep learning algorithms.

3.1 Layer 1 - Computer Simulation

On the path from virtualization to reality, the first station is computer simulation providing background for different proof-of-concept, feasibility but also durability tests. In the new approach, the limitations of the different simulation environments are in focus. In most cases the vehicle dynamics is quite well simulated, but the vehicle surrounding is missing to a certain degree, to be able to put vehicle (VUT) into a traffic scenario or simulate the corresponding V2V or V2I communication. We believe that virtual testing and validation key features should involve integrated vehicle dynamics simulation, integrated traffic simulation, virtual environment composition with real world simulation. The environment should simulate the interaction with other road users and potentially the visibility and the weather conditions. Later region dependent road type and traffic sign simulation could also be added to the comprehensive approach.

Simulation means a mathematical modelling of a well-defined part of the real world. To reach good enough results by simulation it is important to define the required complexity of the models. Knowing the capabilities, the neglected effects and the limits of the simulation model can make the design process efficient.

The next step is to use the available simulation software for modelling road vehicles and the traffic situations. From functional point of view we consider that model-in-the-loop (MIL) and software-in-the-loop (SIL) tests are carried out within this layer.

There are two types of commercially available automotive simulation software. The first type focuses on the vehicle dynamics: the integrated vehicle dynamics simulation software. In the conventional vehicles the earlier important requirements were the safety and the easy handling. Designing a car according to these expectations needs simulation of the vehicle dynamics to evaluate system operation: the engine performance, brake performance, suspension performance and the harmonization of them. These simulation environments implement the longitudinal, the lateral and the vertical vehicle dynamic equations and the role of the stochasticity is small here. Some typical examples for this software are CarSim, CarMarker, VI-CarRealTime, Dyna4 Driver Assistance, Dymola, EB Assist ADTF and dSpace Motiondesk. Most of these simulation environments can handle basic traffic situations too (they can test the present driver assistant systems).

The second type focuses on traffic situations. These simulation environments have been developed for transport engineers, to design the traffic of cities. In the software the vehicle models are very simple. The aim is to make faster the transport in complex traffic networks. Some examples for this software are PTV VISSIM, CityTrafficSimulator, MovSim and UAF.

The simulation environment which represents the future for automated vehicles integrates these two key features, where the vehicle is handled by the part of the environment, not an independent system. A typical example for this is PTV VISSIM which is able to simulate automated vehicles in every SAE level. In the next years many simulation environments will develop in this direction.
Another aspect for traffic situations is to simulate the interactions between the different road users. For example implementing the vulnerable road users (VRU) prepares the possibility of the perception of them and to simulate the V2X communication. There are researches to save the pedestrians and the bicycle users by vehicle sensors, typically based on video camera signals. The shape and the movement are distinctive most of VRU-s, and by this information the position of them can be predicted.

3.2 Layer 2 - Laboratory Tests

Within the laboratory layer, together with our industrial partners we identified the requirements for laboratory testing. The requirements were then categorized into four groups. Technology research laboratories are rather deal with specific technology researches like RADAR technology. Component analysis laboratories will enable to test certain components like a specific RADAR device of a selected manufacturer. This would also enable to produce component benchmarking tests, showing the advantages and the limitation of a certain component design. System integration laboratories are testing environments for more than one component. Besides the component testing part, the interaction of the components are also investigated and evaluated here. The most complex laboratory proposed is the so-called vehicle-in-the-loop laboratory, where according to our imagination an autonomous vehicle can drive in and without any injection (the least possible injection) into the vehicle system, the surrounding would be created in a way that can simulate all the inputs of the automated vehicle in a coherent way in real-time, so that a tested AD vehicle would believe it is driving in a real traffic environment. It would include video frames or rendered LIDAR frames all around the vehicle to make the optical systems believe it is running on real road. It would also include RADAR target simulator devices so that the vehicles RADAR system would also believe there are physical objects in around the vehicle in positions where the video frame shows. The VIL simulator would also have a roller brake test bench under the tested vehicle not just simulating the longitudinal control but also enabling to simulate lateral control by the turning of the steered wheels. Such laboratory is so complex that there are only a few similar existing ones worldwide, they have to be designed and built specifically integrated into several computer simulators.

3.3 Layer 3 - Proving Ground Tests

The main advantage of test tracks in general is the predictable safety, since they are not publicly accessible. The radical difference in our new approach of an automotive proving ground is in the design concept, making it compatible for conventional vehicles and for connected and automated vehicle tests together. In the following design all components fulfil the so-called standard requirements of a conventional test track, and they are also suitable to fulfil the connected and automated vehicle testing and validation requirements. The different proving ground elements are interconnected with road sections enable the formulation of combined testing processes.

The new proving ground is being designed based on the requirement specification of the relevant industrial companies in cooperation with academic participants. Fig. 2 demonstrates the outline of the complete proving ground concept incorporating the basic vehicle dynamics elements and the autonomous vehicle specific testing functions. The proving ground has the following functional sections: High-speed oval (1), Dynamic surface (2), Braking surfaces (3), Handling courses (4), Motorway section (5), Rural road (6), Smart City Zone (7). The proving ground will be built on a 260 hectare area with an overall estimated budget of 130 million EUR.

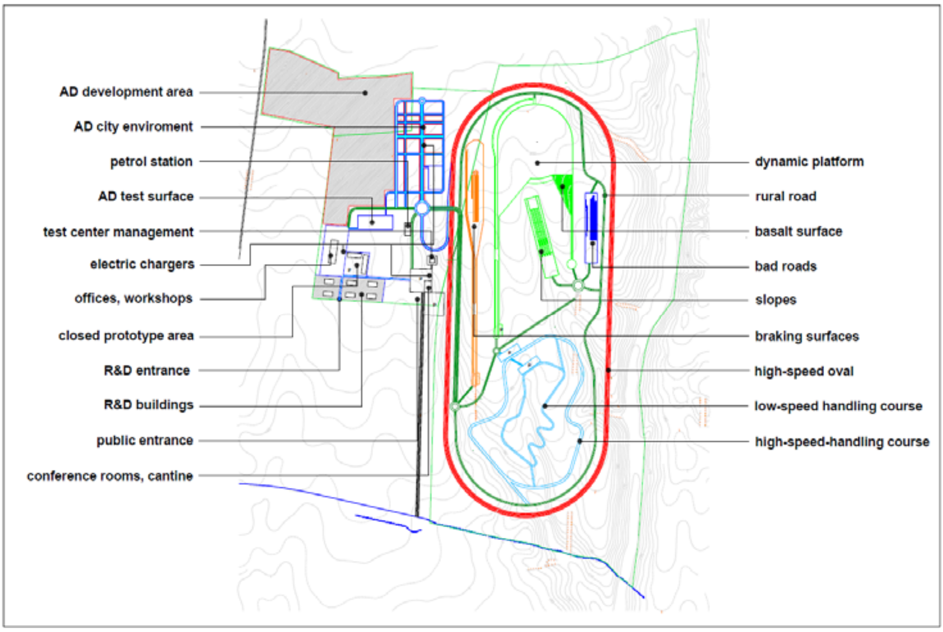

Fig. 2 Automotive proving ground dedicated to connected and automated vehicle testing and validation at Zalaegerszeg

The test track will not only provide a passive environment for vehicle testing but also the active environment (e.g. intelligent traffic control, V2I communication) for the integral testing of automated driving functions. Different test scenarios (obstacles, traffic signs, traffic control, other vehicles, vulnerable road users, etc.) can be prepared and controlled for the analyses of specific situations. In the proving ground, the automated vehicles are in permanent interaction with the surrounding environment.

The objective is to build a proving ground suitable for every type of testing starting from prototype testing till series production testing and validation of connected and automated vehicles. The top use case vision of the proving ground is to provide a comprehensive testing scenario for a level 4 autonomous driving from suburban home to city office and valet parking (rural road, highway traffic, sub-urban area, city environment with continuous transition).

3.4 Layer 4 - Limited Public Road Tests

Closed circuit vehicle tests are essential, but no question that automated vehicles must also be tested on public roads before their type approval process. The controlled proving ground tests are a basis to start a next level testing on public roads. We feel that before the fully open public road testing there has to be an intermediate testing and validation layer. This layer would be a controlled area of a city, where the traffic regulations are modified to guarantee safety. This controlled area would be a dedicated "Test City". It might also be combined with a so-called "smart city"- we would like to use the synergy effect with a Smart City environment. Modified regulation could be an exclusion of certain vehicle categories, typically the vulnerable traffic participants: pedestrians, cyclists, motorcycles, etc. Working closely together with the city of Zalaegerszeg to compose a dedicated „Test City" area within Zalaegerszeg incorporating challenges for the connected and automated vehicles like bridges, tunnels, railway crossing and smart city features. The proposed limited public route can be observed on Fig. 3. that extends the test city zone of the closed proving ground.

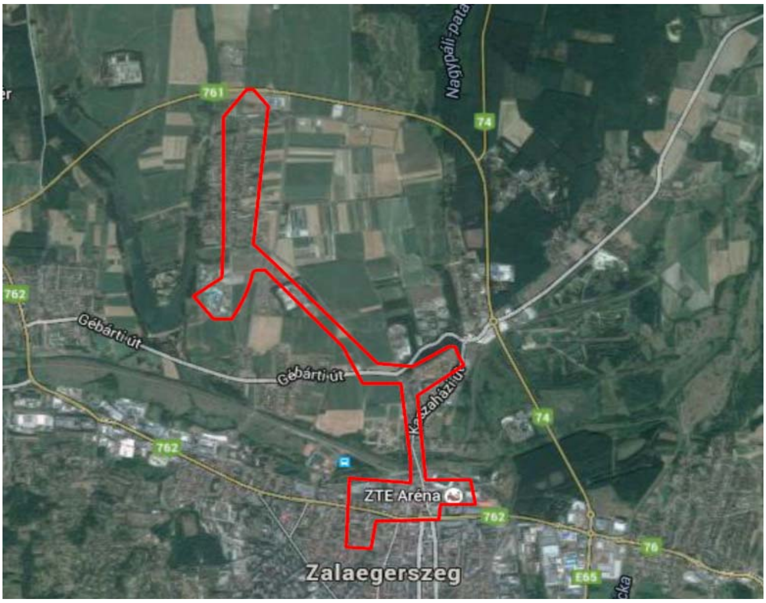

Fig. 3 The extended testing zone in the City of Zalaegerszeg

3.5 Layer 5 - Public Road Tests

It is no question that the automated and autonomous vehicles must also be tested in real public road environment, since the stochasticity of the potential scenarios cannot be produced in closed (partially or fully controlled) locations. On the other hand, one must be sure that before starting the open road testing every safety measures had been carried out before, including simulations, closed proving ground testing and limited public road testing.

In Hungary there are preparations to modify the traffic rules in order to enable open public road testing of CAVs under specific circumstances. Through continuous consultation with the automotive industrial companies a requirement list for the legal modification was prepared and submitted to the National Traffic Authorities. The proposal has prerequisites for the "Vehicle Developer Company", the "Vehicle Under Test" and the "Personnel (Test Driver)" in order to assure safety. After long discussions, the

Hungarian approach shifted to the self-certification direction putting all the liability in the proposal to the highest-ranking officer of the vehicle developer company.

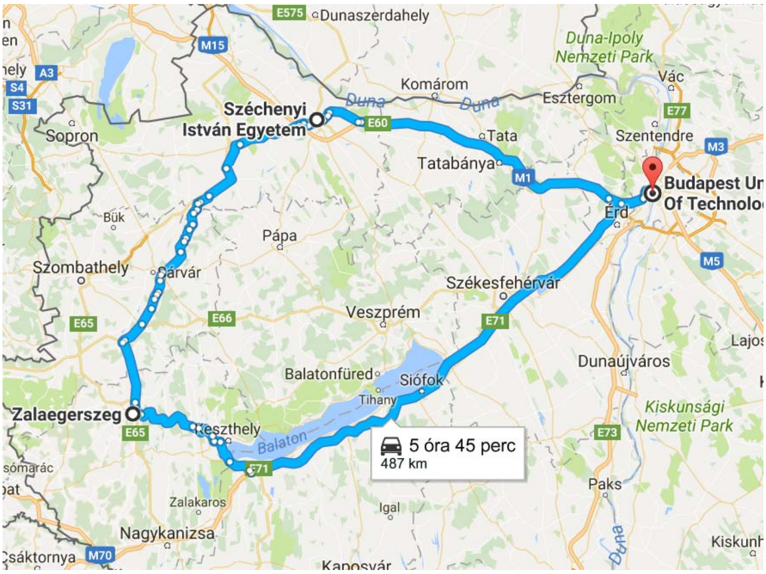

Fig. 4 Suggested smart road test circle for CAVs within Hungary, connecting Budapest and Győr to the Automotive Proving Ground at Zalaegerszeg

The objective is to create a complex and integrated multi-level testing environment with the built-in potential for future extension. This is the so-called ZONE concept, where apart from conventional vehicle testing and CAV closed track testing there is a possibility to do tests in real urban environment (in Zalaegerszeg), on public rural roads and on motorways. The proposal is under public consultation now and is expected to be released officially within months. It is planned that beginning of next year autonomous vehicle functions will be allowed to be tested on Hungarian public roads. Though the proposal does not have territorial limitations, there is a suggested highway and rural road circle (see Fig. 4.) connecting Budapest, the capitol of Hungary with Győr (having high density of Automotive Industry) and the new proving ground at Zalaegerszeg, enabling the testing of automated function through the way reaching the proving ground. The Budapest Győr part of the M1 highway is already equipped with ITS-G5 road side units (RSU) to support connected car function testing as well.

4. CONCLUDING REMARKS

Automated and connected vehicles are unavoidably going to change road transport in the future. The major motivation is to reduce the number of accidents since they can mostly be traced back to human errors. To be able to guarantee the safe operation of connected and automated vehicles we need to have dedicated testing environments including disruptive testing and validation processes for the new autonomous systems and features. In this paper, a new approach was proposed to overcome these structural and architecture problems. Within the framework of the RECAR program the Budapest University of Technology and Economics has worked out a strategic plan for the testing and validation of connected and automated vehicles. This is classified by the layers of the connected and automated vehicle testing and validation "pyramid". The methodology guarantees that every layer of testing and validation is addressed in a systematic way conforming to the requirements of the automotive industry. The proposal contains the plan all of the "pyramid's" layers and we hope that by implementing it we will have the chance to validate our ideas and new testing and validation methodologies can be based on this paper. Apart from that we also hope that the new test track will serve the competitiveness of the region.

5. REFERENCES

[1] SAE International (2014). Taxonomy and Definitions for Terms Related to On-Road Motor Vehicle Automated Driving Systems, SAE standard, nr. J3016_201401, 2014-01-16. URL: http://standards.sae.org/j3016_201401/

[2] **Gáspár, P - Szalay, Zs. - Aradi, Sz.**: (2014). Highly Automated Vehicle Systems. BME MOGI. URL: http://www.mogi.bme.hu/TAMOP/jarmurendszerek _iranyitasa_angol / index.html

[3] PROSPECT project 'Accident Analysis, Naturalistic Observations and Project Implications' (2016) http://www.prospect-project.eu/download/

[4] **Tettamanti, T. - Varga, I. - Szalay, Zs.:** Impacts of Autonomous Cars from a Traffic Engineering Perspective, Periodica Polytechnica Transportation Engineering, Vol. 44, No. 4, 2016, p. 244-250, DOI: 10.3311/PPtr.9464

[5] **Miller, A.:** (2016) 'EuroNCAP roadmap – autonomous vehicles, vehicle and system testing'. Paper presented at Vehicle Test & Development Symposium 2016. 2nd June 2016. Stuttgart, Germany.

[6] **Piperno, A.:** (2016) 'UTAC CERAM first results, testing and homologation worldwide reference'. Paper presented at Vehicle Test & Development Symposium 2016. 2nd June 2016. Stuttgart, Germany.

VALIDATION OF AN AGRICULTURAL DRIVEN AXLE LUBRICATION MODEL

Csaba KOKREHEL and Huba NÉMETH

Department of Automobiles and Vehicle Manufacturing
Budapest University of Technology and Economics
H-1111 Budapest, Sztoczek J. u. 6. Bld. J. 5th floor.
csaba.kokrehel@gjt.bme.hu,

Received: November 9, 2016

ABSTRACT

A mathematical model of a hydraulic system for agricultural vehicle driven axle lubrication has been designed and validated by measurements. The main subject of this paper is the validation process of the model that gives the basis for an oil flow-controlled axle lubrication control design in further researches. The hydraulic system contains a mechanically driven oil pump, oil filter, cooler circuit, piping and nozzles that lubricate several driveline elements in the axle. The main oil consumer parts of the driveline are: bearings, gear contacts, wet brakes. Depending on operation parameters the separated consumers require varying oil flow in time and in share.. The presented axle lubrication system transfers constant oil flow rate to every spot. On the end of the oil circuit dedicated nozzles lubricate the driveline elements. A complex measurement for the whole system is done including driveline mechanical, and lubrication system thermal, and flow states. The validation process is focusing on the states that are in close relation with the lubricant oil flow rate. During the validation tests, the axle input speed was increased step-by-step, and held until the oil pressure in the lubrication circuit has stabilized. Pressure measurement is performed on several points of the hydraulic circuit, so the pressure drop of the lubrication system elements can be validated also. The total hydraulic loss of the lubrication system mainly influences the system eigen-dynamics. A flow-meter is attached serial to the lubrication circuit, thus the precise flow-rate is measured also. The overall validated hydraulic lubrication system model gives a tool for further researches in order to design a control system for a multi circuit, distributed flow lubrication system.

Keywords: axle lubrication system simulation, hydraulic simulation, lubrication model

1. INTRODUCTION

In commercial vehicle industry driven axles are mostly equipped with wet sump stray or guided oil flow lubrication system. Forced lubrication systems are rather tipical in agricultural, ball handling or other heavy duty machines. As the legal regulations on vehicle emissions getting more and more strict the overall driveline efficiency is getting into focus even in the off-highway segment.

In on-highway commercial vehicle categories the driveline „downspeeding" disciple became also a strategy like in engine design. Since the local power losses in the driveline rather depend on the speed and less on the load of the shafts, bearings and gears, the overall driveline losses can be reduced by lowering the axle speed. This process is clearly observable on the ratio tendency of commercial vehicle axles during decades.

Agricultural market is different, because the high torque ratio in the axle is essential. The performance of agricultural machines on the market are between 100 – 400 kW, since the ratio of the axle can be up to 26-30, and in the heaviest categories even more. The high torque ratio means that some of the axle driveline parts are rotating with high speed (like the input pinion), some parts with medium (like differential housing and wheel-hub driveshafts) and some parts with very low speed, but extreme load (like the wheel-hubs). The lubrication system of these axles is usually hybrid designed with both wet sump and forced lubrication elements. Usually the mechanically driven forced lubrication part is overdesigned on high speeds, to meet the oil flow requirements on lowers. This way there is a huge potential in the axle lubrication system, to make the losses much smaller, not only thanks to the high hydraulic losses of the wet sump part, but also to the mechanical and hydraulic losses of the forced lubrication sub-system.

2. SIMULATION TARGET

Target system is a driven agricultural axle with forced lubrication on several points of the drive-chain. The focus of this paper is to build up a detailed, validated model of the lubrication system to support further researches on system performance and efficiency. Hydraulic model therefore is a lumped-parameter, 0D type, not focusing on the longitudinal pressure distribution in time, only calculating temporary average pressure level and temperature values in discrete flow volumes.

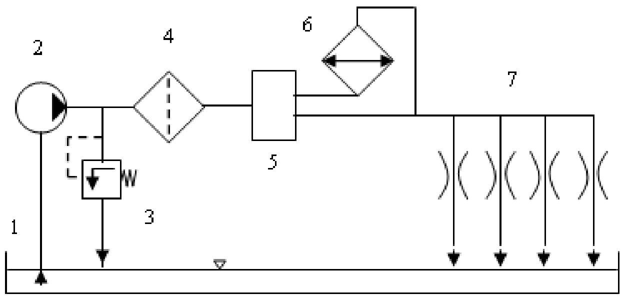

Fig. 1 Hydraulic circuit of the investigated driven axle. 1 – Oil sump, 2 – Oil pump, 3 – Pressure limiter valve, 4 – Filter, 5 – Oil cooler bypass valve, 6 – Oil cooler, 7 – Nozzles (4 pcs.)

Since the modelling target is to get detailed information on the system behaviour, the hydraulic circuit described on the Fig. 1 contains numerous elements that are needed to be implemented in the dynamical simulation.

3. MODELLING PROCESS

According to the references, two basic techniques are used for simulating hydraulic flows. Both of them use the hydro-elastic behaviour of the fluids, that they are only theoretically non-compressible. To reach any pressure rise in a fluid, it must be either elastic, or contain some gas (air) on molecular level, that stands for the compressible feature indeed. The physical feature of the system used in this research is illustrated on Fig. 2. Oil flow generated by a gear-type pump always contains some air. In the simulation the initially estimated air volume is taken as constant all along the hydraulic circuit.

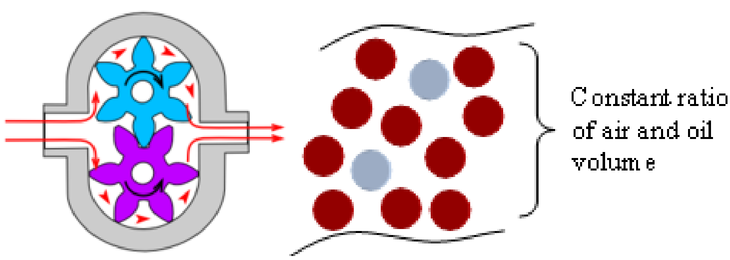

Fig. 2 Hydraulic circuit of the investigated driven axle.

A hydraulic circuit as a modelling target can be divided into pressurized and non-pressurized sub-systems. The modelling process between the two groups is essential for complexity and functionality, therefore the group of the elements being modelled is crucial to be defined previously. Non pressurized system elements are usually the oil pump and oil sump. Pressurized sub-system of a hydraulic circuit is usually built up of two types of system components:

- Hydraulic volume type elements
- Orifice-type elements

Hydraulic volume-type elements are implemented to calculate pressure along the flow, while orifice-type elements calculate the flow between two volumes. Parameter setup defines the functionality of a volume-type element. This way, for modelling a hydraulic system, only a few basic elements need to be modelled, and various system architectures can be constructed easily. Due to parameter diversification, the following model elements can be reached from volume-type base element:

Parameter	Value	Resulting model
Volume	High	Tank
	Low	Piping
Heat transfer coefficient	High	Cooler
	Low	Piping
Contraction coefficient after the volume	High	Nozzle, Filter
	Low	Piping or tank

Table 1 Accessible hydraulic model elements by parameter setup.

Fig. 3 describes the implemented system after modelling simplification.

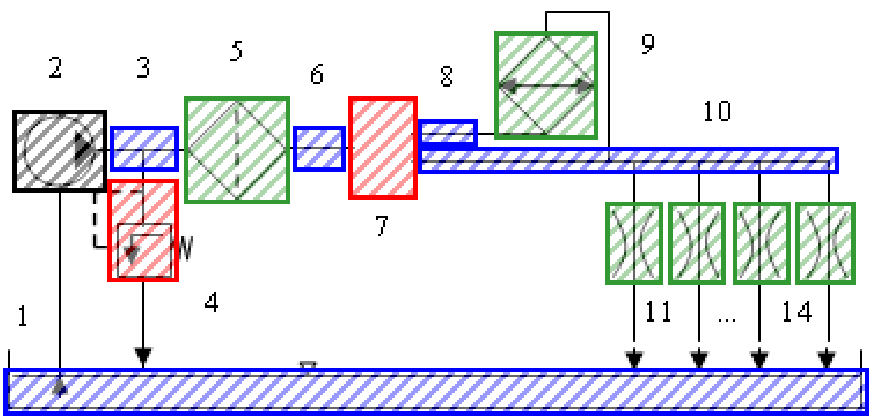

Fig. 3 The implemented hydraulic system. BLACK – excitation (pump), BLUE – Volume type elements, GREEN – nozzle (orifice) elements, RED – Orifice elements with flow distribution.

4. MODELLED ELEMENTS

System element models and equations are described in the following chapters.

4.1. Hydraulical volume-type elements

Oil sump physical model:

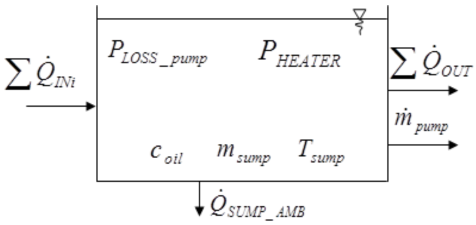

Fig. 4 Oil sump physical model.

Based on the physical model of the oil sump, the following energy and mass balance equiations can be set:

$$\frac{dT_{sump}}{dt} = \frac{1}{m_{sump}c_{oil}}\left(-\frac{dm_{sump}}{dt}T_{sump}c_{oil} + P_{HEATER} + P_{LOSS\_pump} - \dot{Q}_{SUMP\_AMB} + \sum \dot{Q}_{INi} - \sum \dot{Q}_{OUT}\right) \quad (1)$$

$$\frac{dm_{OIL\_sump}}{dt} = \sum \dot{m}_{OIL\_sump\_IN\_i} - \dot{m}_{OIL\_sump\_OUT} \quad (2)$$

Algebraic equiations:

$$\sum \dot{Q}_{INi} = \sum \dot{m}_{OIL\_sump\_IN\_i} c_{oil} T_i \quad (3)$$

$$\sum \dot{Q}_{OUT} = \sum \dot{m}_{OIL\_sump\_OUT} c_{oil} T_{sump} \quad (4)$$

$$\dot{m}_{OIL\_sump\_IN\_i} = \eta \dot{m}_{sump\_IN\_i} \quad (5)$$

$$\dot{m}_{OIL\_sump\_OUT} = \eta \dot{m}_{SZIV} \quad (6)$$

According to the „Modelling process" chapter, the pressurized volume-type elements can be simulated by a common base model. Fig 5. illustrates the model of pressurised volume-type elements.

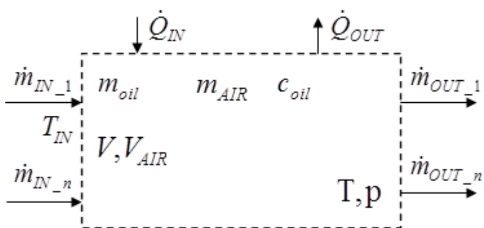

Fig. 5 Model of pressurized-type oil volume elements.

Based on the physical model of the pressurized-type volume elements, the following equations can be set as mathematical model for the „i" model part:

$$\frac{dT_i}{dt} = \frac{1}{m_{OIL} c_{oil}} \left[\sum \dot{Q}_{IN} - \sum \dot{Q}_{OUT} + \sum \dot{m}_{IN} c_{oil} T_{IN} - \sum \dot{m}_{OUT} c_{oil} T_i \right] \tag{7}$$

$$\frac{dm}{dt} = \dot{m}_{IN} - \dot{m}_{OUT} \tag{8}$$

$$\frac{dm_{OIL}}{dt} = \dot{m}_{OIL\_IN} - \dot{m}_{OIL\_OUT} \tag{9}$$

$$\frac{dm_{AIR}}{dt} = \dot{m}_{AIR\_IN} - \dot{m}_{AIR\_OUT} \tag{10}$$

$$\frac{dp_{AIR}}{dt} = \frac{1}{V_{AIR}} \left[\frac{dm_{AIR}}{dt} RT + m_{AIR} R \frac{dT}{dt} - \frac{dV_{AIR}}{dt} p \right] \tag{11}$$

$$\frac{dV_{AIR}}{dt} = \frac{1}{\rho_{OIL}} \left[\dot{m}_{OIL\_OUT} - \dot{m}_{OIL\_IN} \right] \tag{12}$$

As described in the „Modelling process" chapter, the mass of entering and leaving oil and air can be calculated by a constant value, that estimates portion of air in the flow:

$$\dot{m}_{OIL\_IN/OUT} = \eta \dot{m}_{IN/OUT} \tag{13}$$

$$\dot{m}_{AIR\_IN/OUT} = (1-\eta) \dot{m}_{IN/OUT} \tag{14}$$

4.2. Orifice-type elements

Orifice connections between two volume elements are used to calculate the oil flow through the circuit, and also to estimate hydraulic losses in the line. Pressure drop can be observed on every orifice, what is used to generate flow from one volume element, to another. Orifice physical model can be seen on Fig 6.

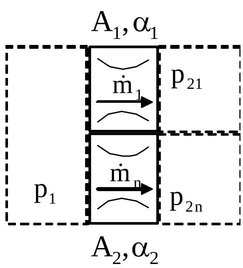

Fig. 6 Model of orifice connections in the system with single input and multiple output possibilities.

Based on the physical model of the orifice elements, the (15) algebraic equation can be set as mathematical model. Mass flow through the „i" nozzle:

$$\dot{m}_i = \alpha_i A_i \sqrt{2\rho (p_1 - p_{2i})} \tag{15}$$

4.3. Other elements

The hydraulic lubrication system of the axle is supplied by a gear-type oil pump that is mechanically driven from the differential gear-set housing, so constant kinematical coupling is present between the axle input- and oil pump speed. Pump model is implemented with a lookup table, where the oil mass-flow is calculated as a function of entering and leaving pressure quotient, and pump speed:

$$\dot{m}_{pump} = f\left(\frac{p_{OUT}}{p_{IN}}, n_{pump}\right) \tag{16}$$

Mechanical pressure limiter model is illustrated on Fig. 7.

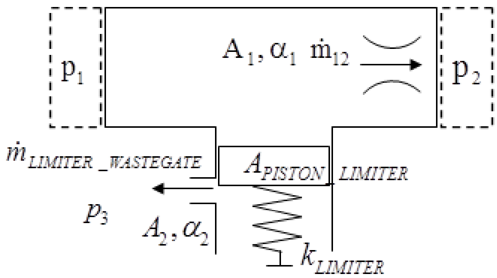

Fig. 7 Mechanical model of the pressure limiter.

Based on the physical model of the pressure limiter, the following equations can be set as mathematical model:

$$\dot{m}_{12} = \alpha_1 A_1 \sqrt{2\rho(p_1 - p_2)} \tag{17}$$

$$\dot{m}_{LIMITER\_WASTEGATE} = \alpha_2 A_2 \sqrt{2\rho(p_1 - p_3)} \tag{18}$$

The effective flow area of the wastegate direction depends on piston displacement. Piston stroke can be calculated with the following equation:

$$y = \frac{(p_1 - p_3) A_{PISTON\_LIMITER}}{k_{LIMITER}} \tag{19}$$

With equation (19) the limiter model for piston displacement is taken as linear. The effective flow area of the wastegate direction is implemented with a lookup table, as illustrated on Fig. 8:

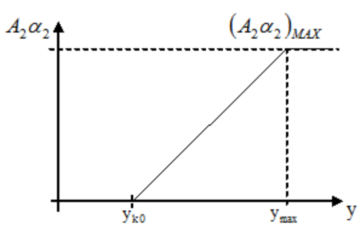

Fig. 8 Pressure limiter effective flow area in function of piston displacement.

5. MODEL VALIDATION

5.1. Validation process

Losses of a hydraulic system are very dependent of oil temperature, overall driveline losses are decreasing as the oil temperature rises. System measurements are done on 30°, 45°, and 60° to get an overview about the loss tendency in function of oil temperature. Since the efficiency is most crucial by long-term work periods, where the oil temperature is increased, the model validation is only performed on 60°.

6. CONCLUDING REMARKS

An axle hydraulic model introduced and validated in this paper, can be useful in further researches. By analysing the main functions in a lubrication system, the necessary pump performance can be estimated and optimized, and the hydraulic losses can be minimized. The model is a base for intelligent lubrication system design, where the necessary oil flow is optimized by distribution and mass-flow for all system speed and load cases. Also a smart lubricating system can avoid driveline parts overheating, harshness and therefore prolong oil lifetime. Further researches in the topic will focus on controlling the system.

ESTIMATION OF THE SLIP RATIO, SLIP SINKAGE, SLIP VELOCITY AND TRACTION OF THE RIGID WHEEL IN DEFORMABLE TERRAIN

Ramadhani Omari KIVUGO[*], Alessandro TASORA[+] and Francesco BRAGHIN[*]

[*]Dipartimento di Meccanica
Politecnico di Milano
Via La Masa 1, I-20131, Milan, Italy
[+] Department of Industrial Engineering
Universita di Parma
Via Università 12, I-43121, Parma, Italy

Received: November 8, 2016

ABSTRACT

Sinkage of tyres is a critical issue for both off-road vehicles and space exploration vehicles. Although well known from an experimental point of view, the boundary conditions that determine sinkage in terms of soil and tyre characteristics as well as the underlying physical phenomena are not fully understood. This paper presents a novel simulation methodology based on CHRONO::Engine for estimating the traction performances as well as the static-sinkage and slip-sinkage as a function of soil characteristics and tyre tread design. Soil is modelled as rigid particles that interact with each other and with the tyre through field forces that reproduce soil rheology and plasticity. The tyre instead is modelled as a rigid body. Traction and sinkage performances have been estimated as a function of various soil parameters showing the relative importance of some of these with respect to one or both performance indexes considered. Moreover, also the influence of wheel speed and weight has been analysed. Thus, some indications are drawn on how to improve traction and avoid sinkage as a function of soil parameters.

Keywords: tyre-deformable ground interaction, particle model.

1. INTRODUCTION

Off-road operation of the vehicle is the field of interest in agriculture, construction, exploration, mining, military applications [1]. Despite the fact that pneumatic tires have decades of replaced rigid wheels in most off-road wheeled vehicles, the mechanics of interaction for the rigid wheels still of interest, as rigid wheels are still in use under certain circumstances such as exploration robot and extremely high temperature conditions or chemically reacting environment, but also pneumatic tires can behave like rigid wheel in soft terrain [2]. The performance of an off-road vehicle to the greater extent depends on the manner in which the vehicle interacts with the given terrain [3]. The mobility of the vehicle and its dynamical characteristics are determined by the tire-soil interaction during these operations [3]. Consequently, understanding the mechanics of the tire-terrain interaction is of importance in the proper selection of the vehicle configuration and design parameters to meet the operation requirements.

Wheel slip and sinkage has been shown to be a prime key variable in estimating and predicting wheel-terrain interaction phenomenon. The deformation of the terrain along the direction normal to the contact surface is known as wheel sinkage [4]. During this deformation, total sinkage of the wheel consists of two parts, which are sinkage due to static axle/wheel load and one due to slip of the wheel under traction [4, 5]. Little attention has been devoted to the study of dynamic effects occurring at wheel-terrain interface such as slip ratio and slip sinkage [3]. These effects compromise the traction performance and may results in the traverse failure of the wheeled vehicle in deformable terrain [5]. Proper techniques of estimating slip ratio, slip-sinkage and associated slip-velocity may leads to the improvement of the off-road vehicle mobility performance [3, 5].

When wheel interacts with ground on running gear, it applies the normal load to the terrain surface which results in sinkage and motion resistance [2, 4]. The torque applied to the wheel initiates the shearing of the terrain layer which in turn results in thrust and associated slip of the wheel [2, 4]. Estimation of static sinkage, slip sinkage, slip ratio and slip velocity are of prime importance in the prediction and evaluation of the running wheel and vehicle performance in deformable terrain [5]. Estimation of the above interaction parameters are based on the terrain response to the applied load of the wheel and the applied tractive effort [2, 4]. Estimation of the static and slip sinkage of the wheel gives pressure-sinkage relationship of the interaction, while estimation of the slip ratio, slip velocity gives the shear stress-shear displacement relationship which are both of prime importance to the evaluation and prediction of traction performance for off-road vehicles.

Finally, the evaluation and prediction of the wheel sinkage leads to realistically prediction and evaluation of the terrain compaction and resistance, which is useful for strategically and planning for control of autonomous off-road vehicles and reducing odometric errors, and also reducing soil compaction, which is the case now days for profitable large agriculture machinery which cause severe soil compaction and leads to low soil aggregates, less productivity if not properly controlled in agriculture activities.

2. CHRONO::ENGINE: WHEEL-TERRAIN INTERACTION MODEL

The model presented in this paper considers only the rigid wheel for analysis simplicity [6]. The study of the rigid wheel is still relevant as some vehicles are equipped with rigid wheel as the case of the robot for extra-terrestrial exploration where rubber compound cannot be used because of the severe environmental condition (extremely high temperatures, unfavourable chemical composition) [2]. The tires are modelled in SOLIDWORKS as the agriculture vehicle tire with dimensions: 1.42 m, 0.74 m and 0.5 m external, internal diameters and width respectively. The lugs used in the model are straight/high, non-directional and combined/low, and their height and inclination are 30 mm, 60 mm and 45°, 90°, 55° to the width of the tire respectively , while material of the tires are chosen to be natural rubber with the respective masses and inertia.

The tire model was then exported to CHRONO::Engine as (wave front object.obj) file, thanks to CHRONO::Engine as a free available C++ general-purpose available software made up of a collection of loosely coupled components that facilitate different aspects of multi-physics modelling, simulation and visualization [7] and an optional module for third-party model import capability which enable the tire model to be imported to CHRONO::Engine model [7]. The soil bin is made as the collection of four walls and ground positioned accordingly, the front wall was made to be transparent to facilitate interaction visibility (see Fig. 1).

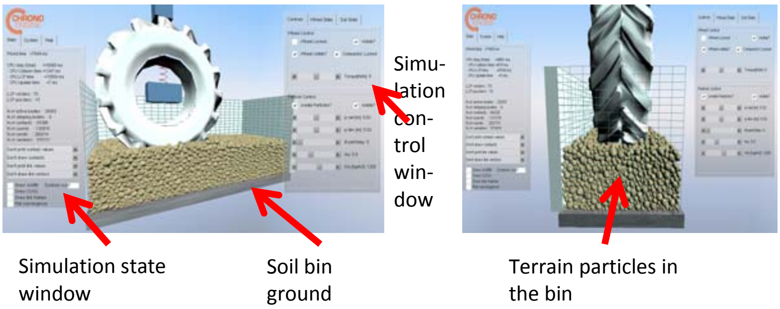

Fig. 1 Tire-terrain model in CHRONO::Engine

Rigid block (truss) was attached to the wheel centre through revolute joint to account as hub, rim and axle masses, and made to be movable with the same linear velocity as the wheel. Furthermore, other rigid block was attached to the system through suspension spring to account for vehicle sprung weight. The motion of the wheel and masses was achieved by adding drive engine which gives angular motion of the wheel.

Thanks to collision detection feature in CHRONO::Engine for handling the large number of colliding bodies and triangle mesh capability which assign collision detection of particles in the terrain with high precision iteration solver of contact and simulation [8]. Since the items in CHRONO::Engine are organised in classes and namespaces, this ensures fast execution of the simulation program even in complex situation like collision between particle-particle and particles-wheel during interaction [7].

To account for issues of dependency and memory footprint, CHRONO::Engine follows the modular approach by splitting the libraries modules that can be dynamically loaded only if necessary [7]. Moreover, in the case of providing compact algebra for managing the quaternion, static and moving coordinate system for the case of free particle and moving wheel, the operator overloading feature has been used with the adoption of modern programming techniques such as shared pointers [8].

CHRONO::Engine has the capability to handle simulation of the non-smooth collision of rigid bodies through differential inclusion approach which calculates the contact forces by penalising the small interpenetration of colliding rigid bodies (DEM-P), this also ensures the correct estimation and calculation of the friction and collision forces in contacts of particles and wheel during interaction [7, 8].

Thanks to physical system object which handles the list of rigid bodies and their constrains which were used to add forces, position, velocity, acceleration and auxiliary references to rigid bodies and specific constrains for the drivers (Engine::Mode) [8].

Finally, global simulation parameters was added on terrain.ccp file, then the project was compiled in CMake compiler, and the solution of the tire-terrain model was built in visual studio in release modes to accomplish the tire-terrain simulation in CHRONO::Engine (see Fig. 1).

3. SIMULATION RESULTS

In this section simulation results are presented to validate the proposed approach. The simulation of the wheel-terrain interaction achieved by commanding the wheel to traverse in a straight line in the soil bin of 2.4 m long by 1.0 m wide across the particles for a period of at least two seconds and resulting the interaction parameters such as traction and slip sinkage.

Furthermore, the wheel was given a constant initial angular speed of 5 and 10 rpm, and slip of the wheel was estimated by the ratio of the difference of wheel circumferential velocity and linear velocity to the linear velocity at the centre of the wheel, while slip sinkage was estimated based on the wheel centre vertical variation with respect to ground during simulation. The resulting resistance of the soil to the wheel longitudinal motion was recorded as the output resistive traction of the wheel.

3.1 Effect of grains size

As shown in Figure 2 both traction and slip sinkage of the wheel are more sensitive to grain size. The traction is high with smaller grains slip ratios below 25%. This is because of long contact of the wheel due to high static sinkage with smaller grains. High slip sinkage can be caused by large space left after rip of the particles under the contact due to slip and deformation of the terrain.

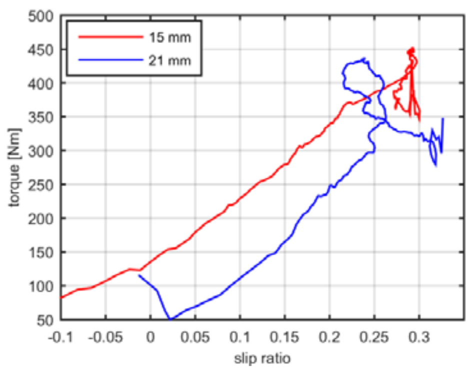

Fig. 2 (a) Wheel traction as a function of slip ratio

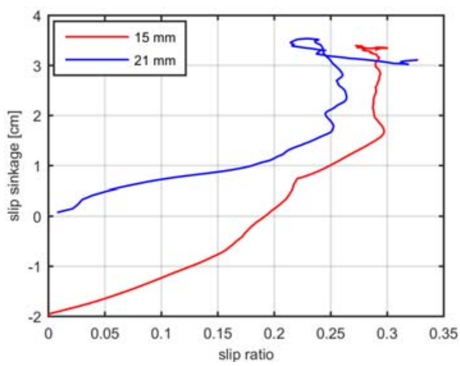

Fig. 2 (b) Wheel slip sinkage as a function of slip ratio

3.2 Effect of the number of grains

Figure 3 show the influence of the number of grains: traction is less sensitive to grains number with slip between 10%-20%. This is because number of particles in the bin does not change the wheel motion resistance with the same slip value. Instead small differences could be due to small increment in static sinkage with more particles in the bin as observed during simulation. Above that slip, the traction with more particles increases significantly until the maximum value is reached which is almost the same at slip value above 20%. Slip sinkage is significantly effected at slip value below 22.5 %. This is due to high resistance to longitudinal deformation of the terrain which increase with high terrain weight density.

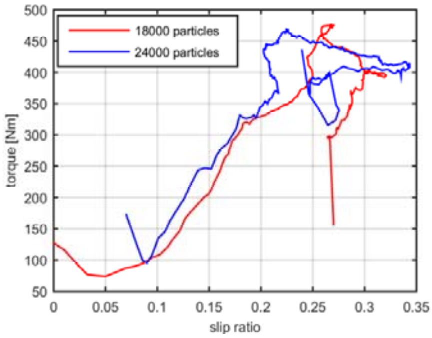

Fig. 3 (a) Wheel traction as a function of slip ratio

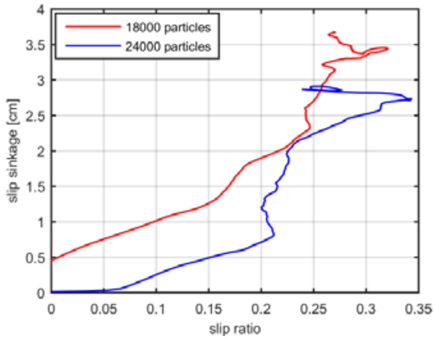

Fig. 3 (b) Wheel slip sinkage as a function of slip ratio

3.3 Effect of lugs number

From the simulation results shown in figure 4 it is noted that there is an increase of traction of the wheel at a slip value between 0-20% with more lugs. This is because of the reducing lug space and increase in number of lugs that are in contact with the terrain which cause increase of deformation rut as well as traction. At a slip value above 30% high traction is noted with 20 lugs and this is due to increase in slip sinkage of the wheel above that slip value. Increasing the number of wheel lugs is beneficial to develop continuous shearing between the wheel lugs and the soil so as to improve traction efficiency and drawbar pull [9]. Slip sinkage increases with increase of the wheel lugs. This is because the time span between smooth surface of wheel and lugs in the soil increase with lugs during interaction and results in increase of wheel slip and slip sinkage this results is comparable with [9].

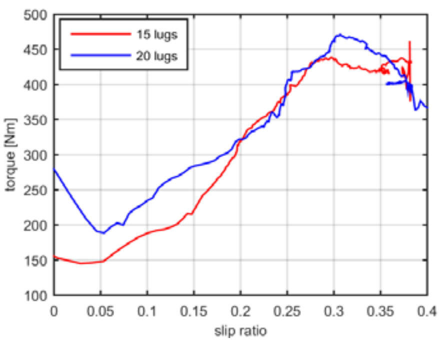

Fig. 4 (a) Wheel traction as a function of slip ratio

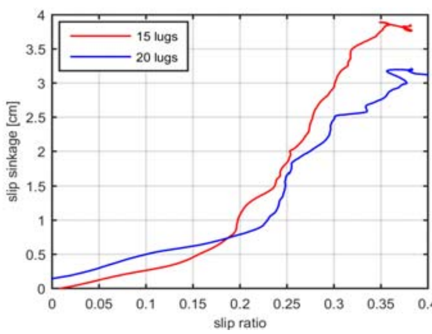

Fig. 4 (b) Wheel slip sinkage as a function of slip ratio

3.4 Effect of lugs height

From the simulation with 30 mm and 60 mm lugs height, shown in figure 5, it is seen that both traction and slip sinkage of the wheel increase with an increase of lugs height. This is due to high digging of soil with higher lugs than with lower lugs [9]. If wheel lugs are low, the slip of the soil mainly occurs at the surface between wheel surface and soil, but it will occur between the steady soil and movable soil adhering to the wheel if the lugs are high enough to form steady shearing loop. The results show that slip velocity is not sensitive to lugs height at the slip value between 0-20%.

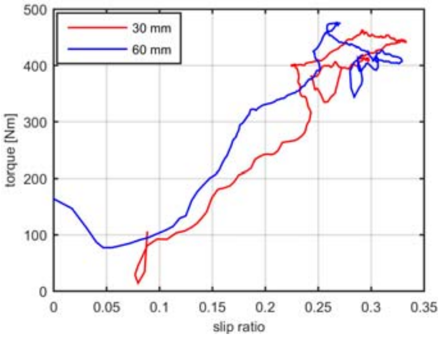

Figure 5 (a) Wheel traction as a function of slip ratio

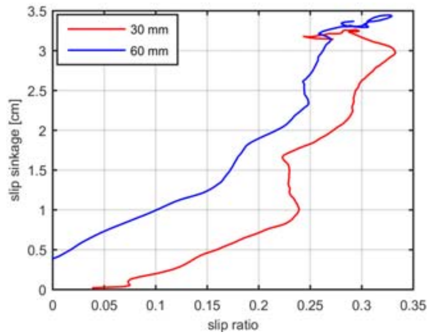

Figure 5 (b) Wheel slip sinkage as a function of slip ratio

3.5 Effect of lugs inclination angle

From the simulation results obtained with two lugs inclination angles shown in figure 6, higher traction is noted with 45° rather than 55° inclination at slip value around 20% while at slip values between 20-27.5% the lugs inclination show almost similar traction to the maximum value of the traction. This is because of higher slip sinkage with 45° lugs rather than with 55° at that slip value and almost similar slip sinkage between 20-27.5% slip values, respectively. Small increase of traction with 55° lugs angle at slip value above 20% could be due to increase of lateral force with increase of lugs angle which increase motion resistance of the wheel [9].

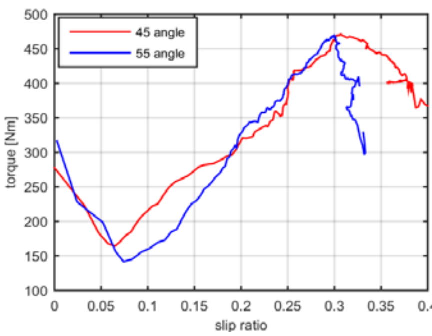

Figure 6 (a): wheel traction as a function of slip ratio

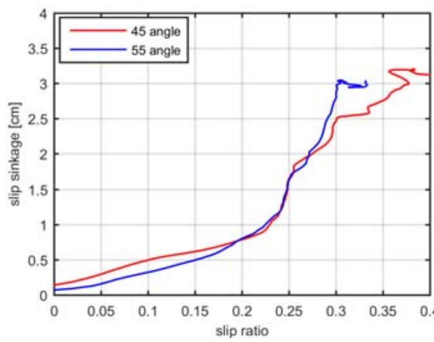

Figure 6 (b): wheel slip sinkage as a function of slip ratio

4. CONCLUSIONS

The capability of CHRONO::Engine was utilised in this modelling of tyre-soil interaction. The rigid wheels with different lugs type and design were used in the simulation with respect to terrain particles characteristics. The simulation results show that the interaction parameters are the function of lugs type, design and soil particles characteristics.

The model gives out the interaction parameters with respect to soil characteristics such as traction, slip ratio, slip velocity, static sinkage and slip sinkage, and from these it can be concluded that soil characteristics and tyre lugs design has to be taken into consideration for the interaction problem.

The performance of the rigid wheel on deformable terrain gives out the promising results, which shows well the effects of discontinuous deformation of the terrain such as build-up and cleaning by considering the longitudinal and lateral deformation of the terrain.

From the fact that, the model shows the sensitive of the tyre design and the soil characteristics, therefore the model can be used for sensitivity analysis and optimisation of tyre tread design with respect to soil characteristics.

Some improvement to the model should be done to account for interlocking mechanism of the soil particles by introducing different particle forms such as box, triangular convexhul particles. Also the model has to include different size of the wheel such as diameter and width which also affect the interaction and performance of the wheel in deformable terrain.

Finally, the model has to be validated with experiment tests or experimental results available in the literature to make appropriate fine turning to the model to have better results of the model with respect to experimental results.

5. REFERENCES

[1] **Ishigami, G. - Otsuki, M. - Kubota, T. – Iagnemma, K.**: Modeling of flexible and rigid wheels for exploration rover on rough terrain, 28th International Symposium on Space Technology and Science, 2011.

[2] **Wong, J. Y.**: Theory of Ground Vehicles, John Wiley & Sons, 2008

[3] **Reina, G. - Ojeda, L. - Milella, A. - Borenstein, J.**: Wheel slippage and sinkage detection for planetary rovers, Transactions on Mechatronics, 11, , 2006, p.185-195

[4] **Ding, L.**: Improved explicit-form equations for estimating dynamic wheel sinkage and compaction resistance on deformable terrain, Mechanism and Machine Theory, 86, 2015, p.235-264.

[5] **Reina, G.**: Methods for wheel slip and sinkage estimation in mobile robots, IN-TECH Open Access Publisher, 2010.

[6] **Hutangkabodee, S. - Zweiri, Y. H. L. - Seneviratne, D. - Althoefer, K.**: Soil parameter identification for wheel-terrain interaction dynamics and traversability prediction, International Journal of Automation and Computing, 3, 2006, p.244-251.

[7] **Mazhar, H. - Heyn, T. - Pazouki, A. - Melanz, D. - Seidl, A. - Bartholomew, A. et al.**: CHRONO: a parallel multi-physics library for rigid-body, flexible-body, and fluid dynamics, Mechanical Sciences, 4, 2013, p.49-64.

[8] **Tasora, A. - Silvestri, M. – Righettini, P.**: Architecture of the CHRONO::Engine physics simulation middleware, Multibody Dynamics, 2007.

[9] **Ding, L. - Gao, H. - Deng, Z. - Nagatani, K. – Yoshida, K.**: Experimental study and analysis on driving wheels' performance for planetary exploration rovers moving in deformable soil, Journal of Terramechanics, 48, 2011, p.27-45.

ADVANCED FLOW MODELLING FOR ENGINE INTAKE MANIFOLD BY MEANS OF COUPLED ANALYSIS OF GT-SUITE AND ANSYS FLUENT

Csilla TÓBIÁS and Árpád VERESS

Department of Aeronautics, Naval Architecture and Railway Vehicles
Faculty of Transportation Engineering and Vehicle Engineering
Budapest University of Technology and Economics
H-1111 Budapest, Műegyetem rkp. 3, Hungary

Received: November 8, 2016

ABSTRACT

Recently, an increasing demand of simulation accuracy can be observed in automotive industry including engine technology and development as well. Meanwhile, computational capacity is still a limiting factor making 3D modelling of the entire system impracticable. 1D-3D coupling pose a compromise solution for this apparent discrepancy. Using co-simulation complex parts can be modelled by 3D approach while the other parts by 1D one, thus detailed information is obtained only where needed. In this work, the model of a generic 4-cylinder diesel engine has been built to test the coupling procedure. The intake manifold is the 3D part whilst the rest of the engine is modelled as 1D. With this approach besides acquiring detailed flow characteristics more realistic boundary conditions can be imposed to 3D simulation to further improve reliability.

Keywords: coupled 1D-3D simulation, co-simulation

1. INTRODUCTION

These days, automotive industry expects more and more accurate simulations and with the advancement in computational capacity facilitates simulation of more complex models, however, in many cases it is still not sufficient for modelling the whole system in 3D.

3D CFD simulations provide detailed information about flow properties, however, they require high computational cost at certain application. 1D simulations can give overall information at system levels but it cannot capture complex 3D features of the flow. With the coupling of the two simulation methods, the most preferred characteristics can be utilized while minimizing the drawbacks. Using co-simulation modelling approach complex parts (exhaust collectors, intake manifolds, catalytic converters) can be modelled by 3D approach and the other parts by 1D method, thus detailed information is obtained only where needed. Moreover, the multi-scale approach avoids the need of imposing approximated boundary conditions to the 3D simulation, which would badly affect the reliability of the simulation. [1] It also allows the simulation of complex physical phenomena including turbulence and secondary gas mixing. [2] In this work, a possible method for 1D-3D coupling, GT-SUITE and ANSYS Fluent coupling was tested.

2. 1D-3D COUPLING

Many methods for simulation accuracy improvement have been developed. Complex 3D geometries can be transformed into a set of suitable 1D components with software tools such as GEM3D or COOL3D for example. Other option can be the coupling of 1D and 3D codes and tools.

There are different methodologies for coupling 1D and 3D simulations. The coupling can be achieved through manual (external coupling) or automatic data transfer between the two simulations. The data transfer can occur in one-way or two-way manner.

During one-way coupling, the 1D simulation provides the time-varying boundary conditions to the CFD part. Two-way (strict) coupling is when 1D and 3D simulations exchange data at each time step.

In case of external coupling, the flow coefficients of the concerned complex components (valves, junctions, and orifices) are determined by steady-state CFD simulations. The characterization of these 3D components allows the definition of an equivalent 1D component. [3] The detailed information gained with the 3D simulations are embedded and used in the 1D system model. [1]

Nowadays, leading simulation software providers enable 1D-3D co-simulations with their programs. GT-Power can be coupled with Fluent, STAR-CD, STAR-CCM+, Fire and OPENFoam as well. [4] WAVE has coupling capability with Vectris, STAR-CD, Fluent, Fire and now it has its own 3D module, WAVE3D. [2]

Applications of 1D-3D co-simulation are EGR mixer simulation [5], simulation of compressed air injection module [6], air induction noise [7], close-coupled catalytic converter [8], a solar thermal system [9], bus cooling system [10], lambda sensor [11] and environmental control systems in aircraft cabins [12].

3. GT-SUITE ENGINE MODEL

The GT-SUITE has been used in the present case and a generic 4-cylinder, naturally aspirated diesel engine model with the firing order of 1-3-4-2 at 1500 RPM has been prepared. There is a restriction that only one GT-SUITE case can be simulated at a time.

The GT-SUITE model includes parts from special CFD templates for coupling: CFDComponent part where the number of pre-cycles, coupled cycles and CFD Species Map (to advert species to and from the CFD model) can be set, the CFDInterface parts to control the transition from standalone GT-SUITE to coupled simulation and CFDConn parts to specify boundary type, geometry and turbulence parameters (Fig. 1). After every attributes and parameters are set a *.dat file can be created from the model at Simulation Utilities. This file will be the input file of the ANSYS Fluent to connect to the GT-SUITE for coupling.

The flow model of the GT-SUITE simulation involves the solution of the Navier-Stokes equations: the conservation of continuity, momentum and energy equations. These equations are solved in one dimension, which means that all quantities are averages across the flow direction, [14].

4. FLUENT MODEL

During the coupled simulation, a transient CFD simulation is executed simultaneously. For all flows, ANSYS Fluent solves conservation equations for mass and momentum.

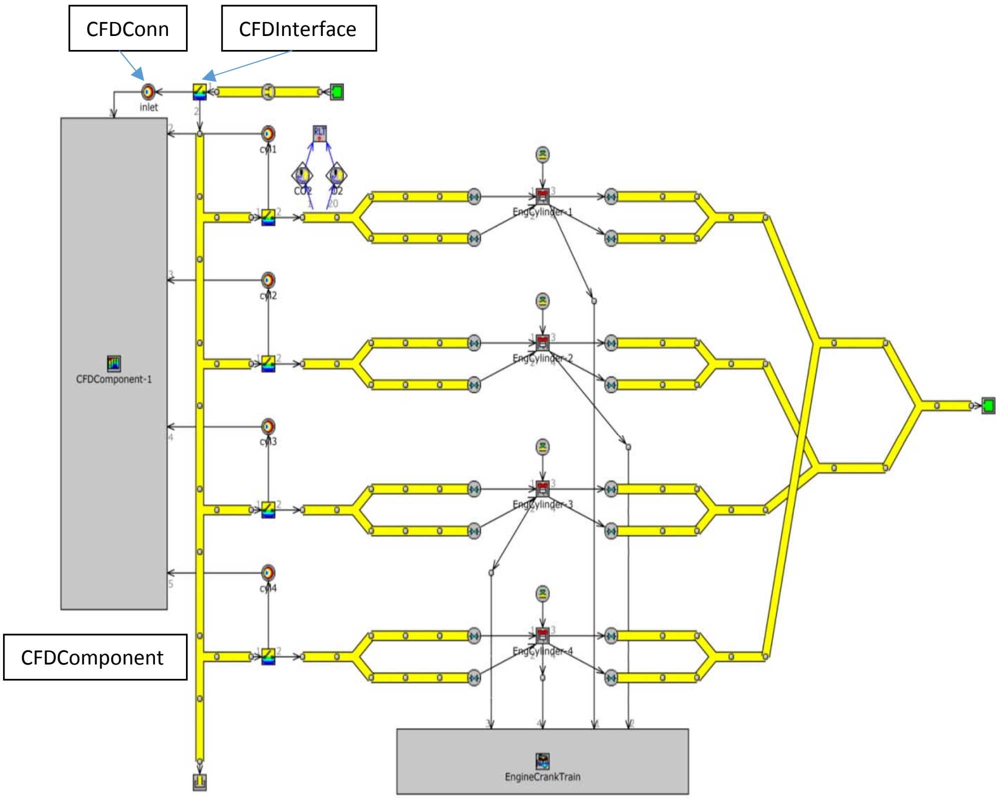

Fig. 1 .GT-SUITE model

For flows involving heat transfer or compressibility, an additional equation for energy conservation is solved. For flows involving species mixing or reactions, a species conservation equation is solved or, if the non-premixed combustion model is used, conservation equations for the mixture fraction and its variance are solved. Additional transport equations are also solved when the flow is turbulent, [13]**Hiba! A hivatkozási forrás nem található.**

The time step of the transient simulation is determined from crank angle degree time step. The number of time steps in ANSYS Fluent simulation should be adjusted to GT-SUITE cycles.

For the coupled simulation species transport and energy equation calculations are activated. For coupling ANSYS Fluent with GT-SUITE UDFs for mass flux, temperature and species mass fractions can be chosen at the boundaries after the User-Defined 1D Coupling and GT-SUITE generated *.dat file are selected.

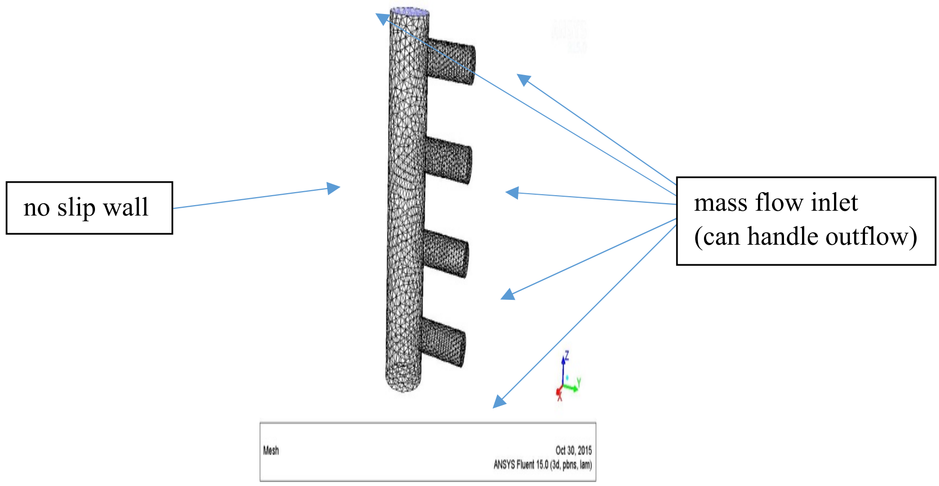

Fig. 2 ANSYS Fluent model

5. COUPLED MODEL

The coupled model has two main parts: the 3D intake manifold (see *Fig. 2* about its mesh), which is the CFD part (simulated in ANSYS Fluent) and the 1D GT-SUITE engine model. At their boundaries, there are the interfaces and connections for coupling (Fig.3).

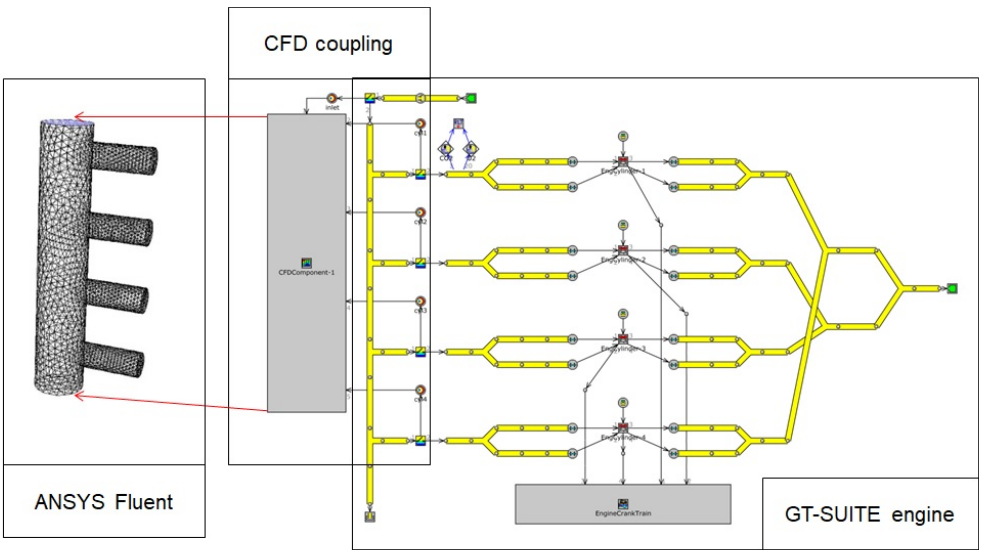

Fig. 3 Coupled model

The effect of mesh resolution and used physical and numerical parameters are not investigated in the present case as the goal was to establish the co-simulation between the mentioned software.

First, the GT-SUITE model is executed without coupling to achieve a more stable solution. Once the pre-cycles are completed the simulation switches to coupling through CFD interface. During coupled simulation, GT-SUITE provides time-dependent boundary conditions of mass flux, total temperature and species mass fractions for ANSYS Fluent. After the 3D simulation part, the appropriate boundary conditions are averaged and these averaged values are given back to GT-SUITE.
When the CFD solver completes the requested simulation duration, it terminates the GT-SUITE solver even if its processes are not completed yet. To prevent loss of post-processing files, extra time steps should be added to the CFD simulation.

6. RESULTS AND CONCLUSIONS

Fig.4 shows the velocity distribution of the intake manifold with time. The velocity vectors are coloured based on the local velocity magnitude.

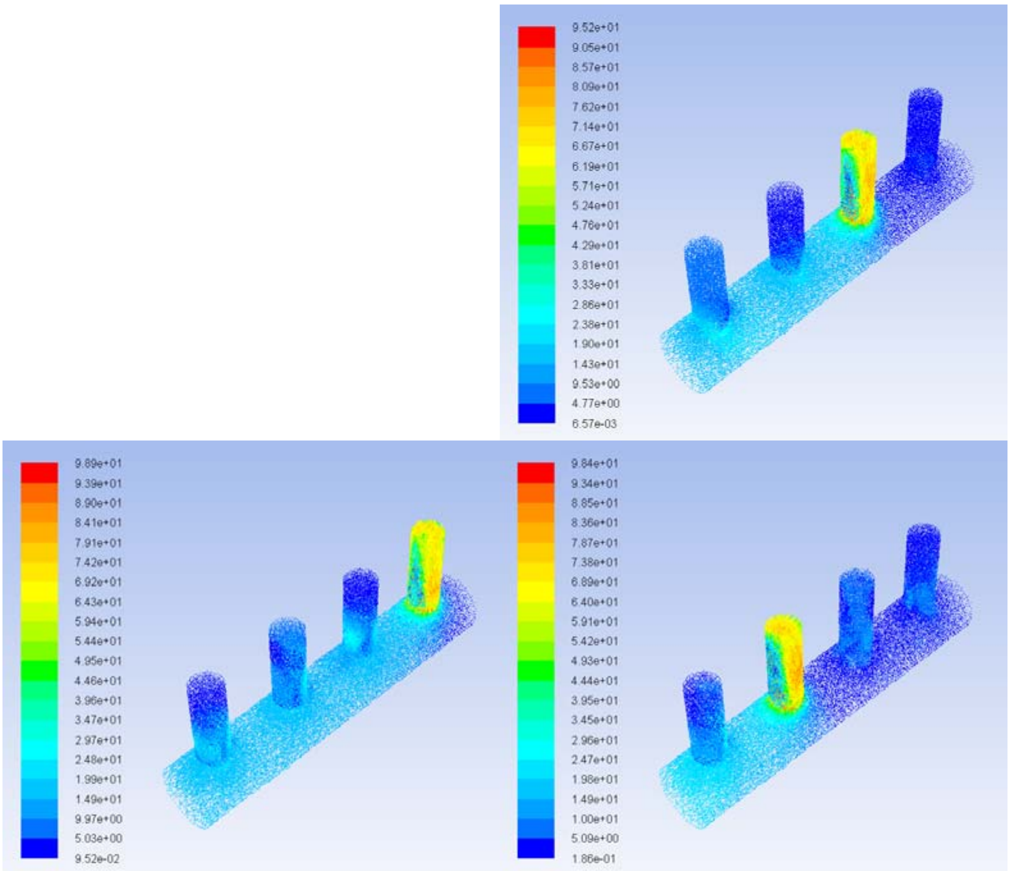

Fig. 1 Velocity distribution

Since it was a method test there is no quantitative results, however it can be seen in Fig. 4 that the results are plausible the velocity distribution is consistent with the firing order.

GT-SUITE and ANSYS Fluent coupling is one of the above-mentioned compromise method for flow simulation. It is suitable for gaining more realistic boundary conditions for the examined component with acceptable computational cost.

7. REFERENCES

[1] **Soumoy, V. –Kelsall, D.**: Coupling 1D and 3D CFD – The Challenges and Rewards of Co-Simulation; Newsletter EnginSoft Year 7 n°4, p.53-55.

[2] 1D/3D CFD Co-Simulation; http://www.ricardo.com/en-GB/What-we-do/ Software/ Products/ WAVE/1D3D-Analysis/; 2015.04.03.

[3] **Gianluca Montenegro**: 1D-3D Coupling for Automobile Power-train Systems

[4] GT-SUITE CFD-Coupling Manual 7.2, 2010.

[5] **Kereszty, B - Kiszely, M. - Németh, H.**: Coupled Simulation Method for Investigating EGR Mixers in Turbocharged Commercial Vehicle Diesel Engines; Conference on Modelling Fluid Flow (CMFF’12); Budapest, Hungary, September 4-7, 2012.

[6] **Németh, H. - Kristóf, G. - Szente, V. – Palkovics, L.**: Advanced CFD Simulation of a Compressed Air Injection Module; Conference on Modelling Fluid Flow (CMFF’06); Budapest, Hungary, September 6-9, 2006; p.388-395.

[7] **Dipali Ghodake, Zakirul Haque**: The Simulation of Air Induction Noise Using 1D-3D Coupling; SAE Technical Paper 2011-01-0500

[8] **Liu, Z. - Benjamin, S.F. - Roberts, C.A. - Zhao, H. - Arias-Garcia, A.** (2003). A coupled 1D/3D simulation for the flow behaviour inside a close-coupled catalytic converter, SAE Technical Paper 2003-01-1875, doi: 10.4271/2003-01-1875; http://dx.doi.org/10.4271/2003-01-1875

[9] **Ljubijankic, M. - Nytsch-Geusen, Ch. - Jänicke, A. – Schmidt, M.**: Advanced Analysis of Coupled 1D/3D Simulation Models by the Use of Solar Thermal System; 12th Conference of International Building Performance Simulation Association, Sydney, 14-16 November; p.1871-1877.

[10] **Kai Shen, Feihong Li, Jimin Ni**: 1D/3D Coupling Calculation Analysis on Bus Cooling System; Energy and Power Engineering 6; 2014, p.550-556. http://dx.doi.org/10.4236/epe.2014.614048

[11] **Silvestri, J.**: Powering the System; ANSYS Advantage, Volume VI, Issue 1, 2012; p.46-48.

[12] **Wolf, K. – Bayrasy, P.**: Generic Coupling of 1D System Codes with 3D CFD Tools; ERCIM News 81, April 2010, p. 27-28.

[13] **ANSYS Inc.:** ANSYS Fluent Theory Guide, Release 15.0, November 2013

[14] **Gamma Technologies Inc.:** GT-SUITE Flow Theory Manual 7.2, 2011.

NOVEL APPLICATION OF INVERSE DESIGN METHOD BY MEANS OF REDESIGNING COMPRESSOR VANNED DIFFUSER IN A RESEARCH JET ENGINE

Foroozan ZARE[*] and Árpád VERESS[**]
Department of Aeronautics, Naval Architecture and Railway Vehicles
Faculty of Transportation Engineering and Vehicle Engineering
Budapest University of Technology and Economics
H-1111, Budapest, Műegyetem rkp. 3.
*fzare@vrht.bme.hu; Phone: +36-1-463-1805
**averess@vrht.bme.hu; Phone: +36-1-463-1992

Received: November 9, 2016

ABSTRACT

The main goal of this article is to introduce the adaptation of a new method for redesigning compressor vanned diffuser in a research jet engine. The applied inverse design method is based on a finite volume and explicit time marching solution of the compressible Euler equations. Stratford's separation prediction method is used for determining the expected pressure distribution along the suction side of the profile on such a way that the cost effective and highly utilized vane geometry – which will belong to the expected pressure distribution: close but certain distances far from the separation – will provide less total pressure drop, higher static pressurize and more axial flow turning than the baseline design. Following the inverse design procedure for determining the new profile and verification of the result by ANSYS CFX inviscid and viscous flow simulations, the viscous module of the CFX software has been used to compare the results of the new and the original vanes with each other. Although the purpose of the present paper is to introduce a design technique for compressor vanned diffuser, the procedure can be extended and applied for other wall bounded flows at strong adverse pressure gradient flow conditions.

Keywords: inverse design, redesigning, jet engine

NOMENCLATURE and ABBREVIATIONS

Variables (Latin and Greek)

C_p	Pressure coefficient, Spec. heat [-,J/kg/K]
M	Mach number [-]
p	Static pressure [Pa]
R	Spec. gas constant, Residual [J/kg/K, var.]
T	Temperature [K]
U	Vector of conservative variables [-]
x	Cartesian coordinate in space [m]
ρ	Density [kg/m^3]

Subscripts and Superscripts

0	Total parameters (e.g.: pressure, temperature)
i,j,k	Variables for spatial and sum indexing
in, out	Inlet and outlet
l	Local variable (static pressure)
stat,to	Static, total

Abbreviations

BC	Boundary Condition
CAE	Computer Aided Engineering
CFD	Computational Fluid Dynamics
Re	Reynolds number
SST	Shear Stress Transport

1. INTRODUCTION

Development and application of different simulation and modelling techniques are widely spread in the vehicle industry; several researches are in progress in those areas: [1-4]. The CFD (Computational Fluid Dynamics) is one of the CAEs (Computer Aided Engineering), by which high number real tests and measurement can be replaced or reduced also and significant amount of cost, capacity and time can be saved. The parameterization of the geometry provides higher reproducibility and flexibility in the model generation. The implemented computational techniques are well established and they were validated over the most representative benchmarks. Their consistency, stability and convergence characteristics were investigated and proved. The accuracy of the available techniques allows designers to turn more effort on the new fields of the engineering practice called simulation driven product development or virtual prototyping in other words, which is going to be the keyword of the next decades. Additionally, in case of applying optimization methods, not only the development process, but the overall effectivity of the product developments can also be increased, so the cost decreased significantly.

Here, in the present research, the main goal was to adapt, apply and verify the correct and plausible operation of the inverse design based optimization tool by means of redesign a compressor vanned diffuser in a research jet engine in the most cost effective way with respect the production cost. ANSYS CFX software was used to crosscheck the results of the inverse design method.

1.1. Optimization Methods and Their Ability to be Coupled with CFD

Beside the developments of the central core of the fluid dynamics solvers, the different optimization techniques, coupled with CFD, are also under intensive research [5]. In case of direct optimization techniques, an attempt has been made to find the optimal solution. They typically utilize some sort of search technique (gradient-based optimizer), stochastic based algorithms (e.g. evolutionary strategies, genetic algorithms) and artificial neural networks for example. These procedures can be computationally expensive because several flow solutions must be completed to specify for example the direction of deepest descent, fitness of individuals in the population in order to determine the shape changes. Furthermore, the required number of flow solutions increases dramatically with the number of design variables.

Several optimization methods have been developed so far, but the optimal shapes for practical CFD design have been the subject of limited methods.

1.2. Inverse Design Based Optimization

In case the inverse design-type methods, the geometry modification is based on the prescribed set of the pre-defined variables at the wall by simple, fast and robust algorithms, which make them especially attractive amongst other optimization techniques. The wall modification can be completed within much less flow solutions for inverse design techniques than for direct optimization methods. Hence, the inverse design methods typically being much more computationally efficient and they are very innovative to be used in practice. The main drawback of the inverse design methods is that the designer should create target (optimum in a specific sense) pressure or velocity distributions that correspond to the design goals and meet the required aerodynamic characteristics. It can be difficult to specify the required pressure or velocity distribution that satisfies all the design goals. Also, one cannot guarantee that an arbitrarily prescribed pressure/velocity distribution will provide mechanically correct airfoils without trailing edge open or cross over [6]. These drawbacks are solved within the frame of the present article. The optimum pressure distribution was found and the trailing edge was closed in the all investigated cases.

Without high performance computing, the earliest methods of inverse design were analytical. Beside *Jacobs*, *Theodorsen* and *Mangler, Lighthill* [7] can be considered as pioneer in this field by developing an inverse design method for 2D incompressible flow past airfoils, making use of conformal mapping and potential flow solution [6]. These methods are limited to the shock-free irrotational flows and difficult to extend to 3D. At the last decades of the twentieth century, the inverse methods are rather based on an iterative solution and they are generally developed together with the newly developed CFD solvers mostly based on the theory of characteristics. The governing equations of those methods are generally the Euler and *Navier-Stokes* equations. The solid wall modification algorithm is performed by means of transpiration technique (*Giles* and *Drela* [8], *Demeulenaere* [9] and *De Vito* [10]). These methods are primarily dedicated to the design of airfoils, wings and turbomachinery cascades, but it has also been applied for design of duct geometries (*Cabuk* and *Modi* [11]) [6].
The general procedure of the iterative type inverse design methods requires an initial geometry and optimal pressure or velocity distribution over the wall to be modified. The prescribed distribution generally comes from the industrial experiences and/or theory. The iterative cycle starts with the direct solution of a CFD solver. Completing the convergence criteria, a new boundary condition is applied at the solid boundary to be optimized, by which the wall become locally opening as inlet or outlet, depends upon the evolved pressure distribution between the boundary and computational domain. The outcome of this analysis is a velocity distribution along the wall, which is not necessarily parallel with it. The final step of the cycle is the wall modification. The wall becomes parallel with the local velocity vector corresponds to a new streamline of the flow field. The mentioned procedure is repeated until the target distribution is reached by the direct analysis and so the new geometry is available [6].
Hereafter, two dimensional inviscid inverse design based optimization method has been adapted, tested and verified by using ANSYS CFX commercial software in case of redesigning vanned diffuser in a research jet engine. The detailed description of the used numerical method is found in [14]. The implementation and application of the *Stratford*'s separation prediction method with the goal of having the optimum pressure distribution is described in the next chapter. It is followed by the introduction of the redesign process of the vanned diffuser by the inverse design method. The outcome of this step is the expected vane geometry. Finally, the plausibility analyses of the results are presented by using ANSYS CFX software in inviscid and viscous flow assumptions at the same geometry, boundary conditions, material properties and physical settings.

2. IMPLEMENTATION OF STRATFORD'S METHOD AND TESTING THE INVERSE DESIGN BASED OPTIMIZATION METHOD

The inverse design methods require optimal pressure or velocity distributions to determine the adherent geometry. Hence, the selection, development and application of flow separation prediction method is described in the present chapter.
In order to maximize the blade loading or flow turning of a profile in a given cascade at given and constant operational (boundary) conditions, the pressure distribution should be as low as possible over the suction side of the vane. However, the adverse

pressure gradient must be present after the location of the maximum velocity (and minimum pressure) in order to recover downstream conditions. The adverse pressure gradient till the trailing edge should be limited in each discretized points to be just below the condition of causing separation. The maximum area bounded by the suction and the pressure side distributions in conjunction with limited values of pressure gradients will provide the optimum solution as a target distribution to be specified for the inverse design method in the present case.

There are several existing methods for predicting separation as *Goldschmied*, *Stratford*, *Head*, and *Cebeci-Smith* for example. The accuracy these methods were examined several times. One of the output of these investigation shows that the operation of *Goldschmied*'s method is unreliable. The other three ones are in reasonable agreement and Stratford's method tended to predict separation slightly early. The *Cebeci-Smith* method is appeared to be the best and the *Head* method is a strong second one [12]. Due to the good accuracy, simple expressions and conservative characteristics for predicting separation, *Stratford*'s method has been used in the present study.

2.1 Determination of the Pressure Distributions

The required pressure distribution for the inverse design method was determined by the application of *Stratford*'s separation prediction method, which is described in [12-15] in detail. The calculation was implemented in Microsoft Excel environment. The reason of the selected computer program was its widespread availability, the fast and efficient data handling and management, calculation, visualisation and data transfer. Concerning the conditions for the application of *Stratford*'s method, the flow is supposed to be incompressible, boundary layer is turbulent and the *Reynolds* number based on unit momentum thickness is around 10^6-10^7. At the start of the process the input parameters such as the total pressure (p_{to}) and temperature (T_{to}) at the upstream of the blade row, static pressure at the downstream of the vanned diffuser and the pressure coefficient (Cp_0) were specified. Then, the far field static parameters (T_∞, M_∞, u_∞ and ρ_∞) were calculated by using the above mentioned total inlet and static outlet conditions. The location of starting pressure increase (the max. flow velocity over the suction side) is denoted by x_0. Afterwards, the static parameters ($p_0(Cp_0, p_\infty, M_\infty)$, $M_0(Cp_0, M_\infty)$, $T_0(T_{to}, M_0)$, $u_0(T_{to}, T_0)$, $\rho_0(T_0, p_0)$ and $Re_0(x_0, u_0)$) belong to this state were determined and supposed to be constant starting from the leading edge of the suction side till the starting of the pressure gradient increment (x_0). Starting from the leading edge, the next step was to change x with sufficiently small steps - keep $x=x_0$ condition, use Stratford's equations for determination canonical pressure distribution - till the pressure on the trailing edge became finally equal with the expected outlet static pressure downstream of the vanned diffuser. By this way, the pressure coefficients and the pressures were determined in every point of the suction side. More information about the described process is found in [14 and 15].

The array of pressure coefficient distribution curves with the inlet total pressure 270000 Pa, inlet total temperature 436.369 K and static outlet (trailing edge) pressure 240184 Pa is shown in Figure 1. The pressure coefficients are in the range of [-2.8, -0.5]. The red curve means the variant with the maximum closed surface area, which is belongs to the Cp=-1.8.

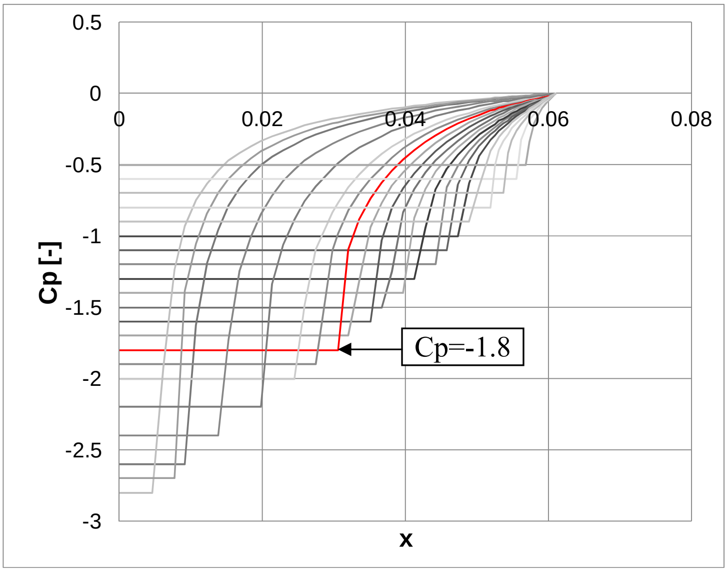

Fig. 1 Pressure coefficient distributions belong to different values of initial Cp

Four different pressure coefficients were selected in order to test the inverse design method. The curve with the largest closed area given at Cp=-1.8, then Cp=-2.2, Cp=-2.6 and Cp=-1.6 were used to test and check the plausibility of the results. The pressure distributions belong to the mentioned pressure coefficients are plotted in Figure 2.

2.2 The Application of the Inverse Design Method and Comparison of Different Test Scenarios at Cp=-1.6, Cp=-1.8, Cp=-2.2 and Cp=-2.6

As the required pressure distributions - along the wall to be modified - and the initial geometry were available, the inverse design process could start. The first step of the iterative cycle was the direct solution of the Euler solver. Roe's approximated *Riemann* solver with MUSCL approach and *Mulder* limiter were used to solve inviscid governing equations by explicit 4^{th} order *Runge-Kutta* time stepping. The number and determination of the physical and numerical boundary conditions were based on the theory of characteristics (see [14] for details). After fulfilling the convergence criteria, a new boundary condition was applied at the solid boundary to be modified, by which the wall became locally opening as inlet or outlet, depends upon the evolved pressure distribution between the boundary and computational domain. The outcome of this analysis was a velocity distribution along the wall, which was not necessarily parallel with it. The final step of the cycle was the wall modification. The wall became parallel with the local velocity vector corresponded to a new streamline of the flow field. The mentioned procedure was repeated until the target distribution was reached by the direct analysis and so the new geometry was available [6].

The boundary conditions of the inverse design applied over the cascade model were the next: inlet total pressure: $p_{tot,in}$=270000 [Pa]; inlet total temperature: $T_{tot,in}$=436.369 [K]; inlet flow angle: 45° and outlet static pressure: $p_{stat,out}$=240184 [Pa].

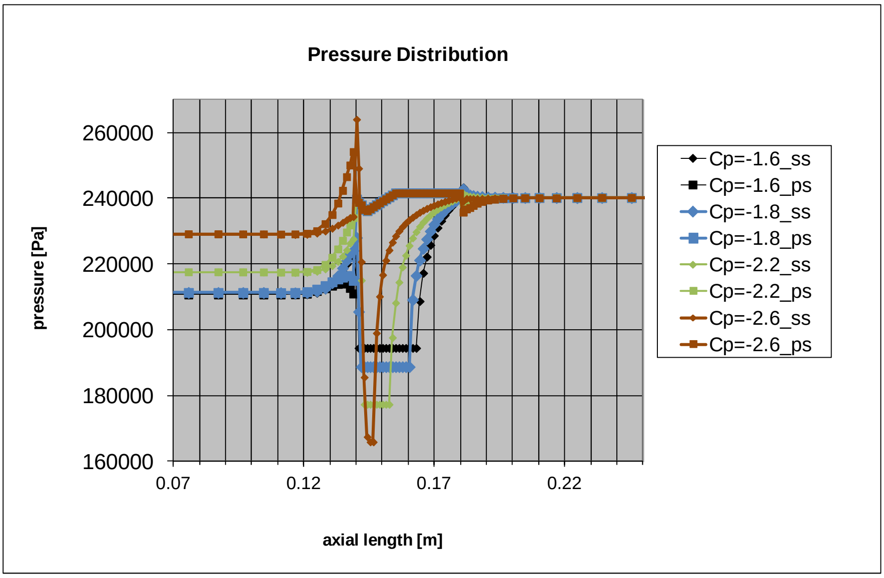

Fig.2 The pressure distribution for the investigated pressure coefficients

Following the application of the inverse design method with the required pressure distributions at Cp=-1.6, Cp=-1.8, Cp=-2.2 and Cp=-2.6, the corresponding blade geometries are shown in Figure 3. The geometries belong to different pressure coefficients are denoted by different colors.

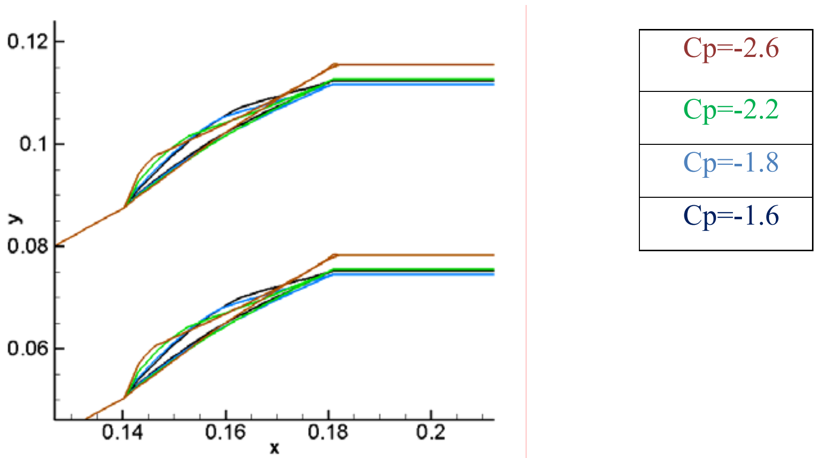

Fig.3 Geometrical configurations of the all redesigned blades in one graph

The design parameters are found in Table 1.

Tab. 1 Design parameters with improvements compared to the initial geometry for all Cp's.

	Initial geometry	**Cp=-1.6**		**Cp=-1.8**		**Cp=-2.2**		**Cp=-2.6**	
		value	%	value	%	value	%	value	%
Flow angle form horizontal at downstream (deg)	26	23	-11.53%	22	-15.38%	28	7.69%	32	23.07%

Static pressure rise (-)	1.119	1.136	1.52%	1.14	1.79%	1.103	-1.42%	1.04	-7.05%
Mass flow rate per unit length(kg/s.m)	15.5	16	3.22%	16.5	6.45%	15.7	1.29%	14.2	-8.38%

As it is shown, the variant with Cp=-1.8 (the optimal pressure distribution) has the maximum flow turning in axial (x) direction, static pressurize and mass flow rate per unit length.

Based on the results above, the existence of a unique pressure distribution on the suction side of the blade in adverse pressure gradient condition from the location of the highest velocity - determined by the Stratford's separation prediction method - is proven and this pressure distribution has the highest closed surface area and the cascade corresponds to this pressure distribution provides (i) the maximum flow turning in axial direction, (ii) the maximum static pressurize and (iv) maximum mass flow rate per unit length, (iv) beside close, but certain distance far from the separation. Hence, this pressure distribution is going to be used in the next chapter of the present work.

3. OPTIMIZATION AND REDESIGN OF THE COMPRESSOR VANNED DIFFUSER OF A RESEARCH JET ENGINE

The numerical simulations and the results of the initial profile and redesigned vane geometry by the inverse design method are presented hereinafter.

The boundary conditions for the both analysis and design were the same as before; inlet total pressure: $p_{tot,in}$=270000 [Pa]; inlet total temperature: $T_{tot,in}$=436.369 [K]; inlet flow angle: 45° and outlet static pressure: $p_{stat,out}$=240184 [Pa].

110×60 H-type mesh was used in the all cases.

The simulations were converged; the residuum's were below 10^{-7} in the all investigated scenarios.

The introduction and the resulted flow fields for the initial and redesigned blade variants with the evaluations and conclusions are found in subchapter 3.1 and 3.2 respectively.

3.1 Determination and Numerical Analysis of the Initial Geometry

A compressor vanned diffuser of a research jet engine was used for creating the initial blade geometry. The 2D projection of the cut section at mean diameter was applied and the splitter vanes were removed with the goal of (i) increasing the cross sectional area, (ii) decreasing weight, (iii) minimizing the drag and losses and (iv) keeping production cost as low as possible by means of using as close configuration to the base line design as possible.

The Mach number, static pressure and static temperature distributions of the initial geometry are plotted in Figures 4-6. The results were plausible; they are within the expected and suitable interval according to preliminary study [16], so they were accepted in physical point of view. The peaks in the flow field at the leading and at the trailing edges were due to the sudden change of mesh and the spatial discretization.

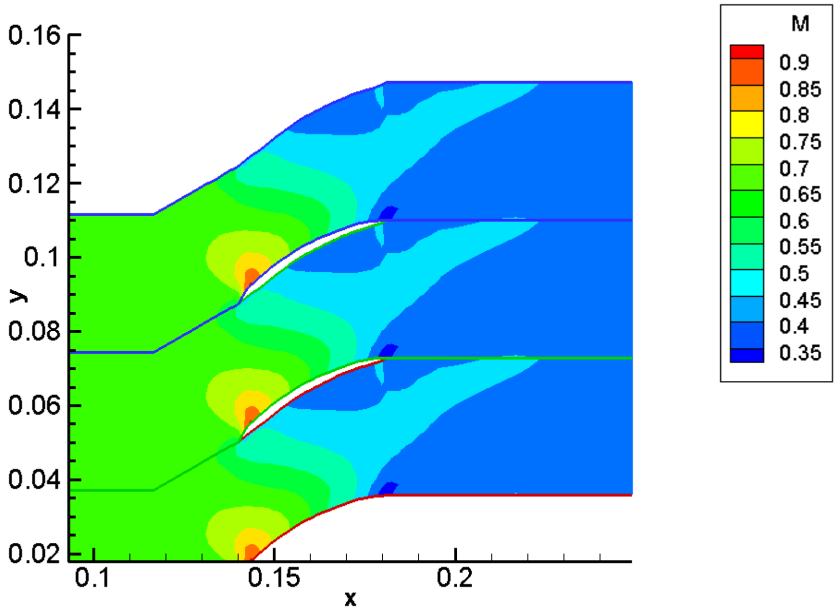

Fig. 4 Mach number [-] distribution in case of initial geometry [m]

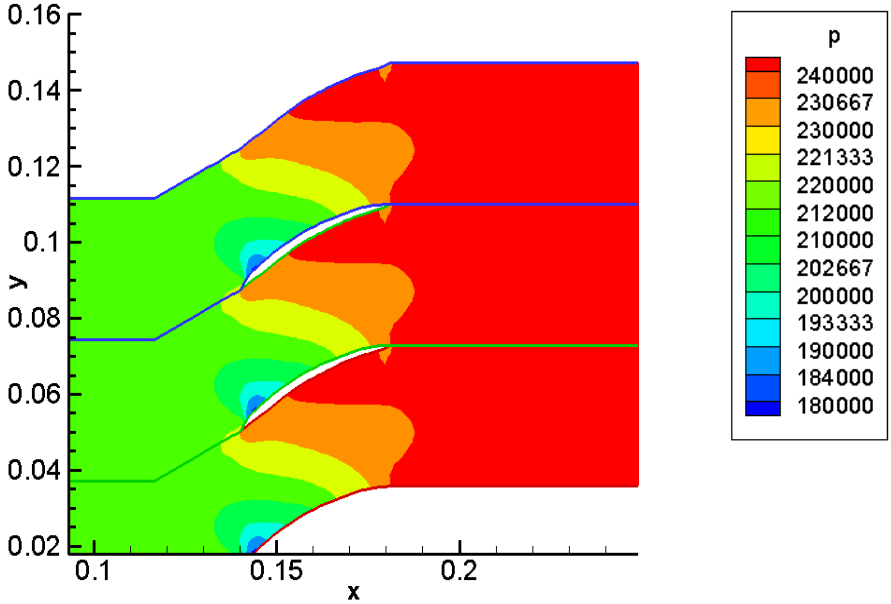

Fig. 5 Static pressure [Pa] distribution in case of initial geometry [m]

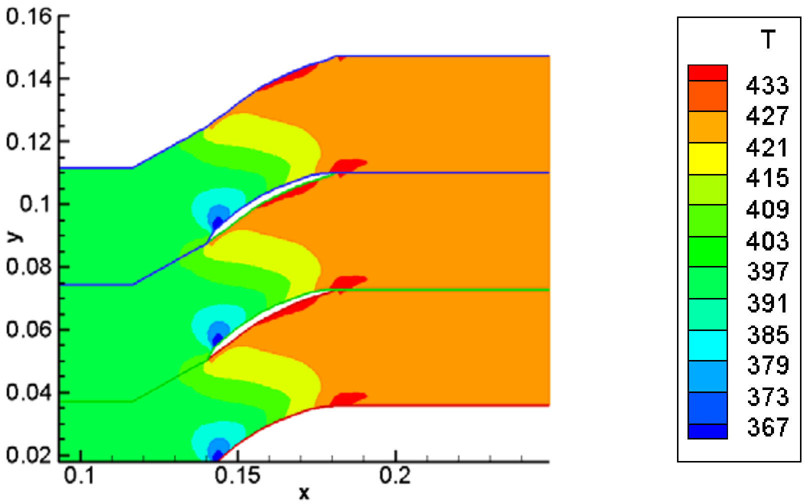

Fig. 6 Static temperature [K] distribution in case of initial geometry [m]

3.2 Inverse Design of the Vanned Diffuser

The vane geometry created in subchapter 3.1 was used for initial blade profile in the present case to be optimized. The determination of the required pressure distribution was already introduced in the subchapter 2.1. The optimum pressure distribution belonged to Cp=-1.8 had the highest closed surface area (see Figure 1. and 2.) and the optimum in this context means the maximum flow turning in axial direction, the maximum static pressurize and maximum mass flow rate per unit length beside close, but certain distance far from the separation.

It can be mentioned also, which is a general procedure at completing the inverse design process, that several points of the target pressures near to the leading edge of the suction side were modified to make the extremely high pressure gradient smoother (see Figure 7). Moreover, an arbitrary (optimal in the present case) target pressure distribution often causes non-realistic geometry as negative thickness, trailing edge opening or cross over. Based on several theoretical investigation and computational tests, it can be noticed, that the expected pressure distribution cannot be arbitrary in case of subsonic flow due to the information propagation into the upstream (leading edge) direction along the streamline bounded by the wall. If the required pressure is differ from the initial one at the certain representative part of the near wall region, the flow can be retarded or sucked depends on the local conditions. This effect has an influence on the flow evolution starting from the leading edge and the pressure should be redistributed by considering higher or lower local kinetic energy along the stream line especially at the first couple mesh points of the leading edge [6].

So, the modified distributions were imposed in the inverse design procedure at the same boundary conditions and meshing than in the case of initial blade profile to determine the geometry, which provides the expected solutions. The inverse design method was converged after 10 iteration cycles of the inverse, wall modification and direct modes. The normal velocity distribution across the solid wall was near to zero at the 10th iteration of the inverse subroutine, which represented that there was no need for further steps, the pressure gradient was infinitesimally small (no flow) across the solid boundary. The corresponding results of the optimization procedure are found in Figure 7.

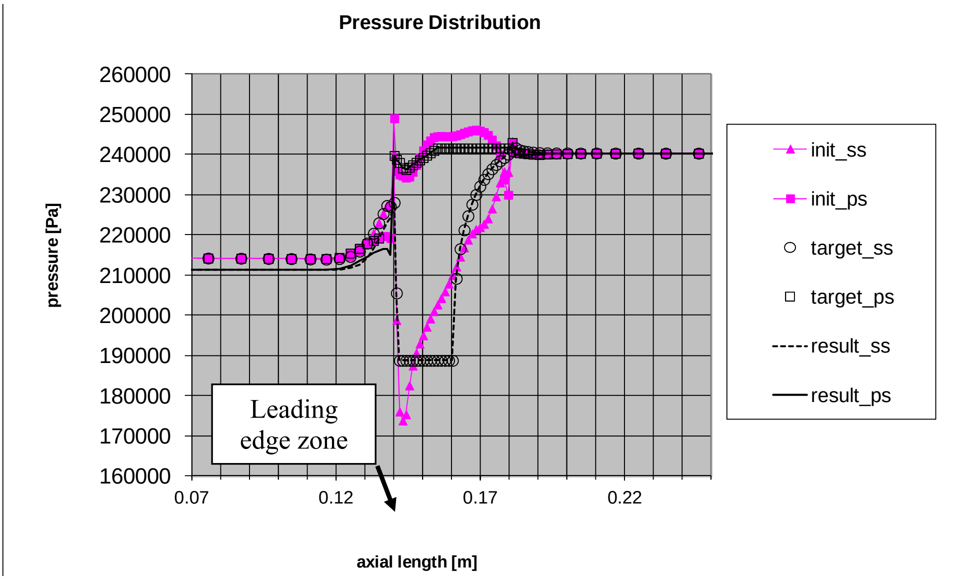

Fig. 7 Comparison of the initial, target and result static pressure distributions along the suction and pressure side of the profile (ss: suction side, ps: pressure side)

So, the modified distributions were imposed in the inverse design procedure at the same boundary conditions and meshing than in the case of initial blade profile to determine the geometry, which provides the expected solutions. The inverse design method was converged after 10 iteration cycles of the inverse, wall modification and direct modes. The normal velocity distribution across the solid wall was near to zero at the 10^{th} iteration of the inverse subroutine, which represented that there was no need for further steps, the pressure gradient was infinitesimally small (no flow) across the solid boundary. The corresponding results of the optimization procedure are found in Figure 7. The target and optimised (result) pressure distribution are compared with each other and the deviation between them is negligible. The average normalized differences between the suction side and pressure side pressure distributions are 0.42 % and 0.34 % respectively. The optimized (redesigned) geometry with the resulted Mach number and pressure distribution are found in Figures 8-9. The both Mach number and pressure distributions show more homogenous and uniform exchange along the blade channel compared to the initial profile.

Concerning the design parameters as the static pressurize, flow turning in axial direction and mass flow rate, the optimized configuration had better performances than the initial profile in the each cases as it is shown in Table. 1. The initial profile in this case namely was the same – together will the all other setting – as it was used the subchapter 2.2, so the optimized blading were also the same. The results confirm the expectations; the optimized vane geometry gave (i) higher flow turning in axial direction, (ii) higher static pressurize and (iii) higher mass flow rate per unit length than the initial blading. The all parameters were improved by 7.9 % in average.

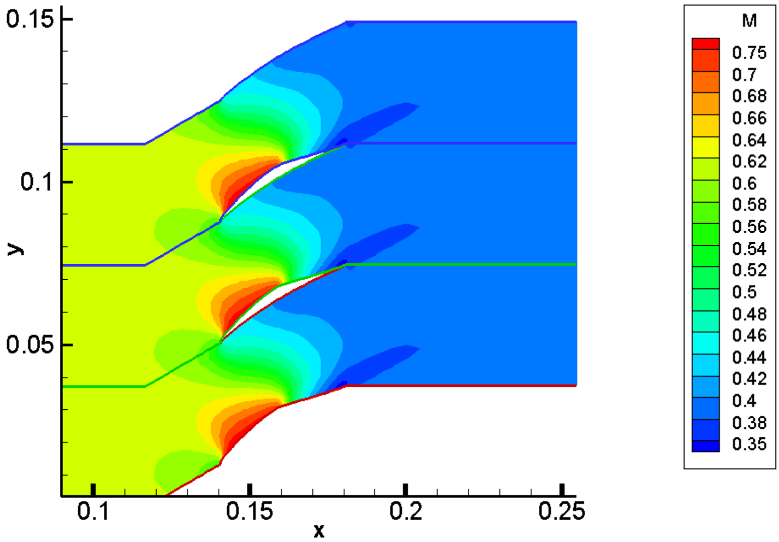

Fig. 8 Mach number [-] distribution in case of redesigned geometry [m]

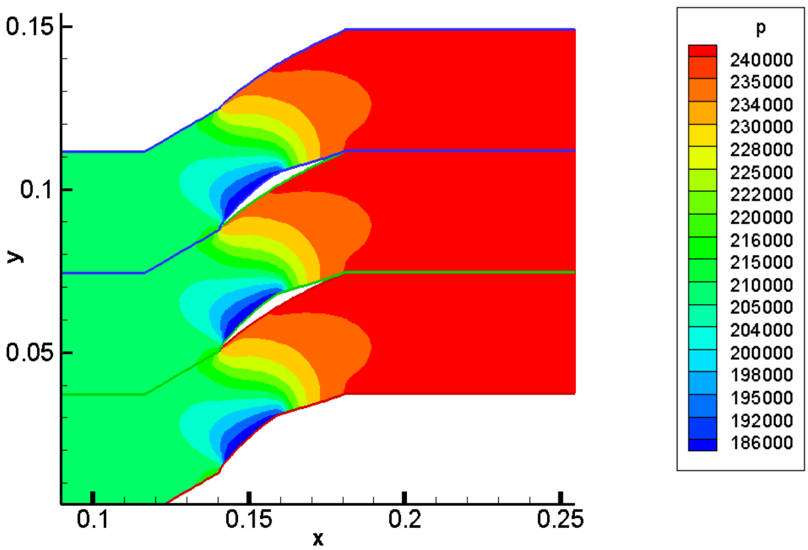

Fig. 9 Static pressure [Pa] distribution in case of redesigned geometry [m]

4. Verification of the Results by Means of ANSYS CFX

The verification in this context means that the output geometry of the optimization process was compared with the results of a highly validated commercial CFD code to crosscheck the correct and accurate operation of the inverse design tool. ANSYS CFX was used for that purpose at the same mesh, boundary conditions and material properties. The simulations in the ANSYS CFX were performed by two different ways as inviscid and viscous flow assumptions to see the differences between them and the (inviscid) in-house code.

4.1 Inviscid Analysis of the Optimized (Redesigned) Blade by CFX

The Design Modeller, which is part of ANSYS Workbench, was used for creating the flow field. The 2D coordinates of the points were imported from the Tecplot_21_10.dat file into the Design Modeller. Concerning the numerical mesh, similar configuration was created in the present case also than in the direct mode of the inverse design method to minimize the differences between the two simulation approaches. The numbers of the elements and nodes to be used in the simulation were 7448 and 6494, respectively.

In CFX-Pre sub module, the properties of the operational fluid through the domain were defined. Air as an ideal gas with zero viscosity was used. The option of heat transfer corresponded to 'Total Energy'. Free slip boundary condition was used for solid surfaces. The boundary conditions were the following: inlet total pressure: $p_{tot,in}$=270000 [Pa]; inlet total temperature: $T_{tot,in}$=436.369 [K]; inlet flow angle: 45° and the outlet static pressure: $p_{stat,out}$=240184 [Pa]. After reaching the convergence criterion, the results of the CFX analysis were evaluated. First, the pressure distributions, as quantitative results, were shown in the upstream and downstream of the periodic pairs at the vane segments and along the suction and pressure side of the profile (see Figure 10). The initial, the target and the resulted pressure distributions of the inverse design method are also shown beside the inviscid result of the CFX at the pressure side (Ansys_inviscid_ps) and at the suction side (Ansys_inviscid_ss).

The average relative deviations between the results of the inverse design code and Ansys inviscid approach were 2 % at suction side and 0.29 % at the pressure side. These data confirms that the inverse design optimization method works correctly and provides plausible and accurate results.

The qualitative results were also presented in case of CFX for comparison (see Figure 11 and 12). The differences between the direct solver of the inverse design method and ANSYS CFX were mostly due to the different treatments of the boundary conditions and averaging techniques over the cells. Additionally, the used discretization methods could also contribute to have slightly different results based on the different inherent mechanism.

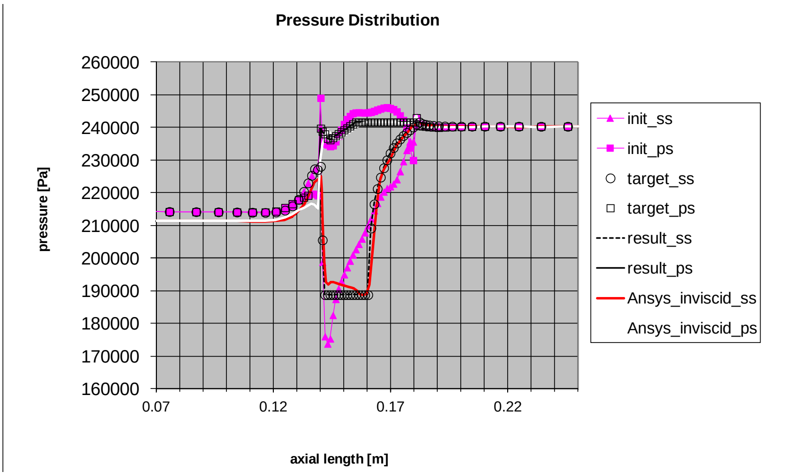

Fig. 10 Pressure distributions of the initial (init), target and redesigned (result) blade configurations in case of inviscid flow analyses by the direct solver of inverse design tool and ANSYS CFX (Ansys) (ss=suction side, ps=pressure side)

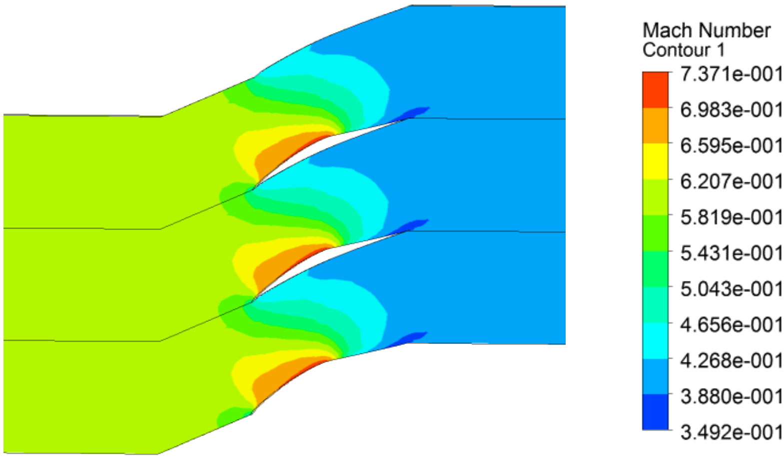

Fig. 11 Mach number [-] distribution of the redesigned blade configuration in case of ANSYS CFX (inviscid analysis)

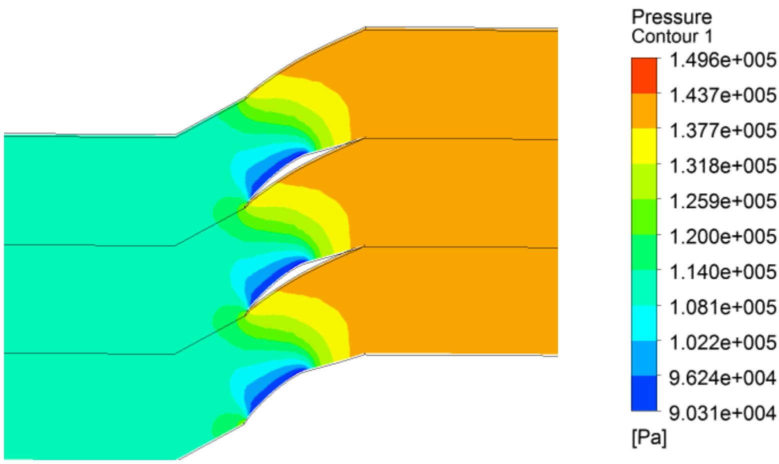

Fig. 12 Pressure distribution [Pa] of the redesigned blade configuration in case of ANSYS CFX (inviscid analysis)

4.2 Viscous Analysis of the Optimized (Redesigned) Blade by CFX

The same procedure was followed in case of viscous flow than in case of inviscid analysis. However, due to the more complex treatment of the physics, there were some differences between the two approaches. The boundary layer was resolved on such a way that the first cell from the wall to be fallen in the log layer region. Hence, dimensionless analytical expressions derived over the flat plate flow were used to determine the distance of the first cell from the solid wall to have y+=21. The inflation layer was build up from 20 layers. The numbers of elements and nodes to be used in the simulation were 87221 and 36756 respectively.

Air was considered as an ideal gas for the operational fluid. The value of the dynamic viscosity was set to be 1.831e-05 Pas. Total energy was used for the heat transfer. Shear Stress Transport (SST) turbulence model was applied.

The boundary conditions were the following: inlet total pressure: $p_{tot,in}$=270000 [Pa]; inlet total temperature: $T_{tot,in}$=436.369 [K]; inlet flow angle: 45° and the outlet static pressure: $p_{stat,out}$=240184 [Pa]. No slip boundary condition was used for the wall boundary condition.
After having mesh independent and converged solution, the initial, the target and the resulted pressure distributions of the inverse design tool were plotted in a same diagram with the inviscid (Ansys_inviscid_ss and Ansys_inviscid_ps) and viscous (Ansys_viscous_ss and Ansys_viscous_ps) flow result of the CFX software (ss=suc-tion side and ps=pressure side) as it is shown in Figure 13. The maximum differences between the inverse design and Ansys viscous wall pressures were 8 %, and the relative average differences between the inverse design and Ansys viscous flow analysis were 3.04 % on suction side and 0.3 % at pressure side. The highest difference was arisen around the leading edge stagnation point.
The qualitative results are also presented in case of viscous CFX simulations for comparison. The relative static and total pressure distributions are plotted in Figure 14 and 15 respectively. These distributions are in line with the results of the CFX viscus analysis and with the results of the direct solver of the inverse design method.
Both, the viscous and inviscid analyses confirmed that the adopted and applied inverse design optimization method provided plausible and accurate results for the presented case, which is acceptable in engineering point of view. Hence, the introduced inverse design based optimization method - after further sensitivity analyses and validations by measurements - can be used in design and developments in the other field of the fluid dynamics, too.
-

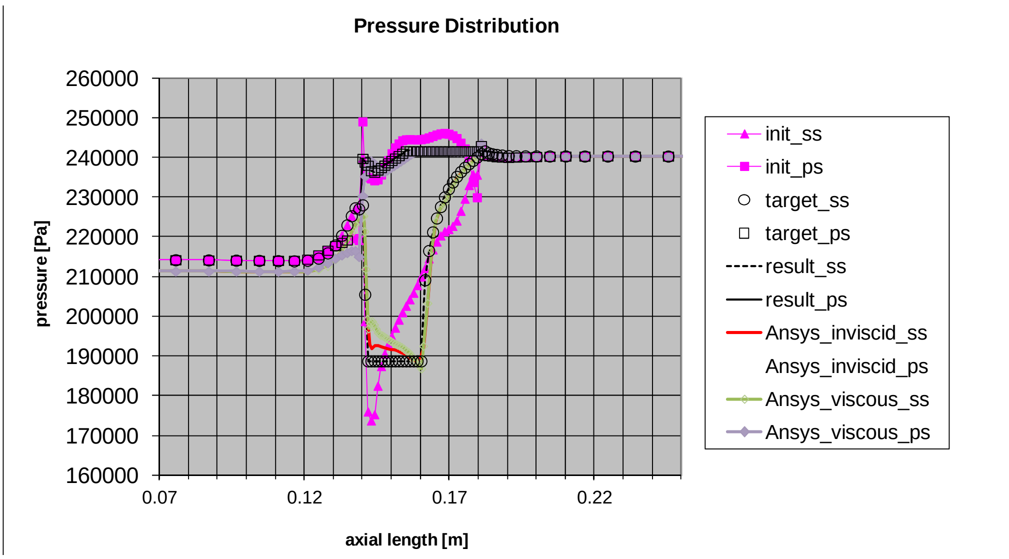

Fig. 13 Pressure distributions of the initial (init), target and redesigned (result) blade configurations in case of inviscid flow analyses by the in-house inverse design code and inviscid and viscous flow analyses by the ANSYS CFX (Ansys) (ss=suction side, ps=pressure side)

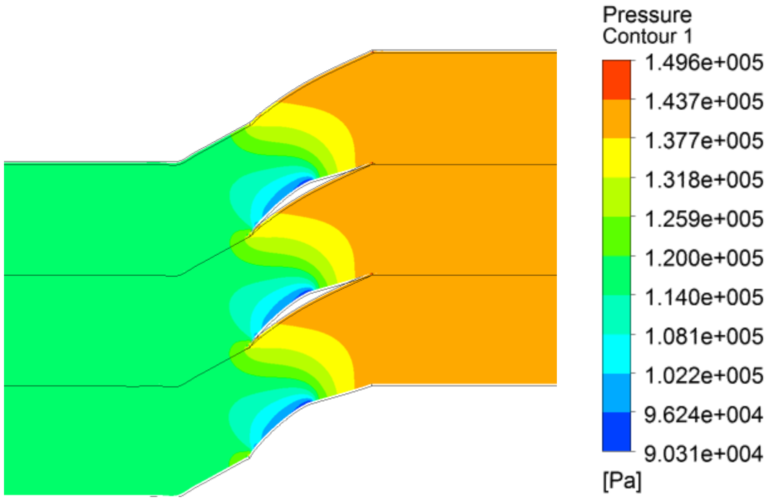

Fig. 14 Pressure distribution of the redesigned blade configuration in case of ANSYS CFX (viscous analysis)

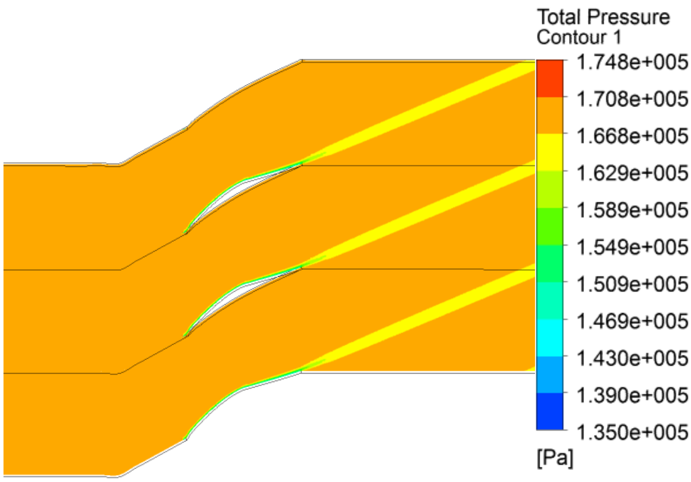

Fig. 15 Total pressure distribution of the redesigned blade configuration in case of ANSYS CFX (viscous analysis)

Finally, the performance of the original vanned diffuser with splitter vanes and the optimized geometry was compared with each other by using ANSYS CFX viscous flow solver. The mesh, the boundary conditions, the physical and numerical setting were the same as before for the both configurations. After having convergent status at the simulation, the qualitative results of the original vanned diffuser with splitter vanes are presented in Figures 16-17.

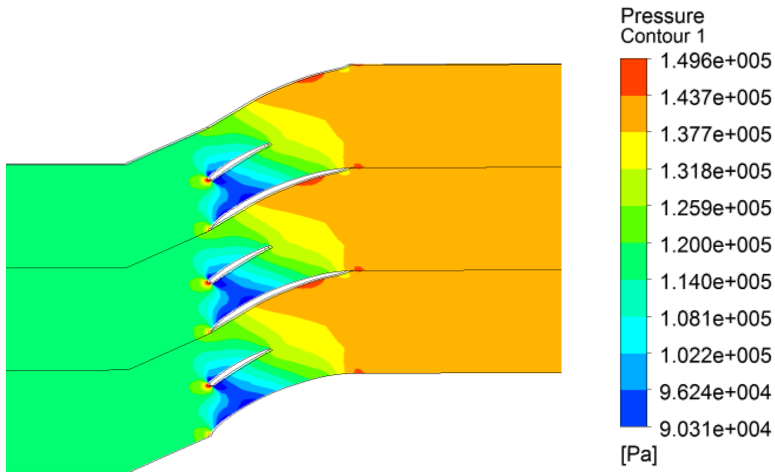

Fig. 16 Pressure distribution of the baseline configuration in case of ANSYS CFX (viscous analysis)

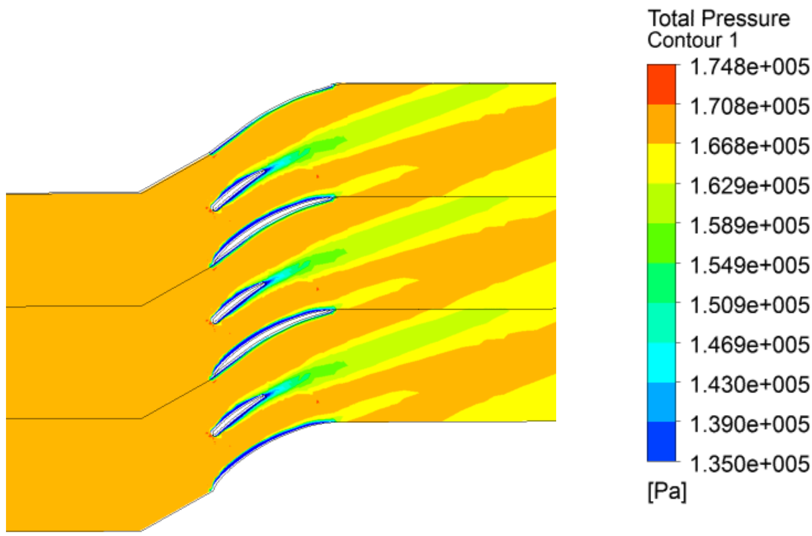

Fig. 17 Total pressure distribution of the original blade configuration in case of ANSYS CFX (viscous analysis)

Following the qualitative results, the quantitative comparison was completed between the original geometry with splitter vanes and the optimized geometry. The total pressure recovery factor, the static pressurize, the flow turning in axial direction and the mass flow rate are found in the Table 2.
It is shown, that the newly redesigned optimum vane configuration provides better performance that the original vane configuration in the all investigated design parameter. The average relative improvements are 5.88 %.

Table. 2 design parameters with improvements compared to the base line design

	Base line design	**Optimized vanned diffuser**	**Improvements**
Total pressure recovery factor (-)	0.96	0.99	3.13%
Static pressure rise (-)	1.1	1.12	1.81%
Flow angle from horizontal at downstream (deg)	26	22	-15.38%
Mass flow rate per unit length (kg/m.s)	15.5	16	3.2%

The combination of the optimum pressure distribution by means of the maximum closed surface area created by Stratford's separation prediction method and inverse design method has provided a suitable tool for determining the most suitable design variant at given operational condition for vanned diffuser of centrifugal compressors.

5. CONCLUSIONS

The adoption and the new application of the inversed design optimization method have been completed in the present research for redesigning the vanned diffuser in an academic jet engine with verification. The goal function of the optimization was to keep the (i) original geometrical configuration and dimensions as much as possible, meanwhile (ii) the maximum flow turning, (iii) the maximum static pressurize, (iv) the maximum mass flow rate and (v) the maximal pressure recovery factor were expected on such a way that (vi) the flow stream to be close but certain distance far from the separation.

Compressible Euler equations are considered as governing equations in the used academic code and a specific finite volume method has been applied to solve the system of the nonlinear partial differential equations. Stratford's separation prediction method has been used to determine and then select the optimum pressure distribution at given boundary conditions along the suction side in adverse pressure gradient flow condition.

The initial 2D profile for the inverse design method was extracted from the original vanned diffuser at the mid-radius of the flow cross section.

The outcomes of the recent investigations were the following:

(i) The combination of
   a. the Stratford's separation prediction method with the maximum closed surface area of the pressure distribution
   b. and inverse design method

   has provided the optimum vane configuration by means of
   a. the highest flow turning in axial direction
   b. the highest mass flow rate and
   c. the highest flow turning in axial direction,
   d. meanwhile the flow is close but certain distance far from the separation and
   e. the relative average difference between the target and the resulted pressure distribution is 0.42% at suction side and 0.34 % at pressure side.

(ii) The initial geometry for the inverse design tool was determined to keep the design change and production cost as low as possible, so
   a. the splitter vanes were removed and
   b. only the longer vanes were kept and used as initial geometry.

(iii) Ansys CFX commercial code has been used for verification, for crosschecking that the outcomes of inverse design method are plausible, correct and accurate.
   a. The inviscid-type verification has provided 2 % and 0.29 % relative average deviations in case of the resulted pressure distribution between the commercial and in-house code at suction side and pressure side respectively.
   b. The average relative difference at the pressure distributions between the CFX at viscous and the inviscid inverse design code is 3.04% at suction side and 0.3 % at pressure side.

(iv) The aerodynamic performance of the base line design and the optimized vanned diffuser has been compared with each other by means of viscous flow analyses. The optimized version has
   a. 3.13 % less total pressure recovery factor,
   b. 1.81 % higher static pressurize,
   c. 15.38 % flow angle decrement measured from the axial (x) direction
   d. 3.2 % higher mass flow rate per unit length

   than the original vane configuration.

Based on the all paragraphs mentioned above, the presented inverse design tool with Stratford's separation prediction method can be used successfully in the developments of vanned diffusers of centrifugal compressors. However, measurement based validation would be indispensable to complete before the introduction that into the R&D processes. Additionally, there are several features to improve its capability as follows: (i) extension in 3D and (ii) viscous flow conditions, (iii) automatic target pressure distribution at the leading edge for guarantying the existence (structural integrity) of the blade geometry (iv) investigate the effect and/or develop other separation prediction methods to increase the overall accuracy and (v) to be suitable with other range of Re and highly compressible flow regime.

6. REFERENCES

[1] **Jankovics, I. - Rohács, D. - Rohács, J.**: Motion Simulation Model of a Special Acrobatic Aircraft, Proceedings of the 12th MINI Conference on Vehicle System Dynamics, Identification and Anomalies (VSDI 2010), (ed. by Prof. I. Zobory). BME, Department of Railway Vehicles, Budapest, 2012. p.393-401. ISBN: 978-963-313-058-2,.

[2] **Beneda, K.**: Numerical Simulation of MEMS-based Blade Load Distribution Control in Centrifugal Compressor Surge Suppression, AIP Conference Proceedings, 1493, 2012, p.116-123.

[3] **Bera, J. - Pokorádi, L.**: Monte-Carlo Simulation of Helicopter Noise, Acta Polytechnica Hungarica, 12:(2) 2015, p.21-32.

[4] **Hargitai, Cs. - Rohács, D.**: Manoeuvring Behaviour Prediction of Inland Vessels by Computer Simulation, Scientific Journal on Transport and Logistic, (under edition), 2016.

[5] **Thévenin, D. - Janiga, G.:** Optimization and Computational Fluid Dynamics, Hardcover, ISBN 978-3-540-72152-9, Springer-Verlag Berlin Heidelberg, 2008.

[6] **Veress, Á. - Felföldi, A. - Gausz, T. - Palkovics, L.:** Coupled Problem of the Inverse Design and Constraint Optimization, Applied Mathematics and Computation, vol. 219, no. 13, 2013, p.7115-7126,

[7] **Lighthill, M.:** A new Method of Two-dimensional Aerodynamic Design, in Aeronautical Research Council, London, 1945.

[8] **Giles, M. B. - Drela, M.:** Two-Dimensional Transonic Aerodynamic Design Method, Journal of AIAA, vol. 25, no. 9, 1987, p.1199-1206,

[9] **Demeulenaere, A.:** An Euler/Navier-Stokes Inverse Method for Compressor and Turbine Blade Design, Von Kármán Institute for Fluid Dynamics, Inverse Design and Optimization Methods, 1997.

[10] **de Vito, L. - Van den Braembussche, R. A. - Deconinck, H.:** A Novel Two-dimensional Viscous Inverse Design Method for Turbomachinery Blading, in International Gas Turbine and Aeroengine Congress and Exhibition, Amsterdam, PAYS-BAS , 03/06/2002.

[11] **Cabuk, H. - Modi, V.:** Optimum Plane Diffusers In Laminar Flow, Journal of Fluid Mechanics, vol. 237, 1992, p.373-393.

[12] **Smith, A.:** High-Lift Aerodynamics, Journal of Aircraft, vol. 12, no. 6, 1975, p.501-530.

[13] **Stratford, B.:** The Prediction of Separation of the Turbulent Boundary Layer, Journal of Fluid Mechanics, vol. 5, 1959, p.1-16.

[14] Z**are, F. - Veress, Á.:** Plausibility Check of the Inverse Design and Optimization Method for Cascade Flow by Means of ANSYS CFX Software, Hungary-Szolnok, 2015, p.182-206.

[15] **Molnár, D.:** Investigation of Inverse Design Utilization for Static Pressurize of a Cascade, Budapest University of technology and economics, Budapest, 2016.

[16] **Pallag, N.:** "A TKT-1 Gázturbinás Sugárhajtómű Áramlástani Vizsgálata", MSc Thesis, Budapest University of Technology and Economics, Department of Aeronautics, Naval Architecture and Railway Vehicles, Budapest, 2013. (In Hungarian)

DEVELOPMENT OF AN INNOVATIVE *UAV* LAUNCHER

Balázs GÁTI

Department of Aeronautics, Naval Architecture and Railway Vehicles
Faculty of Transportation Engineering and Vehicle Engineering
Budapest University of Technology and Economics
H-1111 Budapest, Hungary

Received: November 9, 2016

ABSTRACT

A trebuchet was a kind of siege engine in the middle age that stored the required energy for launching a projectile in the potential energy of the counterweight. We've found a trebuchet-like solution to store the energy demand of a UAV launch in the potential energy of the transport vehicle of the UAV, while the vehicle is used also as a supporting structure of the launching device. This way the device is simpler than common catapults that store energy in rubber bands or in pressurised air. The device is a result of a systematic development started by theoretical investigations. The launcher was described with a multibody model in order to prove that the idea is feasible and the UAV will be released with the right angle of attack, pitch angle, flightpath angle and airspeed. The paper describes the model, the non-linear differential equation system and the simulation results. The theory was verified by different test devices and the prototype performed already 100+ launches and is still in usage. The patent of the solution is pending.

Keywords: UAV, launching device, trebuchet, multibody system, patent

1. INTRODUCTION

A trebuchet was a kind of siege engine in the middle age that was characterized by an arm-and-sling mechanism and a heavy counterweight that stored the required energy for launching a projectile in its potential energy ([1])

Fig.1 Trebuchet in the middle age [2]

The increased release height of this solution appeared to be useful today for fixed wing UAVs, because the widely used catapults ([3],[4],[5]), bungee starts and similar solutions feature low release height and low flight path angle during climb, that require clean, obstacle free area. However a trebuchet releases the projectile in an altitude of several meters i.e. above bushes, small trees, camp accessories, small buildings etc. We started an investigation whether this advantage can be utilized for launching a fixed wing UAV.

2. MOBILE TREBUCHET

2.1 Configuration

After the promising preliminary results we've collected the requirements for a reasonable, full scale device capable of launching a UAV in the class of 10kg. The most important requirements were the mobility: the device had to be easy to transport and easy to install in order to make it competitive to the existing solutions. These requirements could be met only if the counterweight is the vehicle (car, rover, van) itself, that is used to transport the crew and all of the parts of the unmanned system. Additionally the heavy supporting structure of the original trebuchet had to be minimized in order to make it lightweight and simple enough for a single man crew. The following patent pending solution (0) utilizes the transport vehicle as counterweight and even as the most of the supporting structure, too. The operation of the mechanism is similar to the floating arm trebuchet ([6]) but instead of roller-and-track constraints we applied simple, lightweight and easy to maintain linkages.

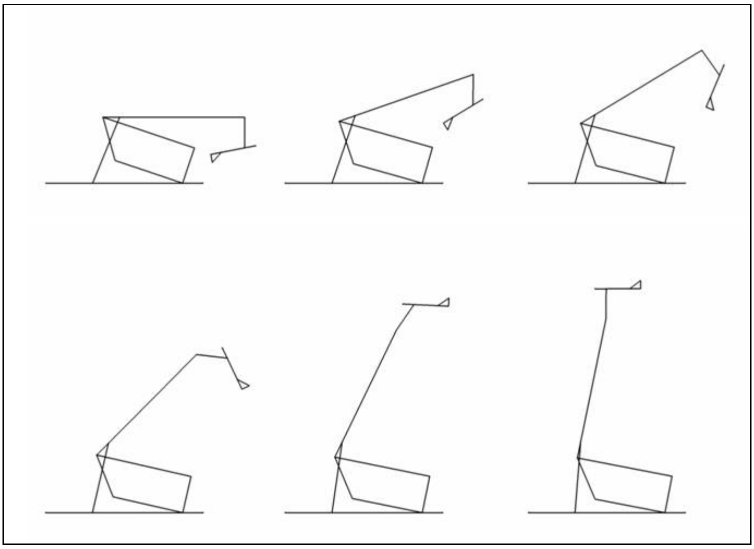

Fig. 2 Kinematics of the mobile trebuchet

This solution seems unorthodox, but in addition to the high release feature it is very cost effective, too. No special high power energy storage device such pneumatics, rubber bands, electric launch motor, etc. is needed, resulting low material, production and maintenance costs. The simple release solution instead of the UAV cradle and the lack of rail make the device more reliable than existing launching systems.

2.2 Simulation

The mobile trebuchet is a typical multibody system, which theory is well known ([7]). This particular system contains five rigid bodies (0). Body m_1 is the transport vehicle. Only one of its axle supported by the ground (S_2), while the other is elevated from it by a force in the retrofitted connection point C_1. Body m_2 is the trebuchet arm, while m_3 is the sling. Body m_5 is the support rod connected to the main pivot C_0 of the arm m_2 and supported by the ground in connection point S_1.

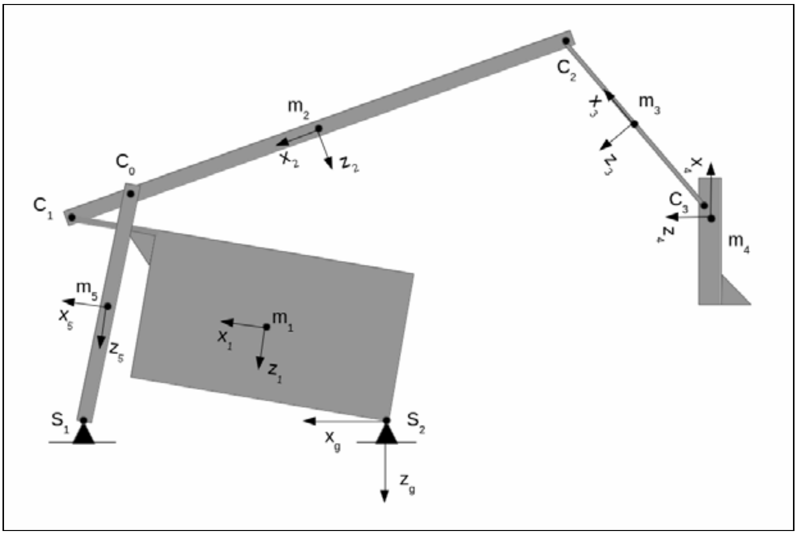

Fig. 3 Multibody model of the mobile trebuchet

These and all other connection points are modelled by an ideal pivot. Each body in the multibody system is affected by its own gravity and the forces in the connection points. The UAV *(m_4)* is the only body we expected to be exposed to the aerodynamic forces, too.

The impulse equation can be formulated for each body in its own body fixed coordinate system:

$$m_i \cdot \left[\underline{{}_i\dot{V}_i} + \underline{{}_i\Omega_i} \times \underline{{}_iV_i} \right] = \underline{\underline{M_{iG}}} \cdot \underline{{}_GG_i} + \sum_j \left(\underline{{}_iCF_j} \right) + \underline{{}_iSF_k} + \underline{\underline{M_{iAi}}} \cdot \underline{{}_{Ai}AF_i} \quad , \tag{1}$$

where

m_i : mass of body *i*

$\underline{{}_iV_i}$: velocity of body *i* in its own body fixed coordinate system

$\underline{{}_i\Omega_i}$: angular velocity of body *i* in its own body fixed coordinate system

$\underline{\underline{M_{iG}}}$: transformation matrix from Earth based coordinate system to body fixed coordinate system of body *i*

$\underline{{}_GG_i}$: gravity of body *i* in Earth fixed coordinate system

$\underline{{}_iCF_j}$: connection force in connection point C_j in body fixed coordinate system of body *i*

$\underline{{}_iSF_k}$: connection force in support point S_k in body fixed coordinate system of body *i*

$\underline{\underline{M}}_{iAi}$: transformation matrix from wind coordinate system Ai of body i to its body fixed coordinate system

${}_{Ai}\underline{AF}_i$:Aerodynamic forces on body i in its wind coordinate system

The momentum equation can be formulated for each body similar way in its own body fixed coordinate system.

$$ {}_i\underline{\underline{I}}_i \cdot {}_i\underline{\dot{\Omega}}_i + {}_i\underline{\Omega}_i \times {}_i\underline{\underline{I}}_i \cdot {}_i\underline{\Omega}_i = \sum_j \left({}_i\underline{r}_{iCFj} \times {}_i\underline{CF}_j \right) + {}_i\underline{r}_{iSFk} \times {}_i\underline{SF}_k + {}_i\underline{r}_{iAi} \times \left(\underline{\underline{M}}_{iAi} \cdot {}_{Ai}\underline{AF}_i \right) + {}_i\underline{AM}_i \ , \qquad (2) $$

where

${}_i\underline{\underline{I}}_i$: inertia of body i in its own body fixed coordinate system

${}_i\underline{r}_{iCFj}$: position vector directed from the CG of body i to the connection point C_j described in body fixed coordinate system of body i

${}_i\underline{r}_{iSFk}$: position vector directed from the CG of body i to the support point S_j described in body fixed coordinate system of body i

${}_i\underline{r}_{iAi}$: position vector directed from the CG to the Aerodynamic Center of body i described in body fixed coordinate system of body i

${}_i\underline{AM}_i$: Aerodynamic moment on body i in its body fixed coordinate system

${}_{Ai}\underline{AF}_i$ and ${}_i\underline{AM}_i$ for the UAV is calculated based on aerodynamic coefficients (lift coefficient C_L, drag coefficient C_D, moment coefficient C_m) provided by the XFLR5 software ([8]) for a typical UAV in the class of 10 kg. The angle of attack is calculated in each time step of the simulation based on the motion parameters of the body m_5 representing the UAV.

The constraints in the connection points are modelled by an ideal pivot that prevents relative translation, thus forces the acceleration of both connected body points to be equal:

$$ \underline{\underline{M}}_{Gi} \cdot \left[{}_i\underline{\dot{V}}_i + {}_i\underline{\Omega}_i \times {}_i\underline{V}_i + {}_i\underline{\dot{\Omega}}_i \times {}_i\underline{r}_{iCk} + {}_i\underline{\Omega}_i \times \left({}_i\underline{\Omega}_i \times {}_i\underline{r}_{iCk} \right) \right] = \underline{\underline{M}}_{Gj} \cdot \left[{}_j\underline{\dot{V}}_j + {}_j\underline{\Omega}_j \times {}_j\underline{V}_j + {}_j\underline{\dot{\Omega}}_j \times {}_j\underline{r}_{jCk} + {}_j\underline{\Omega}_j \times \left({}_j\underline{\Omega}_j \times {}_j\underline{r}_{jCk} \right) \right] \ , \qquad (3) $$

where

${}_i\underline{r}_{iCk}$: position vector directed from the CG of body i to the connection point C_k described in body fixed coordinate system of body i

$\underline{\underline{M}}_{Gi}$: transformation matrix from body fixed coordinate system of body i to Earth fixed coordinate system

The two support points (S_1, S_2) are special connection points, where one of the bodies is the fixed Earth, thus the acceleration of the other body in the support point equal to zero:

$$\underline{\underline{M}}_{Gi}\cdot\left[{}_i\dot{\underline{V}}_i+{}_i\underline{\Omega}_i\times{}_i\underline{V}_i+{}_i\dot{\underline{\Omega}}_i\times{}_i\underline{r}_{iSFk}+{}_i\underline{\Omega}_i\times\left({}_i\underline{\Omega}_i\times{}_i\underline{r}_{iSFk}\right)\right]=\underline{0}\ , \tag{4}$$

Finally the equation system consists five impulse equations (1) and five momentum equations (2) according to the five bodies in the system and six constraints equation according to the four connection points (3) and two support points (4). The rearranging of the equations results a differential equation system in the following form:

$$\underline{\underline{A}}\cdot\dot{\underline{x}}=\underline{b}\left(\underline{x}\right)\ , \tag{5}$$

where the vector of first derivatives of the unknowns is:

$$\dot{\underline{x}}=\left[{}_1\dot{\underline{V}}_1,{}_1\dot{\underline{\Omega}}_1,\dot{\psi}_1,\dot{\theta}_1,\dot{\varphi}_1,{}_1\dot{\underline{P}}_1;\ldots;\ldots;\ldots;\dot{\psi}_5,\dot{\theta}_5,\dot{\varphi}_5,{}_5\dot{\underline{P}}_5;{}_0\underline{CF}_0;{}_1\underline{CF}_1;{}_2\underline{CF}_2;{}_3\underline{CF}_3;{}_1\underline{SF}_1;{}_2\underline{SF}_2\right]\ , \tag{6}$$

where

$\psi_i,\theta_i,\varphi_i$: Euler angles of body i

${}_i\underline{P}_i$: position of the CG of body i in its body fixed coordinate system

${}_i\underline{CF}_k$: connection force in connection point C_k in the body fixed coordinate system of body i

${}_i\underline{SF}_k$: support force in connection point S_k in the body fixed coordinate system of body i

The forces have been included in the vector of first derivatives of the unknowns in order to be able to calculate the value of each unknowns in one step. This way the left division of both sides of (5) with the numerically calculated inverse of the system matrix $\underline{\underline{A}}$ resulted the value of each unknown. Subsequently we applied the above mentioned Runge-Kutta solver to integrate the relevant parameters in the vector of unknowns.

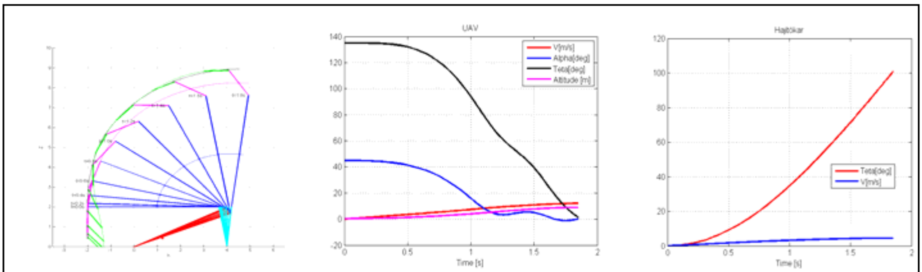

a.) b.) c.)

Fig. 4 Visualisation (a,) UAV parameters (b,) and arm parameters (c,) of the mobile trebuchet

0(a), shows a typical launch sequence of the mobile trebuchet. The green line represents the UAV, the magenta line is the sling, the blue line is the arm, the cyan line is the support rod. The transport vehicle is represented by the red line connecting the axle supported by the ground (left end) with the retrofitted connection point (right end).

The simulation provides all of the important parameters and enable the investigation of the conditions at the release of the UAV. This way we could perform extensive analysis of the effect of UAV parameters such

- Center of Gravity
- position of release hook
- elevator deflection
- wing loading
- drag polar
- initial position and attitude

in addition to the parameters of the trebuchet such

- weight of counterweight
- length of arm
- position of pivot
- length of sling
- weight of UAV

on the flight path angle, velocity, acceleration, angle of attack of the UAV during the launch and the proper time of its release.

2.3 Full scale test launches

The successful simulations proved that the mobile UAV trebuchet is feasibly, thus we started the development of the device. The first full scale version was designed intentionally oversized in order to be able perform launch tests with different position of the main pivot in the trebuchet arm. We've chosen an old fashioned VW Transporter as transport vehicle (and counterweight) because its robust and accessible frame is ideal for the additional fittings. In addition it provides enough volume for crew and test accessories.

Fig. 5 Launch sequence

During the first test campaign we changed the arm ratio step-by-step in order to increase the acceleration moment in reasonable steps and tested the device with projectiles. After we validated the simulation and found the settings for launching a projectile with the desired weight, speed and flightpath, we continued the tests with different freeflight and RC airplanes in order to validate the simulation model.

2.4 Prototype

After the promising tests with the full scale mobile trebuchet we decided to develop a prototype, which parts can be folded on the top of the transport vehicle to be allowed to drive on public roads with but can be installed by a single person in 5 minutes. We analysed several type of cars to find an optimal transport vehicle for the UAV system and for the launching trebuchet. In order to fulfil the strict regulations valid on public roads, and the requirement for the quick installation, we had to rearrange the original layout of the mobile trebuchet. The arm became shorter to compensate the less weight of the new transport vehicle, that caused change in the launch direction, too. To eliminate dangerous parts of the supporting structure during a potential accident on the road, the arm support structure was replaced on the back of the car. The power for the installation and the arming of the trebuchet is provided by a commercial automotive winch mounted on the top of the vehicle.

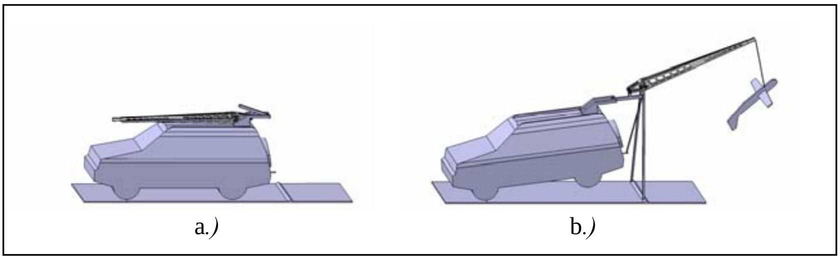

Fig. 6 Prototype in transport (a,) and installed (b,) position

3. CONCLUSION

The goal of the project was to develop a launching device capable not only accelerating the UAV but release it in a safe altitude. We performed feasibility studies, multibody simulations, small scale and full scale tests in order to find the optimal solution. Finally a novel solution has been emerged, that even more simple and reliable than existing UAV launching solutions in additional to the unique high release feature. The patent pending operational product prototype is under testing and fulfilled 100+ launches.

This work has been supported by the National Research, Development and Innovation Office of Hungary, under the grant "Market Oriented R+D Activity" No. KMR_12-1-2012-0121.

4. REFERENCES

[1] **Saimre, T.:** Trebuchet – a gravity-operated siege engine. In *Estonian Journal of Archaeology,* 2006, vol. 10, No.1, p.61-80,ISSN 1406-2933

[2] https://en.wikipedia.org/wiki/Trebuchet

[3] **Reck, R.:** First Design Study of an Electrical Catapult for Unmanned Air Vehicles in the Several Hundred Kilogram Range. In *IEEE Transactions of Magnetics*, 2003, vol. 39, No.1, p.310-312, ISSN 0018-9464

[4] **UAVs:** Launch and recovery. *Air & Space Europe*, 1999, vol. 1, No. 5–6, p.59-62, ISSN 1290-0958

[5] **Miller, B. - Valoria, C. - Warnock, C. - Coutlee**, **J**.: *Lightweight UAV Launcher*. Final project report. San Luis Obispo, California, USA, California Polytechnic State University, 2014, p.51

[6] https://en.wikipedia.org/wiki/Floating_arm_trebuchet

[7] **Shabana, A. A.:** *Dynamics of Multibody Systems.* Chicago, Cambridge University Press, 1989, p.384, ISBN 978-1-107-04265-0

[8] **Meschia, F.:** Model analysis with XFLR5. In RC Soaring Digest, 2008, vol. 25, No. 2, p.27-51.

NEW ADDED MASS CALCULATION METHOD FOR INLAND VESSELS

Csaba L. HARGITAI

Department of Aeronautics, Naval Architecture and Railway Vehicles
Faculty of Transportation Engineering and Vehicle Engineering
Budapest University of Technology and Economics
H-1111 Budapest, Műegyetem rkp. 3, Hungary

Received: November 8, 2016

ABSTRACT

The manoeuvring properties of an inland vessel are important design parameters, and the significance grows with increasing ship sizes. During the sip design the manoeuvring behaviour can be predicted even by model tests or by computer motion simulation. Nowadays the accuracy of computer simulation can be better than the model tests due to the model scale effect. The ship dynamic model for manoeuvring simulation is difficult, and beside the accurate calculation of external forces, the determination of hydrodynamic masses (so called added masses) play a major role in the accuracy of the simulation. This paper demonstrates the significance of added masses and introduces common approximation and calculation methods for added masses. Some motion behaviours of inland vessels are introduced in the paper, which leads simplification possibilities of added mass calculations. A new added mass determination method is also introduced, which based on the momentum thickness calculation around the hull.

Keywords: inland waterway vessel, manoeuvre simulation, motion equations, added masses

1. INTRODUCTION

In vehicle development the computer simulation techniques cover wide range of analysis of motion and control.

The demand for motion simulation increases also in inland navigation, because of the growing traffic on European rivers, the need for fuel consumption reduction, retrofitting of old vessels, environment protection, safer navigation, etc.

The Department of Aeronautics, Naval Architecture and Railway Vehicles at the Budapest University of Technology and Economics has experience in motion simulation of vehicles. The research activity covers wide range of analysis of vehicle motions and control (e.g.: aircraft design [1], pilot's reaction time measurement under pressure [2], aircraft landing technology development [3], simulator development [4] , education by simulators [5], etc.)

The motion simulation research of inland vessels started in 2007 at the Department with a navigability research of a planned port basin on the Danube [6]. The research pointed out a lot of significant questions, of which the present article outlines the added mass problem of inland vessels, and shows some solution possibilities.

2. MEANING OF ADDED MASSES

According to Newtonian mechanics, the momentum and the angular momentum of a point-like rigid body in vacuum changes due to the external forces and its torques acting on the rigid body.

$$\frac{d}{dt}\begin{bmatrix}\boldsymbol{P}_g\\ \boldsymbol{H}_g\end{bmatrix}=\frac{d}{dt}\left(\begin{bmatrix}m\boldsymbol{I}_3 & 0\\ 0 & \boldsymbol{I}_g\end{bmatrix}\begin{bmatrix}\boldsymbol{v}_g\\ \boldsymbol{\omega}_g\end{bmatrix}\right)=\frac{d}{dt}\left(\boldsymbol{M}_{gRB}\begin{bmatrix}\boldsymbol{v}_g\\ \boldsymbol{\omega}_g\end{bmatrix}\right)=\begin{bmatrix}\boldsymbol{F}_g\\ \boldsymbol{M}_g\end{bmatrix}$$

where

- $\boldsymbol{P}_g$: momentum vector of rigid body in the inertia reference system (≈ Earth fixed coordinate system)
- $\boldsymbol{H}_g$: angular momentum vector of rigid body in the inertia reference system
- m: mass of rigid body concentrated in the center of gravity (point-like body)
- $\boldsymbol{I}_g$: inertia matrix of rigid body in the inertia reference system
- $\boldsymbol{M}_{g\,RB}$: mass and inertia matrix of rigid body in the inertia reference system
- $\boldsymbol{v}_g$: translation velocities of the point-like body in the inertia reference system
- $\boldsymbol{\omega}_g$: angular velocities of the point-like body in the inertia reference system
- $\boldsymbol{F}_g$: external force vector acting on rigid body
- $\boldsymbol{M}_g$: torque vector of external forces acting on rigid body

Because the mass and inertia of the body is constant, the external forces and its torque cause acceleration.
But floating bodies like inland vessels are moving in fluid. For this reason the external forces and its torques have to change not even momentum and angular momentum of the rigid body but the surrounding fluid also. Following Zhukovsky, the change of momentum and angular momentum of fluid can be taken into account like the change the momentum and angular momentum of a virtual mass and virtual inertia. This is called in naval architecture as added masses or hydrodynamic masses. Due to the added masses are depending on shape of the rigid body, they have different values in different directions.

$$\frac{d}{dt}\begin{bmatrix}\boldsymbol{P}_g+\boldsymbol{P}_{fluid}\\ \boldsymbol{H}_g+\boldsymbol{H}_{fluid}\end{bmatrix}=\frac{d}{dt}\left(\left(\begin{bmatrix}m\boldsymbol{I}_3 & 0\\ 0 & \boldsymbol{I}_g\end{bmatrix}+\begin{bmatrix}\lambda_{11} & \lambda_{12} & \lambda_{13} & \lambda_{14} & \lambda_{15} & \lambda_{16}\\ \lambda_{21} & \lambda_{22} & \lambda_{23} & \lambda_{24} & \lambda_{25} & \lambda_{26}\\ \lambda_{31} & \lambda_{32} & \lambda_{33} & \lambda_{34} & \lambda_{35} & \lambda_{36}\\ \lambda_{41} & \lambda_{42} & \lambda_{43} & \lambda_{44} & \lambda_{45} & \lambda_{46}\\ \lambda_{51} & \lambda_{52} & \lambda_{53} & \lambda_{54} & \lambda_{55} & \lambda_{56}\\ \lambda_{61} & \lambda_{62} & \lambda_{63} & \lambda_{64} & \lambda_{65} & \lambda_{66}\end{bmatrix}\right)\begin{bmatrix}\boldsymbol{v}_g\\ \boldsymbol{\omega}_g\end{bmatrix}\right)=$$

$$\frac{d}{dt}\begin{bmatrix}\boldsymbol{P}_g+\boldsymbol{P}_{fluid}\\ \boldsymbol{H}_g+\boldsymbol{H}_{fluid}\end{bmatrix}==\frac{d}{dt}\left(\left(\boldsymbol{M}_{g\,RB}+\boldsymbol{M}_A\right)\begin{bmatrix}\boldsymbol{v}_g\\ \boldsymbol{\omega}_g\end{bmatrix}\right)=\begin{bmatrix}\boldsymbol{F}_g\\ \boldsymbol{M}_g\end{bmatrix}$$

where

- $\boldsymbol{P}_{fluid}$: momentum vector of fluid in the inertia reference system
- $\boldsymbol{H}_{fluid}$: angular momentum vector of fluid in the inertia reference system
- $\boldsymbol{M}_A=\begin{bmatrix}\lambda_{11} & \cdots & \lambda_{1j}\\ \vdots & \ddots & \vdots\\ \lambda_{i1} & \cdots & \lambda_{ij}\end{bmatrix}$: added mass and added inertia matrix

For inland vessel motion calculation, the added mass matrix has to be taken into account, because a ship (as rigid body) is modelled as a partially submerged rigid body into the water.

3. MOTION EQUATIONS OF AN INLAND VESSEL

The motion prediction of a ship is always based on a dynamic model. In this paper the dynamic model designed to simulate the motion of single screw self-propelled inland vessels in the common European ship sizes: length between 70m-140m; breadth between 8m-12m; design draft between 1.8m-3.5m; displacement between 1200m^3-3700m^3

In case of inland vessels the six degree of freedom motion equations of a floating rigid body can be simplified by neglecting some motion types.

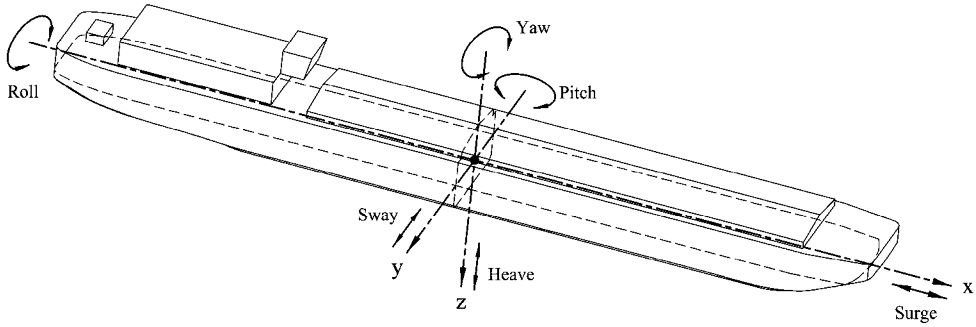

Fig. 1 6DoF motion of a ship

Based on the navigation experiences of boatmasters and full scale test results it can be concluded in normal operation conditions that

- the waves of rivers do not have significant effect on the motion. In 3. navigation zones of [7] the highest waves with 5% probability are 0.6m high, and according to the experiences on Danube the maximum wave length is 4-5m. The waves produce only a small excitation on the ship's oscillating system, because of their amplitudes, time period and relative small energy content.
- the draft of ships do not change quickly (heave), since there are 10-30 waves around the hull and Froude number is $Fn<0.2$. Only the squat effect is important, since by shallow water the stern draft can be increased by 9-10%. The squat effect is taken into consideration during simulation with the minimum 0.4m safety distance between the keel and river bed.
- the longitudinal metacentric radius of a self-propelled inland vessel (in the previously mentioned sizes) is about $R_L = \frac{I_L}{V} = 190 \sim 580m$, because the length-breadth ratio is high ($\frac{L}{B} = 8 \sim 12$). This means high longitudinal stability, which leads almost zero pitching.
- during usual operation (low Froude number, normal manoeuvres, intact hull and systems) the inland vessels do not heel more than 3°-5°, and rolling is almost zero. Higher values appear only if the ship is damaged or the crew has to fulfil an emergency manoeuver.

According to these experiences and considerations the motion of an inland vessel can be simplified as a horizontal, 3DoF motion.

The forces and moments acting on hull can be treated as a resultant force (analytic method after Abkowitz [8]) or as a force system (synthetic method). The force system method fits better to the research goals (preparing a universal inland vessel simulation software), so the forces are divided according their formation.

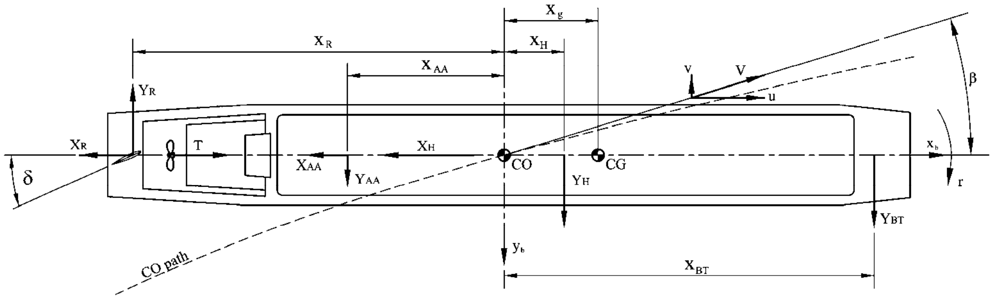

Fig. 2 Forces acting on an inland ship

where

- X_H, Y_H : longitudinal and transversal hydrodynamic forces on hull in body fixed coordinate system
- T : propeller thrust in body fixed coordinate system
- X_R, Y_R : longitudinal and transversal force on rudder in body fixed coordinate system
- X_{AA}, Y_{AA} : longitudinal and transversal aerodynamic forces in body fixed coordinate system
- Y_{BT} : transversal force of bow thruster in body fixed coordinate system
- u : longitudinal velocity of ship in body fixed coordinate system
- v : transversal velocity of ship in body fixed coordinate system
- r : angular velocity of ship around "z" axis of body fixed coordinate system
- $\boldsymbol{V}$: velocity vector of ship in body fixed coordinate system
- β : drift angle of ship

Based on the horizontal motion theory and force definitions, the 3 DoF motion equations in body fixed coordinate system can be written as follows:

$$X_H + X_{AA} + X_R + T = (m + \lambda_{11})\dot{u} - m(vr + x_g r^2)$$
$$Y_H + Y_{AA} + Y_R + Y_{BT} = (m + \lambda_{22})\dot{v} + (mx_g + \lambda_{26})\dot{r} + mur$$
$$Y_H x_H + Y_{AA} x_{AA} + Y_R x_R + Y_{BT} x_{BT} = (I_z + \lambda_{66})\,\dot{r} + (mx_g + \lambda_{62})\dot{v} + mx_g ur$$

where

- λ_{11} : Longitudinal added mass in body fixed coordinate system
- λ_{22} : Transversal added mass in body fixed coordinate system
- λ_{66} : Moment of added inertia in body fixed coordinate system
- m : mass of ship
- I_z : inertia of ship around "z" axis of body fixed coordinate system

4. ADDED MASSES IN 3DOF MOTION OF INLAND VESSELS

The above introduced dynamic model of a self propelled inland vessel has two critical points to achieve accurate motion simulation. The first one is calculation of external forces acting on the hull the second one is determination of added masses.

As mentioned before the added mass matrix is a 6x6 matrix in case of 6 DoF motion [9].

In case of a self propelled inland vessel the added mass matrix can be simplified to a 3x3 diagonal matrix, if the motion is simplified to 3 DoF and the origin of coordinate system of vessel is in the symmetry plane on the water surface in the main section.

$$\boldsymbol{M_A} = \begin{bmatrix} \lambda_{11} & \lambda_{12} & \lambda_{13} & \lambda_{14} & \lambda_{15} & \lambda_{16} \\ \lambda_{21} & \lambda_{22} & \lambda_{23} & \lambda_{24} & \lambda_{25} & \lambda_{26} \\ \lambda_{31} & \lambda_{32} & \lambda_{33} & \lambda_{34} & \lambda_{35} & \lambda_{36} \\ \lambda_{41} & \lambda_{42} & \lambda_{43} & \lambda_{44} & \lambda_{45} & \lambda_{46} \\ \lambda_{51} & \lambda_{52} & \lambda_{53} & \lambda_{54} & \lambda_{55} & \lambda_{56} \\ \lambda_{61} & \lambda_{62} & \lambda_{63} & \lambda_{64} & \lambda_{65} & \lambda_{66} \end{bmatrix}$$

The reasons for simplification are:

- 3 DoF motion: There are no heave, roll and pitch motions, therefore $\lambda_{ij} = 0$ if $i \text{ or } j = 3, 4 \text{ or } 5$
- x-z plane is a symmetry plane: $\lambda_{16} = \lambda_{61} = 0$
- x-y plane = waterplane, where the potential function is zero, like by a symmetry plane, therefore $\lambda_{12} = \lambda_{21} = 0$
- inland vessel is almost symmetrical to the main section (this is a serious simplification), so the y-z plane is a symmetry plane: $\lambda_{26} = \lambda_{62} \cong 0$

Taking into account these considerations, the added mass matrix is:

$$\boldsymbol{M_A} = \begin{bmatrix} \lambda_{11} & 0 & 0 \\ 0 & \lambda_{22} & 0 \\ 0 & 0 & \lambda_{66} \end{bmatrix}$$

5. COMMON ADDED MASS CALCULATION METHOD

In naval architecture the common added mass calculation method is based on the potential flow and strip theory [10]. For counting of λ_{22} and λ_{66} the vessel is divided into sections, where the local added mass components $(\lambda_{22j}\,;\,\lambda_{66j})$ are calculated.

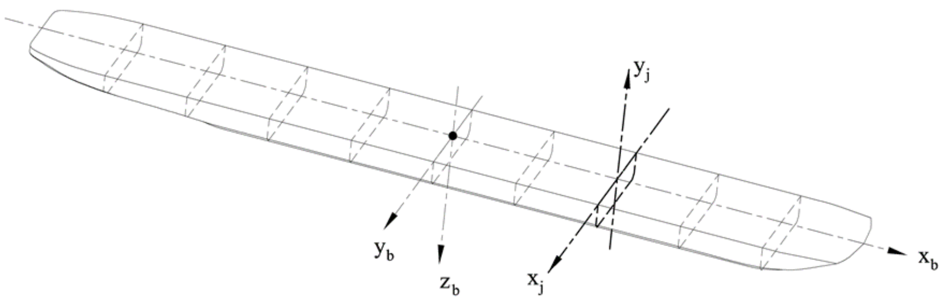

Fig. 3 Splitting the hull for added mass calculation

Based on the added mass components of sections the transversal added mass (λ_{22}) and moment of added inertia (λ_{66}) of the ship are calculated by integration along the hull.

$$\lambda_{22} = \mu_0 \int_0^{L_{WL}} \lambda'_{22}\,dx \cong \mu_0 \sum_{j=1}^{n} \lambda_{22j}\,\Delta x$$

$$\lambda_{66} = \mu_1 \int_0^{L_{WL}} \lambda'_{66}\,x^2\,dx \cong \mu_1 \sum_{j=1}^{n} \lambda_{66j}\,x^2\,\Delta x$$

where

μ_0 and μ_1 are correction factors, taking into account the effect of longitudinal stream on transversal added mass and moment of added inertia.

Calculation of local added mass components in sections can be fulfilled with conformal mapping. The waterline mirrored section usually transformed from an $x - iy$ complex plane (complex number is "z") into an other $\xi - i\eta$ complex plane (complex number is "ζ"), where section is a unit radius circle.

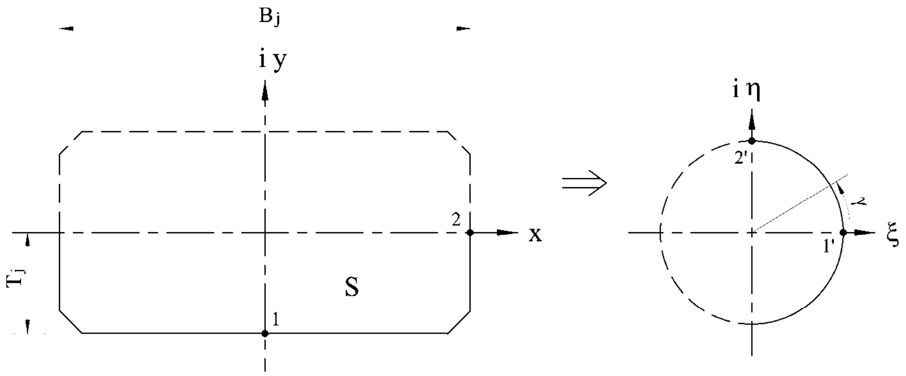

Fig. 4 Conformal mapping of a section

By ship sections the transformation function is usually based on Bieberbach transformation, for example the two-parameter Lewis transformation function

$$z = -\frac{iT}{1 + a_1 + a_3}\left(\zeta + \frac{a_1}{\zeta} + \frac{a_3}{\zeta^3}\right),$$

where $a_1, a_3 \in \mathbb{R}$

According to the potential flow theory, the local added mass components are in $\xi - i\eta$ complex plane:

$$\lambda_\xi = \lambda_\eta = \rho\pi$$

Which can be transformed back to the $x - iy$ complex plane, and so the local added mass components in case of Lewis transformation are [11]:

$$\lambda_x = \lambda_{22j} = \rho\frac{\pi T^2}{2}\left(\frac{(1 + a_1)^2 + 3a_2^2}{(1 + a_1 + a_2)^2}\right)$$

$$\lambda_y = \lambda_{66j} = \rho\frac{\pi B^2}{2}\left(\frac{(1 - a_1)^2 + 3a_2^2}{(1 - a_1 + a_2)^2}\right)$$

The disadvantages of this method are by inland vessels are the follows:

- Due to the potential flow theory the separation of flow and friction are not taken into account, however these are significant factors by inland ships.
- Inland ships have very square sections, therefore the Lewis transformation (or any kind of Bieberbach transformation) cause errors by conformal mapping.
- The effect of shallow water on added masses cannot be taken into account.

6. NEW ADDED MASS CALCULATION METHOD

Because of the disadvantages of potential flow calculation, a new approximation method is suggested by the single screw self propelled inland vessels with usual hull form. The method is based on the theory that the added masses represent the momentum loss $\left(\int_0^\infty [I_0 - I(y)]\,dy\right)$ of water around the hull. Therefore the added masses should be proportional with momentum thickness(δ_I).

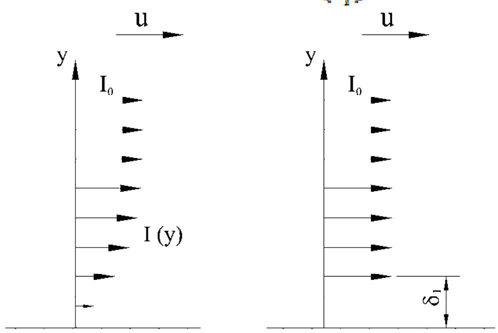

Fig. 5 Definition of momentum thickness

According to the flat plate skin friction researches [12] the momentum thickness (δ_I) can be calculated by the local skin friction coefficient(C_f). In this way the longitudinal added mass is:

$$\lambda_{11} \cong \rho\delta_I S = \rho S \cdot 0{,}0972 \cdot 5{,}14 \int_0^{L_{WL}} C_f\,dx.$$

According to Schultz – Grunow [12] the longitudinal integral of the local skin friction coefficient can be substituted by the average skin friction coefficient $\left(C_{F\,(S-G)}\right)$:

$$C_{F\,(S-G)} = \frac{0{,}427}{\left(\log Re_{L_{WL}} - 0{,}407\right)^{2{,}64}}$$

But in naval architecture practice the ITTC 1957 formula [13] is commonly used for skin friction coefficient $\left(C_{F\,(ITTC)}\right)$:

$$C_{F(ITTC)} = \frac{0{,}075}{\left(\log Re_{L_{WL}} - 2\right)^2}$$

Taking into account the relation between Schultz – Grunow and ITTC 1957 formula, the longitudinal added mass is:

$$\lambda_{11} \cong \frac{\rho S L_{WL}}{8} \cdot 5{,}14 C_{F(ITTC)}$$

But this theory is based on flat plate researches, where the water velocity is constant along the solid surface. Due to the hull form the water velocity along a hull is not constant, which has an impact on the momentum thickness (and on the added mass). In naval architecture practice the water velocity distribution along the hull is taken into account in the residual resistance calculation by the residual resistance coefficient (C_R). Following this practice, the added mass calculation should also take care with residual resistance coefficient. So the final form of the longitudinal added mass formula is:

$$\lambda_{11} \cong \rho S \frac{L_{WL}}{8}(5{,}14 C_{Fx} + C_{Rx})$$

where

λ_{11} : Longitudinal added mass
L_{WL} : Length of waterline
S : Wetted surface of ship
C_{Fx} : Skin friction coefficient by longitudinal motion according to ITTC 1957
C_{Rx} : Residual resistance coefficient by longitudinal motion
ρ : Water density

Following this theory, the added mass in transversal direction can be calculated by width of waterline (B_{WL}), transversal skin friction coefficient (C_{Fy}), and transversal residual resistance coefficient (C_{Ry}):

$$\lambda_{22} \cong \rho S \frac{B_{WL}}{8}(5{,}14 C_{Fy} + C_{Ry})$$

Based on experimental calculations the following formula gives correct result for the moment of added inertia (λ_{66}) of single screw self propelled inland vessels:

$$\lambda_{66} \cong \frac{L_{WL}^2}{2}\lambda_{11}$$

7. COMPARISON OF ADDED MASS CALCULATION METHODS

The comparison of above mentioned added mass calculation methods is fulfilled with a Hungarian sample vessel, named “DET 1”.

source: [14]

Fig. 6 The „DET 1“ sailing upstream in coupled formation with a barge

Main dimensions of “DET 1”:

- Length over all (L_{oA})	85 m
- Waterline length in full load condition ($L_{WL\ max}$)	84 m
- Width over all (B_{oA})	11 m
- Draft by full load (T_{max})	2,8 m
- Draft in light craft condition ($T_{lightship}$)	0,80 m
- Displacement in full load condition	2240 tons
- Displacement in light craft condition	540 tons
- Main engine power (P)	976,8 kW

For comparison of added mass calculation methods, the longitudinal (λ_{11}) and transversal (λ_{22}) added mass, and the moment of added inertia is calculated by different longitudinal (u) velocities.

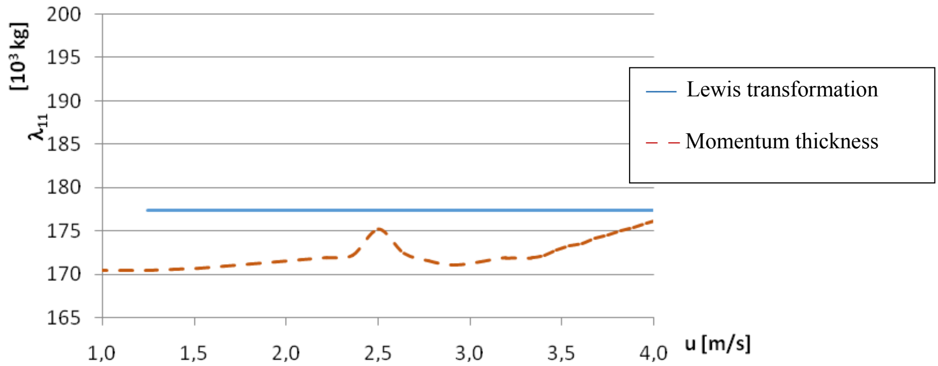

Fig. 7 Comparison of λ_{11} added mass calculation methods

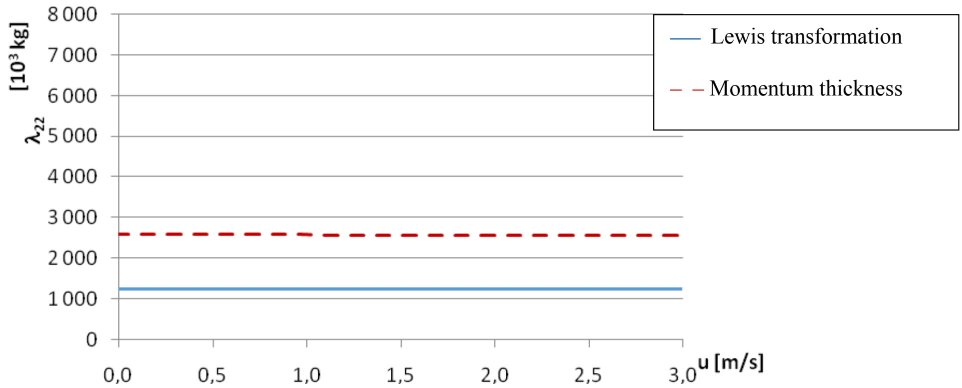

Fig. 8 Comparison of λ_{22} added mass calculation methods

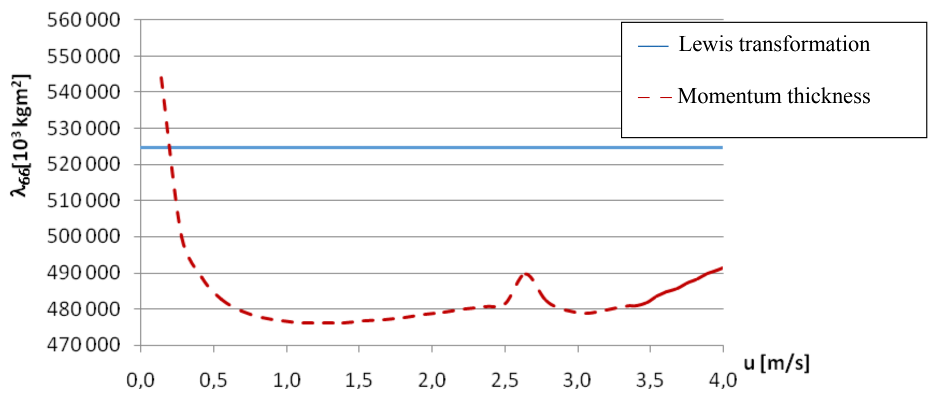

Fig. 9 Comparison of λ_{66} added inertia calculation methods

It can be seen that in range of ship's regular velocity the two methods give max. 4% difference by the longitudinal added mass (λ_{11}), which is a good approximation.

The difference in transversal added mass (λ_{22}) is more serious, but the Lewis transformation cannot handle the rectangular section shapes of inland vessels. The Lewis sections are rounded sections instead of the real inland vessel sections, and that is why the transversal added mass of Lewis sections is smaller than by the momentum thickness theory.
The moment of added inertia (λ_{66}) is smaller by the momentum thickness calculation, because the flat keel of the inland vessels gives less moment of added inertia, than the hull with rounded Lewis sections (not flat keel). But the difference is only max 10%, which is a good approximation.

8. CONCLUDING REMARKS

This paper concludes that the 6DoF dynamic model of a ship can reduced to 3 DoF, while the accuracy of motion simulation enough for manoeuvring behaviour prediction of an inland ship.
The added masses of a self propelled general cargo inland vessel can be also simplified. The commercial potential flow theory gives some inaccuracy in added mass values, due to the special hull form of inland ships. But instead of model tests or CFD calculation, the added masses of inland vessels can be computed by simple formulas based on momentum thickness theory.

9. REFERENCES

[1] **Jankovics, I. R. - Rohács, D - Rohács, J.:** Motion Simulation Model of a Special Acrobatic Aircraft, Proceedings of the 12th MINI Conference on Vehicle System Dynamics, Identification and Anomalies, VSDIA 2010. (Ed by Prof. I. Zobory), BME, Department of Railway Vehicles, Budapest, 2012, p.393-401. (ISBN:978-963-313-058-2)

[2] **Nagy, A. - Jankovics, I.:** Measurement of Small Aircraft Pilot's Reaction Time Variation With Psychological Load in Flight Simulator, Proceedings of AIRTEC, Frankfurt am Main, 2012. p.1-10.

[3] **Rohács, D. - Voskuijl, M. - Siepenkotter, N.:** Evaluation of Landing Characteristics Achieved by Simulations and Flight Tests on a Small-Scaled Model Related to Magnetically Levitated Advanced Take -Off and Landing Operations, Proceedings of the 29th Congress of the International Council of the Aeronautical Sciences (ICAS), St. Petersburg, International Council of the Aeronautical Sciences (ICAS), 2014. (ISBN:3-932182-80-4)

[4] **Nagy, A. - Jankovics, I.:** Tanszéki repülésszimulátor laboratórium modernizálása, Repüléstudományi Közlemények, 2012, p.727-747. (in Hungarian)

[5] **Korody, E. - Gáti, B. - Patyi, B. - Rohács, J.:** Repülésszimulátor az oktatásban és kutatásban, Gép, Budapest, 2004, p.68-74. (in Hungarian)

[6] **Hadházi, D. - Hargitai, Cs.- Simongáti, Gy.:** 2D simulation of inland vessel manoeuvrings, Proceedings of European Inland Waterway Navigation Conference 2007, Budapest, 2007,. p.1-11.

[7] **European Parliament and Council-2006/87/EC:** Directive of the European Parliament and the Council of 12 December 2006 laying down technical requirements for inland waterway vessels and repealing Council Directive 82/714/EEC., Official

Journal of the European Union, Vol. 49, Strasbourg, 2006, p.1-260. (ISSN: 1725-2555)

[8] **Abkowitz, M. A.:** Lectures on ship hydrodynamics: steering and manoeuvrability, Hydro-og Aerodynamisk Laboratorium, Lyngby, 1964.

[9] **Korotkin, A. I.**: Added masses of ship structures, Springer, St. Petersburg, 2007. (ISBN:978-1-4020-9431-6)

[10] **The Society of Naval Architects and Marine Engineers:** Principles of Naval Architecture, Vol.3., SNAME, New Jersey, 1989. (ISBN:0-939773-02-3)

[11] **Lewis, F.M.:** The inertia of the water surrounding in a vibrating ship, SNAME Transaction No.37., New Jersey, 1929.

[12] **Hörner, S.F.:** Fluid-dynamic drag, S.F. Hörner, New York, 1965, p.2-1 – 2-6.

[13] **ITTC Recommended Procedures and Guidelines:** Performance, Propulsion 1978 ITTC Performance Prediction Method, ITTC 7.5-02-03-01.4. 1999, International Towing Tank Conference, 1999.

[14] Unofficial Hungarian vessel register: www.hajoregiszter.hu

CONTROL-ORIENTED MODELLING OF THE VARIABLE-GEOMETRY SUSPENSION FOR INDEPENDENT STEERING PURPOSES

Dániel FÉNYES, Balázs NÉMETH and Péter GÁSPÁR

Systems and Control Laboratory, Computer and Automation Research Institute,
H-1111 Budapest, Kende u. 13-17, Hungary
{fenyes.daniel; balazs.nemeth; gaspar.peter;}@sztaki.mta.hu

Received: November 8. 2016

ABSTRACT

The paper presents the modelling and control design of an independent steering system which is based on the variable-geometry suspension. Through the actuation of the suspension the camber angle of the wheel is modified, which results in the variation of the steering wheel scrub radius. In the paper the model of the independent steering mechanism and the relationship between the steering and the suspension geometry are formulated. Furthermore, the model is validated through a high-fidelity multi-body suspension model Matlab/SimMechanics. In the paper the steps of the robust control design are presented, and the efficiency of the system is illustrated through different vehicle dynamical scenarios.

Keywords: variable-geometry suspension, independent steering, control-oriented modelling

1. INTRODUCTION AND MOTIVATION

The electrification of the vehicle drivelines provides a new possibility to enhance the stability and safety of road vehicles. A novel solution of the electric drive is the application of in-wheel electric motors. It makes possible the distribution of the traction forces between the wheels, by which additional functionalities can be achieved, e.g. the torque vectoring of the vehicle. The in-wheel electric drive offers new challenges in the steering of the vehicle, such as independent steering. The goal of the independent steering concept is to improve the lateral dynamics of the vehicle using individually controlled wheels. The independent steering control for the rear wheels to modify the toe angle is presented by [5]. The analysis of the independent wheel steering system for heavy vehicles is found in [10]. An indirect power steering measure called differential drive torque assisted steering is proposed by [14]. A fault-tolerant control approach for a four-wheel independently actuated electric vehicle to handle fault scenarios is proposed by [4].

In this paper a new solution of independent steering, which is based on the variable-geometry suspension solution, is proposed. The aim of the suspension control is the modification of the geometry, which results in a change in the camber or the toe angle. A rear-suspension active toe control for the enhancement of driving stability is proposed by [3]. The active tilt control system, which assists the driver in balancing the vehicle and performs tilting in the bend, is an essential part of a narrow vehicle system, see [8]. These vehicles require the design of innovative active wheel tilt and steer control strategies in order to perform steering similarly to a car on straight roads but in bends they tilt as motorcycles, see [13]. The advantages of the variable-geometry suspension are the simple structure, low energy consumption and low cost compared to other mechanical solutions such as an active front wheel steering, see [2], [6]. In the paper the control design of an independent wheel steering system for the front wheels is proposed. The novelty of the paper is the application of the variable-geometry suspension in the steering solution. The contributions are the modelling and validation of

the suspension system.
The paper is organized as follows. The modelling of the variable-geometry suspension system is presented in Section 2. The validation and the linearization of the nonlinear model are found in Section 3. Section 4 demonstrates the efficiency of the steering system. Finally, Section 5 summarizes the contribution of the paper.

2. MODELLING OF INDEPENDENT STEERING

In this section the modelling of independent steering is proposed. The variable-geometry suspension performs the modification of the wheel position and orientation. Thus, the wheel camber angle and the scrub radius of the suspension vary. In the following, the formulation of the lateral vehicle model with the consideration of the camber angle and scrub radius is presented.
The goal of the variable-geometry suspension is to perform the wheel camber angle and the scrub radius modification. The camber angle results in a lateral force on the tyre-ground contact. Since the longitudinal force has a rotatory effect on the wheel, the scrub radius of the wheel influences the steering dynamics of the wheel. Therefore, a lateral force results from the wheel steering through the scrub radius modification.
Since the variable-geometry suspension has one actuator in each wheel, it is necessary to find a suspension construction with which the lateral force generation of the camber and the scrub radius is in coordination. Thus, the forces from the wheel tilting and the steering from the scrub radius have the same effect on the vehicle dynamics. In the automotive industry, there are the two commonly used suspension types: Double wishbone and MacPherson. Double wishbone suspension can be manufactured with relatively large nominal scrub radius, while the MacPherson type usually has a small nominal scrub radius, close to zero. Since the variable-geometry suspension has to be able to realize a negative value as well as a positive value of the scrub radius, in the paper the McPherson construction is used. The actuator is incorporated in the suspension between the wheel hub and the wheel. It is able to generate an active torque around B to tilt the wheel. However, it also has a counter effect M_{act} on the hub. In the McPherson construction the suspension is able to rotate around the connection point A of the chassis. Moreover, the arm connects the hub D and the chassis C with joints, which are able to guarantee the rotation and the motion of the suspension. The scheme of the variable-geometry suspension is shown in Fig. 1. Several forces influence the motion of the suspension and the wheel. The force of the suspension compression and damping F_{susp} is formulated as

$$F_{susp} = s_{susp}\left(\frac{z_w + z_{w,0}}{\sin \varepsilon_1}\right) + d_{susp}\frac{\dot{z}_w}{\sin \varepsilon_1} \tag{1}$$

where s_{susp} and d_{susp} are the stiffness and damping coefficients, $z_{w,0}$ is the joint position, resulting from the static suspension compression.
The lateral force acting on the tyre is F_y. It is derived from the Magic Formula, see Pacejka [2004]. F_{tyre} is the force from the tyre compression, which has a direction to the wheel:

$$F_{tyre} = s_{tyre}\frac{(r_w \cos\gamma - l_{tyre}\sin\gamma - r_w - z_w) + z_{tyre,0}}{\cos\gamma} \tag{2}$$

where s_{tyre} is the tyre stiffness, r_w is the wheel radius and $z_{tyre,0}$ is the static compression of the tyre.

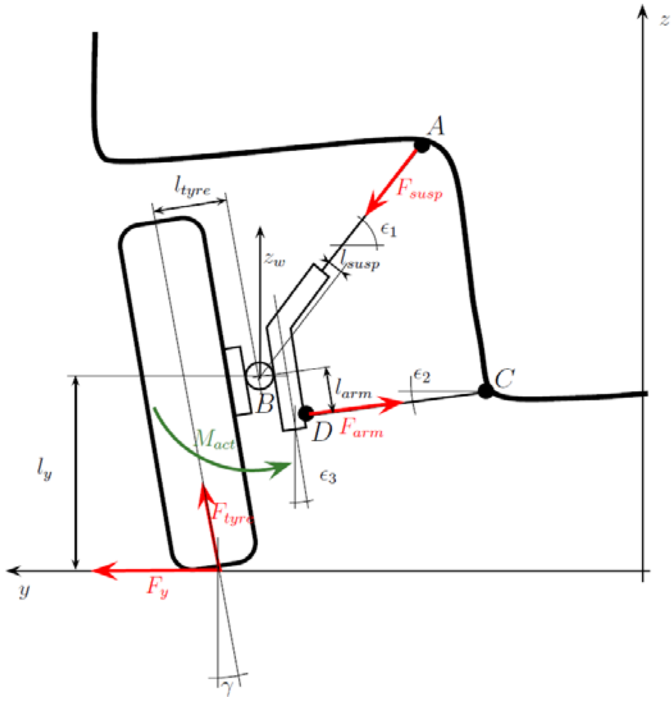

Fig. 1 The scheme of the suspension construction

In the practice ε_3 is constant, thus $\ddot{\varepsilon}_3 = 0$. Therefore, F_{arm} is computed as:

$$F_{arm} = \frac{M_{act} - F_{susp} l_{susp}}{l_{arm}} \tag{3}$$

Thus, it is assumed that $\varepsilon_1, \varepsilon_2$ and l_{arm}, l_{susp} can be handled as constant suspension parameters. More detailed descriptions of the nonlinear suspension model can be found in [15], [16].

3. VALIDATION OF THE NONLINEAR MODEL

In this section the validation of the nonlinear suspension model is presented. The nonlinear variable-geometry suspension model is validated through the complex mechanical simulation system Matlab/SimMechanics. The construction of the suspension has been built in SimMechanics, see Fig. 2.

Each component of the suspension has been modelled as a rigid body. The motion of the suspension has been guaranteed by proper joint elements. The modification of the wheel camber angle has been analyzed. Fig. 3 shows a simulation example, in which the suspension nonlinear model and the SimMechanics model are compared. In the simulations the same chirp input signals M_{act} are realized, see Fig. 3(a). The camber angle of the model is presented in Fig. 3(b). It shows that the resulting camber angles are very close to each other in a high operation range.

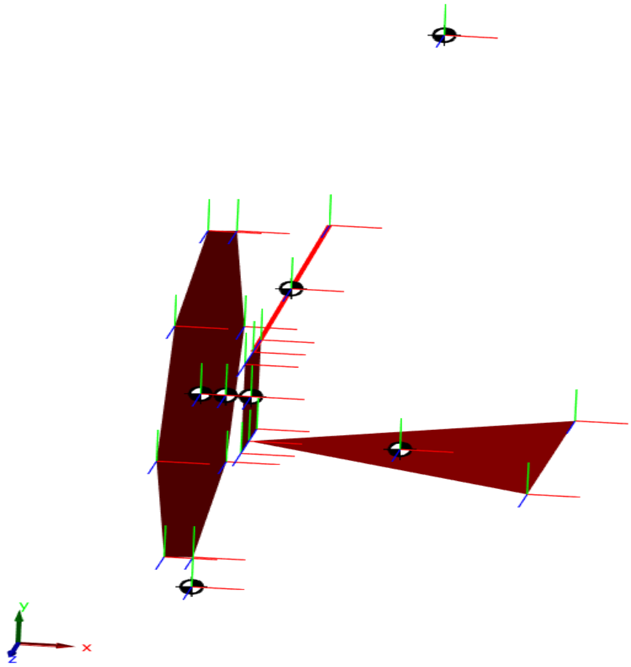

Fig. 2 Suspension model in SimMechanics

Figure 4 shows another example for the validation of the nonlinear suspension model. The step signal of the control input M_{act} is shown in Fig. 4(a). As an effect of the torque modification, the camber angle also varys, see Fig. 4(b). The results show that the steady-state error of the camber angle is below 2%. It means that the proposed nonlinear suspension model (3) well fits the SimMechanics model.

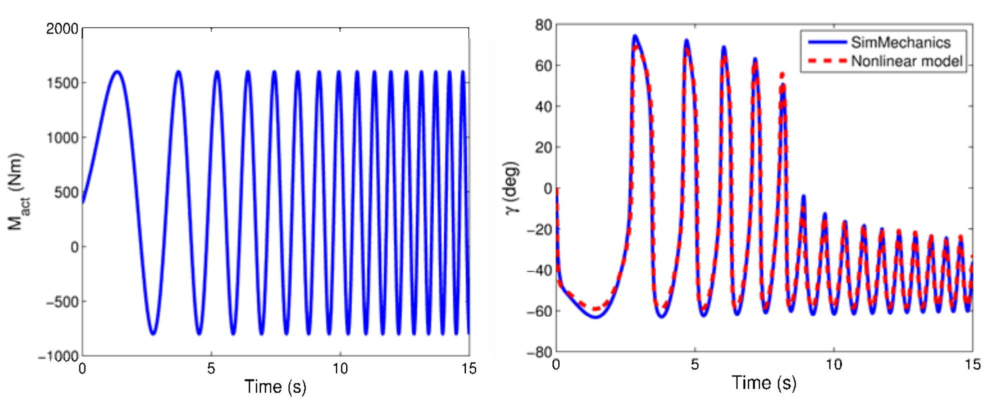

(a) Control input M_{act} (b) Camber angle (γ)

Fig. 3 Model validation - Chirp signal

Since the presented model formulates the motion of the suspension and the wheel, it can be used for control design purposes. Therefore, the nonlinear model is transformed into a linear control-oriented form.

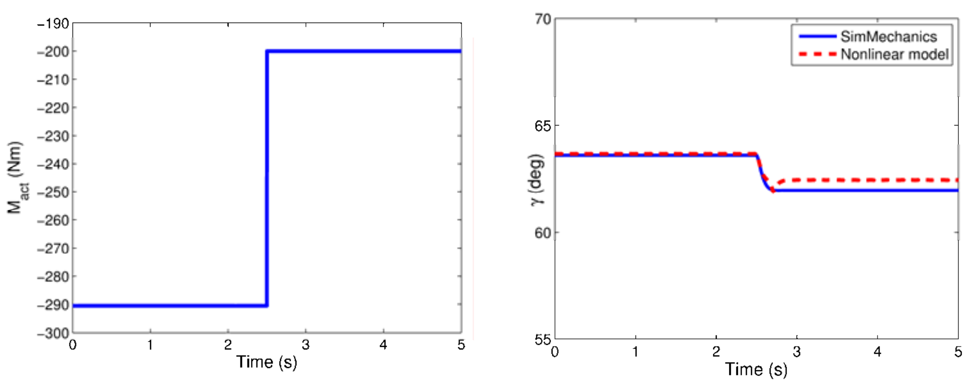

(a) Control input M_{act} (b) Camber angle (γ)

Fig. 4 Model validation - Step signal

During the linearizing the following assumptions are made.

- In the formulation small wheel tilting angels are considered. As a result $\cos\gamma = 1$ and $\sin\gamma = \gamma$.
- Since γ values are small, the lateral tyre force F_y is approximated in a linear form: $F_y = C\alpha$, where α is the side-slip angle of the tyre. During the wheel tilting motion $\alpha = tan\left(\frac{r_w\dot{\gamma}}{v}\right) \approx \frac{r_w\dot{\gamma}}{v}$ results in the lateral side-slip angle, which is the angle between the longitudinal and the lateral component of the velocity vector. Thus, the resulting lateral tyre force is

$$F_y = C\,\frac{r_w\dot{\gamma}}{v} \tag{4}$$

- The static compressions of the suspension and the tyre are neglected see (1) and (2).

The state-space representation of the variable-geometry suspension model can be obtained from the control-oriented form, see (5).

$$\dot{x} = Ax + Bu \tag{5}$$

where the state vector is $x = [\dot{z}_w\ z_w\ \dot{\gamma}\ \gamma]^T$ and the control signal is $u = M_{act}$.

4. SIMULATION EXAMPLE

The aim of the simulations is to show the relationship between the modification of the camber angle and the actual steering angle. The simulations are performed through the complex mechanical simulation system Matlab/SimMechanics.

Fig. 5 (a) shows the intervention on the suspension. The maximum value of the active torque is around $302\ Nm$, which is a reasonable value for the suspension actuator. The camber angles are shown in Fig. 5 (b). It can be seen that the different between the nonlinear model and the SimMechanics model is small. Finally, Fig. 5 (c) presents the resulting steering angle.

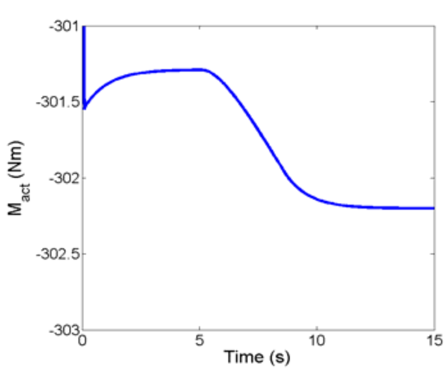

(a) Suspension actuation M_{act}

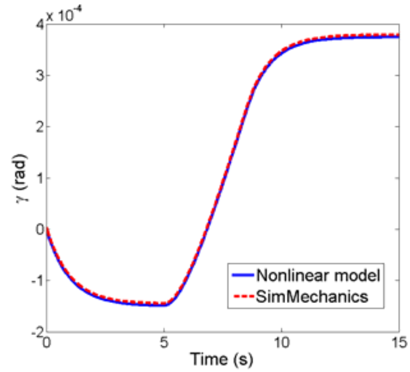

(b) Camber angle (γ)

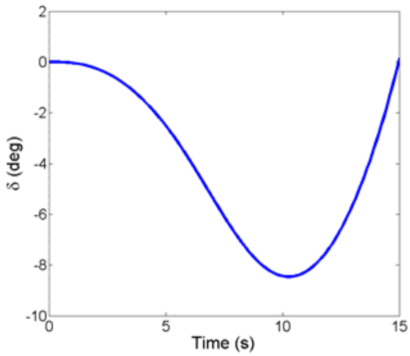

(c) Steering angle (δ)

Fig. 5 Simulation results

5. CONCLUSION

The paper has presented a new independent steering system, which based on the variable-geometry suspension. The nonlinear model of the suspension and its validation has been presented through a complex mechanical simulation system. The main contribution of the paper is to transform the nonlinear model into a control-oriented form. The transformation of the nonlinear equations has been presented. Finally, high-fidelity simulations have demonstrated the operation of the proposed system.
The paper proposed that the variable-geometry suspension can be an alternative way to independent steering control. Since in-wheel electric vehicles are likely to have a significant impact in the future, further research on the variable-geometry suspension control is reasonable.

6. ACKNOWLEDGEMENT

The research was supported by the National Research, Development and Innovation Fund through the project "SEPPAC: Safety and Economic Platform for Partially Automated Commercial vehicles" (VKSZ 14-1-2015-0125). This paper was partially supported by the János Bolyai Research Scholarship of the Hungarian Academy of Sciences.

7. REFERENCES

[1] **Boyd, S. - El Ghaoui, L. - Feron, E. – Balakrishnan, V.:** Linear Matrix Inequalities in System and Control Theory. Society for Industrial and Applied Mathematics, Philadelphia, 1997.

[2] **Evers, W.J. - van der Knaap,- Besselink, A. I. – Nijmeijer, H.:** Analysis of a variable geometry active suspension. International Symposium on Advanced Vehicle Control, Kobe, Japan, 2008.

[3] **Avesta Goodarzia - Ehsan Oloomia - Ebrahim Esmailzadehb:** Design and analysis of an intelligent controller for active geometry suspension systems. Vehicle System Dynamics, 49 (1), 2010. p.333–359.

[4] **Hu, C. - Jing, H. - Wang, R. - Yan, F. – Chen, N.:** Fault-tolerant control of fwia electric ground vehicles with differential drive assisted steering. 9th IFAC Symposium on Fault Detection, Supervision and Safety for Technical Processes, Paris, France, 48(21), 2015. p.1180– 1185.

[5] **Lee, H.S. - Lee, U.K. - Ha, S.K. – Han, C.S.:** Four-wheel independent steering (4wis) system for vehicle handling improvement by active rear toe control. JSME International Journal Series C, 42(4), 1999. p.947–956.

[6] **Lee, S. - Sung, H. – Lee, U.:** A study to the enhancement of vehicle stability by active geometry control suspension (agcs) system. 13th International Pacific Conference on Automotive Engineering, Gyeongju, Korea, 2005. p.1–6.

[7] **Nemeth, B. - Varga, B. – Gaspar, P.:** Hierarchical design of an electro-hydraulic actuator based on robust LPV methods. International Journal of Control, 88(8):1429–1440, 2015. in H. B. Pacejka: Tyre and vehicle dynamics. Elsevier ButterworthHeinemann, Oxford, 2004.

[8] **Piyabongkarn, D. - Keviczky, T. – Rajamani, R.:** Active direct tilt control for stability enhancement of a narrow commuter vehicle. Int. J. Automotive Technology, 5(2), 2004. p.77–88.

[9] **R. Rajamani:** Vehicle dynamics and control. Springer, 2005.

[10] **Ronci, M. - Artuso, P. - Bocci, E.:** Four independent wheels steering system analysis. SAE Technical Paper, 2011. doi: 10.4271/2011- 01-0241.

[11] **Scherer, C. – Weiland, S.:** Lecture Notes DISC Course on Linear Matrix Inequalities in Control. Delft University of Technology, Delft, Netherlands, 2000.

[12] **Sename, O. - Gaspar, P. – Bokor, J.:** Robust Control and Linear Parameter Varying Approaches. Springer Verlag, Berlin, 2013.

[13] **L. Suarez:** Active Tilt and Steer Control for a Narrow Tilting Vehicle: Control design and implementation. Lambert Academic Publishing, 2012.

[14] **Wang, J. - Wang, Q. - Jin, L. – Song, C.:** Independent wheel torque control of 4WD electric vehicle for differential drive assisted steering. Mechatronics, 21, 2011. p.63–76.

[15] **Nemeth, B. - Fenyes, D. – Gaspar. P.**: Independent wheel steering control design based on variable-geometry suspension, 8th IFAC International Symposium on Advances in Automotive Control, Norrkoping, Sweden, 2016.

[16] **Nemeth, B. - Fenyes, D. - Gaspar, P. – Bokor, J.:** Trajectory tracking based on independently controlled variable-geometry suspension for in-wheel electric vehicles, 55th IEEE Conference on Decision and Control, Las Vegas, USA, 2016.

SLIDING FRICTION COEFFICIENT AND WEAR MULTIPLIER AS FUNCTIONS OF THE TRIBOLOGICAL STATE VECTOR

László SÁBITZ and István ZOBORY

Group of Railway Vehicles and Vehicle System Analysis
Faculty of Transportation Engineering and Vehicle Engineering
Budapest University of Technology and Economics (BME)
H-1111 Budapest. Műegyetem rkp. 3, Hungary

Received: November 9, 2016

ABSTRACT

The brake system of vehicles in almost every case based on physical processes is connected with friction elements. When braking with such friction brakes, the kinetic energy of the moving vehicle components are converted into heat energy led out into the environment of the friction pair. Thus, the thermal processes are always present, and determine both the friction coefficient decisive from the point of view of generating brake effect and the wear of the surfaces of the friction partners. The vehicle dynamical simulations nowadays include such procedures, which can take into consideration also the varying pressure, sliding speed and temperature throughout the contact interface of the friction partners. Such simulations need the knowledge of the local friction coefficient function and also the local specific wear function as depending on three variables, namely the pressure, the sliding speed and the contact temperature. Since these functions are of material specific character, extended experimental research is needed for determining them. In this paper a laboratory experiment and measurement results will be introduced, which investigated the friction and wear process of a cast-iron/steel friction pair by using cast iron specimens. The friction interface (the cross section of the specimen) was small: 0.5 cm^2 for approximating the "local" character of the friction interaction in comparison with 200 cm^2 order of magnitude sliding surface area of real frictional brake interfaces used in railway brakes. The paper introduces the test bench, and the measuring results evaluated by graphical extrapolation-based amplification for the three variable sliding friction coefficient and the wear coefficient functions.

Keywords: sliding friction and wear, measurement wheel surface temperature, coefficient of friction, wear coefficient, tribological state vector, thermo-elastic process

1. INTRODUCTION

Several passenger carriages, cargo carriages and locomotives are fitted with cast iron brake blocks, see Fig. 1.

Fig. 1 Bogie equipped with block-brake

There are many studies on mechanical and thermal loads of block-braked railway wheels, by *Vernersson* [1], *Harder* and *Kennedy* [2], etc. Exact knowledge on the friction and wear conditions of the Block/Tyre contact is of paramount importance, both from the point of view of safety and the maintenance costs. The present work is a follow-up to our previous studies, *Sábitz* and *Zobory* [3-6]. The aim of the investigations was to get data on the local – or differential – coefficient of friction and on the local specific wear concerning the cast iron/steel friction pair. Since the local friction and wear history takes a crucial role in generating the thermo-elastic instability process arising in the brake block/tyre sliding interface, cast iron specimens of small cross section were processed and used for the laboratory examinations carried out at the BME, *Department of Railway Vehicles*.

2. LOCAL (DIFFERENTIAL) COEFFICIENT OF SLIDING FRICTION AND THE LOCAL COEFFICIENT OF SPECIFIC WEAR

The local coefficient of sliding friction μ is defined as the ratio of the sliding friction force ΔF_f acting on the small contact surface element ΔA covering the point in the small environment of which the local friction and wear behaviour is examined, and the compressive force ΔF_n acting perpendicularly upon the surface element ΔA, in formula: $\mu = \Delta F_f / \Delta F_n$. This simple definition takes much more complex character, since the friction coefficient can be described with certain approximation by a three variable function $\mu = \mu(p,v,T)$, where the independent variables are the contact pressure p, the sliding speed v and the surface temperature T *at* the point under consideration. The latter three non-negative quantities are the entries of the 3-dimensional *tribological state vector* **a** ordered to the centre point of the friction interface, which state vector depends also on time: $\mathbf{a} = \mathbf{a}(t)=[p(t), v(t), T(t)]^T . \in R^{3+}$, where R^{3+} means the nonnegative *space octant* of the three dimensional Euclidean space. The sliding friction coefficient was tested on a friction test bench of the BME shown in Fig. 2. Vector-valued function $\mathbf{a}(t)$ represents an in-space curve in R^{3+}. The bar-like specimen (2) made of cast iron (type P10) having a cross section area ΔA = 0,5 cm^2 was fixed into a load transferring case jointed by a hinge to the force-exerting vertical arm (3) of the test bench. The force exerted by a hydraulic cylinder (4) pressed the specimen onto the cylindrical jacket of the rotating wheel (1) made of steel. When exerting the hydraulic pressure generated force on the cylinder housing, the fluid pressure acts also on the piston surface and a force, equal and opposite to the cylinder force, is transferred through a helical spring connection to the upper hinged joint at the right hand side vertical force transmitting arm, and in the end to the force measuring cell will be attacked by a force having an action line common with that of the normal compressive force acting on the specimen.

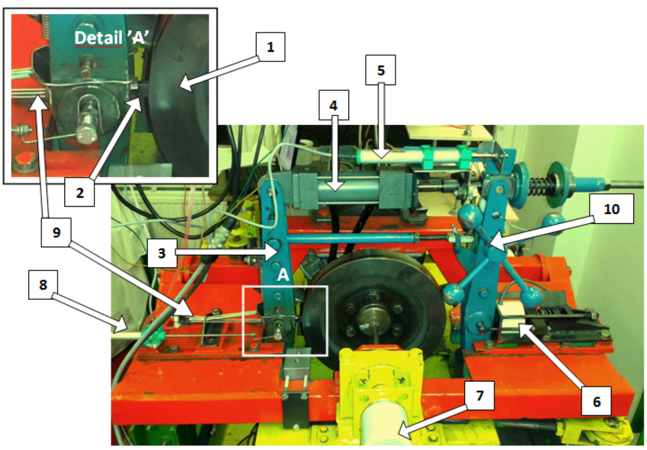

Fig. 2 Roller Test Bench for Tribological Experiments at the BME

The angular velocity of the wheel, and the exerted contact pressure on the friction interface were electronically controlled. The measurements required for the control were ensured by the angular position coder (7), the spring displacement coder (5) and the force measuring cell (6). Each measurement run was started and finished by turning the hand-operated camshaft (10). The wear of the specimen was determined on the basis of the signals of the displacement sensor (8). With the knowledge of the variation in length of the specimen due to wear and the duration, as well as the friction power of the tested loading state, the material removal and the specific value with respect to a unit of the dissipated energy could be determined. The temperature of the rotating cylindrical contact surface of the cylindrical jacket on the wheel periphery was measured by three thermocouples lead through the three longitudinal borings of the cast iron specimen. Thus, the three active measuring tips of the thermocouples were allocated in the close neighbourhood of each other. The order of magnitude of the sliding contact surface of the specimen and the allocation within the latter the three thermocouple tips is visualized in Fig 3.

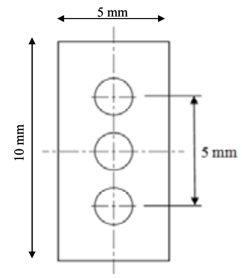

Fig. 3 Cross-section of the test specimen and allocation of the thermocouples

The three parallel borings machined into the test specimen in longitudinal direction can clearly be identified,

- The open-end thermocouples of type NiCr-Ni have wire diameter 0.1 mm. The two wires meet with the contact surface on the rotating jacket of the steel wheel, and the electrical short circuit required for the temperature measurement is ensured)
- Such open-end thermocouples were used previously by *Degenstein* et al. [7].

The cast iron (P10) test specimen used for the experiments are as follows:

Material: P10 cast iron, density: $\rho = 7150$ kg/m^3,
Thermal conductivity (25°C): $\lambda = 48.03$ W/mK
Specific heat (25 °C): $c = 522.3$ J/kgK
Contact surface half-width: $a = 2.5$ mm
The measurements were carried out using the following nominal set-in parameters:
- sliding velocity values: $v = 5.5$, 10.9, 15.5 and 19 m/s
- contact pressure values: $p = 1$, 2, 3, 4 and 5 MPa

The coefficient of sliding friction and specific wear belonging to the specified sliding velocity and contact pressure conditions and to the average temperature prevailing on the contacting surfaces have been evaluated by taking into account the following circumstances:

- The coefficient of friction was evaluated as the ratio of the measured tangential friction force and the normal force acting perpendicularly on the sliding contact surface,
- The measurement of the normal force was carried out by using a load cell placed at the opposite side of the wheel. The load cell was in direct mechanical connection with the force exerting leverage. Due to the symmetry conditions realised in the layout of the brake leverage system the cell was loaded by the same magnitude of force as the perpendicular normal load applied on the specimen/wheel contact area.
- The frictional torque was continuously measured in an indirect way by using force measurement in the support of the *Prony*-brake.
- The wear coefficient was evaluated on the basis *variation in length of the specimen* due to material removal, as well as with the knowledge of the duration of the actual load-state.

3. RESULTS AND DISCUSSION

3.1 Introductory remarks

A total of 136 experiments were carried out. An experiment occurred as follows:

1. the intended sliding speed was set (held constant by a control system),
2. test specimen was pressed against the rotating wheel (contact pressure held quasi const.)
3. wheel surface temperature evolved in the tribological system examined

Each measurement had a certain time interval over which the measured values were evaluated by *moving averaging*. The variation with time of the measured temperatures on the sliding surface are shown in Fig. 4. The *thermoelastic instability* has visibly emerged also on the small contact surface.

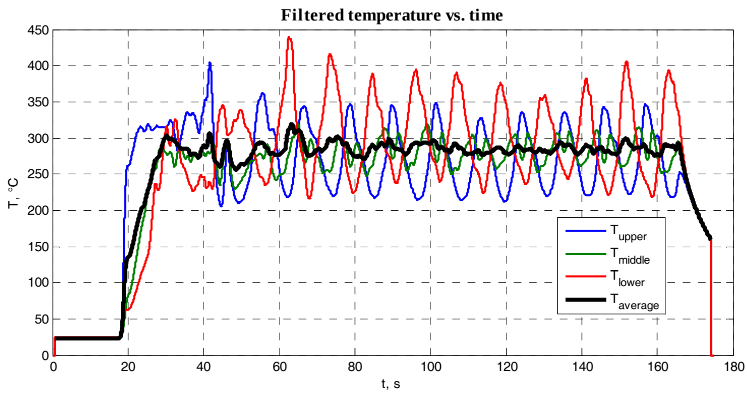

Fig. 4 Temperature vs. time history of a measurement, p = const. and v = const.

3.2 Representation of the executed measurements:

A point-cloud in the 3-dimensional tribological state space is shown in Fig. 5. A meshed surface was fitted on the point cloud by using the method of least squares. The friction and wear properties were traced back to the sliding speed, the contact pressure and the contact temperature conditions.

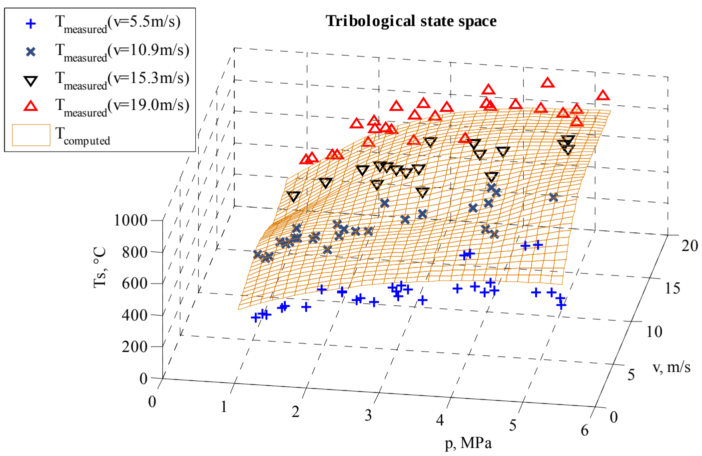

Fig. 5 Measurement results concerning the *tribological state vector* $\mathbf{a}=[p, v, T]^T$ in the non-negative space-octant R^{3+}

3.3 Temperature vs. total heat flow (heat flux) generated

The *polynomial regression function* was determined by using the general method presented by *Zobory* [8]:

$$T(q_{total}) = C_1 \cdot 2^{2k}\left[\frac{1}{2^{2k}} - \left(C_2 \cdot q_{total} - \frac{1}{2}\right)^{2k}\right]$$

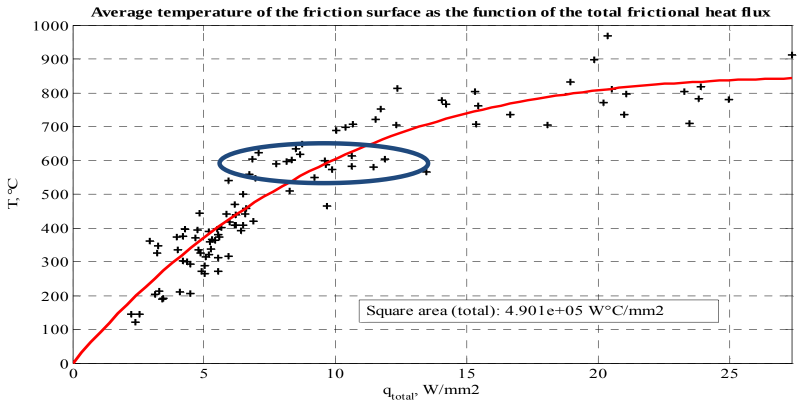

Fig. 6..The contact temperature as a function of the actual frictional thermal energy-flow-density

In the Diagram *T* stands for the averaged local contact temperature (°*C*). On the horizontal axis the friction-generated thermal energy-flow-density values – called specific heat flow densities – are indicated. The heat-flow-density reds: $q_{total} = \mu\, p\, v$ (W/mm^2). In the regression function given above the first parameter *k=2*, and the further parameters are computed on the basis of the *least squares*. The two constant values received are: *C1 = 846.5* °C and *C2 = 0.0134* mm^2/W. The initial increasing tendency in the temperature variation slows down, when the contact surface temperature reaches the value about *600* **°C.**

3.4 The wear rate as the function of temperature

Having exceeded the temperature level 600 °C the wear process accelerates after the

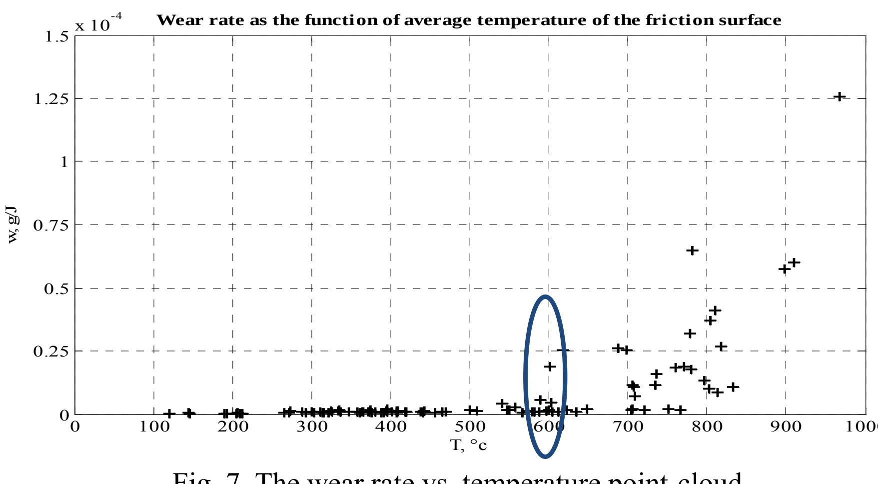

Fig. 7 The wear rate vs. temperature point-cloud

- the increase in wear above 600 °C temperature leads to a *milder* increase in the contact temperature
- increasing the intensity of the heat generation by the total frictional heat-flow-density, the contact temperature changes generate changes in material hardness of the specimen, which changes the wear intensity properties
- a high amount of heat energy is lost with the hot debris flowing out of the contact

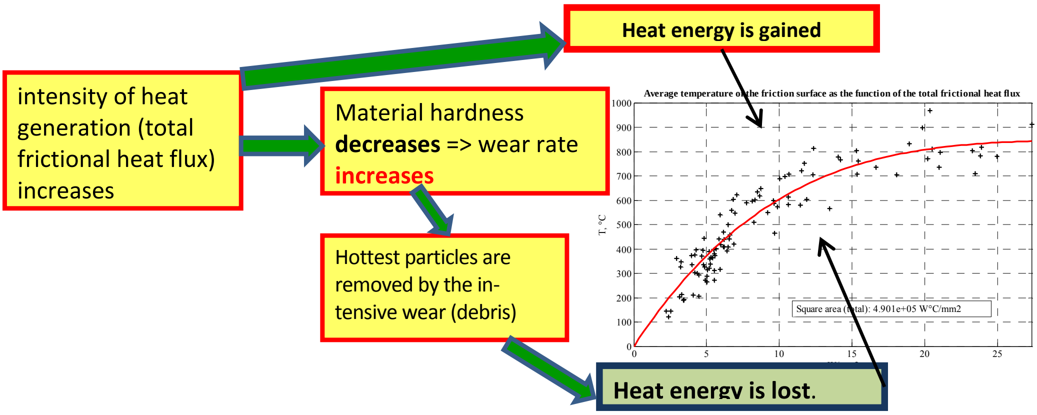

Fig. 8 Contact temperature vs. heat energy-flow-density

3.5 The local (or differential) coefficient of friction as a 3-variable function

The independent variables are the coordinates of the tribological state vector **a**, namely the contact pressure (*p*) the sliding speed (*v*) and the contact temperature (*T*). The function used for approximating sliding friction coefficient in steady sliding state is *a three variable cubic polynomial* with number 20 coefficients has the following form

$$\mu(p,v,T) = a_1 + a_2 p + a_3 v + a_4 T + a_5 pv + a_6 pT + a_7 vT + a_8 pvT + a_9 p^2 + a_{10} v^2 + a_{11} T^2 +$$
$$+ a_{12} p^3 + a_{13} v^3 + a_{14} T^3 + a_{15} p^2 v + a_{16} p^2 T + a_{17} pv^2 + a_{18} v^2 T + a_{19} pT^2 + a_{20} vT^2$$

The measured *value triples* received by sampling went through time averaging and a graphical pre-processing. A numerical condensation of the three dimensional point-cloud of the rough measurement values concerning the tribological state vector and also the measured force values has been realised, which resulted in a *brick-like partition* of the state space range. To each brick centre point belonged a condensed stationary value (smoothed by moving averaging) of the friction coefficient and the wear coefficient. The brick centres were assigned by the three sliding speed values 5.5, 10.9, 15.5 and 19 *m/s*, the nine contact-pressure values 1, 1.5, 2, 2.5, 3, 3.5, 4, 4.5, and 5 *MPa*, and the eight temperature values 200, 300, 400, 500, 600, 700, 800 and 900 in centigrade. For a practical treatment, to the four stationary sliding speed values the bi-variate friction coefficient functions $\mu_i(T,p)$ and wear coefficient functions $w_i(T,p)$ were introduced, for $i=1,2,3,4$.

Since in the brick-centre value tables of the four condensed $\mu_i(T,p)$ and $w_i(T,p)$ function pairs contained also empty bricks an extrapolative graphical estimation became necessary to get estimations for the missing brick centre values. The reasonable graphical estimation was based on the forms and the recognised variation tendencies of the relations among the non empty brick centre values and on the “sense of engineers” concerning the nature of possible variation of the quantities to be estimated.

The originally condensed and the so “amplified” brick centre values were then used for least square fitting, based on the *three-variate cubic polynomial* introduced above. The least square estimation used here was a special one, namely a “weighted” version, so that the entries in the brick-tables, which came from the condensation of real measurement data were taken into consideration with a weight of 90%, while the estimated entries – the results of the graphical “amplification” were taken into consideration with a weight of only 10%. The least square estimation led to the coefficient values: a_1, a_2, …,a_{20} of the *three-variate cubic polynomial*. The necessary numerical procedure was realised by a proper MATLAB program.

3.6 Illustration

The results concerning the friction coefficient functions $\mu_i(T,p)$, $i=1,2,3,4$ belonging to the four constant “brick-centre” sliding speeds are shown with their *three-variate cubic polynomial approximation* in Fig. 9.

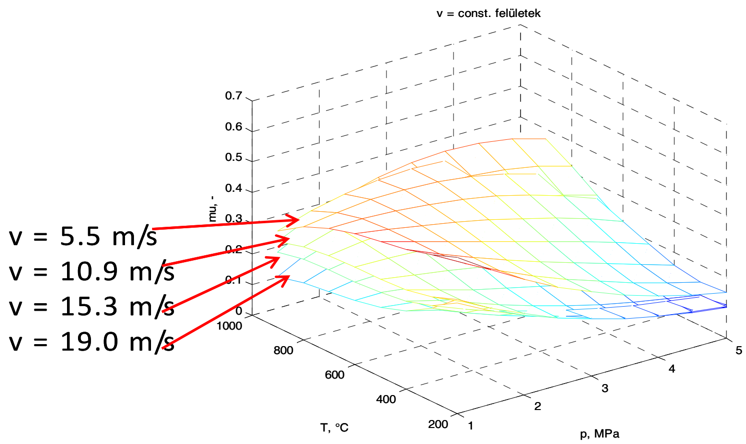

Fig. 9 The friction coefficient functions for constant speeds approximated by three-variate polynomials, fitted by the method of *weighed least squares*

As for the *wear coefficients*, the mass removal due to the sliding friction was detected in the course of the testing by the variation in length of the cast iron specimens. The primary wear data were represented in *mm* values, but with the knowledge of the cross section area of the specimen (=contact surface) and the material density of the cast iron, as well as the knowledge of the duration of the measuring period, it was possible to compute both the mass removed Δm, and the frictional work W done throughout the measuring period. Thus, the wear coefficient for the state vector $\mathbf{a_P}(p,v,T)$ belonging to a brick centre P could be expressed on the basis of formula $w(p,v,T) = \Delta m(p,v,T)/\mathrm{W}(p,v,T)$. The mass was taken into account in g, while the work done in J, thus the unit of measure of w was g/J. The graphically “amplificated“ diagrams of the wear coefficient functions $w_i(T,p)$, $i=1,2,3,4$ are shown in Fig. 10. Here $i=1$ belongs to the stationary brick-centre sliding speed *5.5 m/s*, $i=2$ belongs to *10.9 m/s*, $i=3$ belongs to *15.5 m/s*,and finally $i=4$ belongs to *19 m/s*.

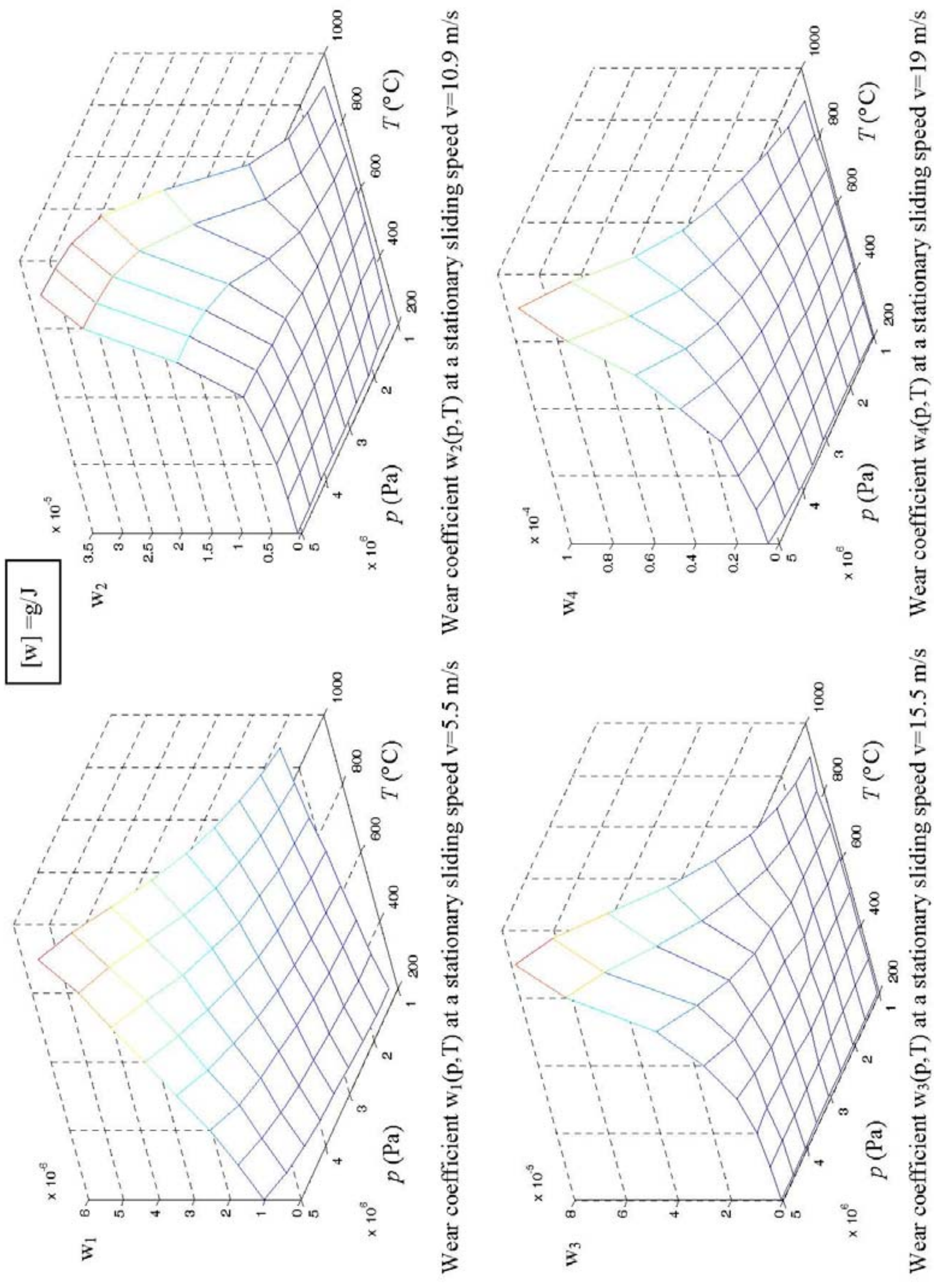

Fig. 10 The wear coefficient functions for constant sliding speed values

4. CONCLUSIONS

On the basis of the evaluation of the measurement results the following conclusions can be drawn:

1. The measurement results indicate that the surface temperature of the sliding friction contact up to a certain temperature level (cca. 600°C) is approximately proportional to the heat-flow-density emerging in the contact interface. Above this level the wear becomes more intensive which leads to the faster removal of the hottest debris particles. As a consequence, the contact surface temperature vs. dissipated heat flux function will have a decreasing slope – though this slope is still positive within the heat-flow-density range measured. The *temperature as a function of the* emerging heat-flow-density was approximately described by a *4th-order polynomial* function.
2. It has been pointed out by processing and evaluation of the measurement results how the coefficient of friction changes with contact pressure p, sliding velocity v and contact surface temperature T. The relations were described by defining a *three-variate cubic polynomial* fitted on the condensed brick-centre values deducted by condensation from the crude measurement results. For fitting the latter polynomial the method of *weighed least squares* was used. The results have been introduced with four p and T dependent performance surfaces belonging to four steady sliding speeds.
3. A reasonable approximation (estimation) method based on graphical extrapolation of the condensed brick-centre values of the contact pressure p and contact surface temperature T belonging to the four constant sliding velocity v values considered has also been elaborated. The results appeared in form of four *bi-variate* wear coefficient performance surfaces. The latter diagrams clearly show that the wear coefficient functions begin with a radically intensive increase when the product $p{\cdot}T$ exceeds a certain bound depending on the constant sliding speed considered.
4. Further efforts are needed for developing the measurement method concerning the friction coefficient and wear coefficient, first of all by making it possible to heat up and cool down in a controlled way the cylinder jacket path contacting with the specimen, for achieving also higher and lower contact temperature conditions, different from those generated by the autonomous friction interaction of the specimen and the cylindrical jacket of the rotating wheel determined by the natural parameters of the test bench.

5. REFERENCES

[1] **Vernersson, T.:** Tread Braking of Railway Wheels – Noise-Related Tread Roughness and Dimensioning Wheel Temperatures, thesis for the degree of Doctor of Philosophy, Chalmers Univ. of Techn., Dept. of Applied Mechanics, Division of Dynamics, 2006, Göteborg, Sweden

[2] **Harder, R. F.- Kennedy, T. C.:** Thermal modeling of railcar wheel braking, Proceedings of the 8th International Conference on Railway Bogies and Running Gears - BOGIE ’10 (Ed. by Prof. I. Zobory). BME, Department of Railway Vehicles and Vehicle System Analysis, Budapest, 2010, p.89-101.

[3] **Sábitz, L. - Zobory, I.:** Finite element modelling of the thermo-elastic processes in tread-braked wheels, Proceedings of the 8th International Conference on Railway Bogies and Running Gears - BOGIE '10 (Ed. by Prof. I. Zobory), BME, Department of Railway Vehicles and Vehicle System Analysis, Budapest, 2010, p.103-113.

[4] **Sábitz, L. - Zobory, I.:** Simulation of local heat processes on the tread of a block-braked railway wheel, Proceedings of the 13th MINI Conference on Vehicle System Dynamics, Identification and Anomalies - VSDIA 2012. (Ed. by Prof. I. Zobory), BME, Department of Railway Vehicles and Vehicle System Analysis, Budapest, 2014, p.245-252.

[5] **Sábitz, L.- Zobory, I.:** On Simulating the Thermal Conditions of Martensite Formation on Railway Wheel Treads. In: Proceedings of the Second International Conference on Railway Technology. Civil-Comp Press, paper 105., DOI: 10.4203/ccp.104.105

[6] **Sábitz, L. – Zobory, I.:** Combined Thermal and Stress Finite Element Analysis of Tread-Braked Wheels. Proceedings of the 12th MINI Conference on Vehicle System Dynamics, Identification and Anomalies - VSDIA 2010. (Ed. by Prof. I. Zobory), BME, Department of Railway Vehicles and Vehicle System Analysis, Budapest, 2011, p. 203-213.

[7] **Degenstein, T. - Günter, M. - Keller, A. - Winner, H.:** Dynamic measurement of the temperature of electro conductive objects used for the example of a wheel brake, AMA Service GmbH, 2007

[8] **Zobory, I.:** Vasúti vontatójárművek terhelési viszonyainak vizsgálata és a terhelésállapot-eloszlás alkalmazása a hidrodinamikus hajtóművek tervezésében. Kandidátusi értekezés, Budapest, 1979. (In Hungarian)

DYNAMICAL PROPERTIES OF CRANK MECHANISMS

Dezső SZŐKE and István ZOBORY

Faculty of Transportation Engineering and Vehicle Engineering
Budapest University of Technology and Economics
H-1111 Budapest, Műegyetem rkp. 3, Hungary

Received: November 9, 2016

ABSTRACT

Some authors introduce a number of simplifying assumptions in the dynamical analysis of crank mechanisms which are either incorrect or cause bias-treatment, thus making it impossible to get an insight into the real dynamical behaviour of the system. A crank mechanism consists of three practically rigid bodies which are interconnected by given constraints. The mass and moment of inertia characteristics of the individual masses are constants, which are known exactly from measurements. It follows from the function of the structure that the mass characteristics of the structure (the mechanism) vary parametrically as a function of time and position. The presence of varying parameters will basically influence the kinematical and kinetic processes describing the system behaviour (parametrically excited system). Together with the computation of motion characteristics, connection forces and the functions describing the uneven running, the measure of balance of the structure will also be dealt with.

Keywords: dynamics crank mechanism, parametric excitation, time domain simulation

1. MECHANICAL MODEL OF THE CRANK MECHANISM

The components of the crank mechanism are the crankshaft, the connecting rod and the piston. The crank mechanism to be analysed is for a single cylinder which is free of work-medium (i.e. no pressure acts on the piston).

When selecting the mechanical model it is assumed, that the crankshaft is statically balanced and rotates around a stationary geometrical axis. In real systems (in internal combustion engines or compressors) the former assumptions are not in force, since in order to balance the reciprocating masses additional masses are mounted on the crankshaft being balanced in itself. The crankshaft is supported in bearings of the housing which is connected to the fixed environment by rubber blocks (mounts). Due to the forces generated by the operation of the mechanism acting upon the housing, the position of the rotational axis changes slightly, thus its bearings are not stiff. For the inertial parameters of the system, see Fig.1.

crankshaft: J_0 rotational moment of inertia about the axis passing through the centre of gravity (CoG). This J_0 includes the crankshaft and the fly-wheel mounted on it.

connecting rod: J_S moment of inertia about the axis passing through the CoG,

m the mass of the connecting rod,

l_{SB} distance between CoG of the connecting rod and the axis of the gudgeon-pin.

piston: m_d the mass of the piston.

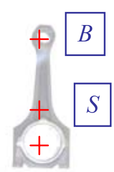

Fig.1 Connecting rod

The parameters used in the simulation model were based on the dimensions for a medium category, internal combustion engine with in-line cylinders. The common moment of inertia of the crankshaft and the flywheel was proportioned for one cylinder.

The objective of this investigation is to dynamically model the most commonly used internal combustion engines

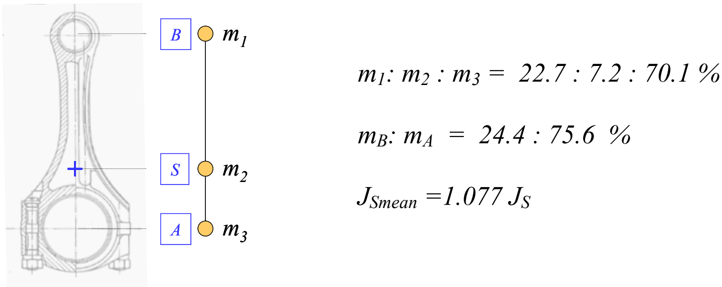

Fig. 2 Mass parameters of the system considered

The kinematics of the crank mechanism is uniquely determined knowing the angular displacement φ and the angular velocity $\dot{\varphi}$ of the crankshaft, see Fig. 3. Thus, the kinematical characteristics can be computed by using the theorem of impulse-moment, knowing the moment of inertia about the principal axis of the system.

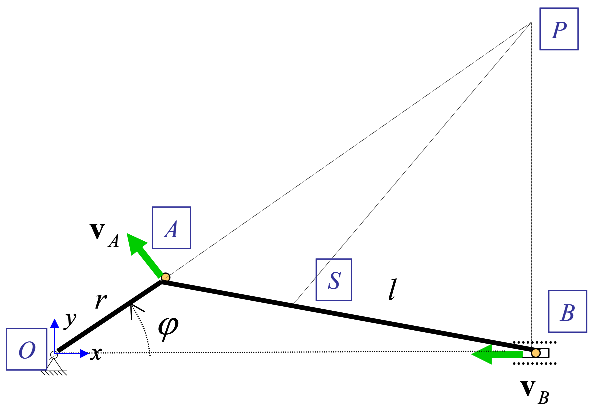

Fig 3. The kinematical characteristics and parameters of the mechanism

The kinetic energy of the system is given by the formula below:

$$E = \frac{1}{2}\left\{J_0\dot{\varphi}^2 + J_P\dot{\varphi}_l^2 + m_d v_B^2\right\},$$

where J_p is the moment of inertia about the instantaneous rotational centre P of the connecting rod, $\dot{\varphi}$ is the angular velocity of the crankshaft, $\dot{\varphi}_l$ is the angular velocity of the connecting rod around its instantaneous centre P and v_B is the velocity of the piston.

The above characteristics can uniquely be expressed as functions of the angular displacement and the angular velocity of the crankshaft, as follows:

$$J_P = J_S + ml_{SP}^2,$$

$$r\dot{\varphi} = l_{AP}\dot{\varphi}_l,$$

$$\mathbf{v}_B = l_{BP}\dot{\varphi}_l \,.$$

Taking into consideration the above relationships the kinetic energy can be rewritten into formula

$$E = \frac{1}{2} J(\varphi)\dot{\varphi}^2 \,,$$

where

$$J(\varphi) = J_O + (J_S + ml_{SP}^2 + m_d l_{BP}^2)(\frac{r}{l_{AP}})^2 \,.$$

is the moment of inertia of the system about the axis of rotation, which depends only on the angular position of the crankshaft for a given structure, since l_{SP}, l_{AP}, $l_{BP} = f(\varphi)$.

2. THE MATHEMATICAL MODEL

The mathematical model of the system, i.e. its motion equation can be generated by using the *Lagrangean* equation of the second kind. The effect of gravity is neglected (the mechanism moves in the horizontal plane). Thus, considering only the kinetic energy and the gas-force acting on the piston, the equation of motion reads:

$$J(\varphi)\ddot{\varphi} + \frac{1}{2} J'(\varphi)\dot{\varphi}^2 = Q(\varphi) = M(\varphi) \,.$$

The moment of inertia $J(\varphi(t))$ also depends on the angular position, while the generalized force (now torque) can be computed from the position and the velocity of the piston, as follows:

$$Q(\varphi) = M(\varphi) = \mathbf{F}\frac{d\mathbf{r}}{d\varphi} = \mathbf{F}\frac{d\mathbf{v}}{d\dot{\varphi}} \,.$$

Here **F** stands for the force vector acting on the piston, d**r** is the infinitesimal displacement vector of the piston, while d**v** is the infinitesimal increment in the velocity vector of the piston. The operation between the vector quantities in the formula is the *scalar product*.

The motion equation is an ordinary, second order, *parametrically excited*, non-linear and non- homogeneous differential equation. The motion of the medium-free system is identical to the solution of the homogeneous equation below:

$$J(\varphi)\ddot{\varphi} + \frac{1}{2} J'(\varphi)\dot{\varphi}^2 = 0 \;;\; \varphi(t) = ? \;,\; \dot{\varphi}(t) = ?$$

As well as a numerical solution, an analytic solution is sought. The following mechanical principle can help find the proper test function: since no external force (torque) acts on the system, the kinetic energy of the system remains constant.

$$E(t) \approx J(\varphi(t))\,\dot{\varphi}^2(t) = \text{constant} \;.$$

Thus, the angular velocity of the crank shaft at a given time instant can only vary obeying the functional relationship:

$$\omega(\varphi) \approx \frac{c}{\sqrt{J(\varphi)}} .$$

All these mean that the signal-form changes a little depending on the angular position of the crankshaft, whereas the amplitude of the signal is determined by the kinetic energy. From these it is clear, that kinematical and kinetic functions of the system with respect to one full rotation are the same depending on the normalized time.

3. DYNAMICAL CHARACTERISTICS OF THE MECHANISM

From among the kinematical and kinetic characteristics of the crank mechanism the following will be investigated:

- position of the CoG
- uneven running (grade of un-equality)
- balanced state (static and dynamical balanced state)
- connection forces
- forces acting upon the environment (forces acting upon the engine-block).

a.) Position of the centre of gravity (connecting rod and piston together)

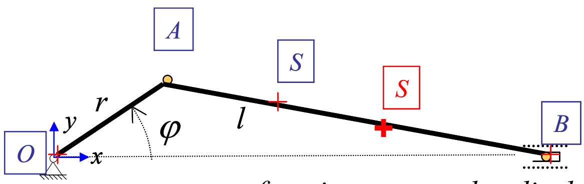

a two parameter function vs. angular displacement

Fig. 4 System descriptive designations

b.) The uneven running (grade of un-equality)

$$\delta = \frac{\omega_{max} - \omega_{min}}{\omega_{mean}}$$

c.) Balancing

statically: the centre of gravity of the system lies on the axis of rotation
(In real systems this condition *is not fulfilled*, since the common CoG of the connecting rod and the piston does not lie on the axis of rotation.)
dynamically: the direction of the impulse moment vector originating at the centre of gravity and that of the axis of rotation is identical
(This condition is met, since the system is symmetric in the plane perpendicular to the axis of rotation.)

d.) Connection forces and forces acting on the environment (supporting forces arising in the bearings and on the cylinder surface).
Knowing the accelerations of the components and their inertial characteristics, the connection forces and the forces acting on the environment can be determined by applying the *gravity-point theorem* and the *impulse-moment theorem*.

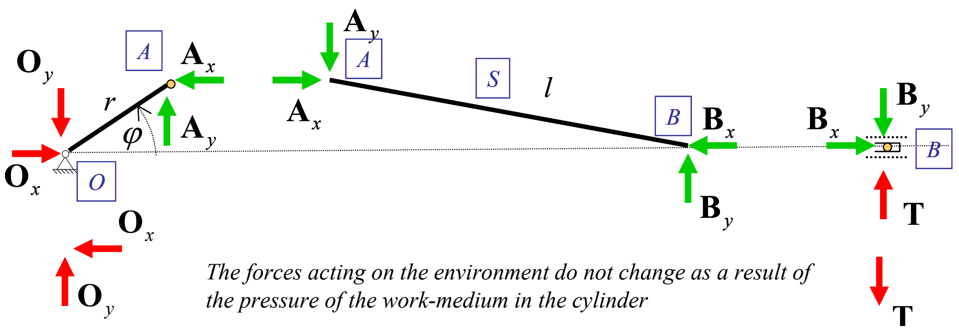

Fig. 5 Connection force components in the dynamical system

The variations of the components of the force system with respect to time is helped by presenting an animation

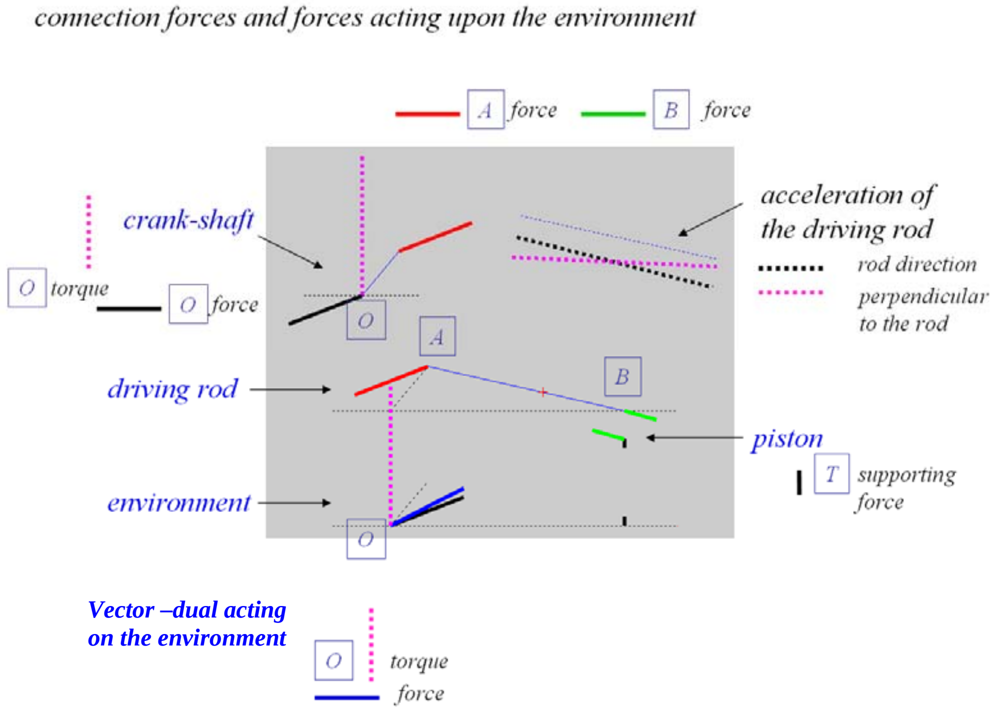

Fig. 6 Connection forces and forces acting upon the environment

4. SIMULATIONS RESULTS

The moment of inertia of the system about the rotational axis is independent of the angular velocity of the crank-shaft, and only depends on the angular position of the crankshaft.

The characteristics of the above variation: The angular frequency of the fundamental harmonic component of the moment of inertia is approximately equal to the twice the value of the angular velocity of the crank-shaft.

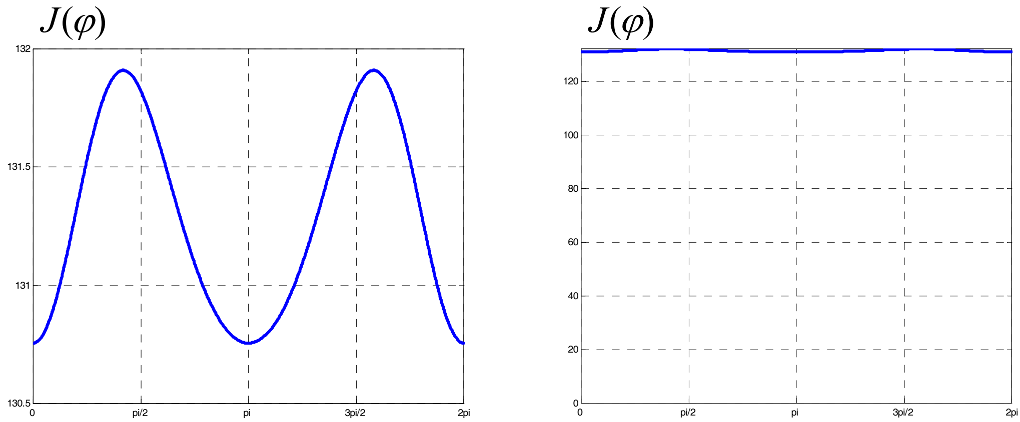

Fig. 7 Variation of the system moment of inertia vs. the angular displacement

Based on the above: the grade of inequality is δ =.88 %.

Due to the changing moment of inertia the angular velocity of the crankshaft also changes, see Fig. 8.

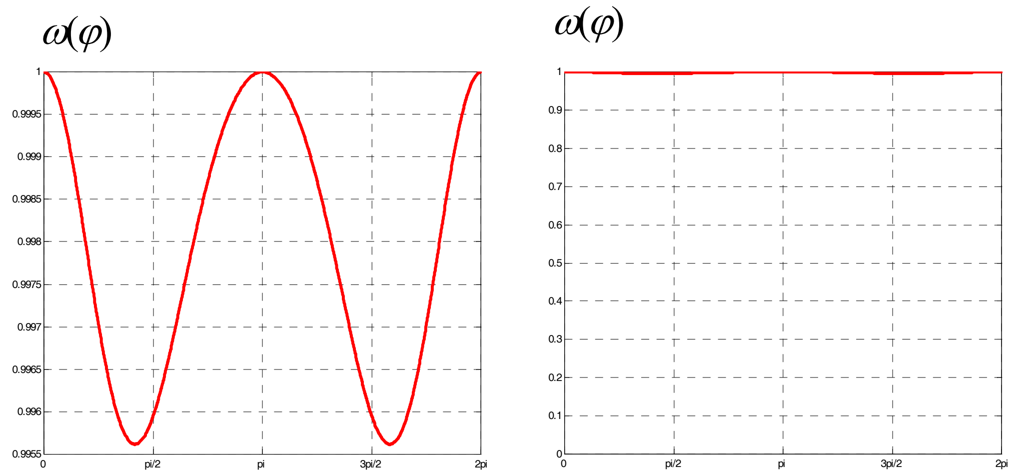

Fig. 8 Variation of the angular velocity of the crankshaft vs. the angular displacement

The characteristics of the above variation are the angular frequency of the basic harmonic component of the angular velocity is approximately equal to the double value of the angular velocity of the crank-shaft. Based on the above: the grade of inequality is δ=0.44 %; (δ=0.4438 % ; δ_{aver}=0.4391 %).

$$J(\phi) = 1 + \varepsilon(\phi)\ ,\ \omega(\phi) = \frac{1}{\sqrt{J(\phi)}} \quad \Rightarrow \omega(\phi) = 1 - \frac{1}{2}\varepsilon(\phi)$$

In the Figure one can see the result of the numerical examinations. The latter result is identical with the results of the analytic treatment. The results are identical concerning the grade of inequality. Since the moment of inertia with respect to the error function

$\varepsilon(\varphi)$ changes only a little, thus with the knowledge of the connection between the angular velocity of the crankshaft and the moment of inertia, the variation of the angular velocity vs. angular displacement can be given also in closed form approximation.

$$J(\varphi) = 1 + \varepsilon(\varphi)$$

$$\omega(\varphi) = \frac{1}{\sqrt{J(\varphi)}} \quad \Rightarrow \omega(\varphi) = 1 - \frac{1}{2}\varepsilon(\varphi)$$

From the above said it also follows, that the impulse-moment of the crankshaft changes, therefore the crankshaft has angular acceleration, thus the gravity point of the system has also a tangential acceleration, and furthermore it is sure that the gravity point performs a displacement of tangential direction.

During operation, the position of the shared centre of mass of the connecting rod and the piston changes, see Fig. 9. Thus, the system is not statically balanced, and *cannot be balanced* by a mass fixed to the crank shaft.

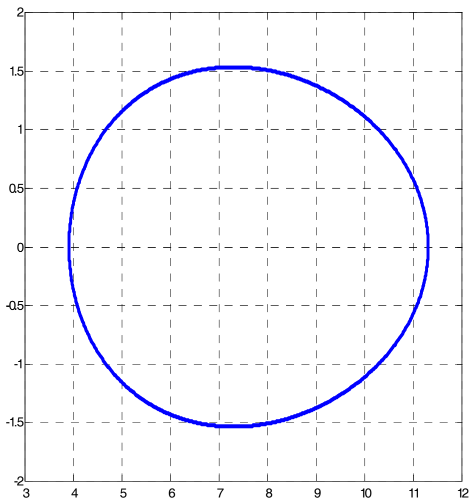

a.) Phase-trajectory of the centre of mass

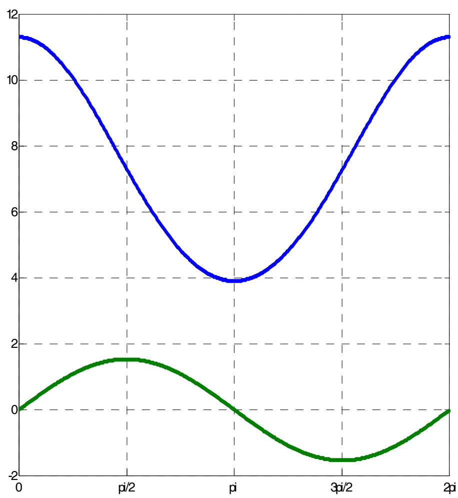

b.) The x and y co-ordinates of the gravity point as a function of the angular position of the crank-shaft

Fig. 9 Performance curves of the motion of the gravity point

As a result of the simulation the angular acceleration, the angular velocity and the displacement of the crankshaft can be visualized as functions of the normalized time ($2\pi/\omega_0$), as well as the acceleration, velocity and displacement functions of the piston, see Figs 10 and 11. In Figs 12 and 13 the components of the forces arising at the ends A and B of the connecting rod are shown.

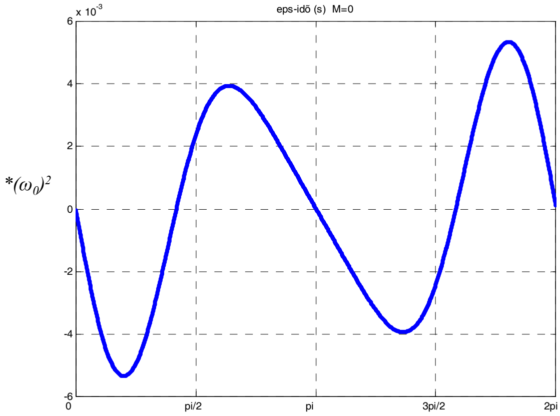

angular acc. of the crankshaft vs. time $2\pi/\omega_0$

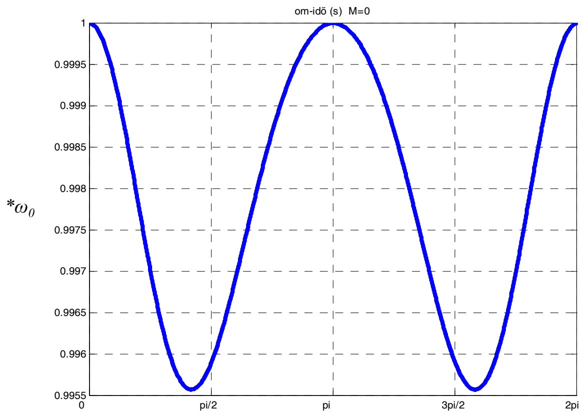

angular velocity of the crankshaft $2\pi/\omega_0$

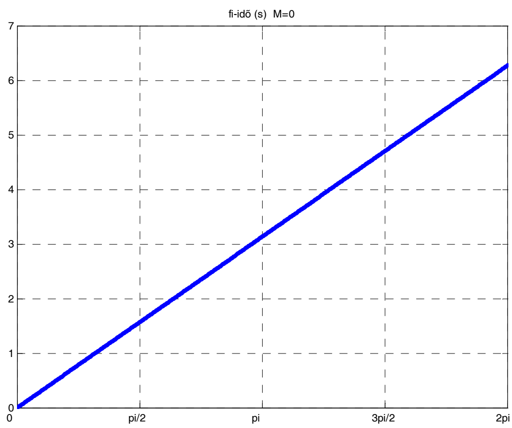

angular position of the crankshaft $2\pi/\omega_0$

Fig. 10 Motion characteristics of the crankshaft vs. the normalized time ($2\pi/\omega_0$)

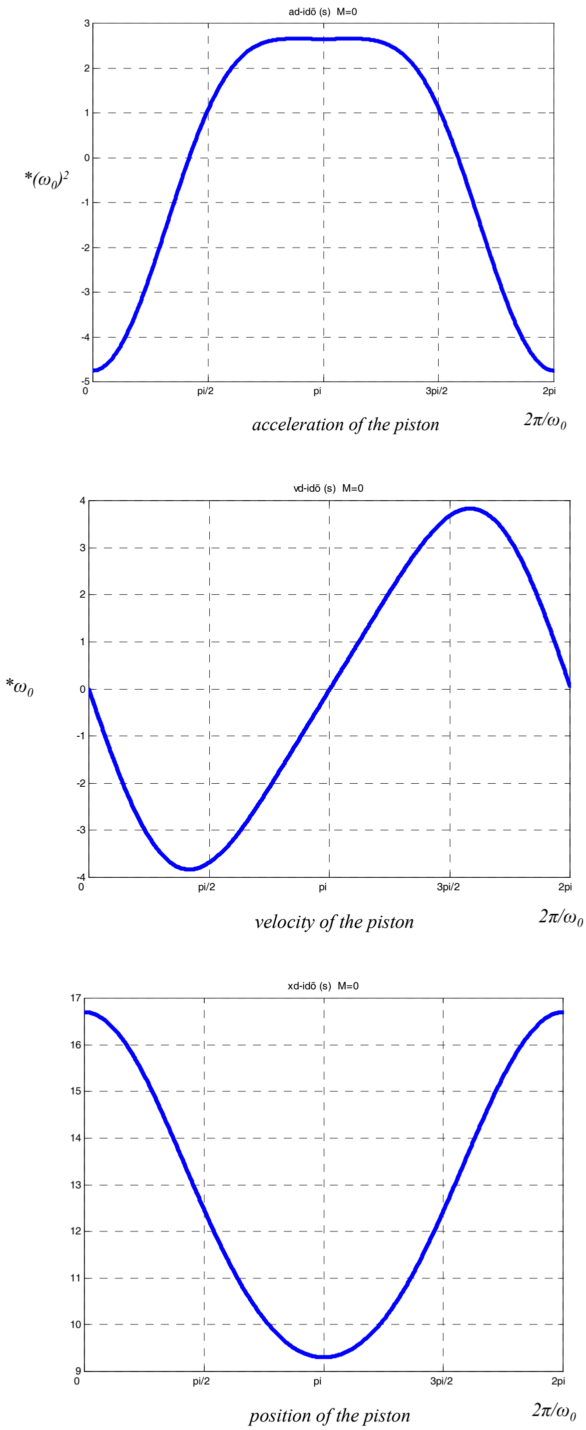

Fig. 11 Motion characteristics of the piston vs. the normalized time ($2\pi/\omega_0$)

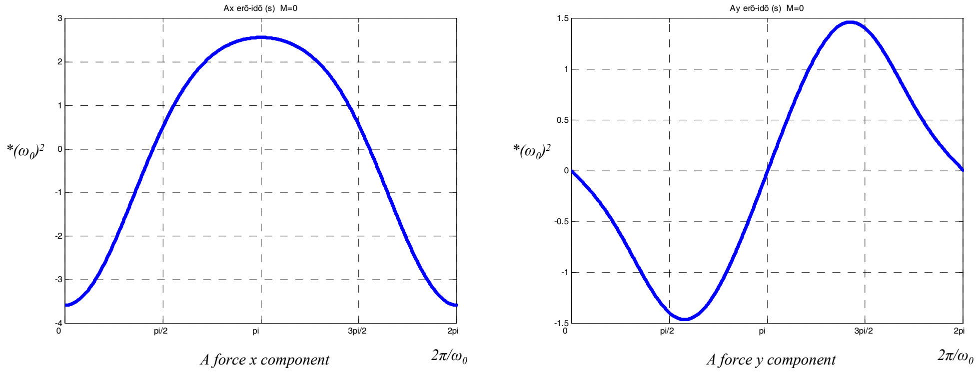

Fig. 12 Force components at point A

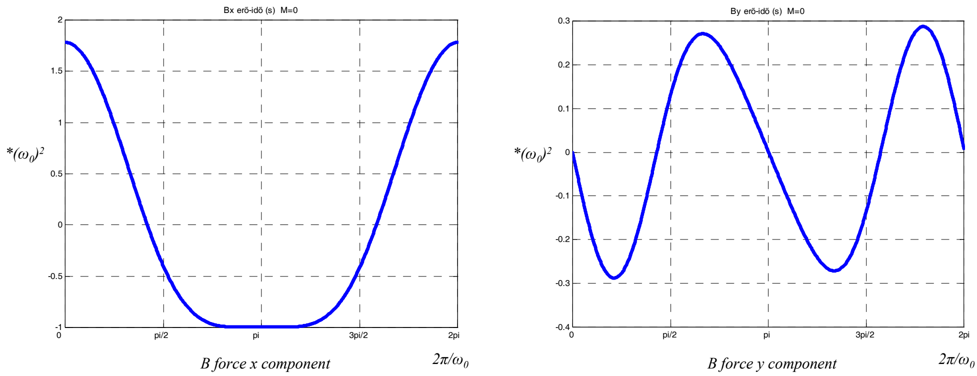

Fig. 13 Force components at point B

5. CONCLUDING REMARKS

The paper presents an exact mechanical model of the crank-mechanism without approximations. It is characteristic for the system that its moment of inertia varies slightly as a periodic function of the angular position of the crank-shaft. The measure of the variation has been described by the *measuring number* of the inertial inequality. Due to the varying moment of inertia the motion (running) of the crank-shaft is non-uniform. The amplitude of the non-uniform motion and its variation with time can be determined in closed form based on the moment of inertia function.

6. REFERENCES

[1] **Gross, D. - Hauger, W. - Schnell, W. – Wriggers, P.:** Technische Mechanik, Springer-Verlag, 1993, ISBN 3-540-56629-5

[2] **Pattantyús, Á.G.:** Gépészeti lengéstan. Akadémiai Kiadó, Budapest, 1952 (In Hungarian)

[3].**Zobory, I. - Szabó, A.:** Járműdinamika és Hajtástechnika. Typotext Kiadó, Budapest, 2012. (In Hungarian)

[4] **Kozsevnyikov, Sz.N.:** Mechanizmusok és gépek elmélete I-II. Tankönyvkiadó Budapest, 1958. (In Hungarian)

LIM AND LSM APPLICATIONS - LINEAR DRIVES FOR VEHICLES

Karoly KEHRER, Sam GUROL and Phil JETER

Eurostile LLC General Atomics
LIM and LSM Applications
Dr. Karoly Kehrer, 670 Barclay Hill Rd Beaver, PA 15009 USA

Received: November 9, 2016

ABSTRACT

An overview of the system requirement definition for LSM control designed for transportation, and the development for the practical application of the same is presented. A system is introduced for controlling movements of a vehicle along a land-based guideway which comprises: a linear array of targets mounted on the vehicle. The array has a length "l", with a distance "d" between adjacent targets accordingly to the required resolution. A plurality of in-line, wayside sensors are placed along the guideway with a spacing "s" between adjacent sensors depending on the length of the vehicle. A signal processor electronically connected to each sensor to receive a signal therefrom, wherein the signal is indicative of a target being within a predetermined range "r" (>13mm, ~0.5 inch) from a sensor. A computer connected to the signal processor for measuring a time interval "Δt" between successive signals to derive parametric values, based on "d", to control of the vehicle movements.

Keywords: Linear Synchron Motor (referred to as LSM), Resolution, Active Computer Control, Safety.

1. HISTORICAL OVERVIEW OF LIM OR LSM DRIVES FOR LEVITATED AND WHEELED VEHICLES

1.1 LIM drives for Maglev

1980 Prof. Goddard designed the first EMS levitation train for Birmingham. 1985 The German team put the first permanent magnet levitated vehicle in service along the Berlin wall. They have used mechanical control for maintaining the levitation gap. 2004 The Japanese deployed a working "Urban" EMS system in Nagoya. (Limino)

Fig. 1 Nagoja Japan the Lim driven levitated car

Fig. 2 Typical arrangement for LIM Gw regardless if it is used either rubber tired, steel wheeled or levitated vehicle

1.2 LSM drives

2004 The Chines deployed the first high speed Transrapid. 2005 The American team in San Diego run a successful full scale demonstration of control-less permanent magnet levitation and successfully applied permanent magnet Halbach arrays in conjunction with the LSM drive system.

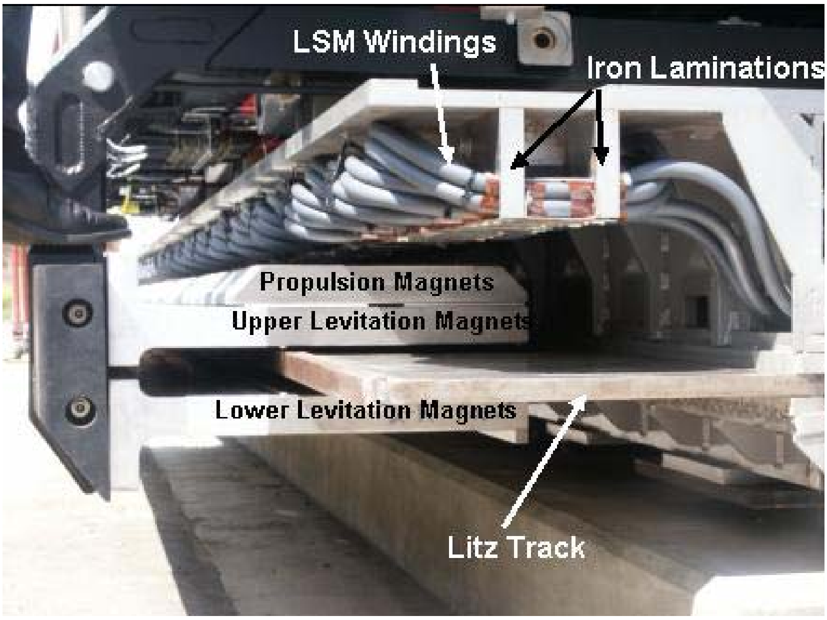
LSM Windings
Iron Laminations
Propulsion Magnets
Upper Levitation Magnets
Lower Levitation Magnets
Litz Track

Fig. 3


LINEAR DRIVES
Container transportation Linear Synchronous Motor (LSM)
Automated transport from LA-LB sea port to intermodal stations in Victorville 12Million container/y cap
Transrapid LSM

Fig. 4

Fig. 5 LSM drive for container transportation

The LSM is the most cost-effective drive for high frequency transportation. Annually **12 million** containers have to be transported from *LSM driven container on the track*
Long Beach and Los Angeles CA see ports to inland intermodal stations and be returned to the port. It means that the containers had to be transferred **in 3 minutes** intervals.

1.3 Superconducting magnet drive

2012 The Japanese began working on ultra-high speed (560 km/h) MLX line between Tokyo and Osaka.

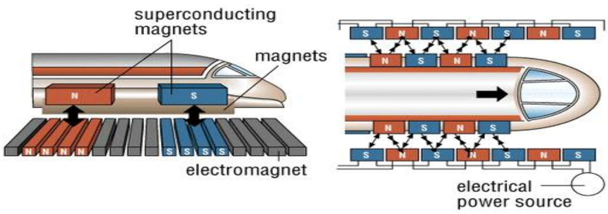

Fig. 6..Principle of Magnet Drive

1.4 Linear Motor drives for wheel supported vehicles.

Scarborough line in Toronto Canada. Elevated transit lines Vancouver British Columbia Canada.
Elevated transit lines Malesia
Kelana Jaya Line in Kuala Lumpur opened 1998
EverLine Rapid Transit System in Yongin) Japan
AirTran JFK in New York opened 2003, Detroit People Mover opened 1987

Fig. 7 Details of Magnet Technology

1.5 LIM motor

Military Application ***Modified LIM for aircraft catapult system (now in service)***
The Aircraft launcher developed by General Atomics has been put in service a few years ago replacing the antiquated steam system. Opposite to the passive LIM guide-way the special LIM winding moves the aluminum plate to which the plane is hocked on. The load capacity is 100 metric tons Acceleration from 0 to 300 km/h is about 8 second.

The most important aspects of LIM and LSM drives are:
LSM is built into the guide ways, has propulsion and lift i.e. it is an active guideway; (the I_d and I_q current can be adjusted independently) the vehicle needs no onboard driving power therefore it is a passive one.
LIM motors are built into the vehicle therefore it needs onboard driving power and is subjected slight forward translational oscillation.
Neither system, - whether it is LSM or LIM - needs friction forces for propelling the vehicle on the guideway, hence no wheel or rail wear. They have no moving parts like rotary motors or gear boxes, hence no friction, wear and no need for expensive maintenance.

Although, both system are still facing the problem of chaotic responses for random disturbance.

In both case, above the critical forward speed, $\mathbf{v_c}$, the origin loses its stability and moves to an isolated closed trajectory.
The vehicle has 6 degrees of freedom that results in 3 translational and 3 angular movements.
The LSM drive can - a certain degree - control the angular movements by altering the I_D current.

The wheelset over-shoots more and more, and at or above the critical forward speed, $\mathbf{v_c}$, the origin loses its stability and moves to an isolated closed trajectory.

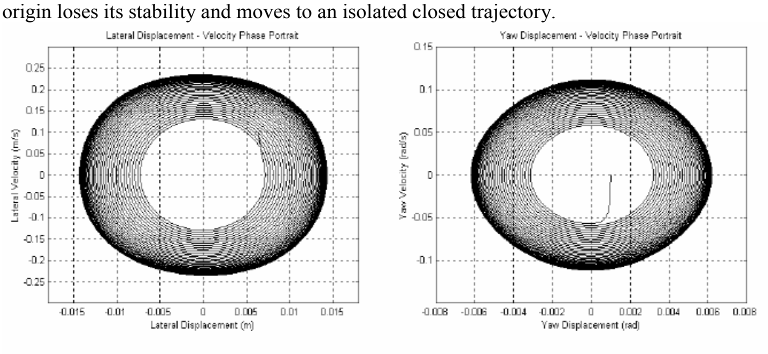

Fig. 8 The LSM I_D current has substantial added stability above v_c,

Advantages and design requiremets for LSM drives
As is well known, the basic components of a Linear Synchronous Motor (LSM) correspond to the standard rotor and stator components of a rotating electric motor. Specifically, the operational interaction of these components is correspondingly similar. Unlike a standard electric motor, however, the components of an LSM are laid out

substantially in-line. Such a configuration lends itself well for use as a propulsion unit for a vehicle that is designed to travel long distances.

However, the linear arrangement poses a serious problem, for there is one significant difference. While the rotating synchronous motor's synchronization is a relatively simple task using assailant poles to pull them in synchronic operation, but to maintain synchronizations of the LSM over hundreds of kilometer long tracks requires a new solution.

Regardless, several advantages can be mentioned for using a hard wired, land-based stator as part of the propulsion unit for a long distance vehicle. For one, in general, the land-based stator will not be influenced by weather conditions or terrain variations (e.g. mountains and valleys) that might otherwise interfere with the reception of radiated radio or satellite signals. For another, it is not affected by vehicle travel through tunnels or other such obstructions. Moreover, by having a hard wire stator, it has been determined that an LSM can be made effectively impervious to electromagnetic interference (EMI) and noise.

Despite the many advantages that can be mentioned for an LSM, **the motor has its sensitivities**. In particular, it is also important to note that maintenance of the motor phase angle (i.e. the electrical phase angle between the vehicle-based rotors - the permanent magnet Halbach arrays - and the land-based stator is crucial. Maximum thrust for a vehicle propelled by an LSM is achieved when the motor phase angle is maintained at ninety degrees (90°).

Otherwise, motor operation can be significantly degraded, and may result in unstable motor fluctuations and possible stoppage, **or can result in a runaway vehicle if the synchronization failed, for in this case the time averaged work becomes zero.** The cure, however, is to have control over the spatial relationship between the rotor and the stator. Stated differently, it is necessary to know the position of the vehicle-based rotor (i.e. the vehicle itself), relative to the fixed, land-based stator.

The applied solutions of vehicle/LSM control are threefold as it is generally required for transportation cargo and passengers, over long distances

Fig. 9 Track with magnet drive

Synchronization test of LSM drive @ San Diego
systems (e.g. trains) that move heavy objects
More particularly: **The presented system design includes stationary, land-based sensors** and an array of ~1 cm^3 1.2 Tesla magnets spaced under the vehicle according to a required resolution, in this case >13 mm to monitor the vehicle movement. The motor wavelength is 435 mm. The signal strength is 15 V

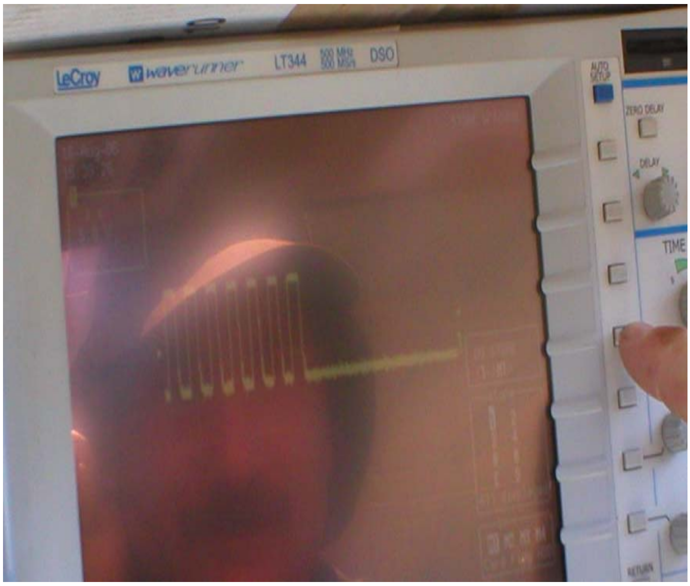

Fig. 10 Testing Screen

Fig. 11 Checking synchronization a typical LSM track

Fig. 12 LSM Guideway @ San Diego

The second control is using high frequency signals injected into the LSM winding and extracted in the control room.

The third control system is using Doppler radar developed by Union Switch and Signal an Ansaldo affiliate company; wherein external sensors provide parametric values for **coordinating the operation of a vehicle's speed control and braking system mainly in case of power failure** which is quite frequent occurrence in the US.

Typical arrangement of a Linear drive for levitated vehicles

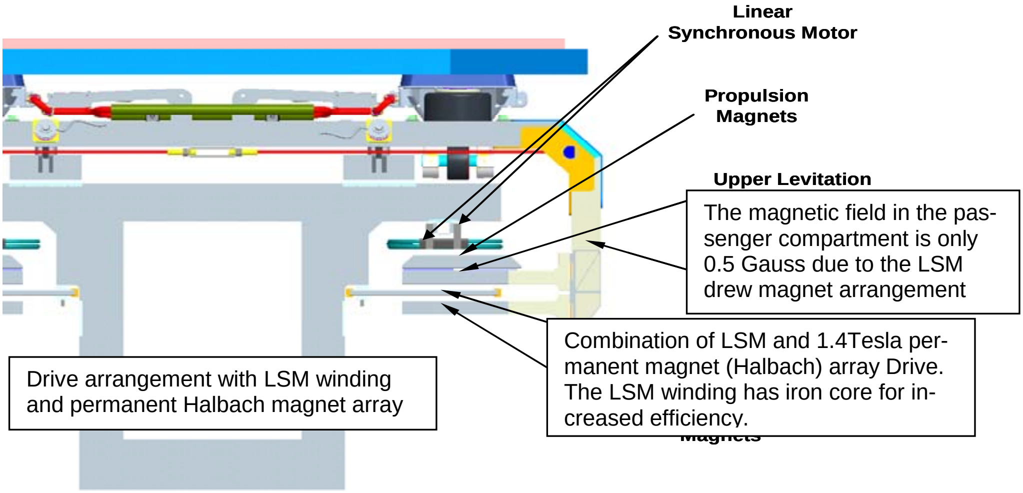

Fig. 13 LSM Drive arrangement

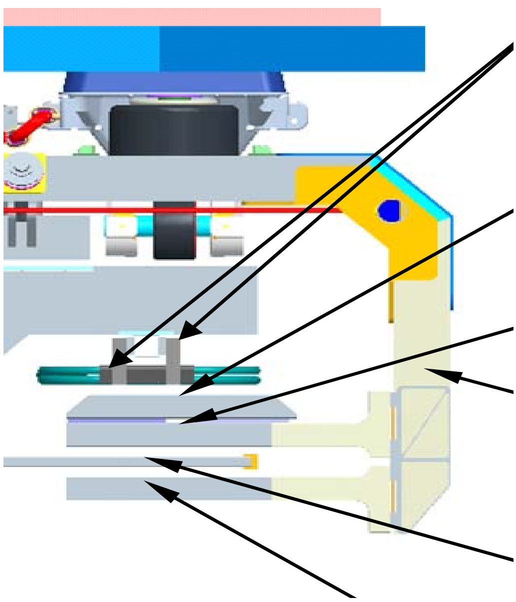

Fig. 14 LSM guideway

2. CONTROL LOGIC FOR LSM DRIVE

2.1 Block switches

The LSM drive is segmented. Block switches are used for energizing the segments in use for safety and energy saving.

Increased safe operation is achieved by keeping one segment between to vehicle not energized. By optimizing the length of the sections substantial energy saving (I^2R) can be archived.

2.2 Microlac Union Switch ad Signal

The system architecture outlined below had required a development of new automatic train control system (ATO). One of the main purposes of the Microlac is to deploy the permanent magnetic brakes in the case of power outage. In addition to this the train based safety arrangement senses the power outage too, and the relay deploys the brakes using only ever present gravitational and magnetic force.

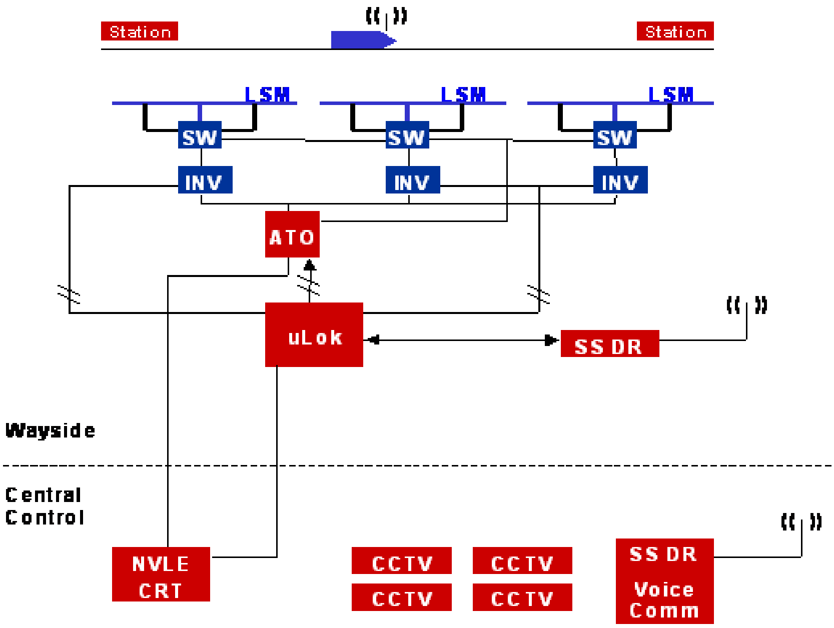

Fig. 15 ATP system is designed to meet transit safety standards

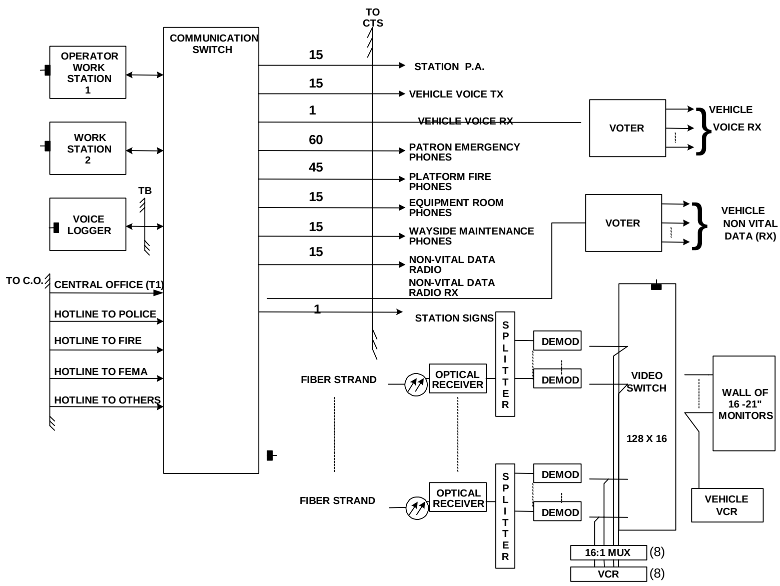

Fig. 16 Central control room constantly monitors and communicates with passengers

3. ECONOMIC ADVANTAGES OF AN LSM DRIVE

Compared to the LIM guideway, or to the simple rail truck the LSM's **ONE TIME investment is high** but it will work with minimal maintenance for 50 years ie. the lifetime cost is significantly lower than any other system that using friction force, rotary motors and gears for propulsion.

Comparative analysis for wheel supported or levitated vehicles. Assumptions: The sample levitated or wheel suppotred fleet consisting 30 **wheel supported** vehicles. Track is 20 km long. Frequency on the average is 1 , 2 or 6 minutes

The **bold** numbers are indicating the assumed system complexity.

Objects	**LSM Drive**	**LIM Drive**	**LRV**
Guideway	**35** *If the vehicle is levitated by electromagnet* ***20*** *with permanent magnet* ***35*** ***If wheel supported 10***	**1** **3** catenary *If the Guideway is elevated* ***5***	**0.7** *3* catenary Conventional street car
Power supply	**30** per fleet	**5** per fleet	**5** per fleet
Control	**10** for all vehicle (1000 wayside transducers)	**30** 90 conductor per fleet 30 Has to be on board at any shift	**30** 90 conductor per fleet 30 Has to be on board at any shift
Human operator	**20** in 2 shifts Driverless. Movement controlled by the LSM built into the GW.	**60** If elevated it can be driverless ***5***	**90** cannot be driverless on surface
Current collector	**0**	**120** 4 per vehicle	1**20** 4 per vehicle
Drive train	**0** .None	**60** None Only 60 LIM motors 2 per car	**95** motors and gears,

		Only rolling friction-less wheels 8 or 12 per car	two per vehicle, Friction wheels 8 or 12 hence rail and wheel ware
Maintenance	**1** **If levitated:** no mowing parts except the doors and climate control. **If wheel supported:** Only rolling friction-less wheels 8 or12	**30** . complicated on board electric and electronics No moving parts except the doors and climate control and frictionless rolling wheels	**60** complicated on board electric and electro-nics 15 years life expectancy for power train wheels, e.c.t Friction dependent drive
Rail and wheel maintenance	**0** frictionless drive	**0** frictionless drive	**480** wheel angle correction, (8 wheel per vehicle), rail correction in every 10 years over 30 years,5 per direction

Sums of **RELATIVE** efficiencies	**96 BEST** ***And the lifetime cost is the lowest***	**339 MEDIUM**	**845 WORST** ***And the lifetime cost is the highest***

APPLICATION OF FUNCTIONAL MOCK-UP UNITS IN DESIGN AND DEVELOPMENT OF VEHICLE SYSTEMS

Csilla TÓBIÁS and Árpád VERESS

Department of Aeronautics, Naval Architecture and Railway Vehicles
Faculty of Transportation Engineering and Vehicle Engineering
Budapest University of Technology and Economics
H-1111 Budapest, Műegyetem rkp. 3, Hungary

Received: November 8, 2016

ABSTRACT

The accelerating pace of technological development in the past few years is expected to result that Original Equipment Manufacturers (OEMs) request not only the products but also their black-box models from their suppliers in order to build them into their own simulations. The standard of Functional Mock-up Interface (FMI) is a constantly evolving way of model exchange and co-simulation through its implementation in Functional Mock-up Units (FMUs) that satisfy the demand for encryption of technology information. Furthermore, FMI approach can facilitate the cooperation between development departments of a company that basically use different simulation tools. In this paper the application possibilities and limitations of FMUs are investigated to gain insight of the utility of FMUs in system modelling and standard simulation platform development.

Keywords: Modelling and simulation, Vehicle dynamics, Functional mock-up units and interface

1. INTRODUCTION

Different models of subsystems are developed in different simulation environments with different standards and with different confidentiality levels, so that different programs should interact to simulate the whole system. Modular structure of simulation models can facilitate faster model or function developments by effective virtual prototyping. Moreover, OEMs may want to integrate components developed by suppliers into their existing system models, hence the protection of intellectual property is inevitable. FMI standard and the use of FMUs can be an applicable approach for reaching the mentioned objectives.

2. FUNCTIONAL MOCK-UP INTERFACE

FMI stands for Functional Mock-up Interface that is a tool independent standard for model exchange and co-simulation. Its main aim is to support the exchange of models between suppliers and OEMs although they may use different development tools. [1] [see Fig. 1]

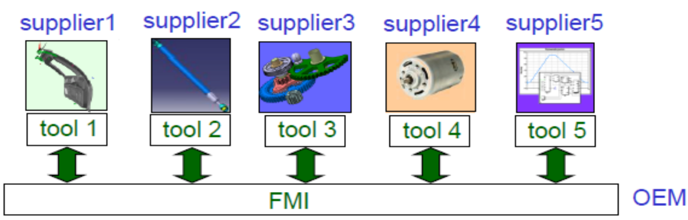

Fig. 1 FMI usage, source:[2]

The FMI standard consists of two main parts: FMI for Model Exchange (FMI-ME) and FMI for Co-Simulation (FMI-CS). During model exchange an input/output box is generated from the dynamic system model, which then can be used in other simulations. Models are described by differential, algebraic and discrete equations with time-, state- and step-events. FMI for Co-Simulation can be applied when at least two simulation tools are coupled. Data exchange between subsystems occurs only at discrete communication points in time. Besides these communication points the subsystems are solved independently from each other by their individual solvers. Master algorithms control the data exchange between subsystems and the synchronization of all slave simulation solvers (slaves). [see Fig. 2] [1][3], [11]

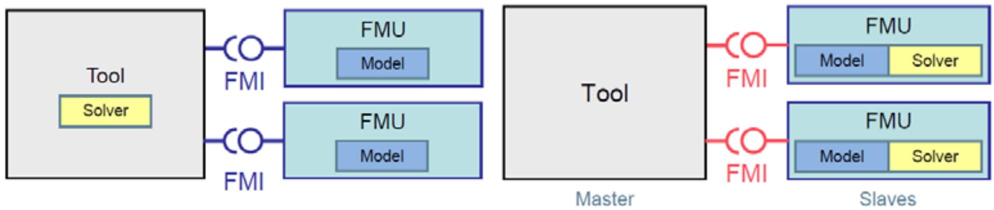

Fig. 2 FMI for Model Exchange (left) and for Co-Simulation (right), source:[40]

Functional Mock-up Unit (FMU) is a component that implements the FMI standard. It is a *.fmu zip-file, which must contain a descriptive XML-file and the source code C-functions/ executables (*.dll, *.so). There might be some further elements such as a model icon, maps, tables, documentation files and object libraries. [1], [11]

Some advantages of the use of FMU are the possibility of creating black-box models for the hiding of technology information, the potential of model integrability and modular structure for virtual prototyping, while it might result decreasing run time.

3. APPLICATIONS OF FMUs AND FMI

After its release in 2010, FMI 1.0 [39] became the subject of investigations about its usability in automotive engineering, building system simulations, thermal and fluid system simulations, etc., and the required steps to implement the standard, in FMI 2.0 [40] new features ease the use and increase the performance especially for larger models [11]. FMI related developments conclude development and testing of import and/or export of Model Exchange and Co-Simulation FMUs in different simulation tools, implementation of missing features and coupling simulations of models built in different tools via FMI.

Many papers deal with FMI related implementation of mathematical methods. Article [12] discusses the means of Jacobian matrix computation in conjunction with FMI 1.0 and Modelica. The paper describes two prototype implementations in JModelica.org and OpenModelica, which are compared in an industrial benchmark and in synthetic benchmarks as well.

Authors of [14] study the asymptotic behaviour of the local error and two error estimates that may be appropriate for automatically determining the suitable communication time step size for the actual solution behaviour by original and modified Richardson extrapolation based step size control. The benchmark is a quarter car model from which two Co-Simulation FMUs (chassis and wheel models) are exported and tested in Fraunhofer master and in MATLAB-based test environment.

In [26] context based polynomial extrapolation for coupled simulation and parallelization via FMI is investigated. The approach is tested on an internal combustion engine (subsystems: 4 cylinder and the air path governed by a basic controller): it speeds up the numerical integration of hybrid dynamical systems that are split into loosely coupled subsystems while integration error caused by slackened synchronization is kept inside the pre-defined bounds.

Article [27] presents the implementation and test of the linearly implicit stabilization method that can handle the issue of strongly coupled system co-simulation that is the trade-off between stability (or accuracy) and computational performance. Using the directional derivatives computation capability of FMUs from FMI for Co-Simulation 2.0 standard and by proposing some minor extensions to the standard, the implemented method allows large communication step size, thus significantly reduce the computation time of the test system (2 DoF hydraulic system of a serially connected pipe and volume).

Another scope of the works is FMI support establishment and testing of FMI supporting tools. The implementation of FMI in Simulation X is described in [3], the work covers FMU import, code generation of Model Exchange and Co-Simulation FMUs and specifying the occurring difficulties.

In [4] the implementation of EAS co-simulation master with simple and advanced algorithms for fulfilling the needs of the actual slave simulators was accomplished and it is tested through simple slave tests and by coupling with ITI Simulation X software where the model consists of two Simulation X FMUs for the plant and the controller and a “C function simulator” FMU for speed function input. This experimental master tool is improved to support FMI 2.0 as well as 1.0 in [35]. For testing its three basic master algorithms, Co-Simulation FMUs from 23 Modelica examples are generated and so the differences of the master algorithms are demonstrated.

A generic FMI Model Exchange interface for FMU import into Modelica simulators is detailed in [5]. FMU import prototype behaviour is investigated by bouncing ball example in OpenModelica environment.

Work in [6] deals with Python-based FMU import interface and FMU export in JModelica.org that are demonstrated by some examples such as Van der Pol oscillator, a Full Robot model from Modelica Standard Library to prove the ability of importing third party generated FMUs and the TwinEvaporatorCycle model to show its capability of large model handling.

In [10] a generic FMI interface of virtual test drive simulator CarMaker for FMU-ME and FMU-CS is presented. In the test application a hybrid truck model from Modelica is exported as FMU and either the standard drivetrain or the complete vehicle is replaced by the exported FMU. Model exchange and Co-simulation approach are both tested.

Application of FMI for integration of classical controller specifications and state chart-based specifications of real-time critical message protocols of cyber-physical systems is described in [16]. As a result, software specifications in MechatronicUML can be automatically translated to ME FMUs while maintaining the original Mechatronic UML semantics.

Paper [20] presents the implementation of FMI support in NI VeriStand to use Co-Simulation FMUs in NI VeriStand environment with real-time hardware. Aim is to perform rapid prototyping and hardware.in-the-loop simulations utilizing FMUs from Modelica models. Simulation of a detailed 6-DoF manipulator model is carried out for validation: LabView and Simulink control algorithms, FMU from Dymola manipulator model as Co-Simulation slaves and VeriStand as Co-Simulation master environment.
Work in [32] describes a plugin developed for FMU ME 1.0 export from Rhapsody (for SysML and UML state chart model execution), the simulation results of the generated FMUs combined with continuous models in different environments and the challenges of semantics preservation. The method is tested on a hybrid model, an FMU from a controller specified as a state chart that is used in a Modelica heater model.
In [22] adding FMI for Co-Simulation support to JGrafchart is conceptually evaluated and possible ways of implementation is described. (Grafchart language is suitable for sequential, parallel and general state-transition oriented automation applications with hierarchical structuring, reusable procedures and exception handling.)
Applications of FMI are heavily investigated in connection with vehicle component and control development and testing. Paper [7] discusses the possibility of converting FMI models to AUTOSAR as well as the requirements and steps of the mapping and conversion. This way, FMI would be an intermediate format in AUTOSAR software component development. The approach is applied to the FMU of a Modelica controller exported from Dymola that is converted into an AUTOSAR software component and thus imported into an AUTOSAR tool.
Design approach of FMI 1.0 Model Exchange based nonlinear observers that can be applied in electric vehicles is presented in [9] along with the framework for generic observer design in Modelica. The usability of the framework is demonstrated through a battery state estimation example. This method is enhanced in [41], an SR-UKF (square root Unscented Kalman Filter) observer extended with obstacle information is developed using Modelica and FMI for semi-active suspension control. The prediction model for vertical dynamics state estimation and tire contact force estimation is a quarter car model with all relevant nonlinear parts (two mass system connected by a nonlinear spring damper unit and the wheel behaviour is modelled by a linear spring damper component). The continuous vehicle model and the discrete observer algorithms are implemented in Modelica-based tools. The continuous time model is exported as FMU and this FMU is imported back to Modelica for system and output evaluation inside the discrete observer algorithm. Further improvements are performed in [31] by proposing a method to automatically utilize continuous-time Modelica models in nonlinear state estimators (SR-UKF) by FMI 2.0 Co-Simulation with a generic interface to manage FMUs in Modelica. To test this approach the previously mentioned application case for vertical dynamics simulation is used but this time with the new method and software for tire load estimation.
Mechatronic gearshift simulation of automated transmissions in commercial vehicles is performed in [17]. Model Exchange FMUs from Simulink control modules are imported into SimulationX 1D multiphysics powertrain model thereafter this combined model is imported into multibody vehicle model in SIMPACK as another FMU-ME. FMI Co-Simulation is tested as well on the powertrain model in pure SimulationX framework.

Paper [15] shows the implementation of FMI in LMS Virtual.Lab Motion that is investigated on a half vehicle model with an opposite wheel travelling scenario in LMS Virtual.Lab Motion and two identical air spring model (ME and CS) FMUs from Modelica code. During validation, output signals from FMU included simulation are compared to the results of the coupled simulation of the same spring model in LMS.Imagine.Lab AMESim and the LMS Virtual.Lab Motion model.

In [33] FMI is inspected from an automotive industrial perspective, the maturity of the standard through problem classification is examined and further steps to improve the standard and its implementations are proposed.

Authors of [29] present an approach to rapidly synthetize HLA-based integrated simulations of FMU-CS components with various specialized simulation packages for the overall composed cyber-physical systems. The FMUs are automatically wrapped as HLA-federates that can be executed in a previously developed model-based multi-model integration platform for integrated distributed simulations. The approach is illustrated by the simulation of a vehicle thermal management system. The model is partitioned into two FMUs: the driver and vehicle models are grouped into an FMU and the fluid and thermal components are grouped into another FMU, thus the simulation architecture consists of three federates: driver-vehicle, thermal management and manager federate.

In [28] a method for High Level Architecture (HLA)-compliant federate development via FMI-CS 1.0 is presented for distributed aggregate level simulations of loosely coupled models. An FMU Federate (FMUFd) is developed from the FMU, and this way, it can join an HLA-compliant federation as a member. In the demonstration simulation, three nodes are connected: the missile node (FMU CS by FMUFd), the target aircraft node (FMU-CS by FMUFd) and the synthetic environment node.

In [25], virtual test driving and in-development testing of ADAS functions considerably reduce validation effort. The work concentrates on CarMaker's implementation of X-in-the-loop approach that makes the integration and validation of all relevant system components (as models, ECU software or hardware) possible. CarMaker's interface architecture supports FMUs, hence component integration become more efficient. An implementation of FMU generation for AUTOSAR controllers is also presented. In the application case, the implementation of dynamic light function FMU into the CarMaker integration platform is carried out, where input signals of the light assistance FMU are received from vehicle dynamics, additional environment sensors, camera systems and driver inputs.

To support development of powertrain controllers for hybrid light trucks, a virtual integration platform using FMUs and other models is implemented in [24]. For the closed loop simulations, vehicle model (including the Motor Control Unit/ Battery Management System and actuators) is imported as an FMU into the integration platform, while the Hybrid Control Unit and Transmission Control Unit control software are imported as *.dll files. Thus, virtual hybrid powertrain model analysis and large coverage testing for system and parameter optimization become feasible.

Paper [23] focuses on the software integration for mechatronic systems and the use of consistent models throughout the integration workflow from model in the loop to hardware in the loop applications in automotive industry that is facilitated by FMI standard.

Authors of [36] explore the possibility to include and execute source code FMUs on electronic control units through a prototypical realization with highly tool-dependent FMI standard modifications with special emphasis on the requirements for the contained C-code and the necessary FMI standard extensions for its usage on automotive embedded real-time systems. The developed prototype is suitable for rapid control prototyping with physical models.

Article [45] details how models from different simulation tools can be connected and simulated on different processors by using FMUs and transmission line element method (TLM). If the system is naturally partitioned the identification of weak links is possible and can be replaced by transmission line elements, and introducing a controlled time delay that makes the parts naturally independent. This way, large aggregated system models can be simulated with good performance on multi-core processors. The simulations are conducted in an in-house distributed simulation environment where FMU import and export are also implemented. The method is demonstrated on a four-wheeled vehicle model with an engine, a mechanical gearbox and hydraulic transmission. The hydraulic transmission, the brake component and the engine are modelled in the in-house tool and exported as FMUs from it and later re-imported again. The vehicle, the wheels and the gearbox FMUs are from OpenModelica, and they are imported to the in-house tool for the simulation. All components are connected through in-house tool's pre-defined transmission line elements that represent the shafts and mechanical connections, and the resulting decoupled system can be effectively solved.

Paper [42] investigates the means of co-simulation of distributed cyber-physical system (a distributed engine control system with thermodynamic models) and its surrounding network for controller development in maritime industry. The network that connects all subsystems is modelled in SystemC network simulation library (SCNSL). FMI for Co-Simulation approach is used to organize the simulation of seven FMUs: a physical crankshaft model and six controllers with the SCNSL network by the implemented SystemC master. Further aspects of engine cyber physical system modelling via FMI is detailed in [44] where the adaptation of embedded control software to meet the requirements of FMI 2.0 for Co-Simulation standard is described. The work suggests a new method for the advancement of real time operating system clock. To test this approach, the control software of a selective catalytic reduction system (SCR) as an FMU is co-simulated with the physical model of the SCR in a different environment.

Article [43] presents a use case for engine control design via FMI where a diesel engine plant model with exhaust gas recirculation and variable geometry turbine in Dymola is exported as FMU and is used for nonlinear air path controller design in MATLAB through FMU import. A DoE analysis is carried out to investigate the system behaviour over the entire engine operating range and to identify a set of characteristic operating points from which linearized engine models can be defined. After a model reduction step LQG control design can be accomplished that implements local linear controllers and by interpolating their outputs a global nonlinear controller can be created.

Besides vehicle industry, many other industrial applications of FMI are present. In Heating, Ventilation and Air Conditioning (HVAC) system simulations, e.g. in [19], it is used for the analysis of indoor environment and energy consumption by coupling of a building envelope simulation and complex HVAC system models exported as FMUs; in [30] occupant behaviour model is coupled with HVAC and building system models via FMI; [37] specifies design guideline and recommendations for thermo-fluid flow components and systems modelling with FMI; while [47] describes a building system simulation with imported FMUs of HVAC equipment and control models. FMI is utilized during large fluid system and power plant system simulations [8], [38], and it is also used for research on smart grids [34], [46], [48], [49],[50]; for nonlinear model predictive control [13], [18], and for state and parameter estimation [21].

4. CONCLUSIONS

As it can be seen from the numerous articles on the subject, FMI-based applications are widely used in industrial simulations and developments, however, at the moment, there are limitations and restrictions of the standard that make it less employable for many tasks. The standard is under continuous development that predicts the gradual elimination of the current difficulties.

5. REFERENCES

[1] **Blochwitz, T. - Otter, M. - Arnold, M. - Bausch, C. - Clauß, C. - Elmqvist, H. - Junghanns, A. - Mauss, J. - Monteiro, M. - Neidhold, T. - Neumerkel, D. - Olsson, H. - Peetz, J.V. – Wolf, S.:** The Functional Mockup Interface for Tool independent Exchange of Simulation Models. Proceedings of the 8th International Modelica Conference, Dresden, 2011.

[2] **T. Blochwitz, M. Otter:** The Functional Mockup Interface for Tool independent Exchange of Simulation Models, presentation. Proceedings of the 8th International Modelica Conference, Dresden, 2011.

[3] **Noll, Ch. – Blochwitz, T. – Neidhold, Th. – Kehrer, Ch.:** Implementation of Modelisar Functional Mock-up Interfaces in SimulationX. Proceedings of the 8th International Modelica Conference, Dresden, 2011.

[4] **Bastian, J. – Clauß, Ch. – Wolf, S. –Schneider, P.:** Master for Co-Simulation Using FMI. Proceedings of the 8th International Modelica Conference, Dresden, 2011.

[5] **Chen, W. – Huhn, M. –Fritzson, P.:** A generic FMU Interface for Modelica. Proceedings of the 8th International Modelica Conference, Dresden, 2011.

[6] **Andersson, Ch. – Åkesson, J. – Führer, C. – Gäfvert, M.:** Import and Export of Functional Mock-up Units in Modelica.org. Proceedings of the 8th International Modelica Conference, Dresden, 2011.

[7] **Thiele, B. – Henriksson, D.:** Using the Functional Mockup Interface as an Intermediate Format in AUTOSAR Software Component Development. Proceedings of the 8th International Modelica Conference, Dresden, 2011.

[8] **Sun, Y. – Vogel, S. – Steuer, H.:** Combining Advantages of Specialized Simulation Tools and Modelica Models using Functional Mock-up Interface (FMI). Proceedings of the 8th International Modelica Conference, Dresden, 2011.

[9] **Brembeck, J. – Otter, M. – Zimmer, D.:** Nonlinear Observers based on the Function Mockup Interface with Applications to Electric Vehicles. Proceedings of the 8th International Modelica Conference, Dresden, 2011.

[10] **Ziegler, S. – R. Höpler, R.:** Extending the IPG CarMaker by FMI Compliant Units. Proceedings of the 8th International Modelica Conference, Dresden, 2011.

[11] **Blochwitz, T. - Otter, M. - J. Akesson, J. - Arnold, M. - Clauß, C. - Elmqvist, H. - Friedrich, M. - Junghanns, A. - Mauss, J. - Neumerkel, D. - Olsson, H. – Viel, A.:** Functional Mockup Interface 2.0: The Standard for Tool independent Exchange of Simulation Models. Proceedings of the 9th International Modelica Conference, Munich, 2012, p.173-184.

[12] **Åkesson, J. - Braun, W. - Lindholm, P.B.:** Generation of Sparse Jacobians for the Function Mock-Up Interface 2.0. Proceedings of the 9th International Modelica Conference, Munich, 2012, p.185-196.

[13] **Kittilsen, P. – S.O. Hauger, - Wasbø, S.O.:** Designing models for online use with Modelica and FMI. Proceedings of the 9th International Modelica Conference, Munich, 2012, p.197-204.

[14] **Schierz, T. - Arnold, M. - Clauß, Ch.:** Co-simulation with communication step size control in an FMI compatible master algorithm, Proceedings of the 9th International Modelica Conference, Munich, 2012, p.205-214.

[15] **Erdélyi, H. - Prescott, W. - Donders, S. - Anthonis, J.**: FMI implementation in LMS Virtual.Lab Motion and application to a vehicle dynamics case. Proceedings of the 9th International Modelica Conference, Munich, 2012, p.759-764.

[16] **Pohlmann, U. - Reddehase, H. - Röckemann, J. - Schäfer, W. – Wagner, R.:** Generating Functional Mockup Units from Software Specifications. Proceedings of the 9th International Modelica Conference, Munich, 2012, p.765-774.

[17] **Abel, A. - Blochwitz, T. - Eichberger, A. - Hamann, P. - Rein, U.:** Functional Mock-up Interface in Mechatronic Gearshift Simulation for Commercial Vehicles. Proceedings of the 9th International Modelica Conference, Munich, 2012, p.775-780.

[18] **Gräber, M. - Kirches, Ch. - Scharff, D. – Tegethoff, W.:** Using Functional Mock-up Units for Nonlinear Model Predictive Control. Proceedings of the 9th International Modelica Conference, Munich, 2012, p.781-790.

[19] **Pazold, M. - Burhenne, S. - Radon, J. - Herkel, S. - Antretter, F.:** Integration of Modelica models into an existing simulation software using FMI for Co-Simulation. Proceedings of the 9th International Modelica Conference, Munich, 2012, p.949-954.

[20] **Palma, C. – Romanoni, M.:** FMI Add-on for NI VeriStand for HiL Simulation. Proceedings of the 9th International Modelica Conference, Munich, 2012, p.963-970.

[21] **Bonvini, M. - Wetter, M. - Sohn, M.D.:** An FMI-based Framework for State and Parameter Estimation. Proceedings of the 10th International Modelica Conference, Lund (Sweden), 2014, p.647-656.

[22] **Theorin, A. - Johnsson, Ch.:** On Extending JGrafchart with Support for FMI for Co-Simulation. Proceedings of the 10th International Modelica Conference, Lund (Sweden), 2014, p.1257-1263.

[23] **Drenth, E. - Törmänen, M. - Johansson, K. - Andersson, B.A. - Andersson, D. - Torstensson, I. - Åkesson, J.:** Consistent Simulation Environment with FMI based Tool Chain. Proceedings of the 10th International Modelica Conference, Lund (Sweden), 2014, p.1277-1283.

[24] **Belmon, L. - Geng, Y. - He, H.:** Virtual Integration for hybrid powertrain development, using FMI and Modelica models. Proceedings of the 10th International Modelica Conference, Lund (Sweden), 2014, p.419-426.

[25] **Schneider, S.A. –Frimberger, J.:** Significant Reduction of Validation Efforts for Dynamic Light Functions with FMI for Multi-Domain Integration and Test Platforms. Proceedings of the 10th International Modelica Conference, Lund (Sweden), 2014, p.395-399.

[26] **Khaled, A.B. - Duval, L. - Gaid, M.B. - Simon, D.:** Context-based polynomial xtrapolation and slackened synchronization for fast multi-core simulation using FMI. Proceedings of the 10th International Modelica Conference, Lund (Sweden), 2014, p.225-234.

[27] **Viel, A.:** Implementing stabilized co-simulation of strongly coupled systems using the Functional Mock-up Interface 2.0. Proceedings of the 10th International Modelica Conference, Lund (Sweden), 2014, p.213-223.

[28] **Yılmaz, F. - Durak, U. - Taylan, K. – Oğuztüzün, H.:** Adapting Functional Mockup Units for HLA-compliant Distributed Simulation. Proceedings of the 10th International Modelica Conference, Lund (Sweden), 2014, p.247-257.

[29] **Neema, H. - Gohl, J. - Lattmann, Zs. - Sztipanovits, J. - Karsai, G. - Neema, S. - Bapty, T. - Batteh, J. - Tummescheit, H. - Sureshkumar, Ch.:** Model-Based Integration Platform for FMI Co-Simulation and Heterogeneous Simulations of Cyber-Physical Systems. Proceedings of the 10th International Modelica Conference, Lund (Sweden), 2014, p.235-245.

[30] **Plessis, G. - Amouroux, É. - Haradji, Y.:** Coupling occupant behaviour with a building energy model - A FMI application. Proceedings of the 10th International Modelica Conference, Lund (Sweden), 2014, p.321-326.

[31] **Brembeck, J. - Pfeiffer, A. - Fleps-Dezasse, M. - Otter, M. - Wernersson, K. - Elmqvist, H.:** Nonlinear State Estimation with an Extended FMI 2.0 Co-Simulation Interface. Proceedings of the 10th International Modelica Conference, Lund (Sweden), 2014, p.53-62.

[32] **Feldman, Y.A. - Greenberg, L. - Palachi, E.:** Simulating Rhapsody SysML Blocks in Hybrid Models with FMI. Proceedings of the 10th International Modelica Conference, Lund (Sweden), 2014, p.43-52.

[33] **Bertsch, Ch. - Ahle, E. - Schulmeister, U.:** The Functional Mockup Interface- seen from an industrial perspective. Proceedings of the 10th International Modelica Conference, Lund (Sweden), 2014, p.27-33.

[34] **Chilard, O. - Boes, J. - Perles, A. - Camilleri, G. - Gleizes, M-P. - Tavella, J-Ph. - Croteau, D.:** The Modelica language and the FMI standard for modeling and simulation of Smart Grids. Proceedings of the 11th International Modelica Conference, Versailles, 2015, p.189-196.

[35] **K. Petridis, Ch. Clauß, :** Test of Basic Co-Simulation Algorithms Using FMI. Proceedings of the 11th International Modelica Conference, Versailles, 2015, p.865-872.

[36] **Bertsch, Ch. - Neudorfer, J. - Ahle, E. - Arumugham, S.S. - Ramachandran, K. - Thuy, A.:** FMI for physical models on automotive embedded targets. Proceedings of the 11th International Modelica Conference, Versailles, 2015, p.43-50.

[37] **Wetter, M. - Fuchs, M. - Nouidui, Th.S.:** Design choices for thermofluid flow components and systems that are exported as Functional Mockup Units. Proceedings of the 11th International Modelica Conference, Versailles, 2015, p.31-41.

[38] **Link, K. - Gall, L. - Mühlbauer, M. - Gallardo-Yances, S.:** Experience with Industrial In-House Application of FMI. Proceedings of the 11th International Modelica Conference, Versailles, 2015, p.17-22.

[39] **MODELISAR Consortium:** Functional Mock-up Interface for Co-Simulation.Version 1.0, October 2010, www.fmi-standard.org

[40] **MODELISAR Consortium:** Functional Mock-up Interface for Co-Simulation.Version 2.0, July, 2014, www.fmi-standard.org

[41] **Fleps-Dezasse, M. – Brembeck, J.:** Model based Vertical dynamics estimation with Modelica and FMI, 7th IFAC Symposium on Advances in Automotive Control, Tokyo, 2013, p.341-346.

[42] **Pedersen, N. - Madsen, J. - Vejlgaard-Laursen, M.:** Co-Simulation of Distributed Engine Control System and Network Model using FMI & SCNSL. 10th IFAC Conference on Manoeuvring and Control of Marine Craft MCMC 2015, Copenhagen, 2015, Vol. 48, Issue 16, p.261-266.

[43] **Nylén, A. - Henningsson, M. - Cervin, A. - Tunestal, P.:** Control Design Based on FMI: a Diesel Engine Control Case Study. 8th IFAC Symposium on Advances in Automotive Control AAC 2016, Norrköping, (Sweden), 2016, Vol.49, Issue 11, p.231-238.

[44] **Pedersen, N. - Bojsen, T. -Madsen, J. - Vejlgaard-Laursen, M.:** FMI for Co-Simulation of Embedded Control Software, Proceedings of the 1st Japanese Modelica Conference, Tokyo, 2016, p.70-77.

[45] **Braun, R. – Krus, P.:** Tool-Independent Distributed Simulations Using Transmission Line Elements And The Functional Mock-up Interface. SIMS 54th Conference, Bergen (Norway), 2013.

[46] **Elsheikh, A. - Awais, M.U. - Widl, E. - Palensky, P.:** Modelica-Enabled Rapid Prototyping of Cyber-Physical Energy Systems Via The Functional Mockup Interface. IEEE 2013 Workshop on Modeling and Simulation of Cyber-Physical Energy Systems, Berkeley, 2013.

[47] **Wetter, M. – Nouidui, Th.S. – Lorenzetti, D. – Lee, E.A. – Roth, A.:** Prototyping the Next Generation EnergyPlus Simulation Engine. Proceedings of the 14th Conference of the International Building Performance Simulation Association, Hyderabad, 2015.

[48] **Schloegl, F. – Rohjans, S. – Lehnhoff, S. – Velasquez, J. – Steinbrink, C. – Palensky, P.:** Towards a Classification Scheme for Co-Simulation Approaches in Energy Systems. IEEE 2015 International Symposium on Smart Electric Distribution Systems and Technologies, Vienna, 2015.

[49] **Galtier, V. – Vialle, S. – Dad, Ch. – Tavella, J.Ph. – Lam-Yee-Mui, J.Ph. – Plessis, G.:** FMI-Based Distributed Multi-Simulation with DACCOSIM. Proceedings of the Symposium on Theory of Modeling & Simulation: DEVS Integrative M&S Symposium, Alexandria (USA), 2015, p.39-46.

[50] **Lévesque, M. – Maier, M. – Béchet, Ch. – Suignard, E. – Picault, A. – Joós, G.:** From Co-Toward Multi Simulation of Smart Grids based on HLA and FMI Standards: A Telecontrol Case Study Based on Real World Configurations, December 17, 2014.

ADVERTISEMENTS

BUDAPEST UNIVERSITY OF TECHNOLOGY AND ECONOMICS

Faculty of Transportation Engineering and Vehicle Engineering

Budapest University of Technology and Economics (BME) was founded in 1782, and is one of the largest higher educational institutions in the field of engineering in Central Europe with about 24.000 students and 1200 teachers and researchers. The university holds an international reputation for excellence in engineering.

One main priority research area is dedicated to the Vehicle Technology, Transportation and Logistics. The Faculty's mission defines the undertaking of high level of scientific activity, research and development, offering expertise and consultation to transport and vehicle industry companies, logistics providers and to industrial policy makers. Concerning the research potential the Faculty has participated in several international research projects, 9 FP7 projects and more than 20 project proposals in the Horizon 2020 European research programme.

Our main research fields in automotive technology are the following:

Engine and driveline research area

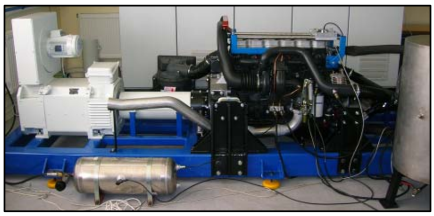

- Comprehensive simulational and computational experiences
- Engine and component analysis
- Powertrain simulation
- Transmission analysis
- Alternative fuels: CNG, hydrogen, biofuels

Chassis and electronics research area

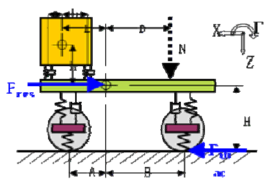

- System overview
- Active and semi-active suspensions
- Development of brake systems
- Steering system design
- Brake system based vehicle dynamical controller

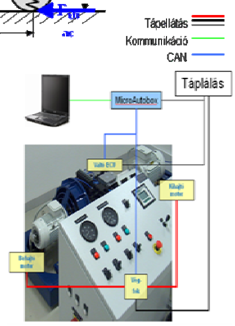

Vehicle operation research area

- Developments related to vehicle recycling
- Irregular vehicle operation – accident analysis
- Monitoring vehicle operation – FMS development
- Reliability analysis and system redundancy


KNORR-BREMSE AG
KNORR-BREMSE
KNORR-BREMSE


KNORR

R&D AND ENGINEERING ACTIVITIES

Within the scope of research and development in Knorr-Bremse Kecskemét, pneumatic and electro-pneumatic systems are being designed and researched, and the manufacturing of these products is being supported.

The Hungarian engineers are partaking in the development of the most state-of-the-art electronic and pneumatic systems. Beyond designing the controlling software of brake systems, they are also responsible for developing mechatronic (mechanical and electronic) elements for products ranging from compressors through wheel brakes up to powertrain components like Pneumatic Booster System.

The ***R&D activities*** carried out by the engineers in Kecskemét can be divided into three major parts:

- Serial development of pneumatic brake system elements,
- Completing analysis for product approval,
- Production and process development.

www.knorr-bremse.com
www.knorr-bremsecvs.com

KNORR-BREMSE

KNORR-BREMSE
Rail Systems Budapest

iCOM Assist (LEADER)

Advanced driver advisory for energy efficient and economic driving with improved punctuality and energy savings up to 15% for passenger and freight operations.

Advantages
- Less costs for energy and operation
- Sustainable improvement for the operation
- Dynamic run optimization
- Reduction of wear and tear
- Simply implementation and semi-automatic integration of topography- and time table data

iCOM Assist (LEADER) is a Driver Advisory System which main function is to advise train drivers how to achieve an efficient usage of energy (fuel or electricity) while still main-taining the schedule. It gives driving recommendations when to power, hold, coast or brake while factoring in target arrival times. All relevant information is displayed in an intuitive way helping the driver to make accurate decisions. iCOM Assist (LEADER) tracks current train position, speed and target times. It shows the remaining route enabling the driver to operate the train more efficiently by being able to better anticipate speed limits, temporary speed restrictions, elevation and curves.

The recent revision of the LEADER® system incorporates hundreds of thousands of source code lines those developed by software developers and testers at Knorr-Bremse's Research and Development division premises including the 30 colleagues at Knorr-Bremse Rail Systems Budapest.

Major benefits
- Energy savings of up to 15%
- Improvement of on-time arrivals
- Reduction of maintenance costs by smoothing train operation
- Reduction of emissions
- High return on investment (typically well above 50% for a three year period)
- Short payback period (commonly between 1 to 2 years)

iCOM Monitor

Monitors and analyzes the vehicle system and the infrastructure and provides information relating to the system status and prognosis of services requirements. From reactive and corrective maintenance to condition based mainentance.

Advantages
- Online monitoring of vehicle and component conditions
- Preventive maintenance to increase vehicle availability and optimizing maintenance and utilization costs
- Own development of dynamic reports, analysis and applications

iCOM Meter

Energy management covering data collection and visualization of consumption and regeneration energy. Measurement of energy consumption is the base for energy efficient operation. According to EN 50463.

Advantages
- Live overview of the energy consumption parameters of the rail vehicle
- Comprehensive data analysis to convert and improve the train operation
- Study of the performance of the vehicle on a specific railway track
- Optimization of maintenance and service works

Knorr-Bremse Rail Vehicle Systems Hungary Ltd. ▪ Knorr-Bremse Vasúti Jármű Rendszerek Hungária Kft.
Address: H-Budapest, Helsinki út 105, Hungary ▪ Telephone: + 36-1-289-4100
E-mail: karrier.vasut@knorr-bremse.com ▪ Web: http://www.knorr-bremse.hu

BME BUDAPEST UNIVERSITY OF TECHNOLOGY AND ECONOMICS

BME ITS NONPROFIT Plc.

ACTIVITY AREAS:

- ***TRANSPORTATION AND VEHICLE RESEARCH***
- ***TRANSPORTATION AND VEHICLE SYSTEM DESIGN***
- ***COST-BENEFIT ANALYSIS***
- ***EVALUATION***
- ***PROJECT MANAGEMENT***
- ***FISIBILITY STUDY***
- ***RISK ANALYSIS***
- ***RAILWAY NOBO & DEBO ANALYSIS***
  Certification of Vehicle Systems
  Certification of Track Systems and Buildings
  Certification of Electric Energy Supply Systems
  Certification of Railway Operation

Postal Address: **H-1111 BUDAPEST, XI. Műegyetem rkp. 3.**
***Directorate*: BUDAPEST, XI. Műegyetem rkp. 3., bldg. K. floor 1. No. 71.**
***Phone*: (36-1) 463 3797 *Fax*: (36-1) 463 3798 *E-mail*: bmeits@bmeits.hu**

Ganz Motor Kft.

Registered seat: 1087 Budapest, Kőbányai út 21., Hungary
Office & factory address: 1089 Budapest, Vajda Péter u. 12., Hungary
Post address: 1475 Budapest, Pf. 263., Hungary
E-mail: info@ganzmotor.hu
Web: www.ganzmotor.hu


TÜVRheinland CERT ISO 9001
Grampet Debreceni
Vagongyár Kft.
Main activities in the freight car industry
Overhaul of freight and tank cars
Rebuilding of railway cars
Reconstruction of damaged railway cars after accident
Building railway cars
Steelworks manufacture, painting, blasting, stamping, welding of aluminium, alloyed and unalloyed steel
Our qualifications:
ISO 9001:2008
DIN EN ISO 3834-2
EN 15085-2
AD 2000-HP0
VPI
445/2011/EU (ECM IV: Maintenance)
TRT 009
DIN 27201-7:2006
www.vagongyar.hu